

AD \_\_\_\_\_

Award Number: DAMD17-98-2-8003

TITLE: Massachusetts Institute of Technology Consortium Agreement

PRINCIPAL INVESTIGATOR: Haruhiko H. Asada, Ph.D.

CONTRACTING ORGANIZATION: Massachusetts Institute of Technology  
Cambridge, Massachusetts 02139

REPORT DATE: March 1999

TYPE OF REPORT: Final III of Phase 2

PREPARED FOR: U.S. Army Medical Research and Materiel Command  
Fort Detrick, Maryland 21702-5012

DISTRIBUTION STATEMENT: Approved for Public Release;  
Distribution Unlimited

The views, opinions and/or findings contained in this report are  
those of the author(s) and should not be construed as an official  
Department of the Army position, policy or decision unless so  
designated by other documentation.

DTIC QUALITY INSPECTED

19990902 076

# REPORT DOCUMENTATION PAGE

Form Approved  
OMB No. 074-0188

Public reporting burden for this collection of information is estimated to average 1 hour per response, including the time for reviewing instructions, searching existing data sources, gathering and maintaining the data needed, and completing and reviewing this collection of information. Send comments regarding this burden estimate or any other aspect of this collection of information, including suggestions for reducing this burden to Washington Headquarters Services, Directorate for Information Operations and Reports, 1215 Jefferson Davis Highway, Suite 1204, Arlington, VA 22202-4302, and to the Office of Management and Budget, Paperwork Reduction Project (0704-0188), Washington, DC 20503

1. AGENCY USE ONLY (Leave blank)	2. REPORT DATE	3. REPORT TYPE AND DATES COVERED	
	March 1999	Final (31 Dec 97 - 31 Dec 98)	
4. TITLE AND SUBTITLE		5. FUNDING NUMBERS	
Massachusetts Institute of Technology Consortium Agreement		DAMD17-98-2-8003	
6. AUTHOR(S)			
Haruhiko H. Asada, Ph.D.			
7. PERFORMING ORGANIZATION NAME(S) AND ADDRESS(ES)		8. PERFORMING ORGANIZATION REPORT NUMBER	
Massachusetts Institute of Technology Cambridge, Massachusetts 02139			
E-Mail:			
9. SPONSORING / MONITORING AGENCY NAME(S) AND ADDRESS(ES)		10. SPONSORING / MONITORING AGENCY REPORT NUMBER	
U.S. Army Medical Research and Materiel Command Fort Detrick, Maryland 21702-5012			
11. SUPPLEMENTARY NOTES			
12a. DISTRIBUTION / AVAILABILITY STATEMENT Approved for public release; distribution unlimited		12b. DISTRIBUTION CODE	
13. ABSTRACT (Maximum 200 Words)			
14. SUBJECT TERMS		15. NUMBER OF PAGES 429	
		16. PRICE CODE	
17. SECURITY CLASSIFICATION OF REPORT Unclassified	18. SECURITY CLASSIFICATION OF THIS PAGE Unclassified	19. SECURITY CLASSIFICATION OF ABSTRACT Unclassified	20. LIMITATION OF ABSTRACT Unlimited

FOREWORD

Opinions, interpretations, conclusions and recommendations are those of the author and are not necessarily endorsed by the U.S. Army.

Where copyrighted material is quoted, permission has been obtained to use such material.

Where material from documents designated for limited distribution is quoted, permission has been obtained to use the material.

Citations of commercial organizations and trade names in this report do not constitute an official Department of Army endorsement or approval of the products or services of these organizations.

In conducting research using animals, the investigator(s) adhered to the "Guide for the Care and Use of Laboratory Animals," prepared by the Committee on Care and use of Laboratory Animals of the Institute of Laboratory Resources, national Research Council (NIH Publication No. 86-23, Revised 1985).

For the protection of human subjects, the investigator(s) adhered to policies of applicable Federal Law 45 CFR 46.

In conducting research utilizing recombinant DNA technology, the investigator(s) adhered to current guidelines promulgated by the National Institutes of Health.

In the conduct of research utilizing recombinant DNA, the investigator(s) adhered to the NIH Guidelines for Research Involving Recombinant DNA Molecules.

In the conduct of research involving hazardous organisms, the investigator(s) adhered to the CDC-NIH Guide for Biosafety in Microbiological and Biomedical Laboratories.

---

PI - Signature

Date

## **Introduction**

This is the third progress report of the M.I.T. Home Automation and Healthcare Consortium-Phase Two. It covers majority of the new findings, concepts, designs, and experiments accomplished in the last six months, October 1, 1998 through March 31, 1999. The Consortium has been hosting diverse research projects of home automation and healthcare, ranging from human modeling, patient monitoring, and diagnosis to new sensors and actuators, physical aids, human-machine interface and home automation infrastructure.

This report contains several patentable concepts, algorithms, and designs. As before, these ideas and inventions have been filed as provisional patent applications. Benjamin Palleiko at the MIT Technology Licensing Office, [benp@mit.edu](mailto:benp@mit.edu), has notified the sponsors, or will notify them shortly of these provisional applications. A few patentable ideas, however, have not yet been filed as a provisional patent. These have been excluded in this progress report. As soon as the patent situation is clarified, we will send the sponsors those reports as an amendment. Should you be interested in pursuing the possibility of using the technologies, please reply to the Technology Licensing Office within six months after signing a non-disclosure agreement.

In addition, the entire contents of this report have been posted at the web site to better disseminate our technology across each sponsor company. Please visit our home page, <http://darbelofflab.mit.edu>, and look at the consortium report section. You need to key in a password, which can be obtained from the representative of each sponsor. Please direct your colleagues and technical staff to the web site. For security, we occasionally change user name and pass word. Please obtain the latest password and username from the contact person at each sponsor.

We hope that this report will provide useful information for your field of research and development as well as for your business.

We appreciate your sponsorship that enabled us to conduct these exciting works in the diverse fields of home automation and healthcare. We look forward to meeting you soon.

H. Harry Asada  
Principal Investigator  
Ford Professor and Director  
d'Arbeloff Laboratory

## Table of Contents

### **Introduction**

**H. Asada**

### ***Patient Monitoring and Diagnosis***

- 1. A Theoretical Evaluation of the Influence of Displacement on Finger Photoplethysmography for Wearable Health Monitoring Sensors**  
**B.-H. Yang, H. Asada, and S. Rhee**
- 2. A New Design of Ring Sensors: A Solution to Signal Artifact**  
**B.-H. Yang, H. Asada, and S. Rhee**
- 3. Sensor Fusion for Cuff-less, Continuous Monitoring of Arterial Blood Pressure**  
**B.-H. Yang, H. Asada, and Y. Zhang**
- 4. The Doppler Necklace: Wearable and Noninvasive Ultrasound Sensors for Continuous Monitoring of Blood Flow in the Common Carotid Artery**  
**E. Awad, and H. Asada**
- 5. SIMSUIT Project**  
**L. Jones, S. Martel, J. Tangorra, and L. Sambol**
- 6. Noninvasive Blood Glucose Analysis Using Near Infrared Absorption Spectroscopy**  
**K. Youcef-Toumi, and V.A. Saptari**

### ***Home Treatment***

- 7. Laser Tissue Modification with Spectroscopic Feedback: the "Smart Scalpel for Treatment of Port wine Stains and Permanent Hair Removal**  
**E. L. Sebern, C. J. H. Brenan, and I. Hunter**
- 8. Minimally Invasive Glucose Sensor and Insulin Delivery System**  
**I. Hunter, L. Jones, L. Sambol, T. Kanigan, C. Brenan, and S. Mihardja,**

### ***Sensors and Actuators***

- 9. Conducting Polymer Devices for the Home**  
**I. Hunter J. Madden, and P. Madden**
- 10. Distributed Photo-Plethysmograph Fingernail Sensors: Finger Force Measurement without Haptic Obstruction**  
**H. Asada, S. Mascaro**

## *Physical Aids*

- 11. Personal Aid for Mobility and Monitoring: A Helping Hand for the Elderly**  
S. Dubowsky, A. Skwersky, H. Yu, F. Genot, and S. Gooding
- 12. Design and Control of an Active Mattress for Moving Bedridden Patients**  
H. Asada, and W. Finger
- 13. Kinematic Design and Analysis of Surface Wave Actuators**  
H. Asada, J. Spano
- 14. Human Interaction with Surface Wave Actuators**  
H. Asada, J. Spano

## *Human-Machine Interface*

- 15. Intelligent Semi-Autonomous Control Architecture Applied to Robotic Holonomic Wheelchairs**  
H. Asada, and K. Tahboub
- 16. Integrating Digital Manuals with Data-Glove Human-Machine Interface**  
H. Asada, and M. Hiratsuka

## *Software*

- 17. Hemodynamic Modeling and State Estimation for Assessment of Cardiovascular Health**  
R. Kamm, Y. Huang, and X. Xiao
- 18. An Intelligent Cardiopulmonary System for the Home Health Market**  
T. Sheridan
- 19. Co-Simulation of Physiological Systems**  
H. Asada, B. Gu, and D. Tarraf

## *Home Networking*

- 20. Status on the IEEE-1394 Based Outlet for Home Automation and Health Care Networks**  
I. Hunter, S. Martel, and S. Lafontaine
- 21. Energy Efficient Codes for Wireless Communications: Source Coding Theory and Error Control**  
H. Asada, K.-Y. Siu, and C. Erin

# **A Theoretical Evaluation of the Influence of Displacement on Finger Photoplethysmography for Wearable Health Monitoring Sensors**

**Dr. Boo-Ho Yang**  
Principle Investigator

**Prof. Haruhiko H. Asada**  
Co-Investigator

**Sokwoo Rhee**  
Graduate Research Assistant

## **ABSTRACT**

This report describes the development of an opto-physiological model of a finger in conjunction with a ring-type photoplethysmography device (the Ring Sensor). This model is a combination of an optical model, a mechanical model, a skin capillary model and the arterial wall dynamics. It describes the photoplethysmographic effects due to the relative displacement and rotation of a finger to a ring-type opto-electric device that monitors the arterial pulsation noninvasively and continuously. Numerical simulations and experiments were conducted to verify and evaluate this model. This model can be used for optimizing design parameters of the ring device to obtain optimal pulse signals and to minimize the influence of noise caused by the displacement of the finger.

## 1. Introduction

Finger photoplethysmography is a technique of noninvasively monitoring the arterial pulse of an individual that offers remarkable convenience and advantages. By integrating the technique with microelectronics and communication technologies, a miniaturized telemetered photoplethysmograph in a ring configuration has been developed by the authors [1] [2]. This device captures the pulsation of the arterial blood flow which is the AC part of photoplethysmography. The Ring Sensor, aiming at providing quality home healthcare, can be worn by the patient twenty-four hours a day. This is a unique form of wearable sensors and, probably, the only thing that the majority of people will accept wearing at all times. Real-time, continuous monitoring with the Ring Sensor allows not only for emergency detection but also for long-term monitoring of otherwise difficult and noncompliant patients such as demented elderly people. However, as a wearable ambulatory sensor, the Ring Sensor is inevitably subject to measurement noise due to the everyday activities of a patient. Especially, the relative displacement and the rotation of the sensor probe to the finger is the major cause of loss of accuracy, and a common problem for all other photoplethysmographic sensors such as pulse oximeters. The objective of the report is to quantify the mechanism of the motion artifact of finger photoplethysmography based on an opto-physiological model of the finger and to facilitate the development of the Ring Sensor which is less affected by the relative displacement of the finger to the ring.

There have been many attempts to analyze and reduce the influence of motion on the photoplethysmography. Many researchers attempted to quantify the movement artifact in pulse and oxygen saturation measurements [3][4], and some researchers have used advanced filtering techniques such as adaptive noise canceler to reduce the impact of motion [5]. However, those attempts did not help understand the nature of the motion artifact since they were based on the input-output matching approach using signal processing techniques without an in-depth understanding of the physiological effects of movement. Thus, it was not possible to conduct an optimization of the design parameters of the device for the best quality of measurement depending on those methods.

In this report, we first examine and categorize a variety of movements that influence photoplethysmographic signals of the Ring Sensor. To articulate and analyze the

influence of each movement, we build a mathematical model of the finger photoplethysmography. The main feature of the model is the integration of multiple domains such as the ring mechanics, finger tissue kinematics, digital arterial wall dynamics and biomechanical optics. Especially, the nonlinear behavior of the arterial wall to external pressure, which is the basis of the oscillometric method of blood pressure measurement, is intensively addressed. Also, the optical property of the finger tissue is profoundly discussed. The resultant opto-physiological model of the finger and the Ring Sensor allows simulation of the influence of mechanical displacement of the finger on photoplethysmographic signals. Extensive simulation is conducted and the numerical results are compared with the experimental data for the validation of the model at the end.

## 2. Approach

One of the most important issues of wearable sensors is the reduction of noise caused by motion artifacts. Many kinds of motion artifacts such as fast and vivid motion of the finger, static relative displacement, and rotation of the ring relative to the finger can interfere with the measurement of the Ring Sensor. However, since the Ring Sensor is mainly to be worn by elderly patients and potential patients of cardiovascular disorders, it is reasonable to assume that the static displacement or rotation of the ring is dominant over fast movements with large accelerations. For example, if any external static force is applied to the ring so that the center point of the ring deviates from that of the finger, the

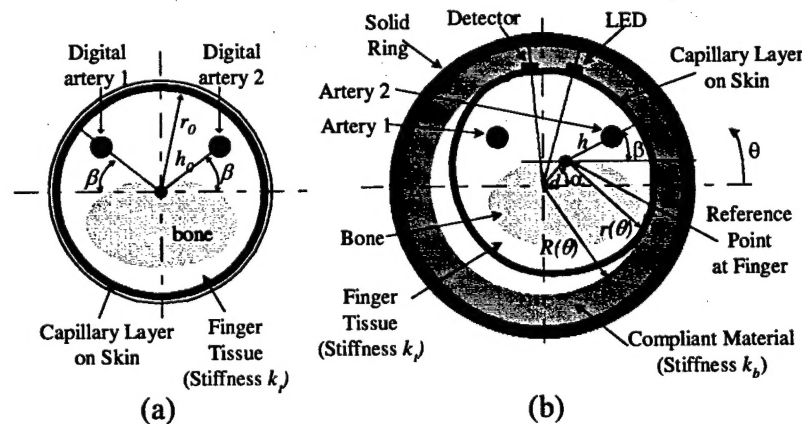


Fig. 1: (a) Uncompressed finger under no external force ( $d=0$ ). (b) Finger compressed by the ring due to an external force. ( $d>0$ )

photoplethysmographic signal will change. The rotation of the ring around the finger will also cause a change in the signal. A mathematical model of the finger and the ring will be very useful in understanding and analyzing the variation of the photoplethysmographic signal due to the displacement and the rotation of the ring. This model has to integrate all of the optical, mechanical and physiological properties of the Ring Sensor. In other words, the optics of the finger tissue and blood, finger tissue kinematics, geometry of the ring, and dynamics of the arteries and the capillaries must all be incorporated into one model to describe the photoplethysmographic behavior. Especially, the dynamics of the arterial wall should be modeled carefully since the compliance of the arterial wall exhibits nonlinear behavior [6]. The modeling of the optical properties is another point that has to be dealt with great care.

Fig. 1 shows a cross-sectional view of the finger. The cross section of a finger is assumed to be a circle when there are no external forces. There are two digital arteries in the finger, and they are both positioned at a distance  $h_0$  away from the center of the finger. The tissue is considered as compliant material with stiffness  $k_t$ . There is also a layer of capillaries of thickness  $t$  beneath the skin. To alleviate sensitivity of the photoplethysmographic signal variation due to movement of the finger, a compliant material of stiffness  $k_b$  is attached inside the solid ring. A light source (LED) and a photodetector are located on the compliant material inside the solid ring. When any external force is applied to the ring, it moves in a certain direction at an angle  $\alpha$  by a certain relative displacement  $d$ . Because of this movement, the pressure at contact point increases and the relative locations of the digital arteries to the optical elements (LED and photodetector) change, which leads to variation in the photoplethysmographic signal. At the same time, deformation of the finger surface occurs and the cross section of the finger is no longer a circle. Due to this deformation of the tissue, the pressure applied to each of the two digital arteries also changes, which results in a change in the volumetric pulsation of the blood vessel. In addition, the volume of capillaries also change due to the change of the pressure. The capillaries occlude more easily than digital arteries since the internal pressure of the capillary is much lower than that of the arteries. In this model, the occlusion of the capillaries is represented as the decrease of effective thickness of skin capillary layer  $t$ . The pulsating signal of photoplethysmograph is caused by the

volumetric change of the digital arteries and capillaries due to the change of the blood pressure.

### 3. Modeling

#### 2.1. Optical Model

The light emitted from the LED passes into the tissue and the number of the paths of photons is almost infinite, which makes it difficult to obtain a good optical model. The light absorption, multiple scattering, and diffusion processes all occur at the same time. It is known that the average photon migration path in the tissue is a banana shape. Assuming that the tissue is optically homogeneous, the cross section of a finger can be

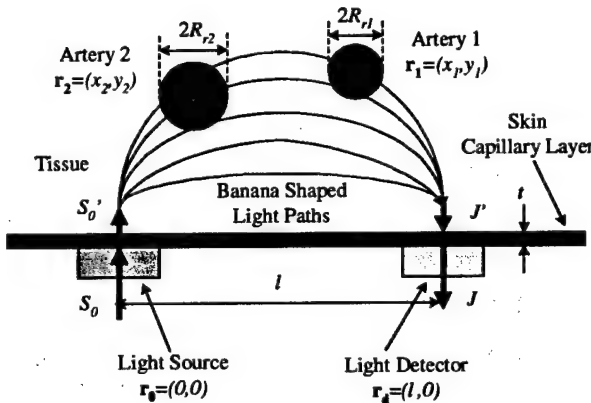


Fig. 2 : Optical model of the finger and optical elements. Blood vessels have different optical properties from the tissue

divided into three regions : tissue, two digital arteries, and capillaries. The blood that flows in the arteries has different optical properties from those of the tissue. Looking at the cross section of the finger, it is possible to consider the digital arteries as two circular regions with different optical properties from the surrounding material. Using the analogy with electrostatics, the photon flux density at the detector can be expressed as a function of the positions of the two arteries, radii of the arteries, the position of the photodetector, and the optical properties of the tissue and the blood. Feng, S., Zeng, F., and Chance, B. derived an analytical formulation of the photon path distributions in the presence of a

spherical region with different absorption and scattering properties from the surroundings in semi-infinite geometry [7]. Fig. 2 shows the geometry of the light source, the photodetector, the arteries and the capillary layer. The light source is in the steady-state condition (constant source intensity of light  $S_0$ ) and is located at the origin  $\mathbf{r}_0=(0,0)$  of the x-y coordinate. The photon flux density at the detector which is located at  $\mathbf{r}_d=(l,0)$  is denoted as  $J$ . Although the LED and the photodetector are placed along a circular ring surface, it is assumed that they are located on a straight line  $y=0$ . This assumption is valid as long as  $l$  is much smaller than the internal perimeter of the ring. As the light emitted from the source passes through the capillary layer of effective thickness  $t$  beneath the skin, the intensity decreases to  $S_0'$  due to the absorption by the blood in the capillaries. This absorption process follows the Lambert-Beer law. The scattering effect at the capillary layer is neglected since the thickness of the capillary layer is considerably thin ( $t \sim 0.1$  mm or less). The light of intensity  $S_0'$  which has passed through the capillary layer is injected and diffused into the tissue. The photons must pass through the capillary layer once again before it reaches the photodetector. The density of the photon flux entering the capillary layer is denoted as  $J'$  and it decreases by absorption process as the light goes through the capillary layer, resulting in a final photon flux density  $J$  at the detector.

In the analogy with electrostatics, the arteries are similar to the dielectric material in the electrical field. Noting the presence of two digital arteries which are located at  $\mathbf{r}_1=(x_1, y_1)$  and  $\mathbf{r}_2=(x_2, y_2)$  with radii of  $R_{r1}$  and  $R_{r2}$  respectively, the relationship between the light intensity  $S_0'$  (after passing through the capillary layer) and the photon flux density  $J'$  at the detector (before crossing the capillary layer) is described as follows.

$$J' = \frac{y_0 S_0}{2\pi} \left( \frac{\kappa}{l^2} + \frac{1}{l^3} \right) \exp(-\kappa l) + J_1(\mathbf{r}_1, R_{r1}) + J_1(\mathbf{r}_2, R_{r2}) \quad (1)$$

where the function  $J_1(\mathbf{r}, R)$  is as follows.

$$J_1(\mathbf{r}, R) = 2Dq(R) \frac{(\kappa|\mathbf{f}| + 1)y}{|\mathbf{f}|^3} \exp(-\kappa|\mathbf{f}|) \Phi_0(\mathbf{r}) - 2Dp(R) \left\{ \frac{[\mathbf{f} \cdot \mathbf{E}_0(\mathbf{r})](\kappa|\mathbf{f}| + 3)y}{|\mathbf{f}|^5} - \frac{E_0 y(\mathbf{r})}{|\mathbf{f}|^3} \right\} \exp(-\kappa|\mathbf{f}|) \quad (2)$$

where

$$\mathbf{r} = (x, y), \quad \mathbf{f} = \mathbf{r} - \mathbf{r}_d \quad (3)$$

$$\Phi_0(\mathbf{r}) = \frac{y_0 y S_0}{2\pi D} \frac{(\kappa|\mathbf{r}| + 1)}{|\mathbf{r}|^3} \exp(-\kappa|\mathbf{r}|) \quad (4)$$

where  $y_0 = 0.7 / \mu_s$ ,

$$\begin{aligned} \mathbf{E}_0(\mathbf{r}) &= (E_0^x, E_0^y) \\ &= \frac{y_0 S_0}{2\pi D} \left( \frac{3\kappa y \mathbf{r}}{|\mathbf{r}|^4} + \frac{3y\mathbf{r}}{|\mathbf{r}|^5} - \frac{\kappa \hat{\mathbf{y}}}{|\mathbf{r}|^2} - \frac{\hat{\mathbf{y}}}{|\mathbf{r}|^3} + \frac{\kappa^2 y \mathbf{r}}{|\mathbf{r}|^3} \right) \exp(-\kappa|\mathbf{r}|) \end{aligned} \quad (5)$$

$$q(R) = -R \exp(\kappa R) \left\{ \frac{\tilde{D}B(1 - \mu_a / \tilde{\mu}_a)}{D(1 + \kappa R) \sinh(\tilde{\kappa}R) / (\tilde{\kappa}R) + \tilde{D}B} \right\} \quad (6)$$

$$p(R) = R^3 \exp(\kappa R) \left\{ \frac{\tilde{D}A - DB}{\tilde{D}A(1 + \kappa R) + DB[2 + 2\kappa R + (\kappa R)^2]} \right\} \quad (7)$$

where the coefficients A and B are given respectively,

$$A = \frac{2 \sinh(\tilde{\kappa}R)}{(\tilde{\kappa}R)} + \tilde{\kappa}R \sinh(\tilde{\kappa}R) - 2 \cosh(\tilde{\kappa}R) \quad (8)$$

$$B = \cosh(\tilde{\kappa}R) - \frac{\sinh(\tilde{\kappa}R)}{(\tilde{\kappa}R)} \quad (9)$$

$\mu_a$  : Absorption coefficient of tissue

$\mu_s$  : Transport scattering coefficient of tissue

$\tilde{\mu}_a$  : Absorption coefficient of blood

$\tilde{\mu}_s$  : Transport scattering coefficient of blood

$D$  : Diffusion constant of tissue ( $= 1/[3(\mu_a + \mu_s)]$ )

$\tilde{D}$  : Diffusion constant of blood ( $= 1/[3(\tilde{\mu}_a + \tilde{\mu}_s)]$ )

$\kappa$  : Inverse diffusive absorption distance of tissue ( $= (\mu_a / D)^{1/2}$ )

$\tilde{\kappa}$  : Inverse diffusive absorption distance of blood ( $= (\tilde{\mu}_a / \tilde{D})^{1/2}$ )

Detailed derivations of Eqs. (1)~(9) can be found in [7].

The absorption process of the capillary layer defines the relationship between  $S_0$  and  $S_0'$ .

$$S_0' = S_0 \exp(-\tilde{\mu}_a t) \quad (10)$$

The final photon flux density is also obtained by the similar equation.

$$J = J' \exp(-\tilde{\mu}_a t) \quad (11)$$

As the absorption coefficient of blood is larger than that of tissue, the DC value of  $J$  increases as the two arteries are located farther from the origin, since more photons reach the detector without passing through the digital arteries. It is also natural that  $J$  increases as the radii of the arteries decrease. However, the amplitude of the AC component of  $J$  decreases as the distance of the arteries from the origin increases, since the change of the diameters of the arteries (which eventually results in the change of the extent of photon absorption) at distant locations does not give significant influence on the photons that reach the detector.

## 2.2. Tissue Mechanical Model

The initial shape of the ring is shown in Fig. 3(a). The LED and the detector are placed such that their mid-point is at an angle  $q_1$  (rad) from the horizontal axis, and both the

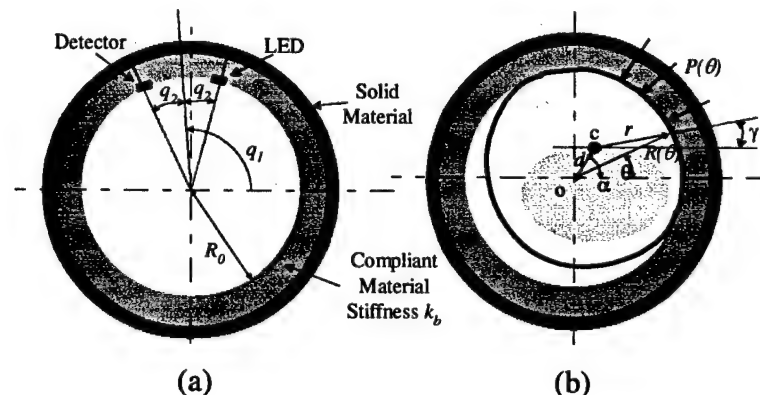


Fig. 3 : (a) Initial state of the ring with LED and photodetector (b) When the finger moves in the ring (Finger tissue is deformed.)

LED and the detector are at an angle  $q_2$  (rad) from the radial line that intersects the mid point. As the finger moves inside the ring, the pressure at the contact point increases and both the finger tissue and the compliant material inside the ring go through deformation. This is shown in Fig. 3(b).

$O$  is the center of the ring and  $c$  is the reference point (initial center point) of the finger located at the bone. As the reference point of finger moves by displacement  $d$  at an angle  $\alpha$ , the distance  $r$  (represented as a function of  $\gamma$ ) from the reference point of the finger to the skin changes from its initial value  $r_0$ . At the same time, the compliant material inside the ring also deforms and the distance  $R$  (represented as a function of  $\theta$ ) from the center of the ring to the ring inner material also deviates from its initial value  $R_0$ . Denoting the pressure at the contact as  $P$ , we can get the force equilibrium equation,

$$\begin{aligned} P &= [r_0 - r]k_t = [R - R_0]k_b \\ P &\geq 0, \text{ always} \Rightarrow r \leq r_0 \text{ and } R \geq R_0, \text{ always} \\ P(\gamma) &= [r_0 - r(\gamma)]k_t : P \text{ as a function of } \gamma \\ P(\theta) &= [R(\theta) - R_0]k_b : P \text{ as a function of } \theta \end{aligned} \quad (12)$$

where  $k_t$  is the stiffness of the finger tissue and  $k_b$  is the stiffness of the compliant material inside the ring. From Eq. (12), we can get the following relationship.

$$R = R_0 + (r_0 - r) \left( \frac{k_t}{k_b} \right) \quad (13)$$

From the kinematics of the tissue, we can also get the following equations.

$$r^2 = R^2 + d^2 - 2Rd \cos(\alpha - \theta) \quad (14)$$

$$R^2 = r^2 + d^2 - 2rd \cos(\pi - (\alpha - \gamma)) \quad (15)$$

Combining Eqs. (13), (14), and (15), the information about the deformation of the finger tissue and the ring inner material is obtained.

$$R(\theta) = \frac{(r_0 + R_0)^2 - d^2}{2[R_0 + r_0 - d \cos(\alpha - \theta)]} \quad \text{if } k_b = k_t \quad (16a)$$

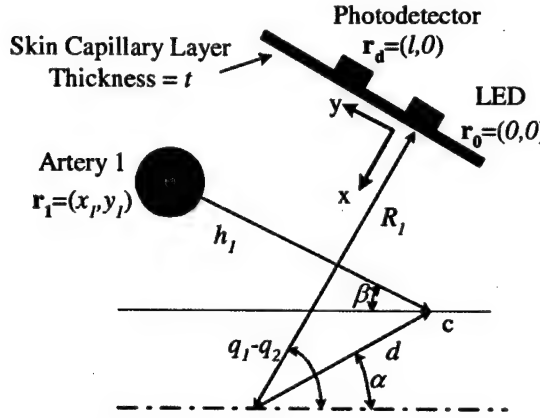


Fig. 4 : Geometry of the LED, the photodetector, the artery 1, and the skin capillary layer

$$R(\theta) = \frac{b - \sqrt{b^2 - ac}}{a} \quad \text{if } k_b \neq k_t \quad (16b)$$

where,

$$a = \left( \frac{k_b}{k_t} \right)^2 - 1, \quad b = R_0 \left( \frac{k_b}{k_t} \right)^2 + r_0 \left( \frac{k_b}{k_t} \right) - d \cos(\alpha - \theta), \quad c = r_0^2 + R_0^2 \left( \frac{k_b}{k_t} \right)^2 + 2R_0 r_0 \left( \frac{k_b}{k_t} \right) - d^2$$

and,

$$r(\gamma) = \frac{(r_0 + R_0)^2 - d^2}{2[R_0 + r_0 + d \cos(\alpha - \gamma)]} \quad \text{if } k_b = k_t \quad (17a)$$

$$r(\gamma) = \frac{b' - \sqrt{b'^2 - a'c'}}{a'} \quad \text{if } k_b \neq k_t \quad (17b)$$

where,

$$a' = \left( \frac{k_t}{k_b} \right)^2 - 1, \quad b' = R_0 \left( \frac{k_t}{k_b} \right) + r_0 \left( \frac{k_t}{k_b} \right)^2 + d \cos(\alpha - \gamma), \quad c' = R_0^2 + r_0^2 \left( \frac{k_t}{k_b} \right)^2 + 2R_0 r_0 \left( \frac{k_t}{k_b} \right) - d^2$$

As shown in Fig. 4, the location of the artery 1 which is  $r_1 = (x_1, y_1)$  in the optical model given by Eq. (1), can be derived using simple kinematics.

$$x_1 = d \sin[\alpha - (q_1 - q_2)] + h_1 \sin[\beta + (q_1 - q_2)] \quad (18a)$$

$$y_1 = R_1 - d \cos[\alpha - (q_1 - q_2)] + h_1 \cos[\beta + (q_1 - q_2)] \quad (18b)$$

where,

$$R_1 = R(q_1 - q_2) \text{ from Eqs. (16a) and (16b)}$$

$$h_1 = h_0 \left( \frac{r_1}{r_0} \right)$$

where,

$$r_1 = r(\pi - \beta), \text{ from Eqs. (17a) and (17b)}$$

The location of the artery 2 which is  $r_2=(x_2,y_2)$  can also be obtained using similar derivations.

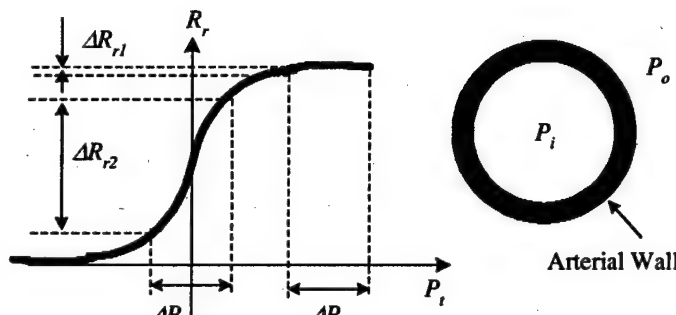


Fig. 5. Change of arterial wall radius ( $R_r$ ) with transmural pressure ( $P_t$ )

### 2.3. Dynamics of the Arterial Wall and the Capillary Layer

The compliance of the arterial wall changes nonlinearly. There are many factors that influence the arterial wall compliance [8], such as temperature, pressure, or even emotion of the person. Among them, pressure is one of the most sensitive factors that change the compliance dramatically. Depending on the transmural pressure  $P_t$ , which is defined as the difference between the internal pressure  $P_i$  and external pressure  $P_o$ , the diameter changes of the digital artery differ even with the same change in blood pressure. Fig. 5 shows the relationship between the arterial wall radius  $R_r$  and the transmural pressure  $P_t$  [6][9]. As shown in the figure, even with the same change of transmural pressure  $\Delta P_t$ , the

change of the arterial radii,  $\Delta R_{r1}$  and  $\Delta R_{r2}$ , are different depending on the operating point of  $P_t$ . The maximum arterial pulsation occurs approximately when the transmural pressure is zero. After this point, the arterial pulsation begins to diminish since the artery becomes occluded by the excessive external pressure [6][9]. This is a well-known principle used in oscillometric blood pressure measurement devices.

The internal pressure of the artery, which is actually what we define as “blood pressure”, is not actively controllable. However, we can change the amplitude of the volumetric pulsation of the artery by changing the external pressure  $P_o$  even under the same blood pressure. In our ring configuration, as the displacement  $d$  increases, the pressure around the contact point increases. This also changes the pressure applied to the digital arteries depending on the configuration and position of the ring. To calculate the radii of the arteries ( $R_{r1}$  and  $R_{r2}$  in Eq. (1)),  $P(\gamma)$  when  $\gamma=\pi-\beta$  and  $\gamma=\beta$  must be calculated from Eq. (12), and this becomes the external pressure  $P_{o1}$  and  $P_{o2}$  applied to digital artery 1 and 2 respectively.

In this approach, we model the relationship of  $R_r$  and  $P_t$  as a sigmoid function for simplicity.

$$R_r = \frac{C_1}{1 + \exp(-C_2(P_t - C_3))} \quad (19)$$

where

$$\begin{aligned} P_t &= P_i - P_o \\ P_i &: \text{blood pressure inside artery} \\ P_o &: \text{pressure outside of artery} \\ R_r &: \text{radius of digital artery} \end{aligned}$$

Finally,  $R_{r1}$  and  $R_{r2}$  in Eq. (1) can be described as follows.

$$R_{r1} = R_r(P_i - P_{o1}) \quad (20a)$$

$$R_{r2} = R_r(P_i - P_{o2}) \quad (20b)$$

where,

$$P_{o1} = (r_0 - r_1)k_t, \quad P_{o2} = (r_0 - r_2)k_t, \text{ from Eq. (12)}$$

where,

$$r_1 = r(\pi - \beta), \quad r_2 = r(\beta), \text{ from Eqs. (17a) and (17b)}$$

The effective thickness  $t$  of the capillary layer can also be obtained using similar derivations except that the operating range of the  $P_t$  is different from that of digital artery. The internal pressure  $P_i$  in digital artery oscillates in the range of 80~120 mmHg. However,  $P_i$  of the capillaries is around 10~35 mmHg, which makes the capillaries occlude more easily in the presence of an external pressure.

Combining the mechanical model describing the locations of the two arteries, the arterial wall dynamics equations given by Eqs. (20a) and (20b), and the optical model equations given by Eqs. (1), (10), and (11), the whole model is completed.

#### 4. Numerical Simulation and Verification by Experiment

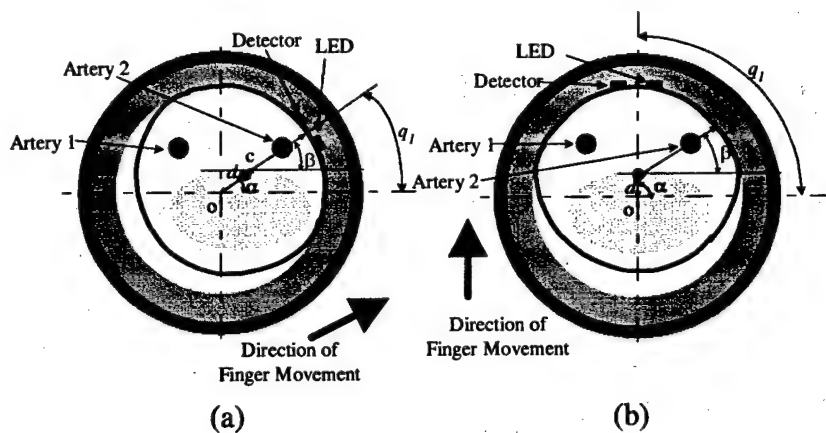


Fig. 6 : Two cases of finger movements in the ring

(a) Case 1 :  $\alpha = \beta = q_1, q_2 = 10^\circ$

(b) Case 2 :  $\alpha = q_1 = 90^\circ, q_2 = 10^\circ$

Numerical simulations and experiments were conducted with different angles of movements. The numerical simulations were performed using MATLAB version 5.2. The first case (Fig. 6a) is when the direction of movement is aligned with that of a digital artery. In the second case (Fig. 6b), the finger moves in the direction of the mid-point of two digital arteries. In the numerical simulations, the blood pressure (internal pressure  $P_i$ ) is given as a combination of two sinusoidal functions, one with a frequency of 1.2 Hz and

the other 2.4 Hz. By this combination, we can closely simulate the two-peak feature of a real heart beat. For the optical coefficients, realistic values of  $\mu_a = 0.002/\text{mm}$ ,  $\mu_s' = 4/\text{mm}$ ,  $\tilde{\mu}_a = 0.05/\text{mm}$ , and  $\tilde{\mu}_s' = 2/\text{mm}$  are used in the numerical simulations. In the experiments, the LED and the photodetector are closely packed in a sensor unit board, and the ring is positioned so that the sensor is aligned in the direction of movement in each case. ( $\alpha=q_1$ )

#### ***4.1. Analysis of the Simulation and Experiment : Case 1***

When the direction of finger movement is aligned with the location of a digital artery ( $\alpha=\beta$ ), it is expected that the amplitude of the photoplethysmograph will change greatly as  $d$  (displacement) increases due to two reasons. First, as the sensor is aligned with a digital artery, the distance from the artery and the photodetector will decrease significantly as  $d$  increases. This will result in a more change of light absorption by the blood with the same change of the diameter of digital artery. Secondly, as the direction of movement is aligned with the location of a digital artery, the external pressure around the artery which is  $P_o$  will increase quickly, resulting in the maximum pulsation point of the transmural pressure more easily. This will also give a more highly pulsating signal at the photodetector. Fig. 7 shows the numerical simulation of the finger and the ring configuration with a gradual increase of the displacement  $d$ . The large outer circle represents the ring, and the inner line which looks like a distorted circle is the finger surface. The two small circles inside the finger represent the two digital arteries, and the plus sign (+) inside the finger represents the reference point of the finger (which was denoted as point  $c$  in previous figures). It can be clearly seen that this reference point moves toward the direction of a digital artery as the displacement increases, and the digital artery goes closer to the LED and the photodetector which were represented as a small square ( $\square$ ) and a small star (\*) on the finger surface at around 20 degree respectively.

From the viewpoint of the arterial wall dynamics, it is expected that the amplitude of the photoplethysmograph will increase as the relative displacement of the finger to the ring increases up to a certain point where the transmural pressure goes to zero. After that peak point, the amplitude is expected to decrease since the digital artery will begin to be

occluded. The simulation results and the experiment results are shown in Fig. 8 and Fig. 9 respectively. The upper plots of Fig. 8 and Fig. 9 are the photoplethysmographs, and the bottom figures are the pressures at the sensor unit. Both results show that there is a certain point of external pressure  $P_o$  that the amplitude of the photoplethysmograph becomes maximum. (The experiment result of case 1 shows a small oscillation even at very high external pressure. This is mainly due to the measurement noise and the signals at this region do not show the typical characteristics of human heart beats such as two peaks waveform.)

#### ***4.2. Analysis of the Simulation and Experiment : Case 2***

The second case is when the direction of finger movement is towards the middle point of the two digital arteries, i.e, to the palm side ( $\alpha=90^\circ$ ). In this case, the change of amplitude of the photoplethysmograph with finger displacement is not expected to be as great as in case 1 since the pressure increase at the artery is not as much as in case 1 with the same extent of displacement. In addition, as the distances of the two digital arteries from the sensor unit are geometrically longer than those of case 1, the overall amplitude of the photoplethysmography signal will not be large. This means that the amplitude of the photoplethysmograph will not change much even though the finger moves significantly to the direction of the palm side. Thus, it is expected that the amplitude of the signal will remain very small regardless of the finger displacement. (This is the worst configuration of the ring and the finger in terms of the signal to noise ratio as we observed in the experiments.) The movement of the finger in the ring is graphically visualized using our model in Fig. 10.

The experimental result is shown in Fig. 11, and the simulation result in Fig. 12. As was expected, the amplitude of the photoplethysmograph shows almost no change in experiment. In this configuration, it is even hard to recognize the pulse, in both experiment and simulation. In both results, the amplitude becomes a little larger with low pressures. This slight increase of the amplitude is from the pulsation of the capillaries on the palm side of the finger. Capillaries usually become occluded at an external pressure of around 10~35 mmHg since the internal blood pressure of the capillaries is around that range. This explains the disappearance of pulsation at higher pressures in the experiment

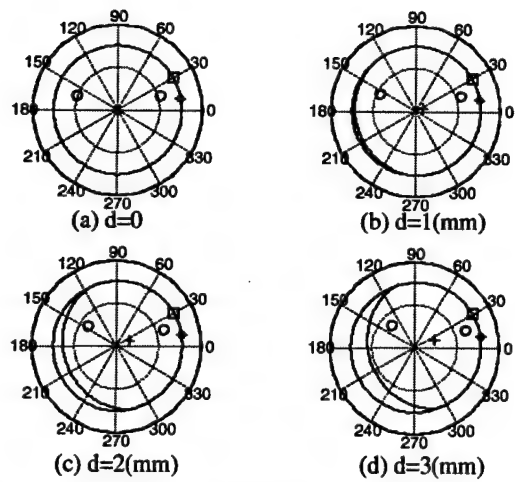


Fig. 7 : Visualization of movement at case 1. It is shown that the finger shape becomes more oval as  $d$  increases.

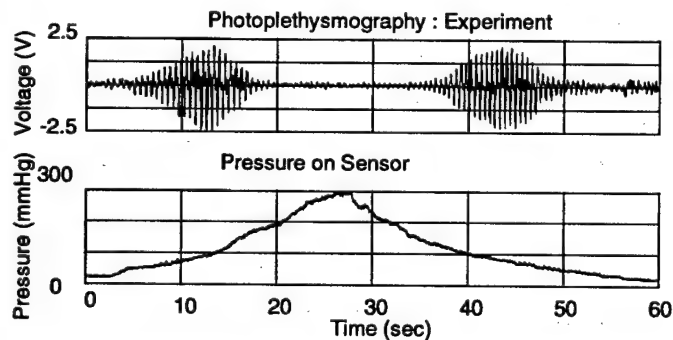


Fig. 8 : Photoplethysmography and pressure at sensor unit from experiment in case 1

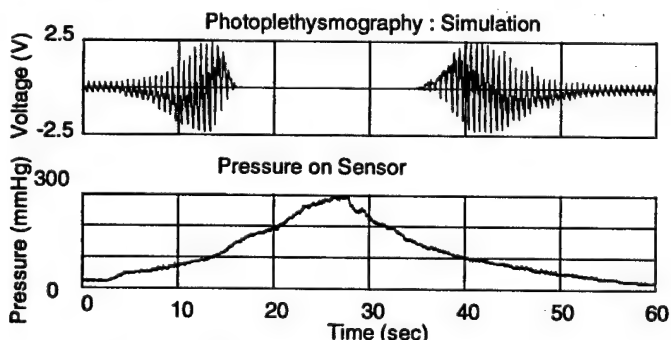


Fig. 9 : Photoplethysmography and pressure at sensor unit from numerical simulation in case 1

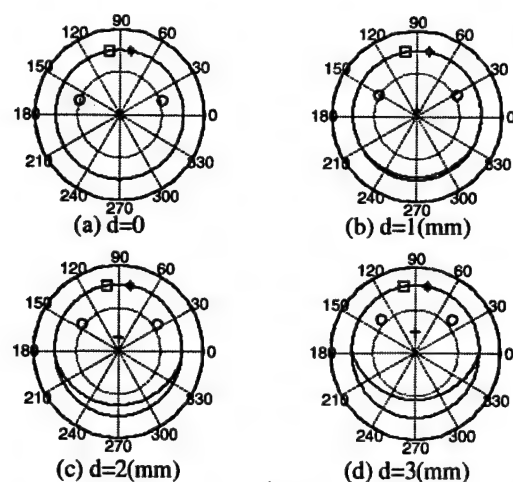


Fig. 10 : Visualization of movement at case 2. It is shown that the reference point (denoted as '+') moves toward the middle point of two arteries as  $d$  increases.

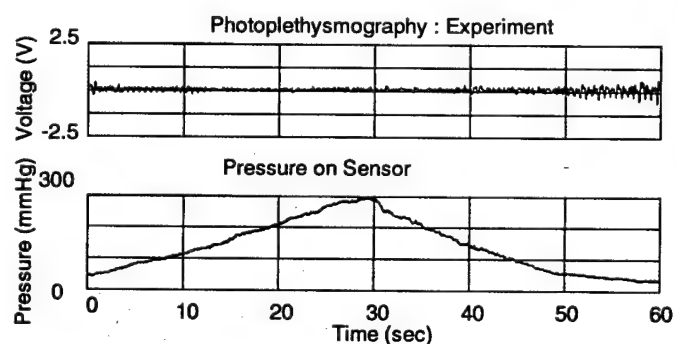


Fig. 11 : Photoplethysmography and pressure at sensor unit from experiment in case 2

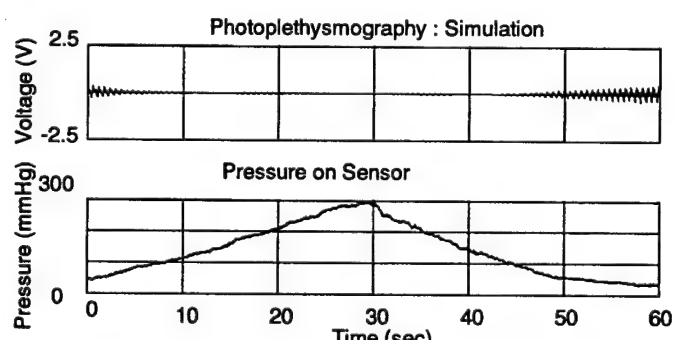


Fig. 12 : Photoplethysmography and pressure at sensor unit from numerical simulation in case 2

result in case 2. (Small oscillation at high external pressures is mainly measurement noise.) In other words, the photoplethysmograph of case 2 catches the pulsation from the capillaries when the external pressure is low. However, as the external pressure increases above 10~35 mmHg, this pulsation disappears as the capillaries become occluded. As the arterial pulsation cannot be apparently detected by the photoplethysmography at this configuration because the distance between the arteries and the sensor is long, we can see almost no pulsation with higher external pressures. Rather, the pulsation of the capillaries plays a major role with a low external pressure, although its amplitude is much smaller than that in case 1 in which the photoplethysmograph is mostly driven by arterial pulsation. The simulation result also exhibits a similar behavior

## 5. Conclusions

A finger model for photoplethysmography of the Ring Sensor was developed. This model is an interdisciplinary physiological model that integrates an optical model, mechanical model, and the dynamics of the arteries and the capillaries. This model was verified by experiments and numerical simulations. This model is especially useful in describing the nature of the finger-based health monitoring device (the Ring Sensor). For example, from the viewpoint of noise minimization issues, there are many advantages of having this mathematical finger model in designing a ring sensor that is strong to noise caused by finger movement. As there are many design parameters that have to be tuned in the development of a ring sensor, this finger model will be a good analytic method in optimizing those parameters such as the compliance of the inner material of the ring and the configuration of the sensor. Further refinement of this model will focus on investigating the non-linearity of the finger tissue, as well as on more detailed modeling of the anatomical elements such as bones and skin layers.

## References

- [1] Rhee, S., Yang, B-H. and Asada, H., "The Ring Sensor: a New Ambulatory Wearable Sensor for Twenty-Four Hour Patient Monitoring," Proc. of the 20<sup>th</sup> Annual International Conference of the IEEE Engineering in Medicine and Biology Society, Hong Kong, Oct, 1998
- [2] Yang, B-H., Rhee, S. and Asada, H., "A Twenty-Four Hour Tele-Nursing System Using a Ring Sensor," Proc. of 1998 IEEE International Conference on Robotics and Automation, Leuven, Belgium, May, 1998
- [3] Barker, S. J. and Shah, N. K., "The Effect of Motion on the Performance of Pulse Oximeters in Volunteers," *Anesthesiology*, 86, 101-108 (1997)
- [4] Plummer, J. L., Zakaria, A. Z., Ilsley, A. H., Fronsko, R. R. L. and Owen, H., "Evaluation of the Influence of Movement on Saturation Readings from Pulse Oximeters," *Anaesthesia*, 50, 423-426 (1995)
- [5] Vicente, L. M., Barreto, A. B. and Taberner, A., "Adaptive Pre-Processing of Photoplethysmographic Blood Volume Pulse Measurements," Southern Biomedical Engineering Conference - Proceedings Mar 29-31 1996 Sponsored by:University of Dayton; IEEE IEEE p 114-117
- [6] Wesseling, K. H., de Wit, B., van der Hoeven, G. M. A., van Groudoever, J. and Settels, J. J., "Physiocal, Calibrating Finger Vascular Physiology for Finapres," *Homeostatis*, 36 (2-3), 67-82 (1995)
- [7] Feng, S., Zeng, F. and Chance, B., "Photon Migration in the Presence of a Single Defect : a Perturbation Analysis," *Applied Optics*, Vol. 34, No. 19, 3826-3837 (1995)
- [8] Tanaka, H. and Thulesius, O., "Effect of Temperature on Finger Artery Pressure Evaluated by Volume Clamp Technique," *Clinical Physiology* (1993) 13, 535-545
- [9] Yamakoshi, K., Shimazu, H., Shibata, M. and Kamiya, A., "New Oscillometric Method for Indirect Measurement of Systolic and Mean Arterial Pressure in the Human Finger. Part 1 : Correlation Study," *Medical & Biological Engineering & Computing* (1982), 20, 307-313

## **New Design of the Ring Sensor: A Solution to Signal Artifact**

**Dr. Boo-Ho Yang**  
Principle Investigator

**Prof. Haruhiko H. Asada**  
Co-Investigator

**Sokwoo Rhee**  
Graduate Research Assistant

### **ABSTRACT**

In this report, we propose a new design of the ring sensor that can alleviate the artifact of motion and ambient light significantly. The ring sensor is a compact, wearable device that was originally designed for continuous physiological monitoring of a human body. One challenging issue in the development of the ring sensor was the high sensitivity of the measurement to movement of the wearer. The signals tend to be distorted and sometimes even ruined by mechanical or optical disturbances caused by the movement. This newly designed ring sensor is composed of two separate rings. The inner ring carries a tiny optical sensor unit for measurement, and the outer ring carries relatively bulky circuit board that includes a CPU, a signal processing module, an RF transmitter, and a battery. These two rings are mechanically isolated from each other except a few thin wires for the electric signal transmission. With this configuration, the inertia-free sensor unit maintain a tight contact with the skin surface even in a highly accelerated motion, resulting in reliable, consistent measurement. The outer ring, on the other hand, works as a mechanical shelter and prevents mechanical contacts from influencing the measurement of the sensor unit. In addition, the outer ring works as an optical seal to block the ambient light, generating more accurate optical measurement.

## 1. Introduction

The Ring Sensor is a miniaturized telemetered ambulatory monitoring device in a ring configuration by combining the technology of pulse oximetry with microelectronics and wireless communication technologies. This device optically captures the pulsation and the oxygen saturation of the arterial blood flow of the patient and transmits the signals to a personal computer in a wireless manner. The light emitted from LED traverses human tissue, and reaches the photodetector, with some of the photons absorbed by the tissue and the blood. As the NIR (Near Infrared) absorption coefficient of blood is much higher than that of tissue, the intensity of received light depends on the amount of the blood in the tissue. As a result, when the digital arteries and the capillaries in the finger expands by the pumping activity of the heart, the intensity of light received by the detector decreases. On the contrary, the measured light intensity becomes higher when the arteries and the capillaries contract. The Ring Sensor can be worn by the patient twenty-four hours a day at home. Real-time, continuous monitoring with the Ring Sensor allows not only for emergency detection of an abrupt change of the patient health condition but also for long-term monitoring of vital signs of otherwise difficult and noncompliant patients such as demented elderly people.

The Ring Sensor, however, is inevitably susceptive to a variety of motion and ambient light artifacts. For example, in a highly accelerated motion of the patient, the inertia force causes the optical sensor unit to move or slide on the skin surface, and, as a result, the optical sensor measurement would be distorted or even ruined completely. Even a static external force causes a similar distortion of the measurement due to the relative displacement of the sensor to the finger. In addition, ambient light is another major source of the artifact on the optical measurement. These kinds of external disturbances can seriously degrade the quality of measurement of the ring sensor.

As the signal detected by the optical sensor is amplified thousands of times, any small disturbance on the sensor will result in a significant change of the amplified signal and eventually ruin the measurement. Therefore, to guarantee stable and clear signal

measurements, it is necessary to develop a new design of a ring-shaped device that can minimize the influence of mechanical and optical disturbances on the signal detection.

## 2. Design

The main objective of this new ring design is to alleviate the influence of the external disturbances on the actual measurement. As stated in the previous section, the major causes of the artifact are the influences of inertia force, static external force, and ambient light. To deal with the influence of the inertia force, it is necessary to separate the sensor unit from the most of the inertia of the device. The separation can be achieved by having two rings which are mechanically independent to each other. By putting the optical sensor unit on one of the rings and the circuit board and the batteries on the other ring, it is possible to protect the sensor unit from the influence of the most of the inertia force. The problem caused by external static forces can also be solved by same approach. We can design the two rings so that one of the ring is enclosed in the other ring. The inner ring floats inside the outer ring so that static displacement of the outer ring does not give influence on the inner ring. The problem of ambient light can be also alleviated by this design since the outer ring works as an optical seal for the sensor unit on the inner ring.

The inner ring is basically a thin band that carries the optical sensor unit including a set of LEDs and photodiodes. This part is made of light material such as plastic or acrylic, or even a rubber band. A rubber band or latex is good in that it is flexible and compliant. From the analysis of the finger model which was described in another progress report in this issue, it was found that giving a certain pressure on the optical sensor on the skin can increase the amplitude of the measured signal, resulting in a higher signal to noise ratio. In addition, using a compliant material for the inner ring helps the ring hold the finger firmly. The second part is the outer ring that carries the circuit board. This second part is made of a stiffer material such as metal or PVC so that it can sustain the circuit board and the batteries. It also works as a mechanical shelter against external forces. The first part is put into the second part, and it can float inside the second part. The sensor unit attached on the first part is connected to the circuit board on the second part with a few flexible,

thin wires that are long enough that the rotation of outer ring does not give influence on the inner ring. These wires are the only connection between the first part and the second part. With this configuration, the first part carrying the sensor unit is virtually de-coupled from the movement of the second part, and it is not bound by the influence of the movement of the second part. A conceptual diagram of this design is shown in Fig 1.

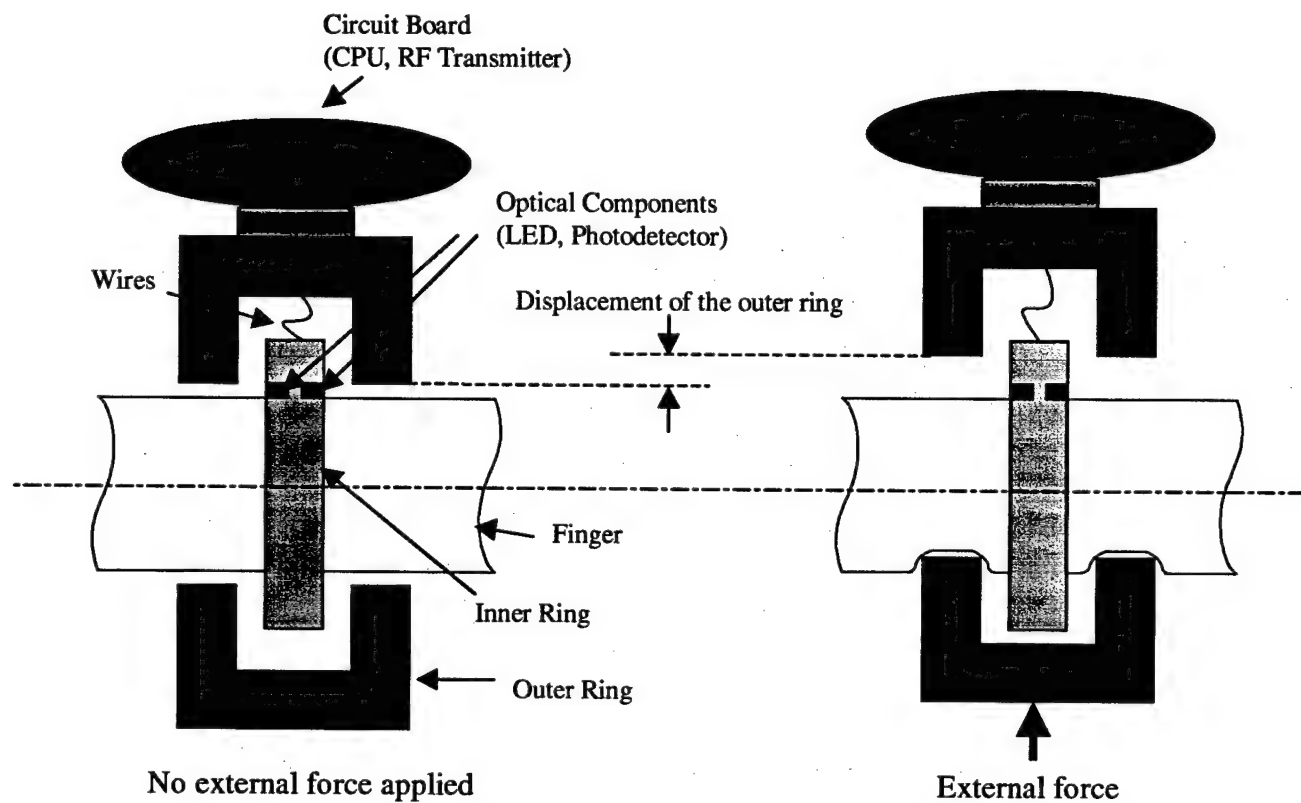


**Fig 1 : Schematic of New Ring Design (With and Without External Force)**

As shown on the diagram of Fig 1, the inner ring moves around inside the outer ring. When an external force applies to the outer ring, the relative position of the inner ring to the outer ring changes, but the relative position of the finger to the sensor unit that is attached on the inner ring does not change. One important point in the design is that the wires that connect the circuit board and the sensor unit have to be thin and long enough. The length of the wire is important when the outer ring rotates by any kind of external torque. We design this ring under the assumption that the ring does not rotate too much.

The wires have to be long enough that the inner ring does not rotate although the outer ring rotates to some extent.

Key points of this design can be itemized as follows.

- (1) A miniaturized sensor unit is attached on the internal ring whose mass is almost negligible. This sensor unit is a small circuit board (5mm × 5mm × 0.8mm) that contains two light emitting photodiodes and a photodetector. As we use point-based light emitting diodes and a subminiature photodetector, the mass of this sensor unit is considerably small.
- (2) The main circuit board and batteries that are relatively heavy and bulky sit on the external ring (Housing). The main circuitry is composed of many small element, most of which are surface mount style or bare die form. Resistors and capacitors are either wire-bonded or glued with conducting epoxy. Integrated circuits are all in die forms and wire-bonded on the gold pads on the circuit board. Although we used small and light components, total mass of this circuit board is not negligible. In addition, the button type batteries used for providing power to the circuit have relatively large mass. These components sit on the surface of the outer ring.
- (3) The inner ring and the outer ring are connected only by a few wires that are flexible and thin. As a result, the inner ring and the outer ring are virtually isolated mechanically. The outer ring is subject to external forces including direct forces and inertial forces, and it may move or rotate around the finger. However, the inner ring is not influenced by the movement of the outer ring.
- (4) The inner ring floats inside the outer ring. When a person wears the ring, the finger puts on both rings simultaneously, but there is no direct mechanical connection between the two rings except a few thin wires for signal exchange.
- (5) Any external force given on the ring set applies only to the outer ring, and the force is sustained mostly by the parts of the outer ring that are in contact with the finger. The external force does not seriously influence the contact point between the finger and

the internal ring since the two rings are virtually de-coupled. As a result, the measurement from the sensor unit can be kept stable even in the presence of external forces applied to the outer ring.

Fig 2 shows a 3-D figure of the new design. The outer ring is divided into two pieces for the person to wear it easily.

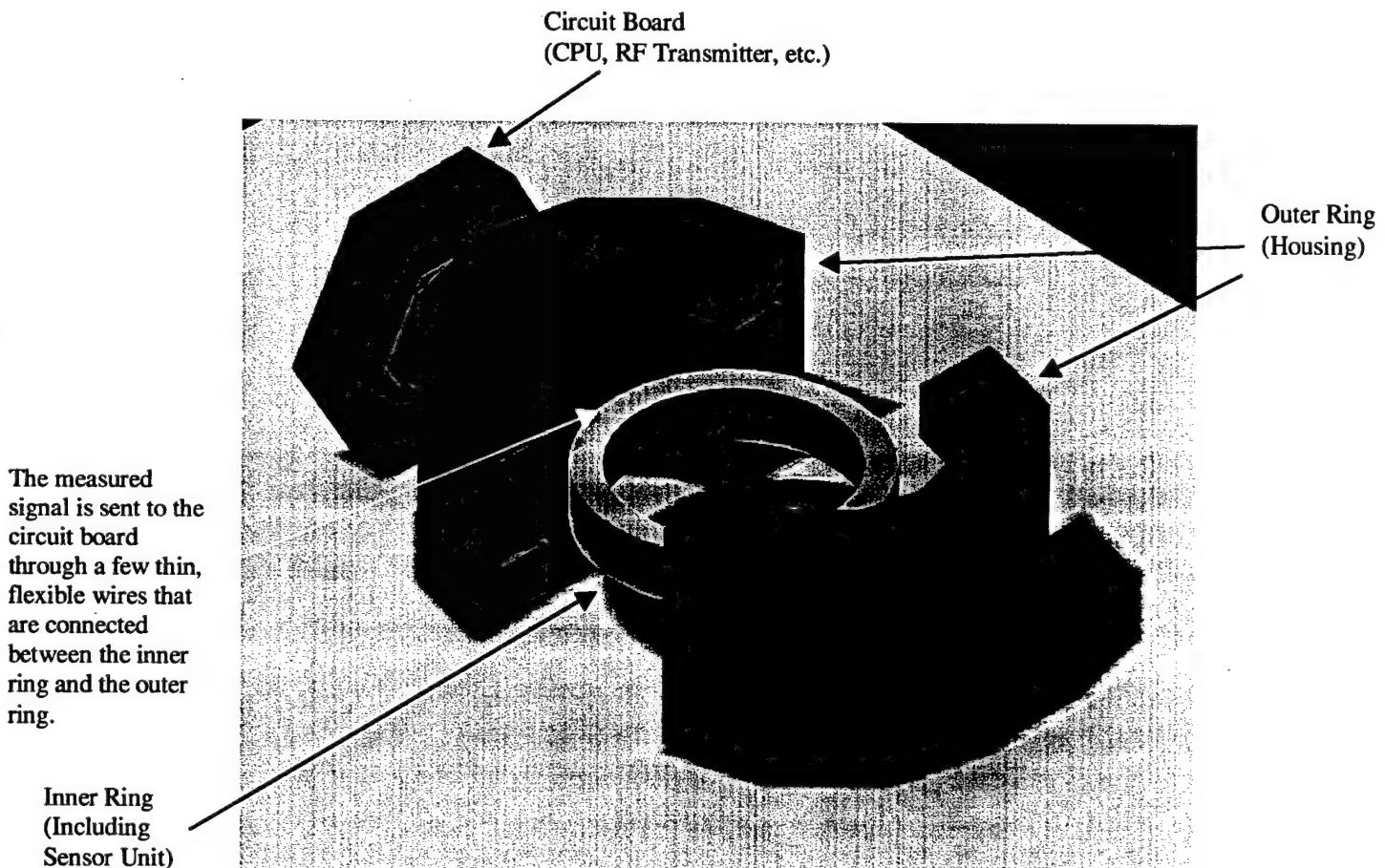


**Fig 2 : New Ring Design for Finger Photoplethysmography**

### **3. Advantages**

This new design is unique in that the sensor unit is protected by the outer ring from external disturbances. There are several advantages in this ring design to be used for finger photoplethysmography. The advantages can be itemized as follows.

**(1) Alleviate the effect of acceleration on the sensor (due to the inertia)**

The inertia of the sensor unit is very small since it only contains a few point-based LEDs and a subminiature photodiode. Due to the small inertia of the inner floating ring, the force applied to the sensor unit can be minimized in the presence of large acceleration. This means that the relative position of the optical sensor does not change much even though the finger moves abruptly, which guarantees stable signal detection.

**(2) Alleviate the influence of external forces applied to the ring**

Mechanical disturbances such as external force are sustained mostly by the outer ring that is in contact with the finger, so that the force does not influence the actual sensor unit floating inside the outer ring.

**(3) Reduce the influence of the ambient light on measurement**

The sensor unit is optical protected by the outer ring. Optical disturbance by the ambient light is blocked by this housing, so that the sensor measurement is not influenced significantly by any external light source.

In summary, the state of the optical detector does not change much in the presence of any mechanical or optical disturbances from outside, which is the ideal condition for obtaining a stable photoplethysmographic measurement from the finger.

#### **4. Verification by Experiment**

To verify the validity of this new design, the measurement obtained from the new ring sensor was compared with that of an old ring sensor. The old ring sensor uses just a simple ring made out of aluminum, which is only one piece. The circuit board is attached on the outer surface of the ring and the sensor unit is attached inner surface of the same ring.

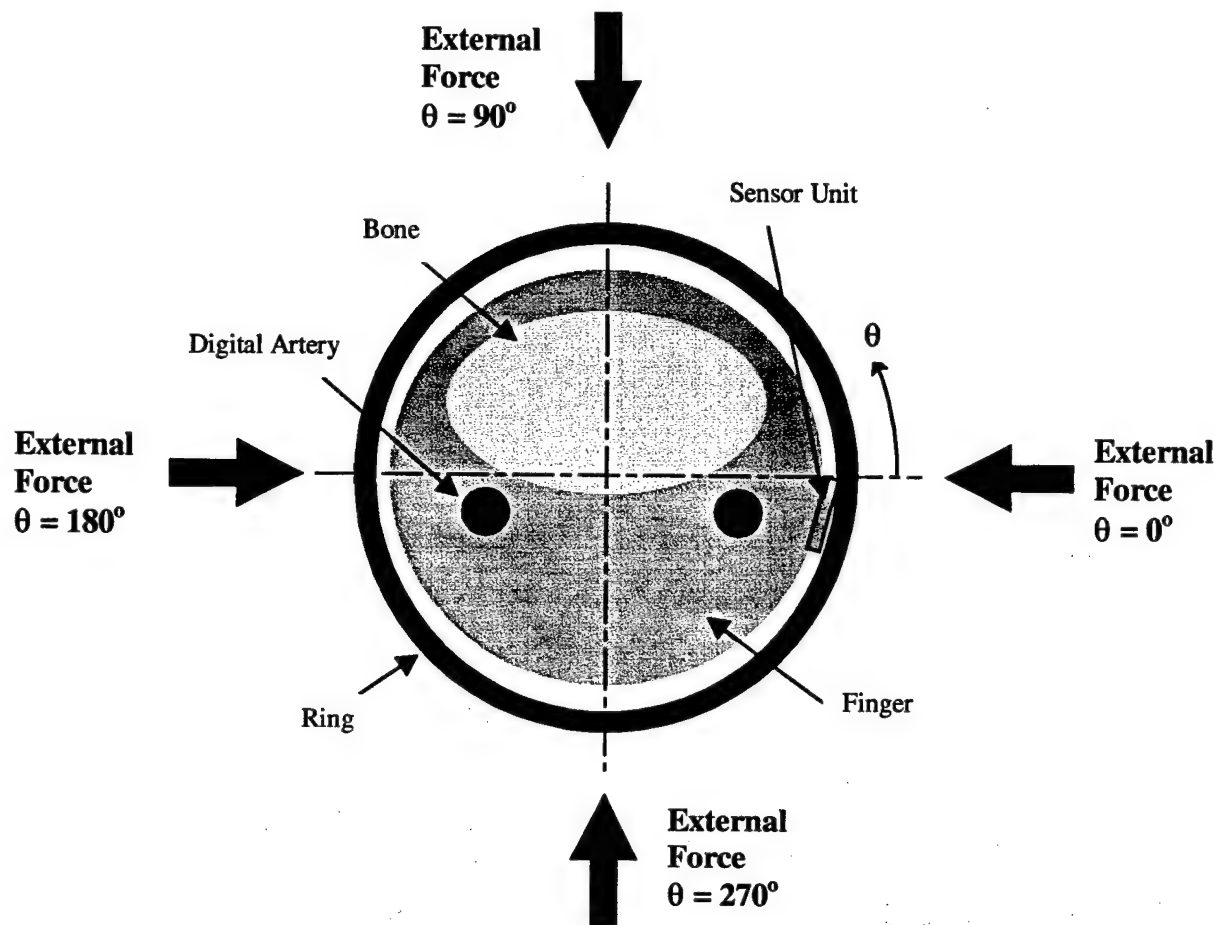
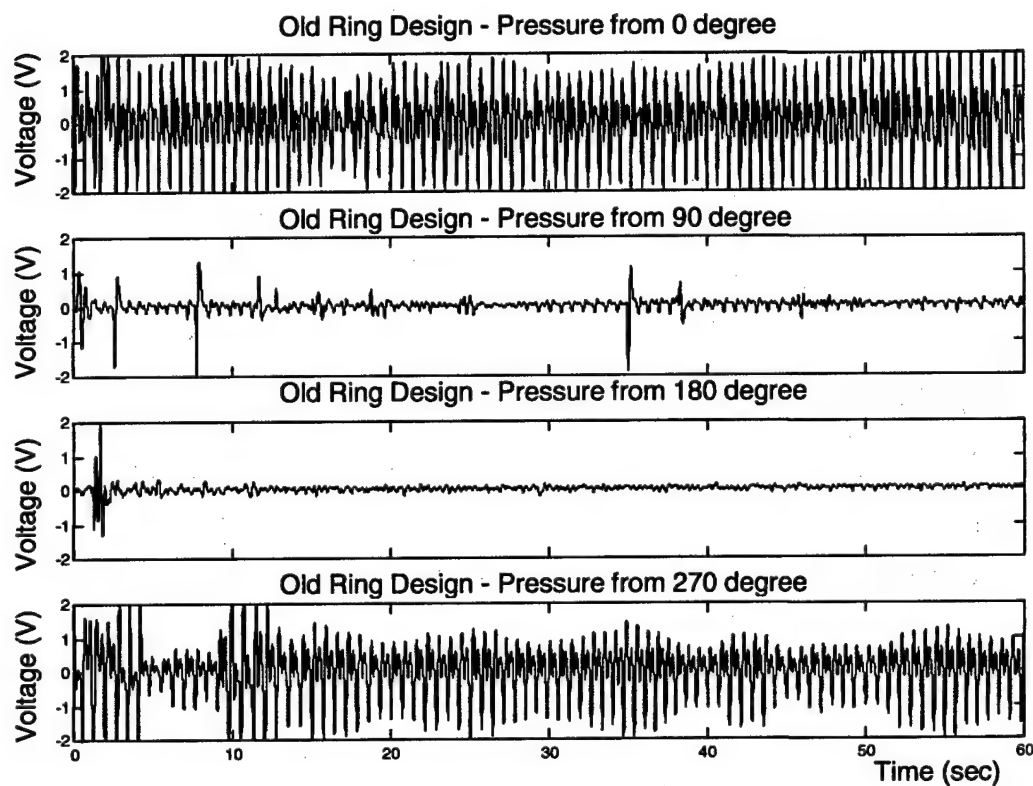


Fig 3 : Experiment Configuration

The experiment was conducted giving an external static force on the ring at various positions. Fig 3 shows the configuration of the experiment. Initially, an external pressure was given on the point of angle  $\theta = 0^\circ$ , and the corresponding photoplethysmograph was measured. The same experiments were conducted with  $\theta = 90^\circ$ ,  $\theta = 180^\circ$ , and  $\theta = 270^\circ$  respectively. The photoplethysmographs from the experiments of the plain (old) ring sensor are shown in Fig 4, and the results of the new ring are shown in Fig 5.

In the case of the old ring composed of one piece, the measurement varies highly depending on the external forces. With an external force at an angle of  $0^\circ$  or  $270^\circ$ , the photoplethysmograph is clear with large amplitude. (In the previous section, the analysis of finger model showed that the signal becomes stronger with a certain pressure on the sensor unit.) In the experiment with an external force at  $0^\circ$  or  $270^\circ$ , the amplitude of

signal is actually larger than the case with no external force due to the pressure applied on the sensor unit. However, when the external force is applied at  $90^\circ$ , the amplitude of the signal is significantly reduced and the pulses are hard to detect. In this configuration, the pressure applied on the sensor unit is almost zero, and even a small air gap can exist between the optical sensor and the skin, which will seriously ruin the measurement. In the case of  $\theta = 180^\circ$ , the air gap becomes even larger and we can hardly recognize the pulses. Actually this is the worst configuration among the four cases.



**Fig 4 : Photoplethysmographs from old ring with external forces at various angles**

Meanwhile, the photoplethysmographs of new ring sensor show much better results. Because of the reason explained above, the signal is most clear and the amplitude is large with  $\theta = 0^\circ$  or  $270^\circ$ . However, even with an external force applied at  $\theta = 90^\circ$  or  $180^\circ$ , the photoplethysmographic signal is still clear and it is not difficult to identify the pulses. Even at the worst configuration which is  $\theta = 180^\circ$ , the amplitude of signal is relatively

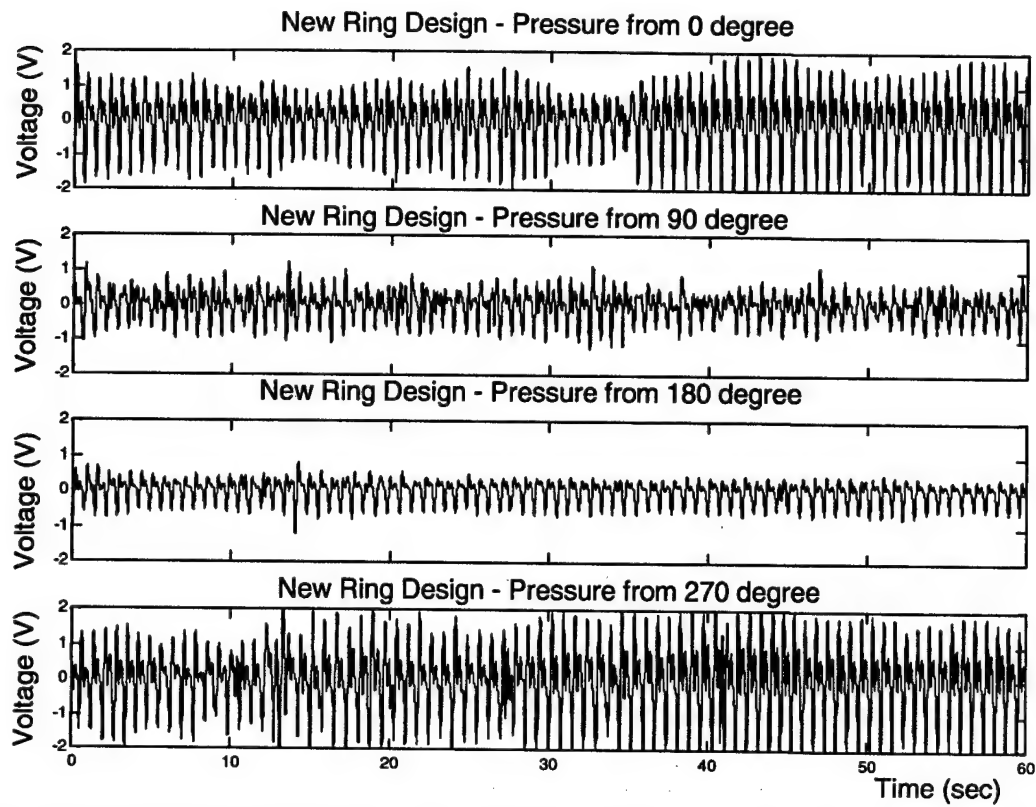


**Fig 5 : Photoplethysmographs from newly designed ring with external forces at various angles**  
 small, but is clearly reflecting the human pulse to the extent that is enough to identify the pulse. With this new ring design, there exists no air gap between the optical sensor and the skin even though the outer ring will move from its original position significantly.

## 5. Conclusion and the Future Work

A new design for the ring sensor was proposed and discussed. One of the most difficult problems in implementing a wearable sensor is motion artifact issue. This new design of the ring sensor does not completely eliminate the influence of the motion artifact. However, it was shown by experiment that this new design can considerably reduce the influence of motion artifact.

In the future, a further verification of the effectiveness of this new design needs to be conducted through more rigorous and quantitative experiment. In addition, a theoretical modeling of the interaction between the finger and this new ring should be developed to fully explain the mechanism in detail.

## **CUFF-LESS CONTINUOUS MONITORING OF BLOOD PRESSURE USING A HEMODYNAMIC MODEL**

Dr. Boo-Ho Yang  
Principal Investigator

Prof. Haruhiko H. Asada  
Co-Investigator

Yi Zhang  
Graduate Research Assistant

### **Abstract**

This report presents a new approach to noninvasive, continuous monitoring of arterial blood pressure for advanced cardiovascular diagnoses. Most of the current noninvasive, continuous blood pressure measurement devices are mechanically intrusive and, therefore, cannot be used for long-term ambulatory monitoring. This new approach requires only simple, noninvasive monitoring devices, such as finger photo plethysmographs and an electrical impedance plethysmograph (EIP), to monitor the dynamic behavior of the arterial blood flow. In this approach, measured signals from these noninvasive sensors on an arterial segment are integrated to estimate the blood pressure in the segment based on a hemodynamic model. A mathematical model of the arterial blood flow is derived and transformed into a state-space representation. In the modeling, we derive a precise hemodynamic model for the arterial segment, on which sensors are located, and combine the model with relatively simplified models of the upstream and the downstream arterial flows to represent an entire arterial stream. Then, a Kalman filter is designed based on the model. It is shown that the internal variables, such as the arterial blood pressure in the arterial segment, can be estimated based on the measurements even though the observability condition of the system may not be met. Simulation results indicate that the approach can generate an accurate estimation of the arterial blood pressure in real-time even from noisy sensor signals.

## 1. Introduction

Noninvasive ambulatory blood pressure monitoring is currently limited to the simple measurements of systolic and diastolic blood pressures at intervals. However, it is known to clinicians that continuous waveforms of blood pressure can provide more useful information about patients' cardiovascular states, which are difficult to obtain from the routine antecubital pressure measurement. For example, the rate of pressure rise at the beginning of systole indicates the strength of cardiac contraction, while the rate of pressure decay during end diastole can be used as a measure of peripheral vascular resistance, both of which are important parameters used in cardiovascular diagnoses. In fact, many numerical algorithms have been developed to estimate left-ventricular and circulatory parameters from the arterial pressure waveform by applying a computer model of the cardiovascular system [1]-[4]. Considering that heart disease is a prevalent cause of death in the modern society, it is obvious that long-term noninvasive continuous monitoring of such pressure waveforms would bring enormous improvement of the quality of healthcare at home as well as in the hospital.

A few devices have been developed for continuous monitoring of the arterial pressure waveform, yet these are either invasive or mechanically intrusive and are not designed for the long-term use. For example, Pressman and Newgard developed a noninvasive method for continuously measuring instantaneous blood pressure by applying the coplanar measurement principle used by tonometry [5]. In this method, called "arterial tonometry," the artery is flattened by applying external pressure non-invasively to squeeze the artery against the bone. Since the circumferential tension of the arterial wall disappears, the applied pressure to maintain the flattened shape indicates the arterial blood pressure. An array of piezoelectric transducers is used for the pressure reading. Penaz, on the other hand, proposed a new noninvasive, continuous blood pressure measuring method based on the principle of vascular wall unloading [6]. In this method, a cuff is inflated to a pressure equal to the pressure in the artery and the cuff pressure is continuously adjusted by a servo control system, which monitors the size of the artery using a photo plethysmograph. This method was further developed by Wesseling [7] and successfully commercialized as "FINAPRES." Yamakoshi and his group also developed a similar device independently by applying the vascular unloading technique [8][9]. The major drawback of these devices, however, is the tight confinement and mechanical intrusiveness of the sensor probes and the resultant discomfort to the patient. As stated above, these methods require a constant and continuous external pressure on the skin surface of the patient, and it could cause vasospasm and pressure drops in the peripheral artery [10]. Therefore, for long-term, ambulatory blood pressure monitoring, a new method for the noninvasive and non-intrusive continuous measurement has to be developed.

In this report, we propose a new approach to noninvasive non-intrusive continuous measurement of pulsating arterial blood pressure without using a cuff. The concept of this method is to process and merge information gathered by multiple sources and sensors to provide a better insight into the phenomena under consideration. We explore the utility of sensor fusion for indirectly estimating arterial blood pressure by integrating simultaneous measurements from noninvasive, non-intrusive sensors such as a photo plethysmograph and a bioelectrical impedance plethysmograph with a mathematical model of the blood flow.

In this approach, we formulate and develop a Kalman filter for the sensor fusion scheme. Kalman filters are standard state estimators or observers that are optimum with respect to the process noise and sensor noise, and many nonlinear extensions have been developed (see [11] for example). The idea of this approach is to derive a state-space equation from a mathematical hemodynamic model and apply a Kalman filter to estimate the internal state variables, such as blood pressure, based on signals from noninvasive and non-intrusive sensors. Figure 1 shows the basic scheme of this approach.

In this report, we first derive a two-dimensional mathematical model of the arterial blood flow as an incompressible, axially symmetric Newtonian fluid in a rectilinear, viscoelastic thick shell of isotropic, incompressible material with a circular section. The modeling method is applied to a small digital arterial segment, from which sensor signals such as a photo plethysmograph and a bioelectrical impedance plethysmograph are obtained. Then, we extend the hemodynamic model of the peripheral arterial segment up to the heart as the proximal boundary and the capillary as the distal boundary to represent an entire arterial stream. A commonly assumed pattern of the cardiac output is used as the system's input. To avoid high-order modeling, the upstream is simply modeled as a three-dimensional extended Windkessel model, and the downstream is modeled as a classical Windkessel model. Finally, a Kalman filter is designed based on the extended model. Since the original local arterial segment are precisely modeled and the output signals are measured from the segment, it is expected that the Kalman filter can estimate the local arterial blood pressure accurately even with the simplifications of the input and the modeling of the upstream and downstream blood flows. An extensive observability analysis is provided. Numerical simulations are also presented to verify the approach.

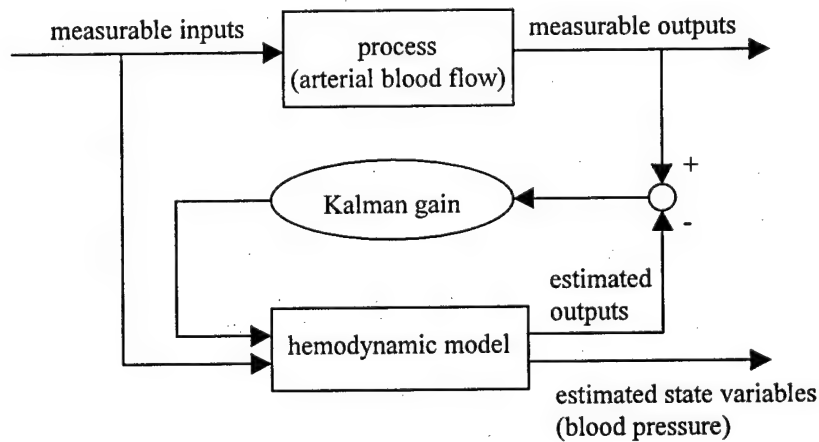


Figure 1: A schematic diagram of the Kalman filter for the instantaneous blood pressure estimation

## 2. State-Space Modeling of Arterial Hemodynamics

The approach proposed in this paper utilizes a mathematical hemodynamic model for the complex behavior of the arterial vessel and blood flow of a peripheral arterial segment and estimates internal variables, such as blood pressure, by comparing the sensor readings from the segment with the simulated outputs. Therefore, the accuracy and fidelity of the local model is a key issue in this approach. Many hemodynamic models have been developed for the study of the two-dimensional nonlinear behavior of the pulsating blood flow [12]-[15]. In this report, we apply a mathematical framework developed by Belardinelli and Cavalcanti [14][15], which describes a two-dimensional nonlinear flow of Newtonian viscous fluid moving in a deformable tapered tube. The upstream and the downstream arterial flows are represented as an extended Windkessel model, and combined with the above nonlinear model of the local segment to constitute the entire arterial stream.

### 2.1 Local Arterial Flow Model

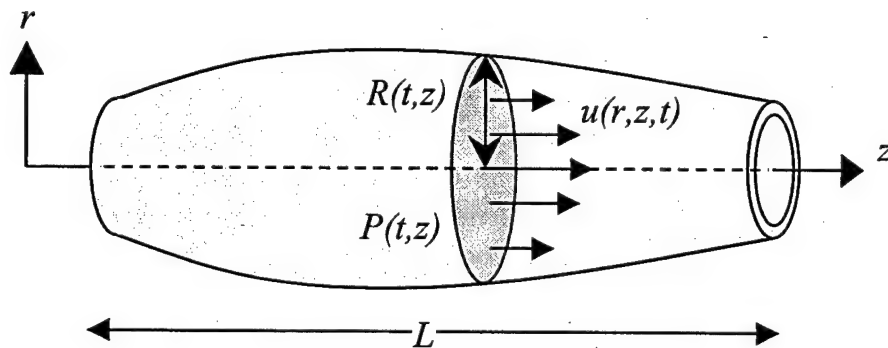


Figure 2: A segment of a viscoelastic artery with length of  $L$

#### Mathematical Model of Arterial Flow

A small segment (distance of  $L$ ) of a small artery, such as a digital artery, is considered in this report, as shown in Figure 2. We assume that the arterial vessel is rectilinear, deformable, thick shell of isotropic, incompressible material with a circular section and without longitudinal movements. Blood is an incompressible Newtonian fluid, and flow is axially symmetric. Two-dimensional Navier-Stokes equations and continuity equation for a Newtonian and incompressible fluid in cylindrical coordinate  $(r, \theta, z)$  are:

$$\frac{\partial u}{\partial t} + w \frac{\partial u}{\partial r} + u \frac{\partial u}{\partial z} = - \frac{1}{\rho} \frac{\partial P}{\partial z} + v \left( \frac{\partial^2 u}{\partial r^2} + \frac{1}{r} \frac{\partial u}{\partial r} + \frac{\partial^2 u}{\partial z^2} \right) \quad (1)$$

$$\frac{\partial w}{\partial t} + w \frac{\partial w}{\partial r} + u \frac{\partial w}{\partial z} = - \frac{1}{\rho} \frac{\partial P}{\partial r} + v \left( \frac{\partial^2 w}{\partial r^2} + \frac{1}{r} \frac{\partial w}{\partial r} + \frac{\partial^2 w}{\partial z^2} - \frac{w}{r^2} \right) \quad (2)$$

$$\frac{1}{r} \frac{\partial}{\partial r} (rw) + \frac{\partial u}{\partial z} = 0 \quad (3)$$

where  $P$  denotes pressure,  $\rho$  density,  $\nu$  kinematic viscosity, and  $u=u(r,z,t)$  and  $w=w(r,z,t)$  denote the components of velocity in axial ( $z$ ) and radial ( $r$ ) directions respectively, as shown in the above Fig. 2. Let  $R(z,t)$  denote the inner radius of the vessel and define a new variable:

$$\eta = \frac{r}{R(z,t)} \quad (4)$$

We also assume that the pressure  $P$  is uniform within the cross section, so that  $P$  is independent of the radial coordinate,  $\eta$ , i.e.  $P=P(z,t)$ . We can rewrite the above equations in a new coordinate  $(\eta, \theta, z)$  as

$$\frac{\partial u}{\partial t} - \frac{1}{R} \left( \eta \left( u \frac{\partial R}{\partial z} + \frac{\partial R}{\partial t} \right) - w \right) \frac{\partial u}{\partial \eta} + u \frac{\partial u}{\partial z} = -\frac{1}{\rho} \frac{\partial P}{\partial z} + \frac{\nu}{R^2} \left( \frac{\partial^2 u}{\partial \eta^2} + \frac{1}{\eta} \frac{\partial u}{\partial \eta} \right) \quad (5)$$

$$\frac{\partial w}{\partial t} + \frac{1}{R} \left( \eta \left( u \frac{\partial R}{\partial z} + \frac{\partial R}{\partial t} \right) - w \right) \frac{\partial w}{\partial \eta} + u \frac{\partial w}{\partial z} = \frac{\nu}{R^2} \left( \frac{\partial^2 w}{\partial \eta^2} + \frac{1}{\eta} \frac{\partial w}{\partial \eta} - \frac{w}{\eta^2} \right) \quad (6)$$

$$\frac{1}{R} \frac{\partial w}{\partial \eta} + \frac{w}{\eta R} + \frac{\partial u}{\partial z} - \frac{\eta}{R} \frac{\partial R}{\partial z} \frac{\partial u}{\partial \eta} = 0 \quad (7)$$

where we assume:

$$\frac{\partial^2 u}{\partial z^2} \ll 1, \quad \frac{\partial^2 w}{\partial z^2} \ll 1, \quad \frac{\partial P}{\partial r} \ll 1$$

The boundary conditions for the above equations in  $\eta$  axis are:

$$w(\eta, z, t) \Big|_{\eta=0} = 0, \quad w(\eta, z, t) \Big|_{\eta=1} = \frac{\partial R}{\partial t}, \quad u(\eta, z, t) \Big|_{\eta=1} = 0, \quad \frac{\partial u}{\partial \eta} \Big|_{\eta=0} = 0 \quad (8)$$

The basic idea of this hemodynamic modeling provided by [14] is to assume that the velocity profile in the axial direction can be expressed in the following polynomial form:

$$u(\eta, z, t) = \sum_{k=1}^N q_k (\eta^{2k} - 1) \quad (9)$$

The velocity profile in the radial direction is also expressed as:

$$w(\eta, z, t) = \frac{\partial R}{\partial z} \eta w + \frac{\partial R}{\partial t} \eta - \frac{\partial R}{\partial t} \frac{1}{N} \eta \sum_{k=1}^N \frac{1}{k} (\eta^{2k} - 1) \quad (10)$$

For simplicity, we choose  $N=1$  in this report, such as

$$u(\eta, z, t) = q(z, t) (\eta^2 - 1) \quad (11)$$

$$w(\eta, z, t) = \frac{\partial R}{\partial z} \eta w + \frac{\partial R}{\partial t} \eta - \frac{\partial R}{\partial t} \eta (\eta^2 - 1) \quad (12)$$

By plugging eqs.(11) and (12) into eqs.(5) and (7), we obtain the dynamic equations of  $q(z,t)$  and  $R(z,t)$  as:

$$\frac{\partial q}{\partial t} - \frac{4q}{R} \frac{\partial R}{\partial t} - \frac{2q^2}{R} \frac{\partial R}{\partial z} + \frac{4v}{R^2} q + \frac{1}{\rho} \frac{\partial P}{\partial z} = 0 \quad (13)$$

$$2R \frac{\partial R}{\partial t} + \frac{R^2}{2} \frac{\partial q}{\partial z} + q \frac{\partial R}{\partial z} = 0 \quad (14)$$

Complete derivations of the above equations are found in [14]. Let us define cross-sectional area  $S(z,t)$  and blood flow  $Q(z,t)$  as

$$S = \pi R^2, \quad Q = \iint_S u d\eta = \frac{1}{2} \pi q R^2$$

Then, eqs.(13) and (14) can be re-written in terms of  $Q$  and  $S$  as:

$$\frac{\partial Q}{\partial t} - \frac{3Q}{S} \frac{\partial S}{\partial t} - \frac{2Q^2}{S^2} \frac{\partial S}{\partial z} + \frac{4\pi v}{S} Q + \frac{S}{2\rho} \frac{\partial P}{\partial z} = 0 \quad (15)$$

$$\frac{\partial S}{\partial t} + \frac{\partial Q}{\partial z} = 0 \quad (16)$$

### ***Viscoelastic Model of Arterial Wall***

To study the hemodynamics of arterial blood flow, a modeling of the viscoelastic behavior of the arterial wall is essential. In this report, we will derive a constitutive law of the arterial wall from stress-strain relationship of the material. Let  $\sigma_\theta$  and  $\sigma_t$  be the circumferential stress and tangential stress respectively, as shown in Figure 3. Ignoring the inertia of the arterial wall and the external pressure, equilibrium with the blood pressure gives:

$$PR = \sigma_\theta e - \sigma_t e R \frac{\partial^2 R}{\partial z^2} \quad (17)$$

where  $R(z,t)$  and  $e$  are the radius of the arterial vessel and the thickness of the arterial wall respectively.

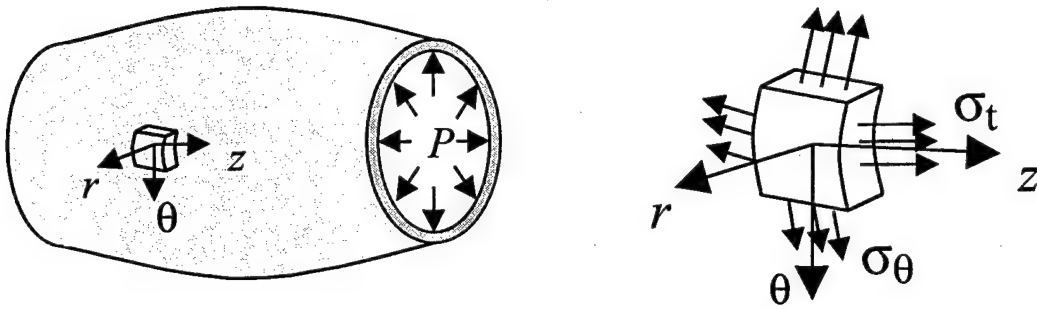


Figure 3: State of stress in a thin-walled, elastic blood vessel

From the geometric compatibility of the blood vessel, we get an expression of strains such as

$$\varepsilon_\theta = \frac{R - R_0}{R_0}, \quad \varepsilon_t = \sqrt{1 + \left( \frac{\partial R}{\partial z} \right)^2} - 1 \quad (18)$$

where  $\varepsilon_\theta$  and  $\varepsilon_t$  are circumferential and tangential strains respectively, and the constant  $R_0$  is the radius of the artery when  $P(z, t) = 0$  and the system is in a steady state.

The most widely used model to describe the viscoelastic properties of the arterial wall is the Kelvin-Voigt model [23], in which the stress-strain relationship is described as:

$$\sigma_\theta = E\varepsilon_\theta + \eta \frac{\partial \varepsilon_\theta}{\partial t}, \quad \sigma_t = E\varepsilon_t + \eta \frac{\partial \varepsilon_t}{\partial t} \quad (19)$$

where  $E$  is the elastic modulus and  $\eta$  is the damping coefficient. By plugging eqs.(18) and (19) with  $S_0 = \pi R_0^2$  and eliminating second and higher order terms, we get the following equation as the viscoelastic constitutive law of the arterial wall:

$$P = \frac{\sqrt{\pi} E e}{S \sqrt{S_0}} \left( S + \frac{\eta}{2E} \frac{\partial S}{\partial t} - \sqrt{S_0 S} \right) \quad (20)$$

### ***Discretization of Partial Differential Equations***

The above nonlinear, partial differential equations given in eqs.(15), (16) and (20) are discretized and transformed into state equations using a finite-difference method. First, the segment of the artery (length  $L$ ) is equally divided by  $N$  grids with a step size of  $\Delta z = L/(N-1)$ . The mesh points in the finite difference grids are represented by  $j$ , where  $j = 1, 2, \dots, N$  and  $N > 2$ . If the length of the arterial element  $\Delta z$  is sufficiently small then it is possible to approximate – in each section – the derivatives with respect to the axial coordinate  $z$  with the following finite difference scheme:

$$\frac{\partial S_i}{\partial z} = \frac{S_{i+1} - S_i}{\Delta z}, \quad \frac{\partial P_i}{\partial z} = \frac{P_{i+1} - P_i}{\Delta z}, \quad \frac{\partial Q_i}{\partial z} = \frac{Q_i - Q_{i-1}}{\Delta z} \quad (21)$$

The constitutive law given in eq.(20) is modeled such that the viscoelasticity applies only at mesh points. An example of the discretization when  $N=4$  is shown in Figure 4. Using the above equations, the hemodynamic model given in eqs.(15), (16) and (20) can be discretized as

$$\frac{dQ_i}{dt} + \frac{3Q_i}{S_i} \frac{Q_i - Q_{i-1}}{\Delta z} - \frac{2Q_i^2}{S_i^2} \frac{S_{i+1} - S_i}{\Delta z} + \frac{4\pi v}{S_i} Q_i + \frac{S_i}{2\rho} \frac{P_{i+1} - P_i}{\Delta z} = 0 \quad (22)$$

$$\frac{dS_i}{dt} = -\frac{Q_i - Q_{i-1}}{\Delta z} \quad (23)$$

$$P_i = \frac{\sqrt{\pi} E e}{S_i \sqrt{S_0}} (S_i - \sqrt{S_0 S_i} + \frac{\eta}{2E} \frac{dS_i}{dt}) \quad (24)$$

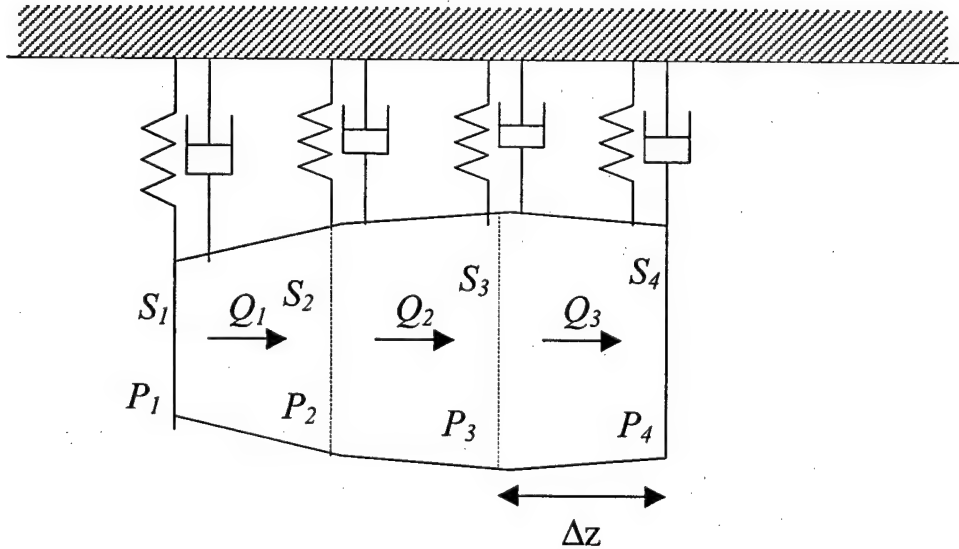


Figure 4: Discretization of the hemodynamic model

To complete the discretization of the hemodynamic model, the boundary condition at proximal ( $P_1, Q_0$ ) and distal ( $P_N, Q_N$ ) extremities of the arterial segment must be defined appropriately.

## 2.2. Upstream Blood Flow

Upstream dynamics extends the proximal boundary ( $P_1, Q_0$ ) up to the heart so that the commonly assumed pattern of the cardiac output can be used as the input to the system. For the simplicity, we use a lumped parameter model to describe the upstream dynamics. A large amount of work has been done in this area. In this report, we apply a four-element modified Windkessel model proposed by Landes [16]. This model has been adopted by many researchers for the analysis of blood pressure waveform of the radial artery [17].

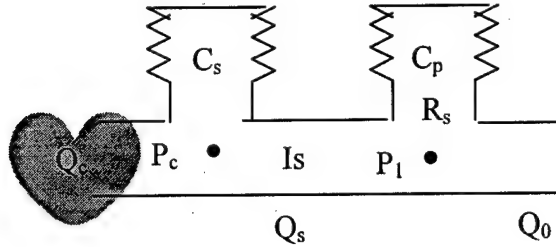


Figure 5: Extended Windkessel model for upstream dynamics

Figure 5 shows the modified Windkessel model. The aorta and major arteries are modeled as a single elastic chamber ( $C_s$ ), which stores the blood ejected from the left ventricle during a systole. The distal vessels are modeled as capacitive ( $C_p$ ) and resistive ( $R_s$ ) elements, through which the blood drains during a diastole. The oscillatory effect of blood propagation is taken into account by introducing an effective mass ( $I_s$ ). The dynamic equations for the upstream are derived as below, where  $Q_c$  is the cardiac output:

$$\frac{dP_c}{dt} = \frac{1}{C_s} (Q_c - Q_s) \quad (25)$$

$$\frac{dQ_s}{dt} = \frac{1}{I_s} (P_c - P_1) \quad (26)$$

$$\frac{dP_1}{dt} = \frac{1}{C_p} (Q_s - Q_0 - \frac{P_1}{R_s}) \quad (27)$$

where  $Q_0$  can be solved from the constitutive law of the arterial wall on the  $1^{st}$  node of the local segment derived in Section 2.1:

$$P_1 = \frac{\sqrt{\pi E e}}{S_1 \sqrt{S_0}} \left( S_1 - \frac{\eta}{2E} \frac{Q_1 - Q_0}{\Delta Z} - \sqrt{S_0 S_1} \right) \quad (28)$$

### 2.3 Downstream Blood Flow

Similarly, the downstream dynamics extends the distal boundary ( $P_N, Q_N$ ) to the end of arteries. Veins can be easily modeled as a reservoir, when our concern is the arterial hemodynamics. Since our approach is currently applied to digital arteries, which is close to veins, the inertia term in the downstream is negligible. The classic Windkessel model is used to model the downstream as shown in Fig. 6, where  $C_d$  is the compliance of the vessels in downstream,  $R_{cd}$  is the characteristic resistance,  $R_{pd}$  is the peripheral resistance,  $P_v$  is an effort source if no interest is in venous dynamics.

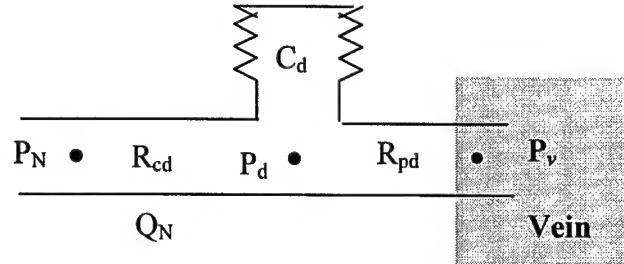


Figure 6: Classic Windkessel model for downstream dynamics

The dynamic equation for the downstream can be written as:

$$\frac{dP_d}{dt} = \frac{1}{C_d} (Q_N - \frac{P_d - P_v}{R_{pd}}) \quad (29)$$

where  $Q_N$  can be solved from the algebraic equation and the constitutive law of the arterial wall on the  $N^{th}$  node:

$$Q_N = \frac{P_N - P_d}{R_{cd}} \quad (30)$$

$$P_N = \frac{\sqrt{\pi E e}}{S_N \sqrt{S_0}} (S_N - \frac{\eta}{2E} \frac{Q_N - Q_{N-1}}{\Delta Z} - \sqrt{S_0 S_N}) \quad (31)$$

## 2.4 Entire Arterial Model

In this section, the models for the local arterial hemodynamics, the upstream and downstream dynamics, described in Section 2.1, 2.2 and 2.3 respectively, are integrated to represent an entire systematic arterial stream.

The entire arterial model has  $(2N+3)$  state variables and two inputs, defined as following:

$$x = [P_c \quad Q_s \quad P_1 \quad Q_1 \quad \cdots \quad Q_{N-1} \quad S_1 \quad \cdots \quad S_N \quad P_d]^T : (2N+3) \times 1 \quad (32)$$

$$u = [Q_c, P_v]^T : (2 \times 1) \quad (33)$$

From the continuity equation given by (23) and the constitutive law of the arterial wall given by (24), the pressures  $P_i$  can be expressed in terms of the above state variables as:

$$P_i = \frac{\sqrt{\pi E e}}{S_0 \sqrt{S_i}} (S_i - \sqrt{S_0 S_i} + \frac{\eta}{2E} \frac{dS_i}{dt}) = \frac{\sqrt{\pi E e}}{2S_0 \sqrt{S_0}} (S_i - S_0 - \frac{\eta}{E \Delta z} (Q_i - Q_{i-1})) \quad \text{for } i = 1, 2, \dots, N \quad (34)$$

For further analysis of the nature of the hemodynamic behavior of the arterial flow, we linearized the dynamic model for local arterial segment given in (22) and (23) as follows:

$$\frac{dQ_i}{dt} + \frac{4\pi v}{S_0} Q_i - \frac{\sqrt{\pi} e \eta}{4\rho \Delta z^2 \sqrt{S_0}} (Q_{i+1} - 2Q_i + Q_{i-1}) + \frac{\sqrt{\pi} E e}{4\rho \Delta z \sqrt{S_0}} (S_{i+1} - S_i) = 0 \text{ for } i = 1, \dots, N-1 \quad (35)$$

$$\frac{dS_i}{dt} = -\frac{Q_i - Q_{i-1}}{\Delta z} \text{ for } i = 1, 2, \dots, N \quad (36)$$

From the dynamics equations for the upstream, eqs. (25) – (28), the downstream, eqs. (29) – (31), and the local arterial segment, eqs. (34) – (36), we can derive the state-space representation of the extended model in the following format:

$$\dot{x} = Ax + Bu \quad (37)$$

where  $A$  and  $B$  are:

$$A = \begin{bmatrix} A_{up:3 \times (2N+3)} \\ A_{local:(2N-1) \times (2N+3)} \\ A_{down:1 \times (2N+3)} \end{bmatrix} : (2N+3) \times (2N+3) \quad (38)$$

$$B = \begin{bmatrix} \frac{1}{C_s} & 0 \\ 0 & 0 \\ \vdots & \vdots \\ 0 & 0 \\ 0 & \frac{1}{C_d R_{pd}} \end{bmatrix} : (2N+3) \times 2 \quad (39)$$

### 3. Design of Kalman Filter

Kalman filters are popularly used to estimate unknown state variables, which cannot be measured directly with limited, noisy measurements of the system. To formulate a Kalman filter for the above hemodynamic system, the observation equation must be defined based on the instrumentation methods to be used. As stated previously, the objective of the Kalman filter is to continuously estimate the blood pressure merely from noninvasive and non-intrusive sensors on a peripheral skin surface. In this paper, we formulate and design a Kalman filter based on an electrical impedance plethysmograph (EIP) and two photo plethysmographs.

A photo plethysmograph employs a pair of LED and photo detector to monitor the variation of the arterial diameter. Suppose that a photo plethysmograph is attached on the skin surface over each of the both ends of the arterial segment under consideration. Then, the two observation functions  $y_1$  and  $y_2$  can be simply described by using state variables as:

$$y_1(t) = S_1(t), \quad y_2(t) = S_N(t) \quad (40)$$

EIP uses four electrodes to measure the electrical impedance of the arterial segment surrounded by the electrodes. EIP is known to provide the absolute measurement of volumetric change of the

arterial segment. Therefore, supposing that the electrodes are located at the both ends of the arterial segment under consideration, the output of EIP  $y_3$  can be described in terms of the state variables as:

$$y_3(t) = V(t) = \frac{1}{2}S_1\Delta z + (S_2 + \dots + S_{N-1})\Delta z + \frac{1}{2}S_N\Delta z \quad (41)$$

Defining  $y(t) = [y_1(t), y_2(t), y_3(t)]^T$ , the observation equation can finally be defined as

$$y(t) = Cx(t) \quad (42)$$

where

$$C = \begin{bmatrix} \underbrace{0 \dots 0}_{N+2} & \underbrace{1 \dots 0}_{N} & 0 & 0 \\ 0 \dots 0 & 0 \dots 0 & 1 & 0 \\ 0 \dots 0 & \frac{\Delta z}{2} & \Delta z \dots \Delta z & \frac{\Delta z}{2} & 0 \end{bmatrix} : 3 \times (2N+3)$$

Since a process noise and a measurement noise inherently exist, the state equations given in eqs. (37) and (42) must be extended as:

$$\dot{x} = Ax + Bu + Fv \quad (43)$$

$$y = Cx + w \quad (44)$$

where  $v$  and  $w$  are white noise processes, having known spectral density matrices,  $V$  and  $W$ , respectively.

Using the above equations, the state variables  $x(t)$  can be estimated by the following dynamic equations:

$$\dot{\hat{x}} = A\hat{x} + Bu + K(y - \hat{y}) \quad (45)$$

$$\hat{y} = C\hat{x} \quad (46)$$

where  $\hat{y}(t)$  is the estimated measurement,  $\hat{x}(t)$  is the estimated state variables, and  $K$  is the Kalman gain matrix, which is updated as:

$$K = MC^T W^{-1} \quad (47)$$

$$\dot{M} = AM + MA^T - MC^T W^{-1} CM + FV F^T \quad (48)$$

where  $M(t)$  is the covariance matrix of the state estimation error  $\tilde{x}(t) = x(t) - \hat{x}(t)$ . In the above derivation, we assume that  $v$  and  $w$  are uncorrelated. By updating the Kalman gain based on the nature of the process noises as described in the above equation, the Kalman filter provides the

optimal estimation of the state variables. Finally, the internal blood pressures  $P_i(t)$  can be estimated by substituting the estimated state variables into (34) as:

$$\hat{P}_i = \frac{\sqrt{\pi} E e}{\hat{S}_i \sqrt{s_0}} (\hat{S}_i - \frac{\eta}{2E\Delta z} (\hat{Q}_i - \hat{Q}_{i-1}) - \sqrt{\hat{S}_i S_0}) \text{ for } i=1,2,\dots,N \quad (49)$$

The main issue in designing the above Kalman filter is whether the system given in (43) and (44) is observable or not. If the system is not observable, we cannot construct a Kalman filter to estimate the whole state variables. As it is found in the next section, the above system is not observable. However, the observability analysis to be provided in the next section will prove that blood pressure given in (49) can be estimated from an observable subspace of the system.

## 4. Observability Analysis

### 4.1 Observability Test

There are many criteria for testing the observability of a system (e.g. [18] for a textbook). The most noticeable test for the observability is so called, “Algebraic Controllability Theorem,” and it simply states:

A system  $(A, C)$  of order  $n$  is observable if and only if the rank of the observability test matrix

$$O = [C^T, A^T C^T, \dots, (A^T)^{n-1} C^T] \quad (50)$$

equals to  $n$ .

This is arguably the easiest criterion to test the observability of a system.

The above observability test was applied to the  $(2N+3)$ -th order system given by (37) and (42), and it was found that the rank of the observability matrix is 4 when  $N=3$  or 3 when  $N>3$ , which is smaller than the order of the system. Therefore, the system is not observable, and a state estimator such as a Kalman filter cannot re-construct the whole state variables. However, it will be found that blood pressure given in (49) can be estimated from a part of the state variables and that part lies in the observable subspace of the state space. Namely, the blood pressure can be estimated from a set of the state variables, which are observable with the Kalman filter designed in the previous section. To prove this argument, we first decompose the whole state variables into an observable subspace and an unobservable subspace.

### 4.2 Observable/Unobservable Sub-space Decomposition

We use a staircase algorithm for the state-space decomposition. Letting  $r$  be the rank of the observability matrix given in (50), for the system described by (37) and (42), there exists a decoupling similarity transformation matrix  $T$ , such that

$$\bar{A} = TAT^T = \begin{bmatrix} A_{uo} : (2N+3-r) \times (2N+3-r) & A_{12} : (2N+3-r) \times r \\ 0 & A_o : r \times r \end{bmatrix} \quad (51)$$

$$\bar{C} = CT^T = [0 \quad C_o : 3 \times r]$$

Namely, the state equation can be decomposed into an observable subspace and an unobservable subspace, and the  $r$ -dimensional observable subspace is represented by  $[A_o, C_o]$ . Suppose  $T$  is expressed as

$$T = \begin{bmatrix} T_{uo}^T : (2N+3) \times (2N+3-r) & T_o^T : (2N+3) \times r \end{bmatrix} \quad (52)$$

Then, the transformed state variables  $z$  are decomposed into the observable state variables  $z_o$  and the unobservable state variables  $z_{uo}$  as:

$$z = \begin{bmatrix} z_{uo} : (2N+3-r) \times 1 \\ z_o : r \times 1 \end{bmatrix} = T^T x = \begin{bmatrix} T_{uo} \\ T_o \end{bmatrix} x \quad (53)$$

Consequently, the set of the transformed state variables  $z_o = T_o x$  is observable from the output given in (42) using the Kalman filter designed in Section 3.

### 4.3 Blood Pressure Estimation from Observable Subspace

#### *Analysis*

Blood pressure can be calculated from state variables, according to eq. (49). This equation can be expressed in a vector form such as:

$$P_i = G_i x \quad (54)$$

where  $G_i$  is a  $(2N+3) \times 1$  row vector.

From the state-space analysis, it is found that there exists a  $r \times 1$  row vector  $H$  such that  $G = HT_o$ . Therefore, blood pressure in (54) can be described as

$$P_i = G_i x = HT_o x = Hz_o \quad (55)$$

Namely, blood pressure can be estimated from the observable variables  $z_o$ .

#### *Example*

We discuss an example when  $N = 3$  to better illustrate the scheme of blood pressure estimation from the observable subspace. In this case, the overall system is 9<sup>th</sup> order, and the state variable is defined as:

$$x = [P_c \quad Q_s \quad P_1 \quad Q_1 \quad Q_2 \quad S_1 \quad S_2 \quad S_3 \quad P_d]^T$$

The local digital arterial segment is depicted in Fig. 7, where the output function is the same as that defined in eq. (42).

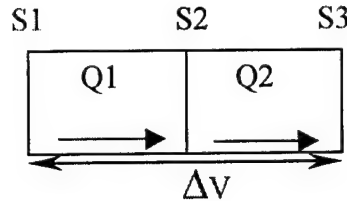


Figure 7: Local digital arterial segment for observability analysis

From the observability test as described in Section 4.1, we find that the observability matrix has the rank of 4, smaller than 9, the order of the system. Thus the overall system is not observable from this set of outputs.

From the state space decomposition, we find the similarity matrix  $T$ , where

$$T^T = \begin{bmatrix} -0.7769 & 0.6296 & 0.0014 & 0.0056 & 0.0056 & 0 & 0 & 0 & 0 \\ -0.6295 & -0.7770 & 0.0012 & 0.0048 & 0.0048 & 0 & 0 & 0 & 0 \\ -0.0106 & -0.0003 & -0.1741 & -0.6963 & -0.6963 & 0 & 0 & 0 & 0 \\ 0 & 0 & 0.9847 & -0.1231 & -0.1231 & 0 & 0 & 0 & 0 \\ 0 & 0 & 0.1741 & 0.6963 & 0.6963 & 0 & 0 & 0 & 0 \\ 0 & 0 & 0 & 0.7071 & -0.7071 & 0 & 0 & 0 & 0 \\ 0 & 0 & 0 & 0 & 0 & -0.0002 & 1 & -0.0002 & 0 \\ 0 & 0 & 0 & 0 & 0 & 0.7071 & 0 & -0.7071 & 0 \\ 0 & 0 & 0 & 0 & 0 & -0.7071 & -0.0003 & -0.7071 & 0 \end{bmatrix}$$

From eq. (53), we know that  $T_{uo}$ , the first  $2N-r$  ( $2N-r = 5$  in this case) rows of the matrix  $T^T$ , transforms the state space into unobservable subspace, and  $T_o$ , the last  $r$  ( $r = 4$  in this case) rows of the matrix  $T^T$ , transforms the state space into observable subspace. So we can see that, in this case,

$$T_o = \begin{bmatrix} 0 & 0 & 0 & 0.7071 & -0.7071 & 0 & 0 & 0 & 0 \\ 0 & 0 & 0 & 0 & 0 & -0.0002 & 1 & -0.0002 & 0 \\ 0 & 0 & 0 & 0 & 0 & 0.7071 & 0 & -0.7071 & 0 \\ 0 & 0 & 0 & 0 & 0 & -0.7071 & -0.0003 & -0.7071 & 0 \end{bmatrix}$$

The observable state variables are  $Q_2-Q_1$ ,  $S_1$ ,  $S_2$  and  $S_3$ . To estimate internal blood pressure  $P_2$  by eq. (49), we need know  $S_2$  and  $Q_2-Q_1$ . So, the blood pressure  $P_2$  can be estimated from the observable subspace.

$$P_2 = \frac{\sqrt{\pi Ee}}{S_2 \sqrt{S_0}} (S_2 - \frac{\eta}{2E\Delta z} (Q_2 - Q_1) - \sqrt{S_2 S_0})$$

### Sensor Design

The above analysis of the state-space decomposition shows that two PPs and one EIP on an arterial segment can estimate the pressure waveforms using a Kalman filter. Based on these results, we designed a cuff-less ambulatory blood pressure monitoring device. Figure 8 illustrates the sensor configuration. Plethysmographic sensors are located on the two bands, which fit a human finger, and the telemetry transmits signals wirelessly.

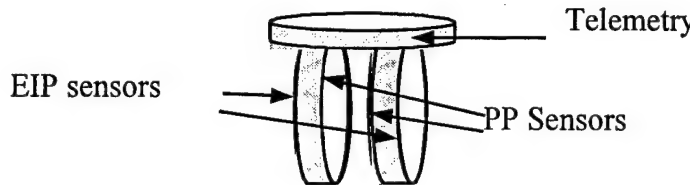


Figure 8: Conceptual diagram of cuff-less ambulatory pressure monitoring

## 5. Simulation

Numerical simulations have been conducted to verify the approach proposed in this paper. The hemodynamic process was simulated using MATLAB on a PC, and the Kalman filter for the blood pressure estimation was applied to the simulated process. The pressure estimated by the Kalman Filter was compared with the digital blood pressure measured by an arterial tonometer.

### 5.1 Simulation Setup

The simulation was conducted using hemodynamic parameters of a digital artery because many finger plethysmographs are commercially available and easy to be miniaturized. The following parameter values were used for the simulation:

Blood density  $\rho = 1.06 \text{ gr/cm}^3$ ,  
 Blood viscosity  $\mu = 0.04 \text{ poise}$ ,  
 Radius of digital artery  $r = 0.5 \text{ mm}$ ,  
 Arterial wall viscosity  $\eta = 100 \text{ dyn}\cdot\text{s}/\text{cm}^3$ ,  
 Arterial wall elastic modulus  $E = 7 \times 10^5 \text{ N/m}^2$ ,  
 Characteristic resistance  $R_{cd} = 1.1 \times 10^4 \text{ dyn}\cdot\text{s}/\text{cm}^5$ ,  
 Peripheral resistance  $R_{pd} = 1.2 \times 10^5 \text{ dyn}\cdot\text{s}/\text{cm}^5$ ,  
 Downstream compliance  $C_d = 1.1 \times 10^{-4} \text{ cm}^5/\text{dyn}$ ,  
 Length of digital artery segment  $L = 1 \text{ cm}$ ,  
 Nodes of the system  $N = 3$ .

The above parameter values were obtained from published literatures such as [14] and [19]-[22]. The distributed model of a digital artery used in simulation is shown in Figure 9. For the simplicity of the simulation, we did not include the upstream dynamic in the arterial hemodynamic model. Instead, we used measured blood pressure signals at Section  $S_1$  as an input

to the arterial model. The definitions of the inputs, state variables and outputs in this simplified model are:

$$\text{inputs } u = [P_1 \ P_v]^T, \\ \text{state variables } x = [Q_1 \ Q_2 \ S_1 \ S_2 \ S_3 \ P_d]^T, \\ \text{outputs } y = [S_1 \ V \ S_3]^T.$$

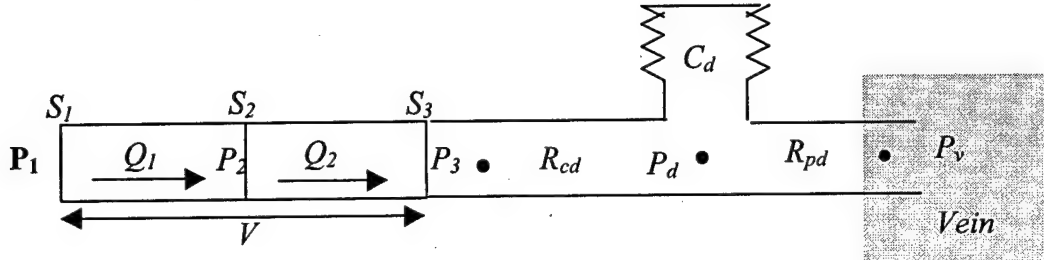


Figure 9: Artery model used for simulation

In this setup of simulation, similarity transformation matrix  $T$  can be calculated numerically:

$$T^T = \begin{bmatrix} -0.0001 & -0.0001 & 0 & 0 & 0 & 1 \\ -0.7071 & -0.7071 & 0 & 0 & 0 & -0.0001 \\ 0.7071 & -0.7071 & 0 & 0 & 0 & 0 \\ 0 & 0 & 0 & 1 & 0 & 0 \\ 0 & 0 & 0.7071 & 0 & -0.7071 & 0 \\ 0 & 0 & -0.7071 & 0 & -0.7071 & 0 \end{bmatrix}$$

where the last four rows of  $T^T$  matrix represent the observable subspace  $T_o$ .

Input  $P_1$  is measured by an arterial tonometer (MILLAR, TX). The other input, venous pressure  $P_v$  is assumed as a constant (20mmHg). A profile of input  $P_1$  is shown in Figure 10.

Outputs  $S_1$  and  $S_3$  are measured by a pulse plethysmograph (CB Sciences, Dover, NH) and  $V$  is measured by an electrical impedance plethysmograph (Parks Medical Electronics, Aloha, OG). The measurements are shown in Figure 11.

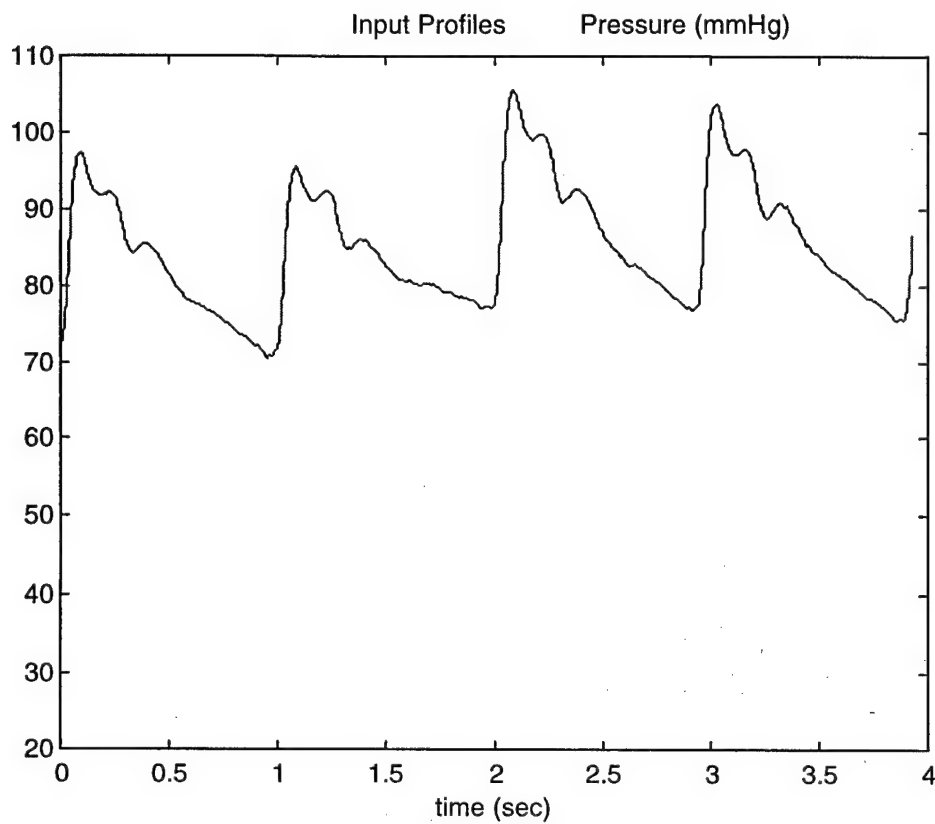


Figure 10: System input – blood pressure on the boundary

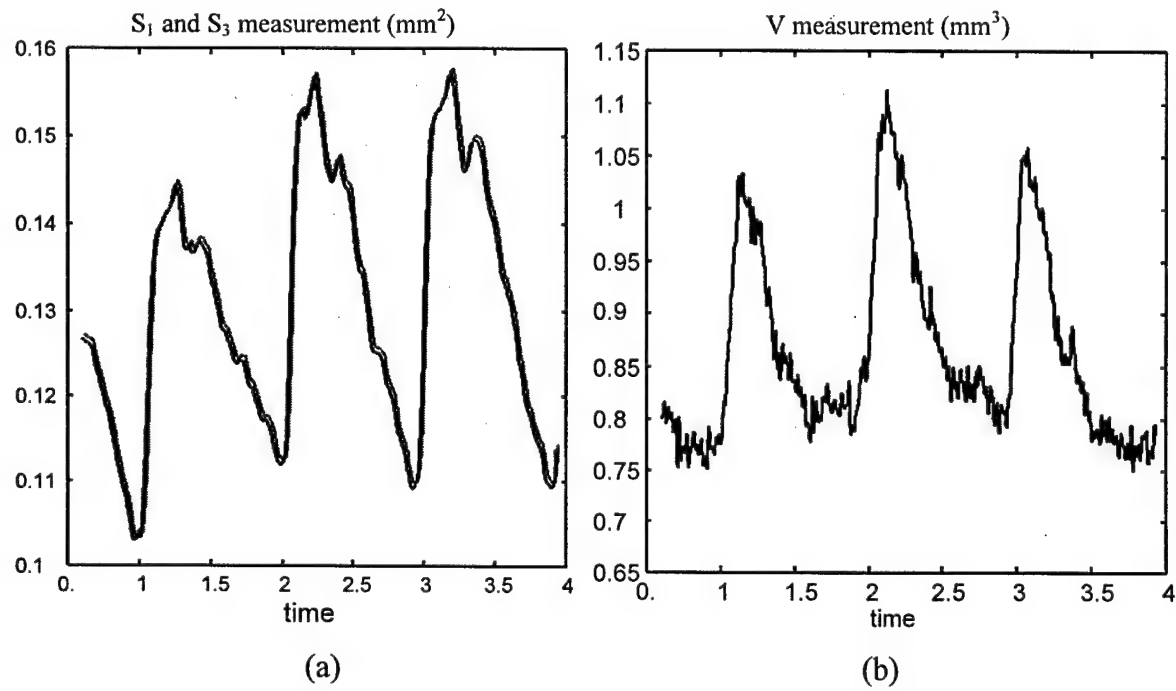


Figure 11: System outputs (a) arterial section area  $S_1$  and  $S_3$  (b) volumetric change  $V$

## 5.2 Simulation Results

The Kalman filter constructed in Section 3 is simulated in MATLAB to estimate state variables and blood pressure.  $P_I$ ,  $P_v$  ( $u$  in eq. (45), depicted in Fig. 9) and measurement  $Y_1$ ,  $Y_2$ ,  $Y_3$  ( $y$  in eq. (45), depicted in Fig. 10) are feed into a Kalman Filter. The Error covariance and Kalman filter gain are calculated for each sample of the sequence and state variables are updated according to eq. (47) and (48). Necessary state variables are then substituted into eq. (55) to estimate blood pressure.

Figure 12 shows the comparison between the measurement and Kalman Filter estimation of the output in which we can see that the Kalman Filter works very well to reduce white Gaussian noises as expected.

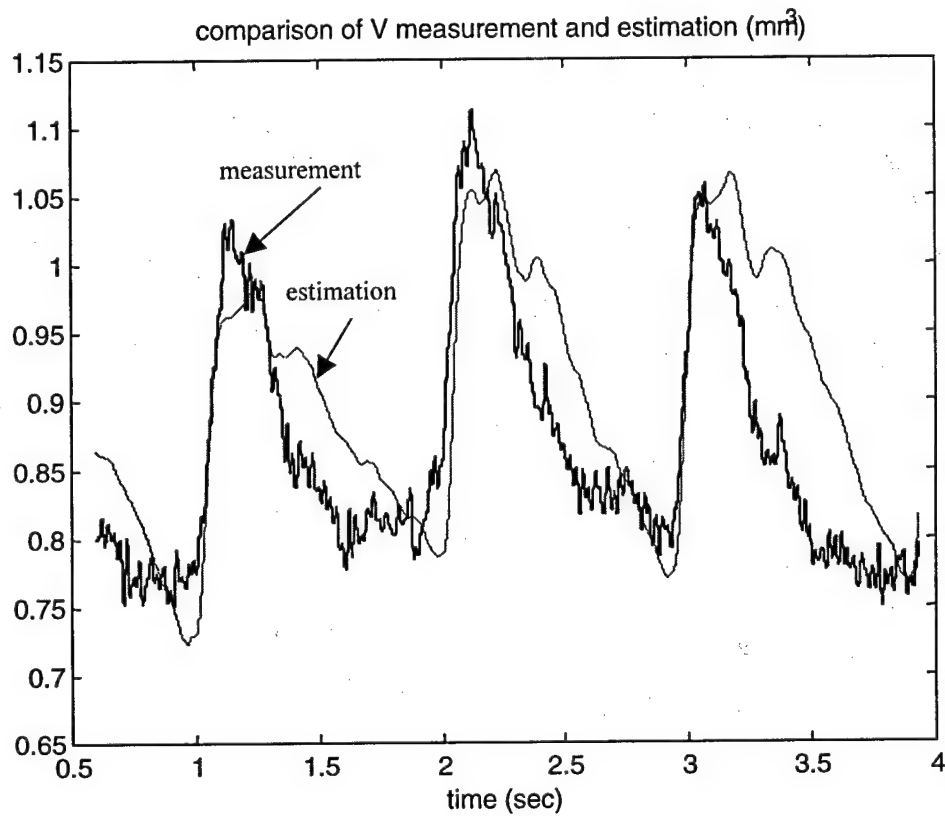


Figure 12: Comparison of output measurement  $V$  and estimation

Figure 13 shows the comparison between the measurement and the Kalman filter estimation of blood pressure.

From the results shown in Fig. 12 and Fig. 13, we can conclude that a Kalman filter is very robust to noise, especially white noise. It is feasible to estimate blood pressure accurately based on the measurements from plethysmographs and a hemodynamic model.

## 6. Conclusions

A new method of noninvasive, continuous monitoring of arterial blood pressure has been presented. A prototype for this approach has been proposed and experiments have been conducted on the fingers to verify the approach.

Fingers are instrumented with two photo plethysmographs and one electrical impedance plethysmograph in order to monitor the dynamic behavior of the arterial blood flow. An observability analysis showed that internal arterial blood pressure in the arterial segment can be estimated based on the measurements of this set of sensor combination, even though the observability condition of the system were not met. Measured signals from these noninvasive sensors on the digital arterial segment are integrated to estimate the state variables in the segment based on a hemodynamic model. A Kalman filter was constructed and simulated to estimate state variables and blood pressure. Simulation results indicate that the approach can generate an accurate estimation of the arterial blood pressure in real-time even from noisy sensor signals.

Unlike traditional blood pressure measurements, this approach uses very simple plethysmographic sensors, which reduces the obstructions of the sensors to the human and makes the miniaturization easier. Meanwhile, it is feasible to continuously monitor blood pressure in a long-term.

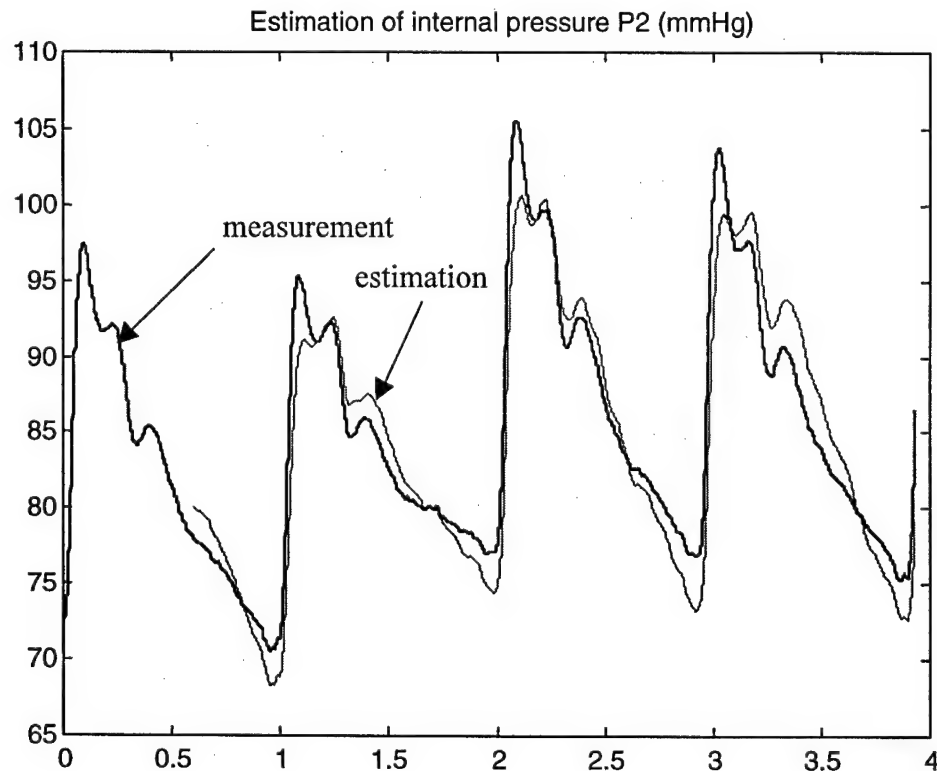


Figure 13: Digital blood pressure – estimation by a Kalman Filter vs. measurement by an arterial tonometer

## References

- [1] J. W. Clark, et al., "A Two-Stage Identification Scheme for the Determination of the Parameters of a Model of the Left Heart and Systemic Circulation," *IEEE Trans. On Biomed. Eng.*, Vol. 27, pp. 20-29, Jan., 1980
- [2] W. Welkowitz, Q. Cui, Y. Qi and J. Kostis, "Noninvasive Estimation of Cardiac Output," *IEEE Trans. On Biomed. Eng.*, Vol. 38, pp. 1100-1105, Nov., 1991
- [3] E. T. Ozawa, "A Numerical Model of the Cardiovascular System for Clinical Assessment of the Hemodynamic State," Ph.D. Thesis, Dept. of Health Sciences and Technology, MIT, Sep., 1996
- [4] M. Guarini, J. Urzua, A. Cipriano, and W. Gonzalez, "Estimation of Cardiac Function From Computer Analysis of the Arterial Pressure Waveform," *IEEE Trans. On Biomed. Eng.*, Vol. 45, pp. 1420-1428, Dec. 1998
- [5] G. Pressman and P. Newgard, "A Transducer for Continuous External Measurement of Arterial Blood Pressure," *IEEE Trans. On Biomed. Eng.*, Vol. 10, pp. 73-81, 1961
- [6] J. Penaz, "Photo-electric Measurement of Blood Pressure, Volume and Flow in the Finger," *Digest of the 10-th Int. Conf. On Medical and Biolog. Eng.*, 1973
- [7] K. H. Wesseling, "Non-invasive, Continuous, Calibrated Blood Pressure by the Method of Penaz," *Blood Pressure Measurement and Systemic Hypertension*, pp.163-175, Medical World Press.
- [8] C. Tase and A. Okuaki, "Noninvasive Continuous Blood Pressure Measurement – Clinical Application of FINAPRES –," *Japanese J. of Clinical Monitor*, Vol. 1, pp.61-68, 1990
- [9] K. Yamakoshi, H. Shimazu and T. Togawa, "Indirect Measurement of Instantaneous Arterial Blood Pressure in the Human Finger by the Vascular Unloading Technique," *IEEE Trans. On Biomed. Eng.*, Vol. 27, pp. 150-155, 1980
- [10] A. Kawarada, H. Shimazu, H. Ito, and K. Yamakoshi, "Ambulatory Monitoring of Indirect Beat-to-Beat Arterial Pressure in Human Fingers by a Volume-Compensation Method," *Med Biol Eng Comput*, Vol. 34, pp. 55-62, Jan. 1991
- [11] M. S. Grewal and A. P. Andrews, "Kalman Filtering: Theory and Practice," Prentice Hall, 1993
- [12] J. C. Stettler, P. Niederer and M. Anliker, "Theoretical Analysis of Arterial Hemodynamics including the Influence of Bifurcations," *Annals of Biomed. Eng.*, Vol. 9, pp. 145-164, 1981
- [13] G. A. Johnson, H. S. Borovetz, and J. L. Anderson, "A Model of Pulsatile Flow in a Uniform Deformable Vessel," *J. of Biomechanics*, Vol. 25, pp. 91-100, 1992
- [14] E. Belardinelli and S. Cavalcanti, "A New Nonlinear Two-Dimensional Model of Blood Motion in Tapered and Elastic Vessels," *Comput. Biol. Med.*, Vol. 21, pp. 1-13, 1991
- [15] E. Belardinelli and S. Cavalcanti, "Theoretical Analysis of Pressure Pulse Propagation in Arterial Vessels," *J. of Biomechanics*, Vol. 25, pp. 1337-1349, 1992

- [16] G. Landes. "Einige untersuchungen an elektrischen analogie-schaltungen zum kreislauf-system." *Z. Biol.*, 101:410, 1943, Written in German.
- [17] K. P Clark. "*Extracting new information from the shape of the blood pressure pulse,*" Master's thesis, Massachusetts Institute of Technology, Cambridge, MA, 1991
- [18] T. Kailath, "*Linear Systems,*" Prentice-Hall, NJ, 1980
- [19] W. S. Spector, "*Handbook of Biological Data,*" Philadelphia Publisher, 1956
- [20] B. M. Leslie, et el., "Digital Artery diameters: An anatomic and clinical study," *Journal of Hand Surgery*, Vol. 12A, No. 5, Part 1, pp740-743, Sep. 1987
- [21] H. Power, "*Bio-fluid Mechanics,*" Computational Mechanics Publications, Boston, 1995.
- [22] K.J. Li, "*Arterial System Dynamics,*" New York University Press, New York, 1987
- [23] Y. C. Fung, "*Biomechanics : mechanical properties of living tissues,*" Springer-Verlag, New York, 1993

# **The Doppler Necklace: Wearable and Noninvasive Ultrasound Sensors for Continuous Monitoring of Blood Flow in the Common Carotid Artery**

**H. Harry Asada**  
Principal Investigator

**Elie Awad**  
Graduate Research Assistant

## **ABSTRACT**

A novel design for a wearable and non-invasive ultrasound Doppler blood flow measuring device is presented. The device consists of an array of piezoelectric transducers that mount at the neck and generate different ultrasonic beams directed at the common carotid artery. The Doppler frequency shift generated by the moving blood is then processed to reconstruct the centerline velocity of the artery as well as to provide an estimate of the velocity profile and other physiological parameters. The presented design covers key issues relevant to making this technology wearable mainly handling the location uncertainty of the artery, securing the transducers to the skin and interpreting the measurement without human assistance with the restriction of keeping the technical complexity of the device low for all cases.

The array of transducers is designed to enable the coverage of a wide sector in the neck that encompasses the artery. Different beams can be produced by the array depending on the number of transducers that are excited. The centerline velocity of the artery is used as a criterion to decide which transducers are favorably oriented and hence should be operated. In addition, the array is designed to minimize the skin coverage area by spacing the transducers.

The report builds upon theoretical analysis and includes computer simulation and experimental illustration of the key ideas.

## 1. Introduction

Cardiovascular diseases are a prevalent cause of death in the contemporary society, and monitoring a patient's cardiovascular system is a critical part of today's healthcare system.

The current practice of continuous non-invasive monitoring of the cardiac state is through the use of ambulatory electrocardiogram (EKG) devices: electrodes are glued onto the chest of a patient and pick up the voltage signals that trigger the contraction of the heart muscles. EKG is thus a measure of a 'control signal' or input to the heart and Miyamoto et al. (1989) considered that it may not reflect the real functions of the heart as good as a measurement of blood flow. From a modeling perspective, the heart is not easily assessed by measuring its input only because it behaves as a nonuniform and nonlinear combination of 'constant volume' and 'constant pressure' idealized pumps [11].

Blood pressure is another important variable of the cardiovascular state. It is one of the most useful diagnostic tools due to the empirical relations that have been established between blood pressure parameters and pathological conditions. However, pressure is not a better index for diagnosis than volumetric flow rates [11]. The more widespread adoption of the former is mainly due to the fact that clinical procedures to measure it were developed earlier and are less complex than the latter. In fact, the occlusive cuff method of measuring systolic and diastolic blood pressure was first introduced by Riva-Rocci in 1896 [12], while measuring blood velocities using continuous wave ultrasound Doppler was first suggested more than half a century later by Satomura in 1957 [1]. Interestingly, pressure measurement has found its way into home healthcare while the ultrasound technology has strictly evolved within the hospital environment: current ultrasound devices are highly sophisticated and often combine velocity measuring capabilities with real time imaging of the heart or the blood vessels. Adapting this technology to home healthcare poses unique issues such as eliminating the need for human assistance while keeping the technical complexity (and hence cost) low. Human assistance plays a dual role of operating the ultrasound equipment and analyzing the measurements. The purpose of our research is to design an easy-to-use wearable Doppler sensor in which the ultrasound transducers are secured to the skin of the patient and a reliable measurement is possible despite motion and location uncertainty of the

target vessel. In addition, the sensor transmits the measurement to a computer that would analyze it in a continuous and systematic way. The device described in this report aims at monitoring the centerline velocity in the common carotid artery which can be used as an index to reflect the cardiac performance [7] as well as diastolic cerebral flow [10]. In addition to that, the arterial wall velocities picked up by the sensor carry information about the time rate of change of the pressure pulse waveform. Also, under conditions of uniform insonification of the artery, the spectral distribution of the measurement can be used to calculate a dimensionless estimate of absolute flow in the carotid artery without the need of measuring the vessel area.

The Doppler Necklace with its ability to monitor the different variables mentioned earlier will have a great impact in healthcare practice. In addition, it will open new opportunities on the research level because the measurement taken with the Doppler Necklace can be combined with other simultaneous physiological measurement (such as that of the ring sensor). This enables a better understanding of the human cardiovascular and thermoregulatory system. In terms of practical applications, the Doppler Necklace is not limited to cardiovascular monitoring but other potential uses also exist. One such application is for the early detection of small amounts of dissolved gas bubbles in the blood stream that give rise to characteristic high pitched 'scratching' signals in the ultrasound reading [4] and that can prove fatal if untreated.

## **2. Design of The Doppler Necklace**

The process of designing wearable ultrasound Doppler sensors starts by selecting an appropriate anatomical site to perform the measurement. The sections below start with a description of the reasons why the carotid artery was chosen. This is followed by an overview of the device itself and later sections on individual design issues.

### **2.1 Site Selection**

In principle, the ultrasound Doppler technology can be adapted to measure the blood velocities in basically any artery (for example the digital artery, aorta...). However, the carotid artery was chosen because it has several advantages:

1. The carotid artery is a main non-peripheral vessel (the left carotid artery branches straight up from the aortic arch (fig. 1 – Appendix B)) and is representative of the

cardiovascular state. In fact Matsumoto et al (1992) have observed a good linear correlation between cardiac output and the blood flow volume in the common carotid artery.

2. The common carotid artery branches off into two vessels (figure 1). The inner branch (inner carotid artery) together with the vertebral artery provide the supply of blood to the brain. Matsumoto et al. (1992) had used the common carotid artery flow as an index of cerebral flow. Champagne and Farget (1980) had also reported that during the diastolic phase, flow in the common carotid artery almost equalled that in the inner carotid artery.
3. The common carotid artery lies at a rather shallow depth (figure 1) and is easily accessible with ultrasound. It also exhibits straightness and has minor secondary velocity components.
4. Aesthetically, the transducers (that emit and receive the ultrasound wave) can be incorporated within a necklace or other form of pendant at the neck.

## 2.2 General Description

The 'Doppler necklace' is basically a continuous wave (CW) Doppler system in which a sinusoidal voltage excites a piezoelectric crystal to create an ultrasonic beam. The beam intercepts the target vessel and its interaction with the moving blood cells gives rise to a frequency shift (the Doppler shift). The backscattered ultrasound carrying the Doppler shift is picked up by a receiving crystal and analyzed. A system employing two transducer crystals for transmitting and receiving ultrasound continuously is shown in figure 2. The Doppler Necklace retains the same operating principle: its electronics hardware supplies a sinusoidal excitation to the emitting transducers and separates the frequency shift in the received signal. However, the Doppler Necklace is unique in the way it handles location uncertainty: it employs an array of transducers that mounts at the neck (at the level of the fourth or fifth cervical vertebra) and allows the generation of different wide ultrasonic beams to track the centerline of the carotid artery. The Doppler Necklace also transmits the information to a computer where it is analyzed. Figure 3 shows a schematic diagram of the device.

## 2.3 Operating Principle

The principle of operation of the device is the well known Doppler effect where motion gives rise to a frequency shift. In our case, this shift is given by:

$$\Delta F = (2F_o V \cos \theta) / c \quad (1)$$

where  $F_o$  is the emitted beam frequency,  $V$  the blood velocity,  $\theta$  the intercept angle and  $c$  the speed of sound in the medium.

The assumptions used in calculating  $V$  from  $\Delta F$  are that:

1. The speed of ultrasound in blood is constant at about 1560 m/sec.
2. The carotid artery runs parallel to the surface of the neck so that the angle of incidence of the beam can be set at 45 degrees by mounting the transducers accordingly (figure 4, left).

These two assumptions are common in traditional ultrasonic diagnostic tests and the error introduced by them is not serious given that the process of monitoring of a patient is essentially relative rather than absolute.

## 2.4 Electronic Instrumentation

The Doppler Necklace is mainly intended for the home healthcare market and it is intentionally designed to employ a simplified configuration of hardware. Thus, the electronics used in the Doppler Necklace is an adaptation of commercially available equipment. The hardware provides a continuous sinusoidal voltage to drive the transducers. It also multiplies the received signal by a quadrature signal of frequency  $F_o$  (the frequency of the emitted signal). The resulting signal contains frequency components equal to the sum and difference of the emitted and received frequencies. A lowpass filter is then applied to remove the higher frequency component and to leave the Doppler shift caused by blood flow and tissue motion. The latter is then tapped and processed on a computer.

## 2.5 Attachment to Skin

Ultrasound propagation from the transducer to the vessel and back necessitates the existence of a coupling medium other than air between the transducers and the skin. This is necessary because ultrasound will get reflected back from any interface that separates two mediums with different acoustic properties as in the case of air and tissue (refer to Appendix A for information on ultrasound reflection). In regular ultrasound diagnostic tests, it is common to use water based gel to provide an acoustically nondissipative continuous medium between the patient's skin and the probe that the operator would be holding. For our application, the transducers have to be secured to the skin with an adhesive (fig 5) that would have a dual role of bonding and providing acoustic continuity. The adhesive should satisfy certain requirements, it should:

1. Adhere to the skin and cause no unacceptable irritation when used for extensive periods of time.
2. Easily removed without mechanically traumatizing the skin or leaving a residue upon removal.
3. Behave as an acoustically matching and nondissipative continuous medium.
4. Provide a stiff bonding because if it is too compliant, the velocity due to the relative motion between the transducers and the skin (which is picked up by the Doppler) will become an unacceptable source of noise in the reading.

The first two criteria can be met with the existing technology in adhesives because they are not more stringent than the requirements on transdermal drug delivery adhesives. Current commercial transdermal drug delivery pads last up to 7 days [14]. In addition, the load carrying requirement of the adhesive for our application is very low because the transducers are very small (0.23 x 2 x 5 mm each). Also, the transducers in the array are spaced to minimize skin coverage and they can be mounted at slightly different locations in order to relieve the skin between usages.

Meeting requirements 3 and 4 listed above is also possible with the current adhesive technology because 'glues' can be produced with different elastic moduli [14] and possibly with different acoustic properties.

## 2.6 Tracking of the Artery

The Doppler necklace has to be used under circumstances when the location of the artery is uncertain or not fixed. This gives rise to a tracking problem. In hospital diagnostic tests, the human operator plays the major role of properly directing the probe at the target artery.

In our application, the uncertainty of the vessel location is in two dimensions: transverse location as well as depth. (If we adopt the coordinate system illustrated in figure 4, the transverse direction is the X-axis and depth is along the Z-axis). The latter uncertainty is handled by using CW beams that will pick up signals from all along their path. This depth insensitivity of CW beams could lead to intercepting flows in neighboring blood vessels in general. However, for the common carotid artery this problem does not arise: in the anatomical section shown in figure 1, it is evident that there are no major artery in the vicinity and any signal received will be representative of carotid flow only. Note that flow in the jugular vein might also be intercepted by the CW beam but can be filtered out because of its opposite flow direction and hence frequency shift. Also intercepting deeper arteries (like the vertebral artery) in the neck is avoided by using high ultrasound frequency (8.1 MHz) that will get significantly attenuated before reaching that depth.

The uncertainty in the transverse direction is resolved by designing an array of transducers that can provide coverage of a wide sector in the neck. Only the transducers that are favorably targeting the centerline of the artery are operated at any one time. Deciding on which transducers to operate is based on tracking the highest frequency shift (that corresponds to the centerline velocity of the vessel) in the signal. The inherent assumption is that the transducers have to be mounted close to the location of the artery initially. This can be achieved by using external features on the neck for guidance (such as pulse sensation) or by implementing a patient specific necklace. Note that receiving the ultrasound signal is not affected by the location uncertainty of the vessel because the backscattered beam is diffuse and to intercept it, the receiving transducer need not be confined to a specific direction. Before presenting the details about the design of the array itself, the following section discusses the principle of beam forming.

## 2.7 Beamforming

*Note: The propagation medium is assumed lossless (i.e. does not attenuate the beam) for now but this assumption is revisited later.*

Huygen's principle [2] states that the radiation pattern from a source of arbitrary shape can be found by modeling the source as a collection of point sources each radiating spherical waves. The summation in magnitude and phase of the contribution of all point sources forms the resulting field. Thus the incremental pressure contribution  $dp$  from each point on the transducer face at the observation point is given by [2]:

$$dp = (kZu_o/2\pi r') \cos(\omega t - kr' + \pi/2) dS \quad (2)$$

where:

$$k = 2\pi/\lambda \quad (\lambda \text{ is the wavelength})$$

$Z$  = acoustic impedance of the medium (appendix A)

$u_o$  = the amplitude of the velocity in the z-direction at which the source surface is vibrating:  $u = u_o \cos(\omega t)$ . For small size transducers as in the case of the Doppler Necklace all points on the surface can be safely assumed to be oscillating with the same velocity and in phase with one another.

$r'$  = distance from the contributing point on the transducer surface to the observation point (see fig 6).

Thus the total pressure at the observation point is given by:

$$p = \int_{\text{source}} dp \quad (3)$$

For the case of rectangular transducers like the ones employed in the Doppler Necklace, there is no closed form solution to find  $p$  and numerical simulation of the field has to be performed. However, a common feature of pressure fields of transducers of all shapes is the existence of a near field and a far field.

In the near field the magnitude of  $p$  is characterized by rapid oscillations and considerable constructive and destructive interference while in the far field it drops at a rate of  $1/z$ . For a circular transducer of diameter  $D$ , the transition from near to far field along the axis of the transducer takes place at a distance of  $D^2/4\lambda$  (figure 7).

The power intensity of the ultrasonic field is defined as [4]:

$$I = p^2/Z$$

Where  $Z$  is the acoustic impedance of the medium.

Another parameter relevant to ultrasonic insonification is the angle at which the beam diverges: a plot of the power density pattern vs off-axis distance at a certain depth from the face of a circular transducer reveals the existence of one main and several side lobes. The majority of the power being contained in the main lobe, the effective width of the beam is commonly taken to be equal to the width of the main lobe at any particular depth. The beam remains collimated in the near field but diverges in the far field with an angle  $\theta$  given by:

$$\theta = \sin^{-1}(\lambda h)$$

where  $h$  for a rectangular transducer is the corresponding dimension in the plane of  $\theta$  [2].

**Note on attenuation:** The effect of attenuation has not been included in the equations above and it was not included in the computer simulations performed. The reason is that although the attenuation is tissue limits the depth from which a useful signal can be obtained, attenuation in blood is low (with a value of about 0.2 dB/cm/MHz compared to a value of 1.5 dB/cm/MHz in fat [1]) and Jensen (1996) reports that 'the signal received from the part of the vessel that is furthest away from the transducer is not much more attenuated than that close to the transducer'.

## 2.8 Array Design

The primary purpose in designing the array of transducers is to handle the location uncertainty of the vessel. The easiest approach to consider is to use a large emitting transducer that would cover the artery and provide for additional spatial uncertainty. However, this design is not flexible nor efficient because it insonifies areas that do not carry information. Another approach that is not flexible but that would minimize the skin area covered by the transducers is to use a convex-shaped transducer to create a diverging beam that would span the artery location. Because on the need to maintain a certain level of energy in the diverging beam this would lead to a concentration of acoustic energy at the face of the crystal (up to 10 times higher than a flat transducer) and could raise concerns for long term usage. This leads us to the

conclusion that a distributed array of planar crystals is the most optimal configuration to radiate the needed acoustic energy safely and in a flexible way. In order to direct or 'steer' the beam to target the artery, phased array are commonly employed in ultrasound devices: by introducing a phase shift between the voltage that drives individual crystals, the resulting wavefront can be directed at will. For the Doppler Necklace, continuous wave ultrasound is used (as opposed to pulsed wave) and the maximum useful phase lag between individual crystals is less than the period of the driving voltage (a delay of one period would create the same wave as no delay at all). This limits the maximum steering angle to about 10° for the desired crystal arrangement in the Doppler Necklace. The approach we adopted is less complex electronically than a phased array system. It consists of using a multitude of crystals that can span a wide sector among themselves. At any one time, only the transducers that are favorably oriented and can potentially cover the centerline of the artery are switched on.

The parameters of such a design are the size of the individual transducer (height  $h$  and width  $w$ ) as well the spacing between them  $s$  (figure 4).

The height  $h$  is determined by two factors: first, it is preferable to have the artery fall within the near field of the transducer in which the beam is not diverging and the resulting intercept angle can be taken as constant. This translates into the need of having  $h > 3$  mm. The other factor in determining  $h$  is the effect of transit time broadening: when the vessel is insonified with an ultrasonic beam, a limited time of observation (equal to the time during which the scatterers are within the beam) is obtained. Thus the smaller the observation window, the lower the relative velocity (or frequency shift) resolution obtained. The relative frequency resolution is given by [1]:

$$\frac{\Delta f_d}{f_d} = \frac{c}{2hf_o} \tan \theta$$

Where the terms are the same as the ones used in equation 1 for the Doppler shift. For a dimension  $h = 3$  mm, this gives a theoretical relative precision of 3%. Note that the actual precision might be lower because of the narrower effective useful dimension of the transducer and a slightly larger  $h$  is preferable.

The remaining parameters are determined as follows: the average diameter of the common carotid artery is about 6 - 7 mm and is unlikely to exceed 8.6 mm [9]. Providing for some location uncertainty, this requires the array to span a total width of about 15

mm. Within this total width the number of transducers to fit is a compromise between the level of flexibility required and the resulting level of complexity (as an initial design we chose to use 5 transducer elements to be operated 3 at a time). Once the number of transducers is set, their width and the spacing between them is governed by the need to span the necessary overall area without having any spatial gaps. Since we are operating in the near field of the transducers, the beams are highly collimated and their individual widths is almost equal to the width of the transducer and the spacing between the crystal cannot be excessive. For example, for an array of transducers whose width is 2 mm, the spacing between the crystals should not be higher than about 1 mm. This results in a skin coverage ratio of 2/3.

### **3. Interpretation of the Signal**

The measurement taken by the Doppler sensor can be interpreted in different ways. Useful information can be derived from monitoring the fluctuations in the centerline velocity of the artery. In addition to that, the reading carries information on the rate of change of the pressure pulse, an indication of cerebral flow and potentially an estimate of flow and velocity profile.

#### **3.1 Monitoring Blood Velocity along the Centerline**

The blood velocity at the centerline of the artery can be easily monitored from the measurement taken by the Doppler Necklace. Due to the existence of high frequency noise in the reading, the highest frequency carried in the signal cannot be taken to correspond to the highest velocity intercepted in the flow field. Instead, signal processing algorithms based on estimating the Doppler shift within which a certain percentage of the spectral energy falls (for instance 95%) can be used to recover the centerline velocity. This velocity cannot provide an absolute assessment of flow because of the fluctuations in arterial diameter and changes in the blood velocity profile over a cardiac cycle. However for monitoring purposes, it can be used as a relative index. A better understanding of the velocity distribution in the artery can be achieved if its area weighted mean velocity can be estimated. This is the topic of the following section.

### 3.2 Estimating the Mean Velocity

One method to determine the dominant frequency component in the signal is to use a zero-crossing detector. This algorithm can be easily implemented electronically but it is vulnerable to both high and low frequency noise. Also, its output is ideally equal to twice the RMS frequency in the signal but differs from that depending on the velocity profiles [1] so that it only provides a crude estimate of mean velocity. A better but more complex method is to digitally process the signal and compute its Fourier Transform. The resulting Doppler frequency spectrum will indicate the amplitude of each frequency component of the signal. If we assume that the angle of incidence onto the blood vessel is fixed and that the beam is illuminating the target volume uniformly, then the amplitude of a Doppler frequency shift component (corresponding to a particular frequency) will be proportional to the number of cells moving at the respective velocity. Thus the frequency spectrum which is a plot of amplitude versus frequency can be thought of as a plot of cell count versus velocity [3]. Figure 8 illustrates this idea and shows the spatial maximum and mean velocities as well.

Due to the existence of high frequency noise, the spatial peak velocity (which is the centerline velocity) cannot be taken to be the maximum frequency in the signal. Rather, it is computed as the frequency within which 95% of the spectral energy falls.

Thus in addition to providing an estimate of the centerline velocity, spectral analysis of the Doppler reading can potentially be used to obtain a flow estimate without knowledge of the vessel diameter. This is possible because the spatial concentration of cells is almost uniform within the vessel and the Doppler spectrum can be thought of as flow area (instead of cell count) versus velocities. A flow estimate is thus provided by taking the first moment about the y-axis of the Doppler power spectrum [3]. This concept is shown analytically in the following derivation [1].

For a typical velocity distribution in any cylindrical vessel can be described by the following equation:

$$V(r) = V_o [1 - (r/R)^p] \quad (4)$$

Where

$r$  = the radial position

$R$  = the radius of the vessel

$V_o$  = maximum velocity at centerline

$p$  = parameter that describes the flow:  $p=2$  for parabolic profile and  $p \rightarrow \infty$  for a plug flow.

Assuming a uniform insonification of the vessel, the frequency shifts  $f_d$  are derived from the Doppler equation:

$$f_d(r) = (2V_o f_o/c) [1 - (r/R)^p] (\cos(\theta))$$

where the incidence angle  $\theta$  has been assumed to be  $45^\circ$  for the carotid artery.

The amplitude of the signal at the corresponding frequencies is found by calculating the number of scattering particles moving with a velocity  $v < v_I$ :

$$n_p(v < v_I) = \int_0^R 2\pi r \rho_p dr = l\pi \rho_p (R^2 - r_I^2)$$

where  $\rho_p$  is the particle density that was assumed to be spatially uniform. The particle density as function of velocity is the derivative with respect to  $v$  of  $n_p$  given above. The result is:

$$p_v(v) = -2l\pi \rho_p r \frac{dr}{dv}$$

since  $v = v_o(1 - (r/R)^p) \Leftrightarrow r = R(1 - v/v_o)^{1/p}$  and  $\frac{dr}{dv} = -R/v_o p (1 - v/v_o)^{1+1/p}$

we get

$$p_v(v) = 2lR^2 \pi \rho_p / [v_o p (1 - v/v_o)^{1-2/p}]$$

the total number of red blood cells is  $n_t = l\pi \rho_p R^2$  and dividing  $p_v(v)$  by  $n_t$  we get the normalized distribution

$$p_n(v) = 2 / [v_o p (1 - v/v_o)^{1-2/p}]$$

Since the velocities are related to frequency shifts received, the normalized power density spectrum of the signal for the range  $0 < f_{doppler} < f_{max}$  (where  $f_{max}$  is the shift corresponding to  $v_o$ ) is given by:

$$G(f_d) = 2 / [p f_{max} (1 - f_d/f_{max})^{1-2/p}] \quad (5)$$

Thus the velocity spectrum is linked to the power density spectrum. Given  $F_{max}$ , if we calculate the mean frequency  $F_{mean}$  in the spectrum corresponding to the mean velocity, we can estimate the velocity profile index  $p$  which for a pipe flow is given by [6]:

$$p = 2 V_{mean} / (V_{max} - V_{mean}) = 2 F_{mean} / (F_{max} - F_{mean}) \quad (6)$$

Note that  $F_{mean}$  is found by dividing the first moment of area (about the y-axis) of the Doppler spectrum by the value of the area.

### 3.3 Monitoring the Time Derivative of the Pressure Pulse

In addition to carrying information on blood velocity, the Doppler sensor also picks up the vessel wall motion. This signal is usually of low frequency (<200Hz) but of high amplitude: 10 to 100 times greater than the amplitudes of blood velocity shifts [1]. It is common practice in medical diagnosis to filter out. However, as the following section shows, the wall velocity is related to the time rate of change of the pressure waveform.

Assuming the artery to be of circular cross-section: the fluid flow in the tube is incompressible so that the equation of continuity is given in cylindrical coordinates by

$$\frac{\partial u}{\partial x} + \frac{1}{r} \frac{\partial}{\partial r} (rv) + \frac{1}{r} \frac{\partial w}{\partial \theta} = 0 \quad (7)$$

where  $u$  is the longitudinal component of the velocity and  $v$  is the radial component and  $w$  is the circumferential component. Assuming the flow in the carotid artery to be axisymmetric so that  $w=0$  and  $(\delta/\delta\theta)=0$ , this simplifies the continuity equation 7 to the following form

$$\frac{\partial u}{\partial x} + \frac{1}{r} \frac{\partial}{\partial r} (rv) = 0 \quad (8)$$

Considering a segment of the carotid artery as an elastic segment of a tube of radius 'a' which undergoes vibrations in the transverse direction only. The instantaneous radius of the tube is given by  $a+\eta(x,t)$  where the vibrations are very small relative to the initial radius namely  $\eta \ll a$ . Eriksen (1992) reports the average percentage variation of the diameter of the carotid artery from its mean as 6.7% so the assumption we just made is not perfectly satisfied, but is valid for a first order approximation.

The average axial velocity is found by integrating the velocity across the tube cross section, since we assumed small vibration, it is given by:

$$\bar{u}(x,t) = \frac{1}{\pi a^2} \int_0^a u(x,r,t) \cdot 2\pi r dr \quad (9)$$

Integrating the equation of continuity (8) across the tube and inserting equation (9) results in the following relationship:

$$\pi a^2 \frac{\partial \bar{u}}{\partial x} + 2\pi r v(x,r,t) \Big|_{r=0}^{r=a} = 0 \quad (10)$$

The radial velocity at  $r=0$  vanishes because of symmetry and the the radial velocity at  $r=a$  is the wall velocity and will be denoted by  $v_w(x,t)$ , it follows that

$$v_w(x,t) = -\frac{a}{2} \frac{\partial \bar{u}(x,t)}{\partial x} \quad (11)$$

Assuming the flow to be non-viscous (ie viscous effects are small over the section being observed) the equations of motion will be given by:

$$\rho \left( \frac{\partial u}{\partial t} + u \frac{\partial u}{\partial x} + v \frac{\partial u}{\partial r} \right) = -\frac{\partial p}{\partial x} \quad (12)$$

$$\rho \left( \frac{\partial v}{\partial t} + u \frac{\partial v}{\partial x} + v \frac{\partial v}{\partial r} \right) = -\frac{\partial p}{\partial x} \quad (13)$$

The approximation of neglecting the viscous terms implies that the wave travels without attenuation, this is definitely wrong for the arterial system as a whole but can be used over a small section of the carotid artery.

Further simplification of the equations above can be performed with dimensional analysis. If the speed of propagation of the wave is  $c$ , its frequency is  $f$  and its wavelength is

$$\lambda = c/f$$

We can use  $\lambda$  and  $1/f$  as characteristic length and time respectively. The average velocity  $\bar{u}$  is used as the characteristic velocity. The ratio of the inertial terms to the acceleration in the equation above become:

$$\begin{aligned}
 \frac{u \frac{\partial u}{\partial x}}{\frac{\partial u}{\partial t}} &\sim \frac{\bar{u} \cdot \frac{\bar{u}}{\lambda}}{\frac{\bar{u}}{1/f}} = \frac{\bar{u}}{f \cdot \lambda} = \frac{\bar{u}}{c} \\
 \frac{v \frac{\partial v}{\partial x}}{\frac{\partial v}{\partial t}} &\sim \frac{\bar{u} \cdot \frac{v^*}{\lambda}}{\frac{v^*}{1/f}} = \frac{\bar{u}}{c}
 \end{aligned} \tag{14}$$

we can safely assume that

$$\frac{\bar{u}}{c} \ll 1$$

since the maximum possible value of this term is  $.4/5=0.08$  (occurring at the aorta) and the average value in the cardiovascular system is 0.01. The equation (14) above also contained  $v^*$  which is the characteristic radial velocity and can be equated to the radial wall velocity:

$$v^* = v_w = -\frac{a \frac{\partial \bar{u}}{\partial x}}{2} \sim \frac{-a \bar{u}}{2\lambda} \tag{15}$$

performing the dimensional analysis for  $v$  gives:

$$\begin{aligned}
 \frac{v \frac{\partial u}{\partial r}}{\frac{\partial u}{\partial t}} &\sim \frac{v^* \frac{\bar{u}}{a}}{\frac{\bar{u}}{1/f}} \sim -\frac{\bar{u}}{c} \ll 1
 \end{aligned}$$

$$\begin{aligned}
 \frac{v \frac{\partial u}{\partial r}}{\frac{\partial u}{\partial t}} &\sim \frac{v^* \frac{v^*}{a}}{\frac{v^*}{1/f}} \sim \frac{\bar{u}}{c} \ll 1
 \end{aligned}$$

Thus the inertial terms can be assumed to be small compared to the instantaneous acceleration and the resulting equations are:

$$\rho \left( \frac{\partial u}{\partial t} \right) = - \frac{\partial p}{\partial x} \tag{16}$$

$$\rho \left( \frac{\partial v}{\partial t} \right) = - \frac{\partial p}{\partial r} \tag{17}$$

Furthermore, comparing the relative magnitude of:

$$\frac{\partial p / \partial r}{\partial p / \partial x} \sim \frac{a}{\lambda}$$

we conclude that since the speed of propagation is very high and the frequency is low (heart beat frequency is about 1 Hz) the corresponding wavelength is large and consequently much greater than the tube radius. Therefore, it can be assumed that pressure is a function of axial distance only and if equation 16 is integrated over the vessel diameter, it follows that:

$$\rho \frac{\partial \bar{u}}{\partial t} = - \frac{\partial p}{\partial x} \quad (18)$$

Now let us analyze the stress in the vessel wall: assuming that the wall has a linear relationship between stress and strain and is incompressible so that its Poisson's ratio is 0.5, we have:

$$\sigma = E \cdot \epsilon$$

and

$$\epsilon = \eta / a$$

The circumferential tension  $T$  is the result of multiplying the stress per unit length by the thickness of the tube  $h$ :

$$T = \sigma \cdot h = E \cdot \epsilon \cdot h = E \cdot h \cdot \frac{\eta(x, t)}{a}$$

Considering that this tension is balanced by the inner pressure and wall inertia, and for an elemental segment we get:

$$\frac{Eh\theta}{a} \eta = a\theta \cdot p - \rho_w (a\theta h) \ddot{\eta}$$

where the angle is considered small for the elemental segment so that  $\sin\theta \sim \theta$ . Rearranging the terms, we get pressure as a function of wall motion as:

$$p = \frac{Eh}{a^2} \eta + \rho_w h \ddot{\eta} \quad (19)$$

at the wall interface, the solid wall and the fluid velocities must match so that no separation results and this gives the following equality:

$$v_w(x, t) = \dot{\eta}(x, t)$$

Assuming the vessel wall to be thin (as in the case of the carotid artery), we can then neglect the second inertia term of equation 19. Taking the derivative of  $p$  and substituting in equation 11 gives the final relation:

$$\frac{dp}{dt} = \frac{Eh}{a^2} \cdot v_w(x, t)$$

This relates the vessel wall motion to the time rate of change of the pressure pulse traveling through the arterial section under consideration.

### 3.4 Carotid Flow as Index of Diastolic Cerebral Flow

As mentioned earlier, Matsumoto et al. (1992) had used the common carotid artery flow as an index of cerebral flow. Champagne and Farget (1980) support this idea by the fact that circulation to the brain is normally of low resistance and diastolic flow in the internal carotid artery is relatively large. On the other hand, the area supplied by the external carotid artery has a high-resistance bed so that diastolic flow is a small fraction of the total flow and is sometimes even absent. Thus the diastolic flow in the common carotid artery almost entirely ends up as internal carotid flow to supply the brain.

## 4. Experimental Illustration and Computer Simulation

The electronics used in the Doppler Necklace is an adaptation of the commercial unit Model 909 directional Doppler produced by Parks Medical Electronics. The signal was tapped out of the device and processed on a computer. The transducers used in the Doppler Necklace are 2 mm by 5 mm each and computer simulation was performed to determine the ultrasonic intensity distribution using the *Ultrasim 2.1* special toolbox in *Matlab* (by Sverre Holm et al). The following convention was used in naming the axes (figure 4, right):

1. The x-axis is along the aperture of the transducer.
2. The y-axis is along the height of the transducer.
3. The z-axis is the depth direction (into the neck)

The origin (0,0,0) is thus at the center of the transducer.

Figure 9 shows the plot at  $y=0$  of the magnitude of the intensity of the ultrasonic field for the 2mm by 5mm crystal used. The x direction of the transducer is the vertical axis in the plot and depth is the horizontal axis. The near field and the side lobes are apparent in the plot. The carotid artery would normally lie at a depth of about 11 mm. Since the transducer is mounted at  $45^\circ$ , the corresponding region of interest in the plot is around a depth 15 mm. In that region, the energy emitted by the transducer is still mostly contained within a 2mm band (same as the x dimension of the transducer).

#### 4.1 Tracking the Centerline Velocity

One arrangement of transducers to be used in the Doppler Necklace is one consisting of 5 crystals of width 2mm each separated by a distance of 1mm. One mode of operation of such an array is to have only one transducer emitting at any one time and another receiving. The emitter, being of small aperture, creates a narrow beam that should intercept the centerline of the artery. The latter condition is met by alternately exciting the different transducers and selecting the one that gives the maximum velocity reading over a cardiac cycle. To illustrate this concept, data was taken when only one transducer was emitting. Switching between the transducers was performed manually and the subject was at rest. The data was sampled at 20KHz. Figure 10 shows the 1024 point spectrogram of the reading (note the existence of noise bands shown in the horizontal streaks).

The signal was then high pass filtered to get rid of all components less than 200Hz. These low frequency components are of high amplitude and correspond to vessel wall activity as well as relative motion between the crystals and the skin. This process of high pass filtering sets the lowest detectable velocity value at about 2.7 cm/sec (corresponding to 200 Hz). The signal was then broken down into overlapping segments (with a length of 512 points each and an overlap of 496 points). The FFT of these segments was computed and the spectrum used to determine the frequency within which 95% of the energy fell (which corresponds to the centerline velocity of the artery). The mean frequency component of each segment was also determined by taking the first moment of area (about the zero frequency axis) of the amplitude-frequency plot and dividing by the area as explained previously. The flow index  $p$  was then estimated by

assuming that the flow in the narrow section insonified by the beam can be assumed to be slit flow and thus  $p = V_{mean}/(V_{max} - V_{mean})$

Figure 11 shows the reconstructed velocity profile versus time. Although the plot reflects the right trend in the pattern of flow established, there are considerable sources of error in the simplified formulation presented. Since  $p$  is calculated from  $V_{max}$  and  $V_{mean}$ , the errors inherent in the approximations of the latters are reflected in  $p$  as well, namely: noise influences the determination of  $V_{max}$ ,  $V_{mean}$  estimation as formulated above assumes the existence of a uniform ultrasonic field. The errors incurred from this final assumption together with that of using the slit flow approximation were estimated for the configuration above and were found to go up to 30% overestimate in  $V_{mean}$  for parabolic flow and tend to decrease as the flow becomes more blunt. This error can be alleviated by further optimizing the geometric arrangement to create a more homogeneous beam.

The configuration presented above has an advantage in low power consumption because it operated only one crystal, however it is sensitive to motion and location disturbances. A more robust insonification can be achieved by operating several of the transducers simultaneously. Figure 12 simulates the field produced by the arrangement of all 5 transducers operating together.

We mentioned earlier that one method to generate a wide diverging beam was to use a convex transducer. Such a configuration would distribute the acoustic energy over a wider sector but fails to create a homogeneous field. Figure 13 compares the simulated intensity fields of a planar and a convex crystal (x-dimension is 5mm and the radius of curvature is 20 mm) and it is apparent that the main and side lobes of the field of the planar transducer seem to have split up into smaller lobes.

Previous investigators have achieved beam uniformity at the expense of complexity in electronics by using annular arrays of independently driven discrete transducers [2]. Although perfect uniformity is theoretically impossible to achieve, one way to alleviate the problem is to have the artery fall in the region just before the onset of the far field. In that region (fig 17) the field varies slowly over distance. Another novel way approach that we are still investigating is to make the maxima and minima closely spaced in the region of interest. Numerical simulation shows that such a field with closely spaced peaks has an 'averaging' effect and tends to decrease the error in the flow

estimate. Figure 14 illustrates the concept where the variations in the field are occurring over smaller and smaller spatial distances.

## **Summary and Future Work**

We presented the design of a wearable ultrasound Doppler device to monitor blood velocity in the carotid artery. The device employs continuous wave excitation and makes use of an array of transducers. These transducers can be operated to generate a varying ultrasonic beam that can be either narrow and intercept the centerline of the vessel or wide and covers a sector in the neck. We also showed the usefulness of the measurement as conveying information about the velocity distribution in the artery and the time rate of change of the pressure pulse in addition to being indicative of diastolic cerebral flow.

Future work will consist of further optimization of the parameters in the design of the multiple transducer probe using computer simulation as well as building a test bed to verify the results.

## Appendix A

The following is a brief review of basic ultrasound equations:

- In the medium:  $Z$  = acoustic impedance,  $C$  = speed of sound,  $\rho$  = density,  $K$  = compressibility and

$$Z = \sqrt{\rho C}$$

- To determine the acoustic field of a transducer,  $dp$  is the elemental pressure distribution due to the contribution of an area  $ds$  of the transducer:

$$dp = \frac{kZu_0}{2\pi r} \cdot \cos(\omega t - kr + \frac{\pi}{2}) \cdot ds$$

Where  $k=2\pi/\lambda$  and  $\lambda$  is the wavelength and  $r$  is the distance between the point of evaluation of  $dp$  and the transducer element  $ds$ . The pressure field  $P$  is the integration of  $dp$  over the area of the transducer.

- The energy density ( $\text{W/m}^2$ ) or intensity is given by  $I = P^2/Z$ .
- When the ultrasonic beam propagates through a medium its power density will decrease mainly due to absorption. Assuming a viscous like damping effect taking place, the solution to the pressure field will be exponentially decaying:

$P = P_o e^{-\alpha z} \cdot \cos(\omega t - kz)$  where  $P_o$  is the pressure at zero depth and  $\alpha$  is the attenuation coefficient. The intensity  $I$  being related to the square of  $P$  will drop at an exponential rate of  $2\alpha$ . However experimental evidence shows that  $I$  only drops at a rate of  $\alpha$  (and not  $2\alpha$  as predicted) due to relaxation effects.

- Reflection and refraction at plane surfaces:

If  $\theta_i$  is the incidence angle of the beam onto a surface,  $\theta_r$  the reflection angle and  $\theta_t$  the angle of transmission into the medium then,  $\theta_i = \theta_r$  and  $(\sin \theta_i)/(\sin \theta_t) = c_1/c_2$  where  $c_1$  and  $c_2$  are the speeds of sound in the corresponding media.

If  $I_i$  is the intensity of the beam incident onto a surface that separates two media 1 and 2 that have different acoustic properties then the transmitted intensity into medium 2 is given by  $I_t = 4Z_2Z_1 \cos\theta_i \cos\theta_t / (Z_2 \cos\theta_i + Z_1 \cos\theta_t)^2$

## Appendix B :Figures

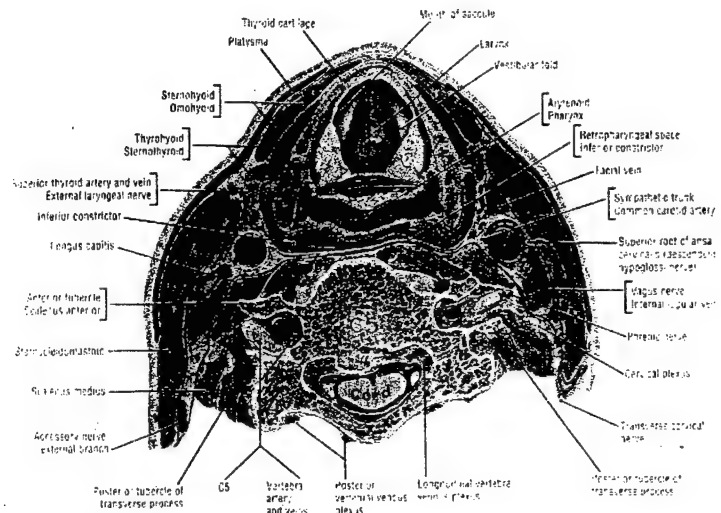
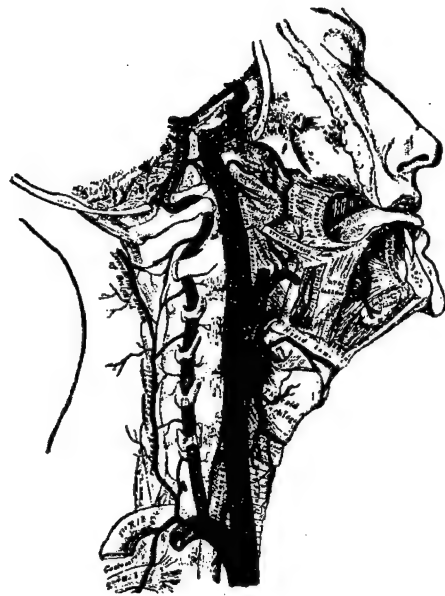
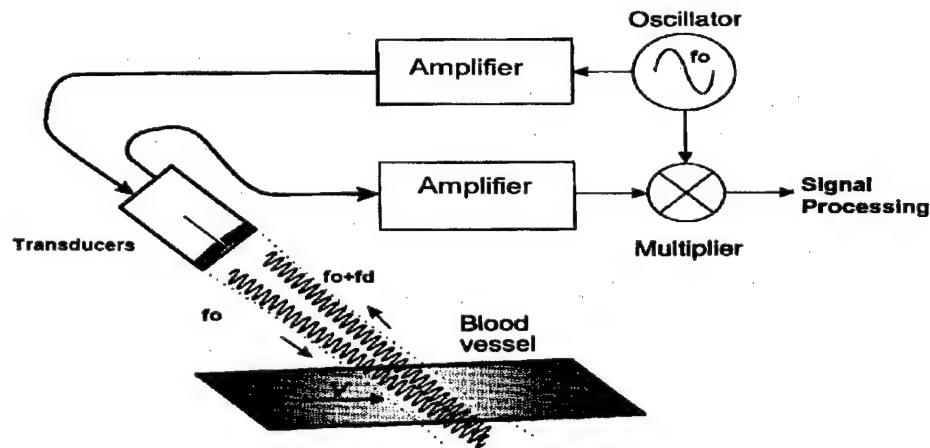


**Figure 1:** Anatomical views showing (left) the common carotid artery going up from the aortic arch and branching into inner and outer carotids [8]. Right: A cross-section through the neck at the level where the Doppler necklace mounts [5].



Continuous wave Doppler system.

**Figure 2:** Diagrammatic representation of a continuous wave Doppler device[1].

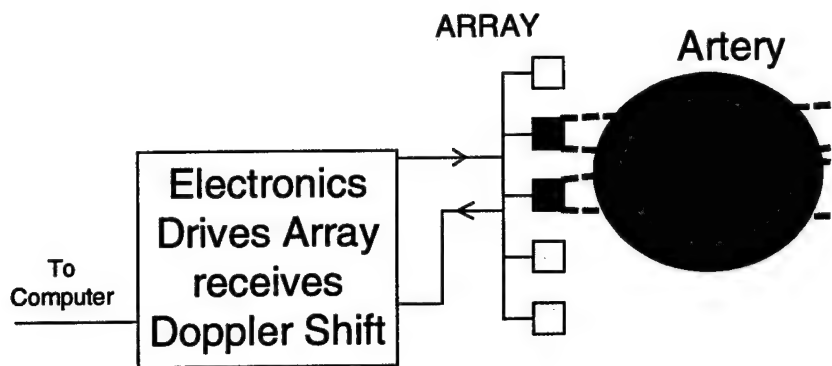


Figure 3: A schematic representation of the Doppler Necklace

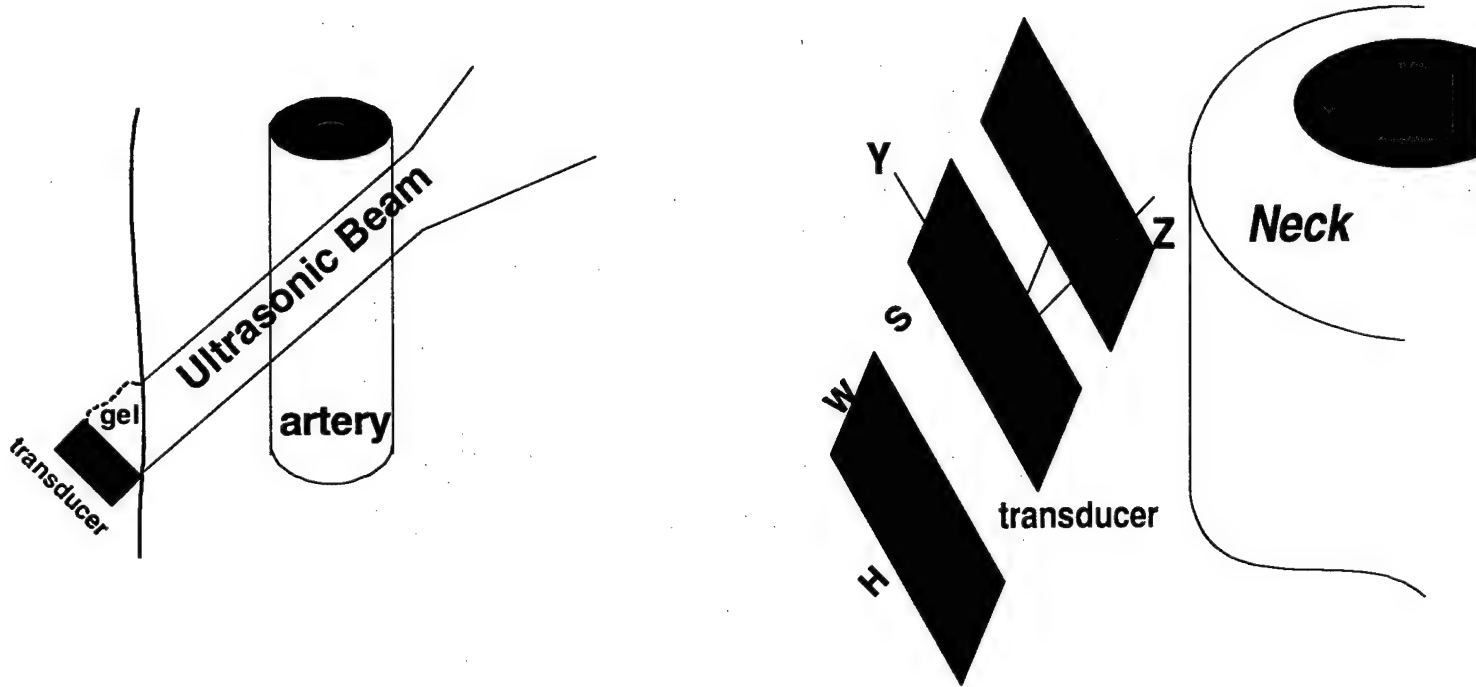


Figure 4: Left: the transducers are mounted at 45 degrees from with respect to the patient's neck and the carotid artery is assumed to run parallel to the surface of the neck. Right: general coordinates adopted in the report

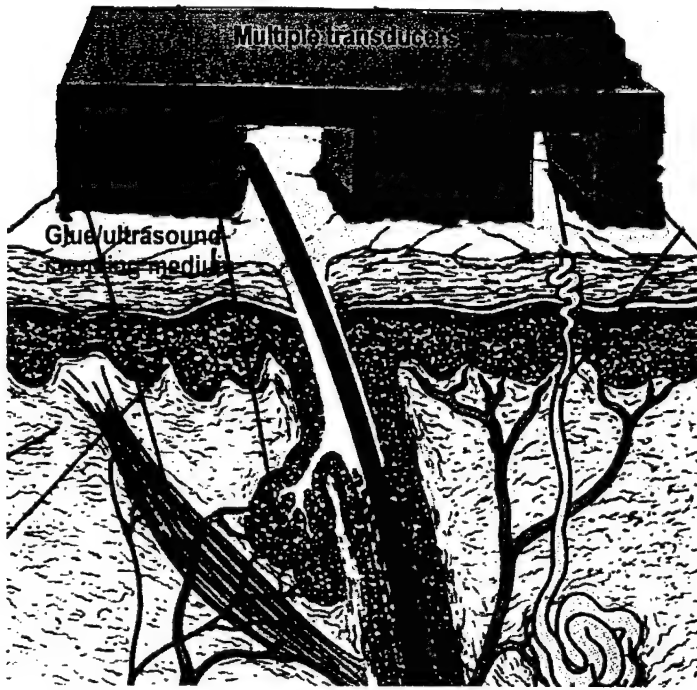


Figure 5: attachment of the transducers to the skin is through an adhesive that also acts as an ultrasound coupling medium

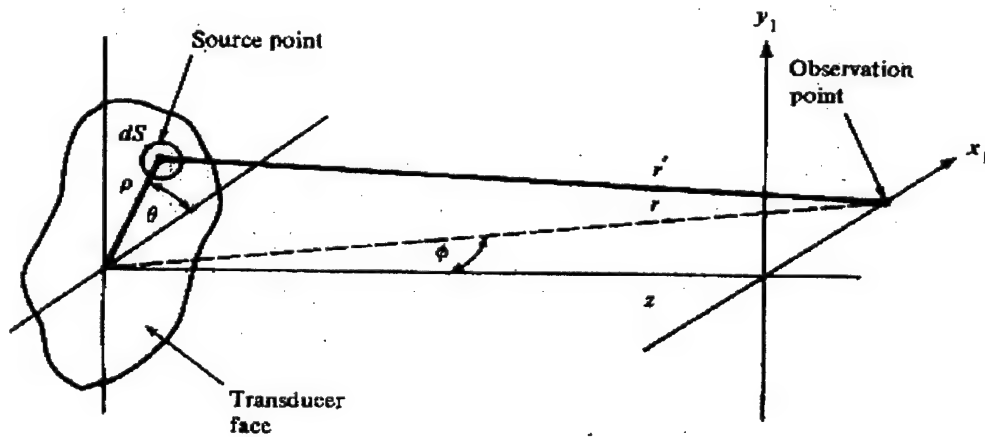
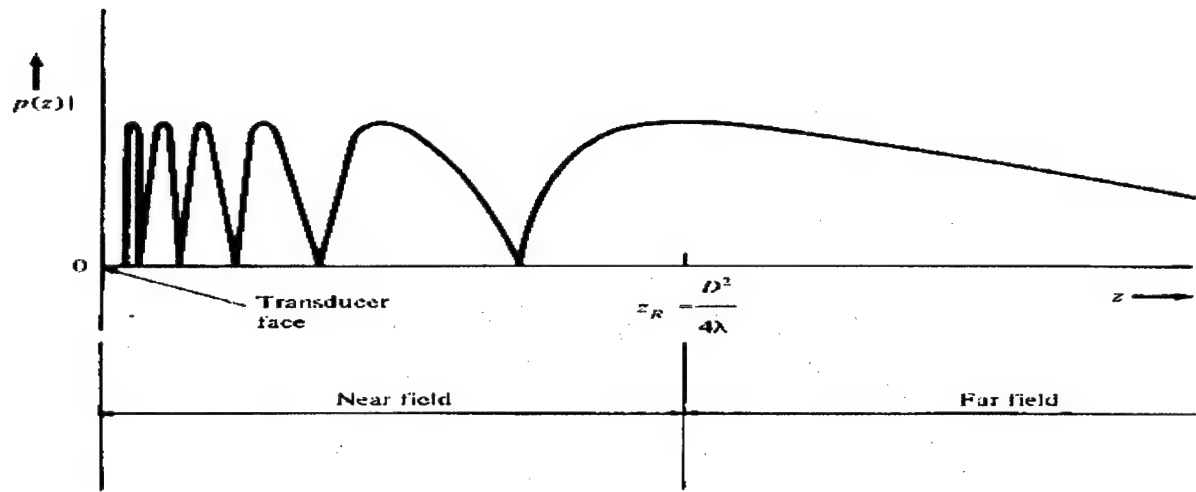
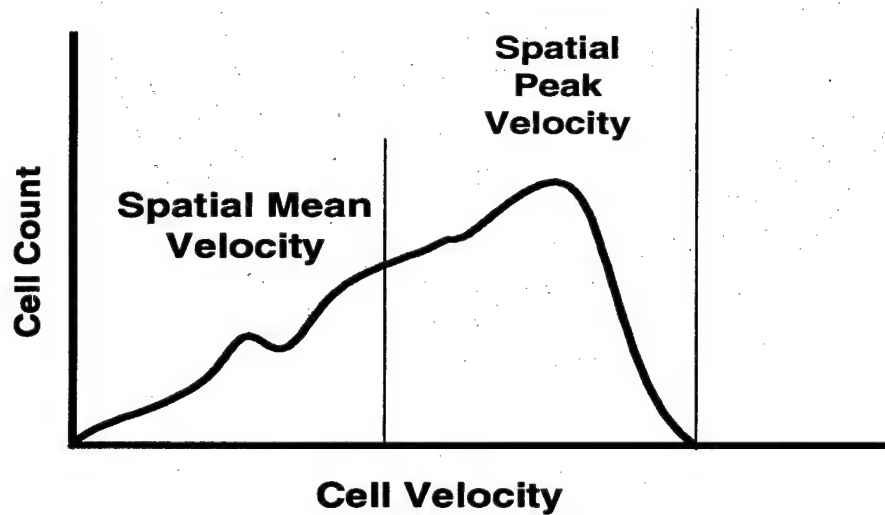


Figure 6: variation of the magnitude of the on-axis pressure field from a circular transducer[2].



*Figure 7: variation of the magnitude of the on-axis pressure field from a circular transducer[2].*



*Figure 8: Doppler frequency spectrum shown as cell count vs cell velocity plot.*

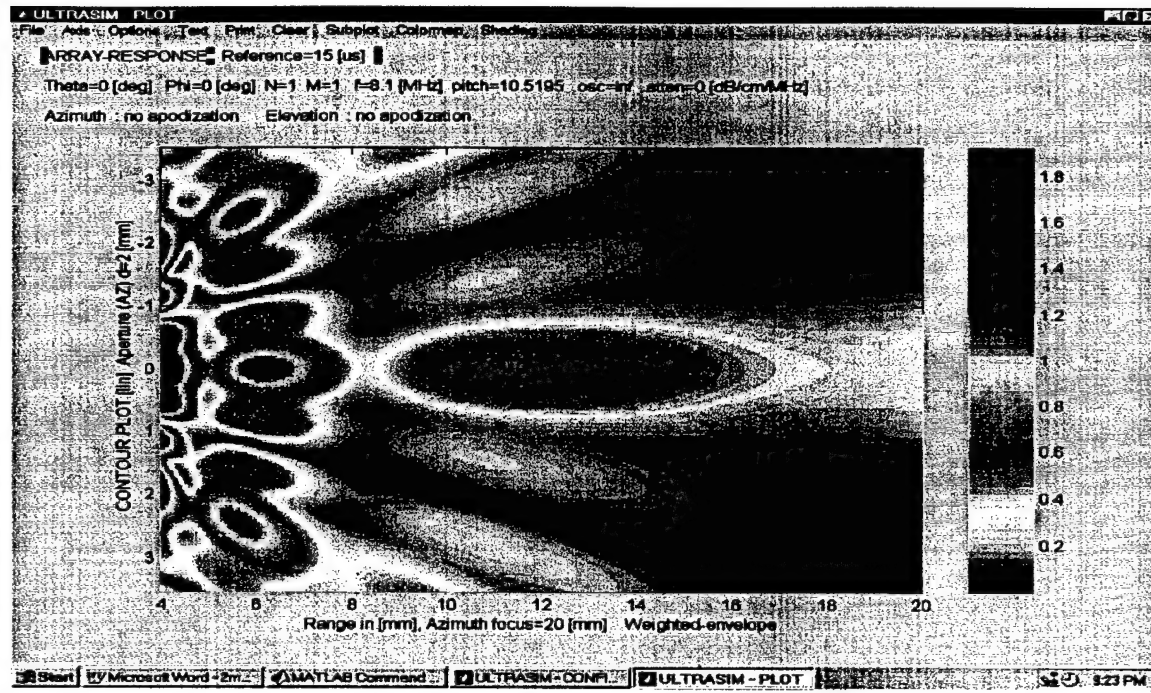


Figure 9: intensity field for 2mm by 5mm transducer at CW excitation of 8.1 MHz

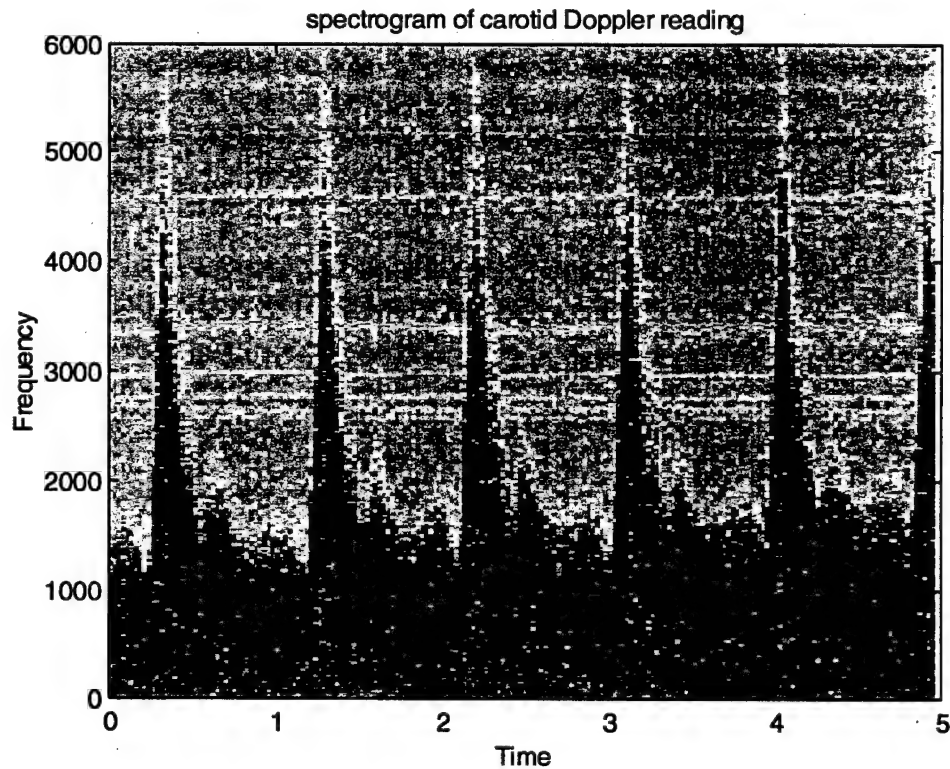


Figure 10 : Spectrogram of the velocity reading from the carotid artery measured with a narrow beam that intercepts the centerline.

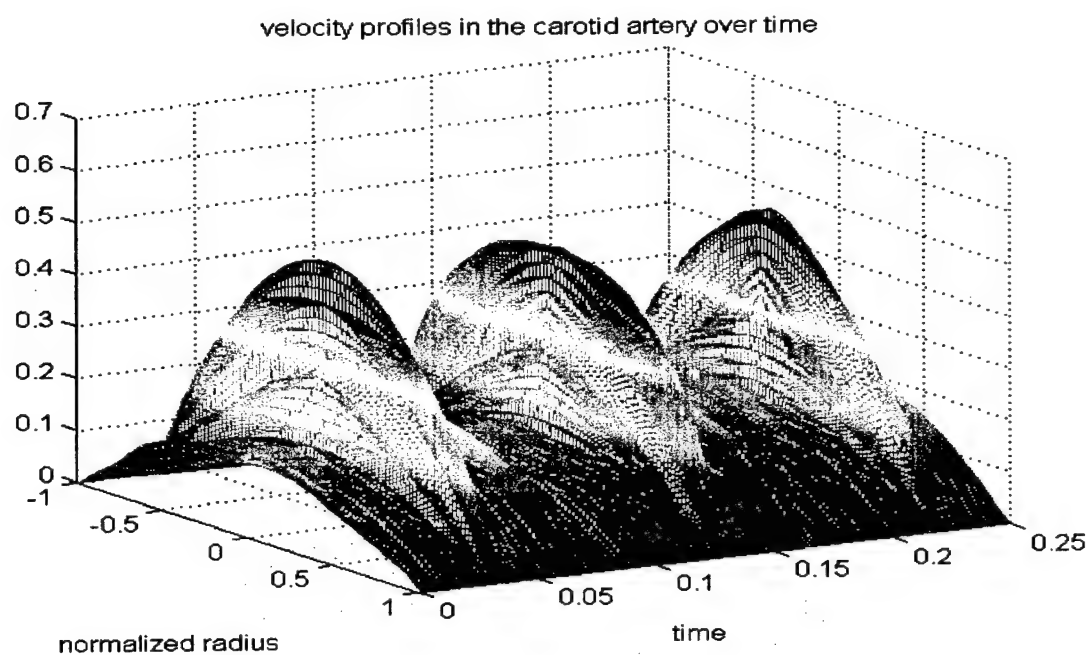


Figure 11: the reconstructed velocity profiles for normalized radius in the carotid artery versus time.

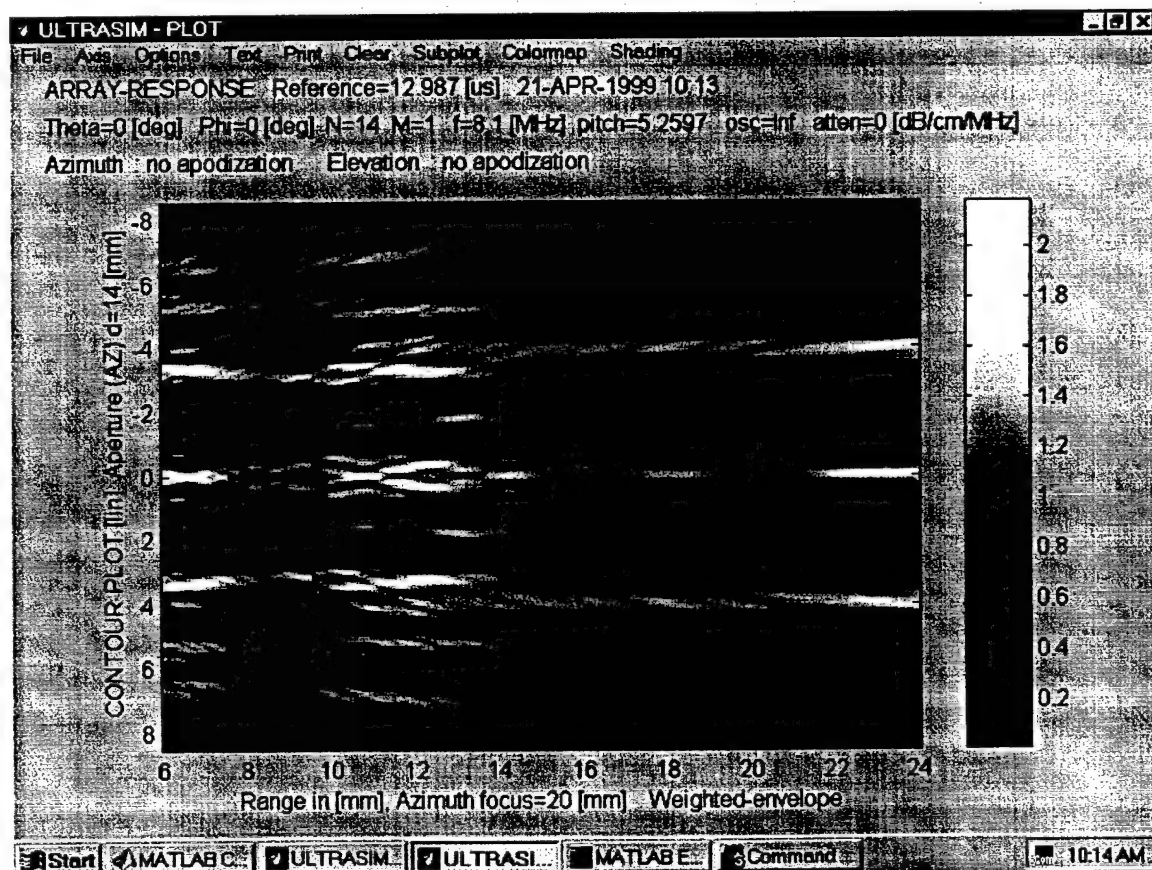
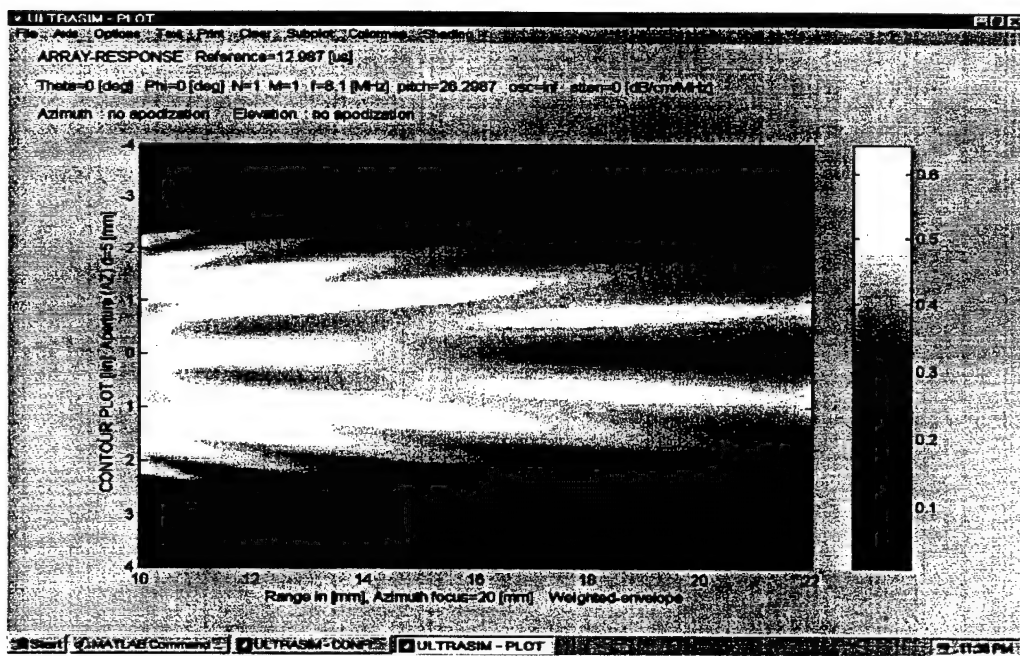
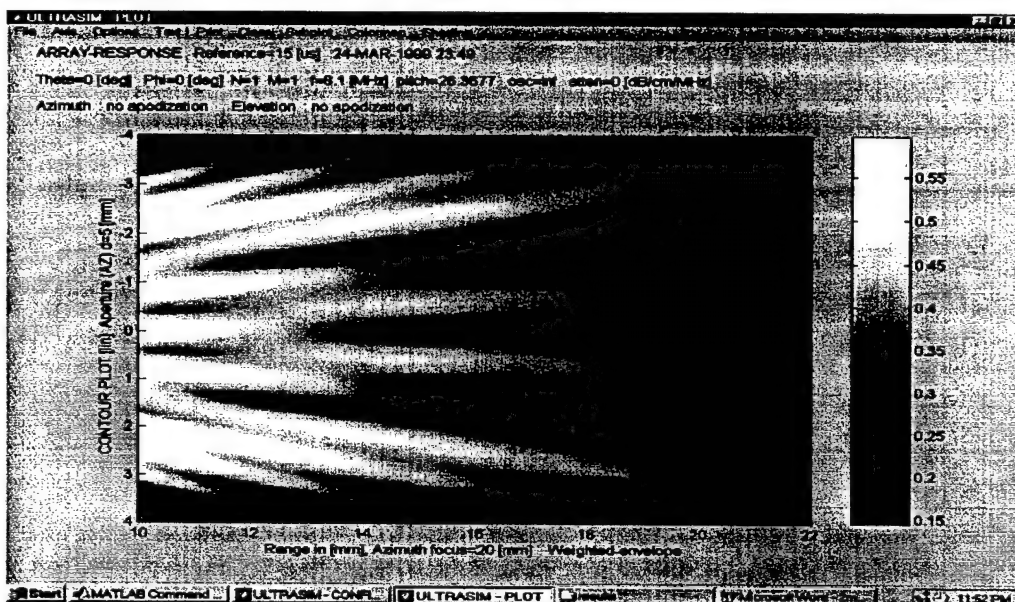
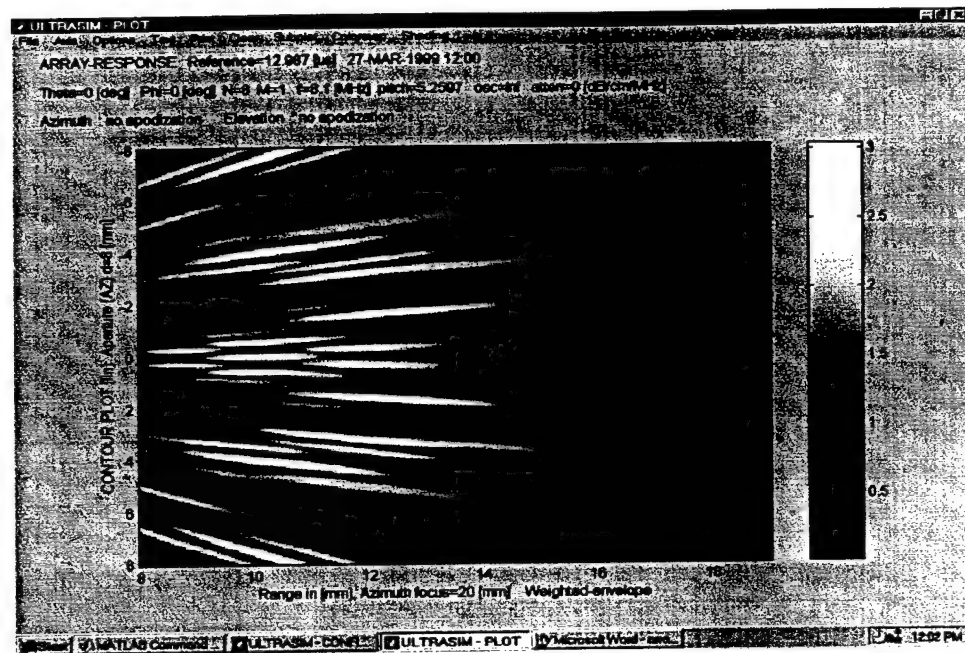


Figure 12: the ultrasound field for an arrangement of 5 transducers of 2mm width each with 1mm between.



*Figure 13: ultrasonic field of flat face transducer (top) and convex transducer (bottom)*





**Figure 14:** an array of smaller transducers (1mm aperture) creates an ultrasonic field with more spatially compact fluctuations.

References:

1. 'Estimation of Blood Velocities using Ultrasound: a Signal Processing Approach', Jorgen Arendt Jensen, Cambridge University Press 1996
2. 'Ultrasonic Bioinstrumentation', Douglas A. Christensen, John Wiley & Sons 1988.
3. 'Doppler Echocardiography' Navin C. Nanda, Igaku-Shoin 1985
4. P.N.T. Wells, 'Biomedical Ultrasonics', Academic Press 1977
5. 'Grant's Atlas of Anatomy', Anne M. R. Agur, Williams & Wilkins 1991
6. Wang, Yuan-Yuan; Wang, Wei-Qi 'Estimation method for blood flow velocity profiles in vessels', Ultrasound in Medicine and Biology v21 n5 1995 p725-7
7. Matsumoto et al, 'Simultaneous cardio-cerebral ultrasonic measurement technique for assessing the interrelationship between cardiac and cerebral circulations in elderly subjects: A preliminary study', Ultrasound in Medicine and Biology v18 n1 1992 p.45-9
8. 'Gray's Anatomy', Lea & Febiger 1973
9. Eriksen M., 'Effect of pulsatile arterial diameter variations on blood flow estimated by Doppler ultrasound', Medical & Biological Engineering & Computing, vol. 30, no.1, Jan 1992, pp 46-50.
10. Ginette Champagne and Daniel Farget, 'Examination of the carotid circulation by means of continuous wave Doppler ultrasound'. Medical Ultrasound 4:9-11 Feb 1980 p. 9-11
11. Uri Dinnar, 'Cardiovascular Fluid Dynamics', CRC press 1982.
12. Chee Wei Chia, 'Characterizing the state of the arterial system through an analysis of the blood pressure waveform', SM thesis in electrical Engineering MIT, 1992.
13. Miyamoto Hiroshi et al, 'Telemetry of Blood Velocity of the Human Carotid Artery' SICE 89 Proc 28<sup>th</sup> SICE ANNU CONF SICE '89: volume 2 jul 25-27 1989 p. 1139-1141

14. Venkatraman et al, 'Skin Adhesives and Skin Adhesion', Biomaterials v19 n13 Jul 1998 p. 1119-  
1136

# Total Home Automation and Health Care Consortium

**March 31, 1999**

## **SIMSUIT Project**

**Lynette Jones**

***Principal Research Scientist***

**Sylvain Martel**

***Post-doctoral Associate***

**James Tangorra, Lisa Sambol**

***Graduate Research Assistants***

**Abstract:** The SIMSUIT project is focused on the development of wearable health monitoring units that can measure different physiological variables and evaluate the status of different sensory systems by perturbing them and measuring the responses to these perturbations. These monitoring systems must be lightweight, wireless, non-invasive and non-intrusive and so considerable effort is being devoted to miniaturizing the component elements and developing appropriate testing protocols. In this report research on the development of the vestibular-ocular testing apparatus will be described. This system is being developed for use as a clinical evaluation tool to examine the functioning of the human vestibular-ocular system particularly for the elderly population, and as a device to measure the alertness in human operators controlling vehicles or machines. Research on a new type of micro-powered EMG recording system has begun with the objective of monitoring the activity of muscles through time as an indicator of human activity and fatigue. The circuit consists of an instrumentation amplifier and a special AC coupling configuration that maintains a high CMRR with a gain of a 1000. All the electronics including two lithium batteries are mounted on a flexible circuit board (FPC). The single FPC has a special shape that allows differential recording at various distances between the electrodes. The whole circuit will be snapped onto the surface EMG electrodes affixed to the skin so that it can be re-used many times.

# A Battery-Powered Dual Active Electrode Unit for EMG Recordings

The measurement of the electrical activity of muscles, known as the electromyogram or EMG provides a useful index of the work being done by the muscles and can be used as an indirect estimate of muscle force. It indicates the start and end of muscular activity, something about the number of active motor units in a muscle and the frequency with which they are discharging. It is one of the most frequently used indices of muscle fatigue as it changes in a predictable and repeatable manner with fatigue.

The objective of this project is to design and implement a single, compact, reusable unit containing all the electronics required for surface EMG recordings from skeletal muscle. Because of the low amplitude of the signals being measured a high gain has to be used that does not cause signal saturation. By using a high gain right next to the recording electrodes, it is likely that a much higher signal-to-noise ratio (SNR) will be achieved in most cases. The unit has to be powered by batteries that are adequate for a relatively long operational life. Battery-powered systems have two advantages: they have very low noise on the power rails and provide isolation. Although the PSRR of the amplifier can reject noise from the power rails, bringing power to a remote unit through relatively long wires would introduce noise at various frequencies that would probably not be fully attenuated by the PSRR and hence would cause alias errors. A high common-mode rejection ratio (CMRR) has to be achieved while providing slow baseline drift removal capability. In this application a recording bandwidth of up to 100 Hz at a minimum gain of 60 dB is required, with an expected maximum signal amplitude of up to +1 mV.

## Architecture

The circuit is implemented on a single Kapton Flexible Printed Circuit (FPC) that has two main sections of size 33.75 mm × 21.78 mm (1.3285 × 0.8575 inch) linked through a narrow bridge. One section contains all the electronics and the second section is used to hold two rechargeable lithium batteries. Both sections have an embedded female snapper that connects directly to a pair of conventional surface electrodes by inserting the female onto the male snappers. The configuration allows two differential electrodes to be placed separately on

the skin to a chosen distance of up to 101.6 mm (4 inches). For shorter distances, the narrow bridge connecting the two sections simply bends upward.

## Amplifier

One of the most critical issues was to select the best amplifier for this particular unit. The AD627 [Analog Devices] has been selected for several reasons. It is a micro-power instrumentation amplifier, which makes it ideal for differential recordings, and it has low power consumption. In dual supply mode, the power rails' voltages can be as low as  $\pm 1.1$  Volt, which is ideal for battery-powered applications. With a maximum quiescent current of  $85 \mu\text{A}$  ( $60 \mu\text{A}$  typically), the unit can operate continuously for several hundreds of hours before requiring battery replacement.

## Batteries

Although 1.5 V batteries such as Zinc-Air batteries or even 1.2 V nickel cadmium or nickel-metal hydride (NiMH) batteries could have been used, 3.0 V batteries such as lithium cells have been chosen for this EMG recording system. With a gain of 60 dB and a maximum negative and positive output swing of  $-V_s + 25 \text{ mV}$  and  $+V_s - 70 \text{ mV}$  ( $R_L = 20 \text{ k}\Omega$ ) respectively. The positive input amplitude would be limited, in the best case, to 1.5 mV and 3.0 mV with 1.5 Volt and 3.0 Volts batteries, respectively. To be capable of recording signals up to  $\pm 1 \text{ mV}$ , 3 V batteries were essential to provide a sufficient margin with respect to the input signals and to deal with various artifacts such as offsets and drifts in temperature. The positive peak input voltage is specified with respect to the amplifier's reference. In the present implementation, the amplifier's reference is simply connected to the analog ground. The main advantage is a simple implementation without additional power consumption and a low impedance connection, which maintains the high CMRR. This configuration is optimal if both the positive and negative portions of the bio-signal are relatively the same, otherwise the amplifier's reference could be changed. Generating a virtual ground that is to be connected to the amplifier's reference could have been easily implemented through a voltage divider using two resistors with high values and the right ratio linking the 3V with the analog ground, with the reference connected between the two resistors. By using resistors with high values, the

power consumption could have been maintained relatively low but this configuration would increase substantially the impedance at the amplifier's reference and therefore, decrease significantly the CMRR which is critical to differential recording. To generate a virtual ground while providing low impedance at the amplifier's reference, an additional amplifier must be used. This configuration was not chosen because of the additional quiescent current required which imposed some serious restrictions on the physical size of the battery that could be used. The standard discharge of the lithium cells with a size sufficiently small for our particular implementation is as low as 100  $\mu$ A. With a 25  $\mu$ A margin from the maximum quiescent current of the AD627, an additional amplifier would, in the best case, require a standard discharge of 200  $\mu$ A. This means that the diameter of the lithium cells would increase, for example, from 10 mm (CR1025) to a minimum of 20 mm (CR2016) in diameter. The discharge current could be increased to the maximum continuous discharge of 0.5 mA for the CR1025, but the voltage at the output of the battery would drop accordingly. Although the voltage at the power rails can drop to as low as 1.1 V for the AD625, it would reduce the maximum output swing which is already tightly restricted. The same reasoning applies when recording bipolar signals with a single lithium cell. In this situation, a virtual ground must be generated, which increases the drain at the battery's output while reducing the output swing amplitude of the amplifier.

Lithium cells have been selected because of their long shelf life, their light weight, and high energy density relative to older primary cells. There are two main lithium products readily available commercially, the carbon monofluoride coin and the manganese dioxide coin, represented with part numbers starting with the standard prefixes BR and CR respectively. Both types have a relatively stable and flat discharge voltage. Since conductive carbon is continuously formed during discharge, the internal impedance of the battery does not increase until the end of the discharge. The lithium manganese dioxide (CR-type) is very popular because of its lower cost and wider availability compared with the lithium carbon monofluoride (BR-type). Although both types of cell can be used with the present system, the operating voltage of the CR-type drops slightly over time because of the rise internal impedance, which does not occur with the BR-type, because of its  $MnO_2$  content.

The EMG unit has a two battery cell holder that accepts CR1025 lithium batteries. The two 10 mm diameter CR1025 batteries with a weight of 0.7 gm, each has a capacity of 30 mAH per battery which can provide an operational life of approximately 700 hours minimum and 1000 hours of continuous operation between recharges.

### **Filtering**

The unit has a 20 dB/dec. bootstrap AC-coupling with a 3-dB cut-off frequency set at 0.5 Hz for baseline drift removal and low-pass filtering above 100 Hz with approximately -20 dB/dec. of attenuation. The high-pass filtering does not require additional components since it is achieved by the limits of the gain versus frequency characteristics of the instrumentation amplifier alone. The amplifier has been selected such that with a gain of 60 dB, a flat response could be observed up to a maximum of 100 Hz with gain attenuation above 100 Hz. Although additional components can be avoided which is critical in developing a compact system, the cut-off frequency becomes highly dependent upon the gain value of the unit. For instance, decreasing the gain to 40 dB would increase the cut-off frequency to approximately 300 Hz in our particular case. Nonetheless, the present implementation provides a perfect match between both the recording bandwidth and a required gain of 60 dB. The bootstrap AC-coupling requires twice the number of components compared with a typical AC-coupling configuration. But unlike conventional AC-coupling, it maintains a much higher CMRR so is critical in differential measurements.

### **Managing Error Artifacts**

It is extremely difficult even with large surface electrodes and very good skin preparation to achieve a skin-electrode impedance below 5 K-ohms. In the best case, input impedance of at least 500 K-ohms is required to maintain the loading error below 1%. Assuming that the skin-electrode impedance may vary between 5 K- and 10 K-ohms, 1 M-ohm input impedance would maintain loading errors below the acceptable thresholds of between 0.5% and 1%.

The AD627 has a maximum bias current of 10 nA (2 pA typically) and of 15 nA over the temperature range of the device (10 nA typically) with a typical average temperature coefficient of 20 pA/°C. Because of the AC-coupling, the bias current at each amplifier's input flows through a return path consisting of two resistors of 499 K-ohms each in series in the bootstrap circuit connected to the analog ground. Over the full temperature range, a maximum input offset created by the bias return path can be as high as 15 mV. Although this would be a problem in single-ended recordings, in our particular implementation this large offset would appear at both inputs and ideally be cancelled by the CMRR. Unfortunately, mismatches between the channels prevent a complete cancellation of the bias offset. First, the AD627 has a maximum input offset current of 1 nA (0.3 nA typically) and 5 nA over temperature with a typical average temperature coefficient of 5 pA/°C. This alone creates a worst case input offset at room temperature of 1 mV, which translates into 1 V at the output. Considering both the input and output offsets of the amplifier, the resulting output offset can reach a value of approximately 1.2 V at room temperature. With a bio-signal of positive amplitude of 1 mV, we still have approximately 800 mV left at the output (800  $\mu$ V at the input) prior to saturation. This result translates into approximately 80 k $\Omega$  of impedance mismatch at the inputs which should be easily achieved with resistors with a 1% tolerance and a maximum impedance mismatch between electrodes of 5 K $\Omega$ .

## **Portable Vestibular Testing Apparatus**

Dizziness and disequilibrium are common complaints in elderly people and associated falls are a major source of injury and death. Neuroanatomical studies of the vestibular system in older people have shown degenerative changes in the inner ear (loss of hair cells) and vestibular nerve (loss of nerve fibers) and neuronal loss in the vestibular nuclear complex (Lopez et al., 1997). The rate of loss of the peripheral vestibular anatomical structures increases in people over 55 years of age (Peterka et al., 1990). It is reasonable to assume that reflex function depends on intact vestibular structures and that associated with the anatomical deterioration in the elderly there is a decline in reflex function as reflected in the vestibular-ocular reflex (VOR). Paige et al. (1992) have shown that the response characteristics of the VOR undergo specific and robust changes as a function of age. These changes are both frequency and amplitude

dependent. The mean gain of the VOR is significantly decreased in older people as compared to younger subjects and there is a significant increase in phase lead of eye velocity relative to head velocity in older people, indicating a shorter dominant VOR time constant in the elderly (Baloh et al., 1993; Paige et al., 1992). The portable VOR testing apparatus that is being developed in the Consortium has as one of its objectives the quantitative measurement of vestibular function in the elderly.

### **Head Perturbation System**

Since October 1998 our main effort has been directed towards investigating different methods of creating horizontal-plane torque perturbations, and determining if they could be used for the head perturber portion of the vestibular testing apparatus. The head perturber creates one of the two controlled inputs for the vestibular-ocular reflex (VOR) testing protocol; the other input being the motion of a visual target. By shaking a person's head in the horizontal plane, the head perturber elicits a response from the horizontal vestibular ocular reflex, which rotates the eyes equal and opposite to the head's motion. The satisfactory performance of the head perturber is crucial for generating an accurate evaluation of a person's vestibular-ocular response, so it is beneficial to explore many possibilities for producing torque perturbations. In addition to evaluating new head perturbation devices, we have continued to develop and refine the vestibular testing protocol and the analysis algorithms. The algorithms and software cannot be fully developed, however, until the head perturber achieves its design criteria, and therefore their development is considered secondary to that of the head perturber.

As described in previous consortium reports, a working head perturber has been used to conduct "proof of concept" horizontal VOR testing, and has served as a platform for developing the other components of the vestibular testing system. This perturber applies a reaction torque to a person's head by using a position-controlled servomotor to accelerate a light aluminum ring about a person's head (see Figure 1).



Figure 1: Head perturber developed from position controlled servomotor and external inertial ring

This arrangement is easily controlled, is capable of producing the desired peak torque levels (1 N-m), is particularly light (0.85 kg) and comfortable to wear. Unfortunately, its low frequency torque output does not meet the 0.5 to 10 Hz input bandwidth necessary to conduct a system level assessment of the vestibular ocular reflex. The servomotor-based perturber has served well for the first stage of system development, but must be improved upon if the system is to produce medically relevant and accurate data. One option that would fix the torque bandwidth problem but would create a different set of issues would be to replace the existing servomotor and aluminum ring with a dc motor and inertial mass tuned to produce low frequency torque perturbations. To produce the low frequency perturbations, it would be necessary either to increase the mass of the inertial ring significantly, or to significantly reduce the magnitude of the torque being applied to the person's head. Before either penalty could be accepted we wanted to explore other technologies and techniques that might be appropriate for producing head perturbations.

To be acceptable for use in the VOR testing protocol the perturbation device must meet the following performance criteria. First and foremost the perturber must be able to produce torque perturbations that span the performance bandwidth of the VOR, which is from 0.5 Hz to above 10 Hz. The torque must be able to be produced as a stochastic output, preferably in a pseudo random binary fashion, and the device must not impede the test subject's natural head and eye motions. A major element of the testing protocol is to evaluate the VOR under normal operating conditions, which means that the person must be free to use natural head and eye motions to track a moving target. Therefore, the perturbation system must be lightweight and completely free to translate and rotate with the subject's head, while still being able to apply torque perturbations to the wearer. Our intent is to make the system useful for clinical and bedside use, as well as for laboratory use, so the perturber must be portable and easily set up. As a medical device that will be used with the elderly, it must be safe to use, comfortable to wear, and must not cause any trauma.

The perturbation methods that have been considered for the head perturber can be divided into two general classifications: those that apply torque to the head via a reaction force, such as the servomotor and inertial ring prototype, and those that use an externally mounted motor to directly apply a torque to the subject's head. The reaction force devices create torque

perturbations by accelerating an inertial mass about the subject's head. The perturbation device is mounted on either a helmet or headband worn by the test subject. Other than a power cable and wiring for the computer control, there are no external connections. The test subject supports the entire weight of the reaction perturber, and as long as the perturber is not cumbersome, the person is free to move their head and neck as they naturally would when tracking moving targets. Since the reaction perturber allows unrestricted head motions, it has the potential to be worn while a test subject conducts normal daily activities. This allows for periodic testing of a person throughout the day, and enables testing of a person in their normal environment which may help eliminate the mental set change that often occurs as a person gets ready for a physiological exam. The main limitation of reaction type devices is their limited ability to create low frequency perturbations. To produce low frequency torque perturbations, while maintaining reasonably slow rotational speeds necessary for safety, a device must either have a large rotational inertia, which would usually make it too heavy to be worn, or the torque applied during the long accelerations must be of low magnitude, possibly too low to stimulate a VOR response.

The second group of perturbation devices that have been considered, the "direct torque application" devices, use mounted motors to apply torque directly to the subject's head. A torque-controlled motor is mounted above the subject's head, and drives a helmet or semi-rigid headband worn by the subject. The motor can be attached to the ceiling, a freestanding frame, or even to a seat back if the test was to be conducted with the subject seated. The motor would have to be gimbaled to allow for pitch and roll head rotations, but rigidly fixed about the horizontal axis so that it would be able to apply a horizontal plane torque to the subject. The main advantage of a mounted system is that it is as easy for the motor to apply a low frequency torque directly as it is for it to apply a high frequency torque. Torque and velocity control would enable a dc motor to produce stimuli that spanned the entire bandwidth of the vestibular system, and would allow the motor to exert torque in the appropriate direction as its angular position changed with the person's head. Another advantage is that the person would not have to support any of the apparatus' weight, as in a reaction perturber, as the apparatus' weight would be supported by the mounting. The main disadvantage of a mounted system is that it could restrict the head motions the person uses to track a visual target. The gimbaled fixture

would allow very little translation of the person's head, only rotations. This might feel unnatural and might encourage the test subject to use mainly eye motions for tracking, rather than the natural combination of head and eye motions that our protocol desires. The elimination of head translation may, however, make the analysis of the data simpler, since all compensatory eye motions from translation would be eliminated. Another disadvantage of the mounted system is that it increases the complexity of the equipment installation and reduces the portability of the system. It also reduces the likelihood that the system could be incorporated into the routine equipment worn by a pilot or worker, or used for intermittent VOR testing during normal activities. Though not considered practical for bedside or industrial testing, where portability is essential, the direct torque application perturber is still useful for laboratory use. The ease with which low frequency perturbations can be created makes it a nice system for evaluating a reaction perturber as it is developed. Specifically, it will allow us to assess how small in magnitude a torque perturbation may be and still elicit a measurable VOR response. This will dictate the necessary rotational inertia for the reaction perturber, and may allow us to produce a lightweight reaction perturber that uses very low torque to test the VOR. A laboratory system will be built over the next month as a means to benchmark other testing devices and to enable the development of the analysis algorithms. However well the mounted system works, it is not considered likely that a direct torque application method could be used outside of a permanently installed laboratory set-up.

One of two tradeoffs must be made to produce low frequency torque perturbations with a reaction perturber that are safe. Either the weight of the inertial ring must be large, or the magnitude of the torque perturbation must be small. When either the rotational inertia of the ring is small, or the torque is large, the inertial ring tends to accelerate to high rotational speed. These speeds may exceed the capabilities of the motor (then obviously the motor would not be meeting the design criteria of the system), may create unsafe gyroscopic effects, or may simply be unsafe by virtue of having an exposed disc spinning at great velocity. The bandwidth of the vestibular-ocular reflex is considered to extend to as low as 0.5 Hz. Testing at this frequency requires an input stimulus with a 2-second period. In the case of a torque driven by a pseudo-random binary sequence, the reaction torque would last for 2 seconds, and therefore the inertial mass being would accelerate for 2 seconds. Consider the simple reaction arrangement where a

central motor drives a single external ring. If the ring has a mass of 1 kg (the upper range of comfort) and a radius of 0.125 m (sized to fit around an average head), a 1 N-m torque applied for 2 seconds would accelerate the ring to 128 r/s (1222 rpm). This would have a significant amount of rotational inertia and could cause a gyroscopic effect on the wearer. This speed also nears the upper rotational speeds of many of the micro-dc motors that would be used for the system. The motor alone could attain these speeds, but not when run through the reduction gear necessary to produce the required torque. If the torque applied to the subject could be reduced to 0.25 N-m, the 1 kg ring would only attain 32 r/s (305 rpm). The 0.25 N-m is only a quarter of the torque that is believed to be needed, but experimentation with the mounted motor perturber may show that it is sufficient. Increasing the mass of the ring is one means of reducing the maximum ring speed, but any ring weighing more than 1 kg feels heavy and is uncomfortable to support on the head. By shaping the torque, the maximum velocity of the ring can be reduced, but generally it is difficult to attain low frequency, torque perturbations of 1 N-m amplitude with a reaction perturber without also causing large final speeds or employing a ring with great rotational mass. This must be resolved before a commercial product can be produced.

Five experimental apparatus have been built to evaluate different methods of generating a controlled reaction torque: a Coanda water jet, an inertial ring driven by a central servomotor (as used in the present helmet perturber system), a solid conductive ring driven by a Lorentz force actuator, a liquid metal driven by a Lorentz force actuator, and a controlled braking system. The goal of each set-up was to determine if the arrangement could generate the desired 1 N-m torque throughout 0.5–10 Hz bandwidth, and if the arrangement could be reasonably modified to meet the comfort, weight, portability, and safety needs of a head-mounted medical testing device. Of the five systems, only the servomotor driven inertial ring system was developed into an actual helmet perturbation device and used for subject testing. The other four methods were evaluated but have not been developed past their initial testing arrangement.

## Coanda Water Jet

The Coanda water jet device is unique among the reaction devices in that it does not accelerate an annulus of material circularly about the head, but creates a reaction force by expelling a jet of water out of nozzles. A Coanda-effect valve (Figure 2) is a bistable-switching device that allows for very quick switching of a water jet between two outlets. It is thus very well suited to creating a pseudo random binary output (PRBS), which alternates between two values, which for our application is between a torque to the left and a torque to the right. The Coanda valve would be mounted on the top of a helmet worn by the test subject. Water would be delivered either from a faucet attachment or from a pressurized tank, through hydraulic lines to the Coanda valve, and expelled through one of two nozzles at the back of the helmet. The PRBS would determine how the jet gets switched between outlets.

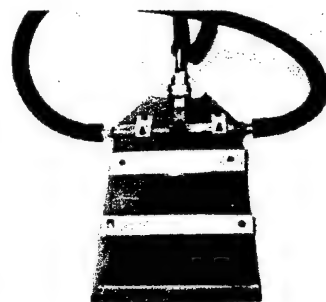


Fig. 2: Bistable Coanda water valve

The system produces the torque requirements needed for our testing protocol. It easily switches between the two outputs, and is capable of producing long periods (low frequency) of continuous torque in either direction. Obvious shortcomings prevent the system from being easily applied as a medical device. A water driven system would need to be used under special conditions, such as in a shower stall, and therefore could not be used as a bedside or routine laboratory testing device. One technical disadvantage with the system is that the hydraulic lines that carry the water to the Coanda valve on top of the head become stiff when pressurized with water. The stiff lines tend to inhibit the wearer's head motion, and could prevent testing the vestibular system with normal head and neck movements. The Coanda system is considered an interesting device, but not appropriate for our needs.

## Helmet mounted servomotor and ring

The most well developed and tested reaction perturber is the servomotor driven inertial aluminum ring. It has been extensively described in past reports, and has served as the reaction device in the helmet perturber used for all of our data collection. It is light, comfortable, and easily controlled with a pseudo random binary sequence, but it does not produce the torque

power spectrum necessary for accurate vestibular testing. As can be seen in Figure 3, its output is limited to approximately 1.5 to 10 Hz, which is not broad enough to produce an accurate impulse response estimate. When used as the input to estimate stochastically the impulse response of a simple rotational mass system, the estimate is close to the expected second order system, but with obvious error (see Figure 4). This error can be attributed to the input created by the perturber not matching the flat spectrum of an impulse input. As previously stated, changing the ring's mass and the motor's torque output could better tune this system to the

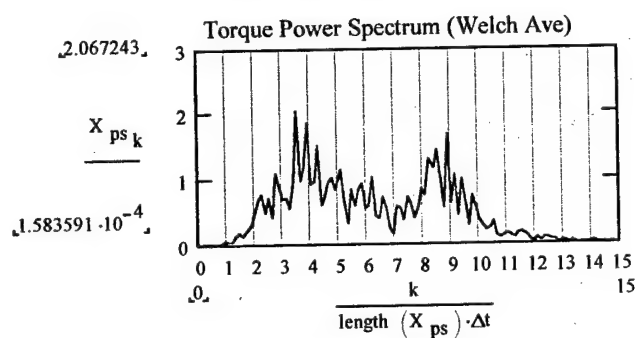


Fig 3. Power spectrum of servomotor

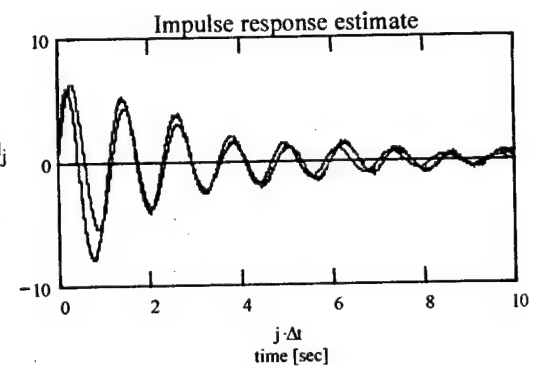


Figure 4: Red: Impulse response estimate of damped, sprung, rotational mass  
Blue: Ideal second order impulse response

needs of the vestibular testing protocol.

### Lorentz Force Actuator with Solid Conductive Ring

The Lorentz force, the force that acts on a charged particle in an electric and magnetic field, is the fundamental force that causes a motor to rotate. In the servomotor driven inertial ring perturber, the result of the Lorentz force is the motor's torque, which is applied to the rotating ring through a mechanical connection. Rather than using a mechanical link to connect the external ring to the motor's Lorentz force, it is possible to directly apply a Lorentz force to a conductive ring. A Lorentz force can be generated to rotate the ring by establishing a horizontal, radial magnetic field across a ring, and then driving current vertically through the ring. By modulating the current flowing through the conductive ring, the force applied to the ring can be controlled and can cause the ring to move back and forth.

The Lorentz force principle was exploited in two perturber experiments: one that moved a solid copper ring about a circular channel, and the other rotated a liquid metal about a similar

circular channel. The liquid metal seemed much more interesting to work with than the copper ring, but required a more advanced design. It had to address viscous flow issues, sealing, potential phase changes of the liquid metal, thermal expansion, and other unknowns. It was more prudent to first build a proof of concept apparatus using the solid ring, and then apply what was learned to the liquid metal.

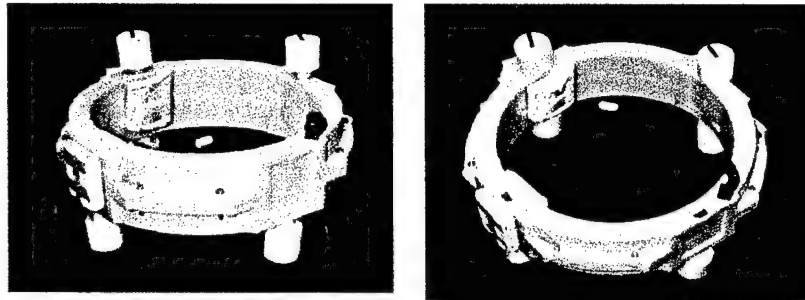


Fig 5: Lorentz force solid copper ring perturber.

A 130 mm radius, 3 mm wide, 70 mm high solid copper ring was placed inside a channel machined into a cylindrical cast nylon housing (see figure 5). The inner diameter of the housing was large enough to fit around an average head, and allowed the housing to be attached to head attachment devices such as a helmet or pair of headphones. Four pairs of neodymium-iron-boron permanent magnets provided a 0.4 tesla magnetic field across sections of the copper ring. Current was delivered to the copper ring through four pairs of graphite brushes that made sliding contact with the copper ring at the top and bottom of the housing. Threaded cylinders allowed the contact force between the graphite brushes and the edge of the copper ring to be adjusted. Each pair of brushes and magnets created a distinct Lorentz force actuator module. To produce the desired 1 N-m torque, the copper ring perturber required over 100 amps of current at each of the four actuator modules. 12-volt lead-acid batteries, wired through automobile ignition switches and 12 gage equipment wire, were used to provide the necessary current. Testing consisted of intermittently applying current to the copper ring and monitoring the ring's motion. We limited the time the current was passing through the ring to 1 sec to reduce the risk of a fusing the ignition switches, or fusing the brushes to the copper ring, and creating a

dangerous low resistance closed circuit with a battery. During testing, currents of up to 65 amps were inductively measured flowing through the wires and brushes of each actuator module. After a few one-second on-off cycles the wires became very hot to touch, but not hot enough to be in danger of fusing. Enough force was developed by the Lorentz actuators to just move the copper ring during the 1 sec of force application. Friction between the ring and the cast nylon housing was high, as no rolling bearings were used to support the copper ring, which severely limited the acceleration of the ring. Smaller, lighter rings, were also tested, and moved significantly farther than the original heavy copper ring. However the smaller width of these rings reduced the effective contact area of the brushes, which limited the current that flowed through the copper ring, and hence the net torque produced by the perturber. Rather than building a bearing system to reduce the friction between the copper ring and the cast nylon housing, it was decided to initiate building the liquid metal Lorentz force perturber.

### **Lorentz Force Actuator with Liquid Metal Ring (Figure 6)**

A perturber was created using a liquid metal that circulated in a horizontal channel, in a similar manner to the solid copper ring Lorentz force perturber. The liquid metal, a gallium-tin-indium alloy that is a liquid at room temperature, is held in a thin circular channel milled out of cast nylon (Figure 6). A reaction torque is created by applying a Lorentz force to the gallium in the direction of the channel. As long as the applied force is greater than the flow's viscous retardation forces, the liquid metal will accelerate around the channel and create a reaction torque that could be used to perturb a head. As in the solid copper ring perturber, the Lorentz force is created by driving a current through the gallium alloy from the top of the channel to the bottom. A horizontal magnetic field is established perpendicular to the current by neodymium-iron-boron permanent magnets placed on either side of the channel. By directing the magnetic field radially across the channel, the resultant Lorentz force is in line with the center line of the channel and pushes the liquid metal along the channel.

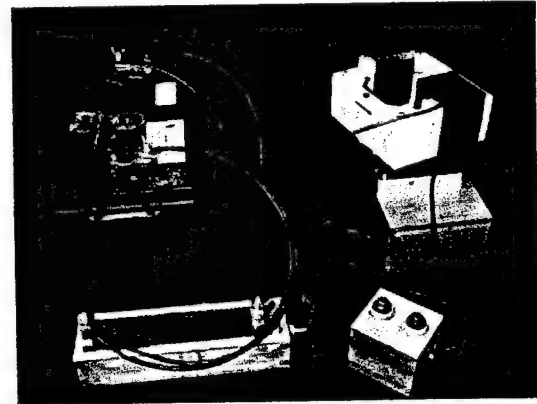


Figure 6: Lorentz force perturber with liquid metal

The channel dimensions significantly impact the theoretical torque that can be produced with the liquid metal perturber. From the perspective of creating large reaction torques by applying as large a Lorentz force to the fluid as possible, it is desirable to have the channel as tall as possible. The height of the channel corresponds to the length of the conductor in the  $F = ILxB$  force on a conductor equation, where  $F$  is the force on a conductor in a magnetic field,  $I$  the current,  $B$  the magnetic field, and  $L$  the conductor length. The resultant torque applied to the fluid loop is just the Lorentz force times the average radius of the channel.

To maximize the torque applied to a given volume of liquid metal, it is therefore desirable to use a very tall channel with a large average radius, and hence a very thin thickness. This puts as much of the gallium at as great a moment arm as possible, maximizing the torque created by the Lorentz force. We are limited in the amount of gallium alloy that can be used because of weight constraints, so when one dimension of the channel is increased, another must decrease in order to maintain a constant volume. The reaction torque created by the liquid perturber is not equal to the Lorentz torque applied to the fluid, but to the resultant time rate change in angular momentum of the fluid. Though a larger Lorentz torque is applied to the fluid ring by making the channel thin and high, the thinner the channel the more pronounced the effects of the viscous boundary layer at retarding the flow and restricting the change in the fluid's momentum. From a simple 2-D fully developed flow model of the channel, it can be shown that the momentum flux of the fluid flow is proportional to thickness to the 5<sup>th</sup> power. We gain great flow benefits by making the channel thicker. Making the channel thicker, however, means that for a given amount of alloy, either the channel height or average radius must be reduced, which then reduces the Lorentz torque acting on the fluid ring. Few flow properties are known about this alloy making a theoretical flow optimization difficult. Although the liquid metal perturber seemed to hold promise as a head perturber, it was deemed more beneficial to determine empirically thickness effects by building scale channels of different thickness.

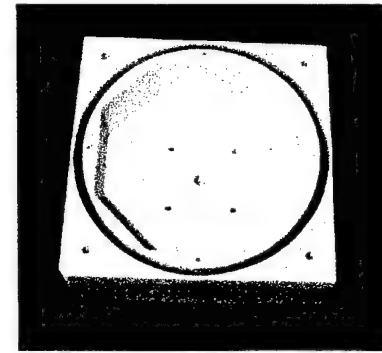


Figure 7: Circular channel cut into cast nylon block for liquid metal perturber.

The thinness of the channel gave rise to another concern, that of the current carrying capacity of the gallium alloy. To attain near the desired 1 N-m torque with a liquid metal perturber of similar dimensions to the copper ring perturber, between 500 and 1000 amps would have to be driven through the metal. The actual current required to develop the torque would depend on the strength of the magnetic field supported across the channel. With a channel thickness of 3.5 mm, and an average radius of 127 mm, a current of 500 amps would yield a current density (flux) of  $1.8 \times 10^5$   $\text{amps/m}^2$ . The actual current capacity of the gallium alloy is unknown, but for copper is  $1 \times 10^7$ . We felt that keeping under  $1 \times 10^6$  for the gallium would be satisfactory.

The proper strength and direction of the magnetic field in the channel is critical for the perturber to work effectively. Ideally the magnetic field would be directed radially outward everywhere through the channel (figure 8), and to complete the magnetic circuit, would follow an inward return path above and below the channel. This horizontal outward magnetic field would ensure that the Lorentz force created by the vertically flowing electrical current would always be directed with the centerline of the channel. Any magnetic field lines flowing through the channel in a direction other than radially out, would change the direction of the Lorentz force away from the tangent to the channel centerline. The only means of creating a field that would meet the strength and would reduce the net Lorentz force acting on the fluid ring, and direction requirements would be to have two radially polarized, continuous, cylindrical magnets, one on the inside and one on the outside of the channel, directing field across the channel. Unfortunately, cylindrical permanent magnets of the size and strength needed for our application would have to be custom manufactured, at a cost nearing \$15,000 a little expensive for a prototype designed to explore the feasibility of an idea. Strong, square plate neodymium-iron-boron magnets are readily available,

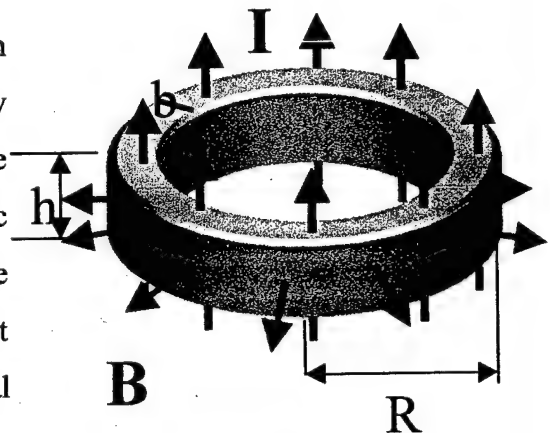


Figure 8: Ideal situation where every where magnetic field (red) is radial

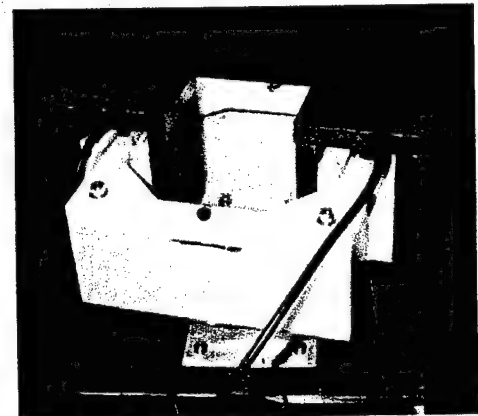


Figure 9: Soft iron horseshoe used to complete magnetic circuit outside channel

so it was decided to maximize a field using stock magnets. A finite element 3-d electromagnetic field software package (Ansoft Maxwell) was used to analyze different arrangements of magnets and iron around the circular channel. The magnetic field was maximized across the channel by connecting pairs of magnets on either side of the channel with a soft iron horseshoe (Figure 9). The iron horseshoe served as a return path for the field after it flowed across the channel. This arrangement resulted in a strong 0.65 tesla field measured across the channel (air filled, not gallium). The penalty for this large, but necessary, magnetic field is the weight of the magnets and the iron. When implemented in the prototype, each pair of magnets and soft iron horseshoe exceeded 1 kg, which is much too heavy to be used for a head perturber in which the total weight of the system should be less than 2 kg. Before testing to determine if the liquid metal perturber could produce the desired torque output, it was known that the system would not be acceptable for a head perturber until the magnetic field could be generated with much lighter magnets. Unfortunately, there do not seem to be permanent magnets, ceramic, iron based, or rare earth that at present can meet our weight and strength requirements.

The liquid metal perturber apparatus was made smaller in diameter than the full scale, 125 mm radius copper ring system. This was to allow experimentation with different channel diameters to see their effects on the torque output, while keeping the total volume of the system under 1 kg. For the system, a 3.175 mm thick, 45 mm deep channel, with an average radius of 76 mm was milled into a 160x160x53 mm cast nylon block. The thin, but deep channel was cut with extended length end-mills. An octagonal shape was cut from the center of the block to a depth of 45 mm, such that only a 2 mm wall existed at the closest point to the channel. The top of the channel was closed with a 13 mm thick Delrin cover plate in which a 5 mm deep channel was milled. When placed together the cover and base block had an overall channel height of 50 mm. The Delrin cover was sealed to the cast nylon block with a silicon sealant, and screws were used to compress the seal and ensure alignment of the channels.

Current was delivered to the gallium alloy through 10 gage Belden wire, insulated with PVC. The wire's overall diameter is 4.2 mm, but the conductor's diameter is only 3.1 mm which just fits into the 3.175 mm channel. Brushes, that made contact with the gallium, were fashioned by stripping the insulation from the end of the wire, and passing the wire through a hole axially machined into a 4 mm diameter nylon screw. The bare wire was sealed to the screw with epoxy.

The screw was threaded into the top and bottom of the channel such that a small length of wire extended into the liquid gallium that sat in the channel. Current, supplied by 12 volt, deep cycle, marine batteries passed from the cable at the top of the channel, through the gallium in the channel, out the cable at the bottom of the channel and through a resistive carbon pile. The resistance of the carbon pile could be adjusted by changing the mechanical force acting on the pile. Changing the resistance of the carbon pile allowed for a resistive control of the current flowing through the system.

During testing, the liquid metal perturber showed that it was capable of producing peak torques near that of what was theoretically estimated for its dimensions and field strength. Increasing the size of the channel would enable the liquid metal perturber to exceed to a peak torque of 1 N-m. The prototype was not, however, able to sustain the torque it developed when the current was initially applied.

After an initial peak, the torque would decay to zero as seen in Figure 10 (the oscillations are attributed to compliance in the mechanical system that connected the perturbed to the force transducer). Inductive current measurements indicated that the current flowing through the system held steady through the test. Therefore current decay was not the cause for the reduction of force. A possible explanation is that the reaction force decayed because the fluid was actually attaining its steady state velocity and no longer accelerating. The steady state velocity is attained when the viscous forces balance the Lorentz force being applied to the fluid. The viscous forces rise with velocity, and a graph of the fluid speed would resemble the decay curve of the torque. However, the time frame for the decay does not seem appropriate for the system. The fluid was expected to require a longer time to attain steady state. Also, the time at which the fluid would attain steady state speed would be proportional to the magnitude of Lorentz force applied. However, the time scale of the decay did not considerably change as the Lorentz force was increased and decreased.

The liquid metal perturber concept was shown to hold some promise – it was able to produce peak forces that matched the needs of a head perturber, and would be relatively simple

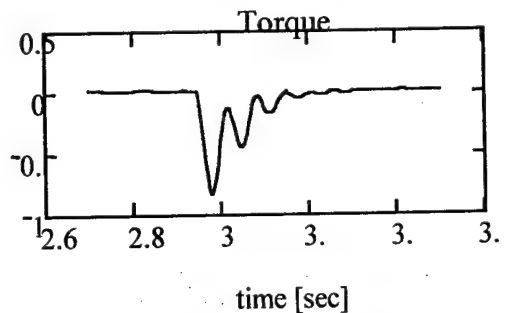


Figure 10: Torque decay of liquid metal perturber

to modulate by controlling current. To maximize the force of our system, there would have to be additional extensive fluid flow analysis, and experimentation to determine why the torque decayed quickly. Before any direct Lorentz force based system could be considered for a head-mounted perturber, though, the weight of the permanent magnets would have to be significantly reduced. Creating the magnetic field is the one area that requires a new technology to make a Lorentz force perturber acceptable for our application.

### **Braked Disc Perturber**

The braked-disc perturber is conceptually a little different from the other reaction perturber devices. It creates a reaction force primarily by slowing a spinning disc from a high initial velocity, rather than by accelerating an inertial ring from rest. The braked-disc perturber is being used to investigate 1) if there are advantages to using controlled braking as the means of changing the angular acceleration of an inertial mass, and 2) if using two discs, spinning in opposite directions, can mitigate the gyroscopic effects that are present when a single disc is spun to high velocities. One of the problems with creating reaction torques by accelerating a single ring in one direction is that a light disc may attain relatively high speeds after a long, low frequency, acceleration. The quickly spinning disc behaves like a gyroscope, and would resist being moved out of the plane in which it rotates by precessing. If the spinning disc was being worn as a head perturber and spinning in the horizontal plane, any head motions outside the horizontal plane would create a gyroscopic torque that would twist the subject's head in an undesirable direction. This would make it difficult for the subject to track a target smoothly that is moving in the horizontal plane, and would elicit saccades or vertical and torsional eye motions to compensate for the out of plane head motion. Though the VOR is the system creating these compensatory eye motions, our initial protocol is directed towards analyzing the horizontal VOR, and other head and eye motions complicate the analysis. It may be possible to reduce the gyroscopic effect of a single spinning disc, by using multiple, lighter discs, spinning in opposite directions. For either system, reaction torques of the same magnitude and duration require the same net change in the system's angular momentum, which would result in the same potential gyroscopic effect. However, it is worthwhile to investigate how closely the speed of the spinning disc can be maintained while eliciting a pseudo random binary sequence torque output

from the system. While one disc was being braked, the other disc's speed could be increased by a light pancake motor. This acceleration would supplement the reaction force created by the braked disc. Since the braking would outweigh the acceleration of the discs, eventually the discs would come to rest. The trick would be to see how closely the speeds of the individual discs could be modulated so that the net rotational momentum of the system was minimized as the kinetic energy was being removed in a pseudo binary manner. The braked disc system has the additional advantage of being lightweight. Since the discs would begin a test session at a high rotational velocity, they could be spun up by an external motor that would not have to be attached to the system or supported by the subject's head.

In order to get an empirical feel for the braking modulation of spinning discs a large prototype was built from high-end bicycle components (Figure 11). It was not thought necessary to build a prototype that met weight constraints of a head mounted perturber until it was established that the braking system had advantages over a perturber using a motor and inertial disc. The intent was to spin two bicycle wheels in opposite directions, brake the wheels in a pseudo random binary fashion, and reduce rotational speed down to zero velocity. The bicycle wheels were mounted into independently rotating forks, upon which a small bicycle disc brake (Figure 12) was mounted. Attached to each wheel hub is the disc upon which the disc brake acts. Disc brakes were chosen over traditional rim mounted, linear push/pull or cantilever brakes because of the disc brake's superior force modulation. The rim mounted, polymer pad, cable actuated cantilever bicycle brakes tend to grab the wheel when even slight pressure is exerted upon the brake's hand lever. The hydraulically actuated disc brake and hand lever is specifically designed for force modulation, and the manufacturer claims it will allow for excellent light force application and modulation. When the moving wheel is braked the reaction force pushes the fork, in

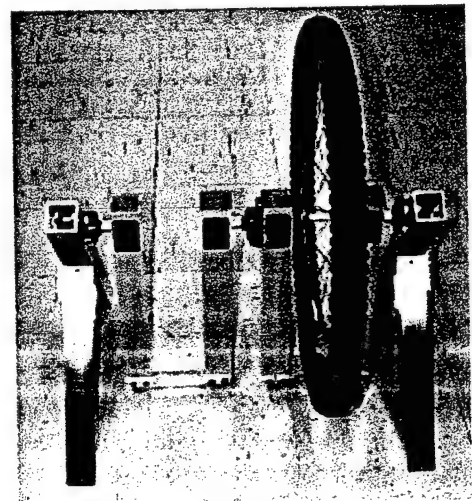


Figure 11: Single bicycle wheel in fork of "disc brake perturber" apparatus. The disc brake is not installed.

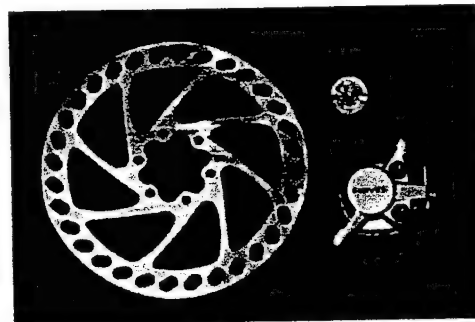


Figure 12: Hayes disc brake system compared to US quarter.  
disc:  $d=160$  mm,  $m=112$  g  
caliper:  $m=141$  g

which the wheel is mounted, against an Entran force transducer which measures and records braking data. The wheels are given their initial velocity by placing a hand drill against the rim and spinning up the wheel.

If the braking experiments indicate that the system has promise as a perturber, the basic system will be miniaturized into a form that can be mounted onto a helmet. The same disc brakes will be used, but the bicycle wheels will be replaced by thin discs rotated by small pancake style motors. Depending on the motors chosen, the pancake motors may, or may not, be used to give the discs their initial velocity. The primary role of the pancake motors will be to increase the speed of their respective discs while the other disc is being braked. There is a very legitimate safety concern in using the braked disc system as a head mounted perturber. Until the end of the test, the spinning discs have a good amount of kinetic energy. If ever one of the brakes was to wedge against the disk causing it to stop very quickly, all the energy would be transferred to the subject's neck in the form of a large torque impulse. This could cause a severe neck injury. Some safety device will have to be incorporated to ensure that the brakes cannot bind against the disc, or that some other failure cannot cause the spinning discs to stop suddenly.

## Conclusions

None of the perturber concepts investigated provides a clear-cut solution for all the requirements of the head perturber. Each perturber concept has some advantages that are unfortunately accompanied by shortcomings that do not meet certain design requirements. Of all the systems investigated, the perturber based on a central motor and inertial ring appears the easiest to implement with the fewest drawbacks. A balance, however, must be found between increasing the weight of the ring and lowering the torque output of the motor before the system will produce the low frequency perturbations necessary for an accurate assessment of the VOR. To determine how low in amplitude torque perturbations may be and still serve as an acceptable input to the VOR, experiments will be conducted with a mounted motor perturber. The mounted motor perturber is capable of producing both low and high amplitude torque perturbations across the entire VOR spectrum, and will allow us to assess how small the torque amplitude may be before a VOR evaluation becomes inaccurate. This will set the minimum

torque that must be output by the reaction perturber, and will dictate the mass of its inertial ring. Of the other perturber concepts, the liquid metal Lorentz force perturber and the braked disc method have the most potential. The liquid metal perturber could be an excellent head perturber method once magnet technology advances, and magnets of strengths comparable to rare-earth magnets are manufactured from lightweight materials. Upcoming experiments may indicate that the braked disc perturber warrants further development so that it can be tested on a subject's head. However, a safety device that prevents sudden lock-up of a disc is paramount before the system could be tested on a person.

## References

Baloh, R.W., Jacobson, K.M., & Socotch, T.M. (1993). The effect of aging on visual-vestibular responses. *Experimental Brain Research*, 95, 509-516.

Lopez, I., Honrubia, V., & Baloh, R.W. (1997). Aging and the human vestibular nucleus. *Journal of Vestibular Research*, 7, 77-85.

Paige, G.D. (1992). Senescence of human visual-vestibular interactions. 1. Vestibulo-ocular reflex and adaptive plasticity with aging. *Journal of Vestibular Research*, 2, 133-151.

Peterka, R.J., Black, F.O., & Schoenhoff, M.B. (1990). Age-related changes in human vestibulo-ocular reflexes: sinusoidal rotation and caloric tests. *Journal of Vestibular Research*, 1, 49-59.

## **Noninvasive Blood Glucose Analysis using Near Infrared Absorption Spectroscopy**

**Prof. Kamal Youcef-Toumi**  
Principal Investigator

**Vidi A. Saptari**  
Graduate Research Assistant

### **Abstract**

A modular Fourier-transform spectrometer was designed and built for the noninvasive blood glucose measurement research using the near-infrared absorption technique. A series of experiments were performed to evaluate the spectrometer's efficiency and its stability. The efficiency, which represents the photon loss through the spectrometer, is proportional to the achievable signal-to-noise ratio. The stability of the instrument is important for measurement repeatability, which would affect the sensitivity of the quantitative assessment of glucose concentration. A preliminary experiment on aqueous glucose solutions was performed, with the purpose of identifying the relevant spectral bands for glucose concentration prediction. It is found that there are two relatively strong bands where glucose molecules affect the water absorption spectrum. One is around  $5950\text{ cm}^{-1}$ , where there is a glucose absorption band, and the other is around  $7250\text{ cm}^{-1}$ , where the magnitude of water absorption is reduced by the presence of glucose molecules. Simple algorithm utilizing spectral information from these two bands may be sufficient for glucose concentration prediction.

## **I. Introduction**

This work is motivated by the profound need for a noninvasive way to measure glucose concentration in the blood. A noninvasive glucose monitoring device would provide a safer and a more convenient method to treat and control diabetes. The goal of diabetes therapy, within and outside hospital, is to approximate the 24-hour blood glucose profile of a normal individual, which necessitates continuous monitoring.

Several optical techniques have received considerable attention over several years, which include Raman, absorption and polarimetry spectroscopy [1-4]. Among them, the absorption technique in the near-infrared region was selected for our research. As discussed in the previous reports, one of the advantages of the absorption technique is its relatively stronger signal-to-noise ratio. Furthermore, it requires simpler and less expensive instrumentation than the other optical methods.

We have completed the development of a modular Fourier-transform spectrometer, which would be used for the subsequent experiments. The work was motivated by the need for a versatile and dedicated instrument for research in the field of noninvasive blood glucose sensing. Great emphasis is placed to ensure that each element is designed or chosen to give maximum signal-to-noise ratio in the near-infrared region. Overview of the system design is presented in the previous report [5].

In this report, we present the performance evaluation of the spectrometer on the basis of measurements chosen because of their impact on the instrument's capability for blood glucose concentration prediction. Identification of relevant wavelength ranges for the glucose analysis, with the experimental results is also presented in this paper. Finally, we discuss challenges and obstacles we anticipate.

## **II. System Description**

### **(i) Theory of Operation**

Figure 1 shows a schematic of the FT spectrometer setup. A white light from a tungsten halogen source is collected and collimated by a concave mirror and a pair of lenses. An aperture is used to limit the amount of divergence of the light entering the interferometer. The interferometer is of Michelson type, comprising a beamsplitter and two perpendicular plane mirrors. One of the mirrors moves linearly in the axis as indicated in the diagram. This produces a variable path difference between the two beams reflected off of the mirrors. The recombined beam is then focused onto the sample and onto the detector. The detector measures the interferogram, which is stored in the computer. This signal is then Fourier-transformed to obtain the spectrum.

A second Michelson interferometer with an HeNe reference laser, as indicated in the diagram, is used for controlling the velocity and position of the linear motion. In addition, it is also responsible for clocking the data acquisition at precise and repeatable locations of mirror retardation. This would enable repetitive scanning to improve the signal-to-noise ratio.

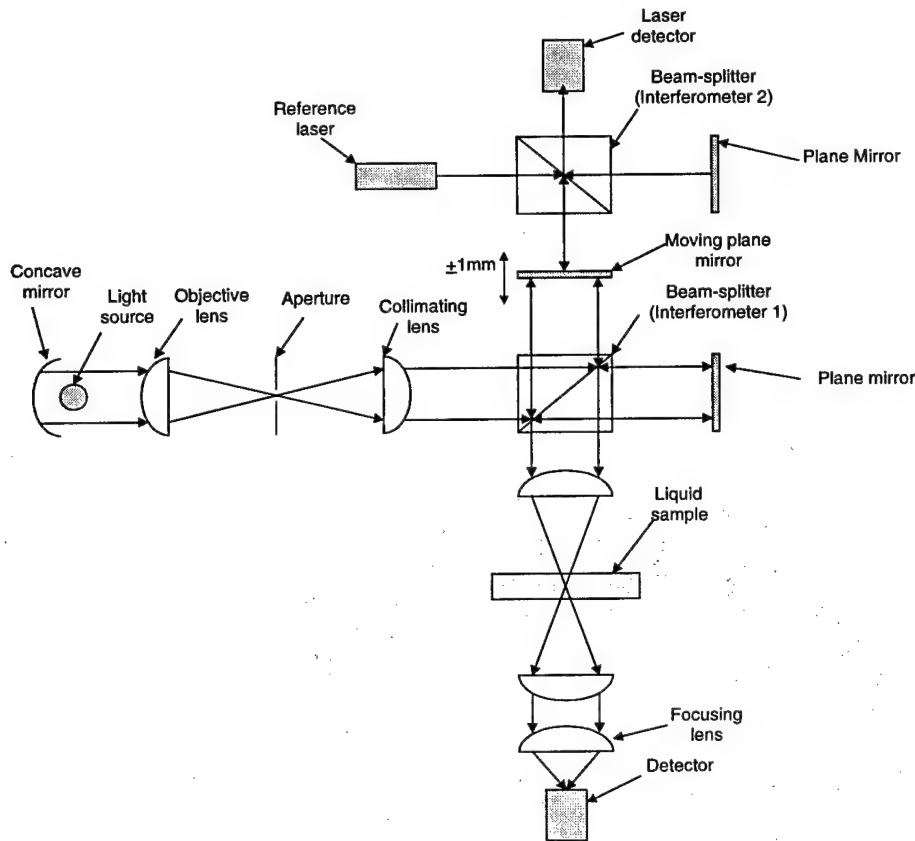


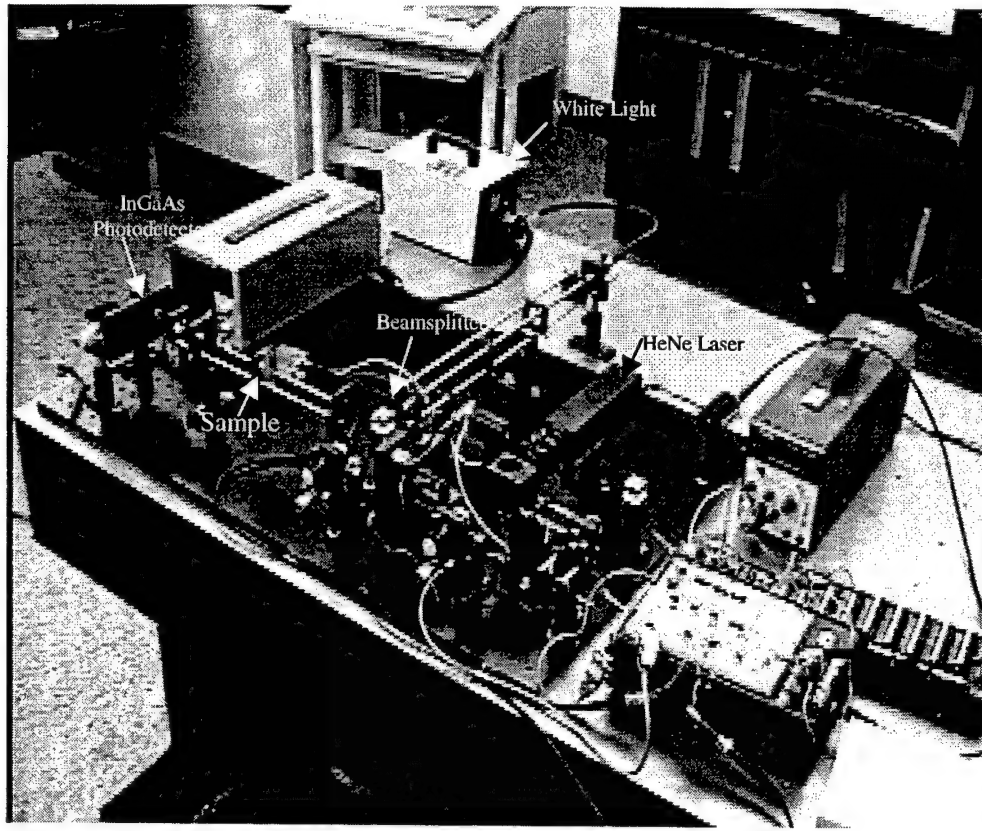
Figure 1: Fourier transform spectrometer layout

## (ii) System Implementation and Components Design Consideration

From the literature and the previous preliminary experiments, it has been realized that signals due to the blood glucose variations in the physiological range are weak. Furthermore, in the noninvasive application, there is further loss of signal due to scattering. As a result, realization of accurate blood glucose quantification would likely be limited by the amount of signal-to-noise ratio achievable. Hence, it is important that each element of the spectrometer is designed to maximize the signal-to-noise ratio.

The spectrometer uses a tungsten-halogen light source that provides a continuous spectrum from the visible through the near-infrared. An extended, thermoelectrically-cooled InGaAs detector is selected for maximum signal-to-noise ratio in the 1000nm - 2200nm wavelength region. For minimum loss due to absorption, Calcium-fluoride lenses are used for light collection and collimation. The photograph below shows the setup of the system.

The absorption spectrum in the near-infrared region is usually broad and overlapping. Therefore, high spectral resolution is not required. Since throughput is inversely related to the resolution, it is advantageous to match the spectrometer resolution to the required resolution [5].



Photograph 1: Fourier-transform spectrometer setup

### III. Spectrometer Characterization and Performance Evaluation

#### (i) Efficiency

Efficiency here is defined as the power of radiation received by the detector as compared with the power emitted by the source. This represents the photon loss through the spectrometer, which may be due to the absorption by the lenses and the beamsplitter, the loss to the environment, as well as the loss due to misalignment of the interferometer. It is assumed to be a constant value throughout the relevant wavelength range.

The equation below shows its relation with the achievable signal-to-noise ratio [6].

$$SNR = \frac{U_{\bar{v}}(T) \cdot \Theta \cdot \Delta \bar{v} \cdot t^{1/2} \cdot \zeta}{NEP}$$

where,

$U_{\bar{v}}(T)$  is spectral density at wavenumber  $\bar{v}$  from a black body source at a temperature  $T$  ( $W / sr \cdot cm^2 \cdot cm^{-1}$ )

$\Theta$  is the throughput of the system ( $cm^2 \cdot sr$ )

$\Delta \bar{v}$  is the resolution of the spectrum ( $cm^{-1}$ )

$t$  is the integrating time in seconds

$\zeta$  is the efficiency accounting for losses due to the optical components

NEP stands for noise equivalent power, which is a sensitivity *figure-of-merit* of the detector ( $W.Hz^{-1/2}$ )

In the equation above, the source is assumed to be a black-body radiation. In the case of noninvasive measurement, the source term  $U_{\bar{v}}(T)$  would be replaced by the radiance of the diffuse-reflected light from the sample, such as the skin.

To assess the spectrometer efficiency, light from the tungsten-halogen source was directed onto the detector through a narrow-band filter at 1600nm. The radiation power at the detector,  $P_1$  at the output of the preamplifier, was recorded. The procedure was done at full throughput, limited by the area of the detector and the speed of the focusing optics. Using the same light source and band-pass filter, an interferogram was recorded using the spectrometer. The peak of the interferogram,  $P_2$ , which corresponded to the radiation power when all the wavelengths interfere constructively, was recorded. Efficiency was then computed as  $P_2/P_1$ , which was equal to 0.085. This value is very good considering the complexity of the system, and is in good agreement with the rule-of-thumb estimations of Fourier-transform spectrometer efficiencies of 10% [7].

## (ii) Stability

Another criterion of importance is the spectrometer stability, which would translate into repeatability of the measurements. The weak glucose signal intrinsic to the absorption technique requires excellent stability of the spectrometer. The repeatability of the spectrum is especially important in the regions where glucose absorption bands are to be analyzed. Irreproducibility of measurements could arise from many sources, such as change in alignment, interferometer thermal expansion, change in sample temperature, scattering and variation due to the light source itself.

To assess stability, water spectra were acquired every 3 minutes over a period of one hour. This duration and periodicity was chosen to simulate an actual experiment. Each spectrum was a result of a Fourier-transformation of 30 averaged, double-sided interferograms. The first spectrum was subtracted from each subsequent spectrum to get the difference spectra, which are plotted in figure 2. To examine the impact of these variations, the plot should be examined together with the difference spectra of glucose solutions, which is presented in the next section.

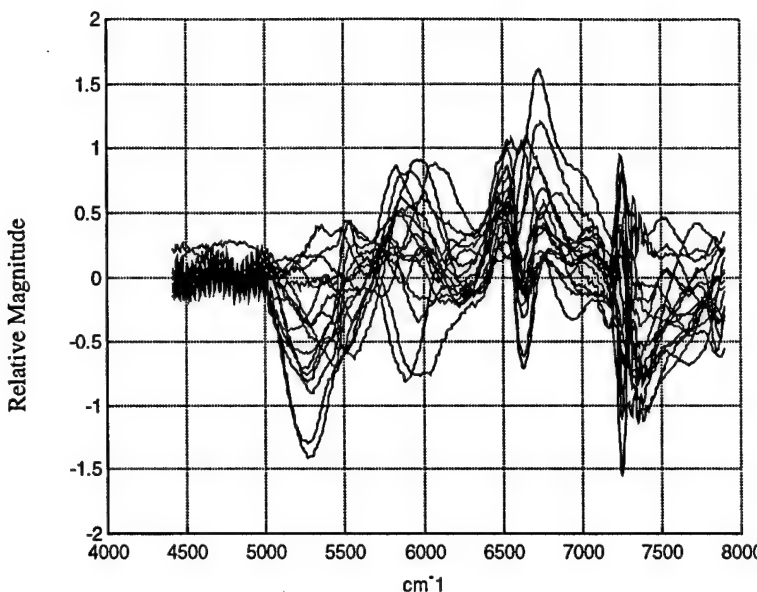


Figure 2: Differential spectra of repetitive water measurements

#### IV. Measurement of Glucose in Water

A preliminary aqueous glucose measurement experiment was done with the purpose of identifying the relevant bands for glucose analysis, as well as examining the capability of the instrument for the task. Glucose solutions with high concentration were used in this study. The lowest concentration was  $50\text{ mmol/L}$ , which corresponded to about 4 times as high as the upper physiological range.

Figure 3 shows the transmission spectra of pure water and glucose solution. Figure 4 shows the differential spectra of glucose solutions with different concentrations with respect to the water transmission spectrum. It can be seen from the two plots that the presence of glucose affects the spectrum of water in two regions. One is between  $5800\text{ cm}^{-1}$  and  $6100\text{ cm}^{-1}$  where there is a glucose absorption band. The other is a narrower band at around  $7250\text{ cm}^{-1}$ , where there is, in fact, more transmission due to the presence of glucose. This might result from the displacement of water molecules by glucose molecules.

In these regions, effects of glucose on water spectra are more pronounced than in the lower wavelength regions, which have been considered by several other investigators [2, 8]. However, water absorption here is much higher. Therefore, in order to probe these bands, a long-wave-pass filter with a cutoff around  $1400\text{ nm}$  was required. Otherwise, they would not be visible at all, as the shorter-wave radiation would dominate.

The water-glucose differential spectra (figure 4) were obtained using the same throughput and detector amplifier gain setting as the experiment to obtain the stability differential spectra (figure 2). Therefore, the magnitudes of the spectra between the two figures can be directly compared. At  $50\text{ mmol/L}$ , glucose altered the water spectrum by 6 units at around  $6000\text{ cm}^{-1}$  and by 3 units at  $7250\text{ cm}^{-1}$ . On the other hand, the extreme values of the variations of water spectra are 1.5 units at  $6000\text{ cm}^{-1}$  and 2.5 units at  $7250\text{ cm}^{-1}$ . This result suggests that for accurate lower glucose concentration prediction, stability needs to be improved.

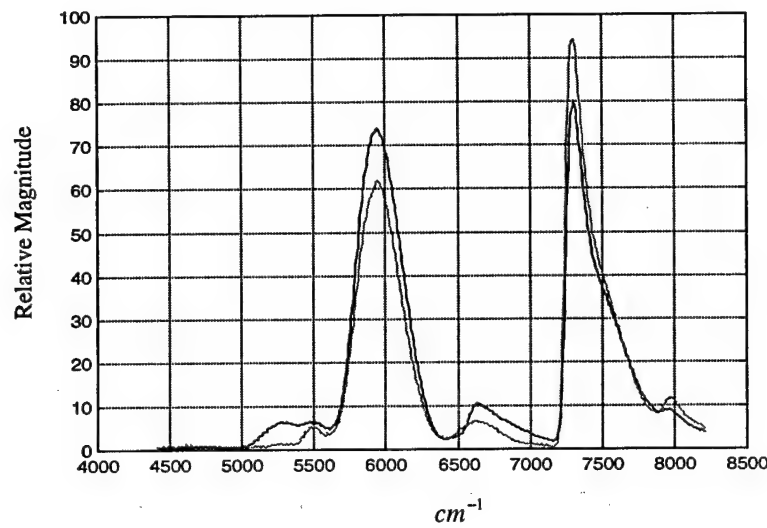


Figure3: Water-glucose solution spectrum (blue: pure water ; magenta:  $100 \text{ mmol/L}$  glucose solution)

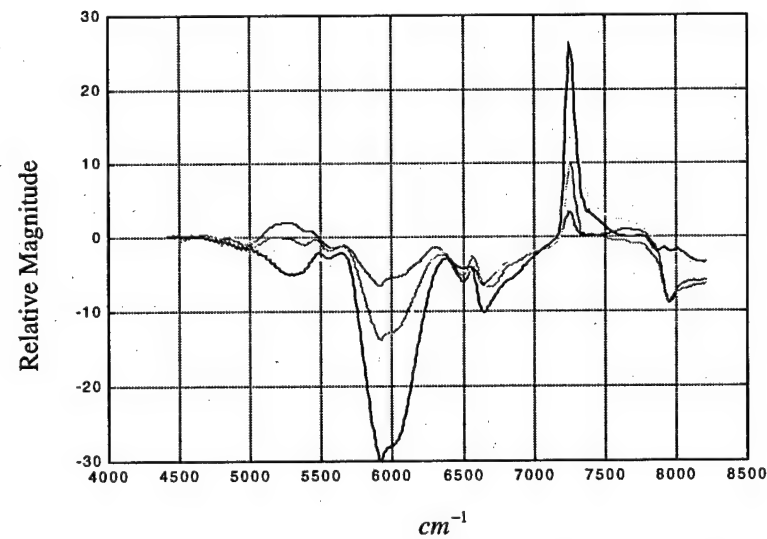


Figure4: Water-glucose differential spectra (red:  $50 \text{ mmol/L}$  ; magenta:  $100 \text{ mmol/L}$  ; yellow:  $200 \text{ mmol/L}$  ; black:  $500 \text{ mmol/L}$  )

## **V. Research Plan**

The experimental result shows that simple algorithm utilizing the two relevant bands might be sufficient for glucose concentration prediction. However, repeatability of the measurements needs to be improved before low concentration prediction could be achieved. Our short-term plan includes improvement of measurement repeatability. This involves identification of the source of error, which may be due to instrumental factor or the sample element.

When this is accomplished, careful analysis of achievable sensitivity for water-glucose and blood-glucose measurement will be attempted. This should be investigated through both experimentation and theoretical studies.

Additional problems with respect to the noninvasive application are signal loss due to light scattering in tissue and physiological variations such as skin temperature changes. Both degrade the signal-to-noise ratio. In this research, we aim to understand the origins of the signals and the sources of errors. This would enable appropriate modifications to the instrumentation design and/or procedural scheme to improve the accuracy of noninvasive blood glucose measurement.

## **VI. References**

1. Marbach R. et. al., "Noninvasive Blood Glucose Assay by Near Infrared Diffuse Reflectance Spectroscopy of the Human Inner Lip", *Applied Spectroscopy* 47 (7): 875-881, 1993
2. Robinson M.R. et. al., "Noninvasive Glucose Monitoring in Diabetic Patients: A Preliminary Evaluation", *Clin. Chem.* 38 (9): 1618-1622, 1992
3. Cote G.L. et. Al., "Noninvasive Glucose Sensing Utilizing a Digital Close-Loop Polarimetric Approach" *IEEE Trans. On Biomed. Eng.* 44(12): 1221-1227, 1997
4. Feld M.S. et. Al., "Rapid, Noninvasive Concentration Measurements of Aqueous Biological Analytes by Near-Infrared Raman Spectroscopy", *Applied Optics* 35(1): 209-212, 1996
5. The Home Automation and Healthcare Consortium Progress Report 2-2
6. Griffiths P.R., de Haseth J.A., "Fourier Transform Infrared Spectrometry", John Wiley & Sons, 1986
7. Mattson D.R., "Sensitivity of A Fourier Transform Infrared Spectrometer", *Applied Spectroscopy* 32(4): 335-338, 1978
8. Muller U.A. et. al., "Non-invasive Blood Glucose Monitoring by Means of Near Infrared Spectroscopy: Methods for Improving the Reliability of the Calibration Models", *Artif. Pancreas and Related Tech. In Diabetes and Endocrinology* 20 (5): 285-290, 1997

# Laser tissue modification with spectroscopic feedback: the "Smart Scalpel for treatment of port wine stains and permanent hair removal

I. W. Hunter

Principal Investigator

E. L. Sebern and C. J. H. Brenan

Research Assistant and Post-Doctoral Associate

## ABSTRACT

While feedback control is widespread throughout many engineering fields, surgical instruments with embedded feedback control systems are uncommon. To improve the effectiveness of microsurgical techniques, we are presently developing a semi-autonomous robotic surgical tool (called the "Smart Scalpel) as an alternative approach to treatment of skin hemangiomas like nevus flammeus (port wine stain or PWS). Current PWS phototherapy relies on selective absorption of optical radiation by the ectatic blood vessels in a PWS resulting in thermally mediated vessel necrosis. Although shown to be effective, heating of the surrounding tissue by photon absorption results in unacceptable collateral damage. The "Smart Scalpel" approach employs optical reflectance spectroscopy to selectively target blood vessels in a PWS for heating with a focused laser beam. Collateral damage to adjacent tissue is substantially minimized and continuous imaging throughout the procedure allows modification of the delivered therapy to optimize therapeutic outcomes. Our work reported here involves optical system design and construction, initial quantification of imaging system resolution and contrast, and preliminary verification of the imaging and targeting strategies. In the context of Home Automation, the "Smart Scalpel" instrument can be applied to cause hair growth delay or permanent hair removal.

# **Laser tissue modification with spectroscopic feedback: the "Smart Scalpel for treatment of port wine stains and permanent hair removal**

E. L. Sebern, C. J. H. Brenan, and I. W. Hunter

Department of Mechanical Engineering, Massachusetts Institute of Technology  
Cambridge, MA 02139

## **ABSTRACT**

While feedback control is widespread throughout many engineering fields, surgical instruments with embedded feedback control systems are uncommon. To improve the effectiveness of microsurgical techniques, we are presently developing a semi-autonomous robotic surgical tool (called the "Smart Scalpel) as an alternative approach to treatment of skin hemangiomas like nevus flammeus (port wine stain or PWS). Current PWS phototherapy relies on selective absorption of optical radiation by the ectatic blood vessels in a PWS resulting in thermally mediated vessel necrosis. Although shown to be effective, heating of the surrounding tissue by photon absorption results in unacceptable collateral damage. The "Smart Scalpel" approach employs optical reflectance spectroscopy to selectively target blood vessels in a PWS for heating with a focused laser beam. Collateral damage to adjacent tissue is substantially minimized and continuous imaging throughout the procedure allows modification of the delivered therapy to optimize therapeutic outcomes. Our work reported here involves optical system design and construction, initial quantification of imaging system resolution and contrast, and preliminary verification of the imaging and targeting strategies. In the context of Home Automation, the "Smart Scalpel" instrument can be applied to cause hair growth delay or permanent hair removal.

## **1. BACKGROUND AND MOTIVATION**

Closed-loop feedback control is widespread throughout many engineering fields, such as manufacturing, robotics, and in other human-machine interfaces. A general characteristic of any feedback control scheme is the comparison of the output of a physical system with its input to generate an error signal. The error signal, in turn, modifies the system to minimize the difference between input and output.<sup>1</sup> Feedback control, therefore, maintains system equilibrium (with respect to its input) by quickly

compensating for changes in the physical system or perturbations imposed on it by the external environment.

An interesting potential application of feedback control is in the field of microsurgery. Many microsurgical procedures require a high degree of physical dexterity, accuracy, and control which degrades rapidly with physician fatigue. This problem could be partially alleviated through inclusion of low-level decision-making embedded in a microsurgical tool to aid in tissue location and removal. Our embodiment of this concept is a device we call the "Smart Scalpel" (Figure 1).

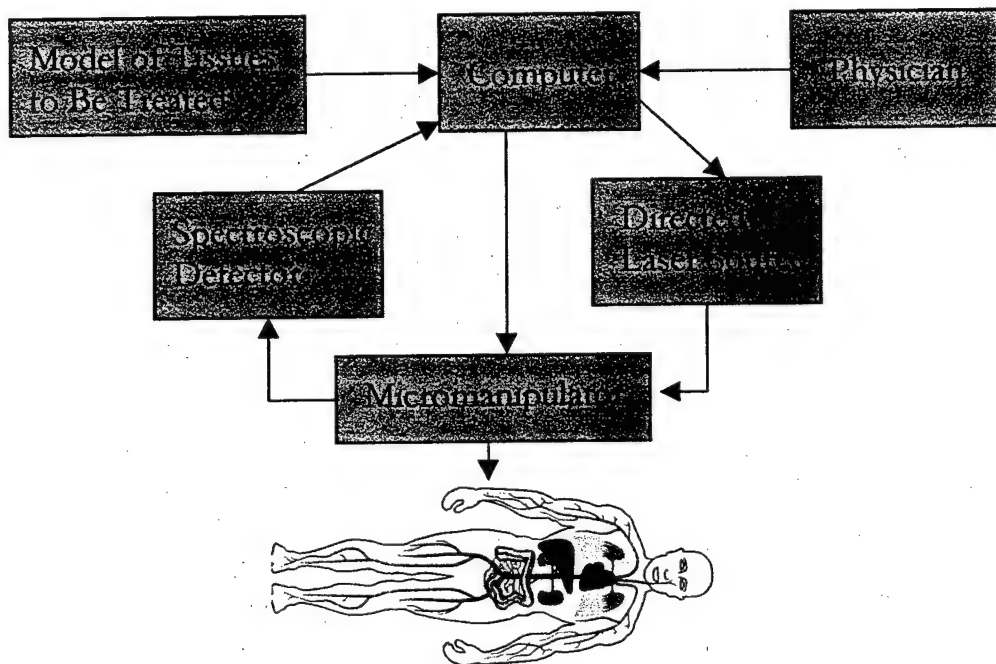


Figure 1: Schematic illustration of the "Smart Scalpel."

Implementation of the Smart Scalpel concept is quite general in both measurement and intervention techniques. Physical properties of normal and diseased/damaged tissue as well as expert knowledge from the physician operator are inputs to a computer model describing the attributes of healthy versus the diseased/damaged tissue to be excised. Histochemical and morphological tissue properties non-invasively measured in real-time provide the feedback needed to selectively identify tissue targets by comparison with the tissue computer model. This tissue selection could be accomplished through any of the following methods: optical reflectance spectroscopy, magnetic resonance imaging, fluorescence optical spectroscopy, Raman spectroscopy, optical polarization detection, fluorescence polarization detection, mechanical impedance measurements, and electrical impedance measurements.

The measurement system for the Smart Scalpel can be either a passive observation or active response to a perturbation of the tissue. The passive strategy makes measurements with little or no influence the tissue of interest. With passive measurements, signal processing techniques are employed to extract information about the system. One example is an electrocardiogram (EKG), which passively measures the propagation of electrical signals throughout the heart, but does not describe the fundamental characteristics of the cells and tissue in the heart, such as stiffness, conductivity, etc.

In contrast, actively probing the tissue enables quantification of these physical characteristics. By comparing input perturbations with the output response, system identification techniques can be used to quantify the tissue properties, and then predict tissue under different conditions. One example is applying a strain to a cell and measuring its stress response. From this input and output information, the stiffness transfer function can be derived for the material, which can then be used to predict its behavior for a wide range of stimuli. Based on the response of a cell, tissue, or organ, to a given input, we can modify our probing signal to maximize the information retrieved from the biological structure. These system identification techniques are applicable to both linear and nonlinear systems.

Using this feedback signal, a spatially localized energy source is applied for removal or modification of the specified tissue. This sequence of events repeats itself until all the targeted tissue has been treated. A micromanipulator serves as the interface between the patient and the "Smart Scalpel," providing a means to extract information about the tissue state and direct the therapeutic energy source to the appropriate targets. This directed energy source could be any of the following: photon beam, electron or proton beam, localized electrical field, directed acoustic energy, and inertial cutting (low frequency mechanical energy).

The many desirable attributes of the Smart Scalpel have the potential to not only improve performance in current microsurgical procedures but also facilitate the development of new treatments not yet feasible with existing technology. The accuracy and reliability of present-day procedures may be enhanced and collateral damage minimized through quantitative, rapid, on-line assessment of the procedure efficacy. This system of real-time feedback has great potential to increase patient comfort,

shorten patient recovery times, and decrease the overall cost per procedure. Additionally, the Smart Scalpel is amenable to integration into a tele-operation system for remote surgery.

We are interested in exploring many applications for the Smart Scalpel. Medical applications considered to date include:

- Removal of port wine stains and other hemangiomas
- Treatment of varicose veins
- Hair removal
- Destruction of cancerous and pre-cancerous tumors
- Photorefractive keratectomy
- Neurosurgery

## 2 APPLICATION TO PORT WINE STAIN TREATMENT

A first demonstration of the Smart Scalpel is the removal of nevus flammeus (port wine stain or PWS) and other hemangiomas. PWS is a congenital, vascular malformation of the dermis, which is estimated to occur in five children per thousand births.<sup>2</sup> On the macroscopic scale, a port wine stain appears pink, red, or purple; lesion color correlates with vessel diameter. Pink lesions have a mean vessel diameter of 16  $\mu\text{m}$  while purple lesions have a mean diameter of 51  $\mu\text{m}$ . Also, pink and purple lesions have significantly deeper blood vessels than red ones.<sup>3</sup> Vessel number is highest in the immediate subepidermal layer and then rapidly diminishes with depth into the subdermal layers; mean vessel depth are found to be  $460 \pm 170 \mu\text{m}$ .<sup>4</sup>

### 2.1 Current clinical practice

Current PWS therapy involves the illumination of ~10 mm diameter regions of skin with the output from a pulsed dye laser ( $t_{pulse} \sim 0.4 \text{ ms}$ ) having a fluence level between 40 - 80  $\text{kJ/m}^2$  at a wavelength coincident with a oxyhemoglobin absorption band (typically 577 nm).<sup>5</sup> Selective absorption of the laser energy by the blood results in thermal necrosis of blood vessels. Over time the body absorbs these vessels, and the PWS fades or completely disappears. In practice, the collateral damage to the surrounding tissue results in patient pain and tissue scarring. Cryogen spray cooling (CSC) is currently

being experimented with in tissue phantoms<sup>6</sup>, animal models<sup>7</sup>, and in pre-clinical<sup>8</sup>, as a means to protect the epidermis from nonspecific thermal injury, while heating blood vessels in the dermal layer. However, CSC is not currently developed and approved for clinical use, and collateral damage still occurs in the dermal layer. The procedure is slow ( $>1$  hour/session  $\times$   $>8$  session/treatment) and treatment response is poor when blood vessels are deep and relatively small. Most important in the context of the Smart Scalpel is, aside from PWS appearance, no feedback is generated to assess treatment efficacy or appropriateness of the photon dosage.

## 2.2 Smart Scalpel approach

The Smart Scalpel approach to PWS treatment requires, first, locating the blood vessels within a volume of PWS and, second, illuminating selected blood vessels with light from a focused laser beam for a time sufficient to increase the local vessel temperature to the point at which permanent physical damage occurs. Major design components of the PWS Smart Scalpel are (1) a non-invasive method to selectively identify and locate blood vessels within the PWS; (2) a means to deliver the heating laser energy to the appropriate spatial location for the required time and (3) a strategy for heating blood vessels within the PWS volume imaged. We now discuss our current system approach to achieve these objectives.

### 2.2.1 Spectroscopic identification of blood vessels

Absorption reflectance spectroscopy with polarized light is the non-invasive method by which blood vessels are discriminated from other tissue in the PWS. The PWS (and skin in general) contains two dominant chromophores: melanin resident in the epidermis and oxyhemoglobin found in blood. Figure 2 shows that whole blood exhibits two strong absorption bands at 540 nm and 577 nm (with two other absorption peaks at 415 nm and 940 nm, not shown), predominately due to the high concentration of oxyhemoglobin chromophore in the blood.<sup>9</sup> In comparison, the relative melanin absorption spectrum generally decreases with increasing wavelength (Figure 2) while its overall magnitude scales with epidermal melanin concentration. Dark and light skin have a melanin concentration of .023% and .008% by weight, respectively.<sup>10</sup> Normalization of the blood absorption spectrum with respect to the melanin spectrum generates a high contrast ratio spectrum with a maximum and minimum relative absorbance at 577 nm and 640 nm, respectively. Thus a ratio of PWS images taken at these two

wavelengths generates a high contrast image from which blood vessels are uniquely identified and their locations determined.

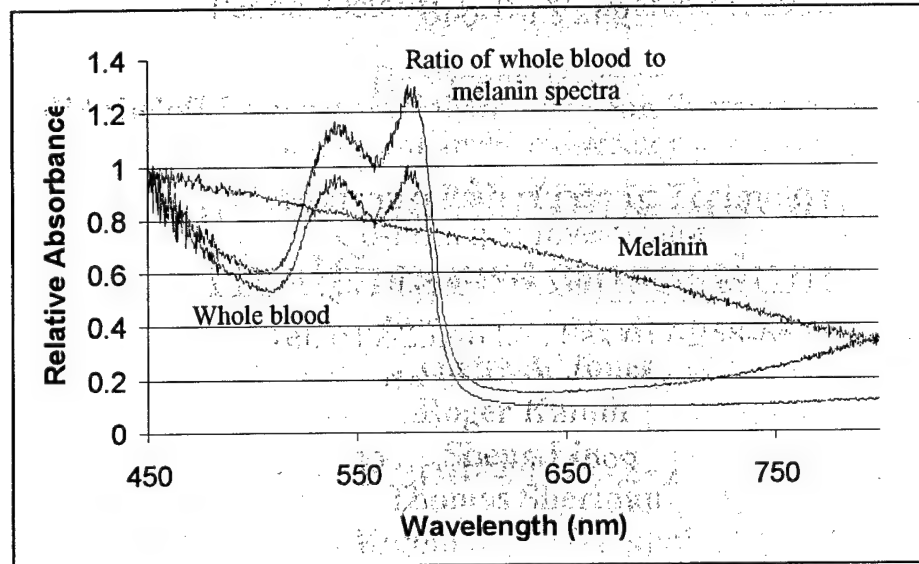


**Figure 2: Relative absorbance spectra of human whole blood and melanin from 450 nm to 800 nm. The ratio of these two signals shows the enhanced contrast used to distinguish blood vessels from the surrounding tissue.**

In addition to absorption, the scattering properties of skin must be considered in selection of an appropriate imaging scheme. The scattering coefficient of skin determines how much of the light delivered to the skin surface reaches the subsurface structures of interest (e.g. blood vessels). In general, longer wavelengths are scattered less and have greater penetration depths. Therefore, although the greatest hemoglobin absorption peak is at 415 nm, this wavelength is too short to penetrate to the depth of PWS blood vessels. At 415 nm, the penetration depth, defined as the distance at which the energy incident on the skin is extinguished by 37% ( $1/e$ ), is 100  $\mu\text{m}$ . The penetration depth of 600 nm light is  $\sim$ 550  $\mu\text{m}$ , which is close to the mean vessel depth of a typical PWS.<sup>11</sup>

Image contrast is further enhanced if specular reflections from the skin surface are minimized. This is accomplished by illumination of the PWS with linearly polarized light and viewing the reflected light through a polarizer oriented orthogonal to the original polarization. Multiple scattering of the incident

optical field by subsurface structures effectively depolarizes the backscattered light thus permitting discrimination between surface specular reflections from light reflected deeper in the tissue.<sup>12</sup>

### 2.2.2 Therapeutic laser

Effective heating of blood in a vessel requires absorption of optical energy by the blood in a vessel at a rate sufficient to overcome thermal losses and raise the local blood temperature to cause irreversible thermal damage. To achieve optimal opto-thermal coupling of radiation into a blood vessel, several criteria must be satisfied. First, the laser wavelength should coincide with one of the oxyhemoglobin absorption bands (415, 540, 577 or 940 nm) and, second, the laser light is focused to a diameter equal to the mean diameter of blood vessels in a typical PWS (ca. 50  $\mu\text{m}$ ). The  $\times 10\,000$  smaller illuminated area compared with the conventional PWS treatment means the incident laser power can be substantially smaller to generate a similar photon flux incident on the targeted blood vessel so as to achieve a similar physiological outcome (vessel necrosis).

## 3 INSTRUMENT THEORY AND SPECIFICATIONS

### 3.1 Optical reflectance spectroscopy

We have chosen optical reflectance spectroscopy for the treatment of port wine stains because the absorbance for blood vessels is much higher than that of the surrounding tissue at the 577 nm wavelength. With ORS we may use a diffuse white light illumination of the port wine stain skin to detect the backscattered light at visible and near infrared wavelengths. We then filter this backscattered light to retrieve only the wavelengths of interest: one wavelength at a peak hemoglobin absorbance, and a second at a lower hemoglobin absorbance for normalization. Alternatively, we may use light-emitting diodes to illuminate the skin at specific wavelengths that are absorbed or reflected by the tissue.

We direct each of the two wavelengths of interest to a photodetector, which converts the incident photons to electrons, generating a voltage signal during the integration time of the detector. Using analog or digital electronics, the ratio of the two signals is calculated. From this ratio signal, a threshold is used to generate a binary image of the region. This imaging coordinate space is then converted to the laser-scanning space to effectively deliver the beam energy to the appropriate vessel targets.

### 3.2 Preliminary results: Identification of blood vessels

The optical system used for the preliminary results is a simple imaging system, which is illustrated in Figure 3. The output of a 100-W tungsten white light source is polarized and then focused on the skin surface. The reflected light is collected by an infinity-correct 10x-magnification objective that collimates the light reflected from the skin surface. The light then passes through a polarizer, which passes light of orthogonal polarization to the illumination. This polarization scheme blocks the specular reflection from the skin surface, making the underlying blood vessels of the camera image more apparent. The collimated light then passes through a liquid crystal tunable filter (Cambridge Research & Instrumentation, Inc., Varispec tunable filter, Model VS-05/30-HC-20-S). This filter can be programmed to wavelengths over a range of 450-720 nm. The 50% bandwidth for the two wavelengths used are 550-590 nm for the hemoglobin signal and 625-680 nm for the normalization wavelengths. The light exiting the tunable filter is then focused onto a charge-coupled device (CCD) array by an achromat to minimize chromatic aberration.

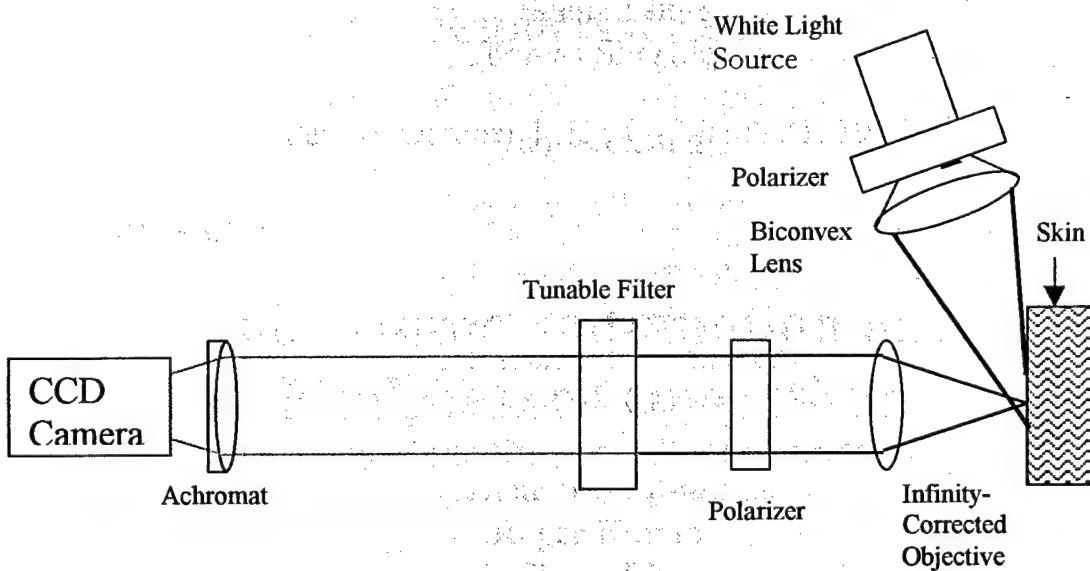


**Figure 3: Schematic representation of optical system used to image and deliver laser energy to the blood vessels.**

Figure 4 shows the contrast enhancement possible with this two-wavelength imaging scheme. Figure 4a is the reflected light absorption image of blood vessels in a mouse ear taken at the ~577 nm blood absorption band. Figure 4b is an image of the same region acquired with non-absorbing 650 nm reflected light and Figure 4c is the ratio image. Note the high degree of background suppression in the

ratio image resulting in an enhanced blood vessel image contrast. If the signal to noise ratio (SNR) is defined as the ratio of the blood vessel signal to the standard deviation of the background fluctuations, the SNR increases from 1.16 to 8.37 from image 4a to 4c using the ratio operation.

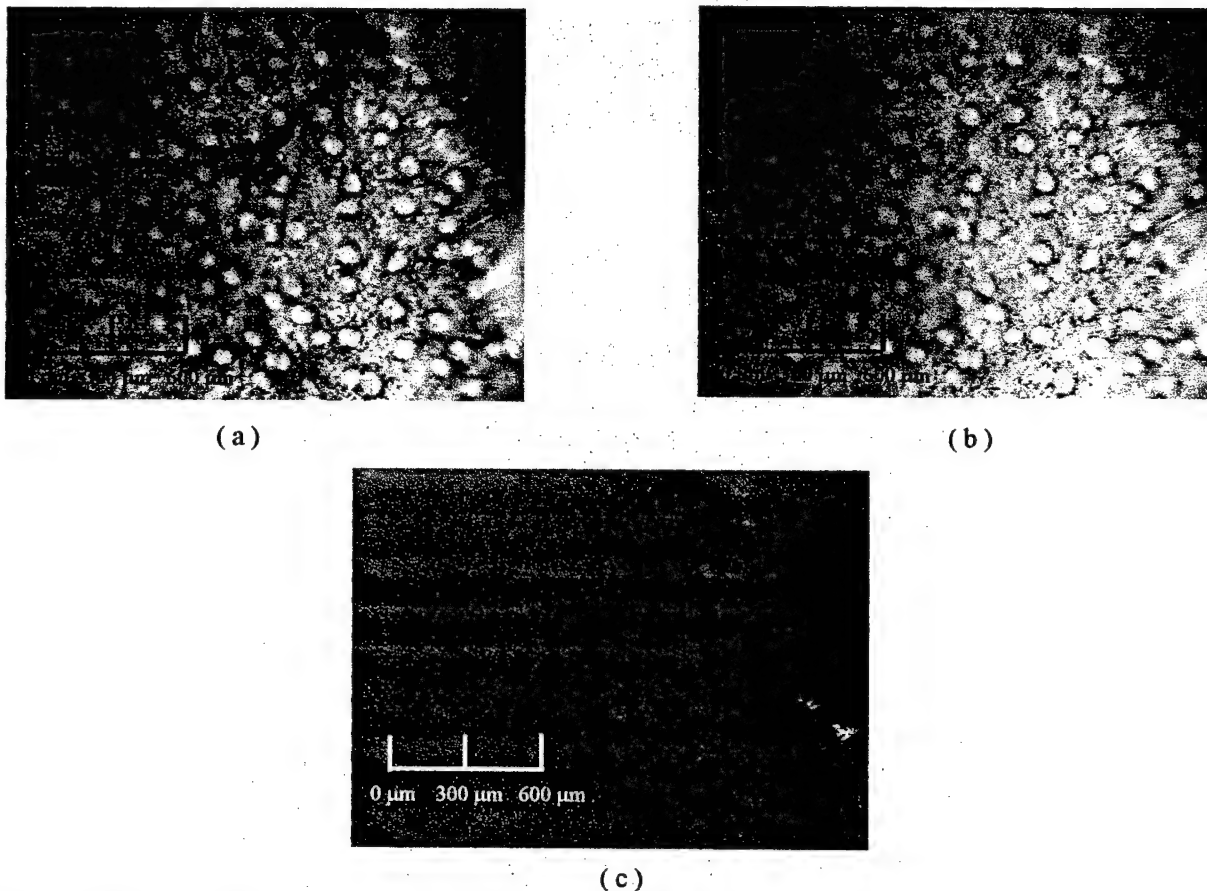


**Figure 4: Optical reflectance imaging of mouse ear blood vessels at (a) 577 nm and (b) 650 nm. Blood vessels appear in the upper right corner of the picture. The circular objects in the background are assumed to be hair follicles. (c) Dynamic range expanded ratio ORS image. Ratio taken of images acquired at 577 nm and 650 nm. Note high degree of background suppression.**

### 3.3 Laser-tissue interactions

The three primary considerations for laser-tissue interactions for this application are thermal relaxation time, energy necessary to coagulate the blood, and the absorption and scattering of light by various skin structures.

### 3.3.1 Thermal relaxation time

Energy absorbed by the vessels is converted primarily to thermal energy if the ratio of illumination time,  $\tau_{ill}$ , to the tissue thermal relaxation time,  $\tau_r$  is greater than one. The illuminated region is in thermal equilibrium with the surrounding tissue and a significant amount of heat diffuses out of the blood vessel. Therefore, it is desirable to deliver the laser energy to the blood vessels in a time shorter than the thermal relaxation period. However, if  $\tau_{ill} < \tau_r$ , energy conversion is primarily adiabatic and substantial mechanical damage to the vessel can result.

The thermal relaxation time for a blood vessel of diameter,  $d$ , is

$$\tau_r = \frac{d^2}{16 \alpha} \quad (1)$$

in which the thermal diffusivity,  $\alpha$ , is

$$\alpha = \frac{\beta}{\rho c} \quad (2)$$

and  $\beta$ ,  $\rho$ , and  $c$ , are the thermal conductivity, density, and specific heat, respectively. For tissue composed of 70% water, the thermal diffusivity,  $\alpha$ , is  $1.15 \times 10^{-7} \text{ m}^2/\text{s}$ .<sup>13</sup> Therefore, assuming a 50  $\mu\text{m}$  diameter blood vessel (typical of many PWS), the thermal relaxation time is approximately 1 ms.

### 3.3.2 Laser coagulation of blood

An estimate of the laser power required to coagulate the blood in a typical PWS blood vessel with a focused laser beam can also be calculated. Assuming thermal equilibrium, a laser illumination diameter equal to the blood vessel diameter (50  $\mu\text{m}$ ), and a blood specific heat and density close to that of water, the energy needed to heat a volume of blood enclosed in the illuminated volume to its coagulation temperature is given by:

$$E = mc\Delta T \quad (3)$$

where  $m$  is the mass of the region of blood treated,  $c$  is the specific heat (assumed to be close to water  $\sim 4.2 \text{ kJ/kgK}$ ), and  $\Delta T$  is the temperature rise required for coagulation of blood,  $\sim 40^\circ\text{K}$  above ambient body temperature.

The mass,  $m$ , of blood treated is given by:

$$m = \rho V \quad (4)$$

$$V = \pi r^2 d \quad (5)$$

where  $\rho$  is the density of blood, again assumed to be similar to water ( $\sim 1000 \text{ kg/m}^3$ ). The volume  $V$  is given by the area of the beam illuminating the vessel ( $\pi r^2$ , where the radius  $r$  of the laser spot is  $25 \mu\text{m}$ ), and  $d$  is the blood vessel diameter, assumed to be  $50 \mu\text{m}$  for these calculations. These equations demonstrate that  $\sim 16 \mu\text{J}$  is the necessary energy incident on the blood vessel to cause coagulation. With a  $\sim 1 \text{ ms}$  laser dwell time (on the order of the thermal relaxation time), this corresponds to an absorbed power of  $\sim 16 \text{ mW}$ .

### 3.3.3 Laser attenuation due to absorption and scattering

Since these blood vessels are located in the dermis,  $\sim 500 \mu\text{m}$  below the skin surface, the light incident on the skin surface will be attenuated, through absorption and scattering as it propagates through the epidermis to the dermis, where the blood vessels are located. Applying a simple Beer's law absorption/scattering model, the estimated laser power incident on the skin required to generate the specified temperature rise is given by:

$$P = P_o e^{-(\alpha_s + \alpha_a)h} \quad (6)$$

where  $P$  is the power required to coagulate the blood ( $16 \text{ mW}$ ),  $P_o$  is the power incident on the skin,  $\alpha_s$  is the human dermis scattering coefficient ( $225 \text{ cm}^{-1}$  at  $633 \text{ nm}^6$ ), and  $\alpha_a$  is the blood absorption coefficient ( $\sim 13 \text{ cm}^{-1}$  at  $580 \text{ nm}^6$ ), and  $h$  is the depth of the blood vessels from the skin surface ( $\sim 500 \mu\text{m}$ ). The parameters  $\alpha_s$  and  $\alpha_a$  have the dimension of  $[1/\text{L}]$ , and the mean free path is the value of  $h$  equal to  $1/\mu$ . Over the distance of one mean free path, the ratio of  $P$  to  $P_o$  is  $e^{-1}$ , so that  $P$  is approximately 35% of  $P_o$ . Beer's law offers the result that  $\sim 2 \text{ kW}$  of power must be incident on the skin within a  $0.002 \text{ mm}^2$  area spot to sufficiently heat the blood vessels and cause coagulation. Since most beams have a  $\sim 1 \text{ mm}$  diameter, a laser power of  $\sim 1 \text{ watt}$  will be required to heat the blood vessels. Several types of lasers exist with this optical power and a wavelength coincident with the oxyhemoglobin absorption band suitable for inclusion as the "Smart Scalpel" therapeutic laser.

### 3.4 Control strategy

We have considered several SmartScalpel imaging and laser targeting strategies, which can be classified into three basic methods. The first is point spectroscopic detection combined with serial scanning to cover affected area. The second is full-field imaging with servo-controlled beam steering. The third strategy, which has been selected for this application, involves line imaging and point laser scanning. The trade-offs among these three strategies will be further developed in the following section.

#### 3.4.1 Serial point-scanning approach

This serial approach relies sequentially scanning a point illumination, using a point detector to determine whether spatial location contains a PWS blood vessel, and if a blood vessel is present, scanning the laser beam to that location for treatment. Figure 5 illustrates one implementation of this approach.

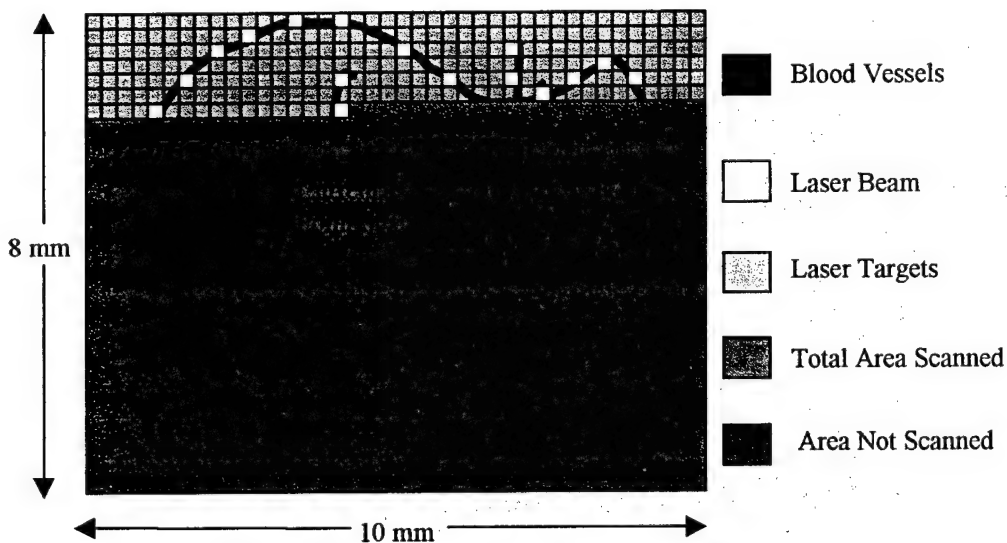


**Figure 5: Illustration of point imaging and point laser-scanning approach.**

This approach has the advantages of simplicity and speed. The imaging illumination and treatment laser can both be positioned with the same scanner. Also, because only one pixel is read before each laser treatment, there is little delay between image acquisition and treatment. Therefore, any relative motion causes minimal shift between the time the image is acquired and the laser energy delivered. We anticipate that an instrument employing this strategy can be easily miniaturized. The physician could scan the Smart Scalpel over the tissue surface, treating  $50 \mu\text{m}$  regions with each laser pulse. Alternatively, the instrument could be stationary, treating a  $\sim 1 \text{ cm}^2$  region. The surgeon holds the Smart

Scalpel on the skin surface, while a two axis scanning system is used to treat the area. Once the first region is treated, the physician moves the instrument to a new area and repeats the treatment process until the entire PWS is treated.

### 3.4.2 Full-Field Approach

The second approach we are considering is a stationary device that images a two-dimensional field, on the order of  $10 \text{ mm}^2$ , and targets specific locations on the vessel network. Figure 6 is an illustration of this control strategy. The advantages of this approach are simplicity in imaging strategy and acquisition of information about the PWS blood vessel in advance of laser targeting. This facilitates pattern recognition of blood vessels, so the laser can be scanned along individual blood vessels rather than randomly hitting points along different blood vessels. In treatment of telangiectasias (skin of larger, more sparsely populated blood vessels than PWS), physicians trace individual blood vessels from the smallest branches inward to the large supply vessels. This strategy routes the blood flow away from the branches, allowing more effective heating of the vessels with the laser light.<sup>14</sup>

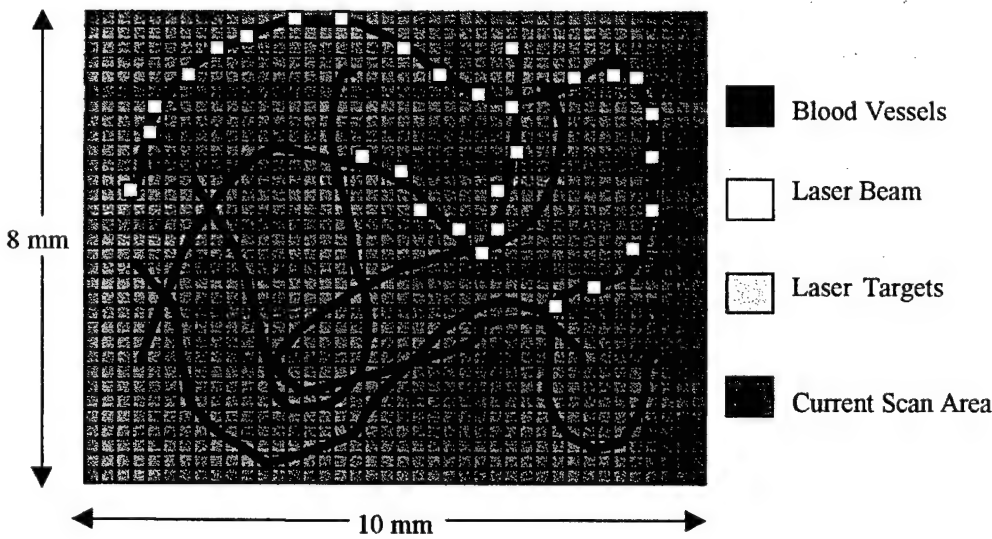


**Figure 6: Illustration of full-field imaging and point laser scanning strategy.**

One disadvantage of this full-field approach is the speed sacrificed in image acquisition. This time delay may cause increased errors, since there is more time for relative motion between the patient and the instrument. For this approach, we considered a 2-dimensional CCD array as our detector. Given the requirements of high resolution ( $\geq 1 \text{ Mpixel}$ ) and relatively low cost, the frame rates for the

cameras considered were too low to image the skin and target fast enough to avoid serious problems with relative motion between the instrument and patient.

### 3.4.3 Scanning of line illumination

The final approach considered, and the one that will be implemented in the first SmartScalpel prototype aims to combine the positive attributes of the serial and full-field imaging approaches. The line imaging approach allows dynamic control of the size of the imaged area. This is helpful in optimizing the trade-off between treating the largest area for each scan versus minimizing the time delay between when the image is acquired and the time the laser energy is delivered to the identified targets because this time delay will allow relative motion between the patient and the instrument. The frequency and magnitude of relative motion between the instrument and patient is largely unknown and variable. This variability arises from many sources, including location of the PWS (since different body parts move differently), position of the patient, calmness of the patient, etc. Also, the density of blood vessels within the PWS is highly variable.

The line illumination can accommodate differences in the frequency and magnitude of relative motion, as well as differences in the density of blood vessels in the PWS being treated. In addition, the line imaging and point laser scanning technique also provides information about the targets in advance of the laser scanning. This may be important if some degree of blood vessel pattern recognition is required in advance of laser scanning.

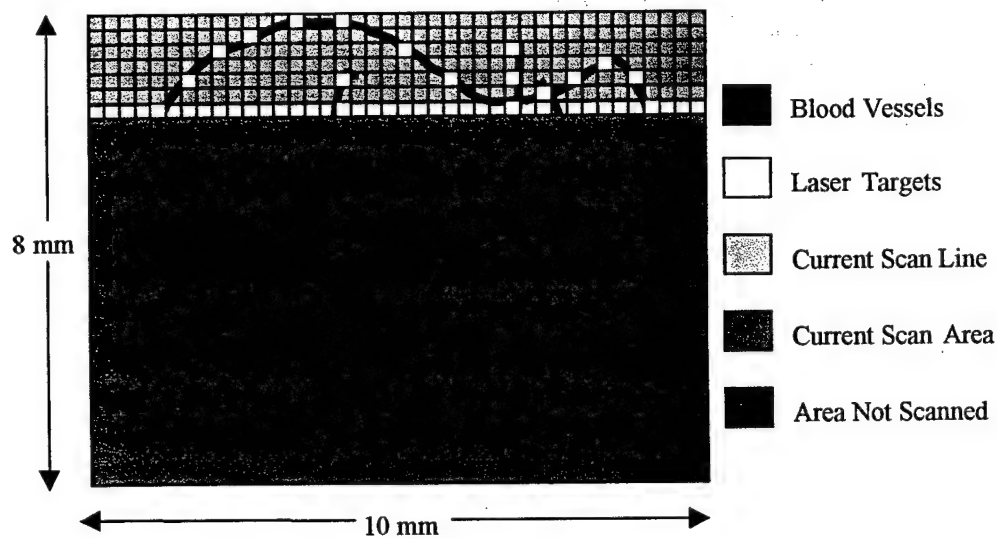


**Figure 7: Illustration of line imaging and point laser-scanning strategy.**

## 4 SMART SCALPEL PROTOTYPE

### 4.1 Line illumination

A diagram of the optical layout for the prototype Smart Scalpel is shown in Figure 8. The desired resolution for the imaging system is  $10 \mu\text{m}$ ,  $\sim 1/10$  the diameter of a PWS blood vessel. A treatment area of  $\sim 1 \text{ cm}^2$  has been specified to conveniently interface with the physician and patient.

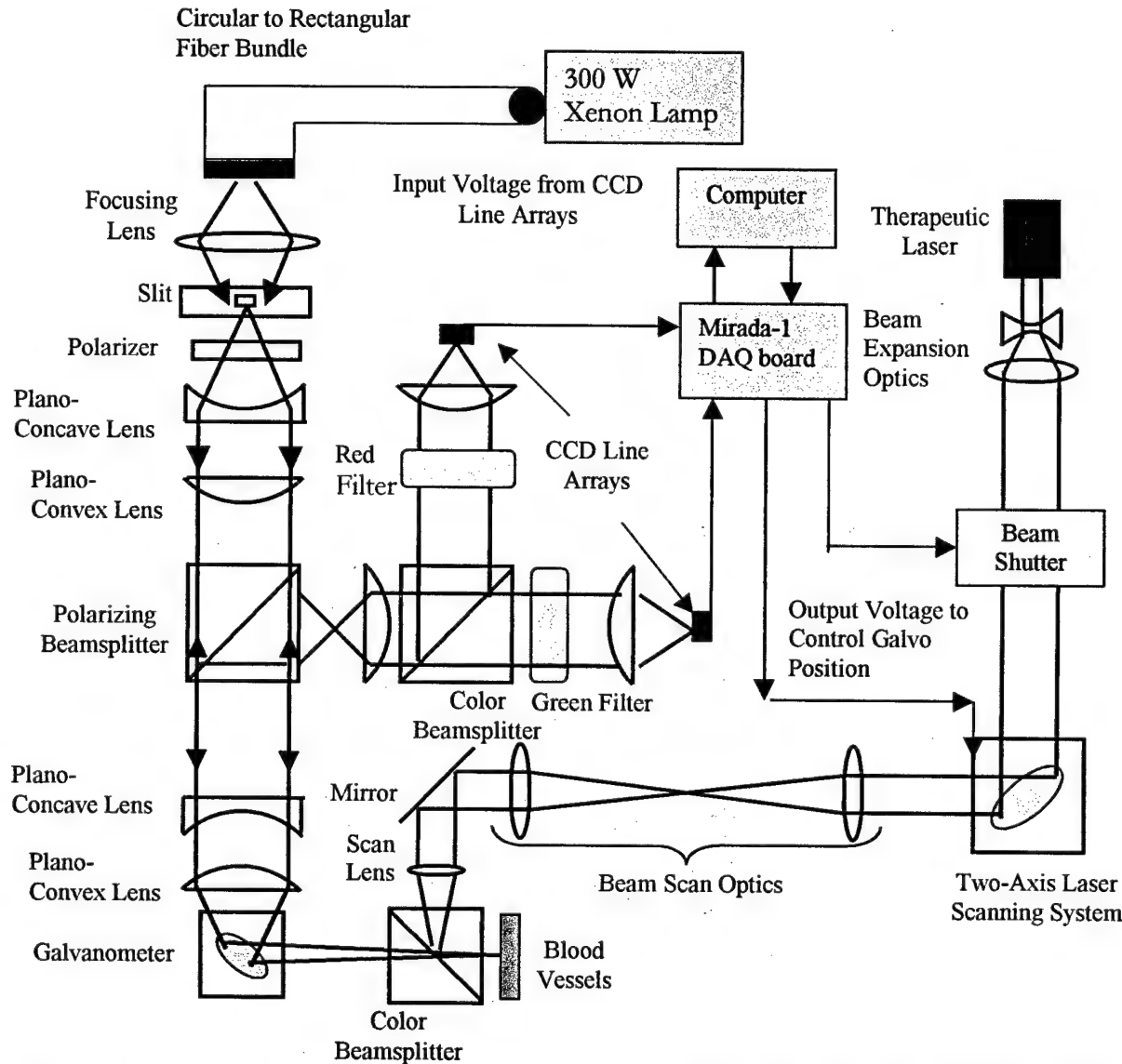


**Figure 8: Schematic representation of Smart Scalpel beam scanning and imaging systems.**

Light from a fiber optic-coupled 300 W xenon lamp illuminates an optical system configured to generate a line of polarized white light on the skin. To do this, an Oriel fiber bundle with a circular cross-section on one end (3.2 mm diameter) and a rectangular output (9.7 mm by 0.8 mm) is used to deliver the light

from the source to the instrument. The output of the fiber bundle is focused onto a slit aperture (50  $\mu\text{m}$  by 6 mm). The ultraviolet and infrared outputs from the xenon are filtered, so only visible light illuminates the skin surface. This light is linearly polarized to enhance the contrast of blood vessel structures beneath the skin surface. The line illumination then passes through a plano-concave to minify the slit image and plano-convex lens to collimate the light. This collimated light is then directed toward a polarizing beamsplitter and the line image is again minified with a plano-concave lens and then focused with a planoconvex lens onto the skin. The polarizing beamsplitter passes light of one polarization for illuminating the tissue and reflects the orthogonal polarization of light backscattered from the skin to the photodetectors. A galvanometer-mounted mirror scans the illumination line across the skin surface.

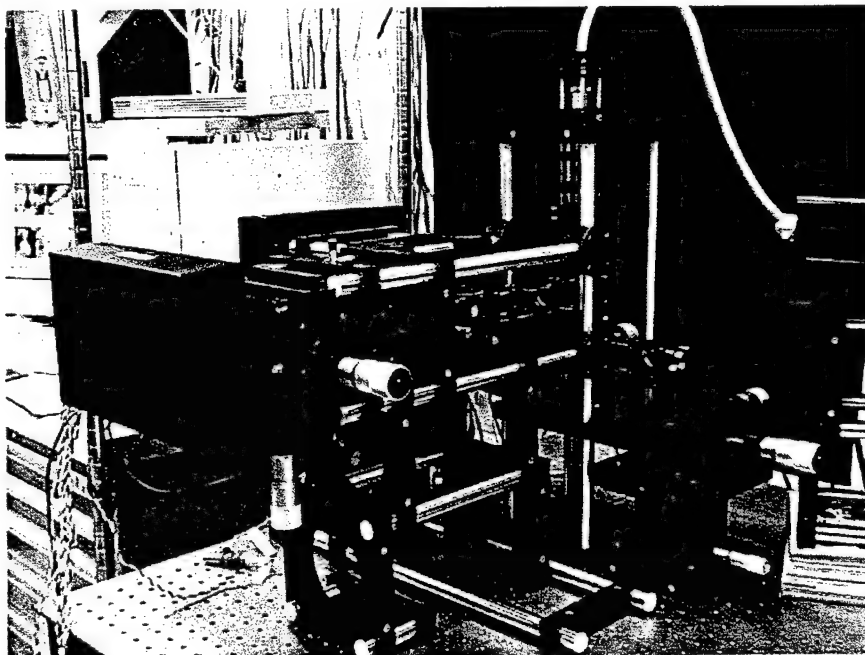


Figure 9: Photograph of Smart Scalpel prototype system.

#### 4.2 Imaging detectors

The light reflected and backscattered from the skin at each galvanometer scan position is de-scanned by the galvanometer, reflected by the polarizing beamsplitter and imaged by a planoconvex lens through a dichroic beamsplitter onto two linear CCD photosensor arrays. Wavelengths shorter than 630 nm are directed toward one array and further spectrally filtered with a 530-590 nm bandpass filter to generate the blood (oxyhemoglobin) signal. Wavelengths longer than 630 nm filtered with a 670-720 nm bandpass filter, and this light is transmitted to the second array to generate a normalization signal against

which the oxyhemoglobin signal is compared. The CCD sensors used for this system are 1024 element CCD spectroscopy line sensors (EG&G Reticon S Series,  $25 \mu\text{m} \times 2.5 \text{ mm}$  pixels, 70,000 dynamic range). Since the desired resolution for the imaging system is  $10 \mu\text{m}$ , the overall magnification of the imaging system is 2.5, so that one pixel on the array corresponds to  $10 \mu\text{m}$  on the skin surface.

#### **4.3 Data acquisition and control: hardware and software**

The photosensor outputs are recorded by the analog-to-digital converters (100 kS/s @ 16 bit/sample) of a home-built data acquisition board (MIRADA-1) resident in a Pentium II PC and controlled by a program written in C. After a line image is recorded, a command is sent via the Mirada board 18 bit digital-to-analog (D/A) converters to rotate the scanning galvanometer to a new position and a new line image is recorded. After the optimal number of line images is acquired, a ratio image is computed and a threshold is set to determine the blood vessel locations. The coordinates of the targeted vessels are sent via the Mirada D/As to a two-axis laser scanning galvanometer to direct the heating laser beam focus onto selected blood vessels. In addition, one D/A channel is used to control the electro-optic beam modulator (Conoptics 380 Series, ammonium dihydrogen phosphate liquid crystal electro-optic light modulator). Because the line illumination is not entirely constant across the width of the scan, the two-wavelength normalization also improves image uniformity.

Processing of the ratio image to identify blood vessels is, at present, algorithmically straightforward. A histogram analysis of the ratio image sets a binary threshold in which all pixels below the threshold value (corresponding to high absorption) are identified as blood vessels. The vessel position in the image field of view is calculated and converted to target coordinates for the two-axis laser scanning system. The step response time of the current laser-scanning system is  $\sim 1 \text{ ms}$  and is comparable to the estimated blood vessel thermal relaxation time,  $\tau_r$ . Therefore, during the transit time between targets, the electro-optic beam modulator blocks the laser beam to prevent heating of the tissue between blood vessels.

#### **4.4 Laser beam scanning**

The heating laser delivery subsystem of the Smart Scalpel is flexible in that any laser can be used with the system. The laser source can be a continuous wave or millisecond-pulsed laser at a wavelength of substantial hemoglobin absorption and minimal scattering and absorption by other tissues. Laser

sources considered to date include: argon (488/514.8 nm), frequency doubled Nd:YAG laser (532 nm), millisecond pulsed dye laser tuned to 577 nm or 585 nm, and a 985 nm laser diode. The laser beam is first expanded to the maximum beam diameter that can be scanned by the mirrors on the two-axis galvanometer system, providing random-access x-y spatial positioning of the laser beam. Standard beam scanning optics are used to transmit the telecentric location between the two galvanometers to the final scan lens, which converts the beam rotation to a displacement scanned on the surface of the skin. The final laser spot is to be approximately 10 to 50  $\mu\text{m}$  to provide the desired spatial resolution for blood vessels targets ranging from 50  $\mu\text{m}$  to 1 mm.

Eventually, a fiber bundle will transmit this line illumination and laser energy from the "Smart Scalpel" system to the skin surface, so the instrument is remote from the physician and patient. Because of the line illumination, the fiber bundle must be coherent to guarantee the line scanned on one end of the bundle corresponds to a line scan on the skin surface.

## 5 IMAGING SYSTEM RESULTS

### 5.1 Resolution and contrast

The line scan image of a standard bar target was used to quantify the lateral resolution of the imaging system (Figure 10). Non-uniformity in the line illumination was compensated for by normalization against the image of a uniformly reflecting target (white photographic paper).

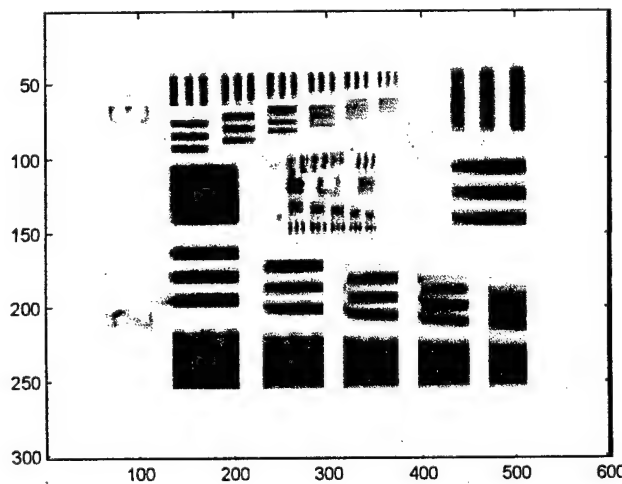


**Figure 10: Test pattern to quantify resolution and sensitivity of imaging system.**

The modulation transfer functions (MTF) for the horizontal and vertical lines of the green and red channels are plotted in Figure 11. The contrast is calculated as the difference between the maximum and minimum signal divided by the sum of these signals. While the contrast generally decreases with increasing spatial frequency, there are unexpected increases in image contrast between 8 and 9 lines per mm and between 15 and 16 lines per mm. This can be explained by considering the way the image is generated. Since, the imaging galvanometer is rotating, the distance between the mirror and the test pattern is shortest in the center of the reticle and longest on the two edges of the image. Given that the bar patterns are located in different parts of the line scan image shown in Figure 10, the parts of the reticle may be slightly out of focus. The extent of contrast non-uniformity throughout the imaged region will be further investigated and quantified to ensure all blood vessels will be identified.

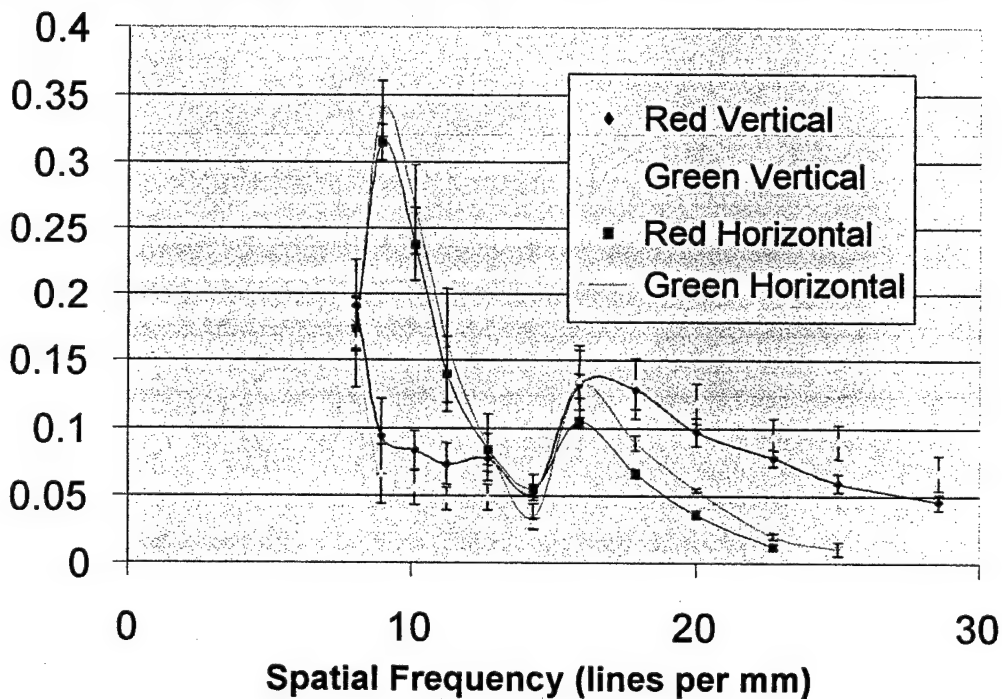


**Figure 11: Modulation transfer function for horizontal and vertical lines on the red and green channels.**

## 5.2 Preliminary blood vessel imaging

Using the Smart Scalpel prototype, preliminary blood vessel images from the ear of a live mouse were generated. The histogram for this image is also pictured, showing the number of blood vessel and background pixels were generated. These images, along with the threshold determined from the histogram will be used to control where the laser energy is delivered.

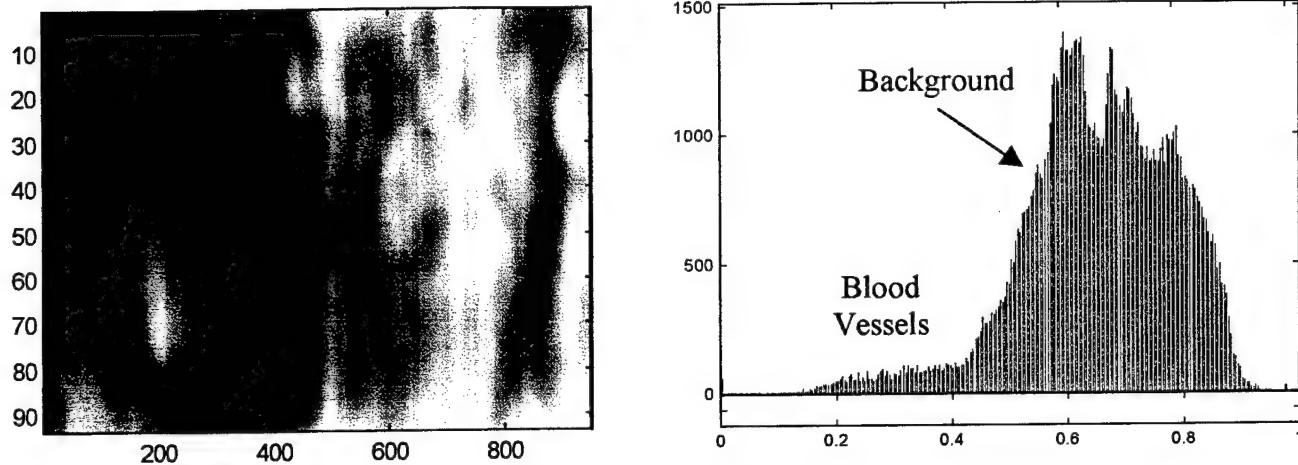


**Figure 12: Preliminary blood vessel image and histogram of a live mouse ear.**

## 6 CLOSED LOOP CONTROL OF LASER

Patterns of oxygenated human blood were created to mimic a blood vessel network in order to test the system's ability to image and identify blood vessel targets. Test pattern images were first acquired at 577 nm and 640 nm (Figure 13) after which the ratio image (577 nm/640 nm) was computed and dynamic range expanded. Next, the histogram of pixel values for this normalized image was graphed to identify the appropriate threshold for blood vessel targets. The 0.7 threshold was used to create the final binary image where pixel values less than 0.7 are assigned as black, representing blood vessels.

Figure 14 illustrates two possible laser targeting strategies with the Smart Scalpel. The line scan image represents the PWS subregion to be treated, with blood vessels interspersed throughout the skin. The gray line represents the line of data acquired at a given instant, while the lighter gray circles are the laser targets. After determining blood vessel positions from a small number of line scans, a randomly selected subset of blood vessel targets are targeted for illumination with the heating laser beam (Figure 14a). However, to effectively heat the blood vessels, it may be important that the laser follow along one vessel at a time (Figure 14b), perhaps in the direction of the blood flow to maximize the efficiency of heat transfer to the blood vessels. Implementation of this targeting strategy will require a larger image to identify and track the spatial position of individual vessels.

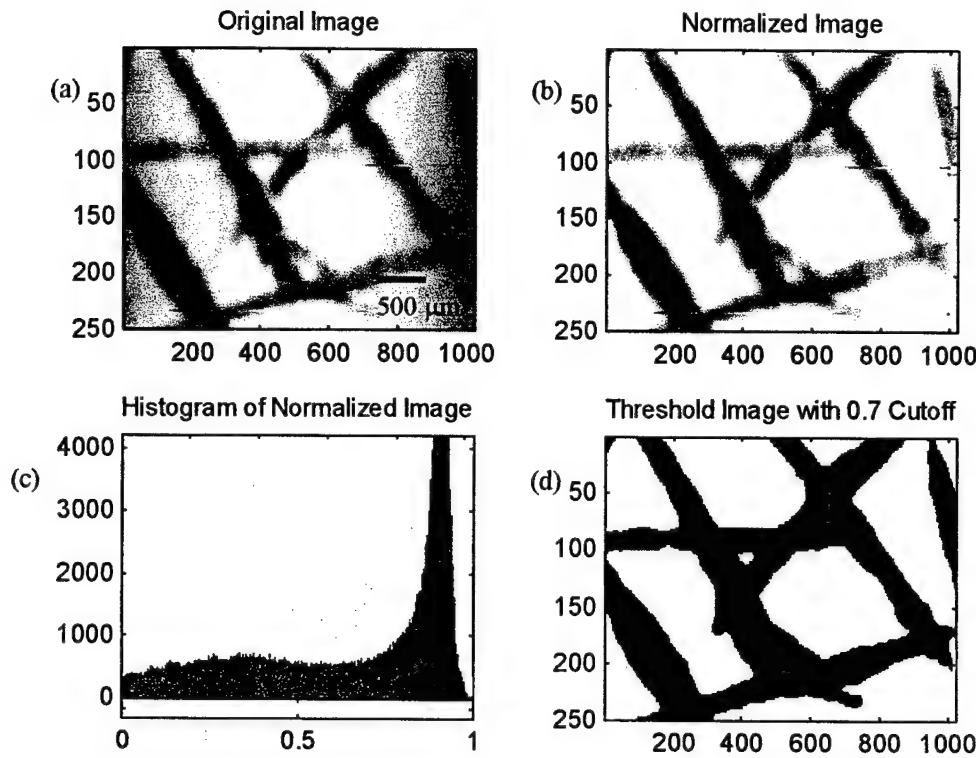


**Figure 13: Succession of steps in identifying laser coordinates. Original 577 nm reflectance image (a), ratio normalized image (b), histogram of normalized image (c), and final image with laser coordinates represented as black using a 0.7 threshold (d).**

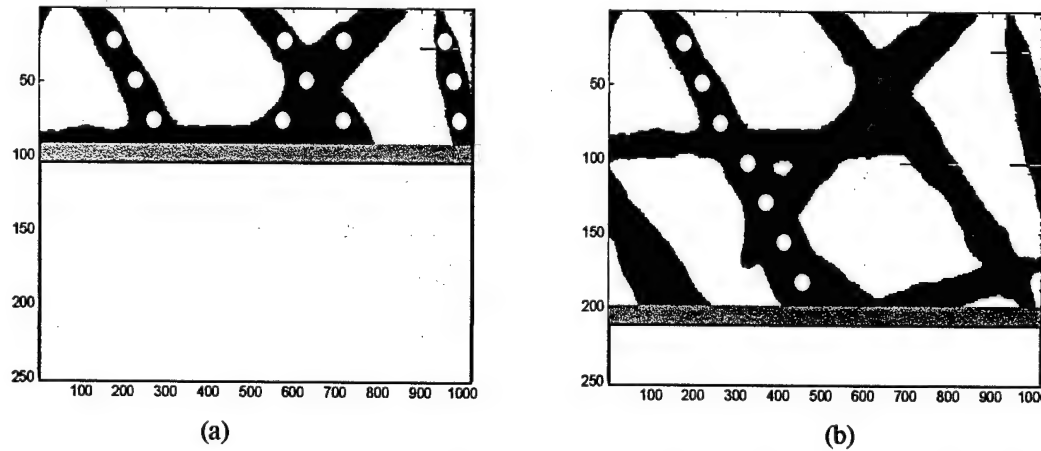


**Figure 14: Two possible control strategies to cover laser targets are illustrated. The first (a) covers one line at a time and delivers energy to the vessel locations within that line. The second (b) requires pattern recognition to identify continuous vessels and follow along one vessel at a time.**

Effective implementation of either laser targeting strategies demands minimal relative motion between the image area and the PWS during the image acquisition, processing and targeting sequence. Tremor is the major source of motion for which the Smart Scalpel must compensate. The result of varied causes<sup>11</sup>, tremor can have a maximal frequency component of 10 Hz with a quasi-sinusoidal displacement that varies across body parts (hands, feet, etc.) and between different people. Accordingly, the maximum number of targets,  $n$ , addressed in one scan is expressed as,

$$n = \frac{T_{move}}{(T_{exposure} + T_{acquisition} + T_{computer} + T_{galvos} + T_{ill})} \quad (7)$$

where  $T_{move}$  is time period of skin displacement (100 ms for a maximum 10 Hz tremor frequency) Time delays in the feedback loop include:  $T_{exposure}$ , the integration time of the line array;  $T_{acquisition}$ , the time required to acquire and convert the photocurrents to an output voltage;  $T_{computer}$ , the data acquisition and processing time of the computer;  $T_{galvos}$ , the step response of the two-axis scanning system; and  $T_{ill}$ , the time required for the laser to thermally treat the blood vessels. By far, the longest time delay is the laser illumination time (~1 ms) resulting in no more than 100 treatment targets within the tremor period.

## 7. SMART SCALPEL APPLIED TO HAIR REMOVAL

### 7.1 Current Clinical Practice

Individuals with unwanted hair are prone to adverse psychological and cosmetic disturbances prompting them to seek medical advice. This has driven the development of methods for temporary hair removal, including shaving, wax epilation, and use of chemical depilatories<sup>15,16</sup>. Electrolysis is a well-established method for permanent destruction of terminal hair follicles. However, the method is tedious, and efficacy has been reported to be between 15% and 50% permanent hair loss<sup>17</sup>. Scarring can result after electrolysis, especially if it is inexpertly performed<sup>18</sup>.

Laser-assisted hair removal methods<sup>19</sup> have been developed recently as an alternative and minimally invasive approach to hair removal. Two general approaches have been identified so far. The first relies on the absorption properties of melanin, an intrinsic chromophore found in high concentration in follicles of pigmented hair. Hair follicles are damaged by selective photothermolysis<sup>20</sup> when illuminated with light at a wavelength absorbed by melanin. In one embodiment<sup>21</sup>, selective thermal injury to both superficial and deep portions of pigmented hair follicles was reported on illumination of the skin with a

3 ms light pulse at 694 nm from a ruby laser having an incident fluence level between 10 to 75 J/cm<sup>2</sup>. The treated area per laser shot is between 10 – 12 mm in diameter. Only 15% to 20% of the incident light penetrate through the dermis to the follicles; the remainder is dissipated in the dermis as heat. Consequently, an actively cooled glass sapphire prism/lens system is used to heat sink the skin to minimize thermal injury to the pigmented epidermis. There is a 2 to 6 month delay reported in hair regrowth after a single treatment for individuals with highly pigmented hair (brown or black).

The second general approach<sup>22,23</sup> to laser-assisted hair removal utilizes long wavelength near infrared light (1064 nm) to increase the penetration of laser energy into the dermis. The low absorption of natural chromophores like melanin at the illumination wavelength is offset by introduction of an exogenous chromophore into the hair follicle to enhance light absorption by the hair follicle cells. Input of the laser energy into the dermis on a time scale much shorter than the follicle thermal relaxation time (<100 ns) results in selective damage of the follicle cells by excessive heat. However, the presence of a mechanical shock wave caused by the superheated fluid surrounding the particle or the fragmentation of the particle itself could also be responsible for causing mechanical damage to adjacent cells. Illumination of the treated area with light from a Q-switched neodymium:yttrium-aluminum garnet (Nd:YAG) laser ( $\lambda = 1064$  nm,  $\tau_p < 10$  ns,  $J = 2-3$  J/cm<sup>2</sup> ) over a 7 mm spot size results a 3 to 6 month delay in hair regrowth.

A common element to both the endogenous and exogenous chromophore techniques described above is the reliance on selective absorption of laser radiation in the illuminated area to damage hair follicle cells. Because of the relatively small difference in absorption between targeted and adjacent cells, collateral damage can be significant resulting in pain and discomfort to the patient both during and after the procedure. Evidence for collateral damage to the dermis stems from reports of postoperative edema and erythema for periods of 24 – 48 hours after the hair removal treatments.

## 7.2 Smart Scalpel approach

One solution to this difficulty is implementation of a SmartScalpel scheme in which the hair follicles are first identified by means of a spectroscopic measurement. A laser beam is then focused on the hair follicle to deliver a radiation dose sufficient to either destroy or inhibit the ability of follicle cells to grow hair. This approach could be implemented in a full-field or line scan imaging format or, as diagrammed in Figure 15, as a hand-held device (known as the LaserShaver) manually scanned across

the skin's surface. In this embodiment, a two-wavelength reflectance measurement identifies the presence of a hair follicle and generates a trigger to fire a laser to selectively heat cells in the hair follicle.

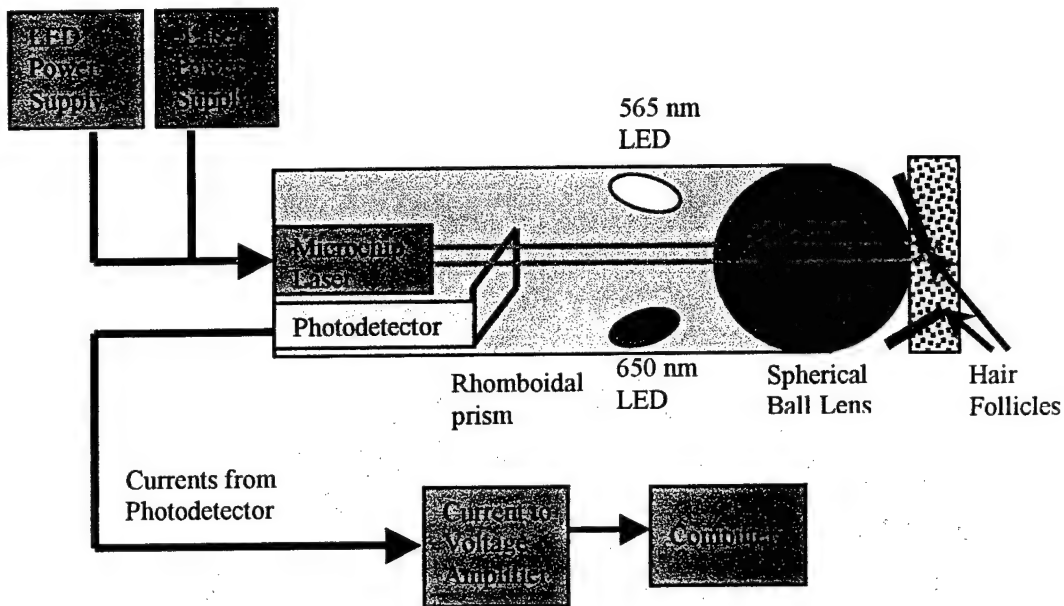


**Figure 15: Schematic of miniaturized Smart Scalpel.**

### 7.3 Application of the microchip laser to laser-assisted hair removal

One of the important steps in our approach towards realization of a SmartScalpel-like system suitable for laser-assisted hair removal is to determine if the Lincoln Lab microchip Nd:YAG laser, a new type of miniature laser, potentially has the beam parameters appropriate for removing hair. The microchip laser is formed from a cleaved  $1\text{ mm} \times 1\text{ mm} \times 0.5\text{ mm}$  Nd:YAG crystal to which is diffusion bonded a  $\text{Cr}^+$ -doped Nd:YAG crystal as a saturable absorber resulting in a passively Q-switched laser cavity. When pumped with light from an 850 nm diode laser, the microchip laser emits light pulses at 1064 nm with a 450 ps duration and a maximum energy of 100  $\mu\text{J}/\text{pulse}$ . The pulse repetition rate –up to 2.5 kHz- is controlled by the magnitude of the pump laser light.

As an initial test, the hair on a  $2\text{ cm} \times 2\text{ cm}$  square section of the forearm of a dark-haired male volunteer was removed by shaving and three regions delineated (Figure 16). A topical solution of glassy carbon particles in water was gently massaged into the skin of Region A while Regions B and C are left alone. Region C is the control and Regions A and B were treated with light from the microchip laser.

The microchip laser output is focused to a 70  $\mu\text{m}$  spot diameter by a 0.25 numerical aperture microscope objective integrated with the laser into a lightweight hand-held assembly. The skin is viewed through a long working distance, wide field microscope and the focused laser beam is manually positioned to illuminate the hair follicles observed through the microscope. The laser repetition rate is 544 Hz and at the skin's surface the fluence level is  $\sim 3 \text{ J/cm}^2$ . Hair follicles in Regions A and B were exposed to the focused laser beam for exposure times from 1-10 s per follicle. The distance between the objective and skin surface was also varied to change the focal depth of the laser beneath the skin surface.



**Figure 16: Shaved forearm of male volunteer showing treatment and control regions.**

#### 7.4 Results

Erythema was observed for several hours after the application of laser energy in both Regions A and B. Illumination of carbon particles on the surface in Region A resulted in a rapid heating of the skin adjacent to the particle thus qualitatively suggesting enhanced selective absorption of laser energy by the carbon particle compared to the surrounding tissue. The high fluence level results in breakdown and plasma formation when the laser light is focused on the skin's surface. Laser light focused onto individual hairs quickly sliced through the hair. Comparison of regrowth rates between Regions A and B with that of the control (Region C) at one week intervals for one month after the laser treatment indicated some of the treated hair follicles were slow in growing back. Selective targeting of hair follicles is difficult because hand tremor introduces an uncertainty in the targeting of the focused laser

relative to the hair follicles. It is clear an improved targeting scheme would greatly enhance the execution and efficacy of the technique.



**Figure 17: Experimental setup for laser-assisted hair removal with a focused laser beam.**

## **8 FUTURE PLANS**

Given the encouraging results in blood vessel imaging and laser hair removal, we see the following as the next steps for the Smart Scalpel project:

- Use of Smart Scalpel imaging system for closed loop control of laser for PWS removal application.
- Testing of Smart Scalpel system in animal model to gain knowledge of optimal parameters such as appropriate laser wavelength, fluence, pulse width, control strategy (e.g. tracing individual vessels or targeting blood vessels in random order).
- Transfer of control scheme developed for PWS application to develop a targeting system for the laser hair removal application, perhaps one based on spectroscopic detection.
- Modification of Smart Scalpel hardware to miniaturize and create an instrument that more conveniently interfaces with the physician and patient.

## REFERENCES

1. R.C. Dorf and R.H. Bishop, *Modern Control Systems*, Addison-Wesley, Reading, MA, 1995.
2. J.B. Mulliken, and A.R. Young, *Vascular Birthmarks- Hemangiomas and Malformations*, Saunders, Philadelphia, PA, 1988.
3. E.J. Fiskerstrand, L.O. Svaasand, G. Kopstad, M. Dalaker, L.T. Norvang, and G. Volden, "Laser treatment of port wine stains: therapeutic outcome in relation to morphological parameters," *British Journal of Dermatology*, 136(3), pp. 467-8, 1997.
4. S.H. Barsky, S. Rosen, D.E. Geer, and J.M. Noe, "The nature and evolution of port wine stains: a computer-assisted study," *Journal of Investigative Dermatology*, 74(3), pp. 154-7, 1980.
5. R.R. Anderson, "Laser medicine in dermatology," *The Journal of Dermatology*, 23, pp. 778-782, 1996.
6. J.H. Torres, B. Anvari, B.S. Tanenbaum, T.E. Milner, J.C. Yu, and J.S. Nelson, "Internal Temperature Measurement in Response to Cryogen Spray Cooling of a Skin Phantom," *Proceedings of SPIE International Biomedical Optics Symposium*, San Jose, CA, 1999.
7. B. Anvari, B.S. Tanenbaum, W. Hoffman, S. Said, T.E. Milner, L.H. Liaw, and J.S. Nelson, "Nd:YAG laser irradiation in conjunction with cryogen spray cooling induces deep and spatially selective photocoagulation in animal models," *Physics in Medicine and Biology*, 42(2), pp. 265-82, Feb. 1997.
8. J.S. Nelson, T.E. Milner, B. Anvari, B.S. Tanenbaum, S. Kimel, L.O. Svaasand, and S.L. Jacques, "Dynamic epidermal cooling during pulsed laser treatment of port-wine-stain. A new methodology with preliminary clinical evaluation," *Archives of Dermatology*, 131(6), pp. 695-700, June 1995.

9. W.F. Cheong, S.A. Prahl, and A.J. Welch, "A review of the optical properties of biological tissues," *IEEE Journal of Quantum Electronics*, 26(12), pp. 2166-2185, 1990.
10. K.P. Watts, R.G. Fairchild, D.N. Slatkin, D. Greenberg, S. Packer, H.L. Atkins, S.J. Hannon, "Melanin content of hamster tissues, human tissues, and various melanomas," *Cancer Research*, 41, pp. 467-472, 1981.
11. R.R. Anderson, J.A. Parrish, "The optics of human skin," *Journal of Investigative Dermatology*, 77(1), pp. 13-19, 1981.
12. R.R. Anderson, "Polarized light examination and photography of the skin," *Archives of Dermatology*, 127(7), pp. 1000-1005, 1991.
13. A.L. McKenzie, "Physics of thermal processes in laser-tissue interactions," *Phys. Med. Biol.*, 35(9), pp. 1175-1209, 1990.
14. W.D. Tope. Personal communication. *SPIE International Biomedical Optics Symposium*, San Jose, CA, 1999.
15. Kvedar JC, Gibson M, Krusinski PA. Hirsutism: evaluation and treatment. *J Am. Acad. Dermatol.*, 1985, 12, 215-225.
16. Richards RN, Marguerite U and Meharg G. Temporary hair removal in patients with hirsutism: a clinical study. *Cutis*. 1990, 45, 199-202.
17. Wagner RF. Physical methods for the management of hirsutism. *Cutis*. 1990, 45, 19-26.
18. Kligman AM, Peters L. Histologic changes of human hair follicles after electrolysis: a comparison of 2 methods. *Cutis*. 1984, 34, 169-176.
19. Wheeland RG. Laser-assisted hair removal. *Lasers in Dermatology*, 1997, 15, 469-477.

20. Anderson RR, Parish JA. Selective photothermolysis: precise microsurgery by selective absorption of pulsed radiation. *Science*, 1983, 220, 524-527.
21. Dierickx CC, Grossman MC, Farinelli WA, Anderson RR. Permanent hair removal by normal-mode ruby laser. *Arch. Dermatol.*, 1998, 134, 837-842.
22. Nanni CA, Alster TS. Optimizing treatment parameters for hair removal using a topical carbon-based solution and 1064-nm Q-switched Neodymium:YAG laser energy. *Arch. Dermatol.*, 1997, 1546-1549.
23. Goldberg DJ. Topical solution-assisted laser hair removal. *Lasers Surg. Med.*, 1995, 7S, 47, Abstract.

# **Minimally Invasive Glucose Sensor and Insulin Delivery System**

**Lisa Sambol, Shirley Mihardja**

Research Assistants

**Tanya Kanigan, Colin Brenan**

Post-Doctoral Fellows

**Ian Hunter**

Hatsopoulos Professor of Mechanical Engineering

**Lynette Jones**

Senior Research Scientist

## **Abstract:**

The goal of this project is to develop a minimally invasive miniature device which has the potential to control the delivery of insulin with feedback from an integrated glucose sensor. This system will be designed to use the interstitial fluid (IF) rather than blood to measure glucose levels since IF can be extracted painlessly from the dermis. The device must be able to accurately measure glucose levels and dispense the appropriate amount of insulin, using the glucose measurement as feedback in the control loop. The device must also be easily mass-produced and miniaturizable. Much progress has been made over the last year in the development of the minimally invasive glucose sensor and insulin delivery device. By creating a biocompatible glucose sensor, these measurements can take place *in vivo*, eliminating the need to remove IF from the patient. We will continue to work towards the development of a closed-loop system for insulin delivery using measured glucose levels as feedback. This technique will then be used to maintain optimum glucose levels in the patient throughout the day, alleviating much of the stress and pain currently endured by diabetics.

# **Minimally Invasive Glucose Sensor and Insulin Delivery System**

Progress Report March 23, 1999

Lisa Sambol, Tanya Kanigan, Colin Brenan,

Shirley Mihardja, Ian Hunter, and Lynette Jones

## **Introduction:**

The goal of this project is to develop a minimally invasive miniature device which has the potential to control the delivery of insulin with feedback from an integrated glucose sensor. This system will be designed to use the interstitial fluid (IF) rather than blood to measure glucose levels since IF can be extracted painlessly from the dermis. The device must be able to accurately measure glucose levels and dispense the appropriate amount of insulin, using the glucose measurement as feedback in the control loop. The device must also be easily mass-produced and miniaturizable.

## **Device Design:**

The current design of this device is that of a hollow microneedle array which only penetrates the stratum corneum layer of the skin. The outer surface of these needles can be made into amperometric glucose sensors using electrochemical methods, enabling them to be used both for sensing and drug delivery.

it cuts. This eliminated the potential problem of closing the needle openings during cutting.

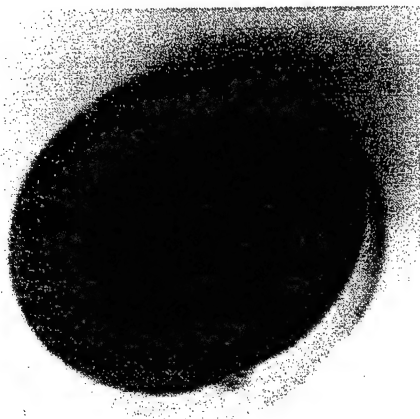


Figure 2: Results of needle cutting using wire EDM.

The needles were inserted into the baseplate manually and positioned such that only 50 micrometers protruded from the array. The needles were then secured in place using epoxy. This manually constructed array was used to show that a viable array can be constructed by combining a baseplate hole array with individual hollow needles.

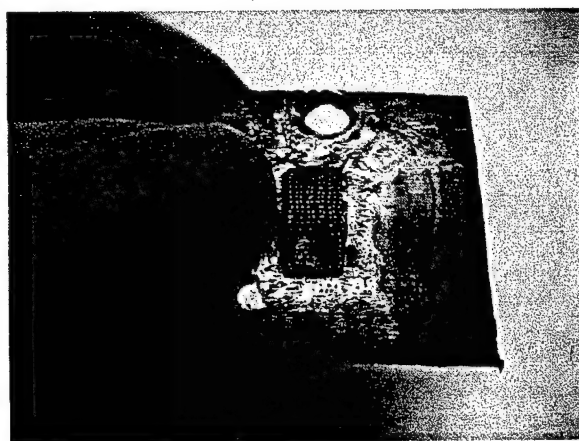


Figure 3: Example of a partially filled array with manually inserted needles.

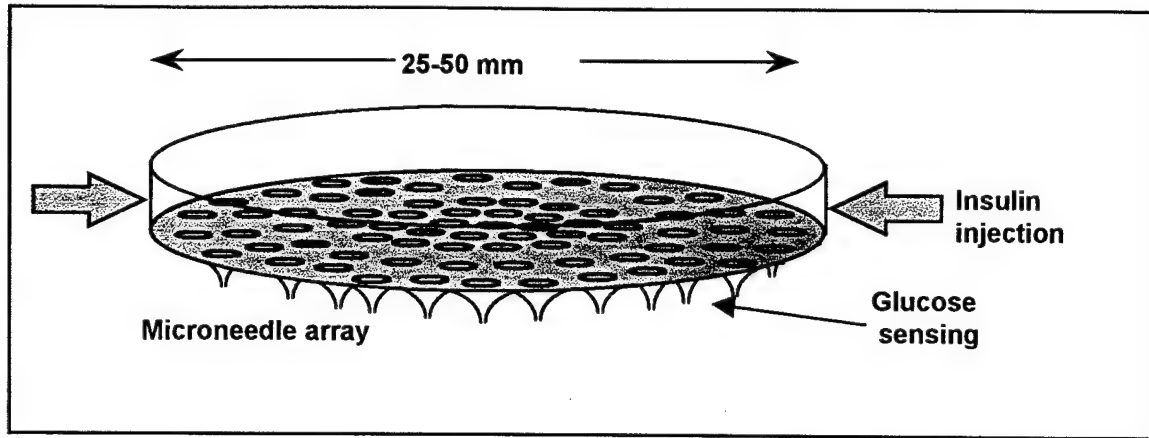


Figure 1: Schematic drawing of an initial design for the glucose sensor/insulin delivery device.

Much effort has gone into developing a low cost method of manufacturing the microneedle array. Our initial approach consisted of forming a microhole array in a base plate of Delrin and then placing and securing the microneedles into these holes. Each of the 200 holes has a diameter of 250 micrometers with a 500 micrometer center-to-center spacing. Delrin was chosen for two reasons: 1) its insulating characteristics allow for each needle to be electrically isolated which will be necessary using a two electrode sensing technique, and 2) it is a soft material in which small holes can be machined at easily attainable speeds.

Standard hypodermic tubing with an outer diameter of 200 micrometers was obtained. Approximately 25 mm length sections of the tubing were tightly packed into a larger tube and then placed in the wire EDM (Electrostatic Discharge Machining) vice. The wire EDM was used to cut the needles to the desired length of 3 mm using an angled cut, thereby forming a pointed tip on each needle for easier penetration of the stratum corneum. The EDM machine was used since it imparts almost no force onto the objects

One possibility is to use solid needles for the glucose detection and have a hollow needle array used solely for drug delivery. Recent lab investigations have also proven that silicon can be machined using the EDM technology. This leads to the possibility of using passivated silicon as the array baseplate in order to electrically insulate the working and counter electrodes. The process for fabrication of this type of design consists of functionalizing the needles of an EDM array as the working electrodes, and then inserting this array into a silicon baseplate predrilled with a matching hole array.

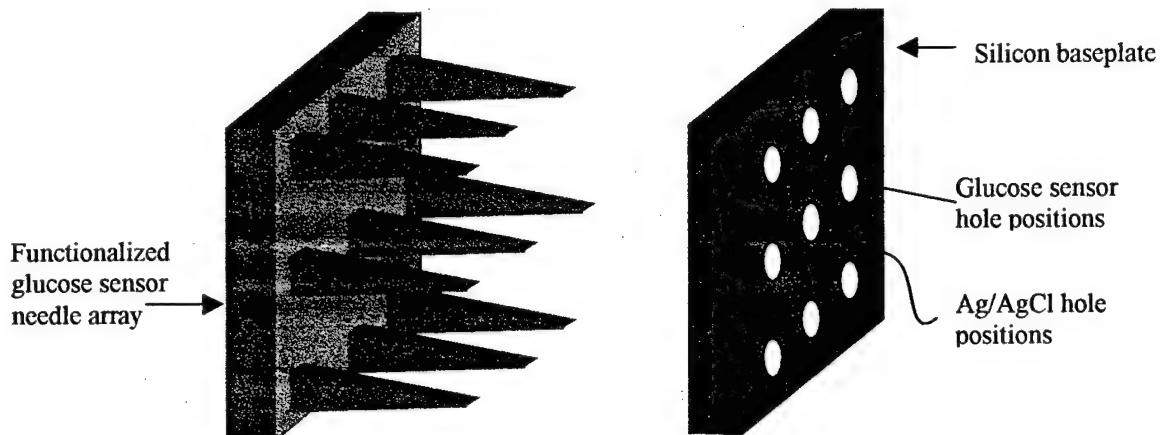


Figure 5: Silicon array fabrication technique

The needle tips would then be imbedded in epoxy to hold them in place while the back end of the needle array is removed by the wire EDM. Once the needles are locked in position, the epoxy can be removed from the tips. This process would then be repeated with an array of counter electrodes (Ag/AgCl). Similar needles could then be electrically connected using gold pads attached to the silicon, allowing the system to record a summed response to glucose levels.

Due to the tediousness of manually inserting needles into the array, alternative insertion methods were investigated. A magnetic shaker system was designed specifically for the insertion task. The needles were placed in a small reservoir positioned directly over the hole array. A magnet was placed beneath the array in such a manner as to align the needles perpendicular to the array and hold the needles in position once they were inserted. A cap was placed over the reservoir and the entire unit was shaken vigorously until the needles were inserted. Although many configurations were tried using this method, only limited success was achieved. Approximately 80 needles were inserted into the array before too much magnetic interference between the inserted needles and the free needles became an issue. The needles were then positioned such that only 50 micrometers protruded from the array and fixed in place using epoxy.

Current work is also being done to determine whether the EDM offers a more appropriate method of array fabrication. Multi-needle arrays have already been fabricated using the EDM, however these arrays contain solid needles rather than hollow ones.

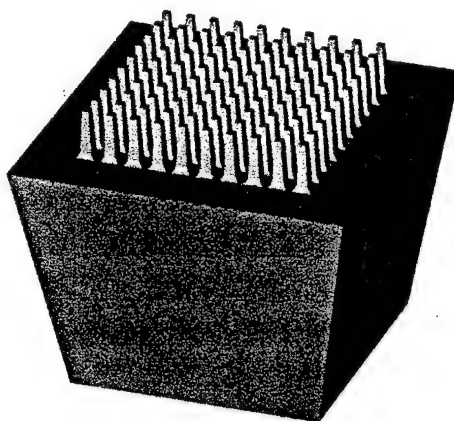


Figure 4: EDM fabricated microneedle array

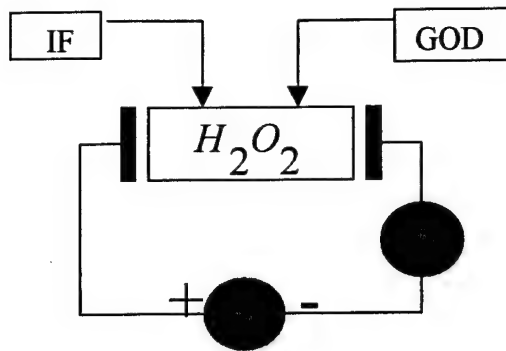


Figure 8: Circuit to detect amount of glucose in IF.

To fabricate the glucose sensor, we have been following an electrochemical depositon method used by Yang (Yang, 1998). This method was chosen because the resulting sensor has a quick response time to glucose (<10 seconds), low operating potential (less than +0.3 V), immunity to chemical interferents, straightforward fabrication method, and potential for miniaturization. The fabrication procedure consists of a series of potentiostatic and galvanostatic chemical depositions onto the needle surface.

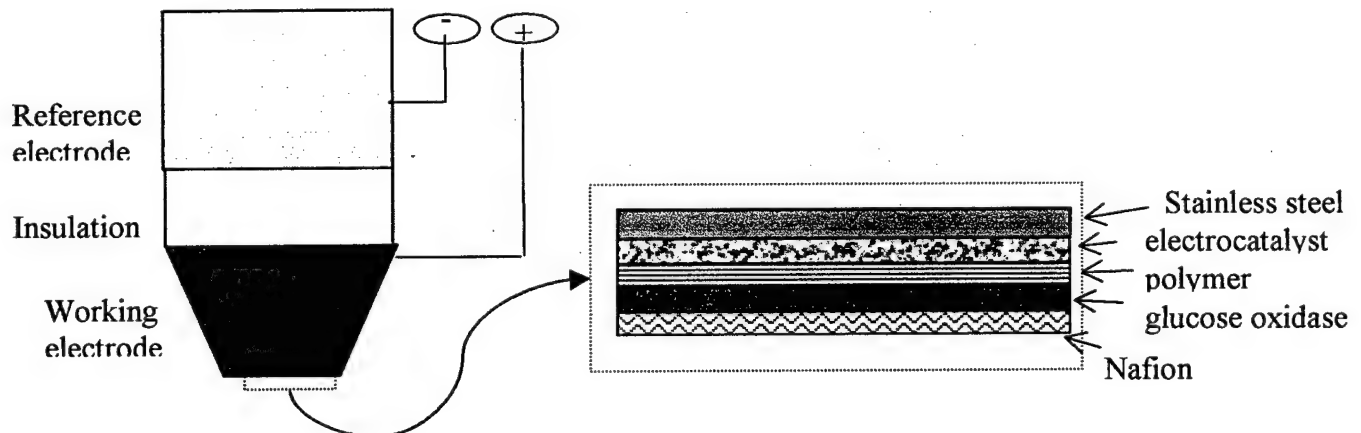


Figure 9: Layers deposited on needle surface.

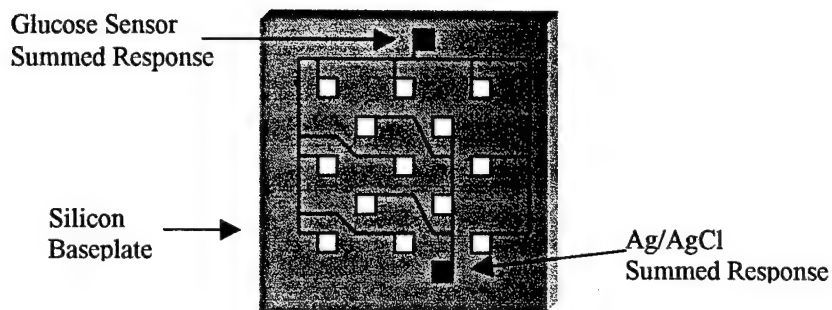


Figure 6: Electrical connections of electrodes on silicon baseplate

### Sensor Design:

Glucose can be detected amperometrically by a two-step chemical process. The enzyme glucose oxidase is used to break the glucose down into hydrogen peroxide and gluconic acid. Electrons are then extracted from the hydrogen peroxide through a subsequent oxidation step.

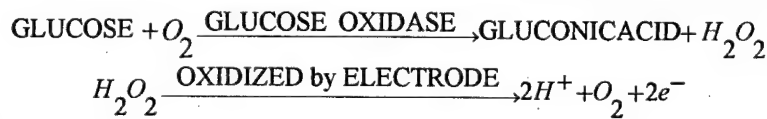


Figure 7: Chemical reactions involved in glucose detection

A circuit can now be set up to collect the electrons produced from this reaction. The current measured in this circuit will be proportional to the amount of glucose present in the IF.

We have been consistently able to sensitize 18 gauge stainless steel needles to hydrogen peroxide, an intermediate step in the process, with this technique. An example of this can be seen in the data collected from one multi-layered needle, as seen in Figure 10. The results here show a distinct and constant rise in current as the hydrogen peroxide concentration increases. This increase in current is evident throughout the expected biological range of hydrogen peroxide concentrations, 0 – 20 mM, and the rise time of the response was less than 5 seconds.

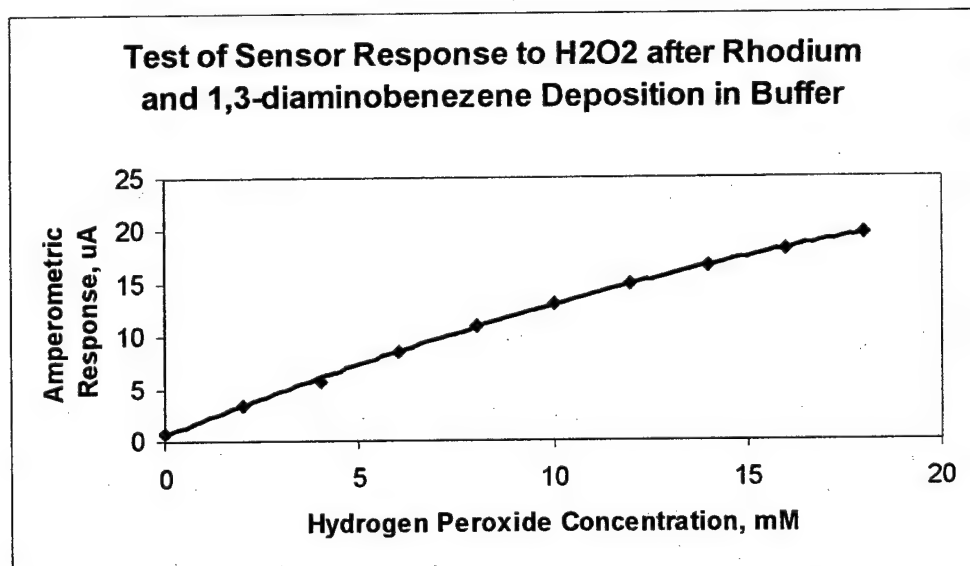


Figure 10: Sensor Response to Hydrogen Peroxide.

Only one of our first experiments produced a sensor which elicited a very weak response to increasing concentrations of glucose (Figure 11). Over the physiological range of glucose, 0 – 20 mM, this sensor showed an increase of less than 3 microamps. The expected response over this range is approximately 12 microamps. Although weak, the response increased consistently as the glucose concentration increased with a rise time of less than 10 seconds, indicating that some measure of success was achieved.

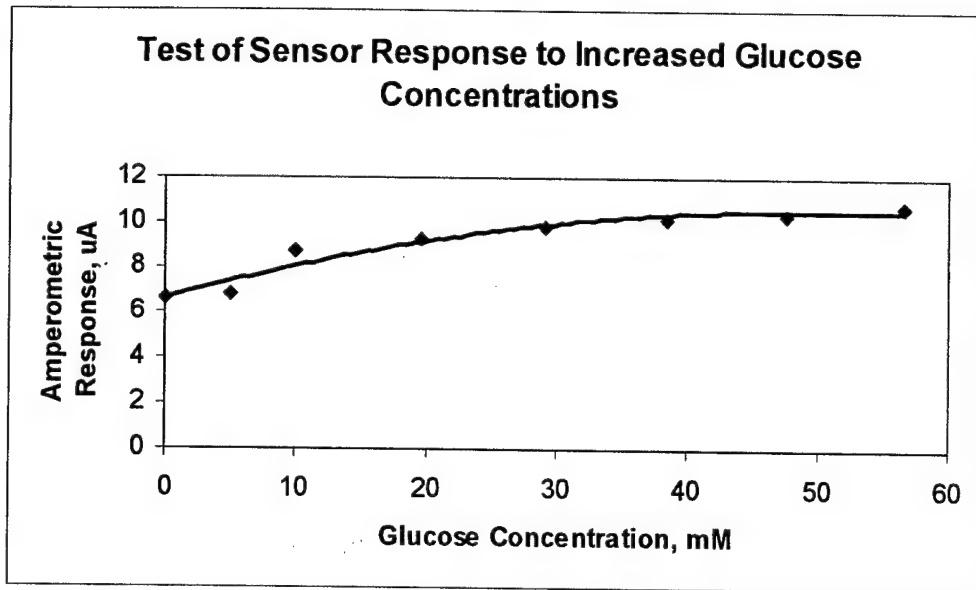


Figure 11: Sensor response to increasing glucose concentrations

This glucose response, while somewhat weaker than expected, indicates the validity of the attempted process. Our goal is to repeat this method with more precision in order to achieve higher current responses to glucose. With subsequent trials, however, we suspect that we have not been able to immobilize a sufficient amount of the glucose oxidase on the needle surface to make it sensitive to glucose because the silver/silver-chloride reference electrode being used for glucose oxidase immobilization was not responding properly. A new protocol has been established to test the electrode before immobilization. With each trial, the silver/silver-chloride electrode will be tested against a silver/silver-chloride reference electrode immersed in the phosphate buffer solution. The electrode will be considered valid only when a voltage of less than 3 mV is measured between it and the reference. We will also work towards the fabrication of our own consistent silver/silver-chloride electrodes which will be adaptable to an array format.

Various other systemic errors have also been eliminated from the procedure. Questions of consistency arose surrounding the means by which potentiostatic and galvanostatic reactions were taking place since the system used had many exposed wires and loose connections. In order to address these issues, we have purchased a single-unit, enclosed potentiostat/galvanostat which will be able to carry out the reactions under constant conditions without the concern of wires being mistakenly moved during the procedure. It was also noted that the needles used in Yang's procedure were epoxy filled. Since our needles were hollow, extra surface area was exposed during the plating procedure possibly causing thinner layers to form on the sensor. As such, we will attempt the process again with filled needles and remove the epoxy after plating is completed.

Based on the successes of past trials to create a consistent hydrogen peroxide detector and the achievement of a weak glucose sensor, we are optimistic that the new protocol will aid in successful immobilization of the glucose oxidase. A few other methods of fixing glucose oxidase on the needle sensor have also been found (Gunasingham, 1989 and Moussy, 1993) should our current attempt fail. Once we are able to consistently produce glucose sensors from 18 gauge stainless steel needles, we plan to adapt the process first to smaller needles and then to arrays of microneedles.

### **Research Plan:**

In the next year of this project, we plan to fabricate a prototype microneedle array that can effectively measure glucose levels in IF. After a sensor is successfully fabricated, we will determine the best array design into which this can be incorporated. One method under consideration is a system of imbedded arrays, one coated with the glucose oxidase catalyst and the other with silver/silver-chloride. We will work to miniaturize our sensor and array designs in order to create a prototype which can sample IF in a painless manner. Once this prototype is developed we will investigate the issues surrounding the control of insulin delivery, including how much insulin needs to be delivered and at what intervals, how fast blood glucose levels change, and whether sensing and drug delivery should take place at the same physical location. Further experimentation will also be needed to determine how much pumping pressure is required to deliver insulin to the tissue.

### **Summary:**

Much progress has been made over the last year in the development of the minimally invasive glucose sensor and insulin delivery device. By creating a biocompatible glucose sensor, these measurements can take place *in vivo*, eliminating the need to remove IF from the patient. We will continue to work towards the development of a closed-loop system for insulin delivery using measured glucose levels as feedback. This technique will then be used to maintain optimum glucose levels in the patient throughout the day, alleviating much of the stress and pain currently endured by diabetics.

**References:**

Gunasingham, Hari and Tan, Chee Beng (1989) "Platinum-dispersed Nafion Film Modified Glassy Carbon as an Electrocatalytic Surface for an Amperometric Glucose Enzyme Electrode." *Analyst*, 114, 695-698.

Moussy, Francis; Harrison, D. Jed; O'Brien, Darryl W.; and Rajotte, Ray V. (1993) "Performance of Subcutaneously Implanted Needle-Type Glucose Sensors Employing a Novel Trilayer Coating." *Anal. Chem.*, 65, 2072-2077.

Yang, Qingling; Atanasov, Plamen; and Wilkins, Ebtisam (1998) "Development of needle-type glucose sensor with high selectivity." *Sensors and Actuators B*, 46, 249-256.

# Conducting Polymer Devices for the Home

Ian W. Hunter  
Hatsopoulos Professor of Mechanical Engineering

John D. Madden  
Research Assistant

Peter G. Madden  
Research Assistant

## ABSTRACT

Conducting polymers exhibit a wide range of tunable properties that make them ideal for use in devices at home, or in health care environments. In this report we update progress in the development of conducting polymer actuators and transistors. The actuator research has produced two important advances. First, power to mass ratios equaling those of mammalian skeletal muscle (50 W/kg) are demonstrated. Actuator strains are observed at frequencies between 0.1 Hz and 30 Hz. The strain falls off in proportion to the inverse square root of frequency in this range, suggesting a diffusion limited process. Diffusion limits can in principle be minimized by reducing polymer thickness. Second, linear actuators are demonstrated operating out of a liquid environment. These actuators feature a gel electrolyte surrounding an active polypyrrole member, the entire device being encapsulated by an outer electrode. The operation of the actuators in air is clearly an important step in widening the scope of applications. Finally, a number of polymer transistor designs are described and characterized, with the aim using these transistors in conjunction with the actuators and conducting polymer strain gauges as integrated, artificial muscle like devices. The actuator/transistor combinations feature properties that are very desirable in home and healthcare applications, including low cost, low voltage (<5 V fast, <0.5 V for slow operation), high active force per cross-sectional area (1-20 MPa) and high power to mass (50 W/kg).

# Conducting Polymer Devices for the Home

*Peter G. Madden, John D. Madden*

*Ian W. Hunter*

## ***Introduction***

Conducting polymers exhibit a wide range of tunable properties that make them ideal for use in devices for use in home, business or health care environments. As has been discussed previously, conducting polymers are being employed, to produce energy storage devices (high energy density batteries and super-capacitors), display technologies (electrochromic windows and flat panel LED displays), logic/memory (transistors, LED controllers ...), actuators, and sensors (chemical, optical, displacement). Furthermore, polymers are inexpensive (\$1/kg), making them suitable materials for use in mass-produced devices. This report highlights developments in the conducting polymer actuator technology, transistor technology, and in the design the first integrated polymer device, namely an actuator/transistor/strain gauge combination that will mimic the behavior of a reflex loops found in mammalian skeletal muscle.

## ***Actuators***

Powerful, efficient, controllable and inexpensive actuators are key for home and health care mass market products. Sense and dispense devices for example, such as air fresheners, air and water quality monitors, and drug delivery mechanisms, rely on actuators to deliver perfumes, antidotes and drugs. For these to be effective, several actuator properties must be considered.

(1) Force and displacement: The volume necessary for an actuator can be significantly reduced if it combines large forces and displacements for a given volume. In effect,

the work performed per cycle is large. If the work density per cycle is low, performing many cycles in the same amount of time can compensate for it. However, often this is inconvenient. For example, a piezo-electric actuator generates small strains (0.1%), at roughly equivalent stress levels to conducting polymer actuators. The generation of the same work requires at least twenty times the number of cycles or twenty times the volume of material as compared with a conducting polymer actuator, which generates strains of 2 to 20%. A larger volume is undesirable and the larger number of cycles may require the use of a ratchet or other additional mechanisms.

(2) Operating Voltage: The ability to operate at a low voltage is a key consideration.

High voltages, as required in piezo-electric drives for example, require heavy and bulky DC-DC converters or transformers. As will be shown, conducting polymers can be operated at potentials of less than 5 V, and even as low as 1 V, allowing conventional batteries and microelectronics power supplies to be employed.

(3) Efficiency: The energy conversion efficiency is important, particularly in autonomous devices, because it affects the size of energy source required. Efficiencies in conducting polymer actuators can be 20 % or higher. Also important is that the actuator can be charged ( the actuator is a capacitor/battery ), and subsequently discharged in order to perform work. No battery or power supply is required in order to perform work, and metering the flow of current from the device can control the degree of contraction.

(4) Power to Mass Ratio: The power to mass ratio is particularly relevant where rate is important. Until recently power to mass in conducting polymer actuators has been

very low – 100 times less than that observed in skeletal muscle. We demonstrate, as described in detail in the next section, that power to mass ratios equaling those in muscle are achievable, and shows that the rate-limiting factor is likely diffusion. Reducing actuator dimensions diminishes diffusion limitations. Employing many small strands in parallel may then be the answer to further improving power to mass ratios in conducting polymer actuators.

(5) Operating Environment: The second section below demonstrates the operation of conducting polymer actuators out of a liquid environment. Until now their operation has largely been restricted by the fact that they were operated in a liquid electrolyte. We have employed gels to show their operation in air.

The following articles detail the current understanding of power to mass ratios achievable in conducting polymer actuators, and the use of conducting polymers in dry environments.

### ***Rapid Strain Rates in Polypyrrole Films***

In this section millisecond scale response to electrochemical activation is investigated, leading to the observation of strain rates two orders of magnitude larger than previously reported, and of continuous power to mass ratios equaling that of muscle. Rapid deflection is shown for polypyrrole actuators operating both in and out of a liquid

environment. The form of the frequency response suggests that diffusion is the rate-limiting factor.

Polymer expansion appears to be the result of ionic and molecular influxes that occur as oxidation state is altered either chemically or electrochemically<sup>3,4</sup>. Mass fluxes resulting from capacitive charging of the polymer may also contribute to material dilatation. Electrochemical experiments show that strain is directly proportional to the magnitude of charge transfer<sup>1,2,9</sup> and, equivalently, that strain rate is proportional to current. Reaction kinetics, mass transport and capacitive charging are hence the candidate rate limiting factors.

Polypyrrole and polyaniline are observed to displace rapidly upon initial application of an oxidizing or reducing potential, but then to slow over time<sup>13,14</sup>. Such an initially rapid, but decreasing rate is consistent with the behavior of diffusion limited processes<sup>15</sup>, and could also result from capacitive charging. The aim is to quantify actuator behavior in terms of strain rate and power to mass, and to study frequency response as a preliminary attempt to elucidate the underlying rate limiting mechanisms. Frequency response is obtained both for devices operating in liquid, and for encapsulated actuators operating in air. Operation in air is of interest as it is a requirement of many potential applications.

To determine strain rate, the amplitude of deflection produced in bilayer conducting polymer actuators is measured as a function of the frequency. Bilayer actuators consist of laminated strips of material in which a differential expansion leads to bending. These devices act as mechanical amplifiers, generating relatively large displacements in response to minuscule deformations, thus allowing ready measurement of small material

strains. Linear elasticity theory is employed to relate bilayer deflections to material strain<sup>9,16</sup>. The effective strain,  $\alpha$ , for a given bilayer deflection,  $\delta$ , is determined by first solving for the change in film curvature,  $\Delta\rho$ , in terms of deflection and bilayer length,  $L$ :

$$\delta^2 = \frac{2\delta}{\rho} + \frac{\sin(L\rho)}{\rho}^2 \quad (1)$$

The strain is then related to the relative thickness of the two layers,  $h_1$ , and,  $h_2$ , as well as the elastic moduli divided by one minus the Poisson's ratio for each layer, as represented by  $E_1'$  and  $E_2'$ :

$$\Delta\rho = \frac{6\alpha}{\frac{\left(E_1' h_1^2 - E_2' h_2^2\right)^2}{E_1' E_2' h_1 h_2 (h_1 + h_2)} + 4(h_1 + h_2)} \quad (2)$$

The active material employed in bilayers operating in both solution and in air is polypyrrole. Polypyrrole films are deposited under two different conditions. Films employed in air are grown from a solution of 0.06 M freshly distilled pyrrole monomer and 0.05 M tetraethylammonium hexafluorophosphate in propylene carbonate, following the procedure of Yamaura<sup>17</sup>. Polypyrrole is deposited galvanostatically on to polished 50 mm x 50 mm glassy carbon substrates at current densities of 1.25 A·m<sup>-2</sup>, resulting in a typical film thickness of 40  $\mu\text{m}$ . Deposition takes place at -30 °C in a nitrogen saturated solution. The resulting films have conductivities on the order of 1 to  $3 \times 10^4$  S·m<sup>-1</sup>, and tensile strengths of 25 MPa. The polypyrrole films employed in liquid environments are synthesized electrochemically from a 0.1 M Pyrrole, 0.1 M sodium

dodecylbenzenesulfonate (DBS) aqueous solution, following the methods of Smela<sup>10</sup>.

Deposition takes place on a 250 nm thick platinum film that has been e-beam evaporated on to mylar tape. Deposition is performed galvanostatically against a large stainless steel counter electrode, 20 times the surface area of the working electrode. 150  $\mu$ A of current are delivered over 8 to 17 hours to yield 30-60  $\mu$ m thick films. Films prepared by both methods have elastic moduli of between 0.5 GPa (wet) and 1 GPa (dry). Creep behavior is observed, with a time constant of roughly 200 s.

In fabricating the liquid-based bilayers, the DBS-doped polymer and the platinum backing are peeled from the Mylar layer and cut to form actuators. Two were employed to obtain the results presented, one being 0.75 mm wide, 7 mm long and 60  $\mu$ m thick and the second having a length of 3 mm, a width of 1.5 mm and a thickness of 31  $\mu$ m. The actuators are immersed in 0.1M sodium DBS aqueous solution. Square wave potentials are applied between the platinum backing and a stainless steel counter electrode. The square wave amplitude is  $\pm$  7 V, and applied frequencies range from 1 Hz to 30 Hz. The current through the actuator is typically several milliamperes. Bilayer deflection, resulting from the expansion and contraction of the polypyrrole layer relative to the platinum, is observed under a microscope. The microscope image is recorded using a CCD camera (Hitachi VK-C630) sampling at 30 frames per second, coupled to a video tape recorder. The magnitude of deflection is determined from these images. Normally digital sampling is limited at the high end by the Nyquist frequency, which is 15 Hz in this case. However, the CCD camera collects light continuously, so that fast moving objects appear blurred on each frame. By analyzing the data frame by frame and between frames, the extent of deflection was determined at slightly higher frequencies. Strain,

strain rate and force are calculated from the measured displacements, bilayer geometry and mechanical properties using the Equations 1 and 2 and standard linear elasticity theory<sup>9,16</sup>.

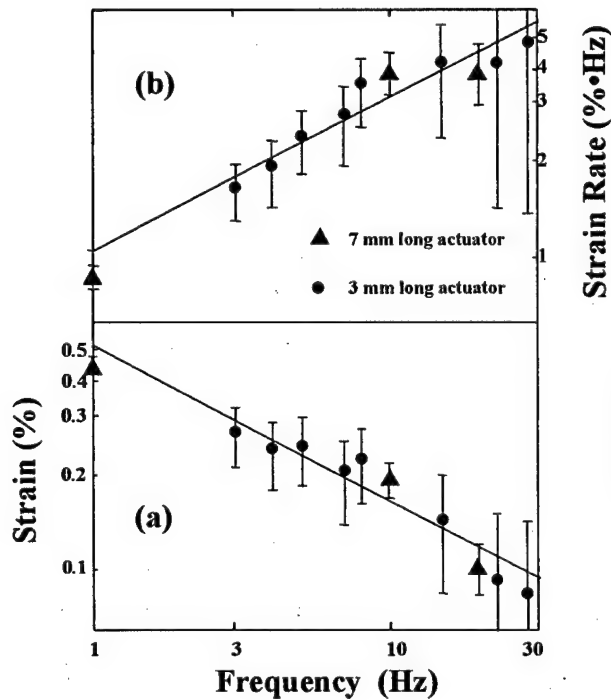


Figure 1: Strain and strain rate as a function of frequency of square wave activation for bilayer actuators in aqueous solution.

Strain amplitudes and the corresponding strain rates from two bilayers are shown as functions of frequency in Figure 1. The magnitude of deflection at 1 Hz is 2 mm for the 7 mm long actuator (triangular markers). The error bars shown account for uncertainties in the measurement of deflection, which are larger for the shorter beam due to its smaller deflections. Uncertainties in the measurement of actuator lengths and thicknesses add a further 10 % error to all points. The average strain rates, Figure 1b, reach a peak of  $4 \pm 1$  %·Hz at 10 and 20 Hz cycling, two orders of magnitude higher than those previously reported. The magnitude of the activation potential influences strain rate. For example,

as applied potential is increased from 4 V peak-to-peak up to 8 V, beam deflection triples. Beyond 10 V peak to peak, the extent of deflection saturates.

The forces generated at the tips of the beams are estimated to be 1 mN using beam bending equations, and exceed calculated drag forces by at least two orders of magnitude. The corresponding stresses generated in the polymer reach 2 MPa. The peak power-to-mass ratio is  $40 \text{ W} \cdot \text{kg}^{-1}$ , exceeding that of electrostatic actuators by an order of magnitude, and matching the steady state power-to-mass ratio of mammalian skeletal muscles<sup>5</sup>. Cycle life is frequency dependent. At frequencies below 1 Hz, delamination occurs after several cycles as hydrogen gas forms at the platinum/polymer interface. However, at higher frequencies, much longer lifetimes are possible. An actuator was left running for 120,000 cycles at 3 Hz, producing strains of  $> 0.25 \%$  at a strain rate of  $1.5 \text{ \%} \cdot \text{Hz}$ . No deterioration in amplitude was observed.

There are several factors that may limit the observed strain rate. These include reaction kinetics, the rate of capacitive charging, the mechanical impedance, and mass transport. The strain rates in Figure 1 appear to follow a square root relation to frequency, as is predicted in the case of semi-infinite planar linear diffusion<sup>15</sup>. The diffusion model is represented by the solid line in Figure 1, which fits the data to within the uncertainties represented by the error bars. This model implies a diffusion of ions to or from the polymer occurring at the liquid interface, where the thickness of the diffusion layer is proportional to the square root of the product of the diffusion coefficient and time, and is less than the film thickness. If the model is correct, then the strain in the polymer near the surface takes place on a time on the order of the width of the layer squared divided by

the diffusion coefficient, suggesting that great gains in speed could be obtained by reducing actuator thickness.

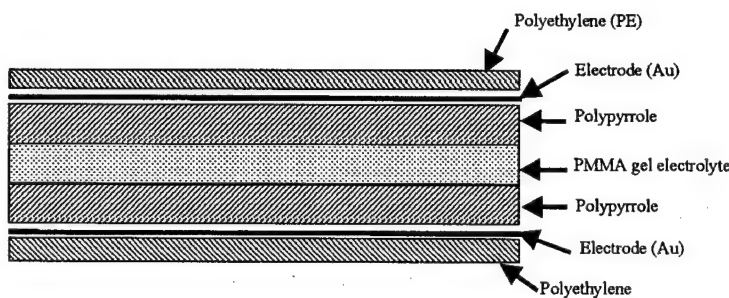


**Figure 2a:** Cross-section of an encapsulated bilayer actuator. The actuator is 40 mm long, and 10 mm wide. Thicknesses of the layers are: Gel: 100  $\mu\text{m}$ ; Au: 100 nm; Polypyrrole: 40  $\mu\text{m}$ ; PE: 20  $\mu\text{m}$ .

For operation outside of solution, two polypyrrole strips 10 mm wide x 20 to 40 mm long x 40  $\mu\text{m}$  thick are cut from the tetraethylammonium hexfluorophosphate doped films. A sandwich structure is formed, as shown in Figure 2, with the polypyrrole strips forming outer layers, and containing a gel electrolyte between them. A gold layer (< 200 nm thick) is sputtered onto the outer polymer surfaces, and the entire actuator is encapsulated in a polyethylene film, as indicated in the Figure 2. The gel layer is approximately 100  $\mu\text{m}$  thick. The gel is synthesized following a procedure related by Reynolds<sup>18</sup>. It consists of 70 wt% acetonitrile, 20 wt% propylene carbonate, 7 wt% polymethylmethacrylate (PMMA), and 3 wt% LiClO<sub>4</sub>. Actuators are soaked for 15 minutes in a solution of 0.05 M tetra ethyl ammonium hexafluorophosphate in propylene carbonate, which renders the

polymer more compliant. Tests are performed as with the bilayer in liquid, except that potential is applied between the two strips of polypyrrole. The square wave peak to peak amplitudes are between 2 V and 10 V, and applied frequencies range from 0.1 Hz to 30 Hz.

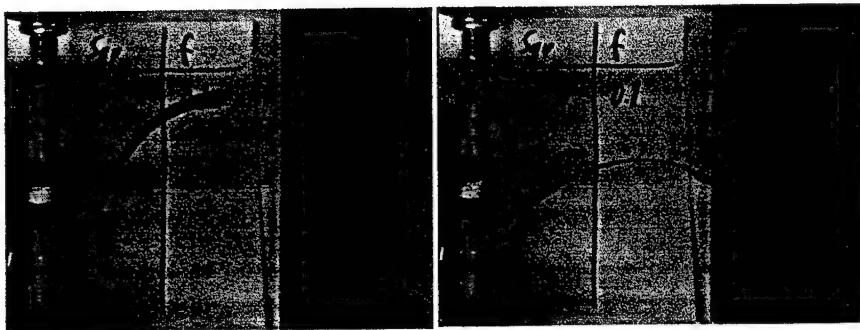


**Figure 2b:** Photographs showing the maximum extent of deflection of an encapsulated bilayer upon activation with a  $\pm 5$  V square wave at 0.1 Hz.

Figure 2b contains a pair of images showing the deflection of the bilayer on activation with a 10 V square wave at 0.1 Hz frequency. Deflection as a function of frequency of activation and for different applied peak-to-peak voltages is shown in Figure 3. Deflection increases as applied potential is increased, with the response saturating beyond 10 V. By comparison, relative deflections at 0.1 Hz with 2 V and 3 V applied are 0.05 and 0.12, respectively. Increasing the excitation frequency in all cases decreases the deflection. This decrease is again proportional to  $f^{-1/2}$  until roughly 15 Hz, above which frequency there appears to be a roll-off. The frequency dependence suggests that rate is

again limited by semi-infinite planar diffusion over this range. In a second film constructed identically, but having twice the length, the roll-off frequency drops by a factor of four. Such a shift as a function of beam length is characteristic of mechanical resonance<sup>16</sup>, suggesting that beam mechanics are at least partly responsible for the drop off at high frequency. The strain appears to flatten at lower frequencies. Another rate limiting mechanism may come into effect at such time scales, explaining the relatively slow rates observed in linear actuators at large deformations. (If the trend in strain rate observed in Figure 1 were to continue over longer time scales, 2 % contractions would occur in 16 s, as opposed to the roughly 60 s observed<sup>1</sup>.)

Strain is not shown in Figure 3 as the mechanical impedance of the gel layer is uncertain. Also the gel layer thickness is somewhat non-uniform, and deflection does not occur uniformly throughout the beam. However, it is possible to generate a lower bound strain estimate, based on the minimum actuator thickness, the polypyrrole glassy modulus and the total deflection. The strain at 0.1 Hz is  $> 0.2 \%$ , and the maximum strain rate, occurring at 15 Hz, is  $> 0.5 \text{ \%}\cdot\text{Hz}$ . Lifetime of these actuators is only several hours. Evaporation of liquid solvent from the gel and the polypyrrole appears to degrade performance, which is then recovered by immersion in a liquid bath. Better encapsulation is likely the key to longer life.

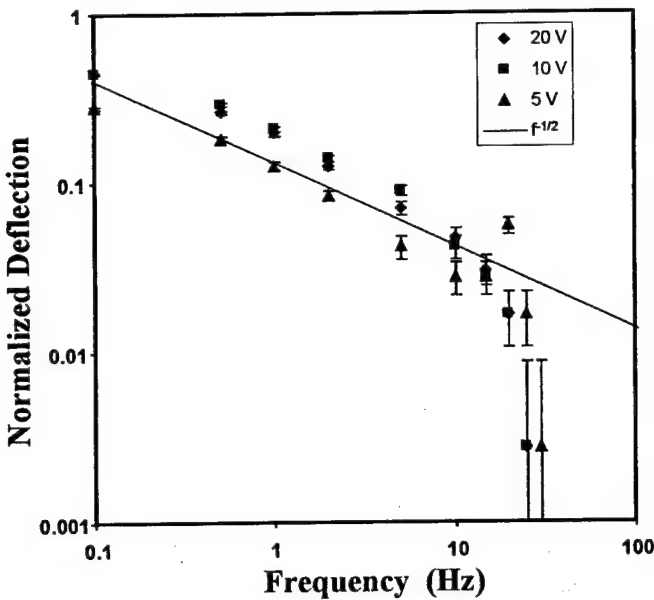


Figure 3: Mechanical frequency response of an encapsulated conducting polymer bilayer at various square wave peak to peak excitation voltages. The solid line represents the expected response assuming semi-infinite planar diffusion. Deflection is normalized to actuator length.

Experiments performed using conducting polymer bilayer actuators demonstrate strain rates of 4 %·Hz, achieved in 30 to 60 micrometer thick polypyrrole films, with corresponding strain amplitudes of 0.2 %. Such strain rates are two orders of magnitude greater than have been previously observed. Power-to-mass ratios are estimated at 40  $\text{W}\cdot\text{kg}^{-1}$ , similar to that of mammalian skeletal muscle. Fast deflections are observed both in liquid and in air. In both cases, the strain rate is proportional to the square root of frequency, suggesting that diffusion is the rate-limiting factor on time scales of 0.05 s to 1 s.

## References

1. A. Della Santa, D. De Rossi, A. Mazzoldi, "Characterization and modeling of a conducting polymer muscle-like linear actuator", *Smart Materials and Structures* 1997, 6, 23.

2. J. D. Madden, C. J. Brenan, and J. Dubow, *Progress Towards An Automatic, Microfabricated Polymer Air -Fluid Sampling Inlet*, NTIS, Accession Number AD-A332 030/6/XAB, Springfield, VA, 1997.
3. R. H. Baughman, I. W. Shacklette, R. L. Elsenbaumer, "Micro electromechanical actuators based on conducting polymers", in *Topics in Molecular Organization and Engineering, Vol. 7: Molecular Electronics* (Ed: P. I. Lazarev), Kluwer, Dordrecht 1991, 267.
4. R. H. Baughman, "Conducting polymer artificial muscles", *Synthetic Metals* 1996, 78, 339.
5. I. W. Hunter, S. Lafontaine, "A comparison of muscle with artificial actuators", *Technical Digest IEEE Solid State Sensors and Actuators Workshop* 1992, 178.
6. T. F. Otero and J.M. Sansinena, "Soft and wet conducting polymers for artificial muscles", *Advanced Materials* 1998, 10, 491.
7. T. E. Herod, J. B. Schlenoff, "Doping-Induced Strain in Polyaniline: Stretchoelectrochemistry" *Chemistry of Materials* 1993, 5, 951.
8. Q. Pei, O. Inganäs, "Conjugated Polymer and the bending cantilever method: electrical muscles and smart devices", *Advanced Materials* 1992, 4, 277.
9. Q. Pei, O. Inganäs, "Electrochemical applications of the bending beam method. 1. Mass transport and volume changes in polypyrrole during redox", *Journal of Physical Chemistry* 1992, 96, 10508.
10. E. Smela, O. Inganäs, Q. Pei, I. Lundström, "Electrochemical muscles: micromachining fingers and corkscrews", *Advanced Materials* 1993, 5, 630.
11. E. Smela, O. Inganäs, I. Lundström, "Controlled folding of micrometer-sized structures", *Science* 1995, 268, 1735.
12. M. R. Gandhi, P. Murray, G. M. Spinks, G. G. Wallace, "Mechanism of electromechanical actuation in polypyrrole" *Synthetic Metals* 1995, 73, 247.
13. J. D. Madden, S. R. Lafontaine and I. W. Hunter, "Fabrication by Electrodeposition: Building 3D Structures and Polymer Actuators", *Proceedings - Micro Machine and Human Science 95*, Nagoya Japan, October 1995.
14. K. Kaneto, M. Kaneko, Y. Min, A. G. MacDiarmid, "Artificial muscle: electromechanical actuators using polyaniline films", *Synthetic Metals* 1995, 71, 2211.
15. A. J. Bard and L.R. Faulkner, *Electrochemical Methods*, Wiley New York, 1980.

16. W. C. Young, *Roark's Formulas for Stress and Strain 6<sup>th</sup> ed.* McGraw-Hill, New York, **1989**.
17. M. Yamaura, K. Sato, T. Hagiwara and K. Iwata, "Memory effect of electrical conductivity upon the counter-anion exchange of polypyrrole films", *Synthetic Metals* **1992**, *48*, 337.
18. S. A. Sapp, G. A. Sotzing, J. L. Reddinger, J. R. Reynolds, "Rapid switching solid state electrochromic devices based on complementary conducting polymer films", *Advanced Materials* **1996**, *8*, 808.

## ***Actuators in Dry Environments***

Actuators exhibiting muscle-like properties<sup>15</sup> are important to the development of life-like robots, artificial limbs, and other bio-mimetic devices. These properties include relatively high stress, and large strain linear actuation at moderate strain rates and efficiencies. While the development of conducting polymer-based actuators is still at an early stage, they already demonstrate some muscle-like properties. Work is derived from material dimensional changes in both conducting polymers and muscle. Stresses are one hundred times those generated in mammalian skeletal muscles<sup>15</sup>, and could reach 200 MPa, 600 times greater<sup>1</sup>. Strains in conducting polymers are typically between 1 % and 10 %<sup>1-3,9,12,14</sup>, compared to 20 % in muscle. Nevertheless, several obstacles to the widespread application of conducting polymer-based actuators remain, including relatively low strain rates, (< 0.03 %·Hz<sup>2,3,12-14</sup>), and the requirement of operation in a liquid environment. In this paper the latter issue is addressed.

The use of a liquid environment stems from the mechanisms employed to stimulate polymer contraction. Chemical activation involves immersion of polymer actuators alternately in aqueous acids and bases<sup>12</sup>. Electrochemical stimulation involves the use of electrolytes, which have in general been liquid-based. Liquid based electrolytes, and in particular polar solvents such as water and propylene carbonate offer environments that allow high ion mobility and concentration, and therefore are generally preferred over solids.

Several exceptions to the use of liquid environments exist. These exceptions have been restricted to bilayer actuators, in which a differential expansion between two thin, adjoining layers results in bending and force generation, as in bimetallic strips. In 1993 Pei reported a polypyrrole/ polyethylene bilayer as a chemical sensor, generating deflection upon exposure to ammonia gas<sup>5</sup>. Other bilayers operating out of solution are electrochemically activated, employing gel or encapsulated liquid electrolytes<sup>11,13,19</sup>.

Bilayers are mechanical amplifiers, generating large deflections, but low forces. An important step in proving the value of conducting polymer actuators is to demonstrate a linear actuator operating in air, thereby fully exploiting the large forces per cross-sectional area of which conducting polymers are capable. However, electrochemical activation of conducting polymers requires a cell, including the polymer as working electrode, an electrolyte, and a counter electrode. The challenge is to find an electrolyte whose mechanical stiffness does not impede the polymer contraction, while offering high ionic conductivity, and which can be readily encapsulated for operation out of bulk solution. Alternatives to the use of bulk liquid electrolytes include solid electrolytes, such as polyethylene oxide (PEO), gels and encapsulated liquids.

Solid electrolytes have the advantage of relatively easy construction. The electrolyte is sandwiched between the polymer and a counter electrode. Unfortunately, solid electrolytes suffer from low ionic conductivities<sup>16</sup>, and provide high stiffnesses against which the polymer actuator must work, reducing the available force and displacement. PEO, perhaps the most widely used solid electrolyte, has the further disadvantage that it only becomes significantly conductive at temperatures above 60 °C<sup>16</sup>. For these reasons, solid electrolytes were not employed.

Liquids offer high conductivity and low mechanical interference, but must be sealed. It is also necessary to prevent electronic conduction between the polymer and the counter electrode, which requires some form of spacer separating them. Adding sealant and spacers not only complicates the manufacturing process, but these elements also provide mechanical impedance to actuator deformation. Gels offer moderately high ionic conductivity, and low mechanical impedance. They also provide sufficient stiffness to separate the actuator electrodes. It is for these reasons that gel electrolytes are chosen.

## Experiment

A representation of the cross-sectional geometry of the actuators constructed, including the active polypyrrole film, the gel electrolyte and the counter electrode, is shown in Figure 1 (inset). The polypyrrole active layer is galvanostatically polymerized on a glassy carbon substrate from mixture of 0.06 M freshly distilled pyrrole monomer and 0.05 M tetraethylammonium hexafluorophosphate in propylene carbonate. Deposition takes place at -30 °C in a nitrogen atmosphere at a current density of 1.25 A·m<sup>-2</sup>, following methods of Yamaura<sup>18</sup>. Film dimensions are typically 35 mm long × 6 mm wide × 40 to 100 µm thick. The resulting material has a density of  $1.4 \times 10^3$  kg·m<sup>-3</sup>, a conductivity in the range of 1 to  $3 \times 10^4$  S·m<sup>-1</sup>, a glassy modulus of 0.5 GPa (wet) and 1.0 GPa (dry), and a tensile strength of > 25 MPa. Two gels were tried, a PMMA-based gel<sup>17</sup> and agar. Agar containing tetraethylammonium hexafluorophosphate salt produces the most repeatable results, as presented here. This was prepared by adding 1 g of agar (Aldrich, Milwaukee, WI) per 150 ml saturated (0.04 M) aqueous tetraethylammonium hexafluorophosphate solution, which is then heated to form a gel. A polyethylene film is sputter coated with a 400 nm thick gold layer to form the counter electrode.

In assembling an actuator, the polypyrrole film is held at each end by gold-coated clamps, as depicted in Figure 1. An approximately 100  $\mu\text{m}$  thick layer of gel electrolyte is applied to each side of the film. Strips of the counter electrode are wrapped around the gel-coated polypyrrole, with the gold contacting the gel. A strand of 75  $\mu\text{m}$  diameter gold wire forms the electrical contact between the counter electrode strips and the test circuit. Electrical contact to the film is made through the clamps.

Actuator displacements are applied via a stepper motor driven linear translation stage, film displacement being determined by the number of motor steps. A load cell measures force on the film. A current source is employed to drive an electrochemical reaction across the actuator cell. The apparatus is under software control from a workstation, interfacing with the actuator circuit via a data acquisition board. Actuator testing begins with the application of 2 MPa of tensile stress to the film. Following a short period (10 to 20 s), equi-amplitude cycles of positive and negative current are applied, with a brief period of no current between each change in polarity. The initial strain is then removed, returning the film to its original length. In the experiments presented force feedback is employed to maintain isotonic conditions (constant force), and the resulting displacements are recorded.

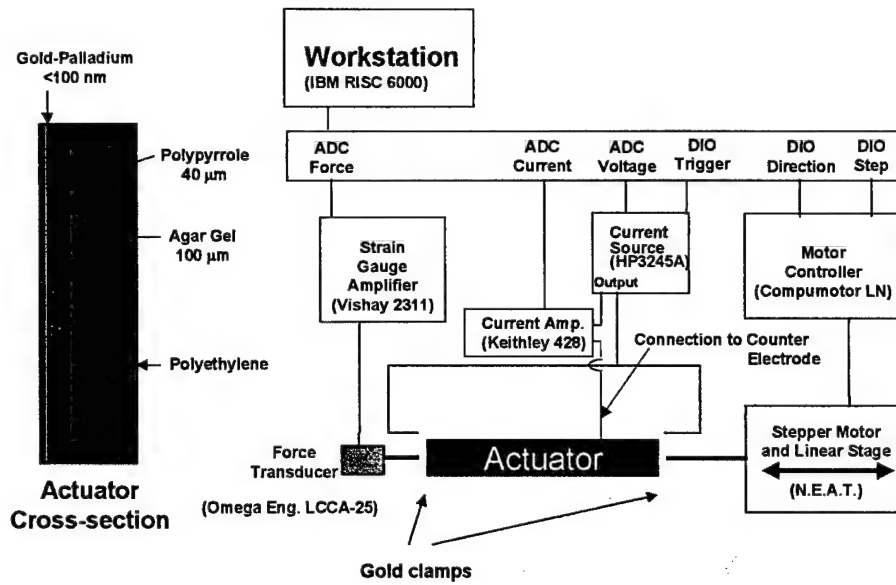


Figure 1: Schematic of electro-chemo-mechanical testing apparatus. Steps in Voltage or Current are triggered from the workstation via the digital output (DIO). The resulting forces, currents and voltages are recorded on the work station via the analog to digital converters (ADC). Strain is applied via computer control of the stepping motor through step and direction DIO channels.

## Results

Figure 2 shows the result of an isotonic test in which a 20 mA current is applied for 80 s, followed by a 10 s relaxation, followed in turn by the application of -20 mA. The applied stress is 2 MPa, as measured relative to the cross-sectional area of the polypyrrole film. When the full actuator cross-section is taken into account, the force per unit area is 0.5 MPa, 50 % larger than that of mammalian skeletal muscle. The total strain is just over 2 %. As has been demonstrated previously in polypyrrole-based actuators, strain is proportional to charge transferred into the polymer. The strain to charge ratio is  $4.5 \times 10^{-10} \text{ m}^3 \cdot \text{C}^{-1}$ , as calculated using the slope of the curve in Figure 2. Note that this corresponds to a volume change per charge (assuming isotropic expansion) of  $2.2 \times 10^{-28} \text{ m}^3$ . The volumes of water molecules and hexafluorophosphate ions are roughly  $0.3 \times 10^{-28} \text{ m}^3$  and  $2 \times 10^{-28} \text{ m}^3$  respectively. Della Santa<sup>3</sup> obtains a strain to charge ratio of  $3 \times 10^{-10} \text{ m}^3 \cdot \text{C}^{-1}$

from polypyrrole films in aqueous solutions of sodium benzenesulfonate salt. Work using identically synthesized polypyrrole films<sup>19</sup> activated in propylene carbonate solution results in a strain to charge ratio of  $2.3 \times 10^{-10} \text{ m}^3 \cdot \text{C}^{-1}$ . The similarity between the strain to charge ratios observed in liquid and gel environments suggests that the gel's stiffness offers negligible mechanical impedance.

The strain rate of  $0.03 \text{ \%}\cdot\text{Hz}$  matches the highest reported<sup>3,9,12,14</sup>. Strain rates and hence power to mass ratios are relatively low in conducting polymer actuators. The rates reported here, at  $0.03 \text{ \%}\cdot\text{Hz}$ , match the highest rates in the literature<sup>3</sup>, but are still three orders of magnitude lower than that of typical mammalian skeletal muscle. Further improvement may be obtained by studying the rate limiting mechanisms.

Force per cross-sectional area of the actuator is a function of both the force generated by the polymer, and the quantity of electrolyte required, as dictated by the geometry of the laminate structure. Since the electrolyte does not directly generate any force or displacement, keeping electrolyte volume to a minimum maximizes force per unit area. However, ions leaving the polymer must be solvated by the electrolyte, and vice-versa.

Given the strain to charge ratio of  $4.5 \times 10^{-10} \text{ m}^3 \cdot \text{C}^{-1}$ , a 1 % strain generates an ionic concentration change of roughly 300 moles per  $\text{m}^3$  of polymer. In the gel/salt combination employed, concentration at saturation is 100 moles per  $\text{m}^3$  of gel. Therefore the gel layer should be several times the volume of the polymer layer in order to store and transfer the required number of ions to the actuator, and the force per cross-sectional area is correspondingly reduced. Further improvement may be obtained by employing gel/salt combinations that are capable of sustaining higher ionic concentrations.

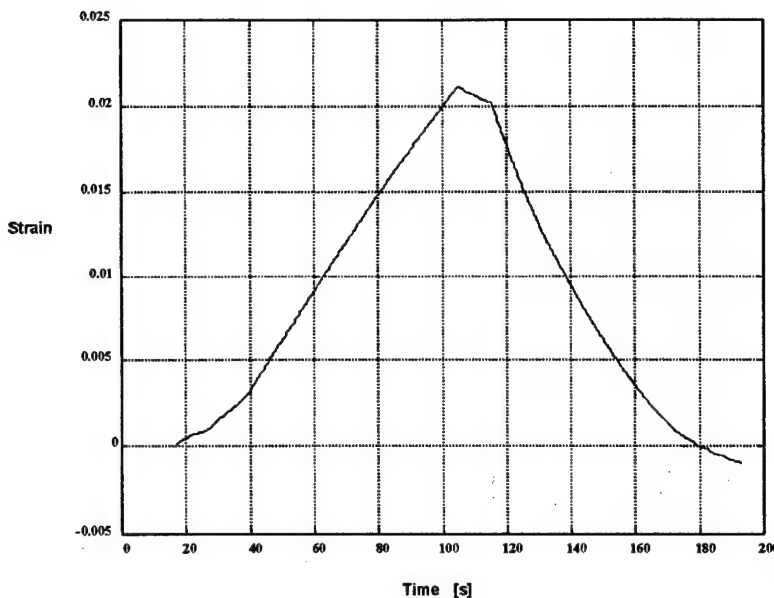


**Figure 2:** Strain in an encapsulated linear actuator with  $2 \text{ MPa}$  applied stress, in response to a  $\pm 20 \text{ mA}$  current.

It is demonstrated that conducting polymer linear actuators may be operated out of solution. The strains, strain rates and strain to charge ratios are very similar to those observed in polypyrrole actuators operating in aqueous environments. Forces per cross-sectional area exceed those of mammalian skeletal muscle. The operation of conducting polymer actuators outside of bulk liquid environments should help pave the way to broader application of this relatively new application of conjugated polymers.

## References

1. R. H. Baughman, I. W. Shacklette, R. L. Elsenbaumer, "Micro electromechanical actuators based on conducting polymers", in *Topics in Molecular Organization and Engineering, Vol. 7: Molecular Electronics* (Ed: P. I. Lazarev), Kluwer, Dordrecht 1991, 267.

2. R. H. Baughman, "Conducting polymer artificial muscles", *Synthetic Metals* **1996**, *78*, 339.
3. A. Della Santa, D. De Rossi, A. Mazzoldi, "Characterization and modeling of a conducting polymer muscle-like linear actuator", *Smart Materials and Structures* **1997**, *6*, 23.
4. Q. Pei, O. Inganäs, "Conjugated Polymer and the bending cantilever method: electrical muscles and smart devices", *Advanced Materials* **1992**, *4*, 277.
5. Q. Pei, O. Inganäs, "Conjugated polymers as smart materials, gas sensors and actuators using bending beams", *Synthetic Metals* **1993**, *55-57*, 3730.
6. Q. Pei, O. Inganäs, "Electrochemical applications of the bending beam method. 1. Mass transport and volume changes in polypyrrole during redox", *Journal of Physical Chemistry* **1992**, *96*, 10508.
7. E. Smela, O. Inganäs, Q. Pei, I. Lundström, "Electrochemical muscles: micromachining fingers and corkscrews", *Advanced Materials* **1993**, *5*, 630.
8. E. Smela, O. Inganäs, I. Lundström, "Controlled folding of micrometer-sized structures", *Science* **1995**, *268*, 1735.
9. M. R. Gandhi, P. Murray, G. M. Spinks, G. G. Wallace, "Mechanism of electromechanical actuation in polypyrrole" *Synthetic Metals* **1995**, *73*, 247.
10. J. D. Madden, S. R. Lafontaine and I. W. Hunter, "Fabrication by Electrodeposition: Building 3D Structures and Polymer Actuators", *Proceedings - Micro Machine and Human Science 95*, Nagoya Japan, October 1995.
11. J.M. Sansimena, V. Olazabal, T. F. Otero, C.N. daFonseca and M.A. DePaoli, "A solid state artificial muscle based on polypyrrole and a solid polymeric electrolyte working in air", *Chemical Communication* **1997**, *22*, 2217.
12. T. E. Herod, J. B. Schlenoff, "Doping-Induced Strain in Polyaniline: Stretchelectrochemistry" *Chemistry of Materials* **1993** *5*, 951.
13. K. Kaneto, M. Kaneko, Y. Min, A. G. MacDiarmid, "Artificial muscle: electromechanical actuators using polyaniline films", *Synthetic Metals* **1995**, *71*, 2211.
14. M. Kaneko, M. Fukui, W. Takashima, K. Kaneto, "Electrolyte and strain dependences of chemomechanical deformation of polyaniline film", *Synthetic Metals* **1997**, *84*, 795.
15. I. W. Hunter, S. Lafontaine, "A comparison of muscle with artificial actuators", *Technical Digest IEEE Solid State Sensors and Actuators Workshop* **1992**, 178.

16. P. P. Soo, B. Huang, Y. J. Jang, Y. Chiang, D. R. Sadoway, A. M. Mayes, "Rubbery block copolymer electrolytes for rechargeable lithium batteries", *Abstracts Of Papers of the American Chemical Society*, **1998**, 216: 093-FUEL , Part 1.
17. S. A. Sapp, G. A. Sotzing, J. L. Reddinger, J. R. Reynolds, "Rapid switching solid state electrochromic devices based on complementary conducting polymer films", *Advanced Materials* **1996**, 8, 808.
18. M. Yamaura, K. Sato, T. Hagiwara and K. Iwata, "Memory effect of electrical conductivity upon the counter-anion exchange of polypyrrole films", *Synthetic Metals* **1992**, 48, 337.
19. J. D. Madden, *Progress Towards An Automatic, Microfabricated Polymer Air -Fluid Sampling Inlet*, NTIS, Accession Number AD-A332 030/6/XAB, Springfield,VA, **1997**.

# Polymer Transistors for Digital Logic and Feedback Control

## ***Introduction***

Conducting polymers enable the construction of actuators, transistors, chemical and light sensors, light emitters, and a wide variety of other elements from a single class of materials. Plastics offer the advantage of being flexible and generally inexpensive. Devices made from conducting polymers will therefore revolutionize the use of actuators, electronics, chemical and light sensors, and light emitters by making a wide range of new applications economically feasible.

## ***Conducting Polymer Transistor Operation***

The conducting polymer transistors that we are working on operate in a manner similar to a field effect transistor. The active region of the polymer transistor is immersed in an electrolyte such as 1 M hydrochloric acid (see Figure 1). The conducting

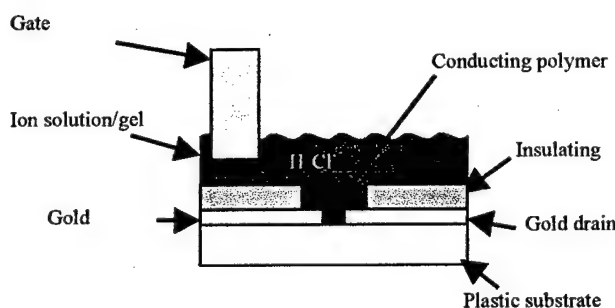


**Figure 1: Polymer transistor structure.**

polymer bridges a gap between two conductors (the source and the drain). A third conductor, the gate, is also immersed into the electrolyte. Changing the voltage applied to the gate electrode drives anions into or out of the

active polymer region. For polymers such as polyaniline or polypyrrole, increasing the concentration of anions in the polymer bulk changes the electronic structure of the polymer backbone and increases the conductivity by orders of magnitude. Decreasing

the anion concentration decreases the conductivity of the polymer. The change in conductivity is used to switch the transistor from off to on or to control the gain of a transistor circuit. As with a FET, the gate potential controls the resistance of a conductive channel and the gate acts very much like a capacitor.

### ***Combination with Other Conducting Polymer Devices***

One of the goals of the conducting polymer project is to integrate different types of conducting polymer devices into a single system (e.g. transistors, strain gages, and actuators to create a polymer feedback loop). In the conducting polymer actuator work, the muscle is activated in exactly the same way that the conductivity is changed. A gate electrode drives anions into or out of the polymer and, instead of (or as well as) the conductivity changing, the polymer expands or contracts. Just as with the transistor, the structure of a polymer muscle includes an electrolyte, a gate electrode (also called a counter electrode), and the polymer itself. Conducting polymer strain gages are likewise made up of an electrolyte, a gate electrode, and a polymer component. We anticipate therefor that the fabrication of integrated devices will be relatively simple as the required components for muscles, strain gages, and transistors are identical.

### ***Digital Logic Implementation***

In order to make a general set of Boolean logic, only two basic logic operators are required. Arranging the two basic operators can create every other logic operator. For example, the logic inverter and an AND gate can be combined to create OR gates (see Figure 2). To show that we can create a full set of digital logic using polymer electrolyte transistors, we need to be able to implement an inverter (or a NOT gate) and an AND gate.

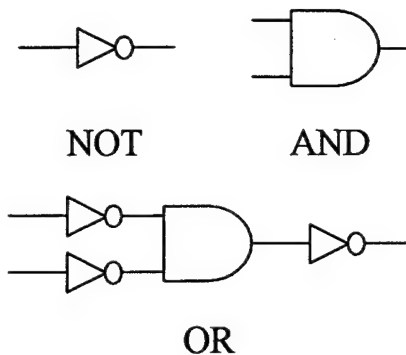


**Figure 2: Combining an inverter and AND gate to make an OR gate.**

between the low and high resistance states) for the gold gate electrode shown is about 0.3 V (vs. the drain voltage).

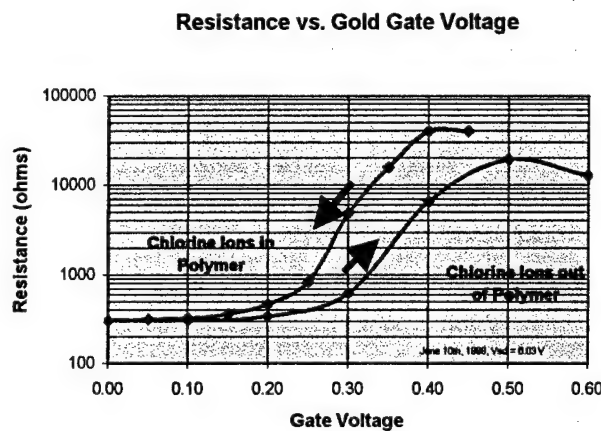


**Figure 3: Resistance between the source and drain as a function of gate voltage (for a gold gate). Gate voltage is measured vs. the drain.**

the source to drain resistance as a function of the voltage of a stainless steel counter electrode (measured vs. the drain voltage). Note that the switching voltage has changed to about -0.4 V. By choosing yet another gate material, we can shift the switching

Our work on polymer transistors so far has focussed on the polymer polyaniline. Polyaniline switches from its high conductivity state to a low conductivity state when the gate voltage increases by about 0.5 V. Figure 3 shows the source to drain resistance as a function of the gate electrode voltage for a polymer immersed in a 1M HCl aqueous electrolyte. The switching voltage (roughly half way

For polyaniline, the difference in voltage between the high and low resistance states is always approximately 0.5 V. However, the switching voltage depends on the choice of gate material. This change in switching voltage is caused by the difference electrochemical potentials of different materials. Figure 4 shows

voltage to an arbitrary value (limited in practice by the range of electrochemical potentials of materials).

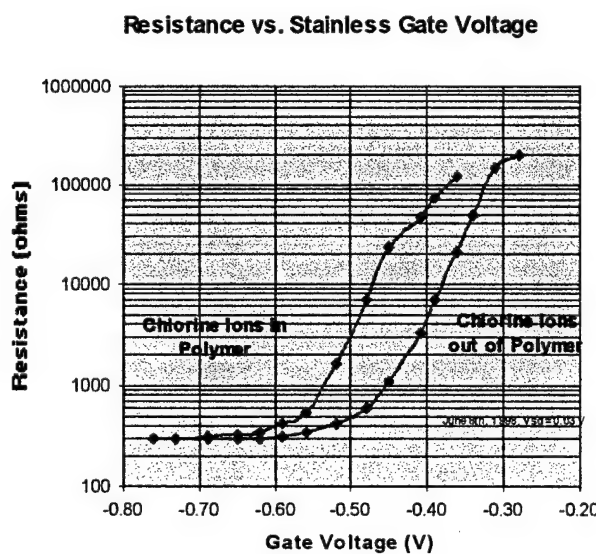


**Figure 4: Resistance between the source and drain as a function of gate voltage (for a stainless steel gate). Gate voltage is measured vs. the drain.**

affect how transistors can be used for implementing Boolean logic. A single transistor with a stainless steel gate can be used to make an inverter while a single transistor with a gold gate cannot.

For digital logic, we would like the switching voltage to be at the midpoint between the voltages we set as the on and off voltages. Furthermore, circuitry will be simpler if we can set either the Boolean ON or Boolean OFF voltage of the gate to be zero volts relative to the drain.

Differences in switching potential for different gate materials

## NOT Gate (Inverter)

For Boolean logic implementation, the operation of a single transistor can be modeled as being in either a high resistance state or a low resistance state. For a polyaniline transistor with a gold gate, the following gate potentials give the following resistance states (see also Figure 3):

$V_{GD}$	$R_{\text{gate}}^{\text{gold}}$ <sup>1</sup>
-0.5	Low
0.0	Low
0.5	High

Compare the resistance states for the gold gate to the resistance states for a stainless steel gate (see also Figure 4):

$V_{GD}$	$R_{\text{gate}}^{\text{stainless}}$ <sup>2</sup>
-0.5	Low
0.0	High
0.5	High

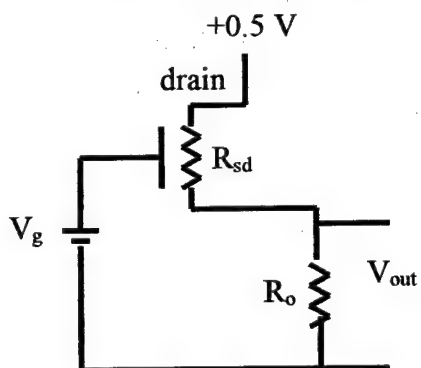


**Figure 5: Inverter configuration for a polymer transistor with a stainless steel gate.**

The only difference is the resistance state at a

gate voltage of 0 V relative to the drain.

However, using the stainless steel gate transistor, it is simple to make an inverter while with a single gold gate transistor it cannot be done.

<sup>1</sup> In the high resistance state in the transistors built so far, the source drain resistance  $R \approx 30 \text{ k}\Omega$ . In the low resistance state,  $R \approx 300 \Omega$ .

<sup>2</sup> The source drain resistance doesn't actually reach its minimum until a gate voltage about  $-0.6 \text{ V}$  vs. the drain but even at  $-0.5 \text{ V}$  the resistance is very close to its minimum.

The configuration for an inverter made with a single stainless steel gate transistor is shown in Figure 5. When the input switches to a low voltage (0 V), the potential from the drain (connected to a +0.5 V voltage supply) to the gate is -0.5 V. The resistance of the polymer junction decreases to the Low resistance state and, if the polymer junction resistance is much less than the output resistance  $R_o$ , the output voltage will be close to 0.5 V<sup>3</sup>. On the other hand, when the gate potential increases to 0.5 V, the gate to drain potential changes to 0 V and the source drain resistance goes to the High state. The output voltage  $V_{out}$  is pulled down to 0 V by the output resistor  $R_o$ <sup>4</sup>.

On the other hand, using the same configuration with a gold gate, the gate voltage must rise to 0.5 V above the drain or 1 V relative to ground to switch the junction resistance to high. This adds a third voltage level (1 V) to the two voltage levels needed for the stainless gate inverter (0 V and 0.5 V). In addition, the output voltage of the inverter with a gold gate cannot be used as the input to a subsequent device. An output of 0.5 V (the ON state) is not sufficient to change the junction resistance from low to high on a following transistor. The stainless steel gate transistor output, on the other hand, can be used to drive a subsequent transistor<sup>5</sup>.

---

<sup>3</sup> The polymer junction resistance and the output resistor act as a voltage divider. The output voltage is given by  $V_{out} = V_{supply} \left( R_o / (R_o + R_{sd}) \right)$ , where  $R_{sd}$  is the source to drain or the junction resistance of the transistor. If  $R_{sd} \ll R_o$  in the low resistance state of the transistor,  $V_{out} \approx V_{supply}$ .

<sup>4</sup> At the high resistance state,  $R_{sd} \gg R_o$  and so, from  $V_{out} = V_{supply} \left( R_o / (R_o + R_{sd}) \right)$  we calculate  $V_{out} \approx 0$  V. Note that the value of  $R_o$  is bounded by  $R_{sd}(\text{Low}) \ll R_o \ll R_{sd}(\text{High})$ .

<sup>5</sup> One of the assumptions that has been made is that the output current from the transistor is small enough that it does significantly affect the output voltage. At steady state, the gate current of the transistors drops to zero. This guarantees that the output voltage of transistors is not affected by the input current needed by a following transistor.

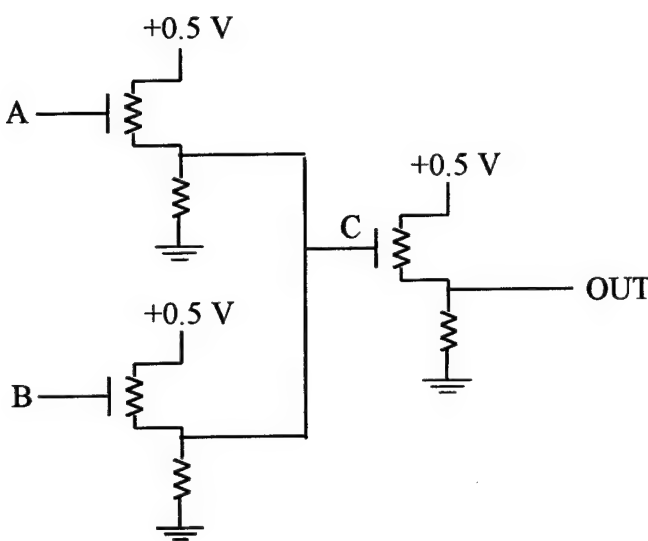


**Figure 6: AND gate configuration for polymer transistors with stainless steel gates.**

### AND Gate

#### The Boolean AND

operation can be implemented using three transistors with stainless steel gates. Fewer transistors can be used but using three transistors allows both inputs to the AND function to be applied to the

transistor gate. In this way, the input current after switching states will be zero thereby reducing the current that must be supplied by the circuitry that drives the inputs. Figure 6 shows the transistor configuration for a polymer transistor AND gate. Here are the states of the point C and the output:

A	B	C	OUT
0	0	0.5	0
0	0.5	0.5	0
0.5	0	0.5	0
0.5	0.5	0	0.5

Each transistor on its own acts as an inverter.

If both A and B are the same, the two input transistors behave identically. The point C in the circuit is the inverse of the input. The output is the inverse of C, which gives the input. Thus if both inputs are 0 V, the output will also be 0 V. If both inputs are 0.5 V the output will be 0.5 V.

If A and B are not the same, the point C is pulled high by whichever input transistor has a low voltage input. Because of the low input, the transistor has a low

junction resistance and supplies current to drive the voltage at C up the high state. With C at a high voltage, the output is at a low voltage. Thus if the two inputs are different, the output will be 0 V.

### ***Implementation***

The ultimate aim of the development of digital logic with polymer transistors is to construct fast integrated devices on a single flexible plastic substrate, with the entire device made of polymer materials. At this stage in the project, we have only built discrete transistors with switching times of about 1 s. The project is proceeding in several directions to reach its goals.

First, to increase the switching time, we are developing methods to shrink the transistor size to an absolute minimum. The switching speed of the polymer transistors is directly related to the distance that anions must diffuse. By shrinking the polymer junction size, the switching speed increases. In this work we will use scanning tunneling microscopy technology to construct transistors with junction sizes as small as tens of nanometers. We expect to achieve switching speeds of a few microseconds (bandwidths of more than 100 kHz).

To integrate the devices onto a single substrate we are using lithography techniques to pattern transistor sources, drains and gates onto a single plastic substrate. We are working to find an inexpensive and simple method to isolate the electrolyte for each transistor. If the electrolytes are not isolated, the transistors will interfere with each other. Using the same integration techniques, we will ultimately be able to build muscles, strain gages, and transistors on the same substrate.

# **Distributed Photo-Plethysmograph Fingernail Sensors: Finger Force Measurement without Haptic Obstruction**

**H. Harry Asada**  
Professor, Principal Investigator

**Stephen Mascaro**  
Graduate Research Assistant

## **ABSTRACT**

Improvement on a new type of touch sensor for detecting contact pressure at human fingertips is presented. A fingernail is instrumented with spatially distributed arrays of miniature LEDs and photodetectors in order to measure changes in the nail color pattern when the fingertip is pressed against a surface. Unlike traditional electronic gloves, in which sensor pads are placed between the fingers and the environment surface, this new sensor allows the fingers to directly contact the environment without obstructing the human's natural haptic senses. The finger touch force is detected by measuring changes in the nail color; hence the sensor is mounted on the fingernail rather than on the fingertip. Photo-reflective plethysmography is used to measure the nail color. Spatially distributed color patterns are used to distinguish touching from motion artifact. Hemodynamic modeling is used to investigate the dynamics of the change in blood volume at multiple locations under the fingernail. The model is simulated and then evaluated by comparison with the experimental dynamic response of the sensor. Applications to human-machine interaction and home health care are discussed.

## 1. Introduction

Electronic gloves have been extensively studied in the past decade in the robotics and virtual reality communities [1]. There are many ways of providing force feedback to the human from sensors on the robot or from a virtual environment, and many electronic gloves now make use of such force feedback [2][3][4]. A good example is the CyberGlove developed by Kramer [5]. However, few electronic gloves collect touch-force data from the human fingers as the human interacts with the environment. The ones that do make use of pressure sensing pads consisting of conductive rubber, capacitive sensors, optical detectors, or other devices which are placed between the fingers and the environment surface [6][7][8][9]. These sensor pads inevitably deteriorate the human haptic sense, since the fingers cannot directly touch the environment surface.

In this paper, a new approach to the detection of finger touch forces is presented in order to eliminate all impediments to the natural haptic sense. Namely, the finger touch force is measured without having to place any sensor pad between the fingertip and the environment surface by using an optical sensor that is mounted on the fingernail. This allows the human to touch the environment with bare fingers and perform fine, delicate tasks using the full range of haptic sense.

In addition to the applications to human-machine interface, the detection of fingernail color may also be useful for home health care through the early detection of a variety of medical conditions. According to several sources [17][18][19][20], many health disorders result in characteristic changes in fingernail color, texture, and shape. As stated in one source [17], “A normal nail bed appears pink, reflecting a healthy underlying blood supply. A white nail bed may be a sign of anemia, while a blue one may indicate heart or lung disease. A physician should regularly examine the nails.” According to another source [18], infection, drugs, topical agents, systemic diseases, and other conditions can result in a variety of visible color changes in the nail – green, yellow, blue, brown, white, and black. All of these color changes could potentially be measured using LEDs of multiple wavelengths.

Other health conditions such as thyroid disorders, cirrhosis, lung disease and others, may result in changes to the mechanical structure or properties of the nail and nail bed [18][19][20]. By using touch force as a

perturbation to the fingernail bed, we may also be able to detect such health disorders by comparing the measured response using the nail sensor with the modeled response for a healthy nail.

Finally, the fingernail sensor may be useful as a means of supplementing the finger ring sensor for measurement of pulse and blood pressure. The use of differential measurement, i.e. taking the difference of measurements at the ring and the fingernail, can be useful for reducing noise and decoupling unknown biases. Furthermore, unlike the rest of the finger, the fingernail provides the unique opportunity of allowing for the rigid attachment of a sensor, relieving the problems associated with a certain class of motion artifact.

In a previous work, the basic principle of such a sensor is described and an initial prototype is implemented [10]. Although the original prototype was successful in measuring the gross change in color of the fingernail caused by touch force, it was not able to distinguish between color changes caused by touch force and color changes caused by finger bending. In order to reliably detect touch force, a two-fold plan for improvement has been implemented. Firstly, the sensor has been redesigned to include a spatial array of photodetectors that can detect the pattern of the color across the fingernail. Miniaturized optical components and circuitry allow the sensor to be disguised as a decorative fingernail covering. Secondly, a hemodynamic model has been created in order to better predict touch force input based on sensor output. The goal of this paper is to better understand, through modeling and experimentation, the physiological behavior that causes the color change in order to obtain design guidelines and signal processing algorithms for the nail sensors.

First, this paper will describe the basic principles and design of the photo-reflective plethysmograph fingernail sensors. The new design using arrays of LEDs and photodetectors is described and implemented. A lumped parameter hemodynamic model is then constructed in order to explain the color change at multiple locations on the fingernail. Dynamic equations are derived for the model, and static and dynamic simulation results are presented. Experiments are performed to measure the actual static and dynamic responses of the sensor, and these responses are compared with the simulation results in order to evaluate the model. Results from different photodetector locations are used to characterize the static and dynamic patterns of color resulting from various touch forces and motion artifacts.

## 2. Principle

### 2.1 Hemodynamics of Fingers and Nails

As a finger is pressed horizontally on a surface with increasing force, a sequence of color changes is observed through the fingernail. In fact, the color change is characteristically non-uniform across the nail, resulting in distinct patterns of color change. Figure 1 shows a typical sequence of noticeable color changes with increasing force. Although the force thresholds may vary from person to person, the underlying physiological principle is universally applicable for a healthy fingernail in an ordinary environment.

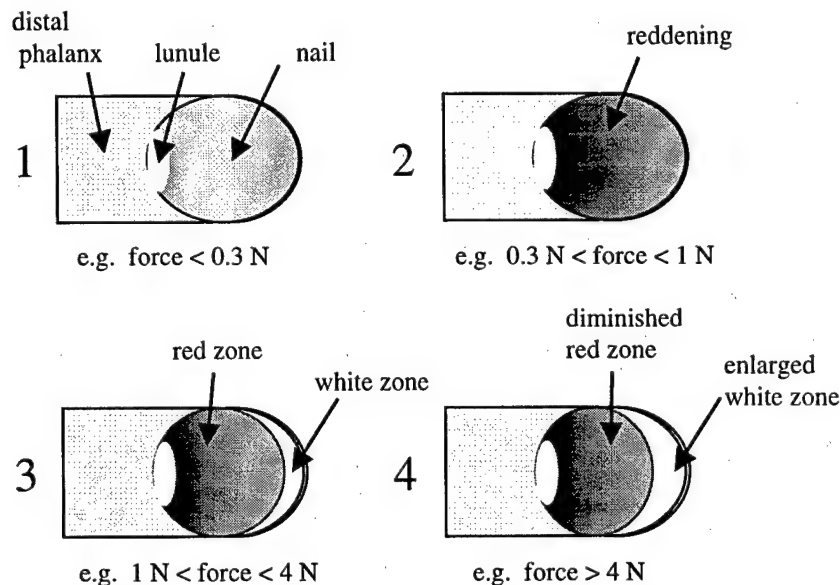


**Figure 1: Typical Fingernail Color Changes**

Above a certain threshold, e.g. 0.3 N, the entire nail begins to redden in color. The dermis is richly vascularized with large arteriovenous shunts [11]. The capillaries run vertically into the dermal papillae under the nail matrix, but run longitudinally under the nail bed [12]. Forces within the 0.3 N to 1 N range are sufficient to cause the venous return of blood in the fingertip to be progressively constricted. This results in pooling of arterial blood in the capillaries underneath the fingernail. This arterial blood is rich in oxy-hemoglobin and is therefore bright red in color. When the contact pressure reaches a point, e.g. 1 N, the veins are completely blocked and the fingernail color stops reddening with further increase in touch pressure.

Further increases in touch pressure begin to constrict the arterial supply at the tip of the finger, which causes the blood to be pushed out of this region, resulting in a white band at the tip of the finger. The rest of the nail remains deep red, as the capillaries are protected from the pressure of the touch force by the bone of the distal phalange, which is connected to the fingernail via a strong matrix of collagen and elastic fibers. The nails are thus described as “immobile over the distal phalange” [12]. In fact, the fingernails have an important tactile function in providing “support and counterpressure for the digital pad, thereby aiding manipulation” [11].

As the force increases, the white band widens until some limit is reached, e.g. at 4 N. Increases in touch force beyond this point have no visible effect. However, forces applied longitudinally to the front of the fingertip and shear forces along the same direction are more effective at exerting stresses on the tissue above the bone, and are capable of increasing the white band even further.

This phenomenon can be utilized to measure touching force/contact pressure by monitoring changes in fingernail color without having to put a sensor between the finger and the surface. The change in color is directly related to the pooling of arterial blood and its oxy-hemoglobin saturation (relative concentrations of oxy- and reduced- hemoglobin). The amount of blood and the oxygen (oxy-hemoglobin) saturation under the fingernail bed can be monitored by shining light into the fingernail and measuring the reflectance.

## 2.2 Construction of the Nail Sensors

An example of the experimental setup is shown in Figure 2. A red LED (660 nm) illuminates the nail bed with red light. A photodiode is mounted nearby and detects the reflected light from the nail bed. As contact pressure increases, more arterial blood accumulates under the nail, resulting in two potentially competing phenomena. The additional volume of blood under the nail tends to increase the absorption of light. As the contact pressure increases, more light is absorbed, less red light is reflected, and the output voltage of the photodiode circuit,  $V_{out}$ , increases.  $V_{out}$  reaches an asymptotic value when the veins are completely collapsed.

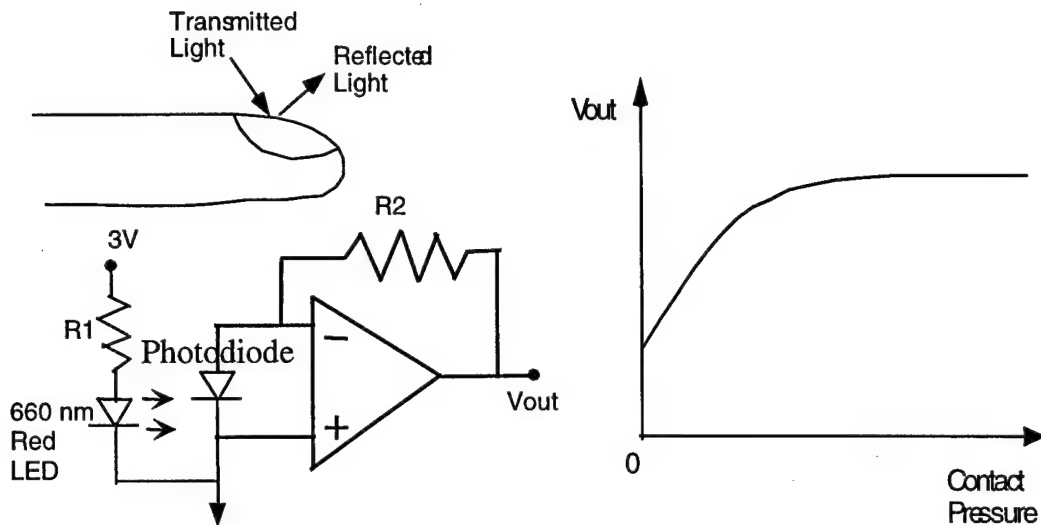


Figure 2: Pletysmograph Fingernail Sensor

Although the absorption of light is also dependent on the oxygen concentration in the blood, the volumetric effect seems to dominate [10]. If the oxygen concentration is of significance, a red LED (660 nm) and an infrared LED (940 nm) can be used in the same sensor to measure the concentration of oxygen in the blood. The two types of LEDs are illuminated alternately and the reflected light is measured by the same photodetector with the aid of sample-and-hold circuitry. Use of a third LED at the isobestic wavelength (770 nm) can provide measurements of absorption that are decoupled from the effect of oxygen concentration.

### 2.3 Prototype Design

Since the key to filtering out color changes induced by finger bending is to measure the *pattern* of the color change, the new prototype sensor is designed to use a spatial array of photodetectors along the longitudinal axis of the fingernail. Furthermore, by using three different wavelengths of LEDs, we can measure the concentration of oxygen in the blood as well as the change in blood volume. Although the oxygen concentration is ignored in our initial model, we may wish to factor this in at a later time.

In order to fit multiple LEDs and photodetecting elements on the human fingernail in a non-obtrusive manner, we will take advantage of modern miniaturization technology. The photodetector arrays have 16 elements each, are 4x1 mm in dimension, and have a broad spectral range across the visible and infrared. The

LEDs are 0.25x0.25 mm and come in a variety of wavelengths. Our prototype will use pairs of LEDs with wavelengths of 660 nm, 770 nm, and 940 nm.

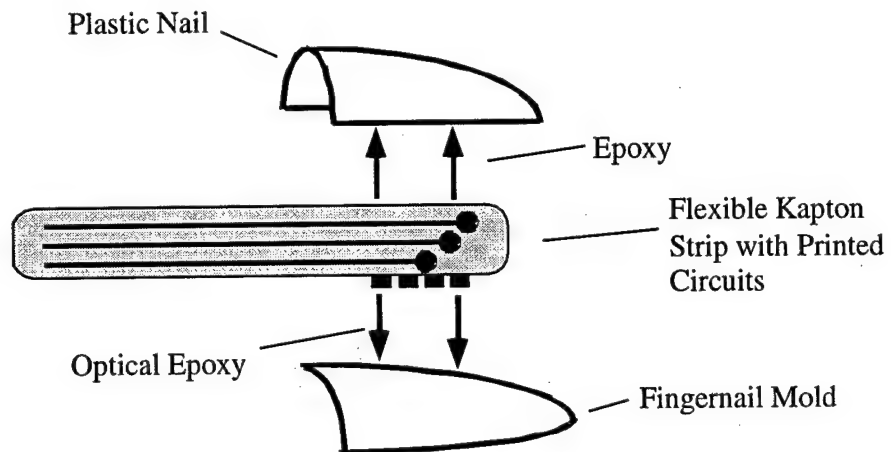


**Figure 3: Prototype Design for the Fingernail Touch Sensor**

### FINGERNAIL SENSOR FLEX CIRCUIT

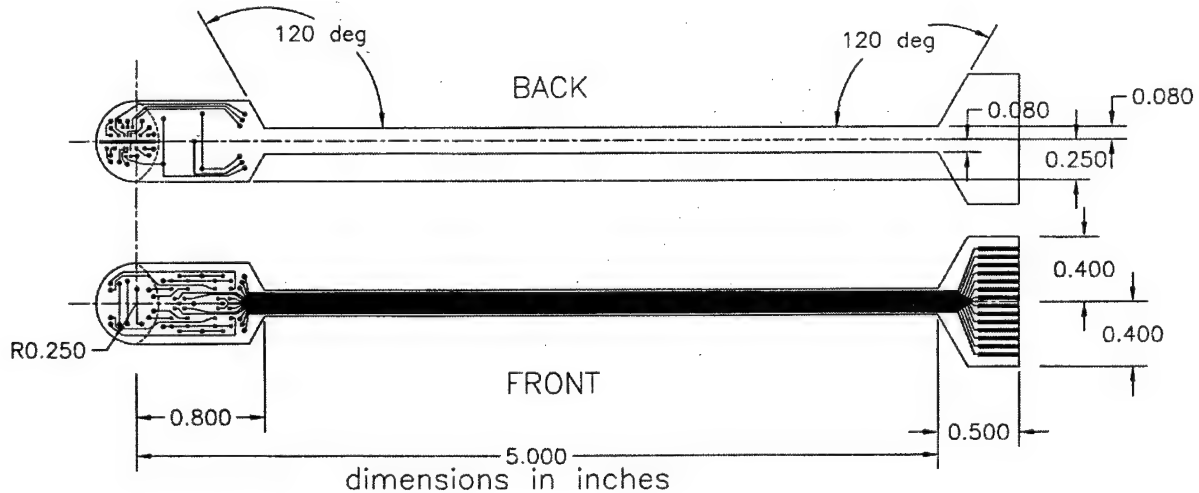


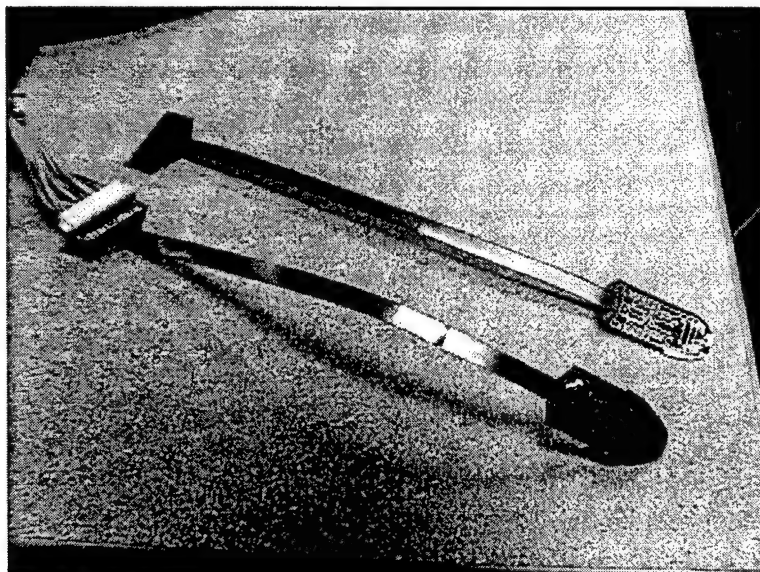
**Figure 4: Design for New Fingernail Sensor**

In order to adjust to the variability in fingernail contours, the optical components will be mounted on a flexible Kapton substrate, which can be bent to the shape of the fingernail before stiffening with epoxy. A

decorative plastic fingernail is bonded to the top of the sensor for cosmetic appearance as well as shielding from ambient light. Figure 3 shows a conceptual drawing of the nail sensor. The sensor can be attached to the nail using transparent adhesive or a ring of adhesive gum around the perimeter. Figure 4 shows the actual schematic for the flex circuit. The nail-shaped section on the left end will fit over the fingernail, while a thin flexible strip will reach back to the wrist, where a cable can be attached. Future designs will incorporate an onboard power source and wireless transmission.

## 2.4 Implementation

The distributed fingernail sensors have been fabricated and assembled, as shown by the pictures in Figure 5. The first picture shows a preassembled Kapton strip lying next to a fully assembled sensor. The second picture shows a close up of the bottom side, where two of the photodetecting arrays have been placed end to end. Although there are 32 total photodetectors, only every 4<sup>th</sup> one is used, resulting in 8 sensing locations along the length of the fingernail. On either side of the photodetector arrays are 3 LEDs, one of each wavelength mentioned previously. The third picture shows a close up of the top side of the sensor, where die form op amp circuits are located just behind the decorative fingernail area. The optical and electrical components are attached using conductive epoxy and gold wire bonding, and are coated with a layer of optically transparent epoxy for protection.



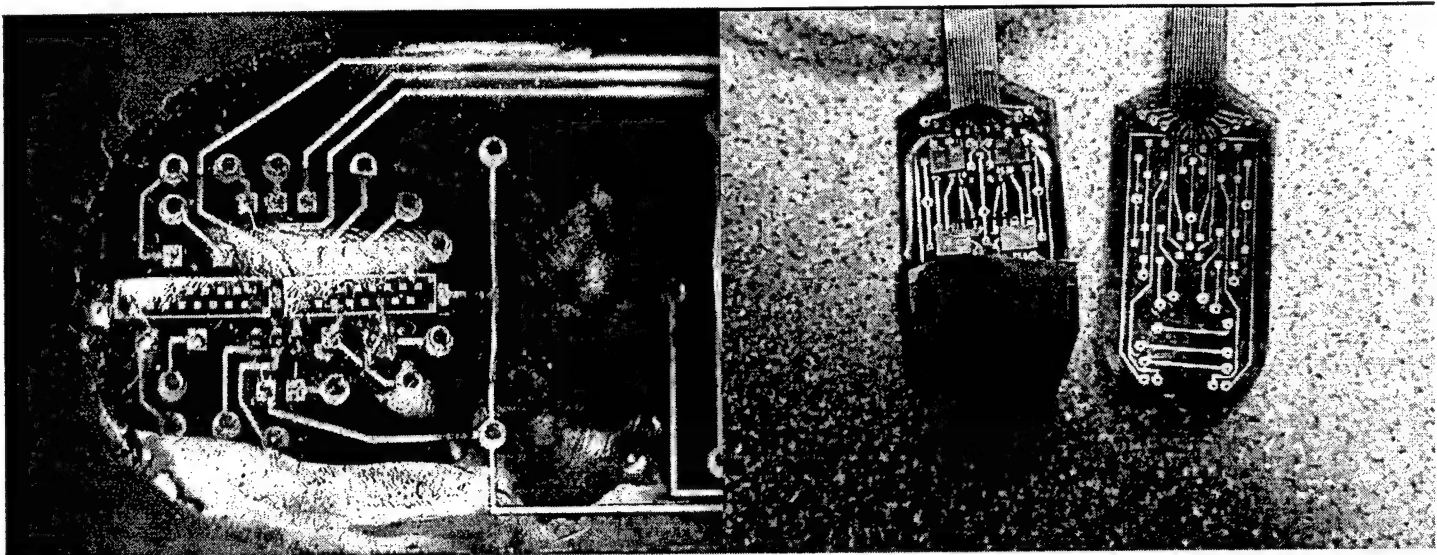


**Figure 5: Distributed Fingernail Touch Sensors**

### 3. Modeling and Analysis

#### 3.1 Problem Formulation and Mechanical Model

Figure 1 showed the typical behavior of the color change of the fingernail with increasing touch force at the fingertip. In order to understand the correlation between the touch force and the observed behavior, we intend to create and verify a hemodynamic model of the blood flow in the fingertip. The goal is a model that can predict the magnitude and location of an input force, based on the measurable color-change output. Specifically, we wish to filter out color changes that are caused by bending of the finger. As a first step towards a model that meets all of the above specifications, we will initially create a lumped parameter model that explains the color change at discrete points under the fingernail. The model in Figure 6 explains the color change at a single point in the reddening zone. This model will be soon be expanded to incorporate multiple points, corresponding to the locations of the photodetectors.

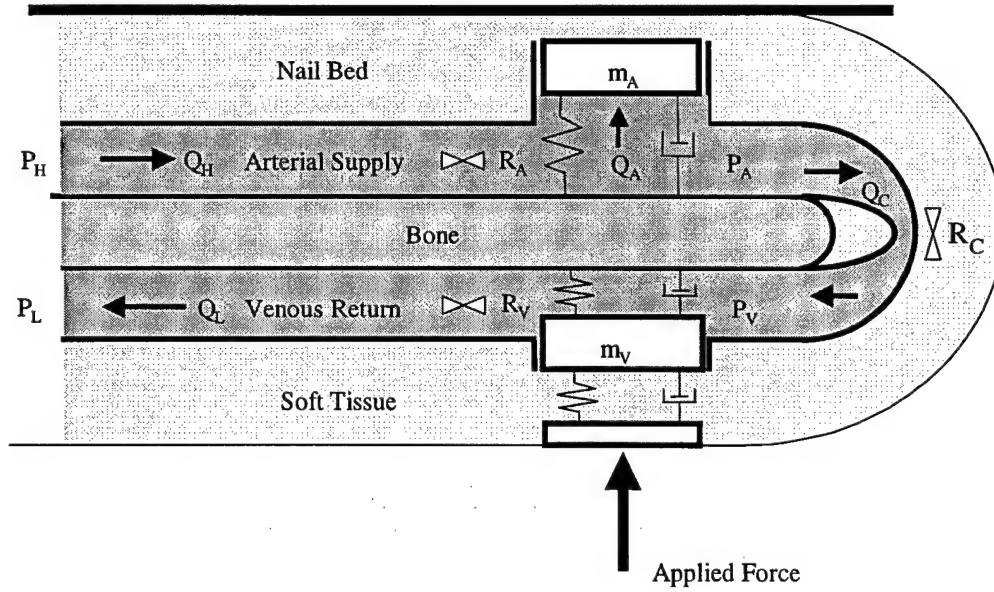


**Figure 6: Hemodynamic Model of Fingertip**

Blood flows into the fingertip through the arterial supply and leaves through the venous return. The arterial supply and venous return are each modeled as a single channel of fluid flow through the finger, and are in series with each other. The walls of the arterial supply and venous return are modeled as mass-spring-damper systems that expand and contract based on external forces and the local blood pressure. As they change diameter, their blood volume capacity and fluidic resistance change. A force  $F_F$  on the soft tissue below the finger will constrict the diameter of the venous return  $x_V$ . This will increase the fluidic resistance  $R_V$  through the veins, driving the pressure  $P_A$  to increase on the arterial side. The increase in  $P_A$  increases the diameter of the arterial supply  $x_A$ . This causes the arterial supply to expand with blood, resulting in a reddening of the nail, and an increase in light absorption.

At this stage we will make several assumptions:

1. The soft tissue of the fingertip can be modeled as a material with linear elasticity and damping.
2. The veins have a linear elasticity up to some sharp cutoff
3. The arterial supply under the nail can also be modeled with linear elasticity and damping, but with a discrete limit
4. The bone effectively shields the arterial supply under the rear portion of the nail from the direct influence of touch forces

5. The increase in blood volume under the nail effectively increases the path length over which light is absorbed by the blood
6. The effects of shear forces are neglected
7. Effects of oxygen concentration are neglected

The model can be expanded to explain the behavior in the whitening zone of the fingernail by adding another capacitive element at the tip of the nail that is directly influenced by the touch force  $\mathbf{F}_F$ . As the  $\mathbf{F}_F$  is increased, the diameter of the arterial supply at that point would decrease, evacuating blood, resulting in a whitening of the nail and a decrease in light absorption.

### 3.2 Bond Graph Model and State Equations

Figure 7 shows an equivalent bond graph representation for the hemodynamic model of the fingertip. The bond graph model elucidates the interactions between the mechanical subsystems of the arterial supply and venous return and the blood flow system which connects them. They not only interact through the fluidic pressures on the arterial and venous walls  $\mathbf{P}_A$  and  $\mathbf{P}_V$ , but also through the modulation of the fluidic resistances  $\mathbf{R}_A$  and  $\mathbf{R}_V$  by the arterial and venous diameters  $x_A$  and  $x_V$ . It is this nonlinear effect of the modulation that is responsible for the reddening phenomenon.

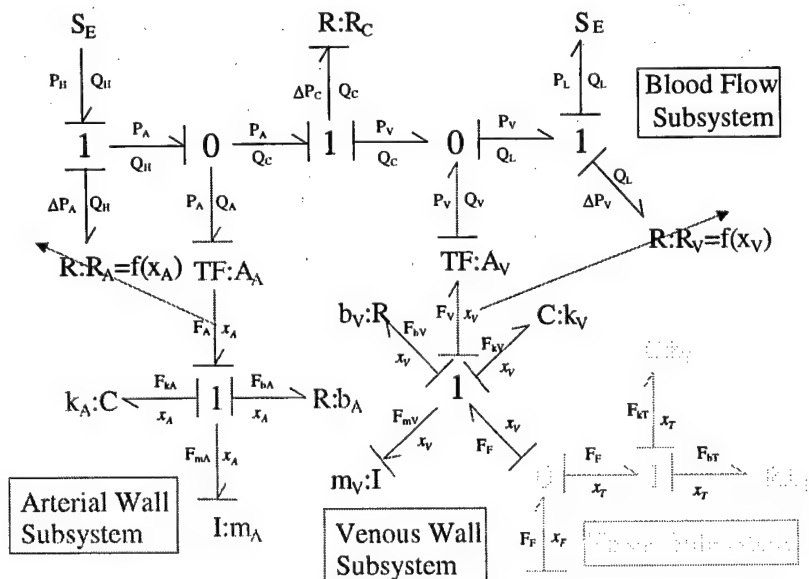


Figure 7: Bond Graph Model of Fingertip

Dynamic state equations can be written for this model as shown below by equation 1. The state variables are:

- $F_{kA}$  = force on the arterial wall
- $F_{kV}$  = force on the venous wall
- $d(x_A)/dt$  = time rate of change in arterial diameter
- $d(x_V)/dt$  = time rate of change in venous diameter

The outputs are the arterial and venous diameters,  $x_A$  and  $x_V$ , respectively. The arterial and venous resistances  $R_A$  and  $R_V$  are modulated by the system outputs as shown by equation 2.

$$\begin{aligned}
 \frac{d}{dt} \begin{bmatrix} F_{kA} \\ F_{kV} \\ \dot{x}_A \\ \dot{x}_V \end{bmatrix} &= \begin{bmatrix} 0 & 0 & k_A & 0 \\ 0 & 0 & 0 & k_V \\ -\frac{1}{m_A} & 0 & -\frac{1}{m_A} \left[ b_A + \frac{R_A(R_C + R_V)A_A^2}{R_A + R_C + R_V} \right] & \frac{R_A R_V A_A A_V}{m_A(R_A + R_C + R_V)} \\ 0 & -\frac{1}{m_V} & \frac{R_A R_V A_A A_V}{m_V(R_A + R_C + R_V)} & -\frac{1}{m_V} \left[ b_V + \frac{R_V(R_C + R_A)A_V^2}{R_A + R_C + R_V} \right] \end{bmatrix} \begin{bmatrix} F_{kA} \\ F_{kV} \\ \dot{x}_A \\ \dot{x}_V \end{bmatrix} \\
 &+ \begin{bmatrix} 0 & 0 & 0 \\ 0 & 0 & 0 \\ \frac{(R_C + R_V)A_A}{m_A(R_A + R_C + R_V)} & \frac{R_A A_A}{m_A(R_A + R_C + R_V)} & 0 \\ \frac{-R_V A_V}{m_V(R_A + R_C + R_V)} & \frac{-(R_C + R_A)A_V}{m_V(R_A + R_C + R_V)} & \frac{1}{m_V} \end{bmatrix} \begin{bmatrix} P_H \\ P_L \\ F_F \end{bmatrix} \\
 \begin{bmatrix} x_A \\ x_V \end{bmatrix} &= \begin{bmatrix} \frac{1}{k_A} & 0 & 0 & 0 \\ 0 & \frac{1}{k_V} & 0 & 0 \end{bmatrix} \begin{bmatrix} F_{kA} \\ F_{kV} \\ \dot{x}_A \\ \dot{x}_V \end{bmatrix} \quad (1)
 \end{aligned}$$

$$R_A = \frac{128L_A \mu_{Blood}}{n_A \pi (D_A + x_A)^4} \quad R_V = \frac{128L_V \mu_{Blood}}{n_V \pi (D_V - x_V)^4} \quad (2)$$

All of the model parameters are listed below and are estimated to order of magnitude with the aid of medical literature [13].

- $k_A$  = arterial wall stiffness  $\sim 10^4$  N/m
- $k_V$  = venous wall stiffness  $\sim 3(10^4)$  N/m
- $m_A$  = arterial wall inertia  $\sim 10^{-3}$  kg
- $m_V$  = venous wall inertia  $\sim 10^{-3}$  kg
- $b_A$  = arterial wall damping  $\sim 10^3$  Ns/m
- $b_V$  = venous wall damping  $\sim 10^3$  Ns/m
- $A_A$  = arterial surface area  $\sim 10^{-4}$  m<sup>2</sup>
- $A_V$  = venous surface area  $\sim 10^{-4}$  m<sup>2</sup>
- $D_A$  = nominal arterial diameter  $\sim 10^{-4}$  m
- $D_V$  = nominal venous diameter  $\sim 10^{-4}$  m
- $L_A$  = arterial length  $\sim 10^{-2}$  m
- $L_V$  = venous length  $\sim 10^{-2}$  m
- $n_A$  = number of small arteries  $\sim 10^2$
- $n_V$  = number of small veins  $\sim 10^2$
- $\mu_{Blood}$  = blood viscosity  $\sim 3(10^{-3})$
- $R_C$  = lumped resistance of capillaries  $\sim 10^{11}$  Pa-s/m<sup>3</sup>
- $P_H$  = arterial pressure input  $\sim 1.3(10)^4$  Pa, gage
- $P_L$  = venous pressure input  $\sim 0$  Pa, gage
- $F_F$  = variable touch force input

### 3.3 Simulations

The state equations for the hemodynamic model were simulated using a step input for the touch force. The step responses of the system outputs are shown in Figure 8 for a range of equally spaced magnitudes (0.1 N) of step force. At time zero, the positive step force was applied, and then at time 2 seconds, the force was stepped back to zero.

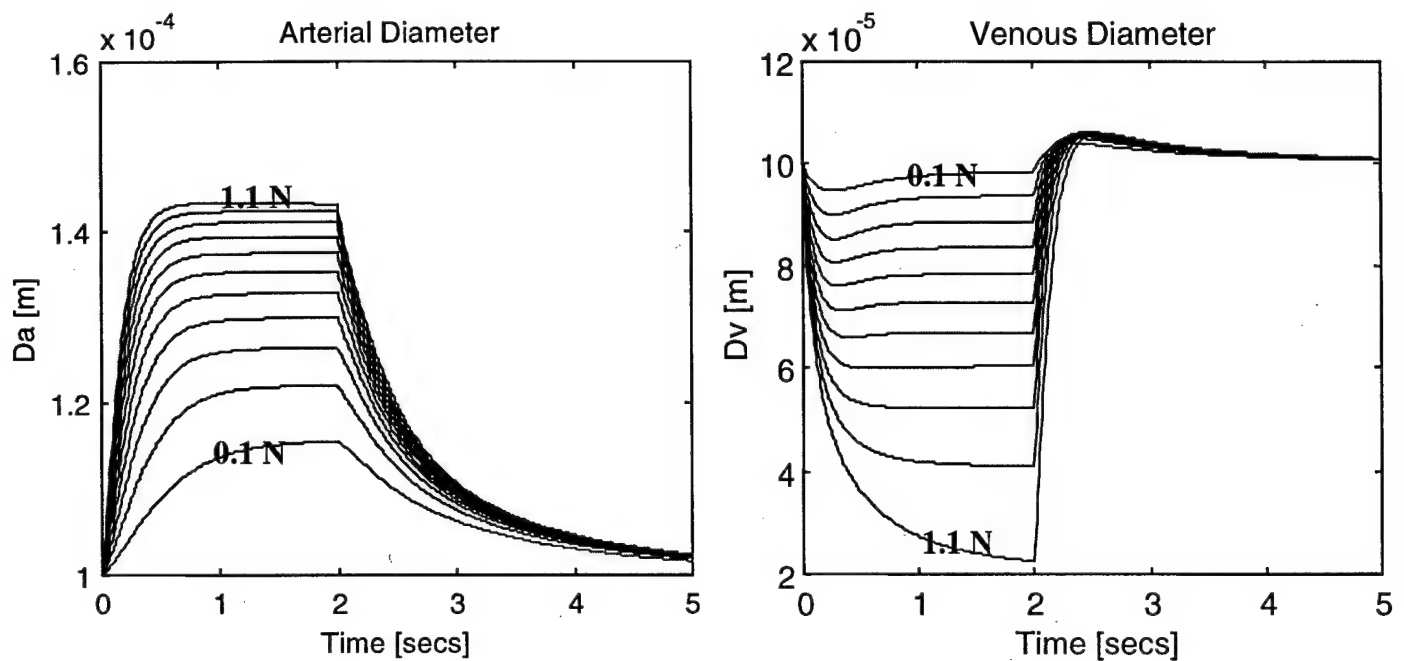


**Figure 8: Simulated Step Response**

The results of the simulation show a characteristically nonlinear behavior. Firstly, the steady state diameters are not linearly proportional to the touch force magnitude. Secondly, the arterial diameter, which is of primary interest, responds much more sluggishly at lower force levels. In fact, the step response back to zero force is much slower than the step response up to a positive force. The venous diameter, on the other hand, responds just as quickly to the negative step as to the positive step. Therefore we conclude that the asymmetry of the arterial behavior is related to the nonlinearity of the fluid dynamics between the arteries and veins. Specifically, the smaller fluidic resistance at low force slows the system response. By linearizing the model about several operating points of different finger force, we see that the slowest pole, which corresponds almost entirely to the dynamics of the arterial diameter, moves to the left with increasing finger force. A second faster pole represents a combination of arterial diameter and venous diameter dynamics lies further and also moves to the left with increasing finger force. The remaining poles, which represent the dynamics of the diameter velocities, are several orders of magnitude faster, suggesting that the inertia elements are not necessary to the model, although they do simplify the derivation of the state equations. There are three zeros in the linearized model, which accounts for the steep initial slope of the step response.

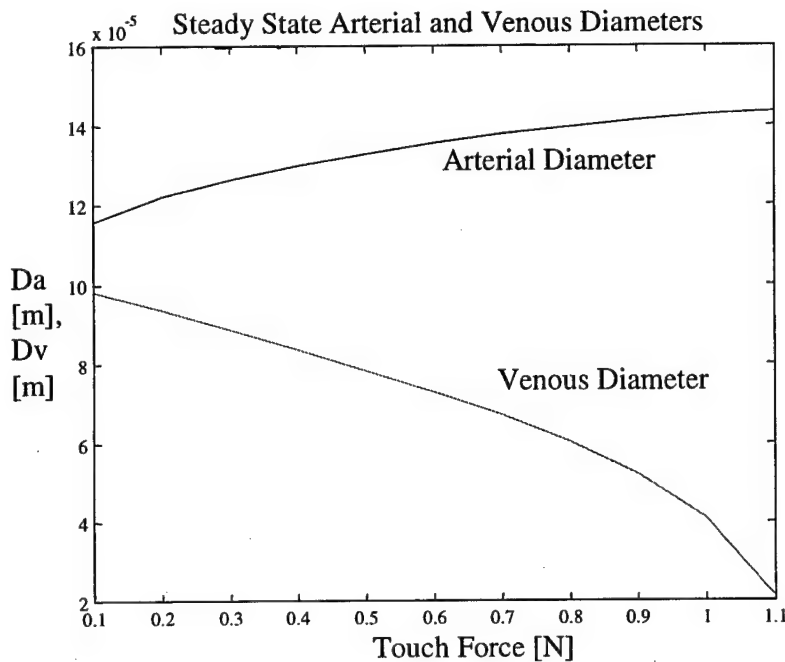


**Figure 9: Simulated Steady State Response**

Figure 9 shows the steady-state relationship between the outputs and the magnitude of the touch force input. As the force increases to just over 1 N, the venous diameter drops to zero and remains there, while the arterial diameter reaches a maximum value and remains there.

It should now be noted that the results in Figures 8 and 9 are not directly proportional to the actual output of the sensor. The intensity of light received by the sensor will be some nonlinear function of the volume of blood in the arterial section. For transmission of light through a solution, the Beer-Lambert Law can be applied, as shown by equation (3).

$$I_{out} = I_{in} e^{-A} \quad (3)$$

$$A = LC\epsilon$$

- $I_{out}$  = output light intensity
- $I_{in}$  = input light intensity
- $A$  = absorption
- $L$  = path length
- $C$  = concentration

- $\varepsilon$  = absorption coefficient =  $\varepsilon(\lambda)$

In the case of blood, however, empirical relations must often be used, especially in the case of reflection photoplethysmography [14][15]. At this point we can only say that the increase in blood volume increases the absorption of light by effectively increasing the path length/concentration in some manner.

### 3.4 New Multi-Element Model

Most recently, work has begun on a new multi-element model that can explain the two behaviors associated with the reddening and whitening zones of the fingernail. Figures 10a, 10b, and 10c, obtained from medical journals [21][22], show details of the arterial structure underneath the fingernail. As shown, the arteries branch out into a tiny network of capillary loops just underneath the fingernail, which are responsible for the apparent color of the nail. Based on this anatomy, the model that seems most reasonable is one in which multiple capillary elements are in parallel with each other, branching off from a main arterial supply and recombining into a main venous drain. Figure 11 shows a sketch of a three-element model, where the proximal arterial element explains the reddening behavior at the center of the nail; the distal arterial element explains the whitening behavior at the tip of the nail, and the venous element functions as before. Using the same methods outlined in previous sections, preliminary simulations show favorable results. Figure 12 shows the step response of the two arterial elements when touch pressure is applied to both the venous element and the distal arterial element. The first arterial element expands as before, while the second arterial element collapses from the touch pressure, causing a whitening at the tip of the nail.

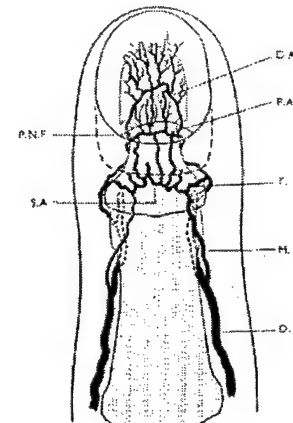
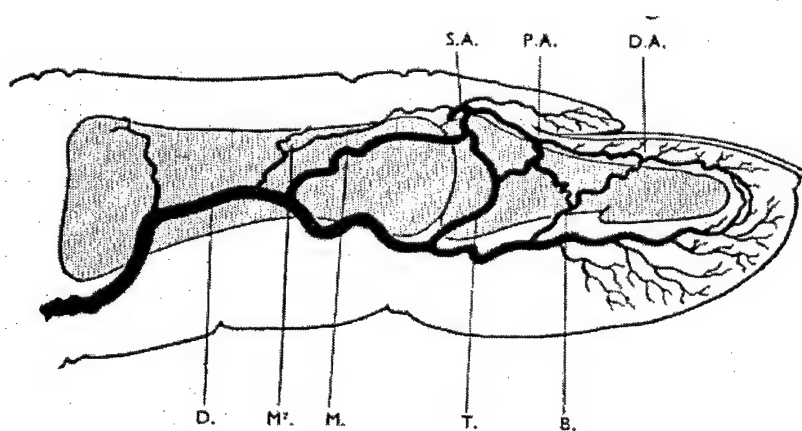
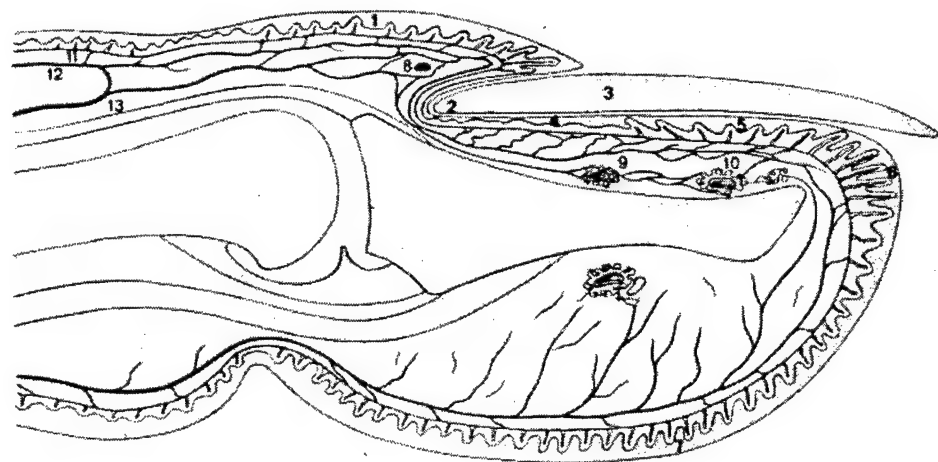
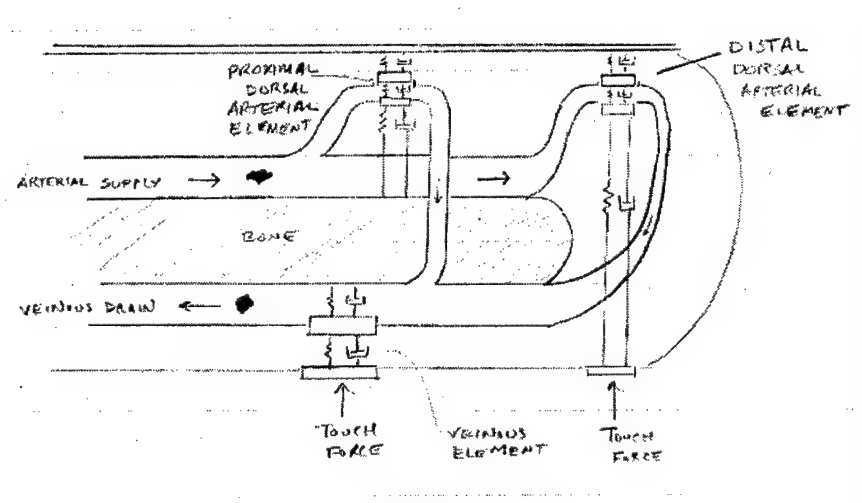


FIG. 3  
Diagram of finger viewed from dorsum showing proximal and distal subungual arcades (P.A. and D.A.). The superficial arcade (S.A.) at the base of the terminal phalanx receives contributions from the middle (M) and terminal (T) segments. Its branches pass deep to nail root to gain the nail bed and proximal subungual arcade. The nail proximal to the proximal nail fold (P.N.F.) is indicated by interrupted line.



**Figure 10: Arterial Structure of the Fingernail: (a) and (b) are adapted from [20], (c) is adapted from [21]**



**Figure 11: Parallel Multi-Element Model**

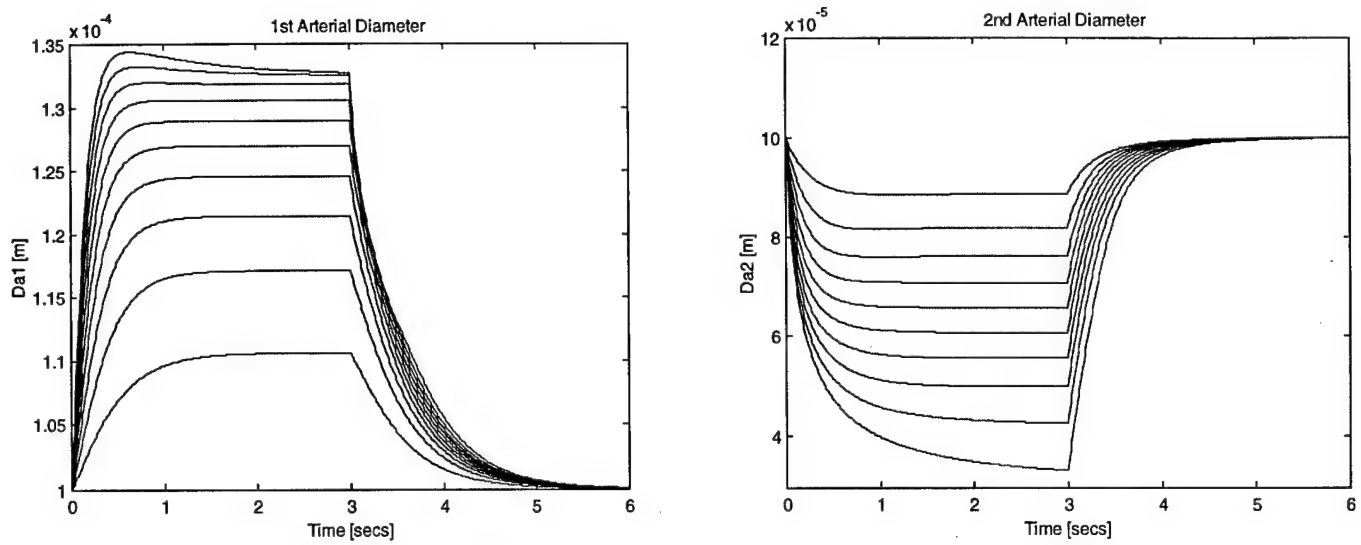


**Figure 12: Multi-Element Simulations**

#### 4. Experiments

In order to test the validity of the model, dynamic and static experiments were performed using the new nail sensor prototypes. Figure 13 shows a typical photodetector output toward the rear of the nail as a function of touch force applied normally to the bottom surface of the fingertip. A thin Archimedian force sensor was used to directly monitor the touch force input.

As seen by comparing Figures 8 and 13, the general behavior of the simulated step response (for the reddening behavior) is very similar to the experimental step response. They both show a relatively instantaneous response to a positive step force, contrasted with a relatively sluggish response to a step back down to zero force. Figure 14 shows the experimental steady-state relationship between touch force input and sensor output. We notice an approximately linear behavior up to approximately 1 N, past which the output exhibits a nonlinear leveling off at 1.5 N, as expected. It is difficult to make any further comparison here without having modeled the optics.

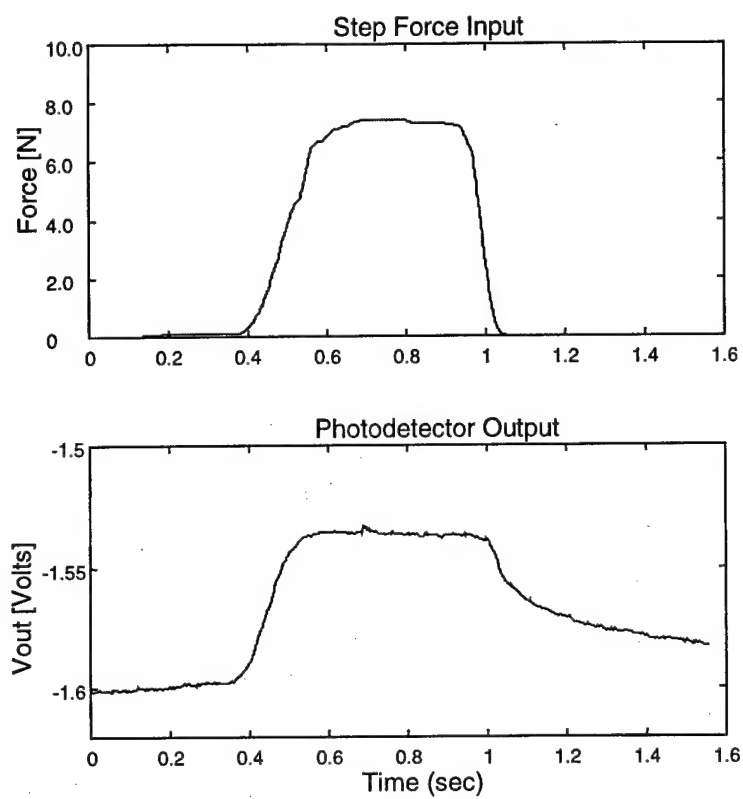


**Figure 13: Experimental Step Response**

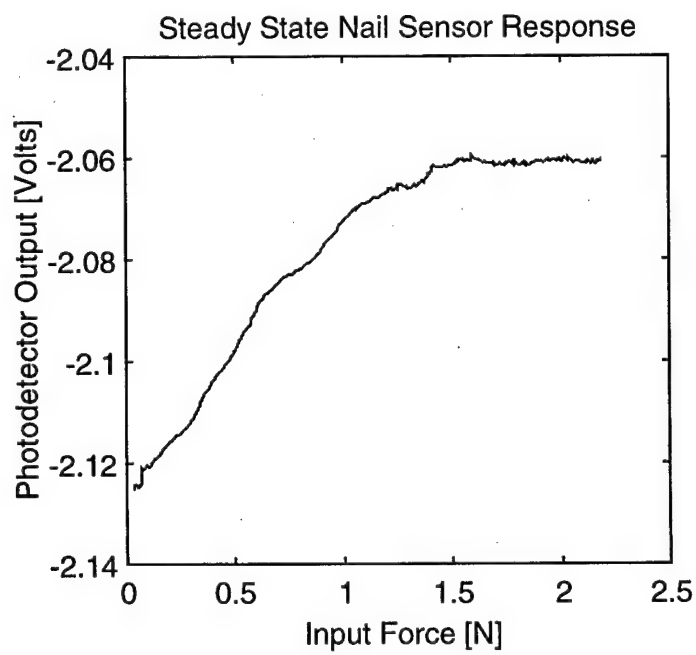


**Figure 14: Experimental Steady State Relations**

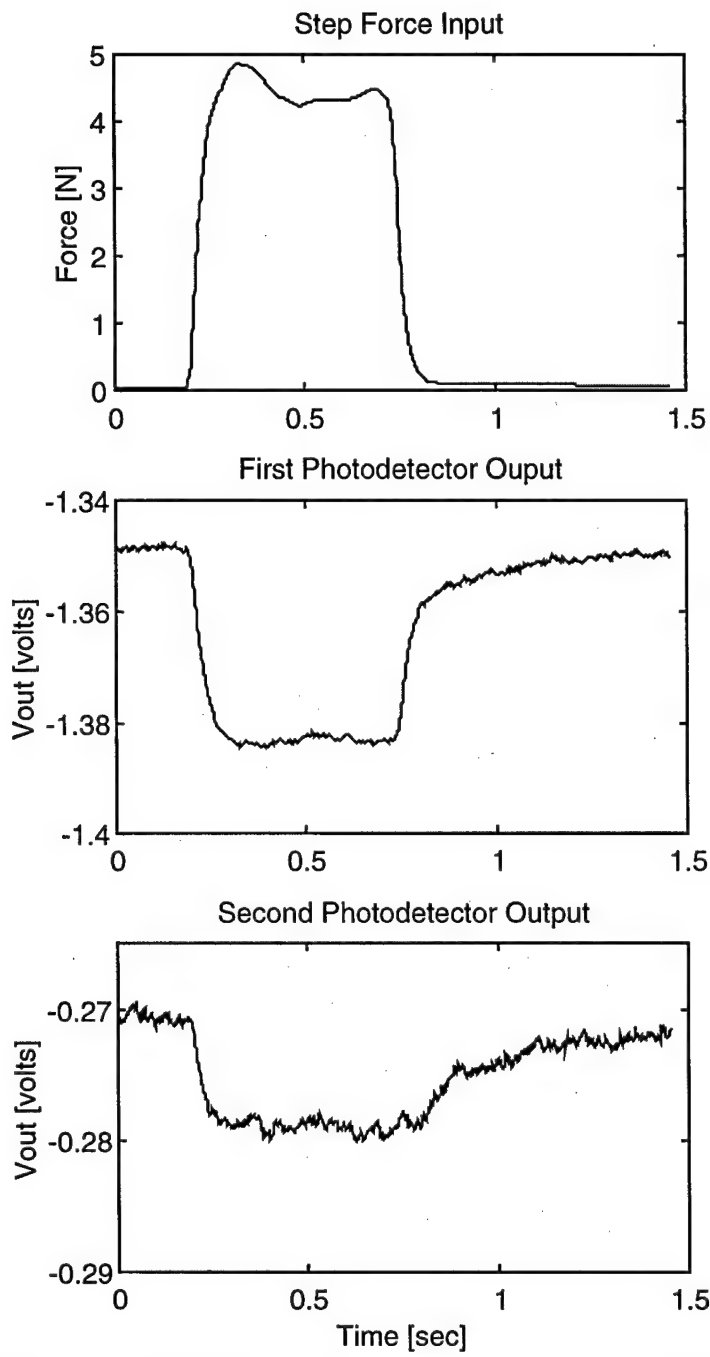


**Figure 15: Experimental Step Response at Tip of Fingernail**

Figure 15 shows the experimental response for a two photodetectors located at the tip of the fingernail when a step touch force is applied and released. The first photodetector is farther forward than the second one. Note that the behavior of the photodetectors at this location is the opposite of that in Figure 13 for photodetectors at

the rear of the nail. As expected here in Figure 15, the data shows a decrease in voltage when touch force is applied, corresponding to a decrease light absorption due to whitening. The dynamics are still relatively instantaneous for the step up and relatively sluggish for the step back down. However this directional difference in speed of response is not as pronounced for the first photodetector, which is farther towards the tip of the nail. This seems reasonable, since we might expect the arterial element at this location to behave more like the venous diameter, whose simulated response is shown in Figure 8.

## 5. Conclusions

Improvement on a new type of touch sensor for detecting contact pressure at human fingertips has been presented. Fingernails are instrumented with arrays of micro LEDs and photodetectors in order to measure changes in the nail color pattern when the fingers are pressed against a surface. Observable behavior of the color change phenomena was described and used to create a lumped parameter hemodynamic model in order to understand the relationship between touch force input and measurable color-change output. The model was simulated and compared to experimental data for multiple sensing locations along the length of the fingernail. The comparison shows that the model does an excellent job of explaining certain key nonlinearities that are observable in the sensor output. The results of both the model and experiments show a relatively instantaneous sensor response to a touch force, with a relatively slow recovery after the touch is released. This information can be used to optimize the strategy for touch force detection. Specifically, the time that the computer must wait before attempting to measure another touch should be on the order of the recovery time demonstrated by the model and experiments. Furthermore, if the dynamics of the color change resulting from finger-bending significantly differ from the modeled dynamics of touch force, we can still detect touch in the presence of finger bending.

Unlike traditional electronic gloves, in which sensor pads are placed between the fingers and the environment surface, this new sensor allows the fingers to directly contact the environment without obstructing the human's natural haptic senses. Several applications for this new technology are being investigated. These sensors could be used for the recording of chiropractic or surgical skills, where neither the patient nor the physician's fingers can be covered with sensors. In another paper [16] we propose the idea of a "virtual switch," whereby a traditional switch is replaced with merely an image of a switch on a surface. Measurements of a person's hand position along with measurements of touch force from the fingernail sensor are used to

activate the virtual switch. Because the virtual switches are merely images, they can be located on all kinds of surfaces, such as the joints of a robot or the surface of a desk without modifying any hardware. They can be completely reconfigured by software and can have different functionality depending on which finger is used to press the switch.

## 6. References

- [1] D.J. Sturman and D. Zelzer, "A Survey of Glove-base Input", *IEEE Computer Graphics & Applications*, January, pp. 30-39, 1994.
- [2] T.B. Sheridan, *Telerobotics, Automation, and Human Supervisory Control*, Cambridge, MA: MIT Press, 1992.
- [3] R.S. Kalawsky, *The Science of Virtual Reality and Virtual Environments*, Addison-Wesley, 1993.
- [4] G.C. Burdea, *Force and Touch Feedback for Virtual Reality*, Wiley, 1996.
- [5] J. Kramer, and L. Leifer, "The Talking Glove: An Expressive and Receptive 'Verbal' Communication Aid for the Deaf, Deaf-Blind, and Non-vocal," tech report, Stanford University, Dept. of Electrical Engineering, 1989.
- [6] D.J. Beebe, D.D. Denton, R.G. Radwin, and J.G. Webster, "A Silicon-Based Tactile Sensor for Finger-Mounted Applications", *IEEE Transactions on Biomedical Engineering* **45:2**, pp. 151-159, 1988.
- [7] J.G. Webster, Ed., *Tactile Sensors for Robotics and Medicine*, New York: Wiley, 1988.
- [8] T.R. Jenson, R.G. Radwin, and J.G. Webster, "A Conductive Polymer Sensor for Measuring External Finger Forces", *Journal of Biomechanics* **24:9**, pp. 851-858, 1991.
- [9] J.S. Son, A. Monteverde, and R.D. Howe, "A Tactile Sensor for Localizing Transient Events in Manipulation", *Proceedings of the IEEE International Conference on Robotics and Automation*, pp. 471-476, 1994.
- [10] S. Mascaro, K.W. Chang, and H.H. Asada, "Finger Touch Sensors using Instrumented Nails and their Application to Human-Robot Interactive Control", *ASME IMECE, Symposium on Haptic Interfaces for Virtual Environment and Teleoperator Systems*, November, 1998.
- [11] *Gray's Anatomy: The Anatomical Basis of Medicine and Surgery*, New York: Churchill Livingstone, 1995.
- [12] R.V. Krstic, *Human Microscopic Anatomy: an Atlas for Students of Medicine and Biology*, New York: Springer-Verlag, 1991.
- [13] Guyton, A.C. *Textbook of Medical Physiology*, Saunders: Philadelphia, 1981.

[14] J.M. Steinke and A.P. Shepherd, "Role of Light Scattering in Whole Blood Oximetry," *IEEE Transactions on Biomedical Engineering*, 33:3, pp. 294-301, 1986.

[15] Y.Mendelson and B.D. Ochs, "Noninvasive Pulse Oximetry Utilizing Skin Reflectance Photoplethysmography," *IEEE Transactions on Biomedical Engineering*, 35:10, pp. 798-805, 1988.

[16] S.Mascaro, K.W. and H.H. Asada, "Virtual Switch Human-Machine Interface Using Fingernail Touch Sensors," *IEEE International Conference on Robotics and Automation*, May 1999.

[17] J.E. Brody, "The Mundane Fingernail, a Little-Understood Barometer to the State of a Person's Health," *New York Times*, 139(48,199): B8, Jan 18 1990.

<http://www.thriveonline.com/health/Library/CAD/abstract12015.htm>

[18] M.A. Pirouzi and P.Pirouzi, "Nail Diseases," *The Canadian Encyclopedia of Dermatology*, 1998.  
<http://www.fortunecity.com/marina/victory/11/nail.htm>

[19] "Your Fingernails: What Do They Reveal About Your Health?" *Mayo Clinic Health Letter*, October 1991. <http://www.mayohealth.org/mayo/9702/htm/finger.htm>

[20] "Nail Abnormalities," *Health Answers*, Healthway Online, 1999.  
<http://www.healthanswers.com/database/ami/converted/003247.html>

[21] M.H. Flint "Some Observations on the Vascular Supply of the Nail Bed and Terminal Segments of the Finger," *British Journal of Plastic Surgery*, No. 8, pp. 186-195, 1956.

[22] R. Wolfram-Gabel and H. Sick, "Vascular Networks of the Periphery of the Fingernail," *The Journal of Hand Surgery*, 20B:4, pp. 488-492, 1995.

## **Personal Aid for Mobility and Monitoring: A Helping Hand for the Elderly**

**Steven Dubowsky**  
Professor, Principal Investigator

**Adam Skwersky**  
Graduate Research Assistant

**Haoyong Yu**  
Graduate Research Assistant

**Frank Genot**  
Visiting Scientist

**Sara Godding**  
Undergraduate Research Assistant

### **ABSTRACT**

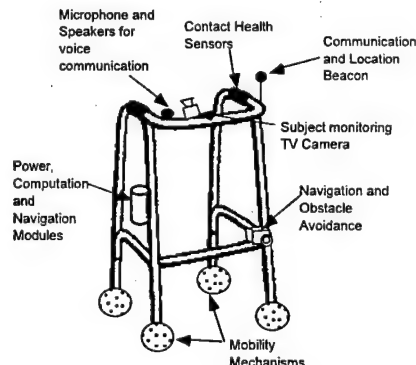
The objective of this research program is to develop the fundamental technology for a Personal Aid for Mobility and Monitoring (PAMM) that meets the needs of elderly living independently or in senior assisted-living facilities. Progress has been made in a number of areas. A prototype cane-based system (MOD I) has been built, and three mobility control modes have been implemented. MOD I was used in experimental trials at an eldercare facility. Based on results from these trials, modifications allowing users to obtain more support while using MOD I were made. The acoustical obstacle detection system has undergone preliminary tests and improvements have been proposed. A preliminary study of object-recognition using acoustics has shown promise, but more work is needed to determine the limits of this approach. Preliminary studies of the MOD II (walker based system) are well underway.

## 1. MOTIVATION AND PROGRAM OBJECTIVE

The objective of this research program is to develop the fundamental technology for a Personal Aid for Mobility and Monitoring (PAMM) that meets the needs of elderly living independently or in senior assisted-living facilities. As an elderly individual moves toward higher levels of care (i.e., from independent living to assisted living facilities to nursing homes), costs increase and quality of life decreases rapidly. The largest change occurs during the transition into a nursing home. A recent summary of reports on caring for the elderly can be found in [1]. According to this summary, an estimated 20-33% of all nursing home residents could be better served by alternatives, if available, within the community. The National Program of All-Inclusive Care for the Elderly Association (PACE), among others, has shown the cost-effectiveness of keeping the elderly out of nursing homes. The preference of most elderly is to stay out of nursing homes for as long as possible. Delaying this transition (with PAMM's) will be extremely beneficial for the elderly and economically for society.



a. Traditional



b. PAMM

Figure 1: A Helping Hand for the Elderly.

This report is broken into three sections. The first section provides a brief review of the PAMM MOD I system concept that was reported previously and a summary of the project goals for October 1999. The second section provides a synopsis of our progress toward these goals during this reporting period. The third section summarizes work that remains to be completed during the remainder of this second year of our three-year research program.

## 2. THE PAMM SYSTEM CONCEPT

The basic PAMM concept is shown in Figure 1 and Figure 2. The concept consists of a "helping-hand" mobility aid that is able to locate itself in a facility by visually reading simple signposts strategically placed

on the ceiling of the eldercare facility. PAMM will use acoustic sensors to locate and identify obstacle and objects in the environment enabling it to maneuver in crowded environments. It will communicate with the facility's central computer to obtain information such as the user's schedule and the facility's updated maps. In addition, PAMM will carry sensors to monitor the health and condition of their users and transmit their status back to the central computer.

A battery powered near omni-directional drive will aid with mobility, navigation, and physical stability. The on-board control and planning systems will "learn" the characteristics of the user and adapt their behavior to maximize their comfort and the PAMM's responsiveness. A sensor for measuring the force and torque applied by the user to PAMM's handle will serve as the main conduit for user interaction with PAMM. In some cases, PAMM will need to override a user's commands.

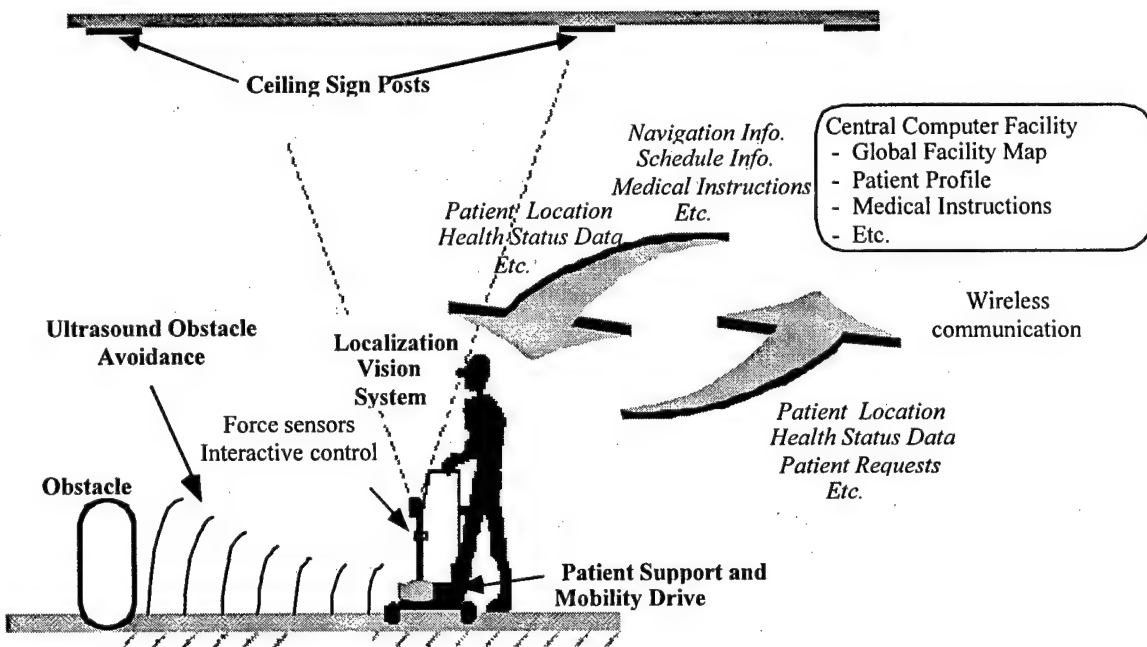


**Figure 2: PAMM System Concept.**

To develop these concepts, a "smart cane" prototype system (MOD I) has been designed and constructed [2]. The cane is simple enough so it could be designed and fabricated quickly, yet functional enough as a mobility-aid so it can be used to obtain practical results. It is being used in ongoing evaluations of the technology envisioned for the final PAMM system. The MOD I system, however, can only provide physical support to elderly individuals with minor mobility impairments. During the second half of this

year, a “smart walker” (MOD II) will be developed to address the needs of users with more severe impairments. Nearly all of the localization, obstacle avoidance, planning, control and health monitoring systems will be directly transferable to the MOD II system.

## **2.1 USERS NEEDS**

Based on studies of physical ailments in the elderly, the basic functionality of PAMM was established. The central function of the PAMM system is to prevent or delay an elderly person's progression into nursing facilities. Table 1 outlines the needs of the elderly and the associated physical infirmities that often necessitate such a transition.

**Table 1: PAMM Functions**

<b>Need</b>	<b>Physical Deficiency</b>	<b>Cause</b>
Guidance	Failing memory, disorientation	Senile dementia, including Alzheimer's.
Physical support	Muscular- skeletal frailty, instability	Osteoporosis, Diabetes, Parkinson's, Arthritis, lack of exercise, failure of vestibular organs.
Health Monitoring	Poor cardiovascular function, susceptibility to strokes and heart attacks.	Poor diet, old age, lack of exercise, illness (e.g., flu or pneumonia)
Medicine and Other Scheduling	Need to take a variety of medicines coupled with failing memory and disorientation,	Senile dementia, general failure health.

## **2.2 SYSTEM PERFORMANCE REQUIREMENTS**

A preliminary set of technical performance goals for PAMM has been defined based on the assumption that the system would be used inside an assisted living facility. The performance goals are summarized in Table 2.

**Table 2: PAMM Performance Goals**

<b>User and operation environment characteristics</b>	
Potential Users	Elderly with mobility difficulty due to physical frailty and/or disorientation due to aging and sickness.
Environment	Assisted-living facilities. Known structured indoor environment with random obstacles such as furniture and people. Flat and relatively hard floor or ramps less than 5 degrees.
<b>System function and features</b>	
Physical stability	Provide equal or better stability than that of a standard walker.
Guidance and obstacle avoidance	Provide guidance to destinations via global sensing, planning and obstacle avoidance strategies.
Health monitoring	Provide continuous health monitoring (details TBD).
Communication	Provide communication with patients and caretakers.
<b>Mechanical specifications</b>	
Mobility device	Compact and robust wheel-based mobility platform with design re-configurability.
Speed	Able to assist the elderly walking up to 0.5m/s.
Loading capacity	Able to support the average body-weight of an elderly person and to provide 2 to 4 kg pulling force for stability and guidance.
Weight	Approximately 15 kg.
Physical size	Approximately equal to a conventional walker
Battery life	About 5 hours between charges.
<b>Sensing and computing</b>	
Computing power	On-board computers sufficient for planning, control, health monitoring and communication.
Sensors and aides to Navigation.	Vision based global sensing for high level planning. Ultrasonic based sensors for obstacle avoidance and mapping. Optical encoders for dead reckoning and motion control. Signpost based localization.

### 2.3 RESEARCH GOALS

The goals for this second year of our three-year study are:

- The development of MOD I planning and control algorithms,
- The performance evaluation of the basic physical system,
- The evaluation of the user interface definition of requirements for user-responsive interface designs, and
- The generation of MOD II system requirements and preliminary design concepts.

### 3. PROGRESS

During first year of the PAMM project, a number of technical challenges were identified, and solutions were proposed. The MOD I system was developed to study these proposed solutions. During this

reporting period (months 12 to 18 of the project), progress has been made in obstacle avoidance and identification and mobility control. The highlight of this period has been the field-testing of the MOD I system at an assisted living facility. Based on these trials, significant improvements to the PAMM technology are proposed. The following sections describe the advances made in each area.

### 3.1 MOBILITY CONTROL

For the MOD I system, three modes of mobility control have been implemented and a fourth is being developed. They are summarized in Table 2. The first mode is user-driven admittance control. The admittance control method is described in more detail in section 3.1.1. The user chooses the path and speed and PAMM provides physical support. The speed and direction of PAMM is based only on the user's pressing on the force-torque sensor. In the second mode, PAMM leads the user to a destination while avoiding mapped and locally detected obstacles. In the third mode, PAMM leads the user along a predefined path, avoids obstacles, provides physical support, and uses a one DOF form of the admittance controller to vary the speed along the path. In the fourth mode, which is being developed, PAMM will allow two DOF (tangential and turning) variations along the path.

**Table 2: PAMM MOD I System Modes**

Mode	Admittance control	Obstacle Avoidance	Guidance
1	Yes	No	No
2	No	Yes	Yes
3	1 DOF (tangent)	Yes	Yes
4	3 DOF	Yes	Yes

#### 3.1.1 MODE 1: ADMITTANCE CONTROL

The admittance-based controller employs a dynamic model. The cane moves in response to the user forces and torques applied to a force/torque sensor as if it were the selected dynamic model [3]. The model is chosen to create a desired feel for the user. The admittance model for MOD I consists of a two DOF (tangential and turning) mass-damper system. Figure 3 shows a block diagram of the admittance controller. Forces and torques are measured and the admittance model is simulated. The resulting motion is then converted to wheel velocities of the skid-steering system using inverse kinematics. These wheel

velocities are then enforced using PI controllers for the motors. The parameters of the admittance model can be varied for different motions and users.

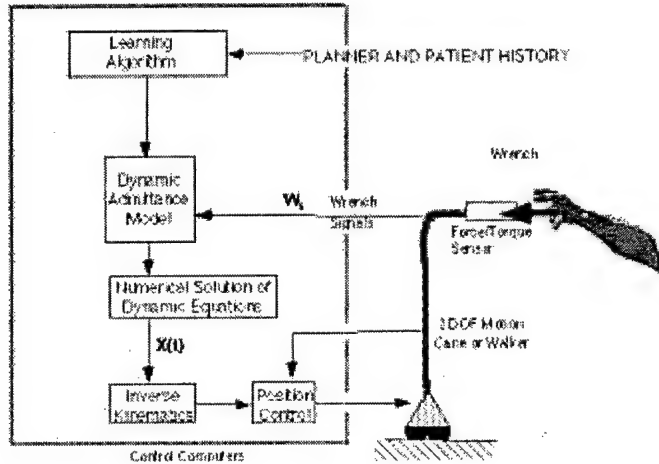


**Figure 3: Admittance controller.**

Due to the complicated nature of the man-machine interaction, the information generated by the force-torque sensor must be analyzed before an effective admittance model can be developed. Various models and parameters were tested in field experiments carried out in an eldercare facility. The results, discussed in section 3.2, suggest that a velocity-dependent damping allowed smoother motion and increased user comfort.

### 3.1.2 MODES 2 & 3: TRAJECTORY TRACKING CONTROL

The non-holonomic mobility drive, while mechanically simple, makes the control of the MOD I cane complex. To control the cane, a trajectory-tracking algorithm using non-holonomic feedback control has been implemented and tested. It is based on the nonlinear feedback posture-tracking algorithm developed by Samson [4]. The controller follows the trajectory by tracking the desired velocities of PAMM. Using this controller, PAMM converges to the trajectory asymptotically.

One advantage of this algorithm over many other non-holonomic control methods is that it has no control action when the desired speed is zero, even when position errors exist. It is thus most suitable for this application as it allows the user to stop and will not force the user to the trajectory. The desired speed along the trajectory can be a constant specified by the planner, emulating a nurse gently guiding the user

along a trajectory. In the third mode, PAMM uses this trajectory tracking controller to guide the user along a trajectory and uses a single DOF admittance model for controlling the desired speed. In this mode, PAMM allows the user to control the pace, without sacrificing its guidance role.

### **3.2 FIELD TRIALS OF THE PAMM INTERFACE**

Several field-tests of the MOD I system were made at the Cadbury Commons eldercare facility in Cambridge, MA. The MOD I system was used by men and women ranging in age from 75 to 95 years old. The system can be seen with an elderly user in Figure 4. The admittance model, ergonomics, and overall user acceptance of PAMM were evaluated.



**Figure 4: Field trials of MOD I System.**

It was first observed that, while walking, users held PAMM too far in front of them for it to provide good physical support. The users had difficulties keeping PAMM close to them possibly because of their fear of tripping over the base. To encourage users to hold PAMM close enough to receive support, an offset handle, shown in Figure 5, has been designed and fabricated.

At first glance, it might seem that the offset handle would not be able to provide physical support to the elderly. Measurements on a common four-point cane, however, show that the maximum downward force applied by a relatively heavy 177 lb. cane-user was approximately 90 N (20 lb.) From this upper bound figure, it was determined that the cane base, with its motors, electronics and batteries, provides sufficient ballast to prevent most users from tipping PAMM over. The offset handle has been evaluated in field

trials, as shown in Figure 4. Results show that this change permits the user to obtain more support from the device.

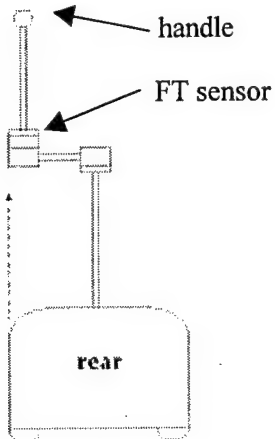


**Figure 5: Design of the offset handle.**

The recent field trials also provided information on user acceptance of PAMM. While users had a bit of trouble controlling PAMM at first, many of them adapted to it with practice. The elderly generally require "training" for common mobility aids, like canes and walkers. This is usually provided by physical therapists. The results show that certain admittance models make adaptation to PAMM difficult. The users, for example, found it difficult to guide the cane accurately when it used an admittance model with large damping. The users also had difficulty applying a forward force to move the cane along without also applying a torque to the handle. This resulted in rotational oscillations of the cane. Some of the users also had trouble adjusting to the non-holonomic nature of PAMM.

It would be premature to make any conclusions about the best type of interface (admittance model, for example) that should be implemented. Nevertheless, preliminary tests on a straight-line motion suggest a non-linear admittance model, that is, a mass-damper model with the damping coefficient that is a function of the cane velocity, would be effective. It is also likely the admittance model will need to be tuned to the user. This could be done off-line or the system could "self-tune" its characteristics to meet the needs of the user.

### **3.3 MAPPING, OBSTACLE IDENTIFICATION AND AVOIDANCE**

The concept is for PAMM to have an initial yet incomplete map of its environment to generate potential paths. Every time PAMM encounters an unknown obstacle, it would update its maps. However, an

eldercare facility is hardly static. People will move around, furniture will be moved and doors will open and close. Building effective maps in such dynamic environments is being considered in our research.

For obstacle detection and mapping, the MOD I system uses a half-ring of five acoustic ranging sensors. Each sensor consists of an electrostatic transducer and a ranging module that are both commercially available [5]. Experimental results show the system can easily detect the distance to people, chairs and sofas with an accuracy of 1.5 inches.

Some of our recent experiments suggested that the acoustic sensors might be able to recognize certain objects. The concept, shown in Figure 6, involves "listening" to an intermediary analog signal generated by the acoustic ranging module. The signal can be thought of as the amplitude of the echo as a function of time. An object like a chair could reflect the acoustic pulse at multiple points, creating a signal distinctly different from that generated by a "smooth" object, such as a wall, a pillar, or a slim person. In an uncluttered environment, the acoustic system was able to distinguish between a chair and a person with 90% accuracy using neural-nets. Initial results are promising, and more studies are being done to determine the limits this approach to object recognition.

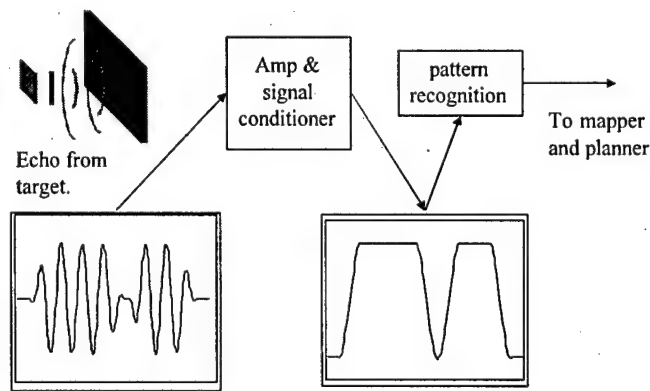


**Figure 6: Acoustic object recognition.**

#### 4. WORK TO BE DONE

This section summarizes areas of research we intend to make progress on by October 1999

##### 4.1 MOBILITY CONTROL

Three mobility control modes have been implemented and are described in section 3.1. A fourth mode is proposed in which MOD I PAMM will lead the user to a destination through a planned path, allowing the user to adjust the speed and deviate partly from the planned path. To implement this mode, we are exploring the application of Coordinated Jacobian Transpose Control method [6]. The controller specifies

a virtual spring and damper between the path and the PAMM. The user will be able to apply a force to the side and force PAMM some distance from the path but PAMM will react by gently guiding the user back. Analysis and experiments will be performed to determine the optimal parameters for this controller.

The admittance-based modes (1, 3 and soon 4) are complicated by the fact that the force/torque measurements are a superposition of two signals:

- (1) the user's intentions interacting with PAMM's motion, and
- (2) the forces exerted by users on the PAMM when it provides the physical support of the user.

The separation these two components is being addressed in ongoing research.

#### **4.2 MOD II MOBILITY DESIGN AND CONTROL**

Canes and walkers are the most common mobility aids for elderly people. A walker gives the user substantially more physical support than a cane would. The goal of the project for the third year is to develop a smart mobility aid in a walker configuration. While it is acceptable for the MOD I cane to use a non-holonomic drive, it is highly desirable for the MOD II system to have omni-directional or near omni-directional mobility. This type of mobility would make it much easier for the user to maneuver a walker through congested areas.

The main considerations in the design of the mobility platform are maneuverability, controllability, traction, stability, environment impact and simplicity. The overall weight and ease of storage are also design issues that concern both the caregiver as well as the user. Various existing mobility forms and wheel configurations were investigated. Due to their holonomic nature, many omni-directional drives demonstrate excellent maneuverability and controllability [7, 8, 9, 10]. These drives, however, can have several drawbacks, including complicated mechanisms, low loading capacity due to material strength limitations, and difficulty when they are used on floors with dirt, spilled food or other irregularities.

An objective of this study was the design of a PAMM mobility platform with conventional wheels that can achieve near omni-directionality. Using conventional wheels would ensure a simpler and more compact mechanism, a higher loading capacity and a greater robustness to poor environmental conditions. The resulting mobility platform consists of three or four assemblies, each of which have two individually controlled driving wheels. In developing such a mobility system, a major challenge will be designing a coordinated control system to minimize wheel slippage. In addition to reducing power-efficiency, wheel slippage may have a significant impact on the system's dead-reckoning accuracy.

#### **4.3 PAMM INTERFACE**

A conceptual design of the user-machine interface for control has been developed, which is based on the force-torque sensor signals measured at handle. PAMM would ideally be able to estimate some measure of mental clarity and interpret intentions of the user. In cases where the user shows signs of confusion, PAMM would take an active role in leading the user to the intended destination. This functionality is still being developed.

#### **4.4 OBSTACLE DETECTION AND MAPPING**

The system has some difficulty detecting tables that have widely spaced legs, and obstacles close to PAMM that are less than a foot high. To remedy this, it is proposed to angle the front 3 sensors downward and angling and an additional three sensors upward. This modification will be completed by October 1999.

### **5. CONCLUSIONS**

Experimental results of the MOD I (cane based system) field tests are very promising. They are providing information that is being integrated into the system design concept. Preliminary studies of the MOD II (walker based system) are well underway.

## 6. REFERENCES CITED

---

- [1] L. J. Barton, "A Shoulder to Lean On: Assisted Living in the U.S.," *American Demographics*, 1997.
- [2] S. Dubowsky, "Personal Aid for Mobility and Monitoring: A Helping Hand for the Elderly," Home Automation and Health Care Consortium Report, 1998.
- [3] N. Stelman, *Design and Control of a Six-Degree-of-Freedom Platform with Admittance*, Master's Thesis, Department of Mechanical Engineering, MIT, 1988.
- [4] C. Samson and K. Ait-Abderrahim, "Feedback control of a non-holonomic wheeled cart in cartesian space," *Proc. IEEE Int'l Conference on Robotics and Automation*, Sacramento, CA, pp. 1136-1141, 1991.
- [5] <http://www.polaroid-oem.com/american/new/usp.htm>
- [6] C. Sunada, D. Argaez, S Dubowsky, and C. Mavroidis, "A coordinated Jacobian Transpose Control for Mobile Multi-limbed Robotic System," *Proc. IEEE Int'l Conference on Robotics and Automation*, San Diego, CA May 8-13, 1994.
- [7] S. M. Kilough and F. G. Pin, "Design of an omni-directional and holonomic wheeled platform prototype," *Proc. IEEE Int. Conference on Robotics and Automation*, Nice, France, May 1992, pp. 84-90.
- [8] M. West and H. Asada, "Design of ball wheel mechanisms for omni-directional vehicles with full mobility and invariant kinematics," *Journal of Mechanical Design*, June 1997, Vol.119 pp. 153-161.
- [9] P. F. Muir, and C. P. Neuman, "Kinematic modeling for wheeled mobile robots," *Journal of Robotics Systems*, 4, 1987.
- [10] H. Hoyer, R. Hoelper, "Intelligent omni-directional wheelchair with a flexible configurable functionality," *Proc. RESNA Annual Conference*, Nashville 1994.

# **Design and Control of an Active Mattress for Moving Bedridden Patients**

**H. Harry Asada**  
Principal Investigator

**William H. Finger**  
Research Assistant

## **Abstract**

A new mechanism for transporting a bedridden patient in an arbitrary direction while lying comfortably on the bed is developed. A wave-like periodic motion is generated on a mattress surface by activating the individual coil springs which constitute the mattress. The whole or part of the patient body is moved by this periodic surface movement. Varying the periodic trajectory and coordination pattern yields various movements of the patient, i.e. translation and rotation of the whole body, changing the posture of the limbs, etc. First, functional requirements for active mattresses are provided, and a prototype system is designed and built. A variety of control algorithms are developed for moving a patient in various ways. Periodic trajectory and coordination patterns are designed in order to move the patient smoothly despite uncertainties in load distribution and actuator dynamics. A discrete-event control system using a Petri net is developed for coordinating and synchronizing many axes of motion. Furthermore, a high-level controller is developed to perform closed-loop positioning of the human body, based on the estimation of the body's location using pressure sensors distributed across the bed surface. Experiments using a prototype mattress demonstrate smooth body motion in both the x and y directions and rotation within the plane of the mattress surface.

## 1 Introduction

Patient mobility is a growing concern for health care facilities in the United States and abroad. In nursing homes alone, there are 1.5 million bedridden patients in the US [HCFA Survey, 1997]. These patients must be assisted in transferring between beds and wheelchairs, as well as transferring to toilets. They must be turned every two hours to prevent decubitus ulcers, or bedsores, from forming. Approximately 25% of all patients in nursing homes will suffer from these painful sores [Decubitus Foundation, 1998]. In order to meet the needs of the patients, caregivers are forced to move the patients manually, a very labor intensive task. According to a survey by [Garg et al, 1992], on average a nursing assistant must perform 50.8 such labor intensive tasks every eight hour shift. As a result, one out of two nursing assistants surveyed received treatment for back injuries in a three year period, and one out of three lost at least one work day. In terms of Lost Work Day injuries, being a nursing home employee was the most dangerous service job in America in 1996, with 8.2 full time employees losing a day for every 100, on average [Decubitus Foundation, 1998]. Many of these injuries are to the back or shoulder; 1 in 22 nursing assistants lost a workday from a back or shoulder injury in 1994 [OSHA, 1996]. These are only the injuries which are reported. Surveys show that 66 to 75% of back injuries go unreported [Owen et al, 1993 ,Garg et al, 1992]. These injuries result in a cost of \$24 billion each year [Garrett et al, 1992].

There have been efforts to train nursing assistants in the proper ways to lift and manipulate patients. However, one biomechanical analysis suggests that the stresses required to move patients manually will always be unsafe for nurses of average strength [Garg et al, 1992, NIOSH, 1981]. Therefore, there is a need for mechanical devices to reduce these stresses. These devices are arranged in three main categories: assistive devices, such as belts, slings, and draw-sheets; hoists; and other devices such as conveyors, turntables, and rollers [Garg et al, 1991]. Although many such devices are available, it has been determined that 98% of patient transfers are still performed with manual techniques [Garg et al, 1992]. Many reasons are associated with this lack of use: insufficient training, danger to patients, uncomfortable for patients, insufficient personnel to operate the equipment, strength requirements, excessive transfer times, etc. Hoists, such as Hoyer, Trans-Aid, and Ambulift were refused by psychogeriatric patients who might cause the hoist to topple [Garg et al, 1992]. In

terms of transfer time, manual lifting operations typically require 18 seconds, while setup and use of a hoist requires about 120 seconds. [Garg et al, 1991].

In the engineering research community, efforts are underway to develop better systems to increase patient mobility. To eliminate bed-wheelchair transfer, a hybrid bed/chair system, RHOMBUS, has been developed and tested [Mascaro et al, 1997]. Recently an active bed with a mechanical linkage mechanism succeeded in moving a human lying on the bed by creating a surface wave in one direction [Spano et al, 1998]. Despite these endeavors, aids for the bedridden that provide diverse functionality have not been developed. Patients must be moved two dimensionally, and individual limbs must be moved, while the patient lies comfortably upon the bed.

The goal of this paper is to establish basic technologies involved with the development of a new type of active bed that provides both high mobility and sleep comfort. Special actuators imbedded into a mattress generate periodic surface movements that transfer the bedridden in an arbitrary direction. A comfortable bed surface has been obtained by making use of the springs available in a commercial mattress. When activated, these springs generate wave-like motions on the bed surface that move the patient. The following sections describe the principle and algorithms used in the surface wave active mattress, control design, prototyping, and experiments performed.

## 2 Design

### 2.1 Functional Requirements and Design Approach

The objective of the active mattress is to assist caregivers in positioning and transporting bedridden patients. The mattress must be comfortable and appropriate for long-term care. Accomplishing this objective requires that the following functional requirements be met:

- 1) The bed surface must provide at least the same level of comfort as that of home-use or hospital beds,
- 2) The whole patient body must be moved in an arbitrary direction on the bed surface without lifting the body,
- 3) The limbs of the patient must be moved individually while lying on the bed, and

4) The motion must be smooth, with minimal jerk and disturbance to the patient.

To meet the first requirement, we employ a standard commercial mattress whose spring characteristics have been tuned to support the patient. To meet the second and third requirements, the coil springs involved in the mattress are instrumented and activated, as shown in Figure 1. Namely, the tip of each coil spring is moved horizontally in both the x and y directions as well as vertically in the z direction, through the use of actuators imbedded in the mattress. The coordination of the motion of the individual coil springs would create a variety of body movements, including both whole body transfer and individual limb movements. Furthermore, these active springs would be controlled in such a way that the jerk and disturbance induced by the activation of the coil springs is minimized while moving the patient body, satisfying the last functional requirement. When these coil springs are not activated, the mattress becomes a standard, passive mattress whose coil springs have been tuned to maximum sleep comfort by the bed manufacturer. Therefore the same level of comfort as the original mattress can be retained.

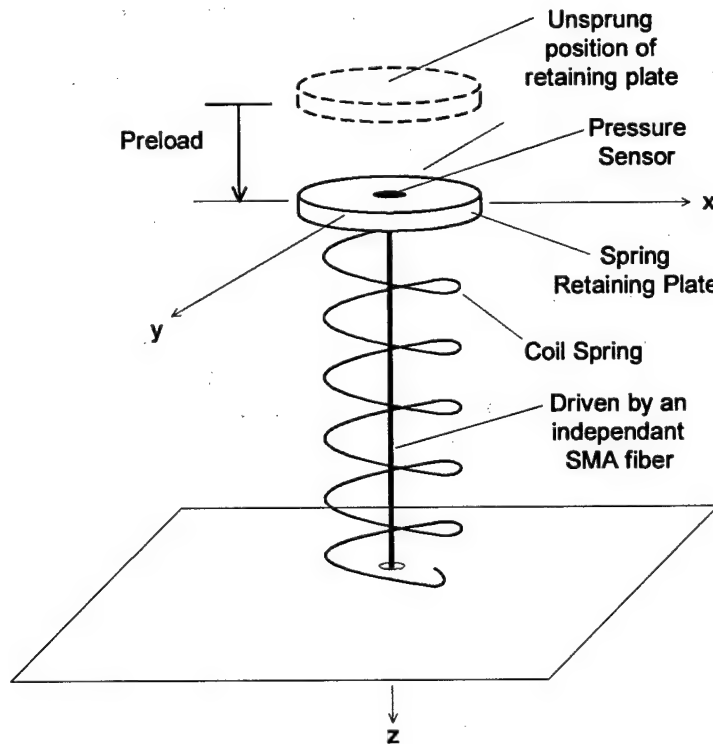


**Figure 1. Active coil spring.**

Figure 2 illustrates how the active mattress works. Coordinating an array of active coil springs creates periodic motions that transfer a body in one direction, e.g., +x direction. First, one set of springs (shown in solid

lines) is moved in the  $+x$  direction (a). Second, it is detached from the body (b), then moved in the  $-x$  direction to its starting position (c). Lastly the set of springs is reattached (d), and the whole process is repeated. If the second set of springs (shown with dotted lines) moves 180 degrees out of phase with this motion, the body may be moved continually in the  $x$  direction. Combined with similar motions in the  $y$  direction we can generate body motion in arbitrary directions. Furthermore, changing the state of  $z$ -axis actuators in coordination with the horizontal axes can cause the body to rotate, or generates localized body motions, as will be addressed in the following sections.

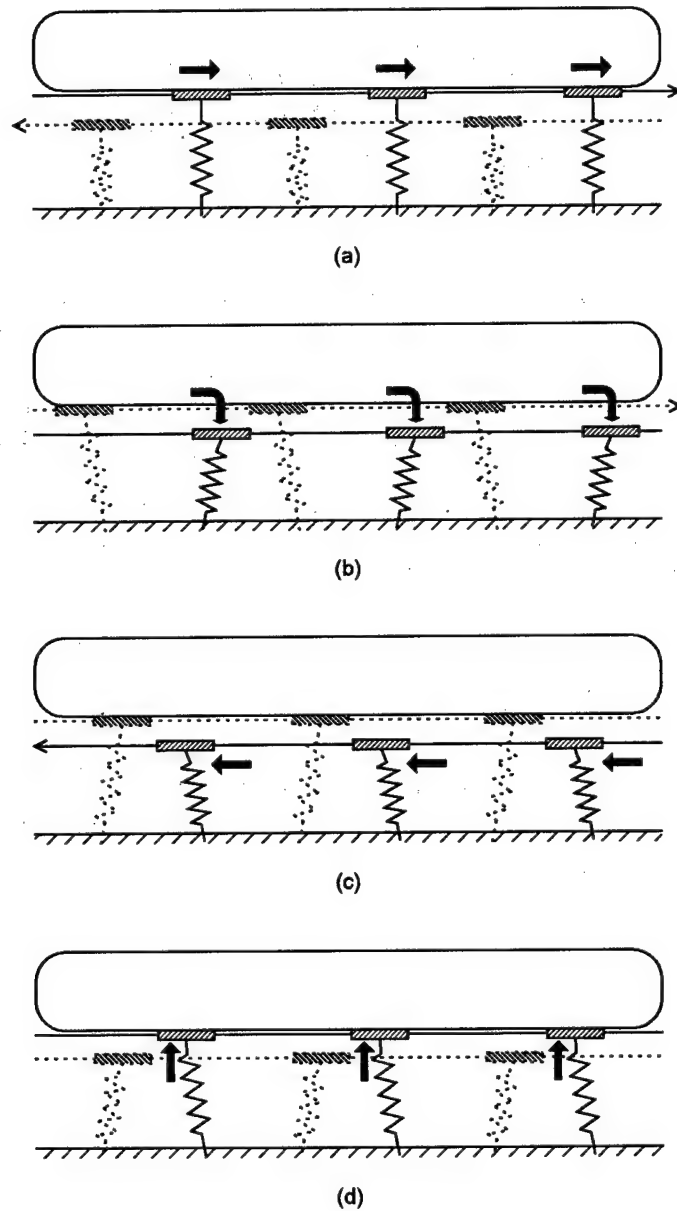


**Figure 2. Periodic motions of connected coil springs for transferring a body in the  $+x$  directions.**

## 2.2 Prototype

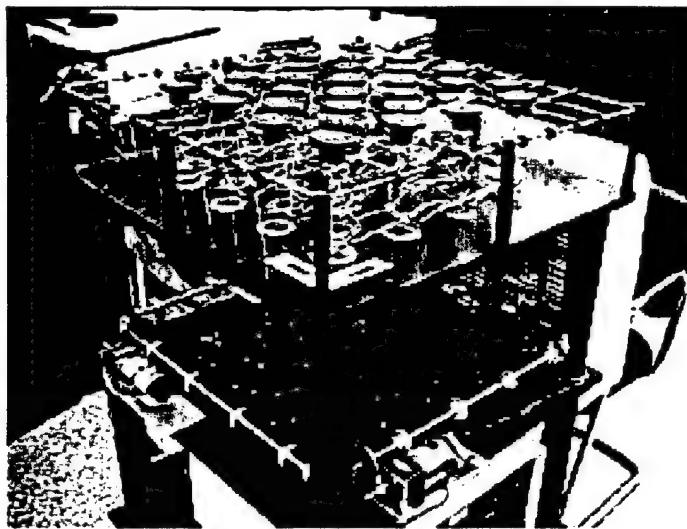


**Figure 3. Surface wave prototype.**

Figure 3 shows the first prototype of the active mattress to meet the functional requirements described above. The mattress contains 32 coil springs taken from a commercial bed. Figure 1 shows an individual coil spring attached to actuators in three directions. Each spring moves independently in the z direction with a shape memory alloy fiber actuator connecting the top plate of the spring to the base frame of the mattress. Shape memory alloy fibers are compact and powerful, as well as inexpensive compared with traditional actuators. Their limitations are low bandwidth and nonlinear behavior. Since in the prototype the vertical axis needs only an on-off motion to detach and reattach with the body, shape memory fibers suffice for the initial design.

During the periodic motion, illustrated in Figure 2, the z axis takes two positions, a high position and a low position. At the high position, the active spring is attached to the patient body and supports it from beneath. At the low position, the active spring is detached from the body and is free to move in horizontal directions. One of the fundamental requirements for the active mattress is to support the patient body at all times, even while some springs are detached. Therefore, the springs in the high position must be able to bear the load of the body, without deflecting so much that the other springs in the lower position cannot be detached. To prevent excessive deflection, the coil springs are given a preload, as shown in Figure 1. Each spring can then support a weight up to the preload before any deflection occurs. In the initial prototype, the preload was adjusted by changing the length of the cable strung between the top plate and the shape memory fiber.

Conversely, the horizontal motion needs higher accuracy and faster speed of response than that of the z axis. Therefore, electromechanical drives using DC servo motors are employed for driving the springs in the x and y axes. As illustrated in Figure 2, the individual coil springs need not be moved independently. The set of all springs can be divided into several subsets and actuated together, in order to generate periodic motions for transferring the body. In the prototype mattress shown in Figure 3, two independent servo motors are used for driving each horizontal axis. Figure 4 depicts the configuration of cables connecting individual springs to servo motors. Along the x axis, every second row of coil springs is connected by cables and thereby moved together with the same actuator, yielding displacement  $\Delta x_1$ , while the remaining nodes are moved by a second actuator an amount  $\Delta x_2$ . Likewise, two actuators in the y direction provide displacements  $\Delta y_1$  and  $\Delta y_2$ , respectively, for columns of coil springs.

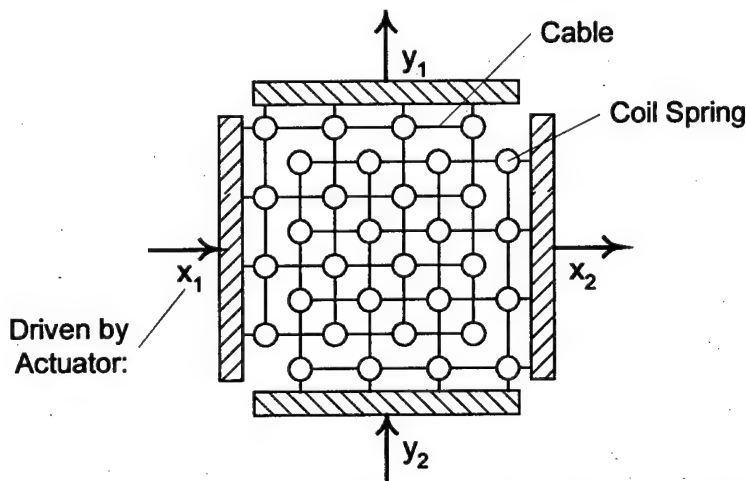


**Figure 4. Horizontal cable configuration connecting coil springs to servo motors.**

The coordination of these four actuators with the z axis actuators creates a variety of periodic motions on the mattress surface that allow the human body to move in an arbitrary direction. A variety of control algorithms will be described in the next section.

### 3 Algorithms

#### 3.1 Notation

The control algorithm briefly described in the previous section is generalized and formally presented in this section. It will be shown that diverse motions of the human body can be created by coordinating horizontal and vertical motions in different modes. To represent diverse motions in a unified manner, we introduce the following notation.

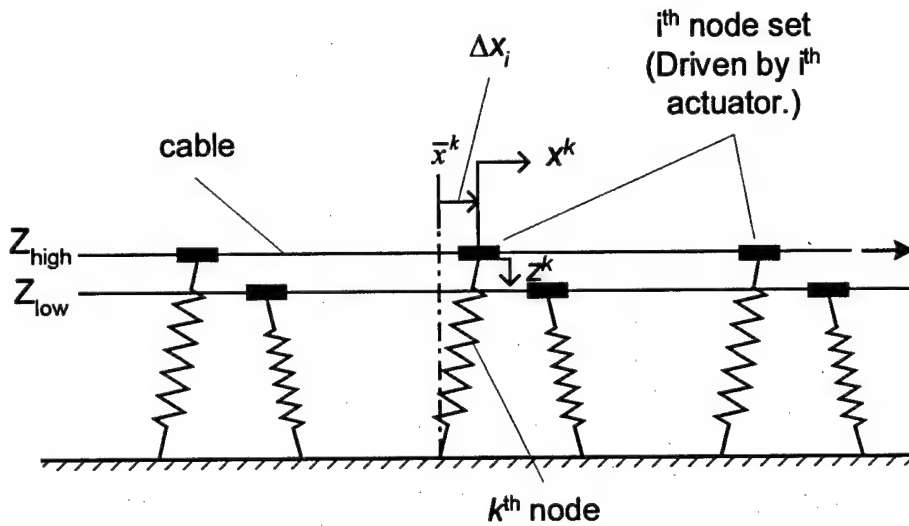


Figure 5. Nodal connections.

Figure 5 shows the schematic of the active mattress system. For the sake of simplicity, the figure shows a single array of active springs along the  $x$  axis, although the actual mattress is two-dimensional. Each active spring, termed a “node”, is numbered 1 through  $n$ . The coordinates of the tip of the  $k^{\text{th}}$  node are denoted  $(x^k, y^k, z^k)$ ,  $k = 1, \dots, n$ .

As mentioned previously, each node is controlled individually in the  $z$  direction to take either a high or low position.

$$z^k = \begin{cases} Z_{\text{high}} : & \text{high position,} \\ & \text{attached to the body} \\ Z_{\text{low}} : & \text{low position,} \\ & \text{detached from the body} \end{cases} \quad (1)$$

In this analysis, we assume that the preload in the node is sufficient to support the body without significant deflection. The horizontal coordinates of the  $k^{\text{th}}$  node are varied from its unforced position,  $\bar{x}^k$  and  $\bar{y}^k$ , to a deflected position by the horizontal actuators driving the  $k^{\text{th}}$  node:

$$\begin{aligned} x^k &= \bar{x}^k + \Delta x_i \\ y^k &= \bar{y}^k + \Delta y_i \end{aligned} \quad (2)$$

where  $\Delta x_i$  and  $\Delta y_i$  are deflections generated by the  $i^{\text{th}}$  actuators of the x and y axes, respectively. As mentioned before, nodes are grouped together for horizontal movements, and are driven by several independent actuators. A set of nodes moved simultaneously by the same horizontal actuator is referred to as an *actuator node set*. Let  $N$  be the number of node sets, and  $S_i$  be the  $i^{\text{th}}$  node set,  $1 \leq i \leq N$ , containing all nodes driven by the  $i^{\text{th}}$  actuators of both the x and y axes.

$$S_i = \{k \mid \text{All nodes connected to the } i^{\text{th}} \text{ horizontal actuators}\} \quad (3)$$

Note that two actuators are used for moving the nodes in  $S_i$ ; one for the x axis and the other for the y axis. Note also that any actuator node sets  $S_i$  and  $S_j$  are exclusive, and every node belongs to one and only one actuator node set.

### 3.2 Body Motion Modes

#### *Whole Body Translation*

In this case we wish to move a body horizontally in the direction of angle  $\theta$  from the x axis. The node sets are coordinated such that:

$$\Delta x_i = h(t_i) \cos \theta \quad (4)$$

$$\Delta y_i = h(t_i) \sin \theta \quad (5)$$

where  $h(t_i)$  is a periodic continuous function of time  $t_i$  that generates a reciprocative motion in the horizontal direction. All node sets move along the same trajectory, and therefore use the same function  $h$ , but have different phase angles. The time  $t_i$  is given by:

$$t_i = t + T \frac{\phi_i}{2\pi} \quad (6)$$

where  $T$  is the period of the function  $h$ , and  $\phi_i$  is the phase difference between node sets  $i$  and  $i-1$ . The node sets will typically be equally spaced in phase:

$$\phi_i = \frac{2\pi}{N}(i-1), \quad i = 1, \dots, N. \quad (7)$$

Figure 5 illustrates a group of hypothetical functions,  $h(t_1)$ ,  $h(t_2)$ , ...  $h(t_N)$ . The functions are monotonically increasing for the period of  $T_I$  and monotonically decreasing for the period of  $T_D$ . The  $N$  functions are out of phase, with  $2\pi/N$  of phase difference between them.

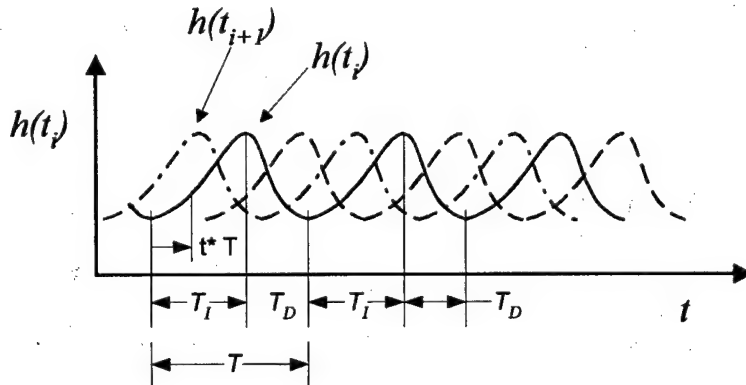


Figure 5. Hypothetical trajectory of horizontal motion.

The vertical motion of each node is synchronized with the horizontal motion so that the node is attached to the body only when the function  $h(t_i)$  is increasing. (i.e., the period  $T_I$  shown in Figure 6.) In this way only forward motion is transmitted to the body. If the  $k^{\text{th}}$  node belongs to the  $i^{\text{th}}$  node set, the  $z$  axis of this node is commanded to take the following position:

$$z^k(t_i) = \begin{cases} Z_{\text{high}}; & 0 < t_i^* < \frac{T_I}{T} \\ Z_{\text{low}}; & \text{otherwise} \end{cases} \quad (8)$$

where

$$t_i^* = \left[ \frac{t}{T} + \frac{\phi_i}{2\pi} \right] \quad (9)$$

Note that the operator  $[\bullet]$  takes on a value between 0 and 1, and  $t_i^*$  represents a time index, normalized by period  $T$  and shifted by phase angle  $\phi_i/2\pi$ , as shown in Figure 6. Nodes in the  $i^{\text{th}}$  node set move forward for  $0 < t_i^* < T_i/T$ , and the z axis is at  $Z_{\text{high}}$  during this period, so that the node is attached to the human body and transmits horizontal motion to the body.

The above control scheme requires all the z axis actuators to be moved, but those actuators that are not under the human body need not be activated. To save energy they should be kept inactive. This control mode provides a general scheme for coordinating horizontal and vertical movements in order to transfer a body by reciprocative motion. Detailed control issues will be addressed in the following sections.

#### *Local Movements*

This control mode allows one or more segments of the body to be moved across the bed surface, while other parts remain stationary. To accomplish this, at least one node set is moved in the same way as in the Whole Body Translation described above, while the remaining node sets are kept stationary in the horizontal direction, so that the body is supported from beneath at all times and the rest of the body is held stationary. To combine these two functional requirements in a non-conflicting manner, the z coordinate of each node is controlled such that:

- Nodes are detached from the body if they are moving horizontally and are beneath the part of the body to be held stationary,
- Nodes are attached to the body if they are moving forward and are beneath the part of the body to be transferred,
- Nodes are detached from the body if they are moving backward in the horizontal direction, and
- Nodes that are kept stationary in the horizontal directions are attached to the body if the nodes are beneath the part of the body to be held stationary, or if there is no other node set supporting the part of the body to be

moved (i.e., in the case of two node sets, when one node set is moving backwards, the other must support the body.)

Let us define a set  $S_A$  as all nodes under the part of the body to be moved, and  $S_B$  as all nodes under the part of the body to remain stationary. Let us assume that node sets  $S_i$ ,  $i = 1, \dots, N_m$ , move both horizontally and vertically as described in Whole Body Translation. The remaining node sets,  $S_i$ ,  $i = N_m + 1, \dots, N$ , remain stationary in the horizontal direction. We then obtain the following expressions for this control mode:

For  $k \in S_i$ ,  $1 \leq i \leq N_m$  :

$$\Delta x_i = h(t_i) \cos \theta$$

$$\Delta y_i = h(t_i) \sin \theta$$

$$z^k(t) = \begin{cases} Z_{high} & \text{if } \left( k \in S_A \text{ and } 0 \leq t_i^* < \frac{T_I}{T} \right) \\ Z_{low} & \text{if } \left( k \in S_B \right) \text{ or } \\ & \left( k \in S_A \text{ and } \frac{T_I}{T} \leq t_i^* < 1 \right) \end{cases} \quad (10)$$

For  $k \in S_i$ ,  $N_m + 1 \leq i \leq N$  :

$$\Delta x_i = \Delta y_i = 0$$

$$z^k(t) = \begin{cases} Z_{high}; & \text{if } \left( k \in S_B \right) \text{ or } \\ & \left( k \in S_A \text{ and } z^j = Z_{low} \right. \\ & \left. \forall j \in S_1 \cup \dots \cup S_{N_m} \right) \\ Z_{low}; & \text{if } \left( k \in S_A \text{ and } \right. \\ & \left. \exists j \in S_1 \cup \dots \cup S_{N_m} \right. \\ & \left. \text{such that } z^j = Z_{high} \right) \end{cases} \quad (11)$$

In general, this requires at least one additional set of nodes than is required to perform a given motion; this node set or sets remains stationary with respect to the x and y directions, and its nodes stay in contact with the stationary portion of the body, while the remaining nodes are detached from the moving portion of the body. In the special case of  $N = 2$ , the stationary node set is required to periodically support the body, while the single moving node set is detached from the body. Note that those nodes which are not under the body (i.e.,  $k \notin S_A \cup S_B$ ) should remain inactive in order to conserve energy.

### *Moving Two Segments of the Body in Opposite Directions*

By modifying the above local movement control mode, two segments of the body can be moved in two opposite directions, such as the legs opened or closed. Assume that body segments  $A$  and  $B$  are to be moved in opposite directions to each other. The  $z$  axis motion of the nodes beneath  $A$ ,  $k \in S_A$ , and the ones beneath  $B$ ,  $k \in S_B$ , are set 180 degrees out of phase so that forward motion alone may be transmitted to body  $A$  while only motion in the opposite direction is transmitted to  $B$ .

For  $k \in S_A$  :

$$z^k(t) = \begin{cases} Z_{high}; & 0 \leq t_i^* < \frac{T_I}{T} \\ Z_{low}; & \frac{T_I}{T} \leq t_i^* < 1 \end{cases} \quad (12)$$

For  $k \in S_B$  :

$$z^k(t) = \begin{cases} Z_{low}; & 0 \leq t_i^* < \frac{T_I}{T} \\ Z_{high}; & \frac{T_I}{T} \leq t_i^* < 1 \end{cases}$$

To keep the remaining part of the body stationary, i.e., the body segments other than  $A$  and  $B$ , the above control mode must be augmented by combining the local movement control mode given by equations (10) and (11). To save energy, those  $z$  axis actuators under the human body alone should be activated. A special case of this algorithm allows us to rotate the entire body: the Whole Body Rotation mode. This is done by creating two anti-parallel velocities, symmetric to and at equal distances from the center of mass of the body, perpendicular to its longitudinal axis.

## 4 Control

### 4.1 Trajectory Design

The active mattress moves a patient body through periodic and intermittent movements of an array of active nodes. To generate continuous and smooth movements, an array of nodes must be coordinated with each other, and the trajectory of each node motion must be tailored so that smooth transitions may be accomplished. While

achieving these goals, we endeavor to move the patient as quickly as possible, limited by safety and patient comfort.

One of the main difficulties in achieving these goals has been the limited performance of the shape memory alloy actuators. They are slow to respond, and their response depends on non-linear heat transfer phenomena which vary depending on ambient conditions. Therefore it is difficult to use them accurately in an open loop configuration, because the time for reconnection and disconnection with the body is uncertain. The node trajectory and coordination method must be optimized so that smooth patient transfer can occur despite actuator limitations. We consider the following trajectories.

### *Circular*

Figure 7 shows a circular trajectory in a vertical plane. Without loss of generality, we assume the plane of the trajectory is parallel to the x axis. The periodic function  $h(t_i)$  introduced in section 3.2 is simply the projection of this circular trajectory onto the horizontal plane. Namely,  $h(t_i) = R \sin\left(\frac{2\pi}{T}t_i\right)$ .

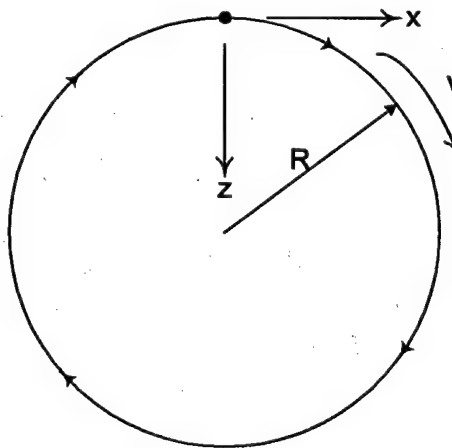


**Figure 7. Circular trajectory**

This trajectory is similar to the motion caused by natural waves observed on the surface of bodies of water. In these waves, water molecules travel through circular trajectories. The circular trajectory is fairly smooth during horizontal motions, as long as the number of node sets  $N$  is large and the phase difference between adjacent node sets is small. However, as  $N$  becomes smaller, there is an undesirable z-axis motion created by

the transfer of weight from one set of nodes to another. The total magnitude of this motion is dependent on the phase difference between the nodes and the radius of the trajectory, as given by:

$$\Delta Z = R(1 - \cos \pi/N) \quad (13)$$

where  $\Delta\phi$  is the phase lag between adjacent nodes, and  $R$  is the radius of the trajectory. The circular trajectory can be created using a piston and crank mechanism, and was used for the surface wave actuator [Spano et al, 1998]. However, since we make use of SMA fiber actuators, this trajectory would be highly distorted, and because the z-axis perturbation which occurs with  $N = 2$  is quite significant, this trajectory is not desirable for our design.

#### *Rectangular*

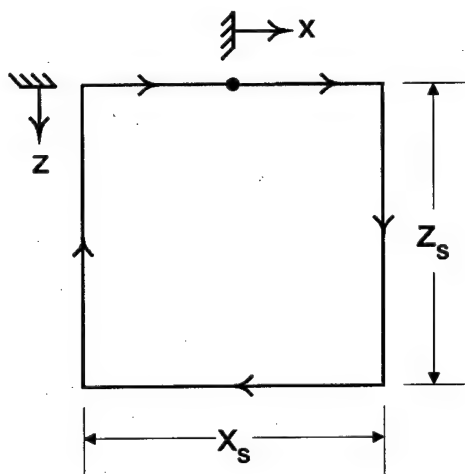


**Figure 8. Rectangular trajectory geometry.**

To eliminate this unwanted vertical perturbation, we can employ a rectangular trajectory, as shown in Figure 8. This trajectory causes no vertical perturbation, since the path in contact with the body is a straight line. Another advantage to this trajectory is its simplicity. It can be easily created using decoupled axes. Also, with two node sets at 180 degrees of phase difference, the nodes are always travelling in opposite directions with this trajectory, so only one actuator per axis is needed. The node sets would be geared so that they move in opposite directions. The simplicity of this trajectory allows it to perform complex maneuvers that might otherwise require many actuators per axis.

The disadvantage of this trajectory is that at the end of each horizontal motion the node must come to a stop, and wait for the adjacent node to complete its motion. Also, at the end of each vertical motion the node must be accelerated quickly, inevitably causing jerky motion. Therefore this trajectory violates our fourth functional requirement.

### *Trapezoidal*

To overcome the limitations of the previous trajectories, a hybrid trajectory has been designed. This trajectory has the benefits of zero vertical perturbation of the body, due to the straight line body contact path, combined with smooth horizontal motion. The horizontal motion is smooth since before the node makes contact with the body, it has obtained the velocity of the body; therefore, the body need not come to a stop for reconnection to occur. The same occurs during disconnection, but in reverse; the node disconnects, and then begins to change its horizontal velocity. Since this trajectory meets our functional requirements, we adopt it and develop a complete control method for coordinating multiple node sets.

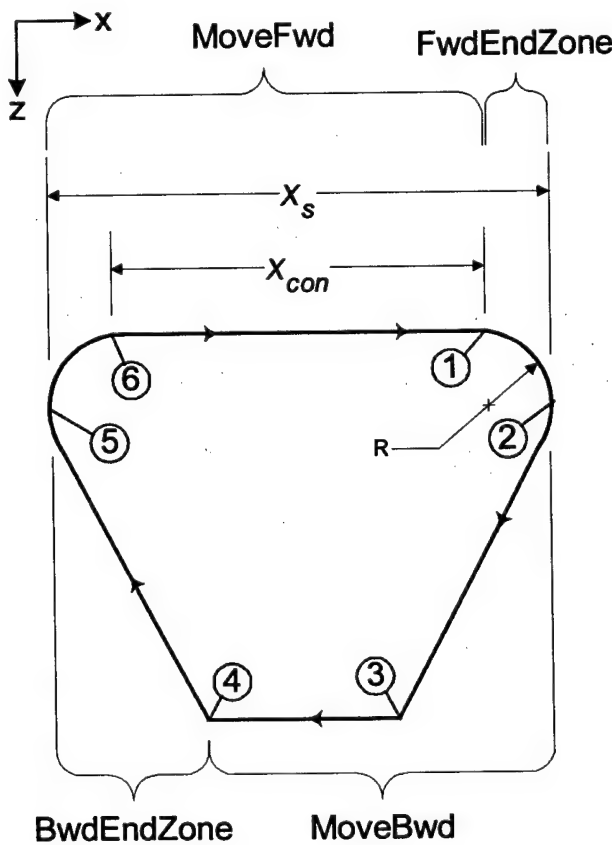


Figure 9. Trapezoidal trajectory.

Let  $v_{fwd}$  be the horizontal velocity of each node set moving forward (from point 5 to 2 in Figure 9), and  $v_{bwd}$  the velocity moving backward (from point 2 to 5). While moving backwards, the nodes do not support the body. Therefore increasing the backward velocity  $v_{bwd}$  reduces the duration when the nodes are not in contact with the body. Reducing this non-contact period means that more node sets may be supporting the body. This results in higher stability and comfort for the patient. Let us obtain conditions on the velocities  $v_{fwd}$  and  $v_{bwd}$  so that only  $\bar{N}_{dis}$  node sets are in time-average disconnected from the body, and  $(N - \bar{N}_{dis})$  node sets are supporting the body during the transfer process.

Let  $x_s$  be the horizontal stroke of each node, as shown in Figure 9. Assuming instantaneous horizontal accelerations, we can derive the following equation for the period of the trajectory:

$$T = \frac{x_s}{v_{fwd}} + \frac{x_s}{v_{bwd}} \quad (14)$$

The time spent by each node set when disconnected or being disconnected from the body is given by

$$T_{dis} = \frac{x_s - x_{con}}{v_{fwd}} + \frac{x_s}{v_{bwd}} \quad (15)$$

In time average, the fraction of  $T_{dis}$  to  $T$  agrees with the fraction of the number of disconnected node sets  $\bar{N}_{dis}$  to the total number of node sets  $N$ .

$$\frac{T_{dis}}{T} = \frac{\bar{N}_{dis}}{N} \quad (16)$$

Substituting equations (14) and (15) into equation (16) yields:

$$\frac{v_{bwd}}{v_{fwd}} = \frac{N - \bar{N}_{dis}}{\bar{N}_{dis} + N(b-1)} \quad (17)$$

where

$$b = \frac{x_{con}}{x_s} \quad (18)$$

Note that in order to reduce the average number of disconnected node sets, the ratio of backward velocity  $v_{bwd}$  to forward velocity  $v_{fwd}$  must be increased. Note also that although the number of node sets is small, the minimum

number of node sets supporting the body at any time may be as many as  $N - 1$ , if the backward velocity is much faster than the forward velocity. The average number of node sets supporting the body will always be greater than 1, because of brief periods of overlap between the node sets, when more than one set is in contact. This phenomenon is demonstrated in Section 5: Experiments.

#### 4.2 Coordination Control

The trapezoidal trajectory has unique features which allow smooth, stable movements. To achieve these movements, however, all actuator motions must be well coordinated. Not merely coordinating the vertical actuators with the horizontal actuators, but the node set as a whole must be coordinated with other node sets. Standard fixed trajectory controls do not apply to this system, since discrete contact/non-contact states must be controlled during the process. Sensors are needed for detecting contact and non-contact between each node and the patient body. Occurrence of connection and disconnection cannot be predicted precisely due to the unpredictable nature of the z-axis shape memory alloy and the uneven surface of the human body. As mentioned in Section 2.2, pressure sensors attached to the top plates of active springs are used for detecting contacts with the patient body in order to synchronize the multiple axes and node sets. This synchronization is based on occurrence of events rather than time, hence the system is treated as a discrete-event control system.

In this section a discrete event controller using a Petri net is developed. Petri nets are powerful tools for describing concurrent discrete-event systems containing many subsystems which are independent but are synchronized with other subsystems based on discrete events [Peterson, 1981]. The active mattress developed in this paper consists of many subsystems, termed *nodes*, which are grouped together as a node set. Furthermore each node consists of horizontal and vertical axes that are controlled by different actuators. It is inconvenient to model this system as a standard finite state machine, since combining subsystems into one large finite state machine incurs complicated problems, including redefinition of states. In Petri nets, states are defined independently for individual subsystems rather than for the whole combined system, and interactions among the subsystems are represented explicitly and effectively.

Figure 10 shows a Petri net representation for discrete-event control of the active mattress system having two independent node sets. For simplicity, only x-axis is shown and the y-axis is eliminated in the figures. All the discrete states, along with input and output symbols, are represented by circles, termed *places*, and transitions among the places are shown by arcs and bars, following the standard Petri net convention. Transitions have been lettered *a* through *n* for the subsystem for node set 1 and others.

The lower part of the Petri net contains the horizontal and vertical axes subsystems comprising the following states:

Horizontal axes:

MoveFwd	Moving forward, from point (5) to (1) in Figure 9
FwdEndZone	End zone of forward motion, from (1) to (2)
MoveBwd	Moving backward, from (2) to (4)
BwdEndZone	End zone of backward motion, from (4) to (5)

Vertical axes:

AllCon	All the nodes in the same node set are at $Z_{high}$ and connected to the body
MoveLow	Moving towards the $Z_{low}$ position
AllDiscon	All the nodes in the same node set are at $Z_{low}$ and disconnected from the body
MoveHigh	Moving towards the $Z_{high}$ position

The left half of the network in the figure represents the first node set; the right half is the second node set. There are two cyclic loops involved in each node set; the outer loop, MoveFwd—FwdEndZone—MoveBwd—BwdEnd-Zone, represents the horizontal motion, while the inner loop represents the vertical motion. These two loops are synchronized at specific transitions. For example, at transition *d* in the network, horizontal motion is reversed from forward to backward after AllDiscon has been achieved, i.e. all the nodes have been disconnected from the body. This is to prevent the body from being pushed backwards by the nodes returning to the original horizontal position. The arc from AllDiscon to this transition bar *d* requires the place AllDiscon to possess a token. Likewise transition *e* is prohibited unless the nodes in the first node set have arrived at FwdEndZone and all the nodes in the second node set have been reconnected to the body, as indicated by a token at AllCon in the right half network. This set of conditions assures that the patient body is supported all the time as the supporting nodes are changed from the first to the second node sets. Transition *g* is fired when the horizontal axis arrives at

the end zone of the backward motion, i.e. BwdEndZone, and all the nodes have been disconnected. Then the vertical actuators begin to move upwards. After transition  $g$  fires, transition  $b$  is enabled, which changes the direction of the horizontal motion. This is to allow these nodes to gain the same speed as the patient body before reconnections occur.

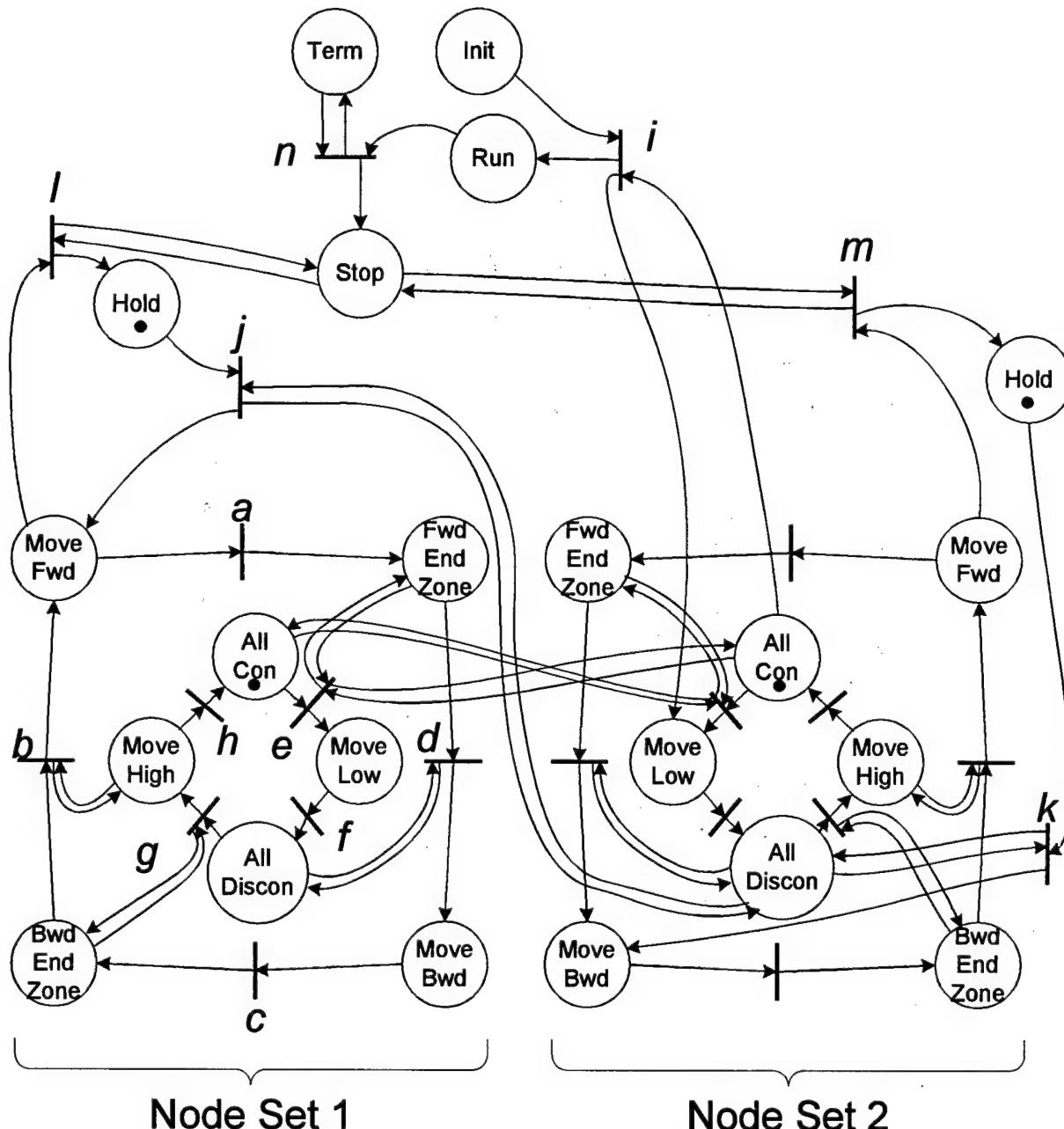


**Figure 10. Petri net for node set coordination.**

In addition to this basic coordination control, startup and termination procedures must be added to the Petri net. Since this active mattress system exhibits cyclic movements for both horizontal and vertical axes, the

process cannot be stopped at an arbitrary state. Before stopping, the process must come to the state where both node sets are at the  $Z_{high}$  position, supporting the body, and the horizontal axes are in the middle or home position. To start the cyclic process, the two node sets must be brought to opposite states with 180 degrees of phase difference. The upper part of Figure 10 represents these procedures, which use the following additional states and inputs:

Init	Input for initiating the cyclic process
Term	Input for terminating the cycle
Run	System is running
Stop	Terminating the cycle and coming to the home state
Hold	Temporarily holding the cycle

To initiate the process, a token is placed at Init. Under normal conditions, this controller holds the process by placing tokens at both AllCon and Hold in both node sets, as shown by dots in the figure. Having a new token at Init enables transition  $i$  to fire. This transition moves a token to Run, removes another token from AllCon in the second node set, and delivers it to MoveLow. This allows all the nodes of the second node set to be disconnected from the body and allows the transition  $j$  to fire, which enables the first node set to move forward. The cyclic movements of the two node sets then begin. To terminate this cyclic process, the token placed at Run is moved to Stop by firing transition  $n$  with an input signal placed at Term. Having a token at Stop enables either transition  $m$  and  $l$  to fire, when the horizontal axis in each node set arrives at MoveFwd. This removes the token from MoveFwd and places it in Hold. This terminates the cyclic movement of the horizontal axis. The vertical axis keeps moving until the AllCon place is reached, but is prohibited to shift to MoveLow, since FwdEndZone of the horizontal axis is no longer reached. Therefore, both node sets are brought to the home state, i.e. the Hold and AllCon states, and stopped there. The actual system includes several other states for switching between forward and backward motion and changing the direction of the motion. These states and associated transitions can be added to the above Petri net in the same way as the initiation and termination procedures. It should be noted, however, that these additional states act as an interface, connecting the discrete-event controller to a higher level controller that observes the human body being transferred, and generates a reference command. Based on this reference, the node set movements are switched.

Note that all of the subsystems involved in this Petri net are *strictly conservative*, in that the number of tokens in each subsystem is not changed by the firing of transitions. The subsystem of vertical axes, which consists of four places, contains only one token at all times. The horizontal subsystem consisting of four places plus the Hold place contains only one token as well. This can be determined by inspection, since the number of arcs into each transition equals the number of arcs out of that transition. Strict conservation is an important property, as it allows the network to represent this discrete event behavior properly. Since the state of every subsystem is represented by a token, the state of the subsystem would be undefined if a token were to be lost. Subsystem conservation can be evaluated by counting the number of arcs which lead from places to transitions outside the subsystem. If the number of input arcs does not equal the number of output arcs, the subsystem is not conservative. Since the subsystems are conservative and only contain one token each, they are *safe*. Every place in a safe subsystem contains either 1 or 0 tokens. Since the subsystems are safe and distinct, meaning tokens do not pass into other subsystems, the entire network is safe. Another important condition to evaluate is *deadlock*. This scenario occurs whenever no transitions are enabled to fire. The systems shown above will not reach deadlock for the initial marking specified earlier.

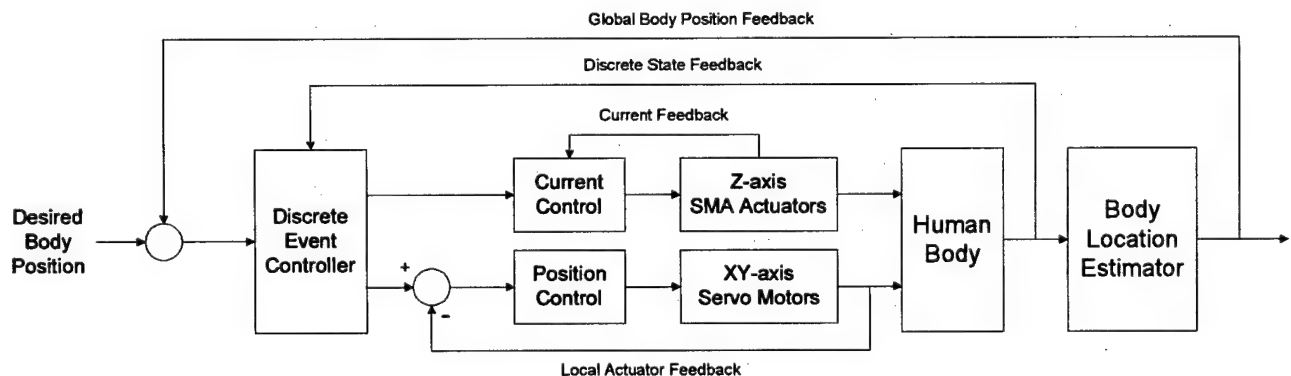


**Figure 11. Overall control architecture including global body position feedback, discrete state feedback and local actuator feedback.**

#### 4.3 Control Hierarchy

Figure 11 shows the overall control architecture of the active mattress control system. Three distinct levels of control exist in the system. The lowest feedback loop is the control of individual actuators; position control of the xy axis servo motors and current control of the z axis SMA actuators. These loops are in turn fed

commands from the discrete-event controller, which coordinates the actuators based on pressure measured at each node.

The highest level control loop shown in the figure is the feedback control of the global body position. Based on the pressure distribution across the bed surface, the mass centroid of the human body is estimated. Several techniques have been developed for body posture and location estimation [Wren, 1998, Nishida et al, 1997]. We apply these techniques for estimating the body position, and close the feedback loop with respect to the patient's position. This allows the user to command the active mattress system at the task level, commanding the patient's position, rather than commanding individual nodes and actuators.

The estimation technique used in the prototype is based on the existing human posture and position monitoring techniques [Wren, 1998, Nishida et al, 1997], but is devised to meet specific requirements for the active mattress system. Like the existing techniques, the body centroid position is determined by computing the first-order moment of the pressure distribution, and the posture is determined by using a simple body model; the body profile is broken down into two dimensional primitives, e.g. circles and polygons such as rectangles. The centroid of each body segment is estimated by the pressure information. One problem of the active mattress in evaluating the centroid of the whole body or a segment of the body is that pressure readings are not available continually and stably, due to the movements of the active nodes. In the prototype system having two node sets, half of the nodes are detached from the body and are unable to measure pressure during the cyclic movement. The information available from the remaining pressure sensors becomes scattered and incomplete.

To alleviate this problem, pressure measurements are taken at specific states. During the motion of the trapezoidal trajectory, there is an interval when all nodes are in full contact. The human body is most stably supported during this period, and a pressure measurement at this time has the highest density. This interval occurs twice during the FwdEndZone and the BwdEndZone.

The pressure measurements at the full contact states, although stable and accurate, are merely intermittent measurements. Continuous estimation is needed for the global body position feedback. To this end, information from the position sensors attached to the xy-axes servo motors is utilized and incorporated into the pressure measurement system.

Let  $\mathbf{x}_c = (x_c, y_c)^T \in \mathbb{R}^2$  be x-y coordinates of the body centroid determined by the previous pressure sensor readings and  $\Delta\mathbf{x}_c \in \mathbb{R}^2$  be the distances traveled by the horizontal actuators since  $\mathbf{x}_c$  was last determined. Then the estimated centroid position  $\hat{\mathbf{x}}_c \in \mathbb{R}^2$  during the interval when one node set is disconnected from the body is given by

$$\hat{\mathbf{x}}_c = \mathbf{x}_c + \Delta\mathbf{x}_c \quad (19)$$

At the end of the motion, the node which was disconnected regains contact with the body. We can then resume the pressure measurement by using all of the nodes to obtain the actual profile of the body. Due to slip between the body and the mattress surface, the estimated body position may have a significant discrepancy. Such errors are corrected periodically by the pressure sensor information.

For whole body motion, all polygon primitives are moved by the same displacement. However, for localized motion, the primitive being moved must be considered separately from the others. The  $\Delta\mathbf{x}_c$  specified in Equation 19 is applied only to that primitive. Human models can be used to determine the locations of the boundaries between primitives.

Whenever a new  $\mathbf{x}_c$  becomes available, the global controller compares the position of the body with its desired position, and generates a reference command, which is passed on to the discrete-event controller. In turn, the discrete-event controller goes through the procedure for changing the direction of movement.

## 5 Experiments

Experiments have been performed to validate the theoretical concepts and control methodologies which have been discussed in earlier sections. The experiments were performed using the prototype, described in Section 2.2, which employs shape memory alloy fibers as the z actuator. Rectangular objects of various sizes and weights were placed on the bed to represent the body. The center of mass of the object as reported by the position estimator was collected, as was the position of each of the horizontal axes. The states of each subsystem of the node sets was recorded, as well as the pressure sensor readings indicating contact with the object at the individual nodes.

In addition to the system's capability of measuring body position, a magnetic position and orientation sensor was also used to measure the position of the body for the purpose of comparison. This device consists of a transmitter unit which generates pulsed magnetic fields, and a tracker which can sense its position and orientation with respect to those fields. Under ideal conditions, this device has a positional accuracy of about 2.5 mm, and an angular accuracy of about  $0.5^\circ$  over its effective range of 1.2 m. Despite the presence of ferromagnetic coil springs and cables, the device performs properly, and maintains an accuracy of roughly the same order of magnitude as given above.

Below we compare the results of the same motion using the rectangular and trapezoidal trajectories. The data was obtained from the active mattress system using the position prediction and estimation algorithm. The object used measured 22.5 cm by 22.5 cm, and weighed 1 kg. It was moved across the surface of the bed in the positive x direction.

Figure 12 shows the x coordinate of the object versus time as it is moved across the bed, from an initial point of 0 cm to a setpoint of 22 cm. Figure 13 shows the velocity of the object versus time for the window between 20 and 30 seconds. We note that the motion for the trapezoidal trajectory is much smoother than that of the rectangular trajectory, while the rectangular trajectory produces more rapid motion in short bursts. The trapezoidal trajectory clearly provides superior performance in terms of smoothness of motion. The rapid acceleration and jerk of the rectangular trajectory is very significant, as observed in Figure 13.

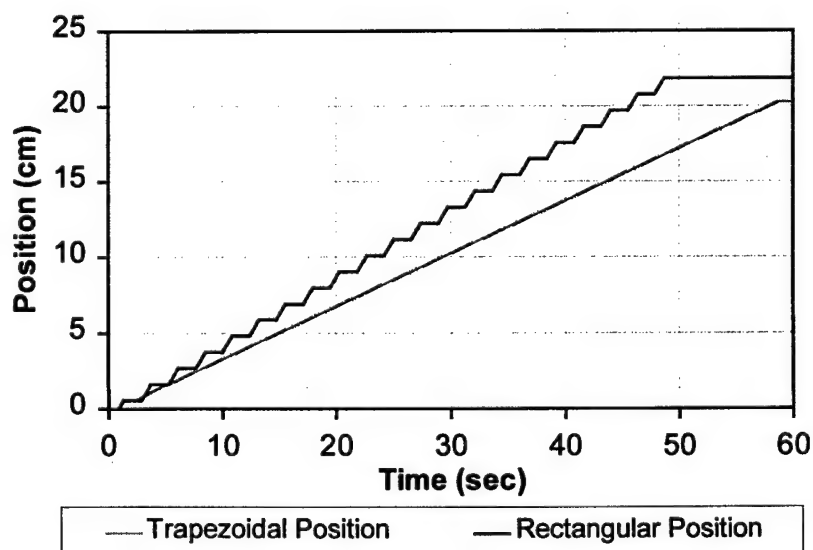
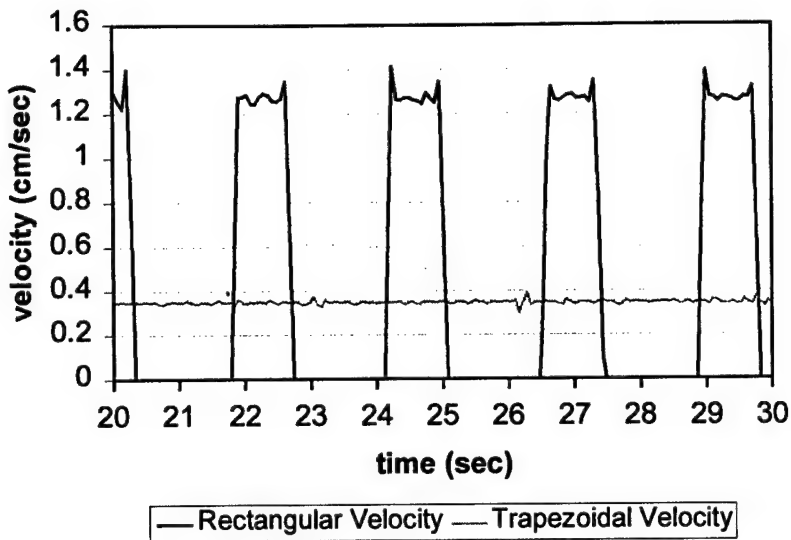
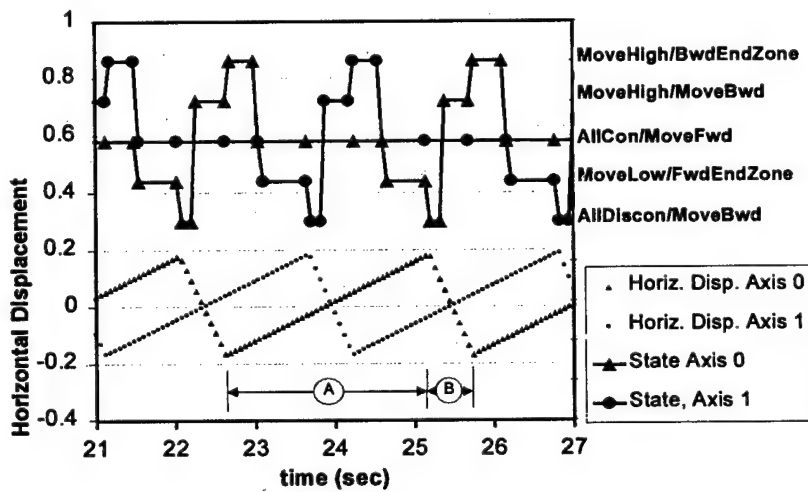


Figure 12. Comparison between rectangular and trapezoidal trajectories, position



**Figure 13. Comparison between rectangular and trapezoidal trajectories, velocity**

Let us examine the trapezoidal trajectory more closely. The plot below shows the position of the two horizontal axes from their centered position, i.e.  $\Delta x_i$ , and the state of vertical and horizontal axes of the associated node set. The combinations of vertical axis state and horizontal axis state are indicated for both node sets. On Figure 14 two regions of motion are marked as **A** and **B**. Note that in the region labeled **A**, the actuator is moving forward at the velocity of the patient, while in region **B**, the actuator is returning to its starting point.

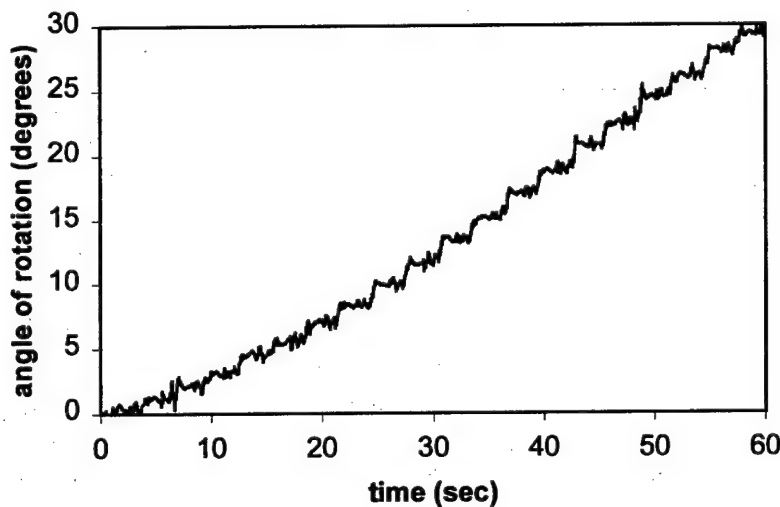


**Figure 14: Plots of Node Set Motion & States**

From these figures we can observe the operation of the system nodes. Note how at least one node set is in the AllCon/MoveFwd state at all times, with brief overlaps while weight is being transferred. While one node set is in the MoveFwd state, the other node set transitions through all the other movement states. Note that the

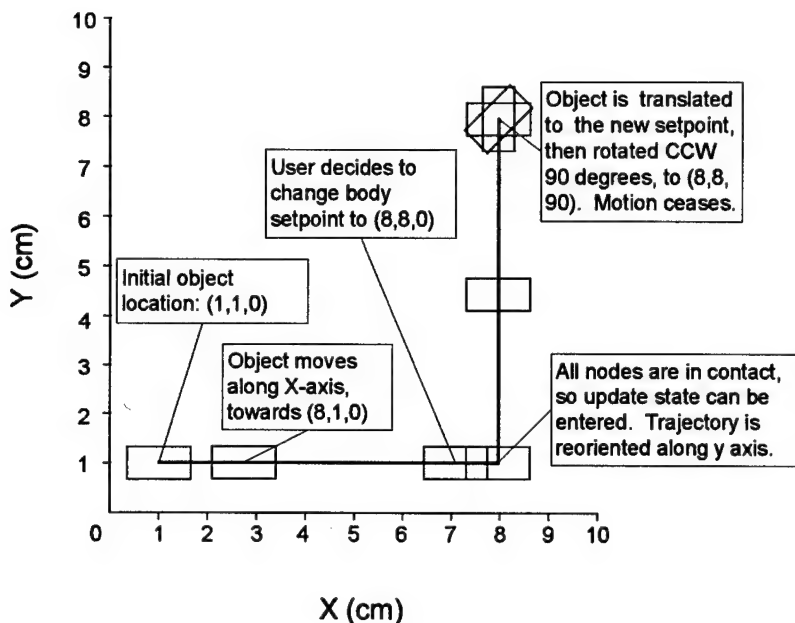
backward velocity is five times faster than that of the forward velocity. From Eq. (17) in Section 4.1, the average number of disconnected node sets is determined as  $\bar{N}_{dis} = 0.75$ , with  $b$  set to 0.75. In other words, the body is supported on average by  $N - \bar{N}_{dis} = 1.25$  node sets, which agrees with the result of Figure 14.

Figure 15 shows the experiment of Whole Body Rotation. The output from the magnetic tracker's yaw sensor is plotted, as the object is rotated on the surface of the prototype. The object was a square measuring 50.8 cm on a side, and weighed 2 kg. The Whole Body Rotation algorithm was employed, with a rectangular trajectory. As can be seen, the object was successfully rotated approximately 0.5 degrees per second. The effects of the rectangular trajectory used can be observed in the periodic nature of the motion.



**Figure 15. Rotation of an object.**

Another important capability of the prototype is its ability to move the body in two dimensions. Figure 16 shows the xy trajectory plot of the body as it is moved across the surface of the bed. The body begins at the coordinates  $x_{body} = 1$  cm,  $y_{body} = 1$  cm, and orientation  $\beta = 0$  degrees, or  $(1,1,0)$  for short, and is initially moved towards the setpoint  $(1,8,0)$ . As it nears this setpoint, the user chooses to change the setpoint to  $(8,8,0)$ . At this time, the trajectory is not ready to accept a new setpoint. Half of the nodes are disconnected, so pressure sensor data will be inaccurate. Therefore, the system waits until the disconnected nodes have finished their motion and reconnected. The horizontal axes then both enter the transition state. An accurate centroid of the object is determined, and the new setpoint is given.



**Figure 16. xy plot of centroid's trajectory.**

The trapezoidal trajectory is reestablished, so as to generate motion in the y direction. At the end, the body is rotated 90 degrees by switching the control mode to Whole Body Rotation. These experiments were repeated for different objects with various weights and shapes. Although the load varied more than 200 per cent, the vertical deflections did not change significantly, thanks to the preload of 10N applied to each node.

The next experiment performed was to evaluate the performance of the system's position prediction and estimation routines. The experiment was conducted with a 22.86 cm x 22.86 cm object weighing 0.9 kg. The object was moved from one end of the bed to the other, along the y axis, using the trapezoidal trajectory and the whole body translation algorithm. The results are depicted in Figure 17. Note that the position returned by the system is in a solid line, while that observed from the magnetic tracker is given as a dotted line. They are in close agreement for much of the duration of motion. The system's prediction is based on how far the horizontal axes have displaced, while in contact with the body. It assumes that there is no slip between the nodes and the body. It also assumes that the initial position of the object is accurate. If the prediction of the object's position is no longer in agreement with the sensors on the mattress surface, the prediction is rejected and the object's centroid is determined from the pressure sensor measurements. This occurs twice during the experiment; once at approximately 13 seconds, and again at about 30 seconds. Both times the actual object position was less than the estimated position, due to slip between the node surfaces and the object.

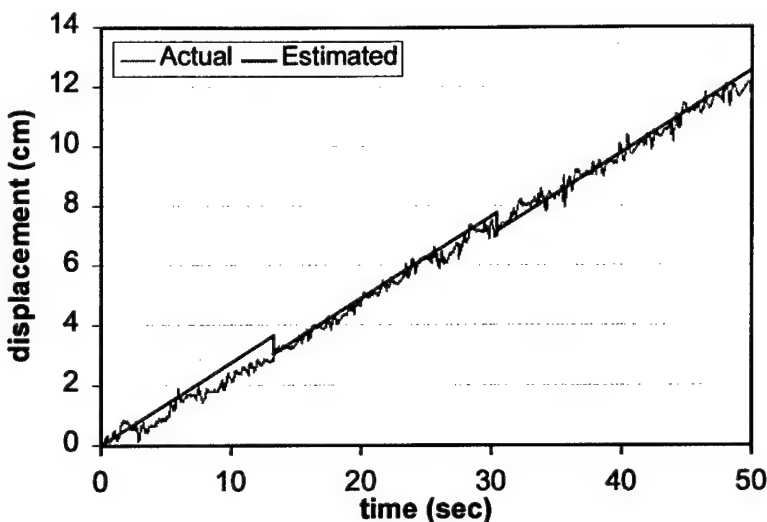


**Figure 17. Evaluation of prediction/estimation of position algorithm, trapezoidal trajectory.**

The experiment described shows that the prediction algorithm is useful for maintaining an accurate estimation of the object's position on the surface wave mattress. It is needed because much of the surface is not in contact with the object during motion, as the nodes need to detach in order to complete their trajectories. However, because of slip the prediction sometimes deviates from the actual centroid, the pressure sensor data, taken at instants when all the nodes are in contact with the body, is used to obtain a more accurate estimate of the object's centroid.

## 6 Conclusion

An innovative system for the transport of bedridden patients has been developed to improve the quality of life for these patients and reduce the strain imposed on caregivers. This work is the first to apply periodic surface movements to the two-dimensional transport of human patients. Successful operation has been accomplished by devising the node trajectory, node coordination method, and sensors. The choice of the trapezoidal trajectory was made to maximize patient comfort, reduce disconnection time to better support the body, and to guarantee smooth and stable connections and disconnections despite uncertainties and actuator nonlinearity.

A discrete-event controller has been built by using a Petri net to deal with complex coordination among multiple node sets and horizontal and vertical actuators. The prototype that has been built to test these

algorithms successfully moves objects across its surface. Translation and rotation have both been successfully demonstrated.

## References

- [1] HFCA's Online Survey, Certification and Reporting Date of March 1997
- [2] The Decubitus Foundation: Press Release. Feb, 1998. <http://www.decubitus.org/press/press.html>
- [3] Nonfatal occupational injury and illness incidence rates per 100 full time workers, by industry, 1996. OSHA. <http://www.osha.gov/oshastats/bls/Serv6.html>
- [4] Bureau of Labor Statistics. Number of nonfatal occupational injuries and illnesses involving days away from work, by occupation and selected parts of the body affected by injury or illness, 1994. Department of Labor, Office of Safety and health, 1996.
- [5] Spano and Asada, "An Active Surface Wave Bed for Transporting Humans and Elastic Bodies", ASME IMECE '98, Anaheim, CA November 15-21, 1998
- [6] Mascaro, Spano, and Asada. "A Reconfigurable Holonomic Omnidirectional Mobile Bed with Unified Seating (RHOMBUS) for Bedridden Patients", IEEE Int. Conf. on Robotics and Automation, Albuquerque, New Mexico, April 1997.
- [7] Garg, Owen, Carlson, 1992. An ergonomic evaluation of nursing assistants' job in a nursing home. *Ergonomics*, 35 (9), 979-995.
- [8] Owen and Garg, 1993. Back stress isn't part of the job. *American Journal of Nursing*, 93, 48-51.
- [9] Holliday, Fernie, Plowman, 1994. The impact of new lifting technology in long term care: a pilot study. *AAOHN Journal*, 42 (12), 582-589.
- [10] Garrett, Singiser, and Banks, 1992. Back injuries among nursing personnel: the relationship of personal characteristics, risk factors, and nursing practices. *AAOHN Journal*, 40 (11), 510-516.

[11] National Institute for Occupational Safety and Health, 1981. *Work Practices Guide for Manual Lifting*. Washington, DC: US Department of Health and Human Services publication No. 81-122.

[12] Garg, Owen, Beller and Banaag, 1991. A biomechanical and ergonomic evaluation of patient transferring tasks: bed to wheelchair and wheelchair to bed. *Ergonomics*, **34** (3) 289-312.

[13] Christopher R. Wren and Alex Pentland, 1998. "Dynamic Models of Human Motion", Third IEEE International Conference on Automatic Face and Gesture Recognition, Nara, Japan, April 14-16, 1998.

[14] Nishida Y., Takeda M., Mori T., Mizoguchi H., Sato T., 1997. "Monitoring patient respiration and posture using human symbiosis system", Proceedings of the 1997 IEEE/RSJ International Conference on Intelligent Robot and Systems. Innovative Robotics for Real-World Applications. IROS '97 (Cat. No.97CH36108). IEEE. Part vol.2, 1997, pp.632-9 vol.2. New York, NY, USA.

## Acknowledgment

This work was supported in part by the National Science Foundation, Grant IRI-9712386, and in part by the Home Automation and Healthcare Consortium at the Massachusetts Institute of Technology.

## Kinematic Analysis and Design of Surface Wave Actuators

Haruhiko H. Asada  
Principal Investigator

Joe Spano  
Graduate Research Assistant

### ABSTRACT

Surface waves are shown to be a viable transport mechanism for large-scale, elastic bodies given certain conditions and constraints on the design. Basic properties of surface waves are presented. In nature, the motion of each node on the surface is coordinated such that it follows an elliptical trajectory with a certain phase lag from adjacent nodes. Inspired by these properties and their potential for tangential transport, a new concept, the extender, augments the system to take advantage to the inherent rotational component of surface wave points. Kinematic analysis is performed to characterize the actuation concept. Inspired by this analysis, modifications to the design are instituted that yield an actuator architecture of significantly reduced order. A proof-of-concept prototype is designed, built and tested. Surface gravity waves in water are studied as a energy propagation media to further reduce the degree of actuation needed to transport lightweight objects. An experiment is designed to test the viability of utilizing the resonance conditions of a water bed for tangential transport. The surface wave actuator has potential as a flexible two-dimensional actuation system capable of transporting elastic bodies. The specific application explored by the authors is the tangential transportation of a human lying on the bed surface.

## 1 Introduction

Bedridden patients require frequent reconfiguration and transport on and off of their support surface for a variety of tasks to be performed. Periodic reconfiguration is the critical activity necessary to prevent the development of painful bedsores. It is also necessary to change linens. Patient transfer from one support surface to the other is necessary when patients need to be relocated for treatment, weighing, or toileting. Traditionally these activities have been handled using the physical exertion and intervention by caregivers in both the home and institutional setting. These exertions are the cause of physical injuries and pain to legions of caregivers. This is a recognized and recently well documented problem. (Owen et.al. 1989) reported that 89% of the back injury reports filed by hospital nursing personnel implicated a patient handling task as a causal factor. Nursing personnel in general show a high level of lower-back pain, (Klein et.al. 1984) reported that based on worker compensation claims nursing ranked fifth among all occupations, trailing only heavy labor groups such as construction. Nursing assistants are recognized as being the most vulnerable of all nursing personnel. (Fuortes et.al. 1994) reported that nursing assistants have back injury rates 3.3 times higher than registered nurses and licensed practical nurses. In particular 51% of nursing assistants visited a health care provider in the last three years for work related lower back pain. (Garg et.al. 1992)

In an attempt to mitigate the difficulties associated with physically manipulating patients, numerous mechanical devices have emerged. The Hoyer lift, Trans-Aid, Medi-Lifter, Molift, Ambulift, etc. are common commercial lifting assistive devices on the market and purchased by hospitals to lessen the physical burden on nursing aids. (Garg, Owen, et.al. 1991) presented an ergonomic study of three of these devices and five common manual techniques for patient transfer from bed to wheelchair and vice-versa. The results showed that two out of three hoists were perceived to be as physically stressful as manual methods by the nurses. Patients found that these two hoists were more uncomfortable and felt less secure than with three of the five manual methods. Ambulift was found to be the least stressful and most comfortable of all methods. This is encouraging in the sense that at least mechanical aids can be beneficial in the care environment. However, (Garg et.al. 1992) through video taping and observations of daily nursing activities, showed that assistive devices such as lifts and belts were used less than

2% of the time. Time to use device, lack of knowledge, patient discomfort, and accessibility issues contributed heavily to their lack of use. While the problem of patient manipulation is well recognized, and the use of mechanical aids has been considered, no clear, widely accepted and implemented solution has emerged.

The development of a manipulator with a high degree of flexibility and capable of planar transportation of objects has wide utility. In robotics, research on distributed actuation originated in the seminal work by [Hirose and Umetani 1976]. They developed a series of distributed actuation systems inspired by biological systems. Snake robots consisting of many servoed joints connected in series can walk in a totally different manner. Later they also developed an abalone robot, a two-dimensional active surface that can reconfigure and move. Burdick extended Hirose's snake robot concept by introducing partial differential equations to describe the distributed nature of snake behavior. [Chirikjian and Burdick 1991] Recently, Messner developed a two-dimensional array of manipulator cells that can transfer and orient an object. [Luntz and Messner 1996] Roller wheels for omni-directional vehicles were placed upside down in order to manipulate an object put on top of the array of the roller wheels. An innovative distributed control system has been developed for the roller wheel transportation system.

Other work related to the use of surface waves as a tangential transport mechanism includes efforts by researchers involved in micro-manipulation. [Tadokoro, 1997] and [Suzumori, 1996] show the use of coordinated pneumatic actuators for small-scale manipulation. However there appears to be no work seeking to exploit surface wave behavior for the manipulation of large-scale, elastic bodies such as humans.

The goal of this paper is to show the validity of flexible, planar transportation by means of large-scale, mechanically generated surface waves. (Figure 1) Although the technology has a wide applicability, the development of the design will reflect the desired goal of addressing the problem of transport of bedridden patients. Humans are flexible and thereby conform to the contour of the surface waves. Moreover, patient health must be assured while transporting the human. The body must be gently supported, and concentration of tissue pressure must be avoided. These create unique issues that require sound understanding of surface wave actuation and careful design and tuning of the equipment.

In this paper, the non-linear kinematic properties of surface waves are examined and basic requirements for transporting humans and elastic bodies are obtained. Design enhancements based on the analysis are made that significantly increase the performance of the actuator system. A realizable design is proposed that reduces the dimension of actuation necessary without significant losses in performance. A low impedance actuator, based on water support is explored without significant loading effect to utilize resonance conditions predicted by linear surface wave theory as a dramatic simplification of the design. Finally, a high impedance actuator based on an array of active nodes is coordinated to generate psuedo-continuum surface waves that are used to transfer a human patient.

## 2 Principle

### 2.1 Surface Waves for Transportation

Figure 1 shows the principle of surface wave actuation for transporting humans and objects. A body supported at the crests of the surface waves is moved horizontally along the bed surface, as the waves propagate. As shown in Figure 2, the waves are created by periodic movements of individual points along the bed surface. First it moves upwards (a), contacts the body, supports the body weight, moves in a horizontal direction (b), moves downwards, detaches from the body (c), and moves horizontally back to the original point (d). The individual points along the bed surface repeat the same trajectory, but with different phase angles. As a result, some segments of the bed surface are in contact with the body and the others are detached from the body, creating a wave-like contour as shown in the figure. When the segment is in contact with the body, it moves together with the body in the horizontal direction and thereby transports the body.

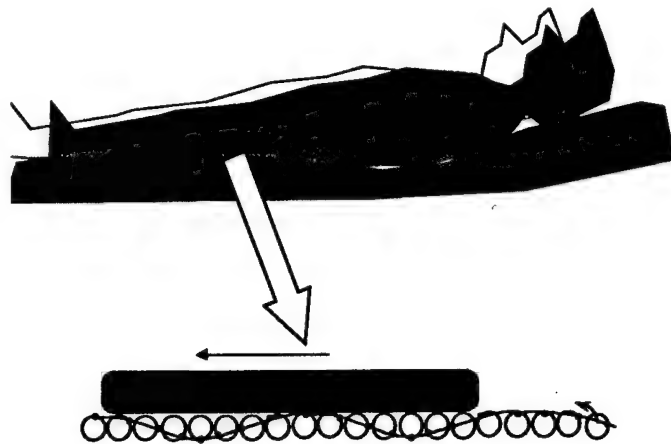


Figure 1 - Human body transported by surface waves

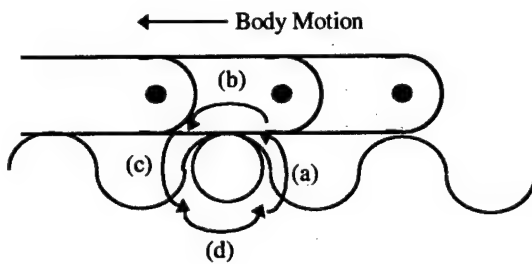


Figure 2 - Detail of flexible object transported by surface waves

This surface wave actuation was inspired by natural surface waves. Figure 3 shows traces of water particles in natural wave motion by [Van Dyke 1982]. Note that each particle motion clearly shows an elliptic trajectory. At the upper portion of each trajectory, a horizontal velocity is generated in one direction, as shown by an arrow in Figure 3. Note also that the two gentle curves in the figure indicate the contours of the waves; one shows the crest and the other shows the trough of the waves. The left-bound horizontal velocity is created along the crest of the waves, which tend to move an object placed on the wave surface.

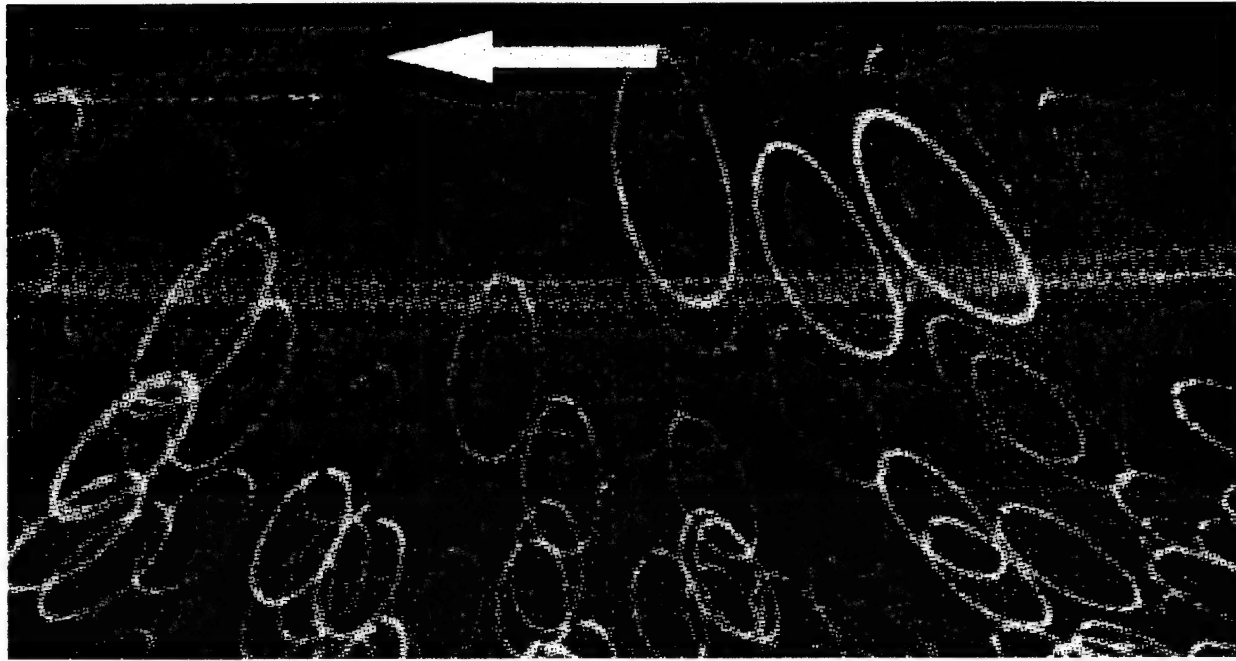


Figure 3 - Traces of water particles in wave motion

This surface wave actuation has several unique features:

- It would allow a body to move horizontally while lying on the bed,
- It would allow a body to move in an arbitrary direction within a plane; two-dimensional motion,
- It can be applied to a water bed, which has been proven to provide excellent sleep comfort, and
- Exploiting the natural resonance of fluidic surfaces would allow small actuators to create large waves.

The natural surface waves are limited in performance and efficiency, and are not optimal for the purpose of transporting humans and objects. Moreover, the natural waves are not necessarily convenient or feasible when they are made by artificial means. In this paper, several modifications and improvements to the surface wave actuation based on the original natural waves will be obtained. The wave pattern will be modified so that it provides faster motion, higher efficiency, and more gentle and comfortable contours while making it easily and simply.

Figure 4 shows one of the improvements, which would significantly increase transportation speed and efficiency. Instead of placing it directly on the membrane, ie, the water bed surface, the body is placed on a membrane with a bed of protrusions, called extenders. As shown in Figure 4, the extender travels a longer horizontal distance than that of the wave surface when repeating a periodic motion. In addition to horizontal motion of each node along the membrane, there is a rotational component of the membrane surface. The extender that is placed normal to the membrane surface magnifies the horizontal motion due to the periodic rotation of the extender body. This additional forward velocity can be utilized in the design of a surface wave actuator to increase the transport speed and efficiency.

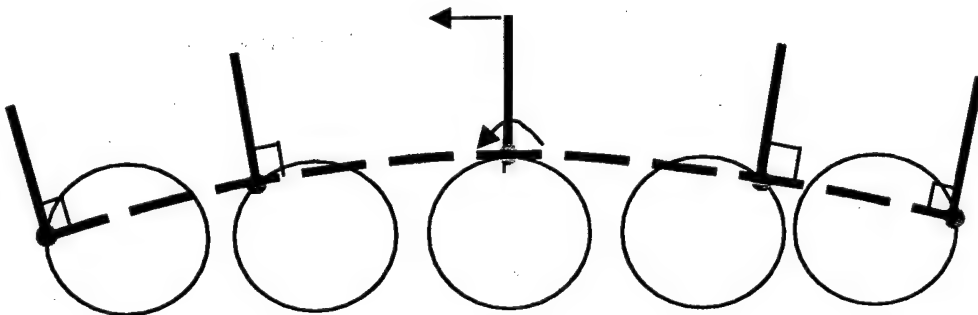


Figure 4 - Extender Detail

### 3. Kinematic Analysis of Surface Wave Motion

#### 3.1 Modeling-Point Motion Position and Velocity Analysis

Surface waves are a particular type of wave created by a periodic elliptical motion of each particle on the surface with a phase lag between adjacent particles. Note that surface waves are not merely longitudinal waves or transverse waves, but are a mixture of the two. As shown in Figure 1, each particle moves in both longitudinal and transverse directions. For the sake of simplicity, it is assumed in this paper that the particle trajectory is a complete circle. In this model we focus only on the point motion of the wave surface.

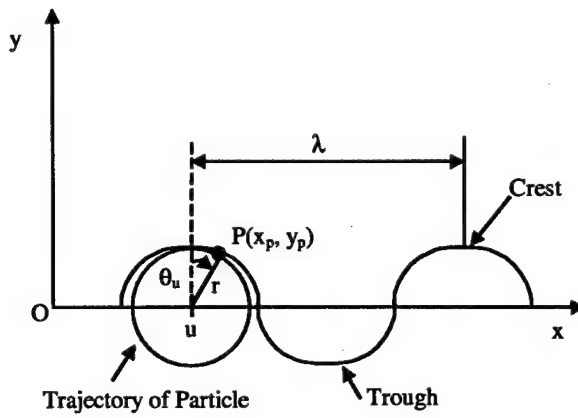


Figure 5 - Nodal Point Motion Kinematics

Let P be a particle at distance  $u$  from origin O along the surface when the wave is not present. The coordinates of particle P when waves are created are given by

$$x_p(u, t) = r \sin(\theta_u) + u$$

$$y_p(u, t) = r \cos(\theta_u)$$

where  $r$  is the radius of the circular trajectory and  $\theta_u$  is the angle given by

$$\theta_u = \omega t + 2\pi \frac{u}{\lambda}$$

where  $\omega$  is the angular velocity of the circular motion measured in radians/unit time, and the second term,  $2\pi u/\lambda$ , is phase lag. The phase lag varies continually along the surface in proportion to distance  $u$ . Parameter,  $\lambda$ , is the wave length, that is, the distance between two successive crests or troughs, as shown in Figure 2. The frequency  $\omega/2\pi$  provides the number of waves passing a fixed point per unit time. Therefore, the wave velocity,  $v_{\text{wave}}$  that is the velocity at which wave crests appear to move, is given by:

$$v_{\text{wave}} = -\frac{\omega}{2\pi} \lambda$$

The velocity of the particle at each crest is given by

$$v_{\text{crest}} = \left. \frac{\partial x_p}{\partial t} \right|_{\theta_u=0} = r\omega$$

while the velocity at the troughs is given by

$$v_{trough} = \frac{\partial x_p}{\partial t} \bigg|_{\theta_u = -\pi} = -r\omega$$

Note that at the crest the wave velocity and the particle velocity are opposed, but at the trough they are aligned for this choice of wavelength parameter.

Note that if we generalize to elliptical trajectories the position equations can be written using the equation of the ellipse and the definition of theta using the parameterization of figure 7. The overall wave shape stretches depending on the proportions of the minor and major axes, but the kinematic limit of physical realizable waveforms stays unchanged and depends on the x-axis dimension. Velocity analysis can be performed, but no real new insight is obtained. For our analyses we focus on circular trajectories to reveal the interesting physics in its simplest analytical form, but recognize that extensions to more general elliptical trajectories can easily be made.

$$x_p = u + \sqrt{\frac{a^2 b^2}{b^2 + a^2 \cot^2 \theta}}$$

$$y_p = \sqrt{\frac{a^2 b^2}{b^2 \tan^2 \theta + a^2}}$$

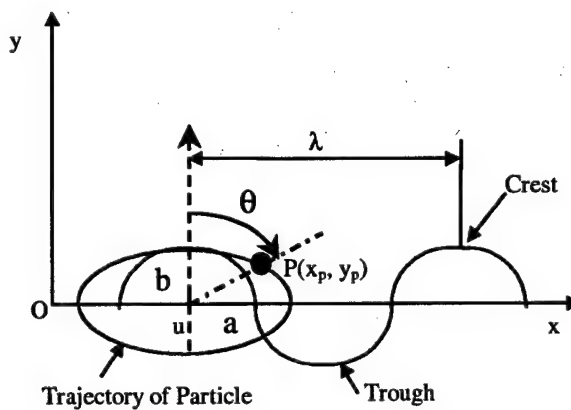


Figure 6 - Schematic of elliptical trajectories

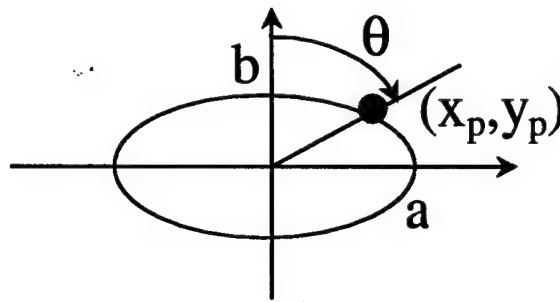


Figure 7 - Detail of particle trajectory

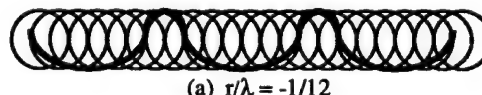
### 3.2 Shaping the Waveform

There are several issues to be overcome to transport a human by surface waves. Since a human body is a multi-d.o.f. system consisting of many flexible bodies connected by articulated joints, it may conform to the wave surface as shown in Figure 1. As it slacks, the body may contact the trough side of the wave surface, which moves in the direction opposite the crests. Therefore the human body may be dragged backwards. This results in low efficiency and, more importantly, leaves the human in an uncomfortable situation.

To avoid slack and uncomfortable situations,

- The wavelength  $\lambda$  must be shortened,
- The waves must be deep, and
- The crest must be gentle and wide (long).

The shorter the wavelength, the less the body slacks, and the more crests the bed surface generates to support the body. The deeper the troughs become, the less likely the body will be to contact the troughs. The design parameters,  $\lambda$  and  $r$ , must be chosen to meet these requirements. The third design guideline addresses the shape of the crests, providing an effective solution to the slack and comfort problem.



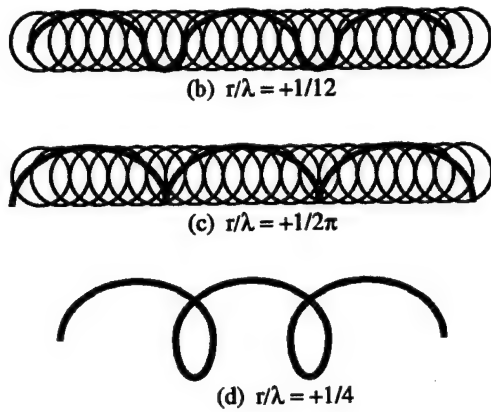


Figure 8 - Surface Waveforms for different  $r/\lambda$

Figure 8b was created by turning the waveform in Figure 8a upside-down by redefining the sign of the wavelength parameter,  $\lambda$ . Note that one side of the wave becomes gentle and long, hence the body can be supported by a broader area of the bed surface. The sharp crests in Figure 8a cause a concentration of stress, which provides an uncomfortable and even dangerous situation for patients with fragile skin conditions. The gradual contours in Figure 8b would significantly reduce the stress concentration and gently support the body. This gentle curvature can be generated by appropriate choice of the sign of the wavelength. Negative wavelength does not exist in natural systems, such as deep water waves, but can be created by artificial means. The proper choice of wavelength is feasible and quite useful for resolving the stress concentration and body slack problems.

In Figure 8, various waves are plotted for different wave lengths,  $\lambda$ . As the absolute value of the wave length becomes smaller, the proportion of the gradual side to the sharp side becomes larger. However, at a certain point the trough becomes a sharp edge and the waves collapse beyond this point. Namely, as shown in Figure 8d, the contour of the wave surface crosses over. This waveform, although very gradual on one side, is not physically realizable because no continuous surface can be manufactured that can continually wrap over itself. Therefore the wave form with the sharp edge, i.e. Figure 8c, provides the lower limit of the wavelength  $|\lambda|$ . The sharp edge is a stagnation point, where the contour of the wave surface has a zero gradient in the  $u$  direction. Namely,

$$\frac{dx_p}{du} = 0$$

Evaluating the gradient at  $\theta_u = -\pi/2$  where the sharp edge exists,

$$\left. \frac{dx_p}{du} \right|_{\theta_u = -\pi/2} = \frac{\partial x_p}{\partial u} + \frac{\partial x_p}{\partial \theta_u} \frac{\partial \theta_u}{\partial u} = 1 - \frac{2\pi}{\lambda} r$$

Therefore, the stagnant condition is given by

$$\lambda = 2\pi r$$

Namely, the lower bound for the absolute value of the wave length is given by

$$|\lambda| > 2\pi r$$

This means that the absolute value of the wavelength must be longer than the circumference of the circular trajectory of radius  $r$ .

By choosing a small wavelength  $|\lambda|$  and a relatively large radius  $r$  that satisfy the kinematic looping condition, one can obtain a broad area of contact surface supporting the human body and thereby reduce the stress concentration. In the kinematic limit the most gentle waveform with adequate depth is generated for point motion surface waves.

#### 4. Kinematics of Surface Wave Actuators with Extenders

##### 4.1 Modeling-Extender Position and Velocity Analysis with Circular Point Motion Trajectories

As discussed earlier the addition of an extender normal to the overall surface can be used to amplify the motion of the surface wave manipulator. This added feature is modeled to put the total system design in parametric form.

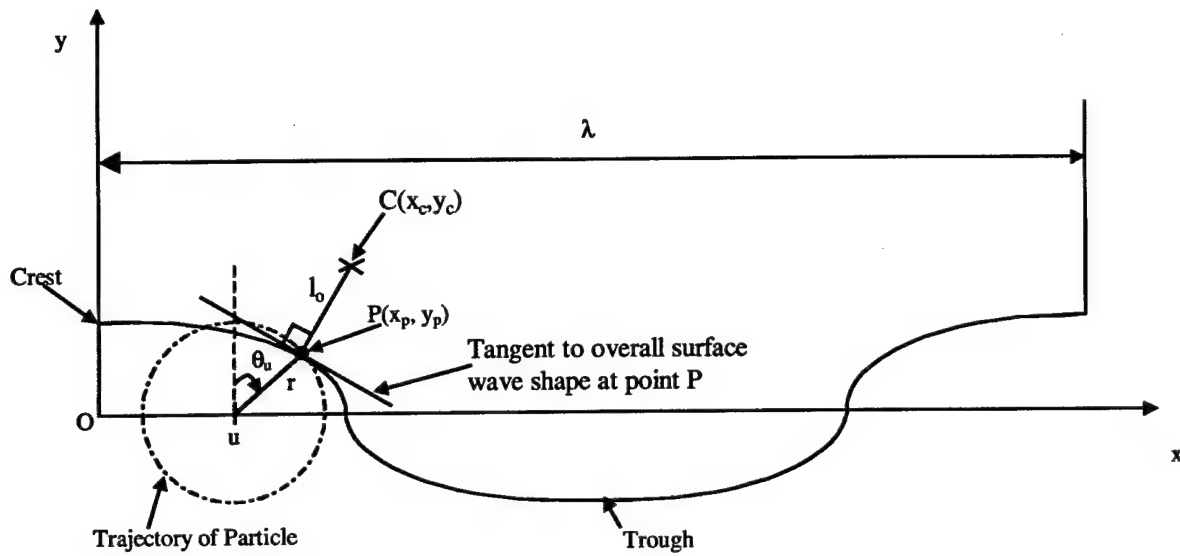


Figure 9 - Extender Kinematics with Circular Point Motion

The position of point C is needed to model what is occurring at the tip of the extender which is in contact with the body undergoing tangential transport by surface waves. First we evaluate the slope of the line tangent to the overall surface wave shape at point P.

$$b = \frac{dy_p(u, t)}{dx_p(u, t)} = \frac{\frac{dy_p(u, t)}{du}}{\frac{dx_p(u, t)}{du}} = \frac{-r \left( \frac{2\pi}{\lambda} \right) \sin(\theta_u)}{1 + r \left( \frac{2\pi}{\lambda} \right) \cos(\theta_u)}$$

Let's examine this slope and introduce the following notation.

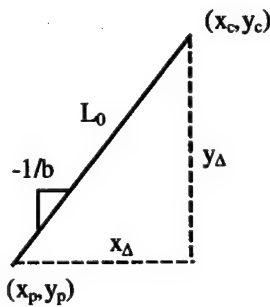


Figure 10 - Extender Detail

Note that

$$x_{\Delta} = -by_{\Delta}$$

$$l_0^2 = x_{\Delta}^2 + y_{\Delta}^2$$

Substitute our derived expression for  $m$  into this set of equations and we with some manipulations one can obtain expressions.

$$x_{\Delta} = \frac{-bl_0}{\sqrt{1+b^2}}$$

$$y_{\Delta} = \frac{l_0}{\sqrt{1+b^2}}$$

With these expressions we can now complete the position analysis for the point c

$$x_c(u,t) = x_p(u,t) + x_{\Delta}(u,t) = r \sin(\theta_u) + u - \frac{bl_0}{\sqrt{1+b^2}}$$

$$y_c(u,t) = y_p(u,t) + y_{\Delta}(u,t) = r \cos(\theta_u) + \frac{l_0}{\sqrt{1+b^2}}$$

With the position analysis completed it is now possible to move forward with the velocity analysis. This is achieved by differentiating the position expressions obtained earlier with respect to time. By simple differentiation and simplification of the expressions one obtains.

$$\frac{dx_c(u,t)}{dt} = r\omega \cos(\theta_u) + \frac{l_0}{(1+b^2)^{3/2}} \left[ \frac{(1+\gamma\omega \cos(\theta_u))}{(1+\gamma \cos(\theta_u))^2} \right]$$

$$\frac{dy_c(u,t)}{dt} = -r\omega \sin(\theta_u) + \frac{l_0 b}{(1+b^2)^{3/2}} \left[ \frac{(1+\gamma\omega \cos(\theta_u))}{(1+\gamma \cos(\theta_u))^2} \right]$$

This equations show that we have increased the x-component of velocity over a range of  $u$  for a given set of design parameters  $\{r, l_0, \lambda\}$ . This range can be calculated by examining when the time derivative of  $x_{\Delta}$  changes sign. By adding extenders, the x-velocity at the point of contact for a particular  $u$  can be increased. In addition one can essentially design beyond the kinematic limit by increasing the velocity further to an equivalent point motion that would loop.

#### 4.2 Modeling-Extender Position and Velocity Analysis with Vertical Point Motion Trajectories

As discussed in the previous section the addition of an extender normal to the overall surface can be used to amplify the motion of the surface wave manipulator and give rise to several interesting properties. These results are very encouraging, however, in situations where a circular point motion trajectory with extenders may be difficult to design in hardware a simplified version involving only vertical motion of each nodal point with extenders can be studied. This version maintains many of the interesting features of the full surface wave version, yet has the advantage of simplified hardware implementation. The kinematic equations for this system are derived below.

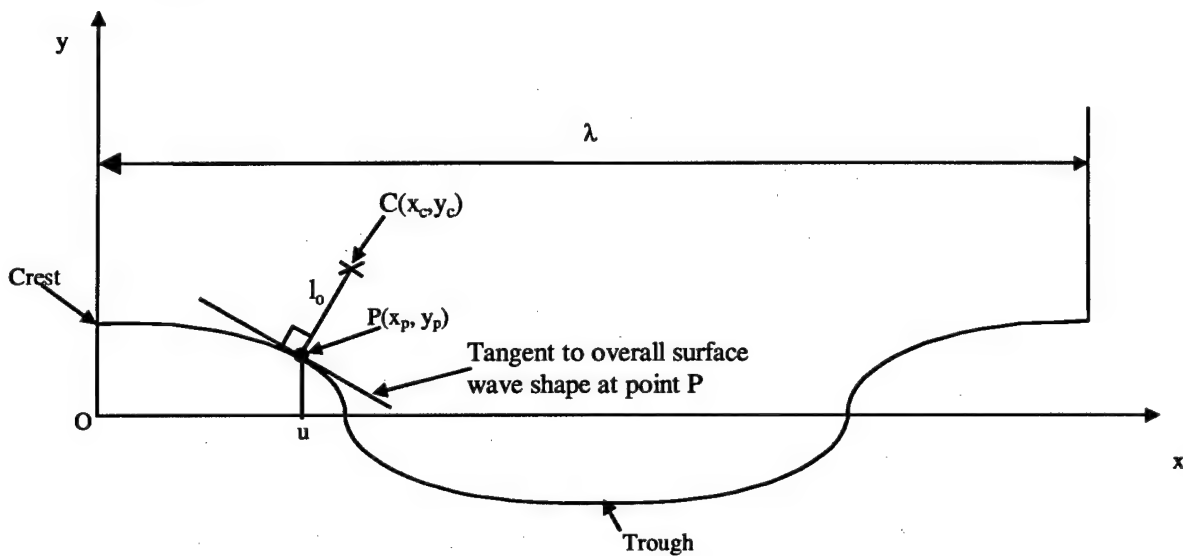


Figure 11 - Extender Kinematics with Vertical Point Motion

The position of point C is needed to model what is occurring at the tip of the extender which is in contact with the body undergoing tangential transport by surface waves. First we can write the position equations for point P.

$$x_p(u, t) = u$$

$$y_p(u, t) = r \cos(\theta_u)$$

Now we evaluate the slope of the line tangent to the overall surface wave shape at point P.

$$b = \frac{dy_p(u,t)}{dx_p(u,t)} = \frac{\frac{dy_p(u,t)}{du}}{\frac{dx_p(u,t)}{du}} = -r \left( \frac{2\pi}{\lambda} \right) \sin \left( \frac{2\pi}{\lambda} u + \alpha \right)$$

Proceeding directly as before in the circular point motion derivation one can reach the following results for position analysis.

$$x_c(u,t) = x_p(u,t) + x_\Delta(u,t) = u - \frac{bl_0}{\sqrt{1+b^2}}$$

$$y_c(u,t) = y_p(u,t) + y_\Delta(u,t) = r \cos(\theta_u) + \frac{l_0}{\sqrt{1+b^2}}$$

With the position analysis completed velocity analysis follows by differentiation.

$$\frac{\partial x_c(u,t)}{\partial t} = \frac{l_0 \omega \gamma \cos(\theta_u)}{(1+b^2)^{\frac{3}{2}}}$$

$$\frac{\partial y_c(u,t)}{\partial t} = -r \omega \sin(\theta_u) - \frac{l_0 \omega \gamma^2 \sin(\theta_u) \cos(\theta_u)}{(1+b^2)^{\frac{3}{2}}}$$

### 4.3 Hidden Trough Conditions

Figure 12 shows the plot of y-component of position vs. x-component of position of the endpoint nodes (Point C in kinematic analysis) using a value of .75 for the shape parameter. This plot is essentially a 'snapshot' of the overall waveform. The solid line represents a  $l_0/\lambda$  ratio of 0.0, which is the case for pure, circular, point motion (no extender), the dashed line represents .15, and the line of squares represents .30. Note that the extenders, which mechanically are simply linear elements can be designed to loop around each other in a way that was not possible with point motion only.

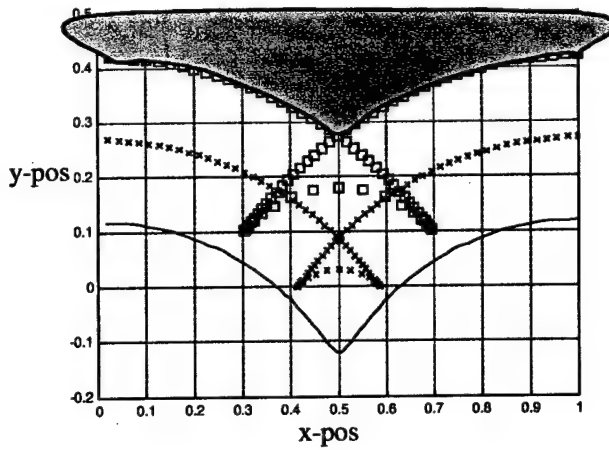


Figure 12 - Node Point 'Snapshot' for  $2\pi r/\lambda = .75$

Figure 13 combines two plots. The first, represented by the top set of lines is the x-component of position of the node (Point C) versus the distance along the x-axis,  $u$ , the coordinate of the base point of the circular trajectory, plotted on the horizontal axis. The second plot is the same except the x-component of velocity replaces x-position as the variable plotted on the vertical axis. What is illustrated in this plot is that depending on the choice of  $l_0/\lambda$ , both x-position and x-velocity change. What is important to us is the nodes that will be in contact with the body shown in the shaded region of Figure 12. These nodes are those associated with a range of  $u$  that have an x-position between zero and .5. Looking at the x-velocity plot it is clear that depending on your parameter choice,  $l_0/\lambda$ , it is possible to design a surface where all of these exposed nodes have positive velocity. This is remarkable considering that the actuation is local in nature.

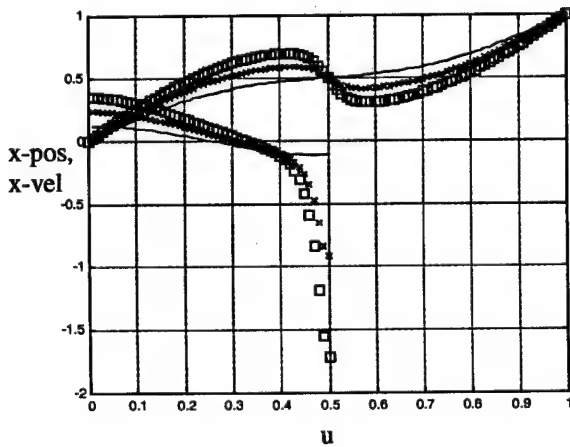


Figure 13- x-direction position and velocity

## 5. Initial Implementation

### 5.1 Experiments with Natural Surface Waves

An experiment was designed to test the feasibility of using water waves as a transportation tool and the effect of using 'extenders' to augment the rotation of the surface normal to enhance transport efficiency. A hydraulic support media offers several advantages. First, a water-based support media has relatively low impedance and offers comfortable support. In addition the infinite number of modes present in the fluid continuum offers the possibility of using resonance as a means to propagate a large number of waves along the surface with a single actuation source. So the net effect is to further decrease the dimension of the actuation and also provide a compliant, comfortable support surface.

The linear theory of surface gravity waves is derived in detail in [Lighthill 1979]. With the assumption that the depth of water,  $h$ , is greater than  $.28\lambda$ , the following dispersion relationship is accurate within 3% and asymptotically converges to the exact solution

$$c = \left( \frac{g\lambda}{2\pi} \right)^{\frac{1}{2}}$$

This relationship defines water as a dispersive media, where wave speed depends on the wavelength. Note also that wave speed is defined below.

$$c = \frac{\omega\lambda}{2\pi}$$

Considering the results of section 4.2 the x-component of velocity at the peak (the transport velocity of the rigid object) of the water base system will be

$$\frac{\partial x_c(u, t)}{\partial t} = \left( \frac{2\pi}{\lambda} \right)^{\frac{3}{2}} r l_0 g^{\frac{1}{2}}$$

The required excitation frequency is given by combining the above equation yielding

$$\omega = \sqrt{\frac{2\pi g}{\lambda}}$$

To transport elastic objects, ideally one would like many wave crests under the object at all times to offer adequate support and prevent sagging of the body into the troughs of the wave. In this case the wavelength will be short and the depth of water needed is defined by the assumption above. The above dispersion relation gives us the appropriate required excitation frequency to achieve a particular resonant wavelength. The trade-off exists due to attenuation of waves due to viscous dissipation. Higher frequency waves, although increasing the transport speed of the object, also attenuate more quickly and thus require more excitation points to sustain them.

For our experiment a 15cm object was selected for transport. A desired wavelength of 5cm was chosen as suitable for transport. The required excitation frequency is calculated to be 5.59hz. The amplitude of excitation is .001m consistent with the limits of the linear surface gravity wave assumption that  $r < 0.02\lambda$ . The extender length is 3/8". The velocity predicted by our derivations is 4.2cm/sec.



Figure 14 - Water support testbed

The experiment shown in figure 14 shows a vat of water of depth approximately 20cm. A Lorenz force actuator is utilized to provide the excitation as specified by a sinusoidal signal generator. A thin plastic sheet was placed over the water to separate the water from the support mat. The extender surface was placed on top of the plastic sheet. A board was fashioned the width of the vat to force waves to travel largely in the

longitudinal direction. A small object was placed on the membrane. The distance traversed by the object was measured by a rule and timed by a stopwatch. Actual experiments yielded an actual transport velocity of 2.0cm/sec. Clearly there is a significant discrepancy with analytical predictions, but by order of magnitude estimates they are in agreement.

## 5.2 Mechanism for Mechanically Generated Surface Waves

A prototype surface wave actuator has been developed in the d'Arbeloff Laboratory. (Figure 15) The prototype is made up of a series of mechanical nodes that are coordinated to generate an overall surface wave behavior. Successive mechanisms trace an elliptical trajectory and cross-bars are set out of phase with each adjacent node, creating a discrete surface wave.

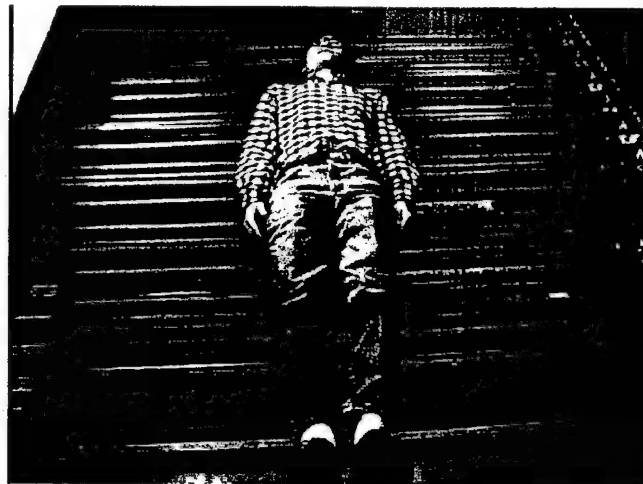


Figure 15 - Surface Wave Actuator

A matching pair of mechanical nodes are driven in tandem and connected by a long bar. Twenty eight of these pairs are driven in a coordinated manner to generate a wave motion that travels across the discretized surface of bars. Overall wave shapes are made by setting adjacent nodes out of phase with one another by the desired amount.

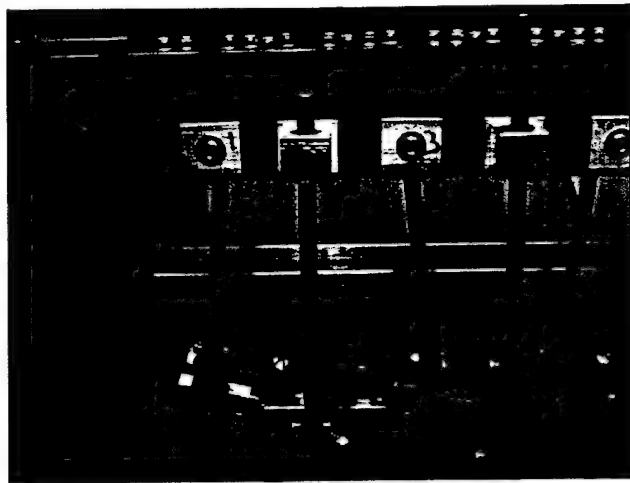


Figure 16 - Detail of Slider-Crank Node Mechanisms

A slider-crank mechanism was chosen as the fundamental mechanism for each node of the surface wave actuator. Using this mechanism one can adjust the shape of the nodal trajectory. By adjusting the length of the radius of the crank one can adjust the vertical displacement of the node and consequently the amplitude of the waveform generated by a set of nodes. By adjusting the position of the cross-bar on the connecting rod one can adjust the horizontal displacement of the node. The drive motor is an Aerotech model 1960 motor with tachometer and encoder used for experimentation. In addition a 25:1 gearhead is utilized to increase torque and reduce speed to levels reasonable for this system. Speed control of this motor sets the angular velocity of the nodes.

The bed dimensions were specified to be 84 inches by 78 inches. These dimensions were chosen to impose waves on both the major and minor axis of the human body. This allows the use of the one degree of freedom surface wave actuator to test the effects of wave propagation on two orthogonal axes of the human body.

The surface wave prototype has been utilized to successfully propagate humans across its surface. This success has illustrated that the surface wave actuator concept indeed shows promise as a unique actuator system capable of exerting tangential forces on elastic bodies, opening a host of application possibilities.

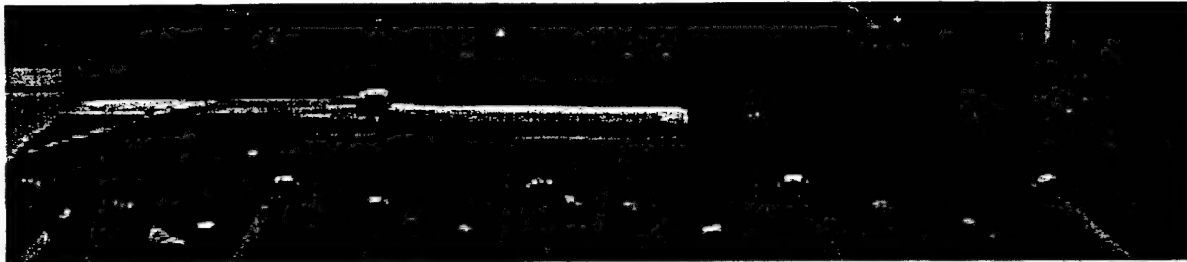


Figure 17 - Extender testbed

Additional experiments were run to evaluate the analysis results in Section 4.2 that showed tangential motion was possible with the extender surface with only vertical actuation. As stated earlier this has the tremendous benefit of decreasing the dimension of actuation significantly while still maintaining the full functionality of the system.

The phase difference between adjacent discrete nodes was set to  $120^0$ . This resulted in a wavelength of 9 inches and an amplitude of wave motion of 1". The mechanism was adjusted to approximate vertical motion trajectories. A rubber mat surface was attached to the surface of each node and interpolated the discrete nodes to make an overall continuous surface. Extenders on this mat were 3/8" in length. The waves were set in motion with an angular velocity of 6.708rad/sec. Using the results of section 4.2 we predict a horizontal velocity of the board equal to the x-component of the extender velocity at a value of  $\theta u = 0^0$ . Evaluating the x-component velocity expression of section 4.2 for this value we obtain

$$\frac{\partial x_c(u, t)}{\partial t} = l_0 \gamma \omega = 1.75 \frac{in}{sec}$$

A magnetic tracker was attached to a board placed on top of the mat to measure the displacement of the board as a function of time during manipulation.

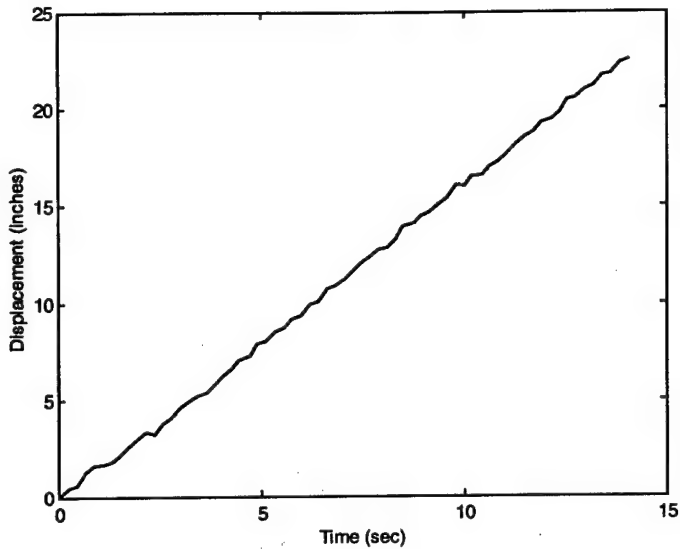


Figure 18 - Displacement-time profile

Figure 18 plots the results of the experiments. One can see a linear displacement-time profile that yields a constant x-component velocity expression of 1.60in/sec. Therefore there is excellent agreement between the analytical predictions and actual experimental results.

## 6 Kinematic Design

The one-dimensional prototype was utilized to demonstrate the feasibility of moving human bodies tangentially across their support surface. It was designed with the large-load bearing capacity needed to safely support a human being. The prototype, however, has limited design flexibility and for this reason other design combinations will be explored in simulation. The design objectives are to provide a gentle, smooth support surface and to provide for efficient transport with as little friction as possible. The set of design variables is  $\{r, l_0, \lambda, \omega\}$ . By carefully constructing simulation experiments and plotting our analytical results for a variety of design variable combinations the sensitivity of the functional objectives on design parameters can be explored.

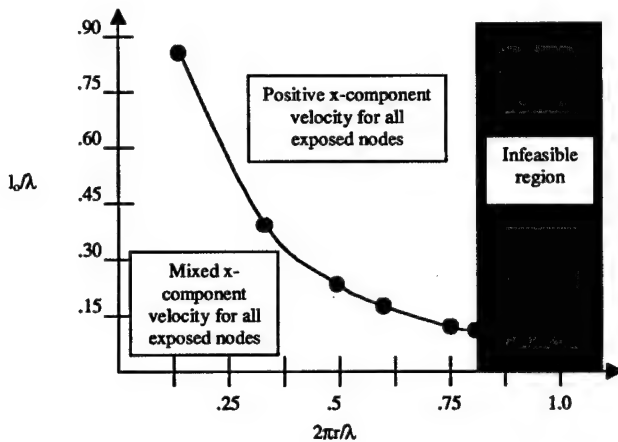


Figure 19 - Results of Parameter Study

Figure 19 illustrates the results of an exploration of the parameter space in simulation. It shows that beyond a shape factor of approximately .8, the extenders begin to loop around the point motion trajectory which is physically difficult to realize. It also shows that the length of extender needed to realize a positive x-component of velocity for all exposed nodes becomes much larger when the shape parameter is decreased. Therefore, to achieve the goal of positive x-component of velocity for all exposed nodes with a minimum extender length it behooves the designer to choose a shape factor as close to the looping constraint as possible.

## 7 Conclusion

This work presents the first consideration of large-scale mechanically generated surface waves as a flexible tangential transport mechanism for bedridden patients. In addition the extender design feature has been introduced to enhance the performance of surface waves that will be synthesized to transport humans or elastic bodies. Position and velocity analyses have been presented that characterize one-dimensional surface waves in terms of four design parameters  $\{r, l, \lambda, \omega\}$ . Performance criteria have been established to characterize the quality of a candidate design in terms of support and transport quality. The analysis has provided a looping condition that represents a kinematic constraint on point motion. However, the introduction of the extender feature has allowed us to bring improved performance beyond the kinematic limit. Finally we have uncovered a set of design parameters that features positive velocity for all exposed nodes, a remarkable feature considering the local nature of the actuator

## Acknowledgments

This work has been supported in part by the National Science Foundation under grant IRI-9712386 and in part by the MIT Home Automation and Healthcare Consortium.

## References

[Tadokoro, 1997] Satoshi Tadokoro, et.al., An Elliptic Friction Drive Element Using an ICPF Actuator, *IEEE Control Systems Magazine*, June 1997

[Luntz and Messner, 1997] Jonathan Luntz and William Messner, A Distributed Control System for Flexible Materials Handling, *IEEE Control Systems Magazine*, February 1997

[Flugge 1962] W. Flugge, *Handbook of Engineering Mechanics*, McGraw-Hill, 1962

[Suzumori, 1996] K. Suzumori, A Linear Pneumatic Rubber Actuator Driven by Mechanical Waves, Japan Society of Mechanical Engineering, Workshop on Robotics and Mechatronics, 1996

[Klein et.al., 1984] B. P. Klein, R.C. Jensen, L.M. Sanderson, Assessment of workers' compensation claims for back stains/sprains, *Journal of Occupational Medicine*, 26, 443-448, 1984

[Garg et.al. 1992] A. Garg, B.D. Owen, B. Carlson, An ergonomic study of nursing assistants' job in a nursing home, *Ergonomics*, vol.35, no. 9, 979-995, 1992

[Owen, et.al. 1989] B.D. Owen, A. Garg, Patient handling tasks perceived to be most stressful by nursing assistants, *Advances in Industrial Ergonomics and Safety*, 775-781, 1989

[Fuortes et.al. 1994] L.J. Fuortes, Y. Shi, M. Zhang, C. Zwerling, M. Schootman, Epidemiology of back injury in university hospital nurses from review of workers' compensation records and a case-control survey, *Journal of Occupational Medicine*, 36, 1022-1026, 1994

[Garg Owen, et.al. 1991] A. Garg, B.D. Owen, D. Beller, J. Banaag, A biomechanical and ergonomic evaluation of patient transferring tasks: bed to wheelchair and wheelchair to bed, *Ergonomics*, vol.34, no.3, 289-312, 1991

[Lighthill 1979] James Lighthill, Waves in Fluids, Cambridge University Press, 1979

[Van Dyke 1982] Milton Van Dyke, An Album of Fluid Motion, Parabolic Press, 1982

[Hirose and Umetani 1976] S. Hirose and Y. Umetani, "Kinematic Control of Active Cord Mechanism with Tactile Sensors", *Proceedings of 2<sup>nd</sup> CISM-IFTOM Symposium on Theory and Practice of Robots and Manipulators*, pp.241-252, 1976

[Chirikjian and Burdick 1991] G.S. Chirikjian and J.W. Burdick, "Kinematics of Hyper-Redundant Locomotion with Applications to Grasping", *Proceedings of IEEE International Conference on Robotics and Automation*, April 1991.

## Human Interaction with Surface Wave Actuators

Haruhiko H. Asada  
Principal Investigator

Joe Spano  
Graduate Research Assistant

### ABSTRACT

Several concepts have been proposed for the design of active support surfaces for bedridden patients that allows for flexible reconfiguration of human posture tangent to the surface without physical caregiver intervention. This work defines healthy support surface conditions using quantified data. Nonlinear finite element analysis is utilized for contact analysis between bulk soft tissue and the surface wave actuator designed in the d'Arbeloff Laboratory at MIT. This actuator features rod-like extenders protruding from the surface with spherical tips. Interactions between human bulk soft tissue and a novel surface wave actuated bed surface are studied for two important scenarios. First a flat support surface for long term support is studied. Specifically the issues of support surface impedance and bone inclusion are solved. Second a spherical support matrix is studied. Static stresses are calculated due to human interaction with the support surface. A preliminary analysis was made to determine the optimal design for the new support surface concept. It was uncovered that a surface could be designed that could safely support the human for long periods of time. Guidelines for surface design based on the analysis is the result.

## 1. Introduction

Two attempts have been made to achieve the tangential manipulation goals of the Consortium for bedridden patient manipulation. [Spano and Asada 1998] designed a mechanically generated one dimensional surface wave capable of moving humans. [Finger and Asada 1999] designed a two dimensional surface wave capable of moving rigid objects. The latest surface concept is shown in Figure 1. [Spano and Asada 1999] details an enhanced surface wave actuator system of relatively low actuator dimension with arbitrary planar motion capabilities utilizing 'extenders' to the conventional support surface. All of these designs require that the human be supported by a wave shape or a set of discrete nodes. To make any of these designs feasible requires that they be studied to ensure that unsafe stresses are not induced.

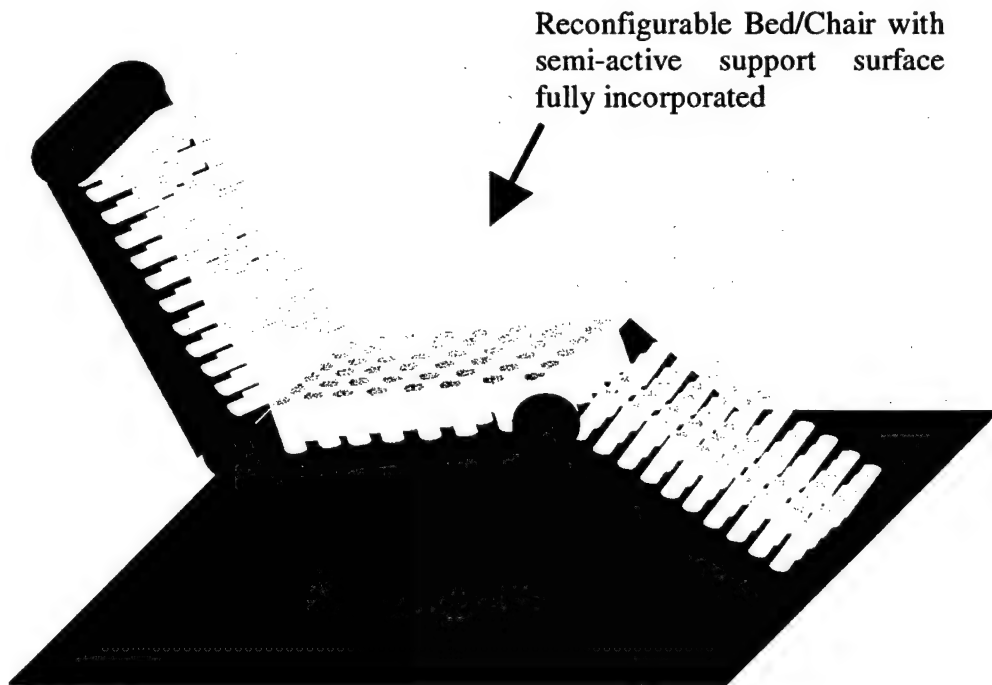


Figure 1 - Reconfigurable bed-chair with extenders

Support surfaces themselves have been studied extensively in the rehabilitation medicine community for the purpose of bedsore prevention. Numerous beds have been developed with the aim of increasing the area of support and reducing stress concentration. Among the numerous designs the fluidized bed concept has been most successful. Numerous other experimental prototypes including sand beds, fluidized beds, and air supports are detailed in [Kenedi 1975]. Work in the application area of soft tissues support systems

has focused on the design of custom contoured cushions and prostheses as a means of reducing peak pressure at the support surface interface. [Brienza 1996] details a test apparatus useful for this purpose.

## 2. Physiologically-based studies

The physiology of soft tissue/support surface interactions has been studied within the fields of rehabilitation, biomechanics, and physical medicine. The literature in these fields offers a wealth of quantitative information that is relevant to this work with some interpretation.

[Ferguson-Pell 1990] has written a primer on the clinical criteria of seat cushion selection. In his report the most important factor that determines functionality, not just comfort, of a support surface is the proper distribution of stress in soft tissues, followed by control of moisture accumulation and heat. Clearly from a clinical and physiological perspective these are the criteria that all support surface designs must meet to be acceptable. This report is a general overview and more detailed quantified data is needed for a rigorous mechanical analysis and design.

Of primary importance is the data showing the relationship between allowable pressure and time duration for 'safe' pressure-time support. This data illustrates clearly the maximum allowable pressure for a given period of time. This data demonstrates that below some pressure threshold, tissue can sustain itself without damage for very long periods of time. This is the region where fluidized beds or special contoured surfaces are designed. These surfaces are used in the treatment of bedsores by keeping pressure as evenly distributed as possible. However, this data also indicates that some higher pressures, above the threshold can be maintained for shorter periods of time.

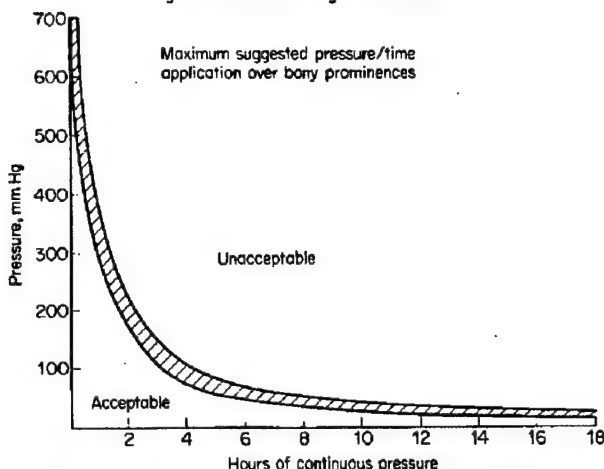


Figure 4. Allowable pressure vs. time of application for tissue under bony prominences. Curve gives general 'guidelines' and should not be taken as absolute

Figure 2 - Pressure-time criteria

The data presented by [Reswick 1975] in Figure 2 is a clinically established pressure-time relationship for normal pressures based on clinical observations of nearly 1,000 patients. However, in a real support surface-human interaction, shear stresses will also be induced and it is important to note the influence of these shear stresses on the human. [Bennett 1979] presents experimental work on blood flow occlusion under shear load. His experimental results show that shear is a contributing factor to blood flow occlusion, but not as dramatically as normal stress. In general it was concluded that normal stress is about twice as effective at producing blood flow occlusion. [Guttmann 1979] makes it clear that shear stress situations must be avoided, citing dramatic examples of plaster casts to treat traumatic paraplegics. It was thought that these rigid, contoured casts would distribute pressure very evenly, however over time, changes in shape of the human body created high shearing actions that produced terrible bedsores. The moral of the story is that both shear and normal stresses must be carefully controlled within the guidelines set by [Reswick 1975]

### 3 Healthy Interactions between Human Soft Tissue and Support Surfaces - The Performance Objective

Healthy interactions between the human and the support surface must be quantitatively defined. Based on these criteria we can establish constraints on our particular design

concept. Based on the clinical results of Reswick, a normal, resting interaction pressure of 4,000Pa is the limit. This ensures a safe interaction of approximately 10 hours duration. Pressure 5-10 times this value are permissible for short periods of time during reconfiguration. Those values are considered the bounds of acceptable pressure for a candidate design.

#### **4. Plane strain models of tissue in contact with a flat support surface**

Models of tissue in contact with a flat support surface have been developed to investigate the contact pressures induced from support by an ideal frictionless surface. Two important features of real support surface scenarios are investigated. First the influence of bone in the tissue close to the surface is determined. Second the effect of varying the impedance of the support surface is also investigated.

I have made several trial mathematical models that explore the problem in a sequential manner. These models include:

- 1) Large displacement, large strain analysis
- 2) Hyperelastic, nonlinear material law
- 3) Contact analysis
- 4) Nearly incompressible material analysis
- 5) Elastic foundation

Each of these components adds to the complexity of the problem and contributes to a more accurate picture of the real physical situation. The physical scenario I would like to model is the human forearm limb in contact with a support surface under gravity load.

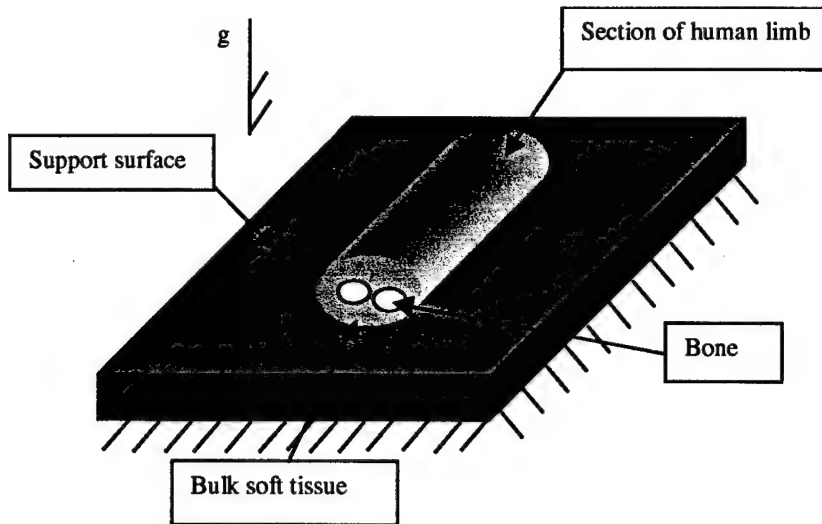


Figure 3 - Human limb in contact with support surface under gravity load

To begin let us assume that the human limb in some portion of the body, say for instance the forearm, is uniform along its length. We will analyze a section of unit length and do a 2-D plane strain analysis.

Let us assume that the bulk soft tissue is homogeneous throughout and the material density and the parameters describing the material properties are kept constant throughout the body. In all of the models a realistic, non-linear, hyperelastic material model for bulk soft human tissue is used due to [Vannah 1996]. The model used is a non-linear Mooney-Rivlin material model. Fully non-linear strain-displacement relations are used and equilibrium is taken in the deformed geometry. Incremental analysis is used to handle the resulting large displacements and strains. (10 time steps) The following strain energy function is used as the constitutive relation.

$$W = c_{10}(I_1 - 3) + c_{01}(I_2 - 3) + c_{11}(I_1 - 3)(I_2 - 3)$$

Material parameters are [Vannah 1996]:  $c_{10} = .0026 \text{ MPa}$   $c_{01} = .00064 \text{ MPa}$   $c_{11} = .0057 \text{ MPa}$

Using the approximation of the initial elastic modulus given in [Bathe 1996],  $E = 6(c_{01} + c_{10})$  and specifying a Poisson's ratio of .4997, one can calculate the bulk modulus to be  $\kappa = 10.8 \times 10^6$ .

#### 4.1 Idealized Mathematical Model #1- No bone inclusion, high-impedance support

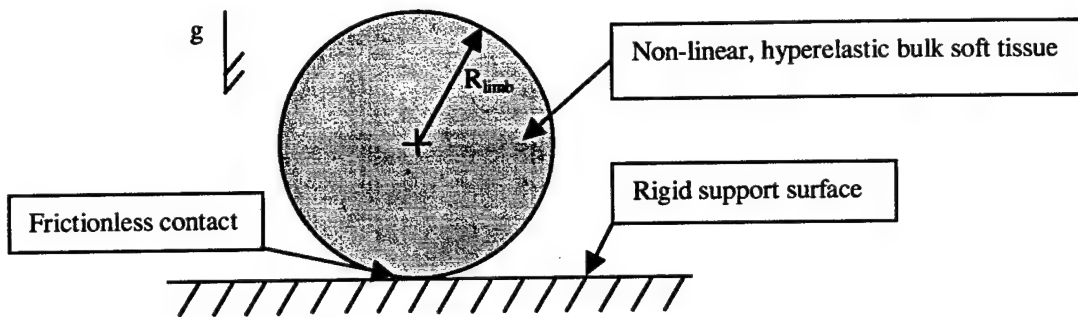


Figure 4 - Model #1 Schematic

Figure 5 is the pressure result for the solution of model #1. Peak pressure at the initial contact point is approximately 3,200Pa. Figure 6 indicates that the strains are in the nonlinear regime ( $>>0.01$ ) and a full nonlinear analysis is needed. Figure 7 illustrates the maximum shear stress which is at its peak above the line of contact. Although this is a non-linear analysis this agrees qualitatively with the Hertz theory which also predicts that shear stress will be maximum within the body on the line of symmetry. For the purposes of bedsores it has been concluded in the literature that pressure is the dominant causal factor and that shearing of the tissues, although not desirable, does not pose as much of a threat.

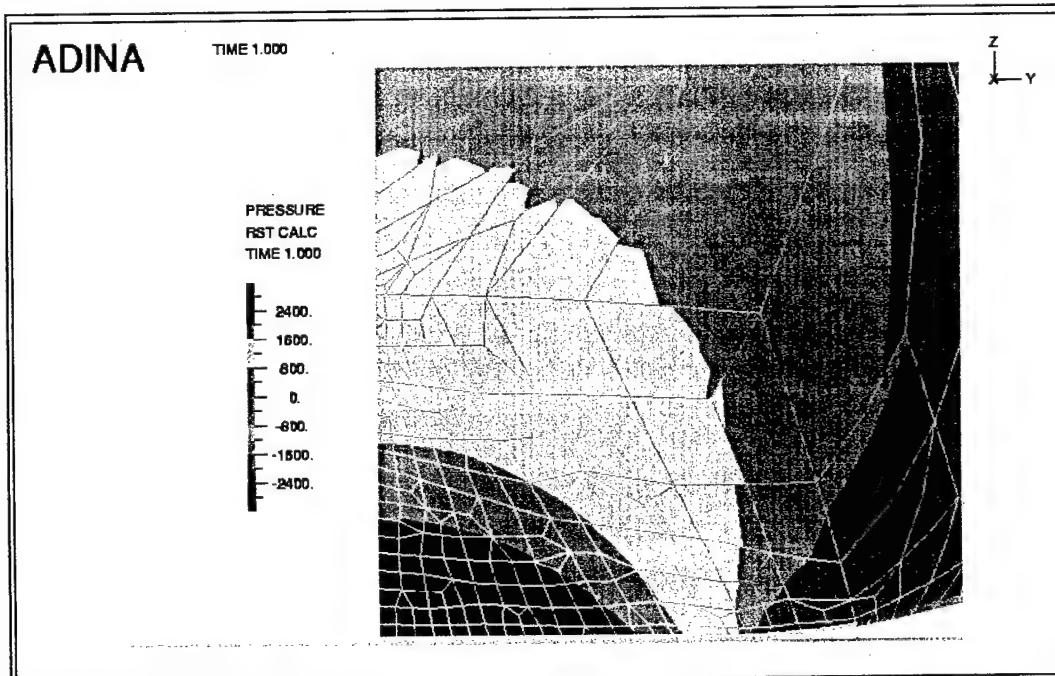


Figure 5 - Model #1 pressure results

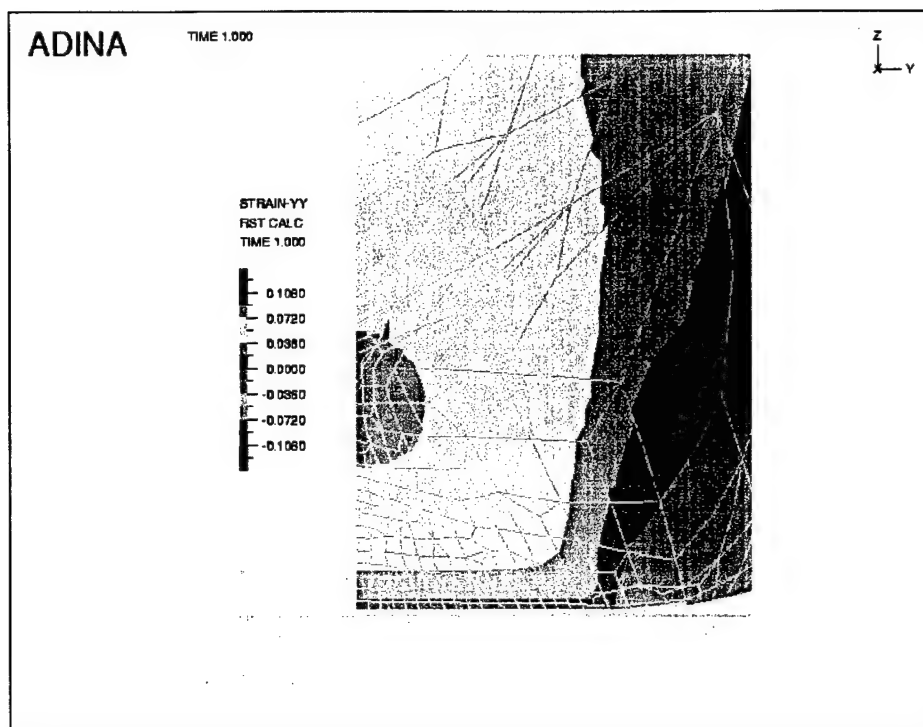


Figure 6 - Strain results for Model #1

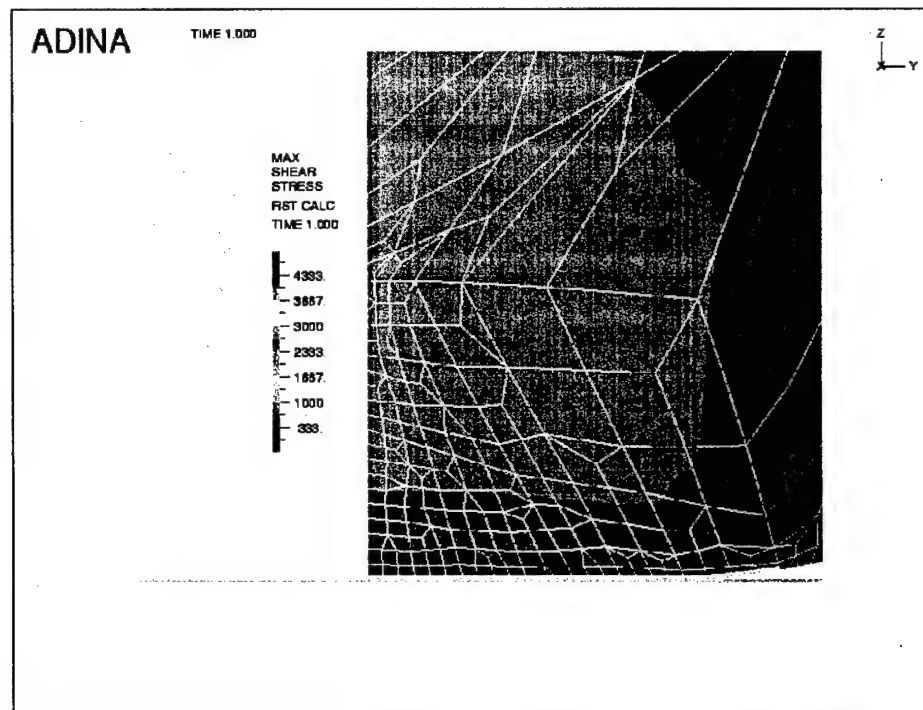


Figure 8 - Shear stress solution for Model #1

#### 4.2 Idealized Mathematical Model #2-With bone inclusion, high impedance support

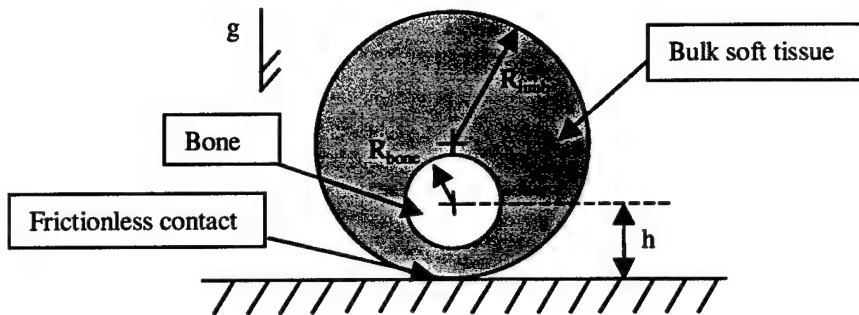


Figure 9 - Schematic of Model #2

To capture the effect of stress concentration due to a thin tissue layer separating bone from its support surface we will introduce a circular bone inclusion close to the contact surface. The bone inclusion will be modeled as perfectly rigid and homogeneous with constant density. The bone inclusion will also be modeled with a no slip boundary condition between it and the surrounding bulk soft tissue as is the case in real human tissue.

Material Properties [Fung 1993]:  $E_{bone}=1.8e10\text{Pa}$   $v_{bone}=.3$   $\rho_{bone}=1950\text{kg/m}^3$

Geometry:  $R_{bone}=.015\text{m}$   $h=.025\text{m}$

With the inclusion of the bone, peak pressure has now increased to 4,000Pa (Figure 10) In addition it is noted that the point of highest pressure is at the bone tissue interface, not at the tissue surface interface. This agrees with the clinical observations that tissue dies from the inside out. The reason for this can be understood physically due to the fact that there is a zero-displacement boundary condition at the bone tissue interface and the bone essentially does not deform. On the other hand there is a frictionless boundary condition at the contact interface so there is some way for stresses to be reduced at the contact interface by frictionless sliding along the contact surfaces.

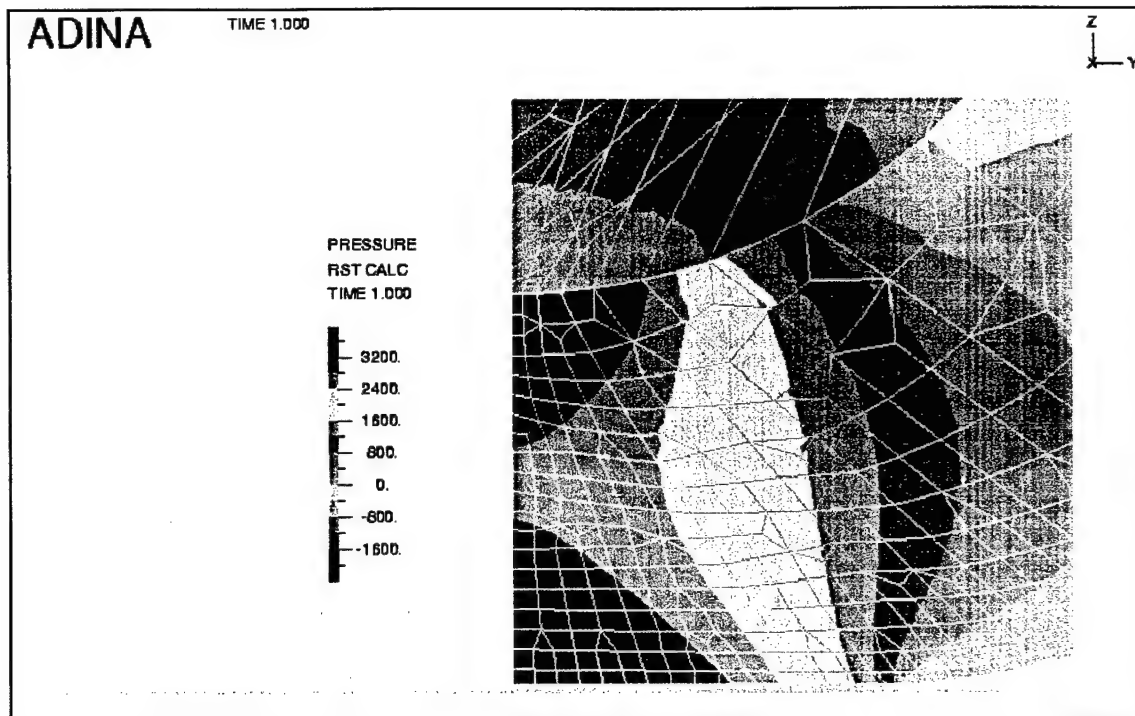


Figure 10 - Pressure solution for Model #2

#### 4.3 Idealized Mathematical Model #3-Bone inclusion, low impedance support

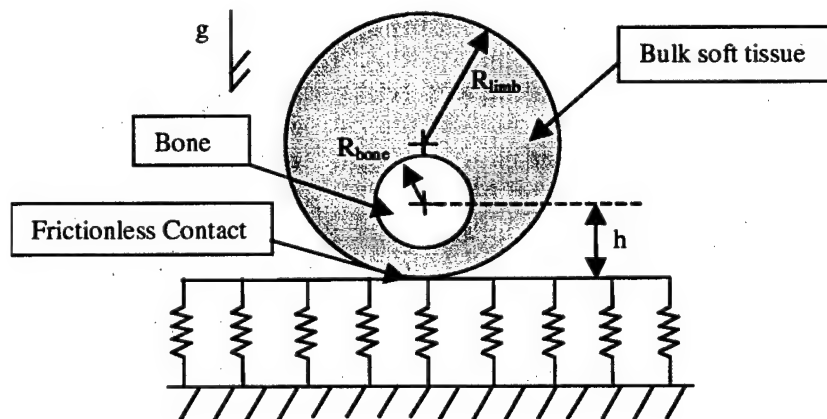


Figure 11-Schematic of Model #3

An elastic foundation supporting the limb has been introduced to illustrate how stress is reduced due to the introduction of a low impedance support surface. Material parameters for support surface were chosen to be the same as soft tissue. The depth of the tissue is .0125m.

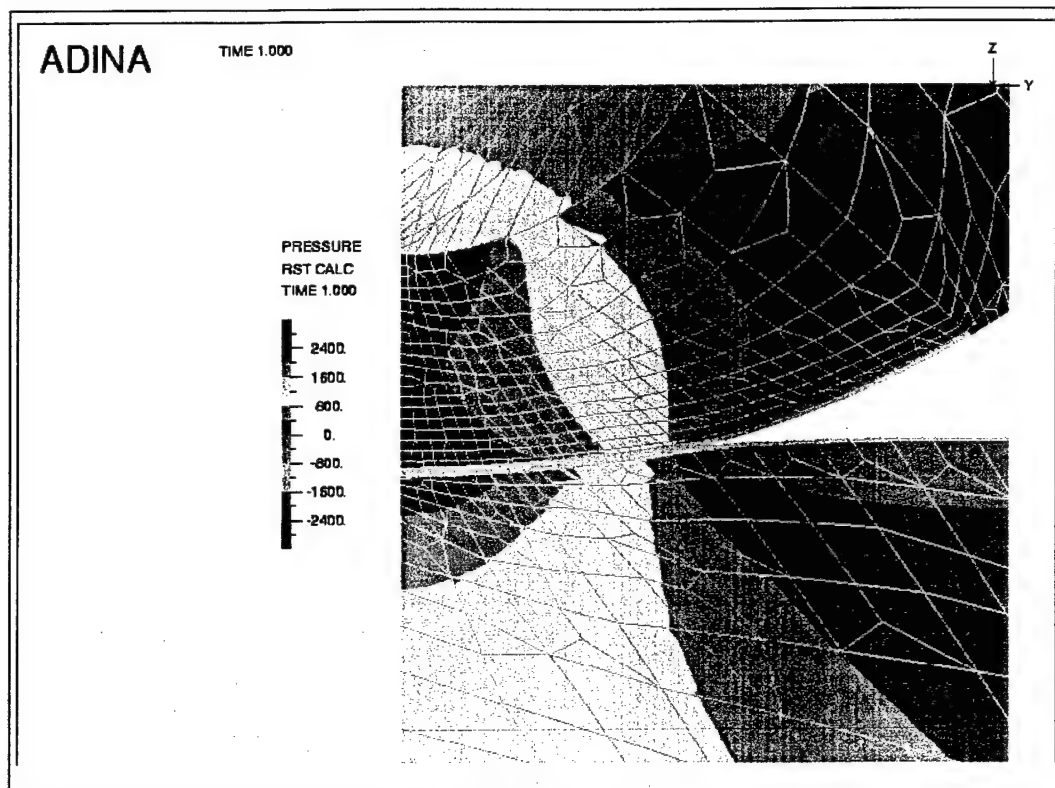


Figure 12 - Pressure results for Model#3

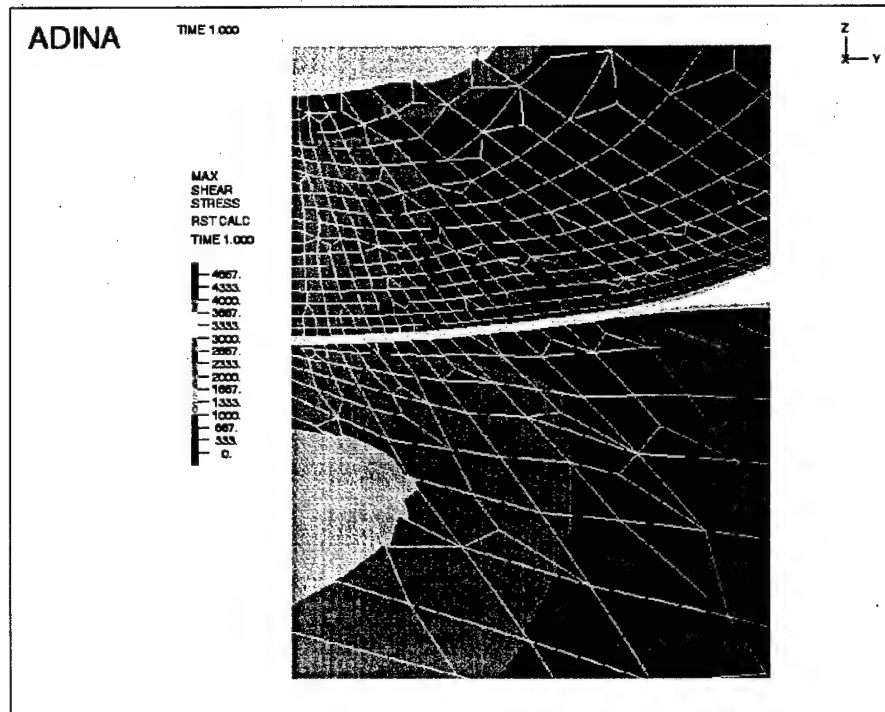


Figure 13 - Shear stress results for Model #3

By introducing an elastic foundation the pressure has been reduced to levels that existed before the bone inclusion. Figure 12 shows the peak pressure has been reduced to 3200Pa which is the result obtained for the case without bone inclusion. This makes sense because I chose the material properties of the support surface to be the same as the soft tissue so one should expect a negation of the effects of the bone inclusion. Figure 13 illustrates the reduction of shear at the contact interface. This makes sense due to the frictionless contact condition. Note that maximum shear stress in the soft tissue has been significantly reduced due to the elastic foundation from approximately 2000Pa in model #2 to approximately 1000Pa in model #3. It would be interesting to study different contact conditions and their effect on shear since they seem to have a strong connection.

## **5. Modeling of spherical tip contact**

With the use of the surface wave actuator with extenders, we will be introducing a spherical foundation matrix as the human support. When an individual lies upon a support surface stresses are induced which deform the soft tissue. The changes in shape result in occlusion of blood vessels and lymphatics, and stimulate nerve endings which could signal discomfort to the central nervous system. We want to be sure that by proper design a physiologically healthy situation will result.

### **5.1 Constraints**

The surface design can be characterized by two parameters, the radius of the spheres,  $R$ , and the distance between adjacent spheres,  $L$ . Two constraints from the machine design itself must be satisfied to ensure adequate machine performance. The distance of separation between adjacent spheres will be bounded by the radius of the spheres as follows:

$$L > 2R$$

### **5.2 Physical model of tissue-support surface interaction**

It is necessary to choose a specific scenario to which the general finite element modeling tools are applied. This choice depends on the specific manipulation goal in mind. The physical scenario I would like to model is the human upper leg limb in contact with a support surface under gravity load. The model is a geometric and static simplification to explore the effects of the spherical foundation.

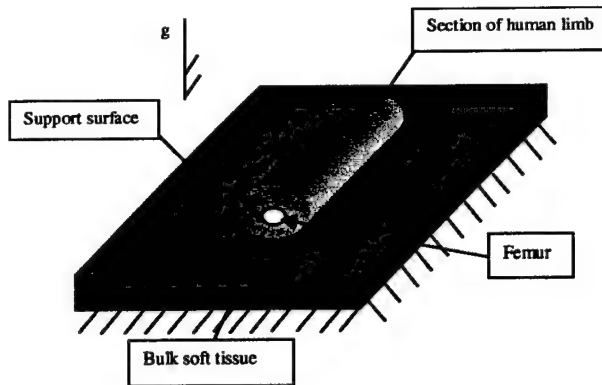


Figure 14 - Model Scenario

**Model Assumptions:**

- 1) Upper leg is statically isolated from pelvis and lower leg, so no load is transmitted through the skeleton
- 2) Lower leg is of uniform cross section
- 3) Bulk soft tissue is homogeneous throughout and material density and material elastic properties are kept constant
- 4) Contact with support surface is frictionless
- 5) Support surface is perfectly elastic and assumes that any contact patch supports the material projected above it only.
- 6) Bone is connected to tissue by zero displacement boundary condition.
- 7)  $R_{sphere} \ll R_{bone}$

With these assumptions we can do a 2-D axisymmetric analysis by examining a 'core' sample of the upper leg subject to the assumptions listed above. In this model the same constitutive model in section 4 is used

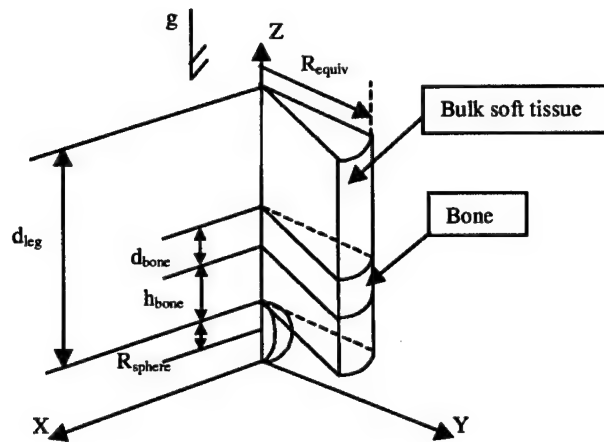


Figure 15 - Model Schematic

To capture the loading on each support sphere it is assumed that each sphere bears the load of a cylindrical portion of tissue equivalent to the mean area of support of each sphere.

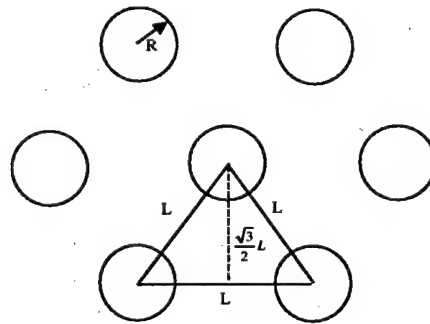


Figure 16 - Spherical foundation matrix layout

By simple geometric arguments it can be shown that the equivalent mean area of support for each support sphere is given by

$$A_s = \frac{\sqrt{3}}{2} L^2$$

and the corresponding equivalent radius of support is given by

$$R_{equiv} = \sqrt{\frac{\sqrt{3}}{2\pi}} L$$

After many trial runs of finite element analysis using different parameters it was found that the major impact on stress was due to the ratio of the sphere radius,  $R$ , and the

spacing,  $L$ . In Figure 17, the results are plotted at the large dots and the regions of constraint are also shown. The infeasible region represents the machine design constraint that  $L > 2R$ . The undesirable region is the peak pressure level that exceeds the long term acceptable pressure levels given in the [Reswick 1975] data. The result is that only very near design constraint  $L > 2R$ , can the surface support the human at safe levels for long periods of time. With larger spacing the design is adequate only for short term support. For all of these trials the deformation constraint was never violated.

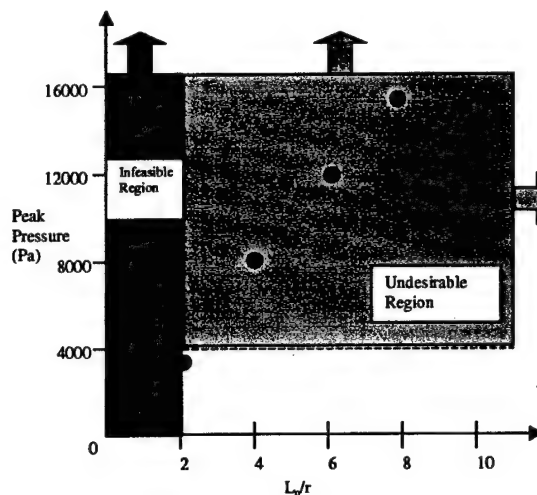


Figure 17 - FEM Results

## 6. Conclusion

A new concept is proposed for the design of support surfaces for bedridden patients that allows for flexible reconfiguration of human posture tangent to the surface without physical caregiver intervention. The attempt is made in this work to define healthy support surface conditions using quantified data. One only has to appeal to physically understood mechanical phenomena to properly analyze the human-support surface interface and synthesize the appropriate geometry to ensure a healthy interaction. A preliminary analysis was made to determine the optimal design for the new support surface concept. It was uncovered that a surface could be designed that could safely support the human for long periods of time, however, the margin of safety was not large.

## References

[Spano and Asada, 1998] J. Spano and H.H. Asada, "An Active, Surface Wave Bed for Transporting Humans and Elastic Bodies," ASME IMECE '98, Anaheim, CA November 15-21, 1998

[Brienza, 1996] Brienza, D.M., et.al., "A system for the analysis of seat support surfaces using surface shape control and simultaneous measurement of applied pressures." in *IEEE Transactions on Rehabilitation Engineering*, pp103-113, June 1996.

[Vannah, 1996] William Vannah and Dudley S. Childress, "Indentor tests and finite element modeling of bulk muscular tissue in vivo," in *Journal of Rehabilitation Research and Development*, Vol. 33 No. 3, July 1996 pgs. 239-252.

[Fischer 1987] Andrew A. Fischer, "Pressure algometry over normal muscles. Standard values, validity and reproducibility of pressure threshold", in *Pain*, 30(1987) 115-126.

[Ferguson-Pell 1990] Martin W. Ferguson-Pell, "Seat Cushion Selection", *Journal of Rehabilitation Research and Development Clinical Supplement*, vol.2, pp. 49-74, 1990

[Reswick 1975] J.B. Reswick and J.E. Rogers, "Experience at Rancho Los Amigos hospital with devices and techniques to prevent pressure sores", Bedsore Biomechanics, 1975

[Bennett 1979] Leon Bennett, et.al., "Shear vs. pressure as causative factors in skin blood flow occlusion", *Archives of Physical Medicine and Rehabilitation*, Vol. 60, July 1979, pp.309-314

[Guttmann 1975] Sir Ludwig Guttmann, "The prevention and treatment of pressure sores", Bedsore Biomechanics, 1975

[Bathe 1996] K.J. Bathe, Finite Element Procedures, Prentice-Hall, 1996

[Spano and Asada, 1997] J. Spano and H.H. Asada, "Design and Control of a Multifunctional Intelligent Bed/Chair System: Concept, Mechanisms, and Sensors," workshop at IEEE ICRA '97, Albequerque, NM, April 1997

[Bennett 1979] Leon Bennett, et.al., "Shear vs. pressure as causative factors in skin blood flow occlusion", *Archives of Physical Medicine and Rehabilitation*, Vol. 60, July 1979, pp.309-314

## **Intelligent Semi-Autonomous Control Architecture Applied to Robotic Holonomic Wheelchairs**

**Professor Harry H. Asada**  
Principal Investigator

**Dr. Karim A. Tahboub**  
Fulbright Visiting Scholar

### **ABSTRACT**

A novel intelligent control architecture for semi-autonomous systems is presented. This has been motivated by the need for an architecture to differentiate between users of different perceptual and cognitive capabilities when interacting and using machines with automatic features and at the same time to comply with user's inputs. A good example for that is a robotic wheelchair. The proposed architecture is hybrid in the sense that the user does the planning (deliberative) while the machine's response is reactive. It evolves around three variables: degree of autonomy to reflect the user capabilities, user's level of confidence in commanding the machine, and strength of conflict between the user's command and the machine's autonomous response. A method is proposed to identify the user capabilities and accordingly to set the degree of autonomy. The analogy between this architecture and horseback riding is demonstrated.

## Introduction

Around the world, millions of young disabled and elderly people rely on wheelchairs in their daily lives. Powered wheelchairs give them more mobility and at the same time save them a considerable physical effort. Although there have been some important achievements towards developing such wheelchairs, navigation and interaction methods still do not satisfy the requirements of all potential users. Safety and maneuverability should be augmented, friendly and simple user-wheelchair interaction tools should be developed to enable physically or mentally disabled people to function with less dependence on the others.

We have designed and manufactured an omni-directional robotic wheelchair [1]. Four balls, actuated independently by DC-motors, enable for moving the wheelchair along any direction in the plane and rotating it around its center while having the ability to change the angle between the beams holding the balls. This novel feature facilitates for varying the footprint configuration to augment stability and change the gear ratio as desired (see figures 1 and 2).

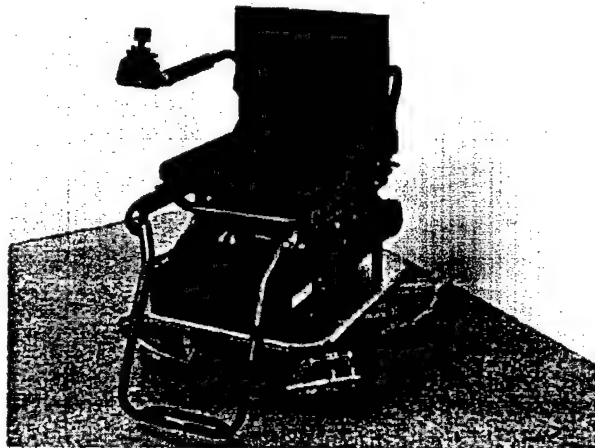


Figure 1: Prototype of the wheelchair

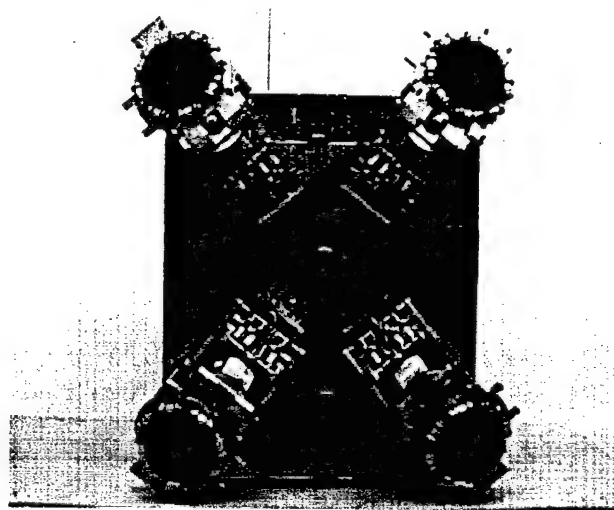


Figure 2: Bottom of the wheelchair

## **State-of-the art in robotic wheelchairs**

Several robotic wheelchair prototypes are produced in different research facilities in the world, see [2, 3] for a review. A variety of cameras, range sensors, joysticks, microphones, head trackers, eye followers, and video screens are deployed on different models to enhance their intelligence and autonomy.

As control architecture, supervisory control (skill-, rule-, knowledge-based behaviors) is suggested in [4]. Depending on the mode of operation, either the user supervises the robot or the robot supervises the user. Man-machine interaction is achieved by the means of a dedicated screen with on-off switches. In [5] the user can select a desired task from a menu. Accordingly and based on a data base and a rule base, a specific man-machine coordination mode is determined.

## **Goals**

It is desired to enhance the intelligent behavior of the wheelchair while maintaining a high standard of safety, to increase maneuverability and navigation capabilities, and to allow for higher autonomy when needed. As not all users are capable of using complicated technology, it is imperative to keep the interfacing tools and sensing system as simple as possible. This leads, as well, to a more affordable price.

## **Hybrid deliberative-reactive intelligent architecture**

The main difference between a mobile robot and a robotic wheelchair is that a user on board controls (in different modes and with variable levels) the motion of the latter. Thus, increasing the system autonomy should be coupled with enhancing the user's trust in the system. As the user's intentions and behavior may change while navigating on the wheelchair the control system should be intelligent enough to understand the user wishes and flexible enough to comply with them while demanding the least amount of information from the user. The man-machine interaction should happen in the most normal possible way that relies on the least possible number of communication devices.

Regarding intelligent control architectures for mobile or autonomous robots two categories are considered: deliberative and reactive. A relatively complete knowledge about the world is required for deliberative behavior where the system uses this knowledge to predict the outcome of its actions. This enables the system to optimize its performance relative to its model of the world. However, this requires the assumption that this knowledge is consistent, reliable and certain. In a dynamic environment where objects may be moving arbitrarily it is potentially dangerous to rely on past information that may be no longer valid [6]. This leads to thinking about reactive intelligence to avoid the use of explicit representational knowledge. Reactive control is a technique for coupling perception and action to produce timely response in dynamic and unstructured worlds. As a deliberative system relies on a hierarchical structure that incorporates a complete world model and a global plan, it is thought to have better predictive capabilities. Thus an architecture that has components from both categories is thought to have a more intelligent, robust, and fast-response behavior. Such architecture is called hybrid deliberative-reactive architecture.

Robotic wheelchairs can be naturally categorized under hybrid intelligence. The user of the system is responsible for planning, global world modeling, and localization. On the other hand, the wheelchair part responds to external stimuli reactively. Accordingly, the important question that arises is how to combine both parts to have the best possible behavior while taking into consideration their limitations. Moreover and especially when dealing with wheelchair users, one should address the issue of variability in their perceptual, cognitive and motoric capabilities.

First, some ideas and methods to deal with reactive behavior of wheelchairs will be presented. Afterwards, the issues of man-machine interaction will be addressed.

## **Subsumption and motor schemas**

A wide range of behavior-based robotic architectures exists. These architectures, in general, share an aversion to the use of representational knowledge, emphasis on a tight coupling between sensing and action, and decomposition into behavioral units [6]. They differ in the granularity of behavioral decomposition, coordination methods used, and response encoding techniques. Two architectures are believed to cover the whole spectrum: the subsumption architecture and the motor schemas architecture.

The subsumption architecture is a layered architecture that uses predefined arbitration strategies and augmented finite state machines as its basis. Motor schemas, on the other hand, is a software-oriented dynamic reactive architecture that is non-layered and cooperative. Vectors serve as the continuous response encoding mechanism with summation as the fundamental coordination strategy [6]. The behavioral units considered for our robotic wheelchair are summarized by the following:

1. Manual footprint configuration: change the angle between the beams manually to augment stability, change gear ratio, or pass through a narrow door. This is achieved by two push buttons.
2. Manual navigation: move the wheelchair arbitrarily in the plane (3 degrees of freedom) according to the direct wish of the user. This is done via the joystick.
3. Automatic stability augmentation: change the beams angle automatically to augment stability.
4. Automatic selection of gear ratio: change the beams angle to automatically select a gear ratio to satisfy torque and velocity requirements.
5. Collision avoidance: automatically avoid any obstacles detected by means of ultrasonic sensors mounted on the wheelchair.
6. Ergonomic posture: rotate the wheelchair automatically around its center to achieve the most ergonomic posture depending on the direction of motion.
7. Hallway navigation: center the wheelchair automatically between two detected walls in hallway navigation or follow a detected wall.
8. Guide following: follow a detected guide automatically. This replaces the usual guide-pushing-wheelchair situation.

Motion playback and motion back tracing are considered to give the user extra tools in handling difficult maneuvers like passing through narrow doors or getting out of a crowded area.

The subsumption and motor schemas architectures are applied to the behaviors considered. The results are shown in a previous work [7]. In the motor schemas architecture, a variable degree of autonomy is introduced to allow for emphasizing different stimulus-response pairs according to their manual/autonomous nature. The degree of autonomy  $A$  can vary between 0 (fully manual) and 1 (fully autonomous). A method of determining  $A$  is presented in the sequel. The footprint configuration group is selected to illustrate the coordination method, see Table 1. On the other hand and as the subsumption method has a predetermined set of rules; manual, semi-autonomous, and autonomous modes are devised to address the degree of autonomy issue. According to the mode of operation certain behaviors are deactivated

Behavior	Response	Weight	Autonomy
Stability	$\dot{\Phi}_s$	3	$A$
Velocity	$\dot{\Phi}_v$	1	$A$
Torque	$\dot{\Phi}_t$	2	$A$
User's input	$\dot{\Phi}_u$	3	$1-A$
Narrow path	$\dot{\Phi}_w$	3	$A$
Total	$\dot{\Phi} = \sum \dot{\Phi}_i * W_i * A_i$		

Table 1: Motor schemas coordination

## **Limitations of current methods**

It is noted that autonomous architectures limit the user in interacting with the system. User's intentions are considered as any other behavior in the system. For example, in case of a detected obstacle and for a given degree of autonomy, some combination of user's command and machine's response will be generated. Here, the user will be prevented from approaching objects closely although it is possible that the user is fully aware of the situation. In such a case, the user should be given the possibility of overriding the machine's behavior. If this is not assured, the user will feel frustrated and will lose trust in the machine.

As a matter of fact, the literature on supervisory-control, artificial intelligence, and behavior-based systems lacks to a semi-autonomous architecture that is capable of addressing the above mentioned issues.

Neither ethology, i.e. animal behavior, nor ecological psychology offers examples of semi-autonomous systems that can be mimicked. However, a man-animal interaction can form a basis for studying autonomous systems.

## **Man-animal interaction**

Horseback riding is a good example of semi autonomous systems and resembles to a great extent driving a robotic wheelchair. The horse, usually, takes care of all low-level tasks such as coordination of leg motions, stability, avoiding obstacles, and providing enough power and speed for different actions. On the other hand, the rider provides for global planning, interacts with horse to achieve tasks, and can override any horse behavior when necessary.

The rider, seen as a system, is completely autonomous as she has adequate perceptual, cognitive, and motoric abilities. The horse, on the other hand, has the same. Although its cognition is limited, it can perform all related tasks autonomously. It can at least wander without any external help. In case of horse riding both parts give up some of their activities. The rider relies on the horse motoric abilities and the horse behavior becomes more intelligent by getting the rider's commands.

The interaction between the two happens in a simple and natural way. The rider commands the horse via the reins, legs pressure at the saddle girth, and by applying and shifting pressure on the seat. The horse interacts with the rider by applying forces upon her with the neck and by raising the front legs (in case of a dangerous obstacle as a snake.)

It is believed that the horse acknowledges the rider commands if they exceed a certain threshold. This threshold depends on the horse training, who is riding (age, maturity, etc) and on the situation at hand. Rider corrects and overrides horse behavior by increasing the level of stimulus (pulling the reins more, pushing harder on the saddle, or increasing the frequency of an action). This continues until the horse changes its behavior as wished by the rider. A lack of proper interaction in show jumping, for example, can end with funny or dangerous scenes.

## **Semi-autonomous architecture**

Mimicking horseback riding calls first for simple and intuitive interaction tools. For powered wheelchairs, joysticks have dominated the market and become sort of a standard interaction tool. Thus, we will concentrate on this tool as a primary interaction tool for robotic wheelchairs. It is shown in a separate section how adding force feedback feature to the joystick will improve the whole system performance and serve as an interaction tool from the wheelchair to the user.

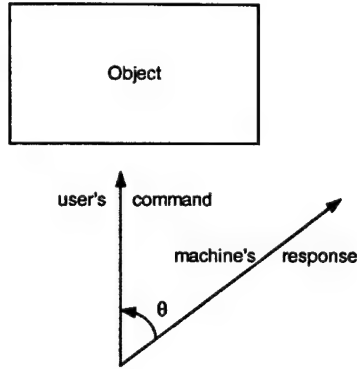


Figure 3: Manual-autonomous conflict

To mimic the threshold behavior described above, consider figure 3 that visualizes a conflicting situation. The user commands the wheelchair to move towards an object, the machine's autonomous response (disregarding user's command) diverts by  $\theta$  degrees from the command. The machine does not know about the user's intention nor the user gives information explicitly. Here, three variables are defined:

1. Level of autonomy  $A$ : as before it takes values between 0 (manual) and 1 (autonomous); this resembles who is riding and how responsible she is.
2. Strength of conflict  $S$ : varies between 0 (no conflict) and 1 (highest conflict). For this example  $S$  is defined as

$$S = \frac{\Theta}{\Pi}.$$

3. User's level of confidence  $C$ : varies between 0 (not confident) and 1 (absolutely sure). For this example  $C$  is defined as

$$C = \frac{\text{amplitude of user's command}}{\text{maximum possible amplitude}}.$$

Based on the value of these three variables, the user's command will be either regarded or disregarded. The following table gives an intuitive decision criterion.

C	A	S	Decision
Low	Low	Low	Regard
Low	Low	High	Disregard
Low	High	Low	Disregard
Low	High	High	Disregard
High	Low	Low	Regard
High	Low	High	Regard
High	High	Low	Regard
High	High	High	Disregard

Table 2: Activation levels of user's command

This intuitive decision criterion can be generalized into an equation form such that the user's command will be regarded if and only if  $C > 2 * A * S$ .

For example, let us apply this criterion to the situation in figure 3. Depending on variable values a certain motion will take place. Two situations can occur

1. The machine complies with user's command and thus no conflict is there
2. The machine does not comply with user's command; here three distinct cases can be identified
  - a) User recognizes that her command was wrong, accordingly she changes her command to comply with the machine
  - b) User feels that the machine is not responding to her commands, accordingly she pushes harder towards her goal and thus she increases her level of confidence until it exceeds the threshold
  - c) User does not notice that, and the machine continues autonomously

This criterion is then imbedded in the modified motor schemas architecture whereas the weight of the manual behaviors can be increased by an order of magnitude. This assures that when the manual (user's command) behavior is regarded, then it forms a dominant factor in the total response. Accordingly, the user has the possibility to shift between autonomous and semi-autonomous modes in a natural and intuitive way with the minimum number of interaction devices. The resulting architecture can be thought of as a hybrid discrete and continuous, competitive and cooperative architecture.

The above argument serves as an implicit user's mental and cognitive model. An explicit human mental model is avoided since deriving it relies on assuming that the user is rational in making decisions [8].

An animation environment has been designed to study and compare different proposed methods and architectures. MATLAB GUI has been selected due to the relatively simple syntax and ease in modifying the structure. One can choose the architecture and activate desired behaviors, set the degree of autonomy and then start animation by commanding wheelchair motions via an animated joystick. This animation environment has helped in better designing the different modules and architectures. Though simulation differs drastically from real world action, this facility gives insight into which problems may occur in implementing different architectures.

## Feedback in semi-autonomous systems

Beside the human usual sensory inputs, it is helpful to provide for extra feedback signals to the human user. This serves two goals:

1. The user will have information about how the wheelchair "sees" the environment and what it will do. This will enable the capable user to correct for the overall behavior.
2. The closed-loop system performance in terms of amplitude and time delay can be improved. This point is discussed in details in the following.

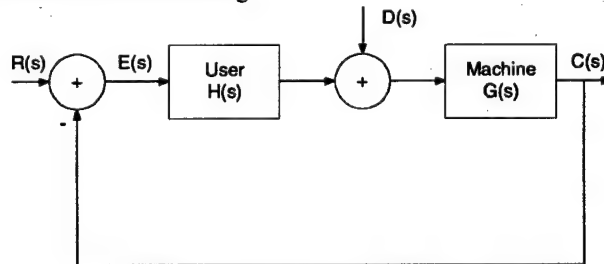


Figure 4: Human-supervisory control loop

It was shown in [9] that a human operator controlling a certain process adapts such that the combined transfer function of the user and the machine is invariant and is given by

$$\frac{C(s)}{E(s)} = \frac{K}{s} e^{-Ts}$$

which is essentially a combined pure time delay and integrator. Users of weak perceptual, cognitive, and movement capabilities are expected to generate transfer functions of long time delays. The effect of a long time delay becomes crucial when the user is moving the chair towards an obstacle in the space. To compensate for this, a prediction tool should be added to the loop. This can be achieved by feeding the command of the user (magnitude and direction) into a motion simulator that calculates the time to the first object in the space, see figure 5. Ultrasonic sensors deployed on the wheelchair give information about the location and distance of the wheelchair from objects in the environment Based on the dynamic model of the wheelchair and the environment, the required time is calculated. The user is then informed about this time by exerting a force on her hand (that moves the joystick) inversely proportional to it.

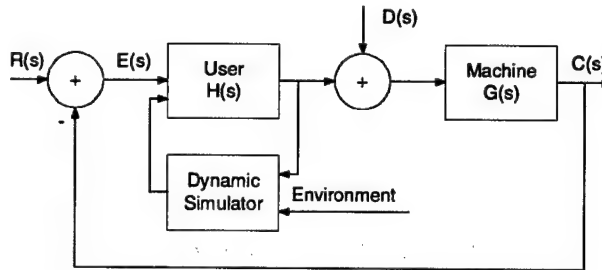


Figure 5: Human-supervisory control with prediction

Feedback via the joystick is advantageous over other visual displays. This is due to the assumption that the user can control the motion of her hand. Moreover, as the force feedback differs in nature from other feedback signals used by the user to detect obstacles, this helps her to overcome any perceptual difficulties and increase her perceptual redundancy. The attention of the user is concentrated on the motion in the environment not on any screens. Finally, the user can be spared from looking behind when commanding the wheelchair to move in that direction.

### Degree of autonomy identification

The presented architecture depends on three variables: level of confidence, strength of conflict, and degree of autonomy. Definitions for the first two have been given above. The degree of autonomy is a variable that ranges from 0 to 1 to reflect the user perceptual, cognitive, and movement capabilities. Considering figure 4, the user transfer function  $H(s)$  is thought to give the required information about the user.

At the beginning of operation the computer onboard will generate step, ramp and other input signals  $D(s)$ . The user is then asked to stop the wheelchair and maintain it stopped  $R(s)=0$ . By knowing the machine transfer function  $G(s)$  and measuring the output  $C(s)$  it is possible to identify the user transfer function. The identified user transfer function can then be parameterized by a metric corresponding to the degree of autonomy.

### Dynamic modeling and identification

A kinematic model is used for the time being to control the motion of the wheelchair. In order to achieve better traction forces (minimize slippage), to minimize power consumption and to have better tracking performance, it is planned to design a control system that incorporates the dynamic model of the wheelchair. In the last few months, a rather complete model has been derived; this includes motor and transmission dynamics, joints and balls friction, twisting torque and wheelchair component masses and inertias. All system parameters have been successfully identified and the model has been verified. Accordingly, the wheelchair transfer function for different modes is available for identifying the user transfer function.

## Conclusions

In this paper, we have discussed the issues of enhancing intelligence, safety, and autonomy of robotic wheelchairs. It is shown that wheelchair systems can be categorized under hybrid deliberative-reactive intelligence where use takes care for planning, world modeling, and global localization whereas the wheelchair controller responds to different inputs (including user inputs) reactively.

Two widely used architectures, subsumption and motor schemas, are modified to handle semi autonomous systems and then applied to the robotic wheelchair problem. The drawbacks of the two methods are identified and discussed.

Horseback riding which resembles a semi-autonomous system is analyzed. Man-animal interaction is studied. Based on the findings, a novel semi-autonomous architecture is developed to mimic horseback riding. For that, three intuitive variables are defined: degree of autonomy, strength of conflict, and user's level of confidence. The values and relationship among these variables determine whether the user's command is going to be regarded or disregarded.

The user can override the autonomous behavior of the system by increasing his level of confidence. In other words, the user can increase the amplitude of his command to exceed a variable threshold and to force the system to acknowledge it.

A joystick with force feedback is proposed as a communication tool between the machine and the user. The user commands the machine by moving the stick in arbitrary direction whereas the machine gives the user feedback about the environment by exerting a certain force on his hand.

It is shown, in principle, that adding this feedback signal not only gives the user extra feedback information but lead to improving the overall system response. Finally, a method for identifying a suitable degree of autonomy for a given user is presented.

## References

- [1] Wada M, Asada HH. "A holonomic omni-directional vehicle with a reconfigurable footprint mechanism and its application to wheelchairs." Proceedings of 1998 IEEE International Conference on Robotics and Automation, pp.774-80.
- [2] Tzafestas S.G "Guest editorial: special issue on autonomous mobile robots in health care services." Journal of Intelligent & Robotic Systems, vol.22, no.3-4, July-Aug. 1998, pp.177-79.
- [3] Miller D. "Assistive robotics: an overview." Book chapter in: Assistive technology and artificial intelligence. Applications in robotics, user interfaces and natural language processing. Springer-Verlag. 1998, pp.126-36. Berlin, Germany
- [4] Bourhis G, Agostini Y. "Man-machine cooperation for the control of an intelligent powered wheelchair." Journal of Intelligent & Robotic Systems, vol.22, no.3-4, July-Aug. 1998, pp.269-87.
- [5] Borgolte U, Hoyer H, Buhler C, Heck H, Hoelper R. "Architectural concepts of a semi-autonomous wheelchair." Journal of Intelligent & Robotic Systems, vol.22, no.3-4, July-Aug. 1998, pp.233-53.
- [6] Arkin R. "Behavior-Based Robotics." The MIT Press, Cambridge, Massachusetts , 1998.
- [7] Tahboub, K., Asada, H.H. "A Semi-Autonomous Control Architecture Applied to Robotic Wheelchairs." Submitted for presentation at IROS'99.
- [8] Proctor, R , Zandt, T. "Human Factors in Simple and Complex Systems" Allyn and Bacon, Boston, 1994.
- [9] Sheridan T., Ferrel, W. "Man-Machine Systems", MIT Press, 1994.

# **Integrating Digital Manuals with Data-Glove Human-Machine Interface**

**H. Harry Asada**  
Principal Investigator

**Mitsuichi Hiratsuka**  
Research Assistant

## **ABSTRACT**

The novel concept of Digital Manual is developed. Digital Manual not only stores information of a task procedure and provides pertinent instructions to the human for completing the task, but also monitors the human in performing the task. By monitoring the human performance, mistakes and malpractice can be identified, and alert and guidance can be provided in the right time. To understand the human performance, Digital Manual needs a model to represent the task structure and the human performance. Human performance in the task procedure is considered as a stochastic process, and a hidden Markov model is applied to modeling the human performance and describing the task structure for Digital Manual. Based on the hidden Markov model, human mistakes, confusion, and failure are detected during the human task performance. Algorithms for identifying and modifying the hidden Markov model are developed. Using a manual assembly task as an example, an experimental system of Digital Manual is designed. The experimental system shows the integration of Digital Manual with a data-glove human-machine interface which can not only measure the human hand motion but also provide an intuitive human-machine interface.

## 1. Introduction

There is an increasing need for better human-machine interface in home automation as well as hospital and factory automation. Active beds and chairs, smart canes, and health monitoring systems are just a few examples that need effective human-machine interface in the Home Automation and Healthcare Consortium project. In the last decade, new technology for human-machine interface is emerging that provide intuitive interface for user-friendly systems and help the human work on the task. Wellner [1] developed a system that gave intuitive human-machine interfaces using projected images onto a working desk. Rauterberg et al. [2] conducted experiments to demonstrate this kind of human-machine interface to be important and helpful especially for elderly people. While these systems had only passive interaction with the human, Sharma et al. [3] proposed a system that gave instructions to the human in manual assembly tasks in accordance with the assembly state. This human-machine interface included the assisting function for the human.

Digital Manual can support the human to complete a task in various situations. Digital Manual retrieves stored instructions and information about the task, and then provides instructions during task performance. These instructions guide the human to appropriate steps of operation toward the task goal. To give right instructions at the right time, Digital Manual has to understand the current status of the human and the objects in the task. Therefore, the task structure and the human performance should be modeled to determine their status. By recognizing the current state of the task and keeping track of the human performance based on the model, Digital Manual can give an effective guidance to the human, and it can detect some errors or confusion in the task.

In this report, a method for modeling human performance and task structure is represented. A manual assembly task is used as an example of human performance. To understand human performance, a hidden Markov model is used as a modeling method. Finally, we design an experimental system of Digital Manual for an assembly task.

## 2. Human performance

Under the umbrella of the Home Automation and Healthcare Consortium, various equipment and devices are being developed in the last several years. Many of them need a special care in operating the system due to safety requirements and involvement of the elderly and caregivers who are lacking in experience in operating machines. Active beds and omni-directional wheelchairs, for example, would not be accepted by the end users unless the system is very easy to operate and safe. Moreover, since those end users are mostly elderly people and caregivers, they are often unable to operate the system properly; they tend to be inconsistent due to confusion, memory loss, or simple mistake. Proper guidance and instructions as well as detection of mistakes and confusion are therefore critical to the design of these systems.

In general, human mistakes are crucial in many tasks and processes ranging from merely manual procedures to operations of complex machines and systems. Mistakes often result in costly repair, injury, or indemnity in many manual procedures and operations at hospitals and factories as well as in the home. The goal of this project is to develop an effective method for detecting mistakes and guiding the end user. This report focuses on

the development of human models that would elucidate the process of fault operations, confusion, and mistakes.

As addressed in numerous references in the human machine systems [1, 2, 3], it is necessary to distinguish actual state of the process and perceived state by the human. A human may perceive the state of the process differently although the information provided to the human remains the same. Sometimes the perceived state significantly differs from the reality, and results in a different action taken by the human. Furthermore the human may take a different action although the same instruction was given to the human. Based on this observation, human behavior can be depicted by the conceptual diagram shown in Figure 1.

The human action is an observable event, while human state is not generally visible from outside. It is an internal state and is often reflecting the mental state of the human. Confusion and misperception occur in this process, and the process is not deterministic. In this report, we treat variability and inconsistency in human behavior as a stochastic processes; both the perception and decision processes in Figure 1 are modeled as stochastic processes. It should be noted, however, that the human behavior is not a totally random process. There exists a certain correlation between a time series of observable outputs and the human state. This allows us to estimate the human state based on the observation of visible outputs, and predict the possible end results and consequence of the sequence of the human actions.

Hidden Markov modeling provides a systematic way of representing and analyzing such stochastic processes, and we employ it in this report. Hidden Markov models have been used in speech recognition [4], robotic performance modeling [5], the human skill acquisition [6] which consist of stochastic processes.

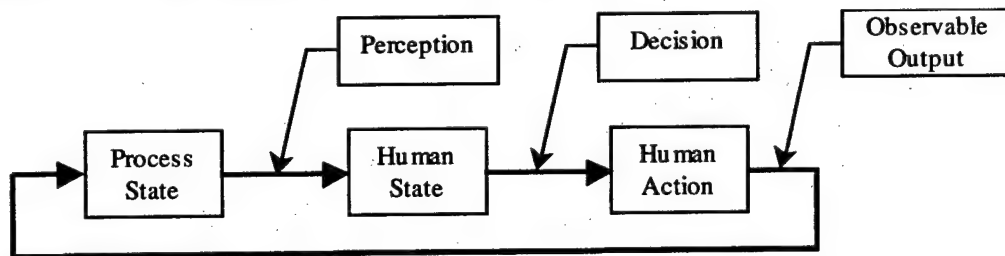


Figure 1. Human and process state

### 3. Representation of human states

We focus on the class of tasks of which process states and human actions can be described using a network representation. Figure 2 shows an example of a graph describing a task procedure. A lot of tasks in home, hospital, and factory automation can be represented by using this network representation, since they can be considered as sequences of process states and human actions and a process state changes to another states according to human actions.

In the network representation, human actions in task procedure can be considered as a stochastic process because of several reasons as follows. First, the human don't completely follow instructions of task procedure. The human sometime ignore instructions and create their own procedure by using their intelligence. They sometime miss to follow instructions due to their carelessness. Second, we can easily find several

ways to reach the goal of the task. It shows that the human might take different actions even if their goals remain the same. These human actions are decided based on the human states which also can be considered as a stochastic process.

Task procedure always has some constraints which have to be taken into consideration when an action is taken. There might exist an action which have to be done before other actions to complete the task. If such constraints are ignored, the task can't be completed. While human actions and internal states are stochastic processes, there should exist some consistent sequences resulting from the constraints. These constraints affect human states. Therefore, to give effective instructions to the human, we have to take their internal states into consideration as well as human actions.

To model these stochastic processes such as human actions and internal states in task procedure, the conventional network representation is not powerful enough, because it can't represent human states which can't be ignored to model human performance. By using a hidden Markov model, we can model some meaningful sequences of human actions and internal states.

In a hidden Markov model, a task procedure is divided into several states that correspond to hidden internal states of the human. At each internal state, actions can be observed with probabilities. These observable outputs consist of human actions by which process states change to another process state. The probability distributions of human actions are different at each internal state. The transitions between internal states also happen with probabilities. Since the hidden Markov model can describe the sequence of human actions and internal states, it also can model the task structure.

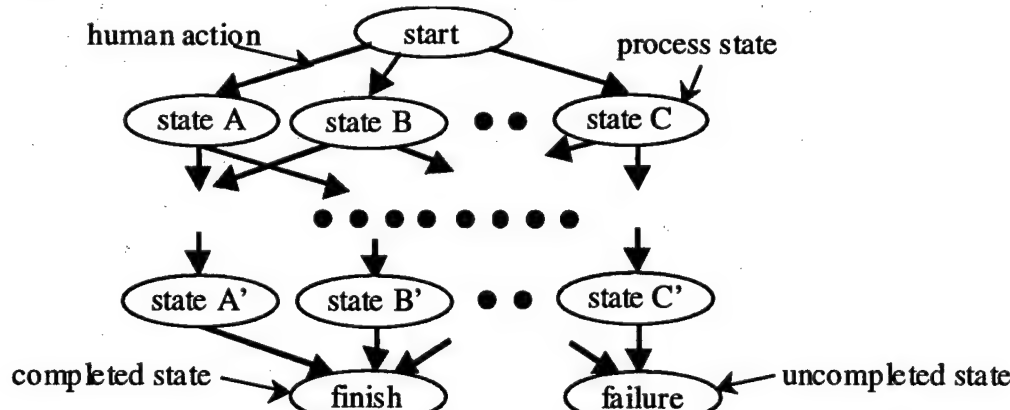


Figure 2. the network representation of a task procedure

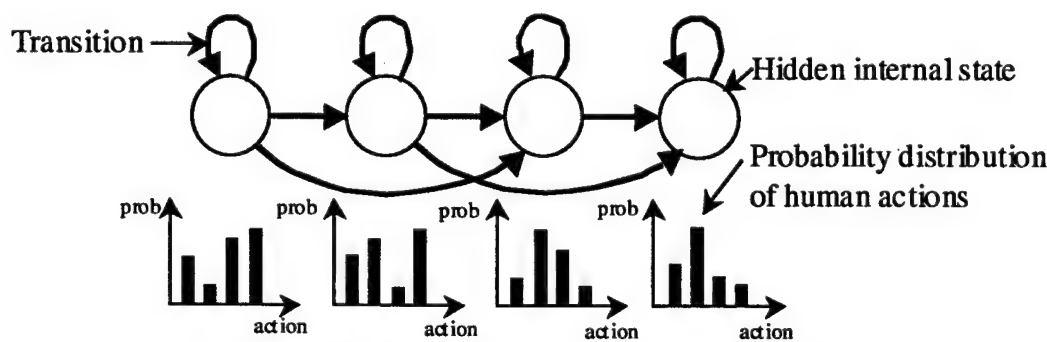


Figure 3. A hidden Markov model for a task procedure

#### 4. Construction of hidden Markov model

A hidden Markov model  $\lambda$  is described using three parameters ( $A$ ,  $B$ ,  $\pi$ ) which are defined as following.

- $A = \{ a_{ij} \}$ ,  $a_{ij} = P(S_{t+1} = q_j | S_t = q_i)$  : a state transition probability distribution from state  $q_i$  at time  $t$  to state  $q_j$  at time  $t+1$ .
- $B = \{ b_j(k) \}$ ,  $b_j(k) = P(O_t = v_k | S_t = q_j)$  : an observation symbol probability distribution, where  $v_k$  is an observation at time  $t$ , given state  $q_j$  at time  $t$ .
- $\pi = \{ \pi_i \}$ ,  $\pi_i = P(S_1 = q_i)$  : an initial state probability distribution at state  $q_i$ .

We have to decide the number of hidden states, the number of observable symbols, and the connections among hidden states.

- The number of hidden states

There is no systematic way to decide the number of hidden states, but we can use a heuristic method based on the prior information such as a network representation. For example, three hidden states are used for a simple task with one procedural constraint. At the beginning of the procedure, the human does some easier operations first. This is a first state. After that, the human has to be cautious to take actions, because a constraint has to be taken into consideration. This can be a second state. At the end of the task, the human has to do some remaining operations to reach the goal. This is third state. Therefor, the human go through three mental states during task procedure. If the task becomes more complicated and more detailed model is needed, there should exist more hidden states.

- The number of observable symbols

The number of observable symbols is the number of types of human actions to complete the task. It can be determined by the task structure.

- The type of hidden Markov model

For the connections among hidden states, a left-right model of hidden Markov model is suitable to represent human internal states during task procedure. It can describe the time-sequencing character of human internal states. As the task is proceeded, a human state transits from left to right. Here we assume that there is no path to go back to a previous state in the task. If the human recognize mistakes, they might go back to a previous state. But we would model this situation as a unsuccessful model. This unsuccessful model represents the human actions and internal states until they recognize their mistakes.

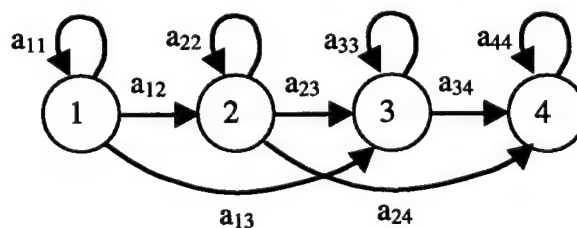


Figure 4. A left-right model of hidden Markov model.

The model parameters  $(A, B, \pi)$  should be reestimated to maximize the probability  $P(O|\lambda)$  for a given observation sequence  $O=O_1O_2\dots O_T$  from time  $t=1$  to  $t=T$ . The reestimated model  $\lambda'=(A', B', \pi')$  using a training algorithm is more likely than the current model  $\lambda=(A, B, \pi)$  in the sense that  $P(O|\lambda') > P(O|\lambda)$ . To compute this model  $\lambda'$  based on the model  $\lambda$ , there is no analytical way, but Baum-Welch algorithm gives an iterative procedure for it [4]. We define the forward variable  $\alpha_t(i)$ , the backward variable  $\beta_t(i)$  as follows.

$$\alpha_t(i) = P(O_1O_2\dots O_t, S_t = q_i | \lambda) \quad (1)$$

$$\beta_t(i) = P(O_{t+1}O_{t+2}\dots O_T, S_T = q_i | \lambda) \quad (2)$$

where  $1 < t < T$  and  $1 < i < N$ . We also define  $\xi_t(i, j)$ , the probability of being in state  $q_i$  at time  $t$  and state  $q_j$  at time  $t+1$ , given the model and observation sequence, as

$$\xi_t(i, j) = P(S_t = q_i, S_{t+1} = q_j | O, \lambda) \quad (3)$$

We can rewrite  $\xi_t(i, j)$  as follows.

$$\xi_t(i, j) = \frac{\alpha_t(i) a_{ij} b_j(O_{t+1}) \beta_{t+1}(j)}{P(O|\lambda)} \quad (4)$$

We define the variable  $\gamma_t(i)$  as

$$\gamma_t(i) = P(S_t = q_i | O, \lambda) = \sum_{j=1}^N \xi_t(i, j) \quad (5)$$

Using the above definition, reestimation formulas for  $(A, B, \pi)$  are given as

$$\pi_i = \gamma_t(i) \quad (6)$$

$$a_{ij} = \sum_{t=1}^{T-1} \xi_t(i, j) \Big/ \sum_{t=1}^{T-1} \gamma_t(i) \quad (7)$$

$$b_j(k) = \sum_{\substack{t=1 \\ \text{s.t. } O_t = v_k}}^T \gamma_t(j) \Big/ \sum_{t=1}^T \gamma_t(j) \quad (8)$$

Training data is a set of the observation sequence  $O$  that is a sequence of the human actions. One action is defined by one operation in a step of a task that change a process state to another process state. These observations can be treated as discrete events. Each set of data has to be prepared for each model that we are interested in.

## 5. Estimation of human performance

Once we obtain the models of human performance in task procedure, we can evaluate a new observation sequence based on these models. By computing  $P(O|\lambda)$ , given observation sequence  $O=O_1O_2O_3\dots O_T$  and model  $\lambda=(A, B, \pi)$ , we can find the most likely model  $\lambda$  which gives the maximum probability  $P(O|\lambda)$ .

For every fixed hidden state sequence  $I=i_1i_2\dots i_T$ , the probability of the observation sequence is

$$P(O|I, \lambda) = b_{i_1}(O_1)b_{i_2}(O_2)\cdots b_{i_T}(O_T) \quad (9)$$

The probability of such a state sequence  $I$  is given as

$$P(I|\lambda) = \pi_{i_1} a_{i_1, i_2} a_{i_2, i_3} \cdots a_{i_{T-1}, i_T} \quad (10)$$

The joint probability of  $O$  and  $I$  is

$$P(O, I|\lambda) = P(O|I, \lambda)P(I|\lambda) \quad (11)$$

Therefor, the probability  $P(O|\lambda)$  is obtained as follows.

$$\begin{aligned} P(O|\lambda) &= \sum_{\text{all } I} P(O, I|\lambda) = \sum_{\text{all } I} P(O|I, \lambda)P(I|\lambda) \\ &= \sum_{i_1, i_2, \dots, i_T} \pi_{i_1} b_{i_1}(O_1) a_{i_1, i_2} b_{i_2}(O_2) \cdots a_{i_{T-1}, i_T} b_{i_T}(O_T) \end{aligned} \quad (12)$$

This computation can be done effectively using Forward-Backward algorithm [4].

For example, we construct two models of a task procedure: a successful task sequence which ends up with a completed state and an unsuccessful task sequence which ends up with a uncompleted state. Based on the models, we can compute three types of estimation for a given sequence of observations. Let  $\lambda_S$  and  $\lambda_F$  be a successful performance model and a unsuccessful one respectively.

- **Guidance to the task goal**

Based on the model  $\lambda_S$ , the most preferable observation sequence can be determined. The next action should be determined to make the probability of this observation sequence maximized. Namely, if an observation sequence  $O=O_1O_2$  is given, the search for the next desired observation  $O_3$  maximizing  $P(O_1O_2O_3|\lambda_S)$  should be done for all possible observation  $O_3$ . The expected observation  $O_3$  is provided as the next instruction.

- **Error detection**

For a given observation sequence  $O=O_1O_2O_3\dots O_T$ , the probabilities  $P(O|\lambda)$  for each model shows how well the observation sequence matches to the model  $\lambda$ . If  $P(O|\lambda_S)$  is nearly equal to zero and  $P(O|\lambda_F)$  has some value greater than zero, we can conclude that the observation is probably an unsuccessful performance.

- **Confusion detection**

We can regard a mistake as a result of confusion of the human. Therefore, confusion is modeled in the unsuccessful model. For a given observation sequence  $O=O_1O_2\dots O_i$ , we can computer the probability  $P(O|\lambda)$ . If we obtain the following change of  $P(O|\lambda_F)$  and  $P(O|\lambda_S)$

$$P(O_1\dots O_j|\lambda_F) < P(O_1\dots O_j|\lambda_S) \text{ for } j < i \quad (13)$$

$$P(O_1\dots O_j|\lambda_F) > P(O_1\dots O_j|\lambda_S) \text{ for } j = i \quad (14)$$

we can consider that confusion may happen at time  $t=i$ .

## 6. Network representation as prior knowledge

For the class of the tasks which can be described by using a network representation, information included in the network can be exploited as prior knowledge. We can obtain insight of the observation of human actions from the network representation. This insight can be useful to determine the initial parameters of a hidden Markov model. In general, we need a lot of training data for training of a hidden Markov model. But by using well-estimated initial parameters, we can expect the reduction of the training data.

For example, a manual assembly task can be represented by using a network graph. Figure 5 and 6 show a 4-part assembly object and its assembly graph used in [7]. In the assembly graph, each state indicates a configuration of assembly parts, and each transition between states indicates a human action to assemble parts. While the task goal is the same, assembly actions of the human can be taken in a stochastic manner. Due to a mechanical constraint, there are unsuccessful task procedure which end up with uncompleted states. By using this example, it is shown how to apply an assembly graph as prior knowledge to a hidden Markov model. Here, we model two assembly procedures: the successful procedure model and the unsuccessful procedure model. An assembly sequence that completes a task is modeled in the successful model, and an assembly sequence that cannot complete a task is modeled in the unsuccessful model. We can find both sequences in the assembly graph.

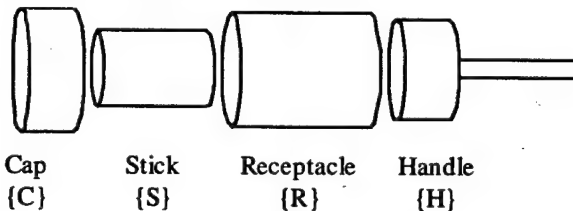


Figure 5. A 4-part assembly object.

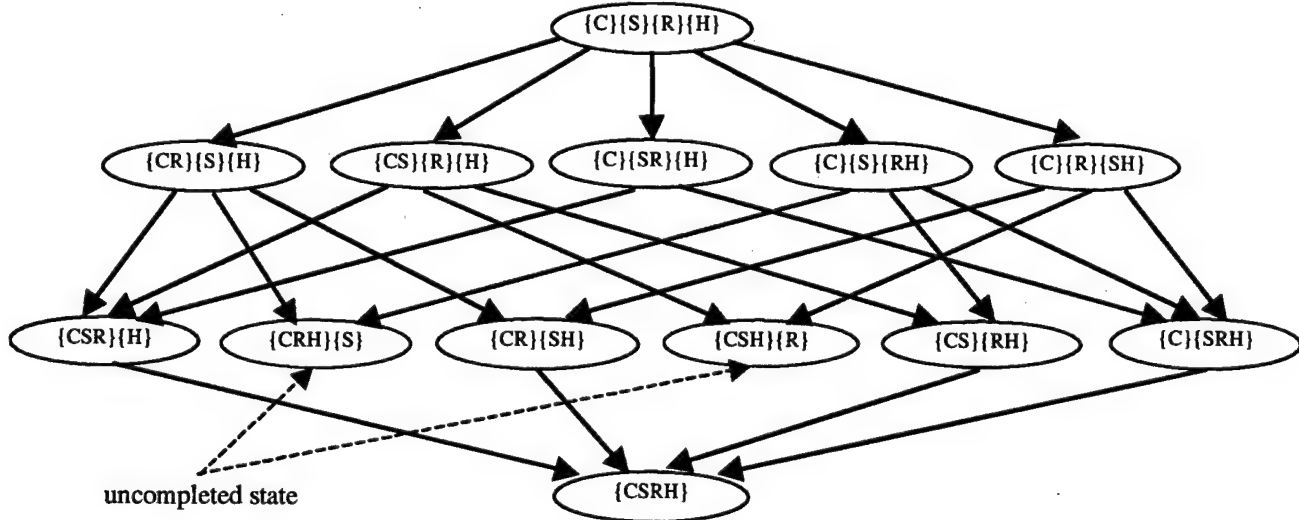


Figure 6. Assembly graph of the 4-part assembly object.

The assembly graph shows that there are two uncompleted states and there are four paths from the initial state to the uncompleted states. These failures happen due to the mechanical constraint. In these unsuccessful assembly sequences, we can find that the

connection between the stick and the receptacle is not included. This connection can not be established at the last step of the assembly sequence. Therefore, in the hidden Markov model of the unsuccessful sequence, the observation to establish the connection between the stick and the receptacle never occurs and its probability should be zero.

On the other hand, in the successful sequence, the connection between the stick and the receptacle is established before the last step of the assembly sequence. The probability of this observation should be larger at the beginning of the assembly sequence and should be zero at the end of the assembly sequence.

By using a conventional network representation as prior knowledge, we can obtain well-estimated initial parameters, especially the probability distribution of the observation. This helps to reduce the training data that is an important and time-consuming procedure to obtain a hidden Markov model.

## 7. Design of Digital Manual for a manual assembly task

We design an experimental system of Digital Manual by using a manual assembly task as an example in the class of tasks which we focus on in this report. A manual assembly task can be considered as a human performance. This task is proceeded by human actions which determined by human internal states. If an assembly task is complicated, some instructions should be provided according to the task procedure. Digital Manual can provide these instructions by understanding the current status of the human and the objects in the system. This system integrates Digital Manual with man-machine interfaces such as a data-glove and a video projector. Figure 7 shows a schematic picture of this system.

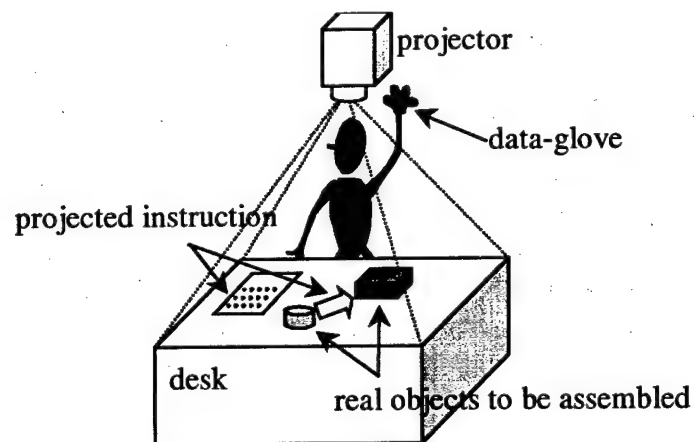


Figure 7. Digital Manual system for a manual assembly task

A data-glove monitors the hand motion in the space and the force acting on the tip of fingers. It also can realize the concept of the “virtual switch” that gives an intuitive and interactive human-machine interface [8]. A video projector gives images onto the desk. These images include the drawings, the task instructions, and other information to assist the human in the task. By applying the concept of the “virtual switch” to the projected images, the images not only are the interface between the human and Digital Manual, but also gives information from Digital Manual to the human.

Digital Manual monitors the human actions from the data of the hand motion and the finger force. When a sequence of the human actions is observed, Digital Manual understands the current status of the system based on the hidden Markov model of the human performance and the task structure. This current status includes the part configuration and the human internal states. Digital Manual finds the instruction of the next desired action to reach the given task goal and gives it to the human through the images of the video projector. Figure 8 shows the flow chart of the task processing with Digital Manual.

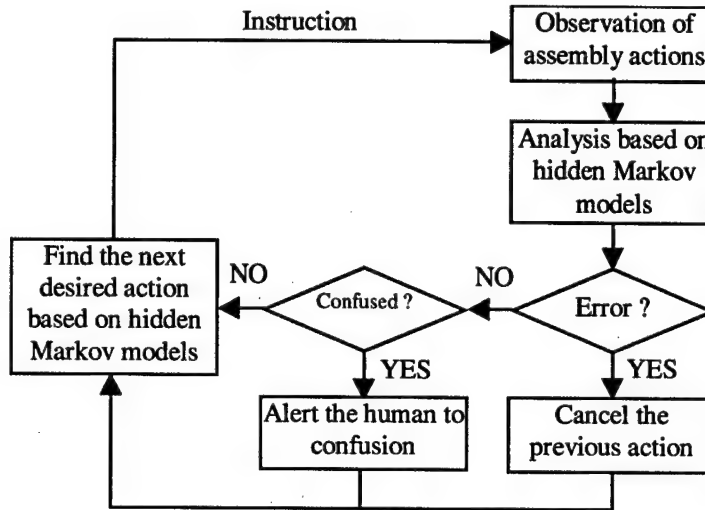


Figure 8. Flow chart of task processing with Digital Manual

## 8. Conclusion

Digital Manual has to understand human actions and internal states to provide effective guidance to the human and to determine what kind of mistakes/contingency is happening. Since human actions are determined according human internal states, and human actions is considered as a stochastic process. Hidden Markov modeling method is applied to model the human performance because a hidden Markov model can represent a doubly stochastic process such as a process including human actions and internal states in a mathematical way. This method can model meaningful sequences of the human performance of tasks in various situation. Finally, by integrating Digital Manual with a data-glove and other human-machine interfaces, we designed an experimental system for an manual assembly task.

## References

- [1] P. Wellner, "Interacting with paper on the DigitalDesk," *Communications of the ACM*, 36(7), pp.86-96, 1993.
- [2] M. Rauterberg, T. Mauch, and R. Stebler, "The Digital Playing Desk: a Case Study for Augmented Reality," *Proceedings 5th IEEE International Workshop on Robot and Human Communication*, pp.410-415, 1996.

- [3] R. Sharma, and J. Molineros, "Computer Vision-Based Augmented Reality for Guiding Manual Assembly," *Presence*, vol.6, no.3, pp.292-317, 1997.
- [4] L. R. Rabiner, "A Tutorial on Hidden Markov Models and Selected Applications in Speech Recognition," *Proceedings of the IEEE*, vol.77, no.2, Feb. 1989.
- [5] B. Hannaford, and P. Lee, "Hidden Markov Model Analysis of Force/Torque Information in Telemanipulation," *The International Journal of Robotics Research*, vol.10, no.5, pp.528-539, 1991.
- [6] J. Yang, Y. Xu, and C. S. Chen, "Human Action Learning via Hidden Markov Model," *IEEE Trans. Syst. Man and Cybern. (Part A: Systems and Humans)*, vol.27, no.1, pp.34-44, 1997.
- [7] L. S. Homem de Mello, and A. C. Sanderson, "Representations of Mechanical Assembly Sequences," *IEEE Trans. Robotics and Automation*, vol.7, no.2, pp.211-227, 1991.
- [8] S. Mascaro, and H. H. Asada, "Hand-in-glove human-machine interface and interactive control: task process modeling using dual Petri nets," *Proceedings 1998 IEEE International Conference on Robotics and Automation*, pp.1289-95 vol.2, 1998.

# **Hemodynamic Modeling and State Estimation for Assessment of Cardiovascular Health**

**Prof. Roger D. Kamm  
Dr. Yaqi Huang,  
Xinshu Xiao**

## **ABSTRACT**

This project encompasses the development of model-based approaches for use in non-invasive assessment of cardiovascular function. In a typical application, measurements of the pressure or velocity waveforms at a peripheral location would be analyzed by means of a computational model of the cardiovascular system to infer parameters of clinical interest. Models of varying degrees of complexity are being developed, from the most detailed, local, three-dimensional analysis of hemodynamic flow patterns, to distributed network models of the arterial tree, to lumped parameter models of the entire circulation and control system. The long-term objective is to develop an array of computational tools having various levels of complexity, to meet a variety of needs. At present, this project links closely with the development of wearable sensors of cardiovascular function, but the realm of application of such models is much broader than this single task.

## I. Introduction

Noninvasive cardiovascular assessment in the home is currently limited primarily to the simple measurements of blood pressure and heart rate. The potential exists to monitor ECG as well, but few devices are capable either of continuous monitoring or of data interpretation beyond the obvious. Yet, there exists enormous potential in the subsequent analysis of these measurements that could potentially lead to more comprehensive, and more useful, information concerning the cardiovascular state of the individual.

Continuous measurement of blood pressure is now a reality with the recent development of systems that can be worn, either on the wrist or, in the case of the Ring Sensor, on the subject's finger. Miniaturized sensors and on-board electronics enable the device to convert the measured signal to a form more easily transmitted to a central computer for further processing and analysis.

The processing of this information is designed to extract all the useful information contained in the signal. In the case of the blood pressure pulse, clinicians have known, and made use of the fact that various aspects of the waveform contain information about the state of the heart or the peripheral vascular network. For example, the maximum rate of pressure rise at the beginning of systole is indicative of the strength of cardiac contraction while the rate of decay of pressure during end diastole is a measure of peripheral vascular resistance, both of which are important parameters used in cardiovascular diagnoses.

The inference of cardiac parameters from peripheral measurements, however, is complicated by the changes in pulse shape that occur as the pressure wave propagates through the intervening arterial tree. Others have sought to overcome this problem by establishing the transfer function that describes the change in shape of the pulse between the aortic root and the peripheral measurement site. This method suffers, though, from the need for periodic calibration requiring arterial catheterization. An alternative approach, developed by our group, involves the use of a comprehensive model of the entire arterial system and heart. This computational model is used to create a *solution library* consisting of an extensive collection of peripheral pressure traces, each corresponding to a different set of system parameters, covering the entire range of possible parameter values. The solution library is further condensed by a two-step process. First, each curve is represented by some small number of features (*feature extraction*). These features are selected so that they describe the shape and magnitude of the pressure waveform, and correspond in number to the set of *critical parameters*, those we seek to predict by our parameter estimation technique. Second, the dependence of each feature on the critical parameters is viewed as an  $N$ -dimensional surface and is mathematically represented by a *surrogate function*. The surrogate function itself is represented by a set of coefficients that are stored for later use in the parameter estimation procedure.

*Parameter estimation* begins with the measurement of arterial pressure by one of several non-invasive methods. The measured trace is processed in the identical manner as the computed waveforms to extract the features. An initial seed is chosen (a particular point in parameter-space) and a measure of the relative error between the features calculated from the measurement and the features corresponding to the initial seed point. Beginning at this point, a minimization routine is used to march down the error surface to eventually identify the point in parameter-space having the smallest error and therefore corresponding to the set of parameters that most closely match those of the subject from whom the measurements are taken.

Progress on this project during the past several months has been made primarily in connection with two tasks: the search for the most efficient method of parameter estimation, and the initiation of experiments on volunteers to further test parameter estimation strategies. These are summarized below.

In addition, we have continued to develop our other two model approaches, discussed in earlier reports. These are the coarse-grained, lumped parameter model of the entire circulation that includes the reflex response of the cardiovascular system, and methods for modeling the detailed, 3-D, unsteady fluid-structure interaction at specific locations in the arterial system. Both of these are progressing well and we will likely provide more information on those aspects in our next reports.

## 2. Approaches to Feature Extraction

One of the new approaches we have used to parameter estimation involves representation of the pressure or velocity waveforms by wavelet analysis. Since this method may be unfamiliar to many of you, we will describe our approach in some detail.

### a. Wavelet Transform

Wavelet transforms are integral transforms using integration kernels called wavelets. These transforms enable the study of nonstationary process (or signals) in that they have good localization properties both in time and frequency. Since the physiologic signal is nonstationary and our system is nonlinear, this seemed a promising approach for feature extraction.

#### Basic Theory

An energy limited signal (i.e. a square integrable signal),  $f(t)$ , can be decomposed by its Fourier transform  $F(\omega)$  as:

$$f(t) = \frac{1}{2\pi} \int_{-\infty}^{\infty} F(\omega) e^{i\omega t} d\omega \quad (1)$$

$$F(\omega) = \int_{-\infty}^{\infty} f(t) e^{-i\omega t} dt \quad (2)$$

Equation (1) implies that the signal  $f(t)$  can be decomposed into a family of harmonics  $e^{i\omega t}$  and the weighting coefficients  $F(\omega)$  represents the amplitudes of the harmonics in  $f(t)$ .

The wavelet transform is defined in a similar manner. However, instead of using the harmonics  $e^{i\omega t}$ , it uses wavelet bases:

$$\psi_{st}(t) = \frac{1}{s} \psi\left(\frac{t-\tau}{s}\right) \quad (3)$$

Where  $s$  represents frequency,  $t$  represents the time shift or "location", and  $\psi(\cdot)$  is called a mother wavelet function. To be "admissible" as a wavelet, this function must have zero mean and be localized in both time and frequency space. An example is the Morlet wavelet, consisting of a plane wave modulated by a Gaussian window:

$$\psi_0(\eta) = \pi^{-\frac{1}{4}} e^{i\omega_0 \eta} e^{-\frac{\eta^2}{2}} \quad (4)$$

Where  $\omega_0$  is the nondimensional frequency, here taken to be 6 to satisfy the admissibility condition. This wavelet is shown in Fig. 1.

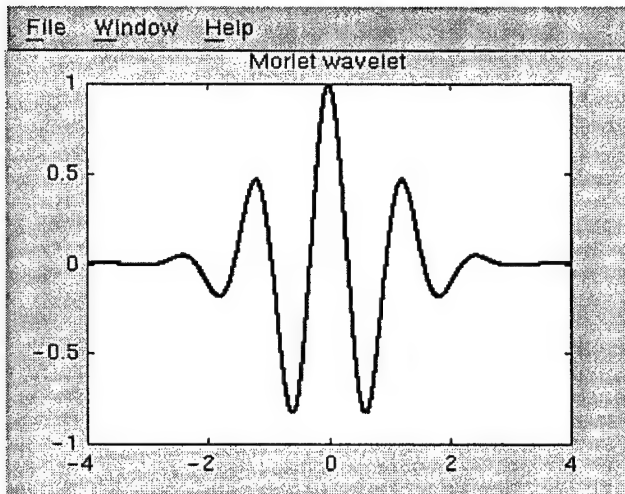


Fig. 1 Morlet wavelet profile

Similar to the Fourier transform, signal  $f(t)$  can be decomposed into:

$$f(t) = \frac{1}{C_\psi} \int_{-\infty}^{\infty} \int_0^{\infty} W_s[f(\tau)] \frac{1}{s} \psi\left(\frac{t-\tau}{s}\right) ds d\tau \quad (5)$$

Where  $C_\psi$  is a constant depending on the base function, and  $W_s[f(\tau)]$  is the wavelet transform defined below:

$$W_s[f(\tau)] = \int_{-\infty}^{\infty} f(t) \frac{1}{s} \psi\left(\frac{t-\tau}{s}\right) dt \quad (6)$$

Equation (6) is called the wavelet transform of  $f(t)$  and equation (5) is referred to as the wavelet inverse transform (or reconstruction formula).

Thus, wavelet transform decomposes a signal  $f(t)$  onto a family of wavelet bases, and the weighting coefficients,  $W_s[f(\tau)]$ , represent the amplitudes at given location  $\tau$  and frequency  $s$ . Compared to the Fourier transform,  $F(\omega)$ , which depends only on frequency, the wavelet transform is a time frequency function which describes the information of  $f(t)$  in various time windows and frequency bands. As a result, the wavelet transform capable of capturing non-stationary information such as frequency variation and magnitude undulation, but the Fourier transform cannot.

#### *Application and evaluation.*

Two kinds of approaches to wavelet transform were tried on the pressure profiles and velocity curves: the Discrete Wavelet Transform (DWT), and the Wavelet Packet Method.

In DWT method that has multiresolution structures, the signal is first split into low- and high-frequency components in the first level. The first low-frequency subband, containing most of the energy, is subsampled and again decomposed into low- and high-frequency subbands. This process can be continued into  $K$  levels. Fig. 2 illustrates the multiresolution decomposition structure with 3 levels. The coarsest signal is the one labeled LLL. Moving from right to left in the diagram, we see progression from coarser to finer signal representation as the high frequency "detail" is added at each level. The signal can thus be approximately represented by different resolutions at each level of the tree.

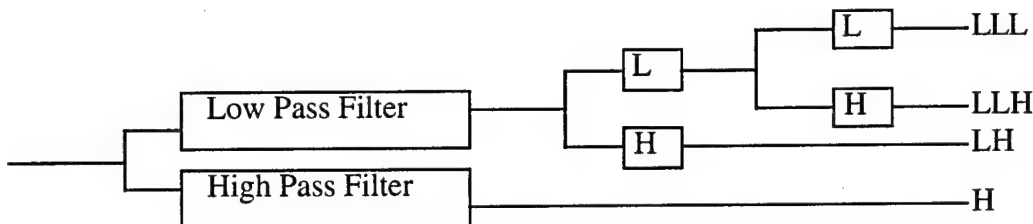


Fig. 2 Multiresolution Structure for 3 levels

In the Wavelet Packet method, at each level, both the low-frequency subband and the high frequency subband are decomposed again, so the original signal  $f(t)$  is decomposed into small number of large packets at lower resolution and large number of small packets at higher resolutions. On the  $j$ th resolution, there are a total of  $2^j$  packets. The signal reconstruction can be done either by using the packets with the same size on the same resolution, or by using the packets with different sizes on different resolutions. Each wavelet packet represents certain information on the signal in a specific time-frequency window. It shows that generally not all the packets in one level contain information, especially at higher resolution, the coefficients of many packets are essentially zero, which you can see from Fig. 3. In feature extraction, the proposed method is to use the wavelet packets that contain large amounts of information as the features, called feature packets. Such feature extraction process is called compression since the selected wavelet packets contains less data than the original signal.

These two kinds of methods are effective to analyze nonstationary and nonlinear signals, they can provide both frequency and time localized coefficients. however, it proved not to be beneficial to employ those approaches in our work since it is difficult to extract 3 or 4 features from the detailed information they provide. In DWT, at each level, the wavelet representation always has the same number of data as the signal  $f(t)$ , each representation has a time and frequency scale, so after DWT, we got 3 times as many data as in original signal. Although in Wavelet Packet method, most of the packets are zero, even one nonzero feature packet contains much more information than can be expressed in 3 or 4 coefficients. We tried to use the first 3 or 4 largest coefficients as features, but all detail was lost, which gives rise to large errors for parameter estimation. A comparison of different feature extraction approaches in influencing errors of parameter estimation is show in Table 1.

#### b. Fourier Transform.

To some extent, Fourier transform is a special form of wavelet transform since it uses harmonics  $e^{iwt}$  as mother "wavelet". Coefficients of the dominant harmonics were initially specified as features, but this approach proved insufficient to describe the pressure and velocity data as functions of the various hemodynamic parameters. The errors for parameter estimation using FFT are listed in Table 1.

#### c. Features from waveform characteristics

This led us to return to the approach we had used earlier using those features that physicians typically apply in their diagnosis of a patient. These may include mean pressure, peak systolic  $dP/dt$ , the slope of the pressure upstroke during early systole, and the systolic ejection period, or the time during the cardiac cycle that the left ventricle is

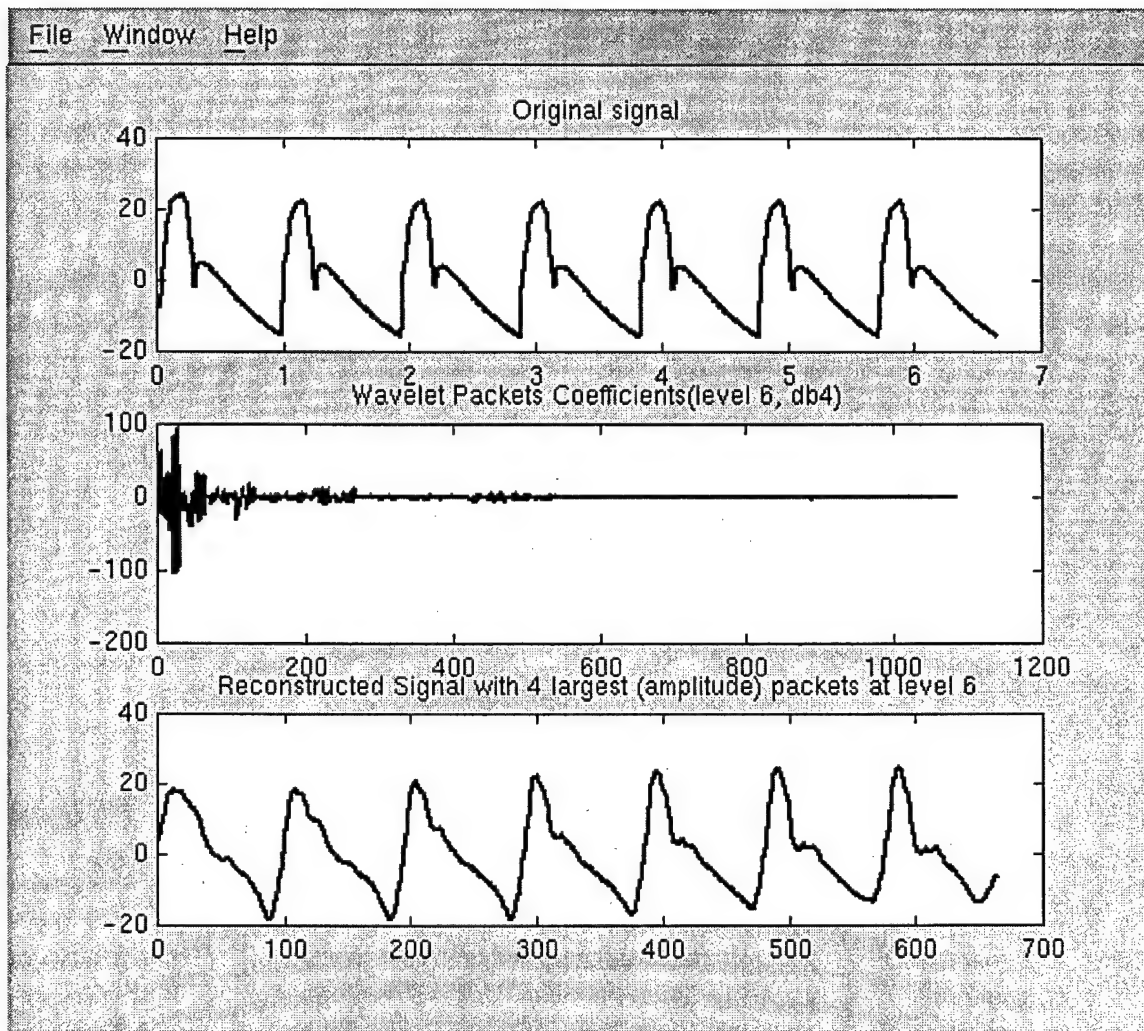


Fig. 3 Wavelet Packet transform and reconstruction.

features\parameters	Elv_max	EDV	SVR
Wavelet Packet	42.0281	25.0410	32.1791
DWT	38.9784	28.0963	12.2098
FFT	31.8283	10.4340	2.5975
Waveform features	14.3867	6.2326	3.5520

Table 1 Errors of parameter estimation using different feature sets.  
 (34 random points generated from model, estimated from pressure curve of carotid artery. Elv\_max: Maximum value of left ventricle elasticity EDV: End Diastolic Volume, SVR: Systemic Venous Resistance.)

actively contracting, the  $dP/dt$  of the pressure during diastole, etc. Ideally, the features should be independent to each other, adequate to specify a unique waveform, and each individually should be a monotonic function of the 4 parameters being estimated. However, in practice, the multi-dimensional relation between features and parameters makes it difficult to define an applicable criterion to evaluate the features. We tried many different combination of feature sets to do parameter estimations and compared the corresponding errors, we also drew 3 dimensional figures to show the relation of each feature to 2 parameter, which can give a direct impression how effectively the features can behave in estimation. The features we have considered include: mean pressure (pmean), difference between maximum and minimum pressure (dp), peak systolic  $dP/dt$  (dpdtmax), mean  $dP/dt$  during diastole, systolic ejection period, the time to peak pressure, the time to dicrotic notch, pressure at 2nd peak, maximum velocity, mean velocity, etc. The smallest set of errors in parameter estimation using 3 of those waveform features is listed in table 1.

### **3. Measurements on Human Volunteers**

#### **a. Objective**

The features extraction and parameter estimation methods mentioned have until now been evaluated using "measurements" of pressure and velocity waveforms generated by the computer simulation. We are now reasonably confident of the parameter estimation methods tested in this manner. A much more stringent test, but an essential one, is to employ these same methods using actual measurements on patient or healthy volunteers. In this section, we describe the methods planned for our recently initiated studies.

For this stage of the study, we have established a collaboration with Drs. Richard Lee and Nancy Sweitzer of the Cardiology Division at the Brigham & Women's Hospital. Dr. Lee is a long-time collaborator of the PI and Dr. Sweitzer is a research fellow.

In order to evaluate our techniques, we require the following measurements:

(a). To provide inputs to the model:

Heart rate, patient height, weight, pressure measured by auscultation at brachial artery, central venous pressure, arterial wave speed, systolic time / ejection period.

(b) To verify the model predictions, we need separate measurements of the following parameters that are to be predicted:

End diastolic volume (EDV), peak ventricular elastance (Elv\_max), cardiac output, systemic vascular resistance (SVR), end diastolic pressure (EDP)

#### **b. Measurement system**

##### ***Measuring instruments***

We measure the pressure pulse noninvasively at locations of carotid, brachial, and radial arteries with a Millar tonometer, which uses a piezoelectric transducer to detect artery wall deflection transmitted through the skin. It converts pressure values to DC voltage outputs with the sensitivity of  $5\mu\text{V/V/mmHg}$  (nominal  $37.6\mu\text{V/V/kPa}$ ).

Velocity data are obtained by the use of a Doppler ultrasound system — Hewlett-Packard Sonos 2000 echocardiography machine with a 7.5 MHz linear array transducer probe. In each patient, the artery of interest is identified using M-mode ultrasound with color Doppler overlay. Once the transducer is positioned over the artery, PW (Pulse Wave) Doppler measurements are obtained over several cycles, which can be recorded or transmitted to a data acquisition system.

In the future, we plan to make invasive clinical measurements (with catheterization) that will be needed to validate our parameter estimation methods.

### *Data acquisition*

A PowerbookG3 equipped with a data acquisition card (National Instrument Corp. DAQCard-516) and related accessories is used, together with the NI-DAQ, LabVIEW and Ultra-recorder software, to convert analog signals from the measuring instruments into digital ones and save them in a readable plain text format.

### *Data processing*

The codes for data processing are mostly written in Matlab with appropriate filter settings implemented to ensure quality signal capture.

### c. Measurement results on healthy volunteers

In the first stage of measurement, normal volunteers were studied to test the measurement system and obtain preliminary data for use in our parameter estimation routines. Fig. 4 shows the pressure and velocity curves at different locations. Table 2 lists some "patient data", including parameters values estimated using the model and their corresponding normal range.

Parameters\values	measured or calculated value	Normal Range Minimum	Maximum
Heart Rate (/min)	75	40	110
Height (meter)	1.63		
Weight(kg)	70		
cuff pressure(mmHg)	110/66		
Wave Speed(m/s)	8		
Venous Pressure (mmHg)*	4	0	30
Systolic time*	0.5	0.3	0.6
Elv_max (dyn/cm <sup>5</sup> )	3500	1000	15000
EDV (ml)	93	30	120
SVR (dyn-sec/cm <sup>5</sup> )	700	400	2660

Table 2 Input and output parameters of the model (measurements done on a normal person) \* denotes estimated values.

For the most part, the estimated parameters fall within a reasonable range for a healthy subject. The value estimated for peak systolic elastance, however, is somewhat lower than expected. This might be explained on the basis that we are currently estimating the zero pressure volume of the ventricle during systole and assuming a single value is suitable to all. This may need to be adjusted to account for body size, or may need to be included as one of the estimated parameters.

We are currently analyzing these results in conjunction with our medical colleagues. Our first step is to make other non-invasive measurements to compare to those we have just estimated. This procedure will be followed in a number of volunteers prior to testing on patients. We are also exploring ways to improve our prediction accuracy, possibly involving additional non-invasive measurements of model parameters of the CV system. Finally, we have discussed the possibility of changing the mix of specified and estimated parameters so as to enhance the ultimate clinical utility of these procedures.

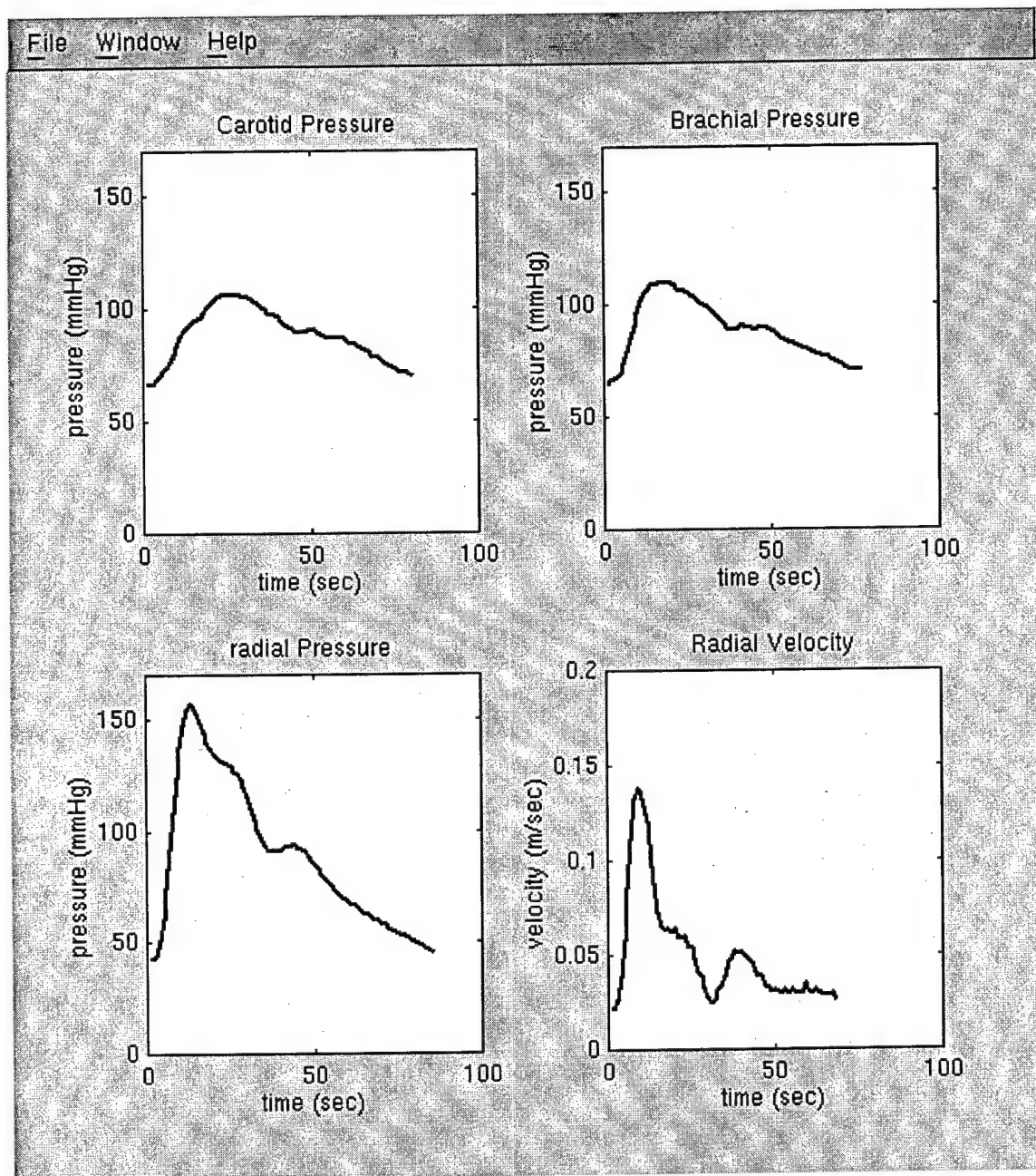


Fig. 4 Pressure and Velocity curves at different locations.

#### 4. Near term plans

- (1) Continue and expand our experiments to include measurements on patients with different diseases and in different therapies.
- (2) Reassess the parameter estimation and feature extraction routines as we examine these new patient data.
- (3) If necessary, verify the model to estimate some more parameters that are important for clinical reference and decision making.

# **AN INTELLIGENT CARDIOPULMONARY SYSTEM FOR THE HOME HEALTH MARKET.**

**Thomas B. Sheridan**

## **HYPOTHESIS**

An intelligent cardiovascular diagnostic system (ICDS) will improve patient care and decrease medical costs by the earlier detection of patient decompensation.

### **1. INTRODUCTION**

The goal of this project is the development of a system designed to acquire, process and analyze blood pressure, heart rate, oxygen saturation, and thoracic signals to make a decision on the relative health of the patient's cardiovascular system. Unfortunately most patients do not have the tools necessary to become an active and informed participant in their own health care. Many of those who end up with serious health problems enter the health care system too late, and thus require more extensive and costly care. The patients selected for monitoring by the intelligent system are those patients who are at a higher risk for decompensation as compared to the general population. These "high risk" patients frequently enter the health care system too late and thus require more extensive and costly care in addition to the emotional and physical strain to themselves and their families. The goals of this program are to decrease the initial acuity, length of hospital stay and readmission rates for patients with congestive heart failure. This will result in substantial savings in health care costs with a decreased burden on the acute health care system.

Why focus on the cardiovascular and pulmonary system? It is estimated that 65 of 239 million Americans have cardiovascular disease. One million die annually, and this is one of every two deaths in the United States. The mortality from cardiovascular disease exceeds that of all other diseases combined. Congestive heart failure (CHF) is estimated

to affect three million people in the United States. It is the final pathway of a variety of primary cardiovascular disease entities, such as coronary artery disease, hypertension, valvular heart disease, genetic disorders, diabetes and the sequelae of infection or toxin exposure, among others. Hospitalizations and mortality from CHF have increased steadily since 1968, despite the overall improvement in mortality from cardiovascular disease. Heart failure is now the underlying cause of death in over 39,000 persons annually. In 1992, it was the first listed diagnosis in 822,000 persons and is the most common hospital discharge diagnosis in persons over 65 years of age. The incidence of death from CHF is 1.5 times as high in black Americans as in whites. The estimated direct economic cost of CHF in the United States be reported to be \$10.2 billion annually. The problem will only get worse, as the elderly segment of the population is increasing at a rate 5.6 times that of the other age groups. There are currently 25 million Americans greater than 65 years of age and 2.7 million Americans greater than 85. Over the next 50 years the >65 age group will see a 140% increase versus 25% in the other age groups. At present, the only cure for end-stage CHF is cardiac transplantation.

Studies have shown that intervention can improve care and decrease costs by decreasing hospital admissions, which account for a large portion of their health costs. Investigators in Los Angeles found that interventions (invasive tests, medication adjustment, patient education and follow-up at a heart failure center) decreased the number of hospital admissions from 429 in the six months before referral to 63 in the six months after referral.<sup>1</sup>

## **2. PROPOSED SYSTEM**

The structure of the ICDS is shown in figure 1. The patient's vital signs and oxygen saturation will be acquired first and will be evaluated by the ICDS. The ICDS will then direct the acquisition of other information as needed by the system. This additional information will be conditioned, digitized, and processed before being put in a form that could be inputted into the ICDS. The ICDS will then make an initial assessment of the patients current state, compare it with a predetermined "optimal state" and make a decision on where to proceed from that point. Options include requesting additional information from the patient, patient education, instructions to hold or to take an

additional dose of a medication, decision to re-evaluate after a waiting period, contact the primary care physicians office, connect to the central system, or call an ambulance for transportation to a medical facility.

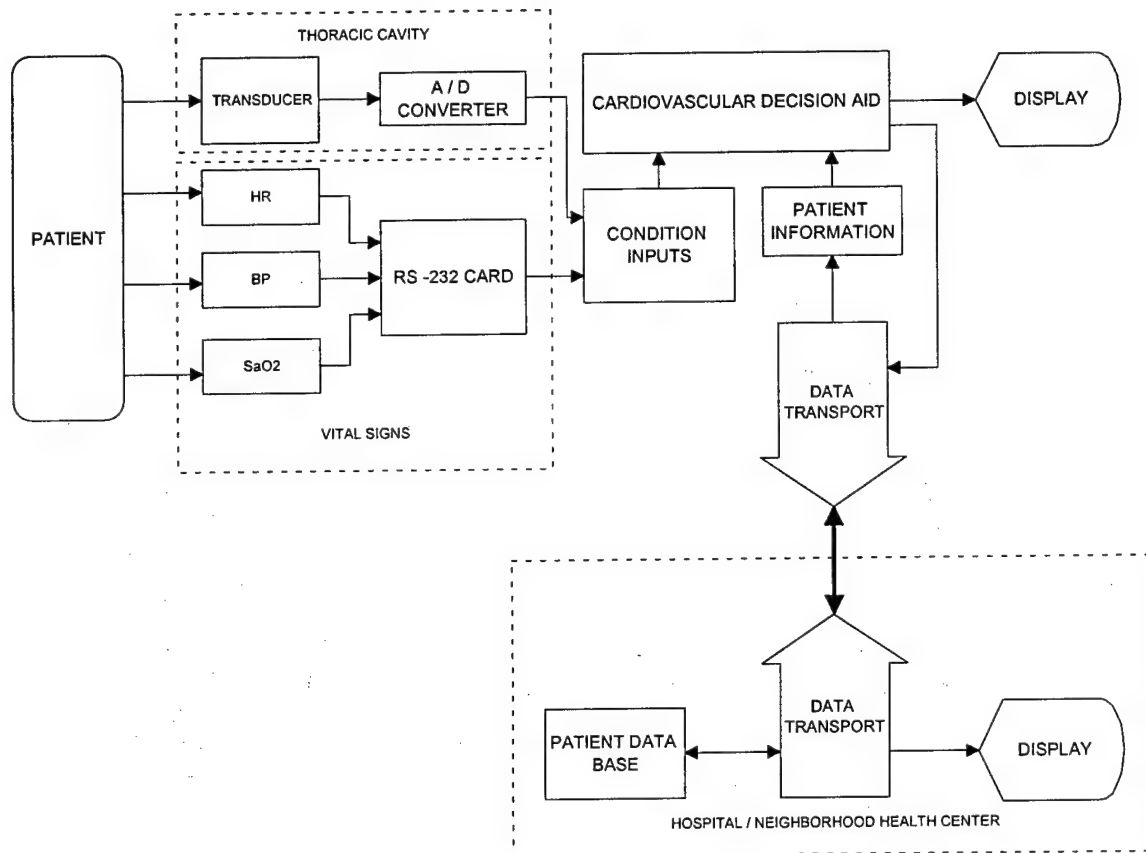


**Figure 1. Structure of the Intelligent Cardiopulmonary Decision System (ICDS)**

### 3. HEART RATE ANALYSIS MODEL

A system was developed to obtain the ECG waveform, as well as digital values for the oxygen saturation, systolic and diastolic blood pressure readings, and time averaged pulse information (Figure 2).

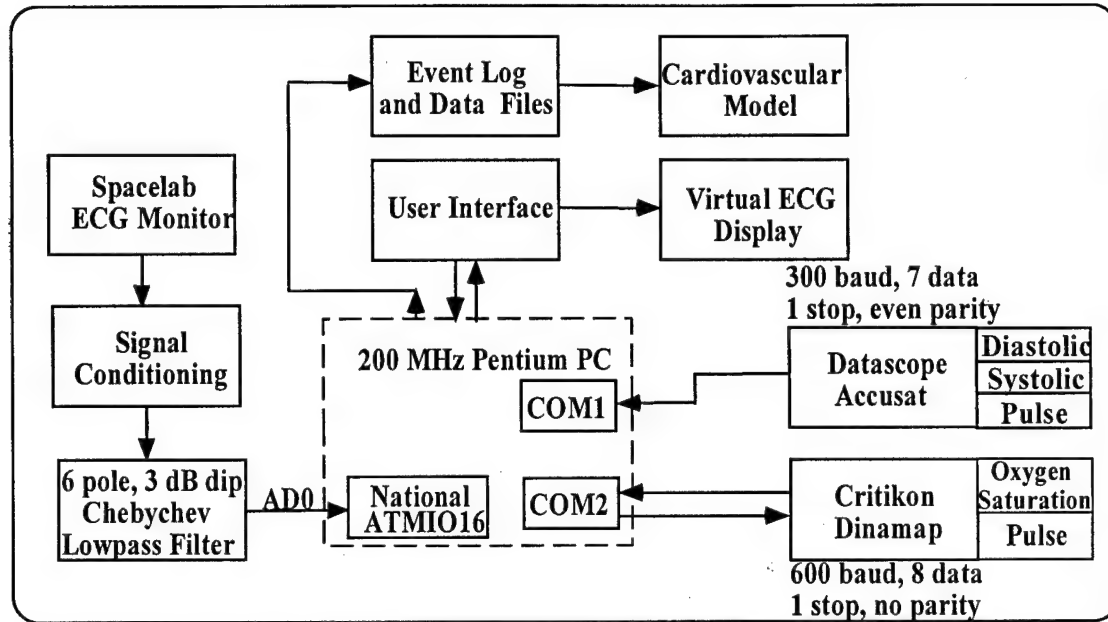


**Figure 2. Heart Rate Analysis System**

The distance in time between two consecutive R-waves of an ECG waveform defines the instantaneous heart rate. With the instantaneous heart rate known over a period of time, it is possible to find the variability of the heart rate. This is accomplished through the use of the power spectral density function, which gives insight into the function of the patient's cardiovascular system. The developed system was tested on four healthy adults, with the resulting data for one patient presented here.

### 3.1 R-wave Peak Detection and Heart Rate Variability

Since the exact location of an R-wave peak is needed for heart rate variability studies, it is highly important to condition the analog ECG signal with not only the normal amplification, but also with an anti-aliasing low-pass filter. In order to produce a sharp falloff from the pass-band to the stop-band frequency range, a sixth order, 3-dB-dip Chebyshev low-pass filter was chosen. A cutoff frequency of 170 Hz was selected since it was above the maximum frequency component of the R-wave of the typical ECG waveform. Figure 3 shows a ten-second window of ECG data taken from one of the test subjects.

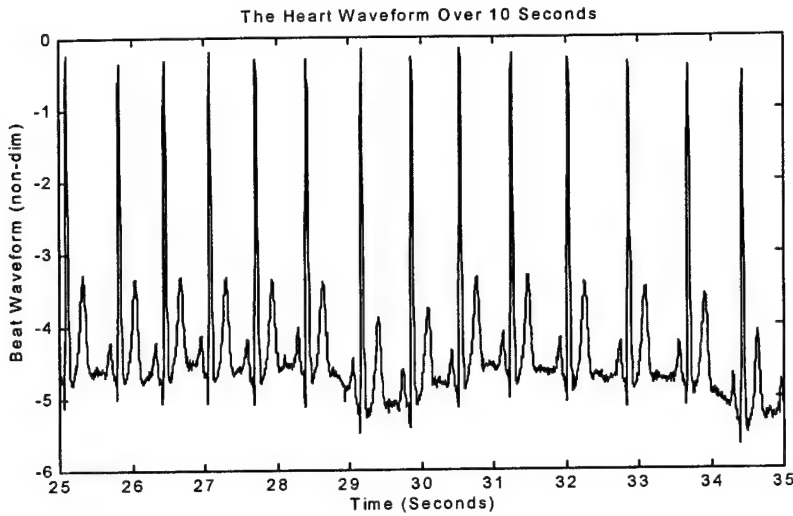


**Figure 3. A Ten Second Window of the Sampled ECG Waveform**

From this ECG waveform, R-wave peak detection was applied so that the interval of time between peaks could be used to produce an instantaneous heart rate waveform. The first step in this procedure was to digitally filter, forward and backward, the ECG data. This forward and backward data was then summed together to eliminate the phase shift associated with digital low-pass filtering. Once the high frequency noise was removed from the ECG signal, a derivative was taken of this sequence. A "window" was then passed through this new sequence,  $g[n]$ , with the magnitude of the derivatives summed over the window. This new sequence can be written as follows:

$$y[n] = \sum_{n-\Delta n_s}^{n+\Delta n_s} \left| \frac{g[n+1] - g[n]}{\Delta n} \right| \quad (3.1)$$

$$\text{where } \Delta n_s = \frac{n_1 + n_2}{2}$$

Since the purpose of this window was to extract the R-wave peak, the time-width of this window was set to be of the order of the inverse of the R-wave frequency maximum:

$$\frac{1}{t_s(n_2 - n_1)} \sim f_{\text{R-wave}} \quad (3.2)$$

where  $t_s$  is the sample time of the analog input. The sample frequency was 500 Hz., and with 170 Hz for the maximum R-wave frequency component, a window three elements

wide in discrete time was needed. Figure 4 shows the results of this windowing enhancement of the ECG R-wave peak.

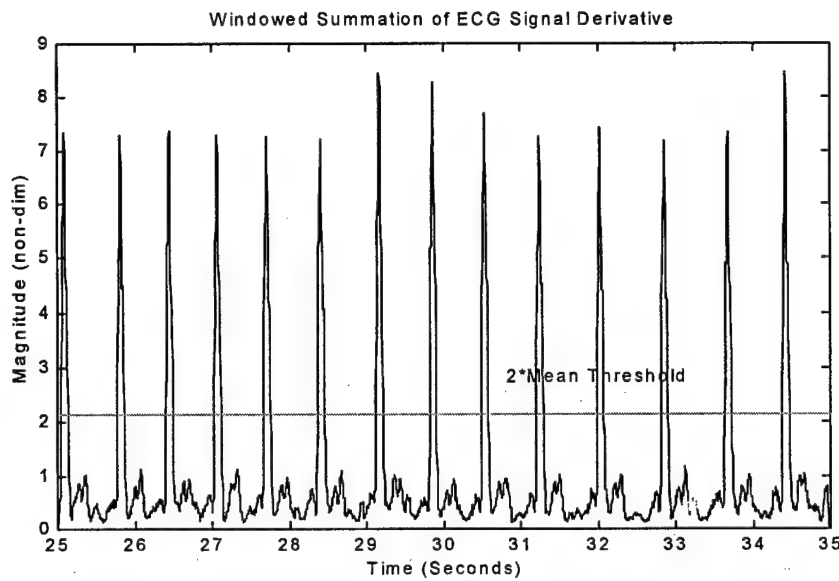


**Figure 4. Enhancement of the ECG Waveform Peaks**

Once the windowing enhancement was accomplished, the mean of the resultant sequence was calculated, and a two-mean threshold was set on the sequence for identification of the R-wave location. Figure 5 shows the after threshold sequence.

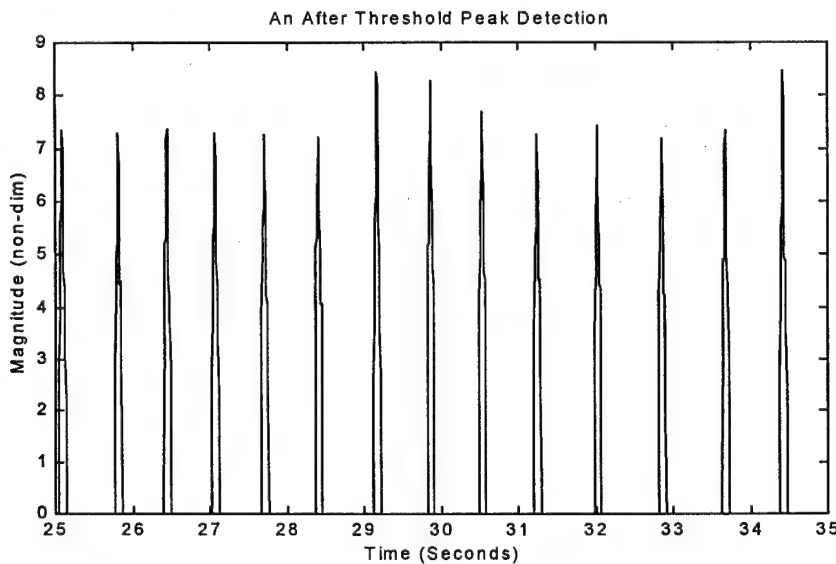


**Figure 5. The After Threshold R-Wave Locations**

It is important to note that since the R-wave changes in frequency makeup and magnitude between patients, in addition to a changing DC value of the ECG mean that may, at times, be above a set threshold, it is not possible to simply set a threshold on the ECG directly to determine the R-wave location. Figure 6 shows the location of the peaks found with respect to the original ECG data.

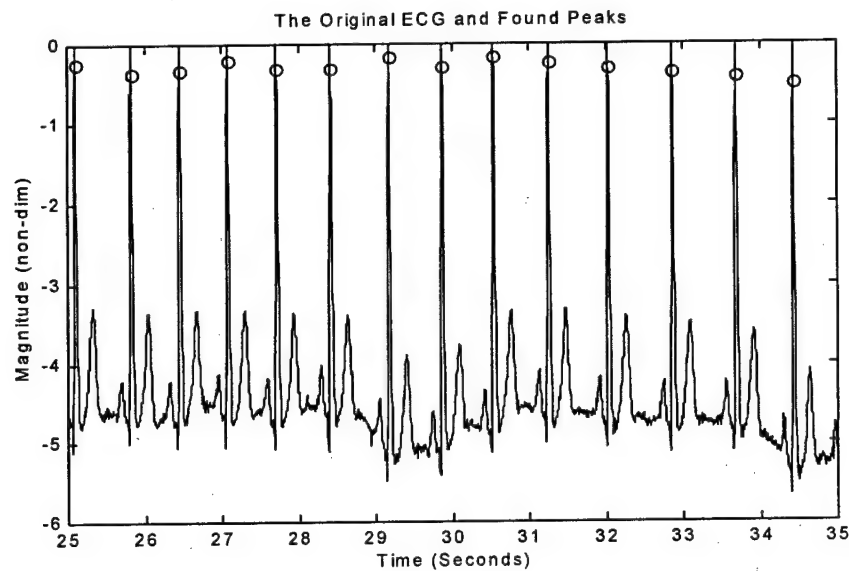


**Figure 6. Peaks Detected Within the Original ECG Waveform**

With the peaks of the R-wave located, the time between the peaks was calculated, and the inverse of this was the instantaneous heart rate. Figure 7 shows the instantaneous heart rate over 10 seconds for one test subject. Since the human heart has beat variation, and beats at unequal increments of time, the instantaneous heart rate waveform is not a straight line. This is not the case with heart transplant patients, in which the heartbeat is well regulated, giving no beat variation, and producing a straight-line instantaneous heart rate waveform. This waveform, which has unequal time spacing between beats, is then sampled at a frequency that is roughly four times the maximum frequency of the instantaneous heart rate waveform. This gives a discrete representation of quasi-continuous data that can be used in variational analysis. After it is re-sampled, it is digitally low-pass filtered again, and then re-sampled again, which basically converts it

from a series of step changes to a more continuous approximation of the true instantaneous heart rate.

It should be noted that there are a variety of methods that were found to be used in producing an equal time spaced instantaneous heart rate waveform, such as using the R-wave location information in a curve fit or passing the data out through a D/A and then a low-pass filter, and then re-sampling it at a higher frequency. Figure 8 depicts the method that was employed to produce an equal time sampled heart rate waveform.

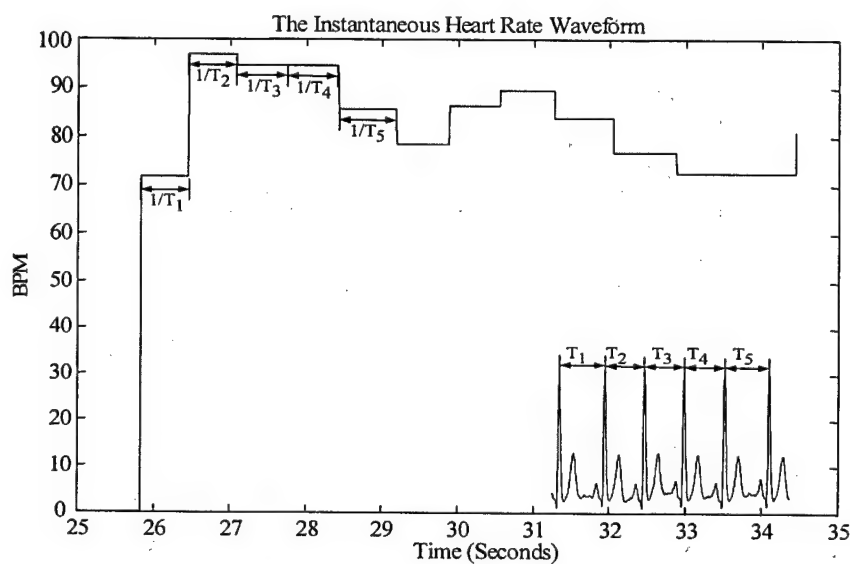


**Figure 7. The Instantaneous Heart Rate Waveform**

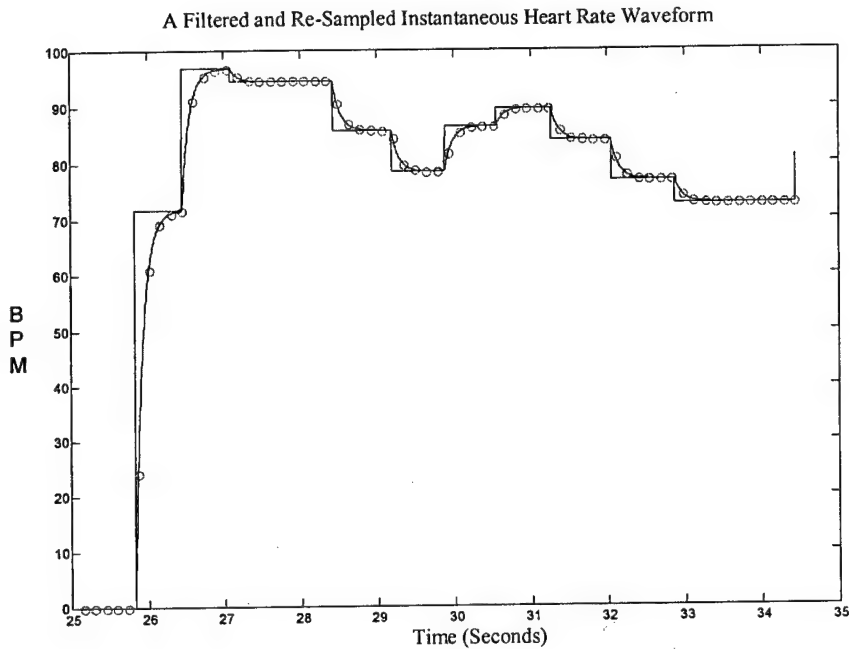


**Figure 8. A Re-sampled Instantaneous Heart rate Waveform**

Although the above is only a ten second window to demonstrate a method, the four test subjects were put through several ten minute sessions in which ECG, oxygen saturation, systolic and diastolic blood pressure, and pulse information were monitored.

In order to measure the heart rate variability, a power spectral density for the instantaneous waveform had to be found. The first step to achieve this was to find the autocorrelation,  $R_x[n]$ , of an  $N$ -point sequence,  $y[n]$  (the re-sampled heart rate waveform):

$$R_X[n] = \sum_{k=-N}^{N} y[k]y[n+k] \quad (3.3)$$

The power spectral density (psd) function is defined as follows:

$$S_x(\omega) = \int_{-\infty}^{\infty} R_X(\tau) e^{-i\omega\tau} d\tau = F[R_X(t)] \quad (3.4)$$

For a continuous function  $g(t)$ , the Fourier transform is:

$$G(\omega) = \frac{1}{2\pi} \int_{-\infty}^{+\infty} g(t) e^{-i\omega t} dt \quad (3.5)$$

From this it can be seen that the psd is nothing more than the Fourier transform of the autocorrelation function multiplied by a constant:

$$S_X(\omega) = \frac{1}{2\pi} F \left[ R_X(t) \right] \quad (3.6)$$

**Figure 9. The Instantaneous Heart Rate Waveform over a Ten Minute Period**

With the instantaneous waveform known over the full ten-minute period, the power spectral density function was then found. Figure 9 shows this waveform.

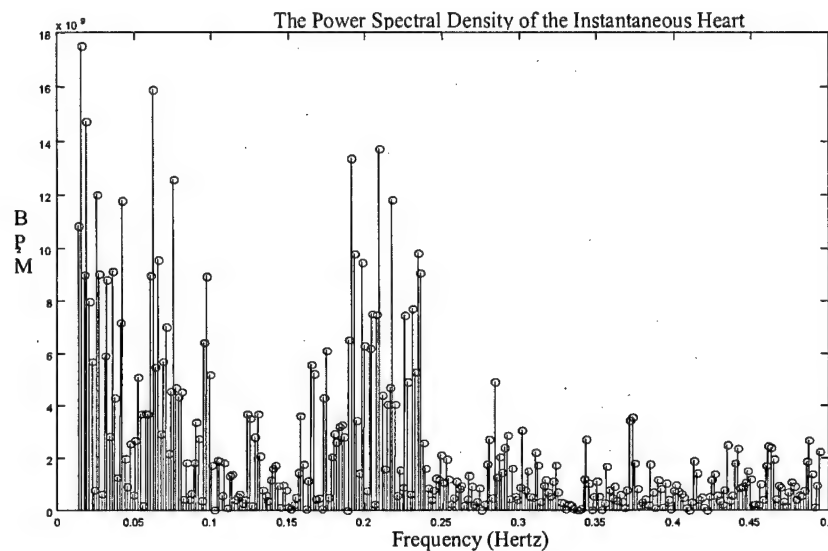


**Figure 9. The Power Spectral Density Function of the IHR**

There are a few important details to note at this point. First, there are roughly three peaks: one at roughly 0.03 Hz, 0.08 Hz, and 0.2 Hz. These are characteristic of healthy patients in variability studies. Second, the spectrum is not plotted below about 0.01 Hz, since the component below this frequency represents the mean drift of the ECG waveform, and has a rather large value. Third, the spectrum is not plotted above 0.5 Hz, since the values above this frequency are roughly zero.

#### 4. INPUT CONDITIONING

In addition to heart rate variability and the ECG information, diastolic and systolic blood pressure information as well as a time averaged pulse was brought in serially from a Critikon Dinamap that was set to automatically sample once a minute. Oxygen saturation and another time averaged pulse was also brought in serially, this time from a Datascope Accusat roughly once every fifteen seconds. This sample rate was limited by the embedded instruction set in each of the two pieces of equipment. Figure 10 shows this information over the ten minute sample taken for the patient.

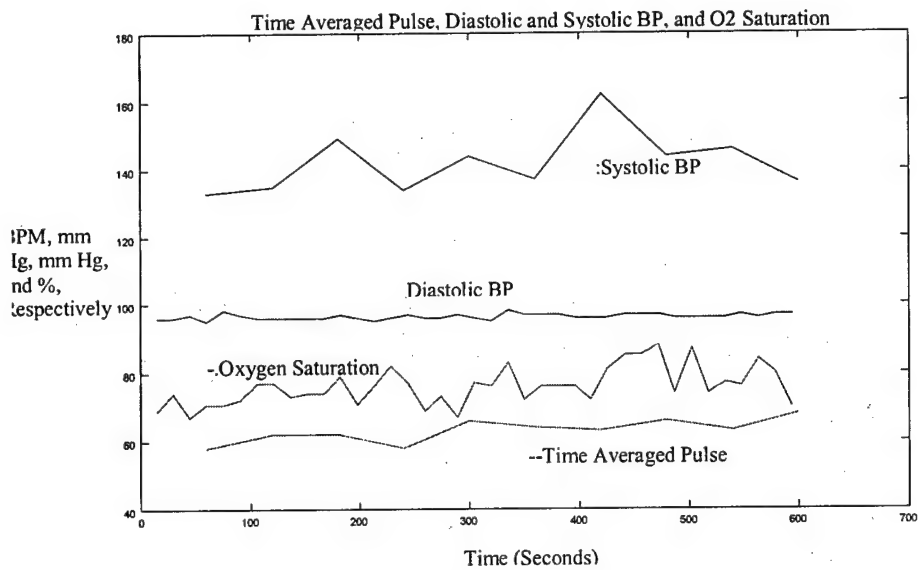


**Figure 10. More Patient Data for the Model**

## 5. CARDIOVASCULAR DECISION AID

Heart rate is important in patients who currently have marginal coronary flow and are sensitive to the physiological consequences of tachycardia. Tachycardia decreases coronary diastolic filling time, which decreases the supply of oxygen to myocardial tissue, especially endocardial. In addition, tachycardia increases oxygen demand, which further contributes to negative myocardial oxygen balance. This initially results in regional wall motion abnormalities, which causes a rise in ventricular end diastolic and end systolic pressures, which further decrease diastolic blood flow, starting the cycle to heart failure. Bradycardia can also have deleterious effects on certain pathologic states.

Patients with mitral or aortic regurgitation can go into congestive heart failure, depending on the magnitude of the regurgitant fraction and the degree of bradycardia. Changes in the other inputs would affect the magnitude of the changes in heart rate that would start the cycle toward CHF. Both an increase and a decrease in blood pressure can have an effect on cardiovascular dynamics that would have a deleterious effect on cardiac patients. Certain types of congestive heart failure are sensitive to changes in afterload, and the presence of blood pressure changes in these patients could start the process toward congestive heart failure. Oxygen saturation, in addition to the heart rate variability, will be used by the model to quantitate the direction / presence of cardiac decompensation.

In the first stage of our intelligent system, the measured patients variables (heart rate, systolic blood pressure, diastolic blood pressure and oxygen saturation) will each be converted to a set of three fuzzy variables using a membership function generated from the patients initial data. Power spectral analysis of heart rate variability of the individual patient will be used to generate three variables to characterize the sympathovagal activity of the patient's cardiovascular state.

The fifteen variables generated from the first stage, along with patient modifiers (to be discussed later), will act as inputs to the second stage of the system, which will then generate an output consisting of three states. Information from a patient information database and drug transducer (also discussed later) will be combined with the output of the second stage of the cardiovascular decision aid to arrive at a recommendation on a course of action for the individual operating our system (patient, primary caregiver, or home health care worker).

---

<sup>1</sup> Fonarow GC et al. *Impact of a comprehensive heart failure management program on hospital readmission and functional status of patients with advanced heart failure*. J Am Coll Cardiol 1997 Sept; 30:725-32.

# Co-Simulation of Physiological Systems

Prof. Harry Asada  
Principal Investigator

Bei Gu  
Graduate Research Assistant

Danielle Tarraf  
Graduate Research Assistant

## ABSTRACT

Simulation of human physiological systems provides useful information for the physiological sensors, patient monitoring and diagnosis, and the control of the home equipment and environment. The human body is a complex system that consists of fluid, thermal, kinematic, chemical and electrical energy domains. It is difficult to model and simulate such a large system by one huge computer model. People unsurprisingly build complex models in a modular fashion. However, there is the need for a technique that can utilize existing simulation software and co-run them on different computers.

Currently, two levels of research topics are being studied in conjunction with the Home Automation and Healthcare Consortium project. One is to deal directly with partial differential equations without reduction of the original distributed system to a lumped parameter model or a finite element model. Boundary conditions involved in the interactions among multiple sub-models are analyzed, and an efficient formulation for co-simulating the sub-models is obtained. The other is to deal with lumped parameter models described by Bond Graphs. Using the theory of Bond Graph, causal conflicts and algebraic constraints arising at the interactions among multiple sub-models are analyzed, and efficient computational procedure for co-simulating the multiple models is obtained.

As an exemplary study, a coupled problem of the circulatory and thermoregulatory systems is addressed. The coupled model in this simulation has been reported in Progress Report No. 2-1. We use this simulator as a demonstration and case study for our long-term goal, which is a simulation environment for co-running several simulators. In this report, we also discuss possible issues of coupling two arbitrary lumped parameter model sub systems. The analysis uses the bond graph as the representation for the dynamic systems. We have explored the possibility of using the bond graph as a simulation tool. We thus developed the junction variable method of dynamic system simulation for bond graph models and discussed the new method's advantages and limitations. Another case study, coupled fluidic/mechanical modeling of the digital artery, is considered as an illustrative example of distributed systems analysis. Recent advances in modeling the visco-elastic behavior of the arterial wall are presented. A systematic means for formulating the coupled systems model, through the use of PDAE systems, is presented and discussed.

## 1. Introduction

Simulation of human physiological systems provides useful information for the physiological sensors, patient monitoring and diagnosis, and the control of the home equipment and environment. The human body is a complex system that consists of fluid, thermal, kinematic, chemical and electrical energy domains. It is difficult to model and simulate such a large system by one huge computer model. People unsurprisingly build complex models in a modular fashion. One simple approach is to build some templates of sub systems and assume the sub systems always connect with each other in an unchanged way. Examples of such approaches can be found in papers by Stein and Louca (1995) and Hassenforder and Gissinger (1996). Another systematic and flexible way of building complex system models is the object-oriented modeling. The object-oriented modeling has features like class and object, encapsulation, polymorphism and inheritance. DYMOLA is such an object-oriented modeling language (Elmqvist, 1979). Users of the object-oriented modeling tools have to build the entire complex system model from scratch if no standard object-oriented sub models available. The compiled code will be executed on one computer. Apparently, this is not the most efficient way of simulating human physiological systems. Therefore, there is the need for a technique that can utilize existing simulation software and co-run them on different computers.

We will report a simulation program simultaneously running the circulatory and thermoregulatory systems simulation. The model in this simulation was reported in the progress report No. 2-1. We use this simulator as a demonstration and case study for our long-term goal, which has been described above. In this report, we also discuss possible issues of coupling two arbitrary sub systems. The analysis uses the bond graph as the representation for the dynamic systems. The bond graph is a powerful tool for inter-energy domain modeling (Karnopp et al, 1990). Since the bond graph greatly helps the understanding of dynamic systems in modeling practice, we have attempted to explore the possibility of using it as a simulation tool. We thus developed the junction variable method of dynamic system simulation for bond graph models and discussed the new method's advantages and limitations.

At the end of this report, research progress on the co-simulation of distributed systems mathematically modeled as partial differential equations is summarized. This is

done through the use of an exemplary case study: the coupled fluid/structure dynamics of blood vessels. A systematic means of formulating the coupled problem, through the PDAE structure, is presented and analyzed. The highlights of this form of mathematical representation are outlined, in particular; flexibility, modularity, projected ease in analysis of system order/complexity and in defining a consistent set of initial and boundary conditions.

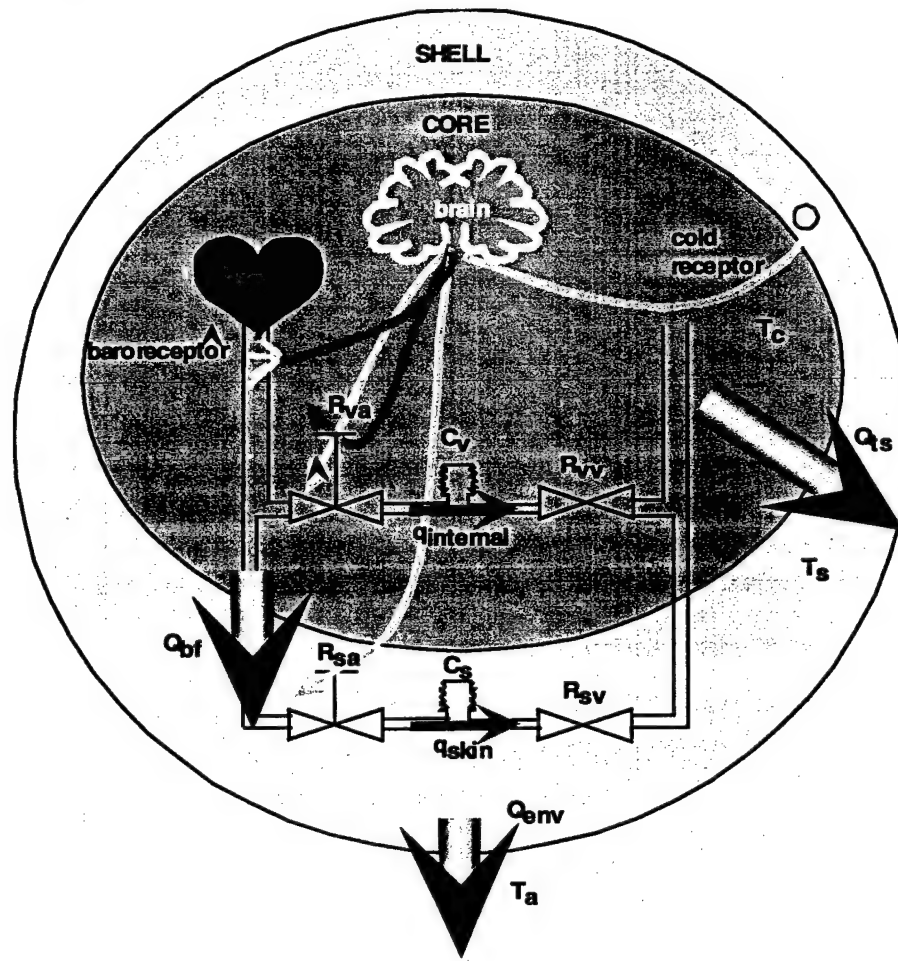


Fig. 1. The coupled model of circulatory and thermoregulatory systems.

## 2. Co-Simulation of Coupled Circulatory and Thermoregulatory Systems

### 2.1 Modeling of Circulatory and Thermoregulatory Systems

Human body generates most metabolic heat in organs and muscles. The skin surface is the dominant place of heat dissipation. The body can be separated into a core and a shell

as shown in Fig. 1. The core temperature must be maintained at a certain value to ensure normal functioning of organs. The heat transfer from the core to the shell by blood flow is the major mechanism that the human body uses to regulate its core temperature. When the body is too hot, the blood vessels in the subcutaneous region expand. The vasodilatation in turn causes more blood to flow from the core to shell. The increased

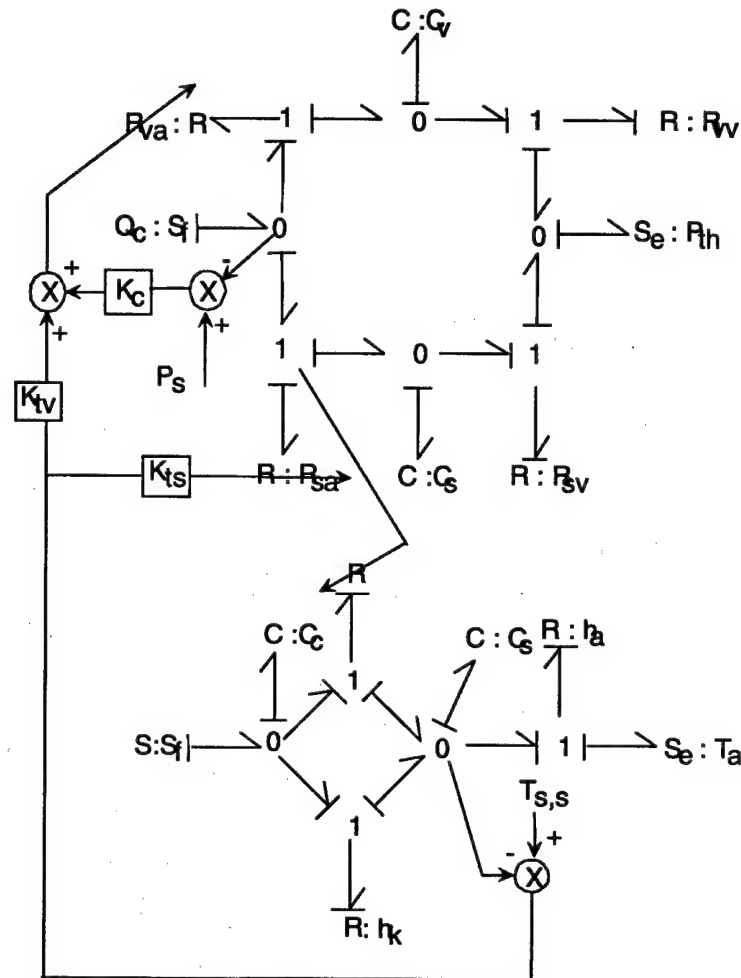


Fig. 2. The bond graph of coupled circulatory, thermal and neural control system.

blood flow carries more heat from the core to the shell increasing the heat dissipation rate. When the human body is subjected to cold environments, the subcutaneous blood vessels contract. The vasoconstriction can cause the peripheral blood flow rate to decrease to almost zero to help maintain the core temperature. Because of the involvement of the circulatory system in body temperature control, the circulatory system is excited by the body temperature variations. Vasoconstriction will raise blood pressure but the human body has various mechanisms to maintain the blood pressure. The

expansion of vessels is the most important short-term measure that the body takes to suppress high blood pressure. Therefore, environmental thermal excitation is able to excite circulation dynamics so we can use thermal excitation as a tool to study circulatory system properties. The bond graph of the coupled circulatory and thermoregulatory model is given in Fig. 2.

The model shown in Fig. 2 yields the following state equations:

$$\begin{aligned}
 \begin{pmatrix} \dot{P}_s \\ \dot{P}_v \end{pmatrix} &= \begin{bmatrix} -\frac{1}{C_s} \left( \frac{1}{R_{va} + R_{sa}} + \frac{1}{R_{sv}} \right) & \frac{1}{C_s} \frac{1}{R_{va} + R_{sa}} \\ \frac{1}{C_v} \frac{1}{R_{va} + R_{sa}} & -\frac{1}{C_v} \left( \frac{1}{R_{va} + R_{sa}} + \frac{1}{R_{vv}} \right) \end{bmatrix} \begin{pmatrix} P_s \\ P_v \end{pmatrix} + \begin{bmatrix} \frac{1}{C_s} \frac{R_{va}}{R_{va} + R_{sa}} & \frac{1}{C_s R_{sv}} \\ \frac{1}{C_v} \frac{R_{sa}}{R_{va} + R_{sa}} & \frac{1}{C_v R_{vv}} \end{bmatrix} \begin{pmatrix} Q_c \\ P_{th} \end{pmatrix} \\
 \begin{pmatrix} P_1 \\ Q_s \\ Q_v \end{pmatrix} &= \begin{bmatrix} \frac{R_{va}}{R_{sa} + R_{va}} & \frac{R_{sa}}{R_{sa} + R_{va}} \\ \frac{1}{R_{sv}} & 0 \\ 0 & \frac{1}{R_{vv}} \end{bmatrix} \begin{pmatrix} P_s \\ P_v \end{pmatrix} + \begin{bmatrix} \frac{R_{sa} R_{va}}{R_{sa} + R_{va}} & 0 \\ 0 & -\frac{1}{R_{sv}} \\ 0 & -\frac{1}{R_{vv}} \end{bmatrix} \begin{pmatrix} Q_c \\ P_{th} \end{pmatrix} \\
 \begin{pmatrix} \dot{T}_c \\ \dot{T}_s \end{pmatrix} &= \begin{bmatrix} -\frac{\bar{h}_k + (\rho C_p)_{be} Q_s}{\bar{C}_c} & \frac{\bar{h}_k + (\rho C_p)_{be} Q_s}{\bar{C}_c} \\ \frac{\bar{h}_k + (\rho C_p)_{be} Q_s}{\bar{C}_s} & -\frac{\bar{h}_k + \bar{h}_a + (\rho C_p)_{be} Q_s}{\bar{C}_s} \end{bmatrix} \begin{pmatrix} T_c \\ T_s \end{pmatrix} + \begin{bmatrix} \frac{1}{A_{Du} \bar{C}_c} & 0 \\ 0 & \frac{\bar{h}_a}{\bar{C}_s} \end{bmatrix} \begin{pmatrix} H \\ T_a \end{pmatrix}
 \end{aligned}$$

with information influence resulted from the neural control:

$$R_{sa} = R_{sa,s} + K_{ts}(T_{s,s} - T_s)$$

$$R_{va} = R_{vas,s} + K_{tv}(T_{s,s} - T_s)$$

$$R_{vv} = R_{va,s} + K_c(P_s - P)$$

## 2.2 Co-Simulation Implementation

A real time simulator has been constructed for the coupled circulatory, thermal and neural systems based on the model components. The co-simulator takes the measured ambient air temperature as the input and simulates the skin temperature, peripheral blood flow, and blood pressure dynamics. Sensors were mounted on a human to obtain experimental

data. The measured physiological information and the real time simulation results were compared. This information could also be used for automatic tuning of the co-simulator.

The simulator was built in a modular fashion. There are three modules: the circulatory, thermal and neural control subsystems. The circulatory and thermal modules are stand-alone simulators. They can independently simulate the corresponding physiological systems. After they are connected together, they interact with each other so that they become a co-simulator overall. The ambient air temperature is the only input to the co-simulation, and it is the driving force for the dynamics of the circulatory system. The structure of the program is shown in Fig. 3.

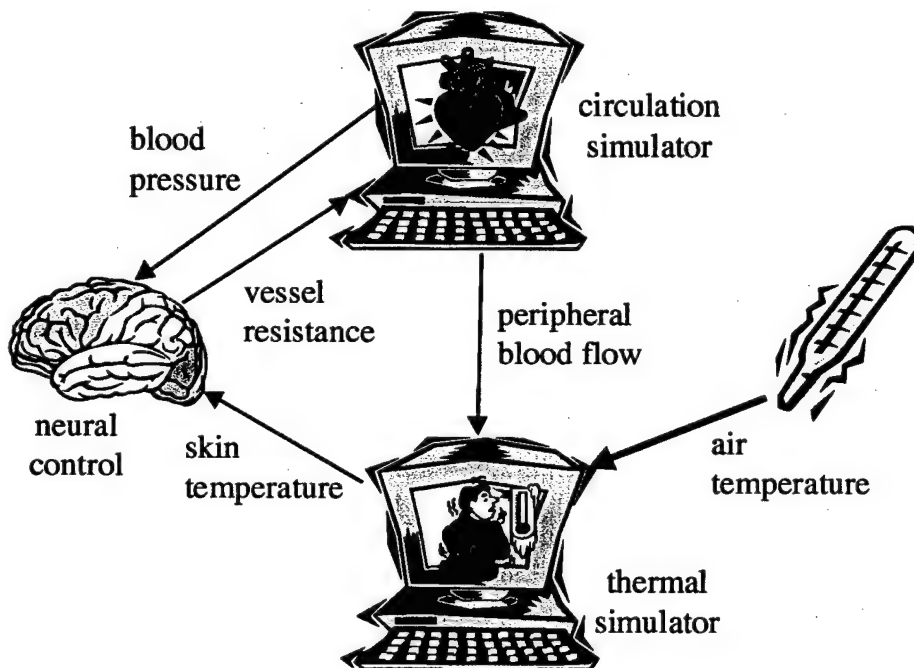


Fig. 3. The software structure of the co-simulator.

LabView was chosen as the programming language to implement the simulation (National Instruments, 1998). The graphic programming language provided an easy way to make a graphical user interface and collect sensor readings. C functions were used to solve differential equations for the circulatory and thermal systems. The simulated skin temperature and peripheral blood flow rate is displayed on the monitor, and so is the real measurement. For initial implementation, this combination turned out to be a good solution.

## 2.3 Experimental setup

To test the co-simulation program, we prepared two adjacent rooms maintained at different temperatures. The hot room was about 35 °C and the cold room was about 15 °C. Thermocouples and photoelectric phethysmographic sensors were attached to the human subject to measure the skin temperature and the peripheral blood flow, respectively. The photoelectric plethysmography measures a tissue's light absorptivity that is correlated to the amount of blood flowing through the tissue. The detail design and calibration procedure of the blood flow sensor was given by Zhou (1997). Another thermocouple for air temperature measurement was used which also moved with the subject to provide the simulator with the current air temperature that the subject was experiencing. A digital blood pressure monitor based on the occlusion method was also implemented. The blood pressure can be sampled every two minutes. The subject wore a T-shirt and shorts which the thermal model required. The subject rested for more than 30 minutes before the experiment started. This was to eliminate any additional effects on the human body except the thermal excitation. During the experiment, the subject stayed under one temperature for at least 5 minutes before moving to another thermal environment.

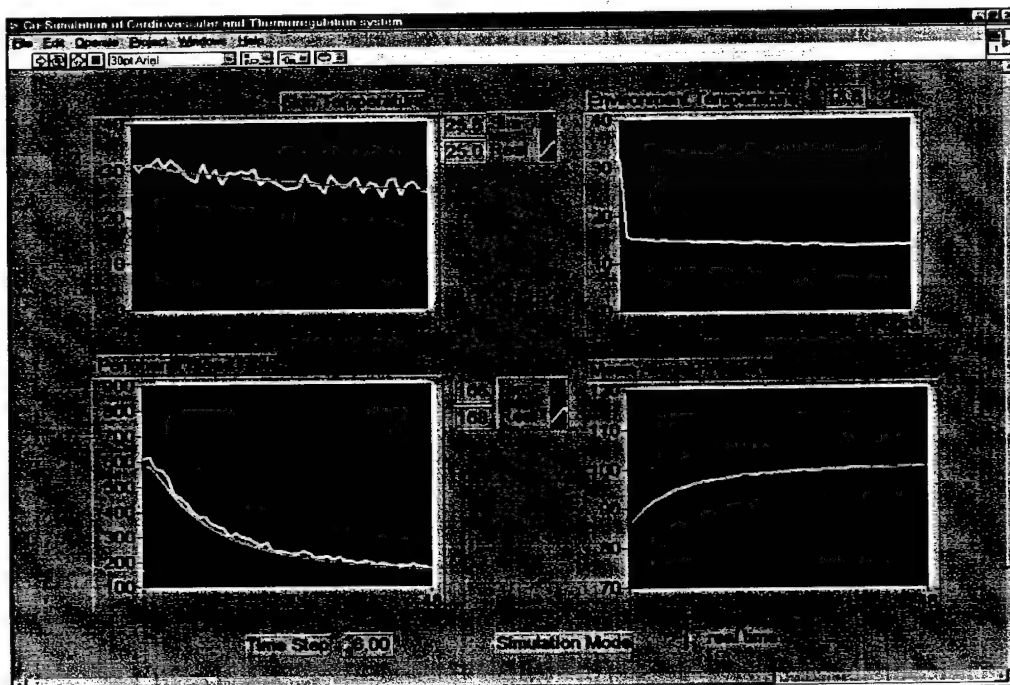


Fig. 4. The graphic user interface of the co-simulator.

## 2.4 Results

As shown from the screen snapshot in Fig. 4, the simulation captured the trend of real physiological measurement quite well. However, the simulation program does not compare or show the blood pressure on screen. The reason is that we found in our model validation process that the blood pressure was subjected to many unpredictable or unaccountable factors, such as emotion. We found that the model prediction of blood pressure agreed with the measurement after averaging several measurements although a real time comparison might give fewer consistencies between the measurement and the prediction.

## 3 Issues about Coupling of Bond Graph Models

### 3.1 The Proposed Complex System Modeling Environment

We intend to integrate existing simulation programs and let them work together to simulate a large system. The rational is that many physiological systems have been already modeled and simulations have been implemented. It is a good idea to use existing specialized resources. Another reason is that some sub simulators may take real time measurement and estimate parameters so independent hardware for these sub simulators is appropriate.

A system integrator running on top of the network of simulators is needed. We propose to use this integrator to specify the inter-connections among individual simulators. We start the research from the lumped-parameter model. Such a dynamic system can be represented in different forms, such as state space equations, bond graph, block diagram, signal graph, etc. The bond graph is a tool to model dynamic system over different energy domains (Karnopp et al, 1990). It is a unified representation in terms of energy. It has clear physical meanings that can help us to understand the system dynamics and interaction. The connection between two systems can be modeled as simple as one bond while a single connection can change the state equations substantially. The bond graph also conveys more structural information than the state equation does. The extra information provided by the bond graph is very useful for many bond graph based analyses. Thus there is a clear advantage for the bond graph representation.

The connections between bond graph models have several forms. Therefore, we start with classification of possible connections and identify what are the critical issues when two systems are to be connected. A classification of all possible connections between two sub systems is given in Fig. 5. The detailed discussion will follow the flow chart shown in Fig. 5.

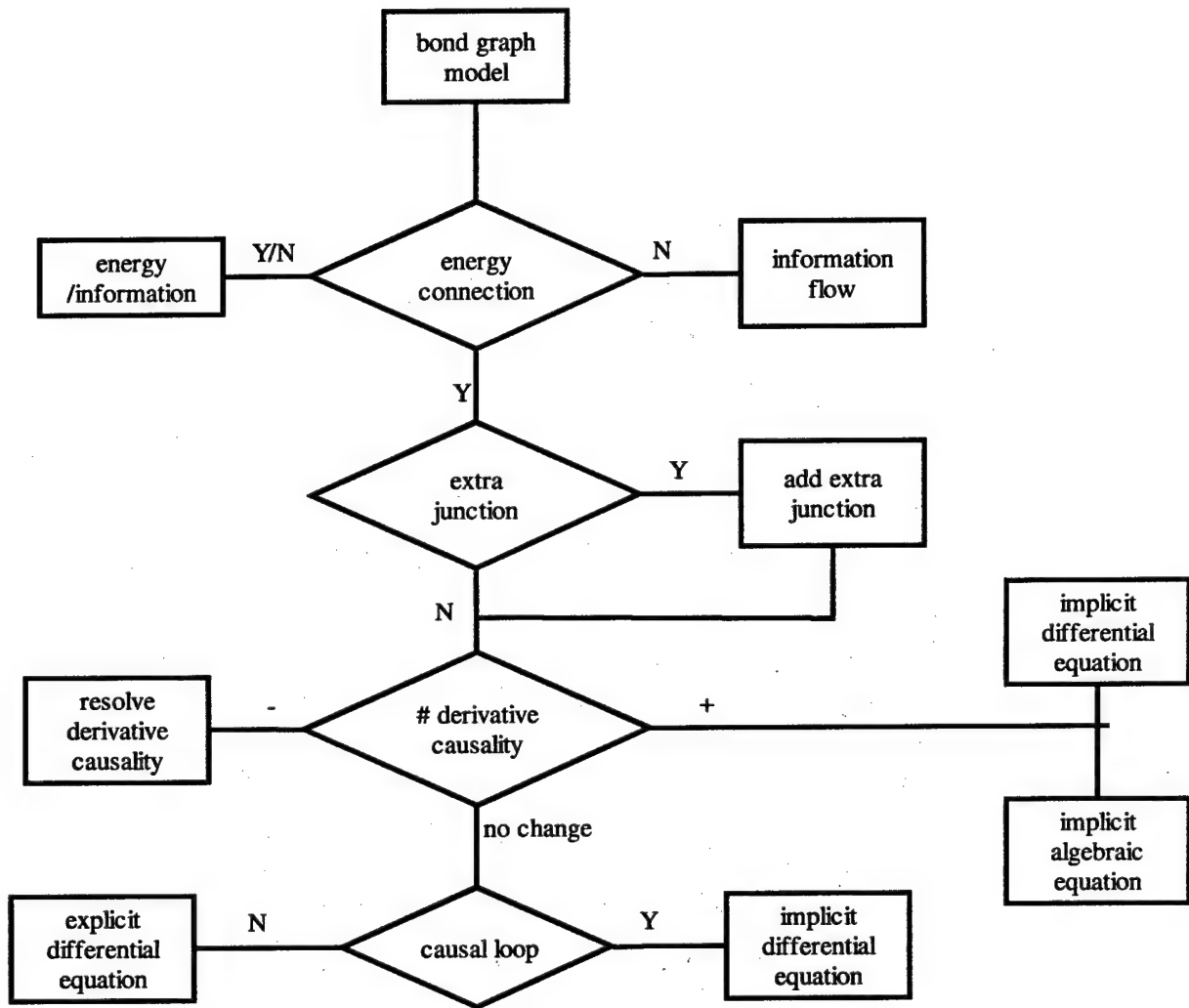


Fig. 5. The classification of different connections between systems.

### 3.2 Different Types of Connection between Two Systems

#### 3.2.1 Whether connection is through energy or information

First of all, what is a coupling? The coupling is a mutual interaction between two systems. In the real dynamics systems, when one system influences another system,

energy transfers from one to another system. The energy transfer can be very small but finite. This is the physics behind all actuators and sensors. We want a non-zero energy transfer for an actuator and zero energy transfer for an ideal sensor. In the bond graph representation, the energy flow per unit time is power, which is the multiplication of the effort and the flow variable. We often distinguish a connection between the energy coupling and information flow. The energy coupling is a two-way influence and the two systems interact with each other by means of the energy flow in bond graph modeling practice. The information flow is a one-way influence and the energy associated with that flow is negligible. A regular bond of the bond graph carries energy. It has a causal stroke assigned at one end. The causal stroke specifies the direction of the influence. The effort of the stroke free side decides the effort of the stroke side. The flow of the stroke side decides the flow of the stroke free side. Therefore, once the energy flow is non-zero, both effort and flow exist. So it is a two-way influence situation. On the other hand, when either the effort or the flow is negligible, there is no energy flow and it is a one-way influence situation. In the bond graph terminology, the information flow is called an active bond, which is the signal flow. Thus, regular bond is a two-way coupling and the active bond is a one-way influence. The fundamental difference is explained by the definition of the bond. According to different bond type of the connection, we can classify the connections into three categories: pure information, information/energy and pure energy.

#### *Pure information influence*

As discussed before, the information flow is one-way influence. That the parameters of non-energy storage elements of system on the left-hand side are controlled by a variable in system on the right-hand side is the case of pure information coupling as shown in Fig. 6.

However, when the granularity or the operation condition changes substantially, the pure information assumption may be no longer valid. For example, the electrical resistivity is a function of operation temperature. If we consider a system consists of coupled electrical and thermal sub systems, the resistor of the electrical system is modulated by a temperature state variable of the thermal system. It is an information one-way influence case if we ignore the entropy change caused by the material property,

i.e. electrical resistivity, change. When the electrical system is to be coupled with a detail thermal system model and the ignored entropy change is comparable to those considered in the thermal model, the information influence should be considered an energy coupling. The difficulty may be that the sub system was modeled as information influence that is only a one way effect. The coupled model is now an energy coupling which is a two way coupling. The software model structure should be able to accommodate this change.

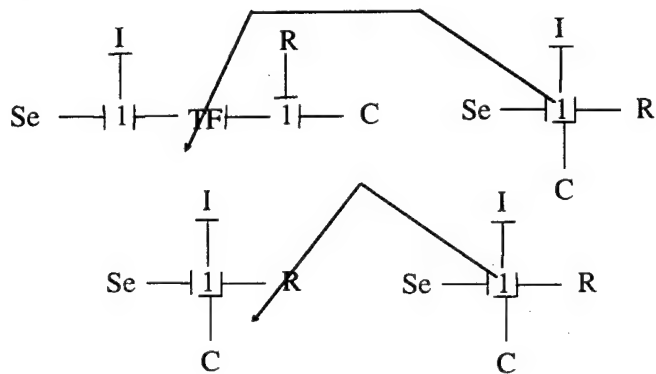


Fig. 6. The bond graph examples of pure information flow.

#### *Energy/information connection*

Often the constitutive law of an energy storage element is controlled by a variable from another system but the energy needed to make change is not supplied from the controlling system. There is another energy source to supply the energy needed to perform the modulation. For example, in the human physiology system, some blood vessels can contract or enlarge to control the blood flow under skin. The blood flow change is to control the heat dissipation to surrounding environment. When the diameter of the blood vessel changes, the compliance of the vessel also changes a small amount. The contract or enlarge is controlled by the body temperatures. The dynamic system of the body temperature regulation sends command to change vessel compliance but the blood vessel muscles change the vessel diameter. Therefore, the energy needed to change a compliance in the circulation dynamic system is from neither circulation system nor temperature regulation system but from somewhere outside. The bond graph of this example is given in Fig. 7.

### *Energy coupling*

Most of the interconnections between two systems are the energy couplings. Two sub systems can be linked through a transformer or gyrator. If the parameter of the transformer is 1, the coupling reduces to a single bond. Sub systems can also be connected through energy storage fields, such as C, I and IC fields.

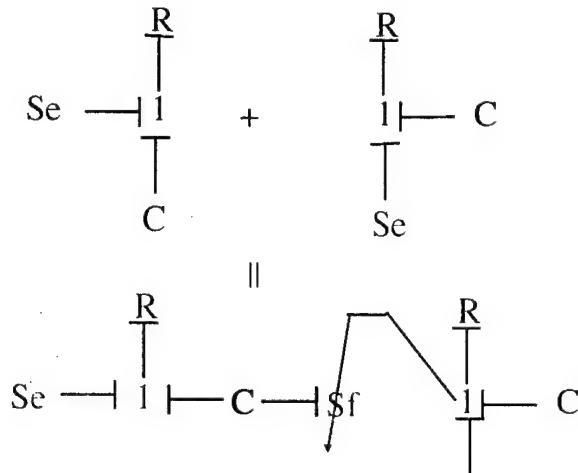


Fig. 7. The bond graph example of energy/information connection.

#### 3.2.2 Whether the variable to be connected is available from a junction

We usually get an effort from a zero junction or a flow from a one junction. However, there are chances that the system does not have a zero or one junction for effort or flow connection, respectively. In this case, we need to add an additional junction to the sub system bond graph model. For example, the two electrical systems are to be connected shown in Fig. 8. The bond graph model is also given. We need use the voltage over the capacitor of the first circuit as the input for the second circuit. Since there is no available zero junction that can supply an effort from system on the right, we have to add a zero junction to it first. Then, we make a connection from the new zero junction to the system on the left as the effort source. The presence of the system on the right actually changes the system structure of the system on the left.

#### 3.2.3 Whether the number of derivative causality changes

Let us consider the cases that no extra junction is needed or the extra junction has been added. When two systems are to be coupled, the overall order of the coupled system can be the same of the total order of individual systems or it can be less or more than that. If

there is a causal conflict between the two systems, the overall order of the coupled system is less than the total state variables of the individual systems. The causal conflict makes some of the energy storage elements change from integral to derivative causality. The derivative causality causes troubles in the equation generation and simulation. The causal conflict problem can be easily solved if the systems are linear. For example, two inertia share a same velocity can be combined into a single inertia. However, if one of the systems to be coupled is nonlinear, the solution is not that simple. There are two cases when the nonlinearity is involved.

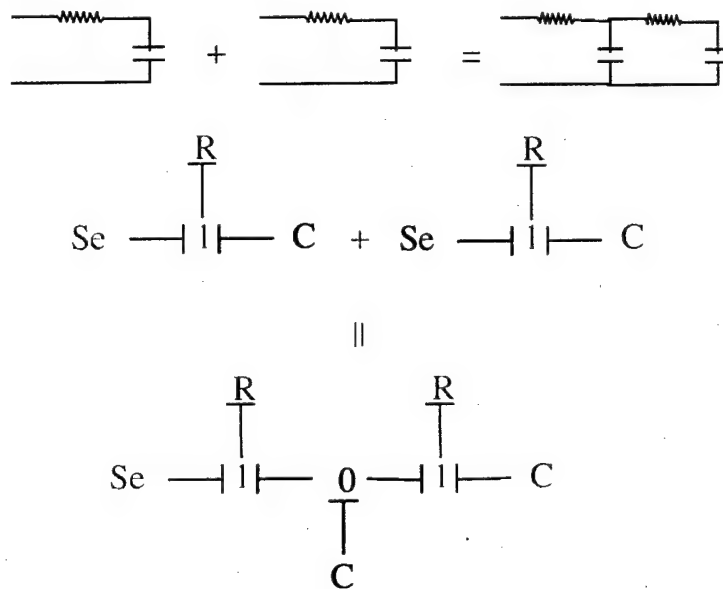


Fig. 8. The bond graph example of the extra junction case.

#### *Energy coupling with order reduction due to implicit algebraic equation*

The first situation results in implicit algebraic system. Fig. 9 shows the schematic drawing of an aqua pump used in fish tank. The overall system considered here is consisted of a mechanical system and a fluidic system. The bond graph of each system is given in Fig. 9. As we can see in the bond graphs, the two sub systems are both causal. However, since the check value is nonlinear and cannot be inverted, the causality of the mechanical system has to be reassigned when the two systems are connected. The causality of the inertia has to change from integral to derivative. The overall order of the system after connection is one that is less than the total order of uncoupled systems. The equations for this system is in flowing form:

$$\dot{\mathbf{X}} = f(\mathbf{X}, \mathbf{U}, t, \mathbf{Z})$$

$$\mathbf{0} = g(\mathbf{X}, \mathbf{U}, t, \mathbf{Z})$$

It is an explicit differential equation with an implicit algebraic equation.

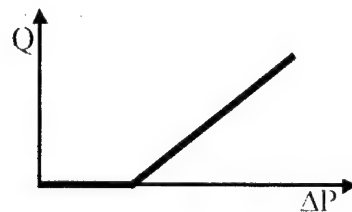
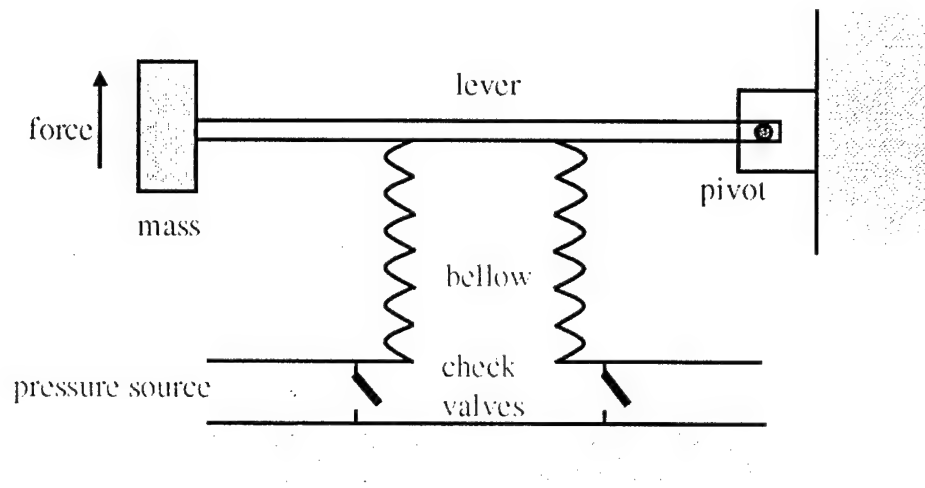


Fig. 9. Schematics of the aqua pump.

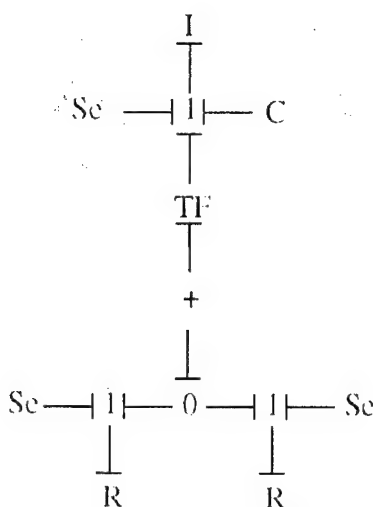


Fig. 10. The bond graph model of the aqua pump.

### *Energy coupling with order reduction due to implicit differential equation*

The second situation is the implicit differential systems. For example in the system depicted in Fig. 11, the two capacitors are nonlinear. The system order after coupling is one, which is lower than uncoupled total order. The system equation can be easily obtained for this simple example. The equation will take following form:

$$0 = f(\dot{\mathbf{X}}, \mathbf{X}, \mathbf{U}, t)$$

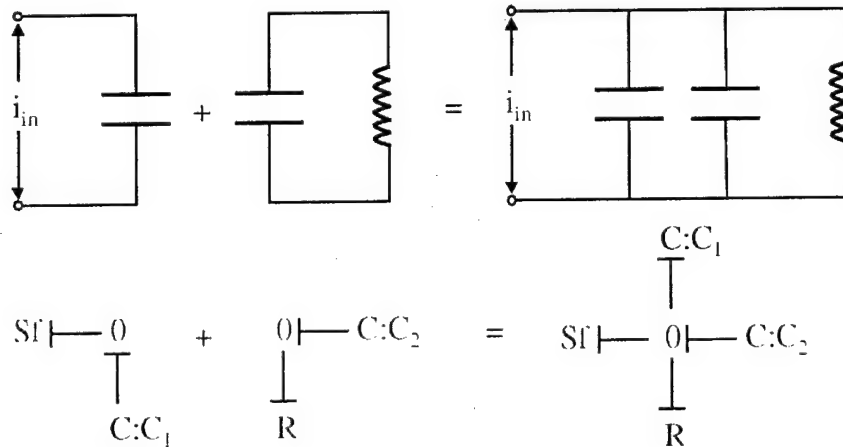


Fig. 11. The coupling of two non-linear capacitors.

The combination of energy storage elements may not necessary work because the combined capacitor may not have a closed form representation. Therefore, the simulation program still has to iterate even if the differential equation becomes explicit. The combination approach indeed transforms the implicit differential problem into the implicit algebraic problem.

#### *Extra states after coupling*

It is also possible that the coupling may resolve the causality conflict so that the total order of the coupled system is higher than the sum of the previous systems.

#### 3.2.4 Algebraic Loop Formed due to Coupling

Even if there is no causal conflict due to coupling of two systems, the coupled system may still contain algebraic loops. The algebraic loop (Gawthrop, 1991; Van Dijk and Breedveld, 1991) may cause difficult in some automatic state equation derivation schemes. Figure 12 shows the coupling between two very simple sub systems. The

coupled bond graph has an algebraic loop. A derivative appears in the right hand side of the equation during the equation derivation. It will be a problem for a large bond graph although the state equation of this trivial example can be easily obtained by manual derivation.

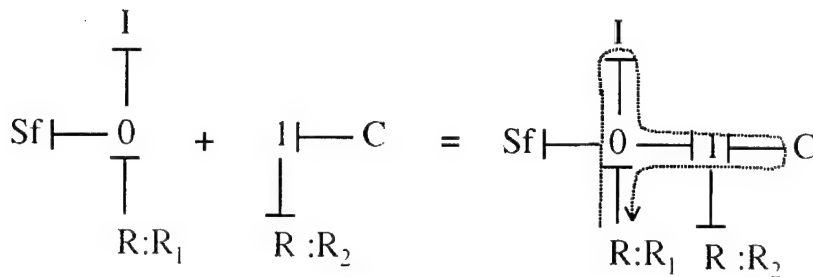


Fig. 12. An example of the causal loop.

## 4 Simulation Using Junction Variables

### 4.1 Physical Ground of Junction Variable Method

Figure 13 shows a simple spring-mass-damper system. The free body diagram of the first two elements, namely mass 1 and damper 1 are also given. The corresponding bond graph for these two elements consists of I, R, and Se elements. Let us assume a force  $F$  is applied at time 0 to the right side of the mass 1. Assume all 0 initial condition. The friction force from the damper is 0 because of 0 initial condition. Therefore the velocity of the mass can be integrated using Newton's second law for time step 1. We store the velocity of the mass in the one junction. We then calculate the force of the damper for time step 1. The velocity of the one junctions connected to the zero junction is used. The time step 0 velocity of the two one junctions are 0 so the constitutive law of the damper gives the force of the zero junction which is 0. The force is stored in the zero junction for next step calculation. We can do the same calculation for mass 2 and other system components. After we scan and calculate the time step 1 values for all the junction variables, we start the time step 2 calculation for the mass 1. Mass 1 integrates the force difference and updates the velocity in junction 1. We then use non-zero value of step 1 stored in junction 1 to calculate the force of junction 0. The resulting non-zero force will again update the zero junction. The procedure covers the rest of the system. The calculation mimics the dynamic effect of the applied force spreading through the spring-

mass-damper system. It indeed is a more straightforward method than the standard state space method. However, they fundamentally share the same physics.

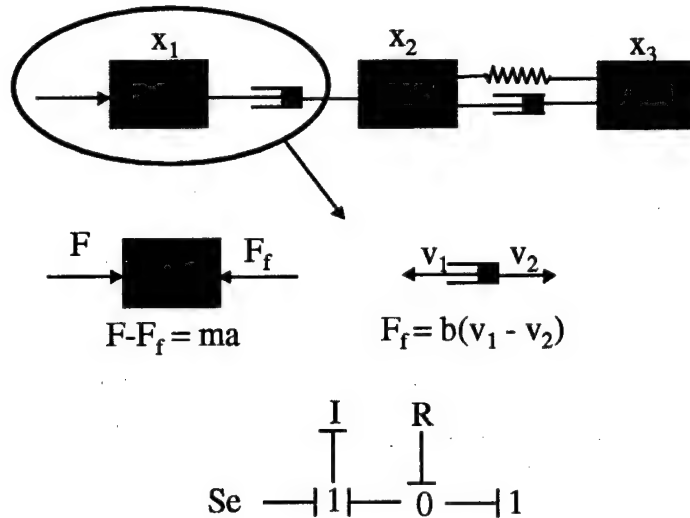


Fig. 13. Physical explanation of the junction variable method.

#### 4.2 Method Validation

A Matlab procedure is written to compare the two different integration methods for solving the dynamic system shown in the Fig. 13. The state space method uses the Matlab function lsim and the junction variable method uses the simplest Euler integration. The three velocities of three masses and the two forces between three masses are given in Fig. 14a and 14b, respectively. The input is a step function. The thick lines are the result of state space method and the thin lines in the center of the thick lines are the output of the junction variable method. The result shows good agreement of the two methods.

#### 4.3 Potential Advantages of the Junction Variable Method

Since the junction variable method of solving dynamic system described by the bond graph reveals more physical meanings, it can help us to understand and then optimize the simulation. Considering a dynamic system given by the bond graph in Fig. 15a. Let us assume the left and right part of the bond graph separated by a thick bar are simulated on two different computers. The two computers have to exchange information over network

to simulate the coupled system. The junction variable method simulation of the left part needs a force from the zero junction of the right part of the bond graph to execute one step. The right part needs also a velocity from the one junction of the left part to integrate one step. The total value passing for a step is two. Figure 15b is the system matrix of the dynamic system described by the bond graph in Fig. 15a assuming linear for simplicity. All non-zero elements of the matrix are marked and zero elements are kept blank. The system is also assumed being solved on two computers. The thick lines in Fig. 15b divide the boundary of the two computers. It is clear that integration of the third row of the left system needs three values from the right system. The right system needs only one value passed from the left system. Thus the total value passing is four which is two times as that in the junction variable method. This demonstrates the saving on network communication of the junction variable method.

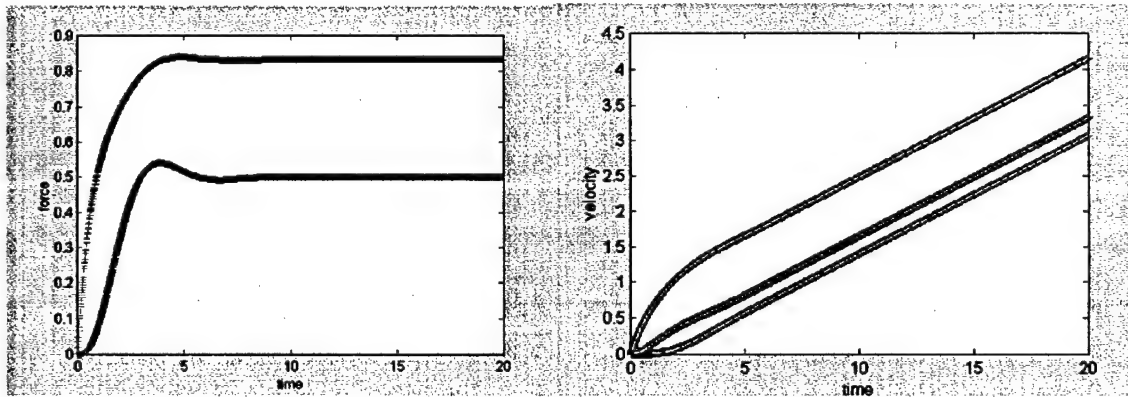


Fig. 14a and b. The results of junction variable method compared with the results of the standard method.

The junction variable method may have another advantage in parallel computation. Figure 16 shows the computation sequence of the junction variable method. If we initiate value passing at the same time of an integration step, the indicated computation sequence will minimize the latency time. The value passing thread can utilize the time, which the integration thread takes to finish its job.

#### 4.4 Remarks of the Junction Variable Method

The junction variable method provides us more physical insight to the simulation. However, it has difficulties in solving algebraic constraints. Nevertheless, we can adopt some ideas of the junction variable method and use them in solving state space systems.

For example, we can pack the three values needed to pass to the left system in Fig. 15b and only send them as one value. We may also study the bond graph structure and use the computation sequence indicated by the junction variable method in the standard state space form.

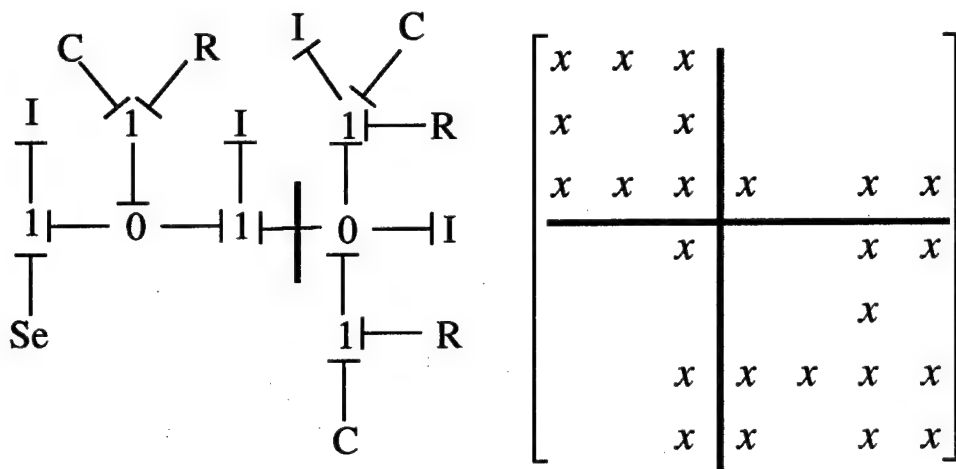


Fig. 15a and b. Passing value between two sub systems.

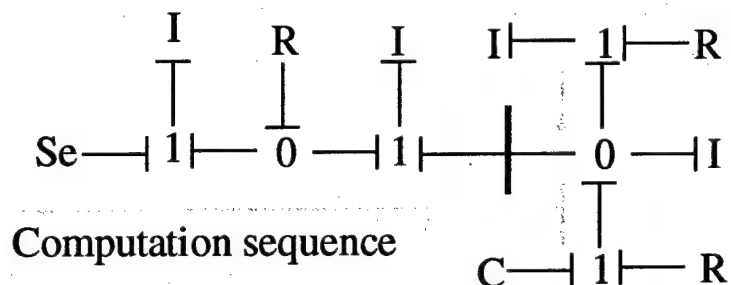


Fig. 16. Computation sequence.

## 6. Analysis of Coupled Distributed Systems: Case Study of Coupled Mechanical/Fluidic Model of Digital Artery

The human body is a distributed system. While many reasonably accurate lumped parameter models of various physiological systems exist, it is reasonable to expect better performance from distributed models. Hence the need for basic research in coupling distributed systems governed by systems of partial differential equations.

The problem of coupling distributed systems is normally studied within the numerical analysis and FEM communities. Coupled problems can be classified into 2 distinct categories, each having its own general numerical treatment: coupled problems where the various domains overlap, either totally or partially, and problems where coupling occurs only on domain interfaces (that is, only through the boundary conditions imposed) (Zienkiewicz, 1984). This is directly analogous to ‘information’ and ‘energy’ coupling in bond graphs. Thus, it is not surprising that the second class of systems is more challenging numerically, since coupling can change the structure and order of the sub-systems. It is this class of problems that we focus our attention to. Typical numerical coupling techniques follow a general sequence of steps: discretizing the equations, followed by iterative attempts to match the kinematic and dynamic variables at the interface. Thus, the procedure is problem dependent, the iterations lengthy and the number of required boundary conditions is not clear. We propose a different formulation of the coupled problem, within the framework of PDAE (Partial Differential and Algebraic Equation). We believe that this formulation will allow us to model and analyze the coupled problem first, leaving the discretization to the last step. As a result, we can, at worst, ensure flexibility and modularity, and at best, provide a systematic means for analyzing the coupled problem and determining a consistent set of initial and boundary conditions.

Our efforts for the past half year have been directed at studying the feasibility of the proposed method. We did that through an exemplary case study that is of high interest to the Consortium goals (Ring Sensor project): the coupled fluid-structure modeling of digital arteries, under the influence of external load transmitted through the tissue. Progress has been made in developing a viscoelastic model for the digital artery. The new model is reported in this section, as well as the coupled problem analysis as introduced above.

## 6.1 Blood Vessel Model

The blood vessel is modeled as a series of thin rings interacting with each other and with their environment, as shown in Fig. 5. The rings can contract and expand in the radial direction, while remaining centered about the blood vessel axis (z axis). Torsional and longitudinal deformation modes are neglected. Smooth muscle action is also neglected, and hence the stress free dimensions of the blood vessel are constant ( $R_o$ , the inner radius

and  $h_o$ , the wall thickness). The blood vessel material is assumed to be incompressible, and stresses are assumed constant across a cross-section of the vessel, taking on some average value. The constitutive behavior of the blood vessel is non-linear time dependent (viscoelastic). Finally, the environment acts as effort sources to the blood vessel: the fluid medium and the tissue medium impose pressure  $P$  on the inner surface and stress  $\sigma_t$  on the outer surface of the blood vessel, respectively.

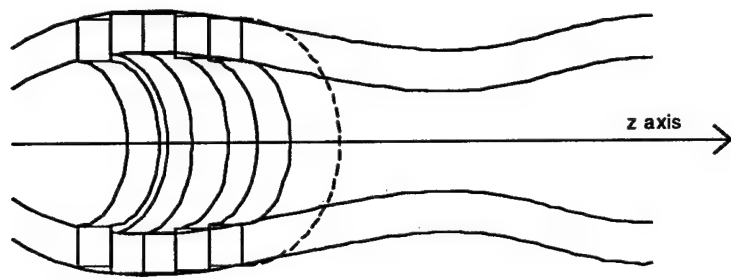


Figure 5.

Consider, within a ring (thickness  $\Delta z$ ), a small wedge element subtended by an angle  $\delta\theta$  (Fig. 6). The relevant dimensions are  $R$ ,  $h$  and  $r$ : the inner radius, the wall thickness and the distance from blood vessel axis to the element centroid, respectively.

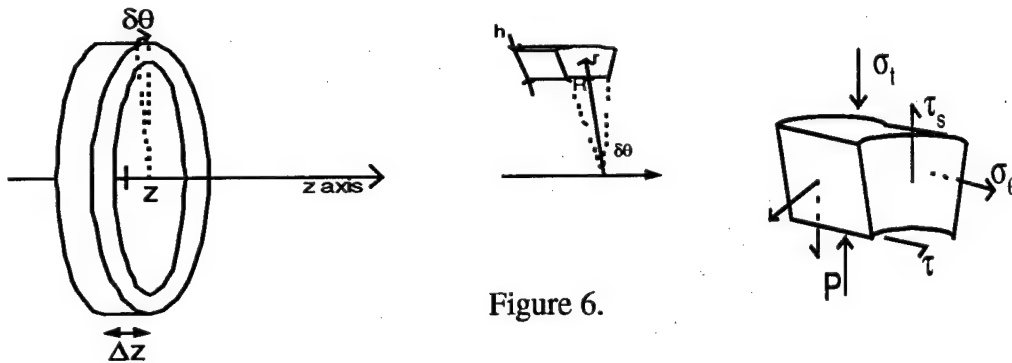


Figure 6.

- Momentum Balance, written for the limiting case where  $\Delta z \rightarrow 0$ :

$$PR \delta\theta - \sigma_t [R + h] \delta\theta - 2F_{\theta,r} + \frac{\partial F_s}{\partial z} = \rho \frac{[R + (R + h)] \delta\theta}{2} h \frac{\partial^2 r}{\partial t^2}$$

- Mass Conservation:

$$(2R + h)h = a_o$$

- The viscoelastic behavior of the blood wall is modeled with the help of the Kelvin model (Fung, 1997). The Kelvin model, shown in Fig. 7, is a lumped parameter system that faithfully mimicks the dynamic behavior of linear viscoelastic material (mainly polymers). It can be extended to model the nonlinear behavior of biological tissue by replacing the linear springs and dashpots by their non-linear counterparts. The resulting equations are given below.  $F_{\theta,r}$  is the radial component of the hoop force while  $F_s$  is the shear force between two adjacent rings.

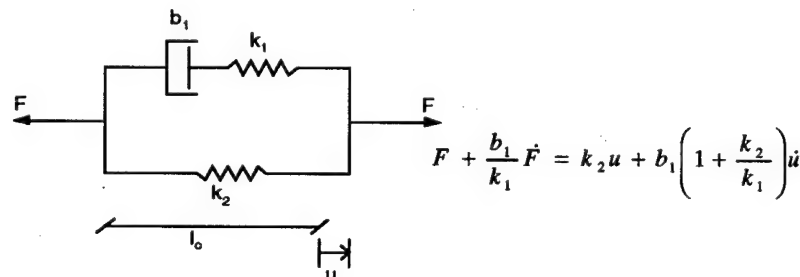


Figure 7.

$$F_{\theta,r} + \tau_{\varepsilon,\theta} \frac{\partial F_{\theta,r}}{\partial t} = E_{R,\theta} (r - r_o) + E_{R,\theta} \tau_{\sigma,\theta} \frac{\partial r}{\partial t}$$

$$F_s + \tau_{\varepsilon,s} \frac{\partial F_s}{\partial t} = E_{R,s} (r - r_o) + E_{R,s} \tau_{\sigma,s} \frac{\partial r}{\partial t}$$

- Finally, the geometry of the element dictates the following relationship between  $r$ ,  $R$  and  $h$ :

$$r = R + \frac{5}{9}h$$

## 6.2 Blood Flow Model

Blood flow is modeled as viscous, laminar, with an assumed parabolic velocity profile satisfying radial symmetry and no-slip condition at the wall. The environment, once again, acts as flow sources. The cardiovascular system and the blood vessel impose a

pressure gradient on the system. Consider a control volume of fixed width  $\Delta z$  and whose boundaries can move with the flow in the radial direction (Fig. 8).

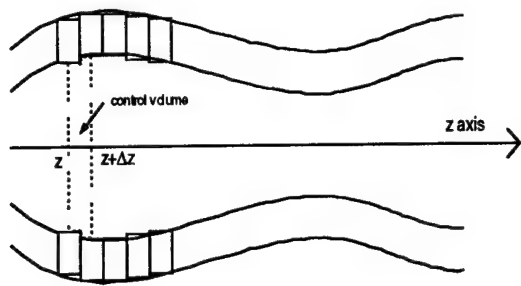


Figure 8.

- Momentum Balance, applied to the control volume in conjunction with the assumed velocity profile (Q: volume flow rate, S: cross-section):

$$\frac{\partial}{\partial t}(Q) + \frac{4}{3} \frac{\partial}{\partial z} \left( \frac{Q^2}{S} \right) = - \frac{1}{\rho} \frac{\partial}{\partial z}(PS) - 8\pi\nu \frac{Q}{S}$$

- Mass Conservation:

$$\frac{\partial S}{\partial t} + \frac{\partial Q}{\partial z} = 0$$

### 6.3 The Coupled Model

In practice, the fluid dynamically interacts with the blood vessel at the inner surface of the latter. The basic physics governing each of the systems remains the same regardless of whether the two systems are interacting or each is acted on by sources. The mathematical model of the coupled system should ensure kinematic and dynamic compatibility of the systems at their common boundary, in addition to satisfying the basic equations of each subsystem. Kinematic compatibility requires the flow area to match the inner cross-section of the blood vessel. Dynamic compatibility requires the fluid pressure to equal the pressure acting on the inner surface of the blood vessel at any given axial

location. Additionally, the conservation equation (mass, momentum) and constitutive equations should be satisfied in each domain.

### 6.3.1 Minimal Formulation

For this particular case, the systems at hand are “nice” enough so that, in spite of the nonlinearity, we can explicitly solve for intermediate variables. As a result, we can eliminate these variables (namely  $P$ ,  $R$  and  $h$ ) from the system equations. To reduce the second order term ( $d^2r/dt^2$ ), we can define a new variable  $=dr/dt$ . Fluid mass conservation indicates that  $v$  is a dependent variable. Once again, the equations permit us to explicitly solve for  $v$  and plug it back into the equations. The result is the following minimal formulation (variables  $r, F_{\theta,r}, F_s$  and  $Q$ ):

$$\left\{ \begin{array}{l} \frac{\partial r}{\partial t} = -a_{1(r)} \frac{\partial Q}{\partial z} \\ \frac{\partial F_{\theta,r}}{\partial t} = \frac{E_{R,\theta}}{\tau_{\epsilon,\theta}} (r - r_o) - \frac{E_{R,\theta}}{\tau_{\epsilon,\theta}} \cdot a_{1(r)} \frac{\partial Q}{\partial z} - \frac{1}{\tau_{\epsilon,\theta}} F_{\theta,r} \\ \frac{\partial F_s}{\partial t} = \frac{E_{R,s}}{\tau_{\epsilon,s}} \frac{\partial r}{\partial z} \Delta z + \frac{E_{R,s} \tau_{\sigma,s}}{\tau_{\epsilon,s}} \frac{\partial v}{\partial z} \Delta z - \frac{1}{\tau_{\epsilon,s}} F_s \\ I \frac{\partial^2}{\partial z^2} \left( \frac{\partial Q}{\partial t} \right) + G \frac{\partial}{\partial z} \left( \frac{\partial Q}{\partial t} \right) + \frac{\partial Q}{\partial t} + H = 0 \\ I = I_{(r)}, G = G_{(r, \partial r / \partial z)}, \\ H = H_{(r, Q, \partial r / \partial z, \partial Q / \partial z, F_{\theta,r}, \partial F_{\theta,r} / \partial z, \partial F_s / \partial z, \partial^2 F_s / \partial z^2 \sigma_s, \partial \sigma_s / \partial z)} \end{array} \right.$$

The first 3 equations can be discretized in space, at  $n$  discrete locations, to give a set of  $3(n-1)$  explicit state equations in the variables  $r, F_{\theta,r}$  and  $F_s$ . The values of these variables at  $z=0$  need to be known (thus the need for 3 boundary conditions) as well as  $3(n-1)$  initial conditions are needed. The fourth equation can be discretized to give  $(n-2)$  implicit state equations, that have to be solved for  $dQ/dt$ . The required boundary conditions here are the flow rates at the two ends of the blood vessel, in addition to  $(n-2)$  initial conditions. The discretized system order has decreased, probably because the coupling changed the source from effort to flow, and forced inertia elements to go into derivative

causality, thus reducing the number of independent energy storage elements in the discretized system. Note that in this formulation, it is very easy to see how many boundary and initial conditions are needed for each variable.

### 3.2 PDAE Formulation

Instead of seeking to eliminate the intermediate (non-independent) variables, this formulation concatenates three sets of equations, 2 representing the physics of each domain and 1 representing the compatibility conditions at the boundary. The resulting system is:

$$\left\{ \begin{array}{l} F_{\theta,r} + \tau_{\varepsilon,\theta} \frac{\partial \mathbf{F}_{\theta,r}}{\partial t} = E_{R,\theta} (r - r_o) + E_{R,\theta} \tau_{\sigma,\theta} v \\ F_s + \tau_{\varepsilon,s} \frac{\partial \mathbf{F}_s}{\partial t} = E_{R,s} \frac{\partial r}{\partial z} \Delta z + E_{R,s} \tau_{R,s} \frac{\partial v}{\partial z} \Delta z \\ \frac{\partial \mathbf{r}}{\partial t} = \mathbf{v} \\ \delta \theta \cdot f_{1(r)} P - \delta \theta [f_{1(r)} + f_{2(r)}] \mathbf{r}_t - 2 F_{\theta,r} + \frac{\partial F_s}{\partial z} = M \frac{\partial \mathbf{v}}{\partial t} \\ \frac{\partial \mathbf{S}}{\partial t} + \frac{\partial \mathbf{Q}}{\partial z} = 0 \\ \frac{\partial \mathbf{Q}}{\partial t} + \frac{1}{\rho} \frac{\partial}{\partial z} (P S) + \frac{4}{3} \frac{\partial}{\partial z} \left( \frac{Q^2}{S} \right) + 8\pi v \frac{Q}{S} = 0 \\ S - \pi \left( \frac{4}{13} r + \frac{9}{65} \sqrt{25r^2 - 65a_o} \right)^2 = 0 \end{array} \right.$$

The advantages of this formulation are flexibility and modularity. The individual system models can be simply changed by modifying the relevant equations. Other interacting systems can be incorporated into the model by simply adding another system of equations. The disadvantages of this formulation is the lack of all those features that make the minimal formulation attractive, namely physical insight into system and its order (upon discretization) and simplicity in defining a consistent set of initial and boundary conditions. It is not clear, without further analysis, which variables are independent and which aren't.

The subject of DAE's (differential algebraic equations) has been studied extensively during the past 20 years (Campbell et. al, 1991). It has been shown that the differential index of a DAE plays a substantial role in determining the complexity of the computational problem, as well as the number of independent variables in the model (from which we can deduce the number of initial conditions required). Although from a modeling point of view, temporal and spatial variations are completely different issues, the mathematics does not differentiate between time and space derivatives. Hence, it is highly likely that, in a manner analogous to differential index for DAE's, there exists a differential space index for PDAE's which gives insight about the number of boundary conditions required, in addition to the temporal differential index. This concept has been explored for the case of linear PDAE's (Lucht et. al, 1997), and our goal is to apply and extend these techniques further, as required for the study of physiological coupled systems.

## 7 Conclusion

The simulation of human physiological system is an important tool for the home automation and healthcare consortium. Different modeling approaches for complex system of multi-energy domain have been surveyed. The object-oriented modeling is a powerful tool for building complex models using re-useable sub system classes. However, the most important aspect of co-simulation is integration of existing software. A co-simulation of circulatory and thermoregulatory systems has been implemented based the coupled dynamic model reported in previous report. Although this co-simulation program involves only one computer, the circulatory and the thermoregulatory simulators are independent and self complete. The simulation result is compared with the real time measurement from a human subject. The simulation catches the trend of peripheral blood flow and skin temperature excited by environment temperature change pretty well. The report has analyzed different possibilities when two bond graph models are to be coupled together. A new simulation method based on the bond graph has been proposed and it passes the junction variables instead of state variables between different sub simulators. The junction variable method thus can save time for coupled simulation on passing data over the network. However, the new method only works with integral causality models but the idea of minimization of passing information between simulators

can be applied to the standard method. Additionally, an exemplary case study of a coupled distributed system was discussed. A newly developed viscoelastic blood vessel model was presented, and the coupled fluid/structure dynamic behavior of the blood vessel was modeled. Two formulations were developed, and their advantages and disadvantages were stated and compared.

## Reference

Borutzky, W. and Cellier, F., 1996 "Tearing Algebraic Loops in Bond Graphs," *Transactions of the Society for Computer Simulation*, Vol. 13, No. 2, pp. 102

Cellier, F. E., Elmquist, H., Otter, M., and Levine, W. S., 1996, "Determining Models," *the Control Handbook*, Levine, W. S. Eds., CRC Press, Inc.

Elmquist, H., 1979, "DYMOLA - a Structured Model Language for Large Continuous Systems," *SCSC Summer Computer Simulation Conference, AFIPS*, pp. 8-14, Montvale, NJ.

Gagge, A. P., Stolwijk, J. A. J., and Nishi, Y., 1971, "An Effective Temperature Scale Based on A Simple Model of Human Physiological Regulatory Response," *ASHRAE Transactions*, Vol. 77, Part 1, pp. 247-262.

Gawthrop, P., 1991 "Causal Augmentation of Bond Graphs with Algebraic Loops," *Journal of the Franklin Institute*, Vol. 328, No. 5-6, pp. 959-980

Hassenforder, M. and Gissinger, G. L., 1996, "Object Oriented Modelling Approaches to Variable Granularity: Application to a Diesel Engine," *SAE Special Publications Modeling of SI and CI Engines, Proceedings of the 1996 SAE International Congress & Exposition*, Feb 26-29 1996, n1168, pp. 231, Detroit, MI.

Hogan, H., 1987, "Modularity and Causality in Physical System Modelling," *ASME Journal of Dynamic Systems, Measurement, and Control*, Vol. 109, pp. 384-391.

Karnopp, D., Margolis, D. and Rosenberg, R., 1990, *System Dynamics: A Unified Approach*, Wiley-Interscience, New York, NY.

National Instrument Corp., 1998, *LabView User Manual*, National Instrument Corporation, Austin, TX.

Ozawa, E. T., 1996, "A Numerical Model of the Cardiovascular System for Clinical Assessment of the Hemodynamic State," *Ph.D. Thesis*, Massachusetts Institute of Technology, Cambridge, MA.

Prata, S., *C++ Primer Plus: teach yourself object-oriented programming*. 2<sup>nd</sup> ed., the Waite Group, Inc., Corte Madera, CA.

Rosenber, R. C., 1987, "Exploiting Bond Graph Causality in Physical System Models," *ASME Journal of Dynamic Systems, Measurement, and Control*, Vol. 109, pp. 378-383.

Rosenberg, R., 1971, "State-Space Formulation for Bond Graph Models of Multiport Systems," *Journal of Dynamic Systems, Measurement, and Control*, March, 1971, pp35-40

Stein, J. L. and Louca, L. S., 1996, "A Template-based Modeling Approach for System Design: Theory and Implementation," *Transactions of the Society for Computer Simulation*, Vol. 13, No. 2, pp. 87.

Van Dijk, J. and Breedveld, P., 1991, "Simulation of System Models Containing Zero-Order Causal Paths I. Classification of Zero-Order Causal Paths," *Journal of the Franklin Institute*, Vol. 328, No. 5-6, pp. 959-980

Werner, J., 1989, "Thermoregulatory models," *Scandinavia Journal of Work Environmental Health*, Vol. 15, Suppl. 1, pp. 34-46.

White, R. J., Fitzjerrell, D. G., and Croston, R. C., 1983, "Fundamentals of Lumped Compartmental Modelling of the Cardiovascular System," *Advances in Cardiovascular Physics*, Vol. 5, Part 1, pp. 162-184.

Zhou, M., 1998, "Human-Centered Control of the Indoor Thermal Environment," *Ph.D. Thesis*, Massachusetts Institute of Technology, Cambridge, MA.

## Nomenclature

$P_s$	Blood pressure in skin vessels
$P_v$	Blood pressure in viscera vessels
$C_s$	Compliance of skin blood vessel
$C_v$	Compliance of viscera blood vessel
$R_{sa}$	Artery resistance of skin blood vessel
$R_{sv}$	Venous resistance of skin blood vessel
$R_{va}$	Artery resistance of viscera blood vessel
$R_{vv}$	Venous resistance of viscera blood vessel
$P_I$	Mean artery pressure
$Q_s$	Skin blood flow
$Q_v$	Viscera blood flow
$Q_c$	Cardiac output
$P_{th}$	Right atrium pressure
$T_c$	Core temperature
$T_s$	Shell temperature
$\rho$	Blood density
$C_p$	Specific heat of blood
$\bar{h}_k$	Tissue conductance
$\bar{h}_a$	Skin heat transfer coefficient
$\bar{C}_s$	Shell thermal capacitance
$\bar{C}_c$	Core thermal capacitance
$A_{Du}$	Skin area
$T_a$	Air temperature
$H$	Metabolic heat generation
$T_{ss}$	Skin temperature set point
$P_s$	Mean artery pressure set point
$K_{ts}$	Skin thermal reflex gain
$K_{tv}$	Viscera thermal reflex gain
$K_c$	Baroreflex gain
$R_{sa,s}$	Skin artery resistance set point
$R_{va,s}$	Viscera artery resistance set point
$X$	Vector of state variables
$Y$	Vector of output variables
$u$	System input

## **Home Automation and Health Care**

### **March 1999 Report on the HANET Project**

### **Status on the IEEE-1394 Based Outlet for Home Automation and Health Care Networks**

**S. Martel, Ph.D.\*, S. Lafontaine, Ph.D., and I. Hunter, Ph.D.**

Bio-Instrumentation Laboratory, Dept. of Mechanical Engineering,  
Massachusetts Institute of Technology, 77 Massachusetts Ave. RM 3-147,  
Cambridge, MA, USA, 02139

\*E-mail: [smmartel@mit.edu](mailto:smmartel@mit.edu)

### **ABSTRACT**

This report describes the status of a new outlet intended for a future home and health care network based on the IEEE-1394 serial bus. The new outlet has been built and tested and it is fully operational. The state of the project allows several units to be distributed at the present time throughout the home to provide high-speed interconnection among various systems designed for home automation and/or health care applications. The system has been fully tested by transferring video images in real-time.

### **INTRODUCTION**

The IEEE-1394 serial bus also known as "FireWire" is a versatile, high-speed, and low-cost method of interconnecting a variety of personal computer (PC) peripherals and consumer electronics devices. The high speed FireWire and the low speed Universal Serial Bus (USB) will be in a near future the only interconnections available on PCs. Hence, by choosing the high-bandwidth IEEE-1394 serial bus, an home automation and/or health care network could be connected directly to any PCs without additional adapters. The integration of IEEE-1394 drivers

as part the PC operating systems will ease the implementation and compatibility issue of the proposed home automation network with unlimited access to information and services across the nation and around the world.

If the IEEE-1394 succeeds in the home automation and health care areas, then one of the fundamental requirements will be to provide an easy and low cost method to interconnect together these IEEE-1394 compatible devices throughout the home. A proposed solution is to have multiple special wall outlets providing the link between various types of devices and the IEEE-1394 network. A first implementation of such outlet is described briefly.

## **OVERVIEW OF THE IEEE-1394**

FireWire provides a direct digital link between up to 63 devices. The number of accessible devices within the same house can be expanded to 65535 if seemed necessary. The present implementation of IEEE-1394 can deliver 100 Mbps, 200 Mbps, or 400 Mbps of data payload and control signals. Future versions that support data rates exceeding 400 Mbps are under development. An important feature of FireWire is its isochronous data transmission mode that lets even the 100 Mbps implementation to support two simultaneous channels of full-motion (30-frames-per-second) video and CD-grade stereo audio. This is ideal for many applications including home security and entertainment. The actual maximum distance between two successive IEEE-1394 outlets is 4.5 meters. An advantage of this technology is its low cost. The IEEE-1394 technology uses a flexible, six-conductor cable and connectors derived from Nintendo's Gameboy to interconnect devices. Use of FireWire for consumer electronic gear, such as camcorders and VCRs, will provide the high-volume market needed to achieve low-cost implementation. Furthermore, FireWire extends

Plug and Play (PnP) features far beyond the confines of the PC. When you add or disconnect a device within the house or office, the network will automatically detect it and reconfigure itself without user's intervention.

## **IEEE-1394 OUTLET**

The proposed outlet implements the network's physical (PHY) layer. The three primary functions of the PHY layer are the transmission and reception of data bits, arbitration, and provision for the electrical as well as the mechanical interface. The block diagram of the outlet is shown in Fig. 1.

The new outlet represented in Fig. 1 has three IEEE-1394 connectors (C1, C2, and C3) and one optional link interface connector (LIC). Each connector has an associated line termination (LT) block for the signals. The LIC has also an optional galvanic isolation (GI) block to prevent excessive ground loop noises when several units are connected through the serial bus. The signals from C1, C2 and C3 are connected to respective cable ports (CP1, CP2, and CP3) to be handled by the received data decoder/re-timer (RxDD/R) and the transmitted data encoder (TxDE). If a link layer controller (LLC) located on a device connected to the LIC is detected through the LLC detector (LLCD), data would be exchanged through the link interface (LI) block. A 24.5760 MHz parallel resonant fundamental mode crystal (OSC) acts as the internal clocking source for the outlet. The crystal oscillator/phase-lock loop/clock generator (CO/PLL/CG) block derives from the OSC all additional synchronization signals required for the unit's proper operation. Bias voltage and current for the line termination blocks, are provided by the bias voltage and current generator (BVCG).

The power management (PM) block is responsible for voltage regulations and conversions for the unregulated IEEE-1394 cable power lines as well as providing filtered ground interconnections. A shield connection (SCH) block has the required circuitry to connect the IEEE-1394 cable's shield to the outlet's shielded box. The central operational control of the outlet at the network's physical layer is achieved with an "arbitration and control state machine logic" (ACSLML) block. More details on the outlet's functionality can be found in [1] and [2].

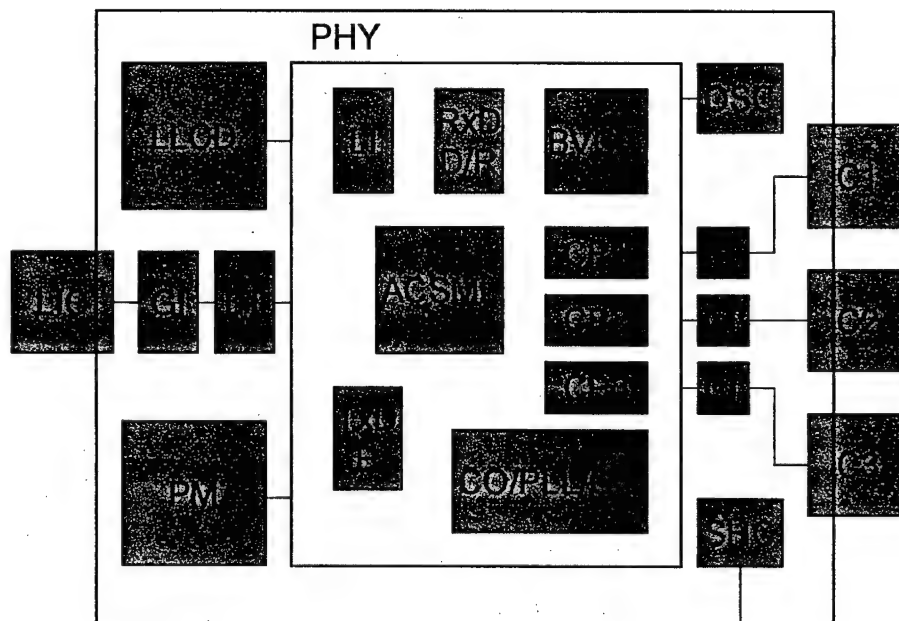


**Figure 1.** Block diagram of the HANET IEEE-1394 outlet.

## IMPLEMENTATION

The present implementation was designed for research and a much simplified and lower cost unit better suited for the commercial market but with less flexibility can be derived easily from this model. By depopulating the unit, several versions can be implemented. The physical model can also be altered. One commercial alternative would be to use a vertical version of C1, C2, and C3, with two connectors on one side of the PCB and one connector on the opposite side. The unit could be mounted on any sides depending if one or two ports (facing the internal wall) are used for networking, making the free port(s) available to the consumer. A photograph of the present outlet implementation is shown in Fig. 2. The size is  $76.2 \times 76.2$  mm (3.0  $\times$  3.0 inches) with height of 15.25 mm (0.6 inch).

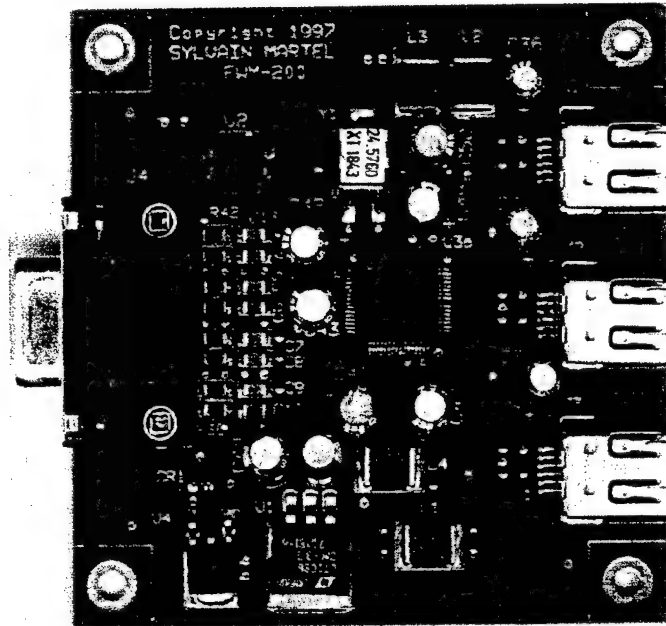


**Figure 2.** Photograph of the outlet's electronic circuit.

The size of the outlet can be reduced further. For instance, by eliminating the optional link layer connection; the LIC, GI with corresponding LT, as well as the LLCD could be eliminated from the block diagram depicted in Fig. 1 reducing the size of the PCB significantly. Furthermore, the electrolytic capacitors could be replaced by capacitors with lower vertical dimension, reducing the overall height of the outlet down to approximately 10.5 mm (0.4 inch). The present unit has 4 plated mounting holes as shown in Fig. 2 which can be used for mounting the unit, attaching a shielded box and providing shielding connection between the outlet's shield and the IEEE-1394 cable shield through the SHC block.

The present unit is referred to as "FWM-200" which stands for FireWire Module running at 200 Mb/s (196.608 Mb/s). The unit could be easily upgraded to the "FWM-400" (393.216 Mb/s). The PHY block for the FWM-200 as depicted in Fig. 1 has been implemented with the TSB21LV03 triple-cable transceiver/arbiter [2] also shown in the middle of the outlet in Fig. 2. Also as depicted in Fig. 2, the crystal oscillator is next to the TSB21LV03 to minimize EMI. To minimize the effect of potential EMI and other switching noises such as cross-talk and ground bounces, the FWM-200 has also several ferrite beads with high impedance above DC distributed throughout the various grounds and power lines as well as ceramic capacitors and low ESR electrolytic capacitors. We designed the unit for worst case scenarios since no exact data of the anticipated noise level were available prior to the implementation. Based on our measurements, the unit could be further simplified by removing some of the beads and de-coupling capacitors and using other part numbers having smaller physical dimensions including the possibility of replacing the electrolytic by tantalum capacitors with potentially higher ESR.

The outlet does not need batteries or transformers since it is entirely powered by the IEEE-1394 cables. Part of the PM has two voltage regulators for +5 VDC output (78M05CDT) and +3.3 VDC output (LT1086CM-3.3). The 5 VDC output is protected against large voltage fluctuations by a SOT-23 5.6V zener diode. The unregulated 12 VDC of the IEEE-1394 cable is connected to the input of the 78M05. A tiny surface-printed jumper allows the input of the LT1086 to be connected directly to the unregulated 12 VDC or to the 5 VDC generated by the 78M05 which is possible considering the low drop out of the LT1086. The advantage of the last scheme is a reduction of the LT1086 power dissipation. This configuration allowed us more flexibility for experimentation and testing. Future versions of the outlet could be easily simplified with the use of only one voltage regulator. The PM block also includes a power-reset circuit to initialize the outlet's PHY layer properly after connecting the first IEEE-1394 cable on any of the three available connectors.

The LLCD block consists of resistors and an optocoupler (TIL191A) for isolation purpose. The LLCD can detect the presence of a LLC through a reserved connection on the LIC providing the link power status (LPS). Monitoring the LPS can be achieved by sensing the LLC power line or a pulsed signal between 200 kHz and 5.5 MHz present when the LLC is powered. To minimize EMI from high-frequency signals passing through inductive connections on the LIC, the LLC power line was selected as indicator for the FWM. Because of the DC component, this choice forced us to use an optocoupler instead of a transformer or a capacitor to provide isolation within the LLCD. The isolated output of the LLCD depending on the LPS then selects one of the two modes of operation of the PHY layer namely, LLC support or repeater mode [3].

The present unit implements the PHY-LLC interface isolation shown as GI in Fig. 1 (and next to the LIC in Fig. 2), using the capacitive-isolation circuitry as mentioned in Annex J of the IEEE 1394-1995 Standard. Several 1206-type jumpers can replace the isolation capacitors when isolation is not required. When doing so, a signal available on the FWM is set internally to force the LI to disable the internal differentiating logic. Other types of implementations of the GI block as described in [4] for instance can also be implemented in future versions.

The LT block for the LIC consists simply of several pull-up and pull-down resistors. The LT blocks associated with C1, C2, and C3 provides an external  $112 \Omega$  line-termination through pairs of  $56 \Omega$  resistors for each twisted-pair cable required for drivers operating in high-impedance current mode. The terminals are also coupled to ground through RC networks with values chosen to meet the IEEE-1394 draft specifications.

The PCB layout [5] was also performed to minimize transmission line effects, differential and common noise interference and antenna effects. As such, the etch length between the PHY and C1, C2, and C3 had to be minimized with a maximum distance depending upon the edge rates, the propagation time, and the matching impedance provided by the three LT blocks depicted in Fig. 1. With a simpler implementation without matching impedance, a rule of thumb from Texas Instruments specifies a maximum etch length " $L_e < (T_r \bullet (c / e_r^{1/2})) / 6$ " where  $T_r$  is the signal's rise time,  $c$  is the speed of light ( $2.997 \times 10^8$  m/s), and  $e_r$  is the PCB's dielectric constant. From the recent 1394a specifications limiting the minimum rise time to 0.5 ns and considering FR-4 maximum dielectric constant of 5.3, we have  $L_e < 1.0$  cm (0.4 inch). This specification has been met between PHY and C2 but could not be realized with C1 and C3. Practically, a maximum  $L_e =$

2.0 cm (0.8 inch) as in the present implementation would be more acceptable for the PCB layout, providing adequate distances between C1, C2, and C3. As such, the dielectric constant of the PCB needed to be at most  $\epsilon_r < (c T_r) / (6 L_e)^2 < 1.5625$  which is practically not possible to achieve at low cost. Even a minimum FR-4 dielectric constant of 4.0, only extends the maximum PCB trace by an extra 0.25 cm. Therefore, the three LT blocks were implemented to fulfill the 1394a specifications. Furthermore, the trace's length of twisted pair was matched as closed as possible and run in parallel. To do so, the LT blocks were implemented on the opposite side of the PCB at the expense of one via implemented per signal since C1, C2, and C3 were surface mounted. The clearance size around each via was increased slightly to minimize capacitance. Through hole connectors could have eliminated the need for via but were not selected because of significant inductance created by the pin-through holes.

The traces on the PHY-LLC interface were maintained as short as possible to minimize coupling and signal losses with equal length to minimize propagation delay mismatch. The present implementation uses a shielded D-type subminiature DB15 connector (LIC). The LPS, PHY-LLC transmission synchronization clock, and link request signals use one terminal each. The control signals uses two terminals, four terminals are reserved for half-duplex data transfers while the remainder pins are used for the unregulated PHY-12 VDC and the LLC isolated ground. All but the LPS, power and ground passes through the GI block. The ground is connected to the PM block through  $1 M\Omega \parallel 0.1 \mu F (10^6 \Omega / (0.1 jw + 1))$  where  $w = 2\pi$  freq.). The maximum frequency derived from the CO/PLL/CG block and passing through the LIC is 49.152 MHz (independent of the IEEE-1394 transmission rate). Although at such transmission rate, the measured signal characteristics were quite satisfactory providing a full working unit, we are aware that more

studies need to be conducted to select the most appropriate connector and pin-out configuration for the PHY-LLC link. As an example, two additional terminals dedicated to data transfer would be required to support the 400 Mb/s transmission rate on the IEEE-1394 cable. Furthermore, three additional connections could be assigned for the power class indicators and one more for power down feature instead of the actual jumper settings on the FWM.

## INSTALLATION

The outlet is targeted for the cable environment as described in the IEEE Std. 1394-1995. As such, any physical topologies can be created provided that the resulting network is non-cyclic (no closed loops) with finite branches and extent. The FWM is a module and a node as defined in the IEEE Std. 1394-1995. A module is defined as a physical packaging concept and a node as a logical entity with a unique address. Each module consists of one or more nodes. In the present implementation, each module has only one node. When nothing is connected to the LIC, the module is the outlet itself. When another circuit with a LLC is connected to the LIC, then the new circuit and the FWM combined becomes one module independently of the architecture, units or logical entities (as defined in the IEEE Std. 1394-1995), and functionality of the new circuit. This new module built from an outlet will be designated here as an extended module. An extended module has one node or single address supported by the outlet. We will refer as a functional module a module where both the PHY and the LLC are embedded together and cannot be separated. This is the case of typical IEEE-1394 commercial products.

Although the number of nodes can be expanded through several bridges, up to 63 nodes can be installed per serial bus. Since the outlet is a node, then up to 63 outlets can be interconnected per

serial bus. Although implementing an extended module will have no impact on the maximum number of outlets, each functional module will implement an additional node and therefore, reduce the maximum number of outlets that can be installed. This is the price to pay for increase flexibility. Hence, the maximum number of outlets will depend on the number of ports among the outlets available to connect the functional modules.

An outlet can either be a branch (more than one connected ports), or a leaf (only one connections) as defined in the IEEE Std. 1394-1995 where the number of connections or IEEE-1394 ports initially used for networking will vary among outlets. A leaf outlet (one at the end of a branch) can connect two additional functional modules. When doing so, the outlet becomes a branch. Because interconnections between outlets are somewhat permanent, whereas functional modules' connections are not, we use the term leaf and branch outlets assuming that no functional modules are initially plugged to the serial bus. Therefore, each leaf outlet will reduce by two the maximum number of outlets per serial bus. If we define outlets with two or three initial IEEE-1394 connections as branch-2/3 (2 ports out of 3 used for networking) and branch-3/3 outlets, than each branch-2/3 outlet will reduce the maximum number of outlets by one. The branch-3/3 outlet will have no impact on the maximum number of outlets but will not provide any connections for the functional modules. In summary, the maximum number of outlets per serial bus is  $N = 63 - 2 \cdot N_{LEAF} - N_{BRANH2/3}$  where  $N_{LEAF}$  and  $N_{BRANH2/3}$  are the number of leaf and branch-2/3 outlets in the same serial bus. The cable medium also limits the number of physical connections or cable hops (length of 4.5 meters each) to 16, giving a total cable distance of 72 meters between any two devices. Hence, we know that in a configuration with a maximum number of outlets, at least 4 will

be leaf, already reducing the number of outlets by at least 8 unless the number of available ports per leaf outlet is reduced.

As shown, installing an IEEE-1394 based network will have an impact on the number of IEEE-1394 ports available for the user. Improving the availability of the number of such connectors will have an impact on the number of outlets that can be interconnected, making the installation more difficult. Therefore, the installation and interconnection between the outlets is a trade-off between accessibility among distant sites and number of IEEE-1394 ports available to the user. More importantly, reducing the number of IEEE-1394 ports available will restrict the added networked functionality provided by the functional modules.

With the present version of the outlet, maximum functionality independent on the above factors can be maintained with our concept of expansion modules. Since connecting an LLC-based circuit to the LIC will maintain unchanged the number of nodes in the network, up to N expansion modules per serial bus can be added to the number of possible functional modules. The only drawback is that unlike functional modules that can be installed up to 4.5 meters from an outlet, the expansion module must be tightly connected with short terminals to the respective outlet.

## **SUMMARY**

The implementation of an outlet intended to connect any IEEE-1394 devices to a home/health care network has been briefly described. This fully functional unit can be used as a reference for future versions.

## REFERENCES

- [1] IEEE Std 1394-1995, *IEEE*, 372 pages, 1996.
- [2] "TSB21LV03 IEEE 1394-1995 triple-cable transceiver/arbiter". Data Sheets, Texas Instruments Inc., 23 pages, 1996.
- [3] R. Raybarman and B. Henehan. "Configuring the TI 400 Mbit PHY as a 1394 Repeater Node". Application Brief SLLA016A, Texas Instruments Inc., 15 pages, 1998.
- [4] B. Henehan, D. Yaklin, B. Gugel, and J. Akgul. "Galvanic Isolation of the IEEE 1394-1995 Serial Bus". Application Report SLLA011, Texas Instruments Inc., 30 pages, 1997.
- [5] R. Raybarman and B. Henehan. "PHY Layout". Application Report SLLA020, Texas Instruments Inc., 17 pages, 1997.

# Energy Efficient Codes for Wireless Communications

## Source Coding Theory and Error Control

H. Harry Asada  
Principal investigator

Kai-Yeung Siu  
Co-investigator

Cem Erin  
Graduate Research Assistant

### **Abstract**

Source coding and error control coding algorithms minimizing the battery power needed for RF transmission are presented. Digital RF transmitters in portable devices consume energy only when high bits are sent and virtually no energy is consumed when low bits are sent. Therefore, energy consumption can be minimized by devising codes that minimize the occurrence of high bits in transmitting information. In this report, we first formulate the minimum energy coding problem for RF transmission. Next, we derive the optimal memoryless and noiseless coding algorithm from the source statistics. Then, we improve the memoryless and noiseless coding performance via a simple memory mechanism. We continue by formulating the energy efficient and reliable information transmission problem. We propose various linear block codes for energy efficient information transmission over noisy channels. Overall, we take a first step towards a novel energy saving wireless communication protocol.

# Table of Contents

<b>1</b>	<b>Introduction</b>	<b>4</b>
<b>2</b>	<b>RF Transmitter Power Consumption</b>	<b>5</b>
<b>3</b>	<b>Energy Efficient Source Coding</b>	<b>7</b>
3.1	Memoryless ME Coding . . . . .	7
3.1.1	ME Coding . . . . .	7
3.1.2	Fixed-Length ME Coding . . . . .	8
3.1.3	Optimality Bound to ME Coding . . . . .	9
3.2	ME Coding with Memory . . . . .	11
3.2.1	Extension and Concatenation . . . . .	11
3.2.2	Mechanisms of Concatenation for Improving Energy Efficiency . . . . .	12
3.2.3	Concatenation Theory . . . . .	16
<b>4</b>	<b>Energy Efficient Error Correction</b>	<b>20</b>
4.1	Setting the Scene . . . . .	20
4.1.1	The Channel . . . . .	20
4.1.2	The Decoder and Error Probability . . . . .	22
4.1.3	The Main Energy Efficient Error Correction Problem . . . . .	25
4.2	Energy Efficient Linear Codes . . . . .	27
4.2.1	Minimum Energy Hamming Codes . . . . .	27
4.2.2	Minimum Energy Golay Codes . . . . .	30
4.2.3	Minimum Energy Reed-Muller Codes . . . . .	33
<b>5</b>	<b>Major Findings and Conclusions</b>	<b>36</b>

## List of Figures

1	Digital RF Transmitter . . . . .	5
2	Direct Concatenation. (a) ME Coding, (b) Direct Concatenation. . . . .	12
3	Concatenation Mechanism . . . . .	13
4	Generating Direct Concatenation (Probabilities in Percentages) . . . . .	14
5	Codebook Optimization for Direct Concatenation (Probabilities in Percentages)	15
6	Coding Optimization for Direct Concatenation (Probabilities in Percentages)	16
7	Concatenation Improvement Conditions on Codebook Parameters . . . . .	18
8	Relations among different concatenation orders: $\bar{n}_{ME}^P/p$ decreases in the direction of arrows . . . . .	18
9	Block Diagram of a Communications System . . . . .	20
10	Discrete Memoryless Channel . . . . .	21
11	Binary Symmetric Channel . . . . .	22
12	Decoder . . . . .	23
13	The Main Energy Efficient Error Correction Problem . . . . .	25
14	Single Error Correcting Hamming Codes . . . . .	27
15	Single Error Correcting and Double Error Detecting Hamming Codes . . . . .	29

# 1 Introduction

Wireless networking is enjoying its fastest growth period in history, due to the enabling technologies that permit wide-spread deployment [1]. However, this growth is still limited due to the limited battery power at the portable terminals. Since the progress in battery technology is rather slow to meet the rapidly increasing application demands, new technology for energy efficient wireless communication must be created [2-5].

In an attempt to devise new technology for energy efficient wireless communication, we optimize the power consumption in digital RF transmitters. Digital RF transmitters constitute the major power consuming component in many portable communication devices. Current efforts on transmitter power optimization aim to minimize the transmitted power while satisfying some quality of service constraints. These efforts aim to achieve optimal transmitter performance via transmitter power level adaptation [6], error control strategy adaptation [2, 7], or a combination of the two [8] for varying channel conditions. While these efforts are of considerable value, they do not provide the ultimate optimal performance. In this report, we propose a formulation of the energy efficient RF transmission problem, solution of which can be combined with the previous efforts to yield the ultimate optimal performance. In an attempt to solve this problem, this report aims to find special codes that minimize power consumption in RF transmission.

In this report, we will

1. develop a novel source coding algorithm extending battery life in portable communication devices,
2. present the extensions of this source coding algorithm for improved battery life,
3. describe linear block codes for energy efficient error correction.

The outline of this report is as follows. Section 2 introduces RF transmitters and formulates the power consumption problem in RF transmission. Section 3.1 describes the Memoryless ME Coding algorithm, proves its optimality, and proposes a bound on optimal performance. Memory utilization, which improves memoryless coding performance, is discussed in Section 3.2. Section 4.1 introduces the problem of energy efficient error correction. Linear block codes for energy efficient error recovery are discussed in Section 4.2. The report closes with some conclusions in Section 5.

## 2 RF Transmitter Power Consumption

In this section, we formulate the power consumption optimization problem for digital RF transmitters. Digital RF transmitters modulate the information to be communicated onto a carrier waveform, amplify the waveform to the desired power level, and deliver it to the transmitting antenna [9]. Many digital transmitter components are similar with the major power consuming component being the oscillator. The oscillator is the circuitry responsible for the modulation of the message signal (i.e., the bit stream of encoded data) onto the transmitted waveform.

An attempt to formulate the power consumption optimization problem requires understanding the oscillator operation. Oscillators are actuated upon the receipt of high bits only (see Figure 1); hence, power consumption in the transmitter occurs only when high bits are sent and virtually no power is consumed when low bits are sent. Each bit period  $t_b$

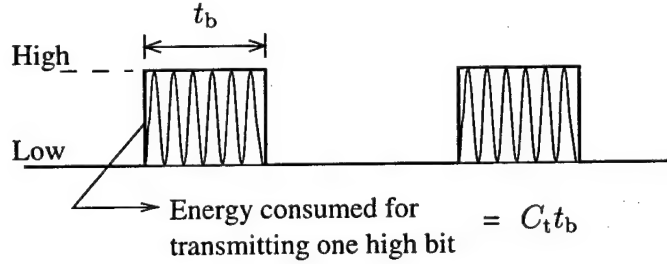


Figure 1: Digital RF Transmitter

is assigned a minimum detectable value that is determined from the channel characteristics. Since this period is much longer than the oscillator period (a factor of nearly  $10^6$ ), the transient period when the oscillator begins to oscillate is negligible in evaluating the power consumption. Therefore, the total energy consumed in the RF transmitter in one second,  $E_{\text{total}}$ , is proportional to the total duration of high bits, namely, the total number of high bits,  $n_{\text{total}}$ , times the bit period  $t_b$ :

$$E_{\text{total}} = C_t t_b n_{\text{total}}, \quad (1)$$

where  $C_t$  is the power consumption coefficient. Let  $M$  be the number of symbols transmitted in one second and  $\bar{n}$  be the average number of high bits involved in each codeword. The average power consumption per symbol,  $\bar{C}$ , is therefore given by

$$\bar{C} = \frac{E_{\text{total}}}{M} = C_t t_b \bar{n}. \quad (2)$$

Equation (2) suggests several ways of optimizing power consumption. Power consumption can be optimized by (i) improving the transmitter circuitry to minimize  $C_t$ , (ii) minimizing

$t_b$ , and (iii) minimizing  $\bar{n}$ . The first two are determined by the physical conditions of the transmitter and the channel, and require modifications to the physical layer. The third one, on the other hand, is a non-physical factor, which would allow us to further enhance energy efficiency beyond the physical limit. The average number of high bits per codeword,  $\bar{n}$ , is determined by the source symbol probabilities and the number of high bits in each codeword:

$$\bar{n} = \sum_{i=1}^q P_i n_i, \quad (3)$$

where  $q$  is the number of source symbols,  $n_i$  is the number of high bits in the  $i$ -th codeword, and  $P_i$  is the probability of the  $i$ -th symbol. *The objective of this report is to reduce this average high bit number,  $\bar{n}$ .* Next, we introduce Memoryless ME Coding, a novel source coding algorithm optimizing power consumption in RF transmission.

### 3 Energy Efficient Source Coding

#### 3.1 Memoryless ME Coding

##### 3.1.1 ME Coding

ME Coding is a source coding algorithm that aims to optimize the energy efficiency in RF transmission by minimizing the average number of high bits used in coding the information source. ME Coding is generated through two distinct steps: Codebook Optimality and Coding Optimality. The former is to determine a set of codewords, termed a codebook, that has fewest high bits, and the latter is to assign codewords having less high bits to symbols with higher probability. The following two theorems underpin the theory of ME Coding.

**Theorem 1: Coding Optimality.** *Let  $S = \{s_1, s_2, \dots, s_{q-1}, s_q\}$  be a source alphabet with symbol probabilities*

$$P = \{P_1 \geq P_2 \geq \dots \geq P_{q-1} \geq P_q\}. \quad (4)$$

*Given a codebook of  $q$  codewords, each of which contains  $n_i$  high bits,  $1 \leq i \leq q$ , the optimal code that minimizes the average number of high bits  $\bar{n} = \sum_{i=1}^q n_i P_i$  is given by assigning the codewords to symbols such that*

$$n_1 \leq n_2 \leq \dots \leq n_{q-1} \leq n_q. \quad (5)$$

*In this optimal coding, all the codewords are arranged in the ascending order of the number of high bits involved in each codeword, and the symbols are assigned to these codewords in the descending order of symbol probabilities. This coding algorithm provides optimal codes for a given codebook with respect to power consumption.*

*Proof.* See Appendix.

Let  $W$  be a codebook of  $q$  codewords arranged in the ascending number of high bits involved in each codeword. The code  $C(W, S)$  assigns the  $q$  codewords in codebook  $W$  to  $q$  symbols in source  $S$  in such a manner that equations (4) and (5) determine the minimum  $\bar{n}$  for the given  $W$ . Hence, the minimum of  $\bar{n}$  varies depending on properties of the codebook used. The remaining question is how to obtain a codebook that provides the overall minimum of  $\bar{n}$ . Let  $W_o = \{w_1, w_2, \dots, w_i, \dots, w_{q_o-1}, w_{q_o}\}$  be the entire set of codewords that are usable for ME Coding;  $q \leq q_o < +\infty$ . We first number each codeword in the ascending number of high bits involved in it, namely,  $n_1 \leq n_2 \leq \dots \leq n_i \leq \dots \leq n_{q_o-1} \leq n_{q_o}$ , where  $n_i$  is the number of high bits in codeword  $w_i$ . Then, we generate the codebook used for ME Coding by taking the first  $q$  codewords having the least high bits.

**Definition: Minimum Codebook.** Let the codewords of the whole codeword set  $W_o = \{w_1, w_2, \dots, w_q, \dots, w_{q_o}\}$  be numbered in the ascending number of high bits involved

in each codeword,  $n_1 \leq n_2 \leq \dots \leq n_q \leq \dots \leq n_{q_0}$ . A minimum codebook of  $q$  codewords,  $W_{\min}$ , consists of the first  $q$  codewords of the whole codeword set  $W_0$

$$W_{\min} = \{w_1, w_2, \dots, w_{q-1}, w_q\} \subset W_0 \quad (6)$$

It can be noticed in the previous example that the overall minimum energy coding cannot be obtained unless the above minimum codebook is used.

**Theorem 2: Codebook Optimality.** *Let  $S$  be a  $q$ -symbol source with symbol probabilities  $P = \{P_1 \geq P_2 \geq \dots \geq P_{q-1} \geq P_q\}$  and  $W$  be a codebook of  $q$ -codewords taken from the usable codewords set  $W_0 = \{w_1, w_2, \dots, w_{q_0-1}, w_{q_0}\}$ ,  $q \leq q_0 < +\infty$ ;  $W \subset W_0$ . The necessary condition for a code  $C(W, S)$  to provide the minimum average number of high bits  $\bar{n} = \sum_{i=1}^q n_i P_i$  is that the codebook  $W$  is a minimum codebook of  $W_0$ .*

*Proof.* See Appendix.

Combining Theorems 1 and 2, the following Corollary is easily obtained.

**Corollary 1: ME Coding.** *Let  $S$  be a  $q$ -symbol source with symbol probabilities  $P = \{P_1 \geq P_2 \geq \dots \geq P_{q-1} \geq P_q\}$ , and  $W_0 = \{w_1, w_2, \dots, w_q, \dots, w_{q_0}\}$  be the entire set of usable codewords,  $q \leq q_0$ . The optimal code  $C(W, S)$  that minimizes the average number of high bits  $\bar{n} = \sum_{i=1}^q n_i P_i$  where  $n_i$  is the number of high bits involved in the codeword  $w_i$ , is given by*

- (i) *Using the minimum codebook  $W_{\min}$  of  $W_0$  for the codebook;  $W = W_{\min} \subset W_0$ , and*
- (ii) *Assigning the  $q$  codewords of  $W_{\min}$  in the ascending order of number of high bits to the  $q$ -symbols of the descending order of source probabilities.*

*This optimal coding is referred to as ME Coding.*

Consider a special case where  $P_1 = P_2 = \dots = P_{q-1} = P_q$ . The average number of high bits in this case equals the total number of high bits in the codebook divided by  $q$ . Therefore, the following Corollary holds.

**Corollary 2.** A minimum codebook contains the minimum number of high bits;  $\min_{W_0} \sum_{i=1}^q n_i$ .

### 3.1.2 Fixed-Length ME Coding

Of practical importance is ME Coding with fixed-length codewords. As shown by Theorem 2 and Corollary 1, use of a minimum codebook is the necessary condition for obtaining ME Coding. Thus, we must first generate a minimum codebook. For  $L$ -bit fixed-length codewords, Table 1 shows the entire set of usable codewords sorted by the number of high bits;  $W_0 = \{w_1, \dots, w_{q_0}\}$ . Note that the total number of usable codewords is  $q_0 = 2^L$ . The first column has only  $\binom{L}{0} = 1$  codeword with zero high bit, the second column has  $\binom{L}{1} = L$  codewords with one high bit, the third column has  $\binom{L}{2}$  codewords containing two high

Table 1:  $L$ -bit Codewords

Codeword	$w_1$	$w_2 - w_{L+1}$	$w_{L+2} \dots$			$\dots w_q$	$w_{2L}$
Number of Codewords	$\binom{L}{0}$	$\binom{L}{1}$	$\binom{L}{2}$		$\binom{L}{a}$	$\binom{L}{L-1}$	$\binom{L}{L}$
Codeword Pattern							
Symbol	$s_1$	$s_2$	$\dots$		$a=L-2$	$\dots s_q$	

bits and so on. All the codewords are numbered 1 through  $2^L$  in the ascending order of the number of high bits. The last codeword,  $w_{2L}$  consists of all high bits. Selecting the first  $q$  codewords from this exhaustive list of  $2^L$  codewords yields the minimum codebook needed for ME Coding.

It is clear from Table 1 that, as the codeword length  $L$  becomes longer, the total number of high bits involved in the first  $q$  codewords becomes smaller. An extreme case is the *unary coding*, where  $L$  is long enough to express all  $q$  symbols with only one high bit per codeword, e.g., 00010000. Since a longer codeword takes a longer transmission time if the bit period  $t_b$  is kept constant, transmission rate decreases. Hence, this constitutes the trade-off between energy efficiency and transmission rate.

### 3.1.3 Optimality Bound to ME Coding

In Sections 3.1 and 3.2, we proved the optimality of ME Coding and introduced fixed-length ME Coding. Since a closed form solution for the optimal performance of fixed-length ME Coding is not available, we derive the following optimality bound

$$\frac{k^{(H_k - \bar{n})}}{B_k} \leq 1, \quad (7)$$

where  $H_k$  is the source entropy and  $B_k$  is the codebook capacity defined as

$$B_k = \sum_{i=1}^q k^{-n_i}. \quad (8)$$

where  $k$  is an arbitrary constant greater than 1. The derivation of this bound is included in the Appendix.

Inequality (7) suggests that source entropy  $H_k$  and codebook capacity  $B_k$  provide a lower bound on the optimal energy performance. As the entropy  $H_k$  decreases and the codebook capacity  $B_k$  increases, the bound to average number of high bits becomes lower. For a codebook consisting of  $q$  codewords of fixed-length  $L$ , the maximum codebook capacity  $\text{Max}(B_k)$  can be obtained from Table 1. Namely, the minimum codebook consisting of the first  $q$  codewords in the table provides the maximum codebook capacity given by

$$\text{Max}(B_k) = \frac{1}{k^0} \binom{L}{0} + \frac{1}{k^1} \binom{L}{1} + \dots + \frac{1}{k^a} \binom{L}{a} + b \frac{1}{k^{a+1}}, \quad (9)$$

where  $a$  and  $b$  are positive integers shown in Table 1. In the  $(a+1)$ st column, the  $q$ -th codeword exists at the  $b$ -th position. In other words,  $q = \sum_{i=0}^a \binom{L}{i} + b$ . Note that any exchange of the first  $q$  codewords with the other  $(2^L - q)$  codewords decreases the value of codebook capacity unless exchanging codewords within the  $(a+1)$ st column. Note also that, as the codeword length  $L$  increases, maximum codebook capacity  $\text{Max}(B_k)$  tends to increase, hence a longer codeword tends to lower the average number of high bits and the energy consumption.

## 3.2 ME Coding with Memory

### 3.2.1 Extension and Concatenation

Section 3.1 introduced ME Coding as the optimal, memoryless source coding algorithm for energy-efficient RF transmission. Given this optimal memoryless coding algorithm, this section takes a step further and introduces a technique, termed *concatenation* or *extensions of ME Coding*, that improves the energy-efficiency of memoryless ME Coding by using a simple memory mechanism.

Concatenation is a source coding technique that is intended for improving the energy efficiency of ME Coding by encoding higher extensions of the source alphabet. Let  $S^1$  be a  $q$ -symbol source with known statistics  $P^1$ . The  $p$ -th extension of  $S^1$  is given by the  $q^p$ -symbol source  $S^p = \{s_{i_1} s_{i_2} \dots s_{i_p} \mid 1 \leq i_1 \leq q, \dots, 1 \leq i_p \leq q\}$  with a probability distribution  $P^p = \{Prob(s_{i_1} s_{i_2} \dots s_{i_p}) \mid 1 \leq i_1 \leq q, \dots, 1 \leq i_p \leq q\}$ . Accordingly, a codebook with  $q^p$  codewords  $W^p = \{w_1, w_2, \dots, w_{q^p-1}, w_{q^p}\}$  is needed for coding the  $p$ -th extension  $S^p$ .

For the sake of simplicity, this section assumes statistical independence among source symbols in performing the concatenation analysis, namely,  $Prob(s_{i_1} s_{i_2} \dots s_{i_p}) = P_{i_1} P_{i_2} \dots P_{i_p}$ . This is not only the simplest case to analyze, but also the worst case in terms of energy performance. If the symbols are not statistically independent, that is, if the mutual information between source symbols is not zero, then further energy efficiency improvement is possible. In what follows, a particular type of extension, termed concatenation, is explored.

**Definition: Concatenation.** Let  $S^1$  be a source with known statistics, coded into an  $L$ -bit fixed-length codebook  $W^1$ . The  $p$ -th concatenation of  $S^1$  and  $W^1$  is a source coding algorithm that encodes the  $p$ -th extension of the source alphabet,  $S^p$ , using a  $pL$ -bit fixed-length codebook,  $W^p$ .

Concatenation uses memory. One drawback of using memory is that it increases delay, which might be undesirable in some applications. Another issue is that concatenation becomes impractical as the concatenation order increases. Since the encoding is in the form of a look-up table, as the concatenation order increases, the source alphabet becomes very large resulting in impractical memory requirements and computational complexity.

A special case of concatenation is direct concatenation. As illustrated in Figure 2, a new codeword of length  $pL$  is created by directly concatenating the  $p$  codewords used in the original coding to form a single codeword of length  $pL$  ( $p=2$  in Figure 2). Note that the bit stream of this elongated codeword is exactly the same as the original bit stream. Direct concatenation results in codewords having a total number of high bits that is equal to the sum of the number of high bits in the original codewords. These newly formed codewords are assigned to symbols having probabilities that are multiplication of the original symbol probabilities (symbols are statistically independent). Higher-order direct concatenation of

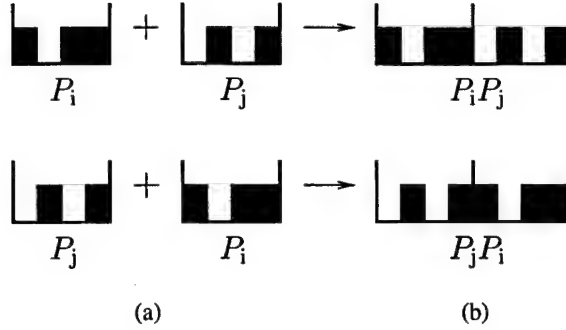


Figure 2: Direct Concatenation. (a) ME Coding, (b) Direct Concatenation.

fixed-length ME Coding is performed in a similar manner. Next, we will utilize direct concatenation to elucidate the performance improvement mechanism in concatenation.

### 3.2.2 Mechanisms of Concatenation for Improving Energy Efficiency

With an expanded codeword length and a new probability distribution, concatenation would further improve energy efficiency of ME Coding. In applying the ME Coding method, concatenation intertwines two separate mechanisms that would yield improved energy efficiency: (i) probability distribution alteration due to source extension from  $S^1$  to  $S^p$ , (ii) variation in the number of high bits due to codeword elongation from  $L$  to  $pL$ . These two mechanisms are illustrated in Figure 3. Figure 3-(a) demonstrates the original ME Coding, where the set on the left is the codeword set with the number of high bits shown, while the set on the right is the set of source symbols with the accompanying probabilities. Figure 3-(b) and (c) demonstrate source extension and codeword elongation, respectively. In Figure 3-(b), source extension is represented as the newly formed source symbols in the ellipses in the set  $PP1$ . In Figure 3-(c), codeword elongation is reflected as the newly formed codewords in the set  $C2$  with the corresponding number of high bits per codeword label attached to them. Notice that, originally, we had 4 symbols and 4 codewords in Figure 3-(a), and we ended up in 16 codewords and 16 symbols in Figure 3-(c). In this section, we will investigate these mechanisms and derive some insight as to how and when concatenation improves energy efficiency in ME Coding. We will use this insight to derive some theoretical results in Section 3.2.3,

Let us begin with direct concatenation introduced in the previous section. The energy efficiency of direct concatenation is exactly the same as the non-concatenated ME Coding, as will be formally proved in Section 3.2.3. This means that concatenation provides at least the same level of energy efficiency as non-concatenated ME Coding and would provide a better efficiency by modifying the direct concatenation case. Direct concatenation does not guarantee the codebook and coding optimality. A loss of optimality in either of the two

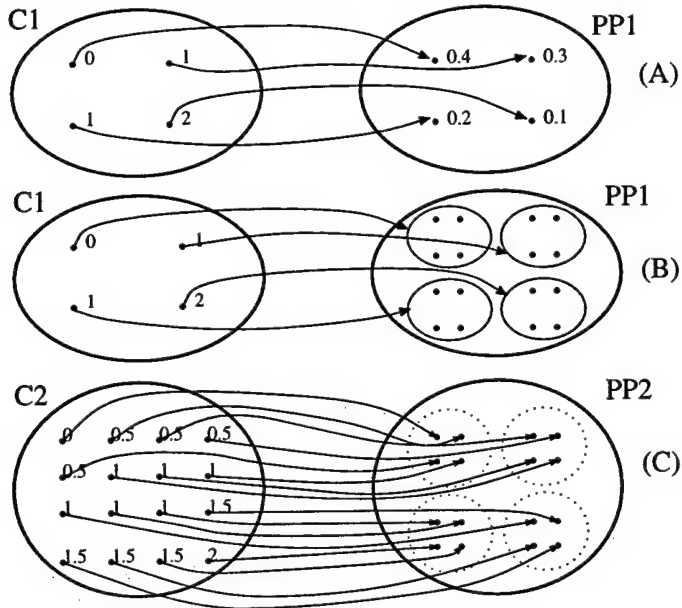


Figure 3: Concatenation Mechanism

will warrant an improvement in overall energy efficiency of the code. Hence, to understand the energy efficiency improvement with concatenation, the codebook optimality and coding optimality should be examined for direct concatenation.

In Section 3.1, Theorem 2 stated that codebook optimality is a necessary condition for overall code optimality. Hence, let us start by investigating the codebook optimality of direct concatenation. Codebook optimality is decoupled from coding optimality, since it is determined only from codeword length,  $pL$ , and number of symbols to code,  $q^p$ . Direct concatenation uses a particular type of codewords restricted to the repeated pattern of the original codewords. Although there are  $2^{pL}$  usable codewords, the codebook of direct concatenation uses only this restricted part of the usable codewords. As shown in the following numerical examples and theoretical analysis, there are some unused codewords having less high bits. The presence of such unused codewords having less high bits implies that the codebook of direct concatenation is not a minimum codebook, hence reduction in the average number of high bits is possible for the direct concatenation.

Coding optimality is determined by the mapping between the codewords and source symbols. In direct concatenation, the symbol-to-codeword assignment is predetermined, and is not necessarily an optimal one. Since the number of high bits in a concatenated codeword is the sum of the individual numbers of high bits of the original codewords, while the joint probability is the product of the individual probabilities, the ascending order of high bits may differ from the descending order of probabilities. Thus, the coding optimality must be

re-investigated. The following numerical examples illustrate this performance improvement mechanism through codebook and coding optimization.

Consider a source  $S^1$  of  $q = 6$  symbols having the probability distribution  $P^1 = \{45, 44, 5, 4, 1, 1\}$  in percentages. Let this source be coded using  $L = 3$  bit codewords according to the ME Coding algorithm. Figure 4-(a) shows the resulting ME Code. The

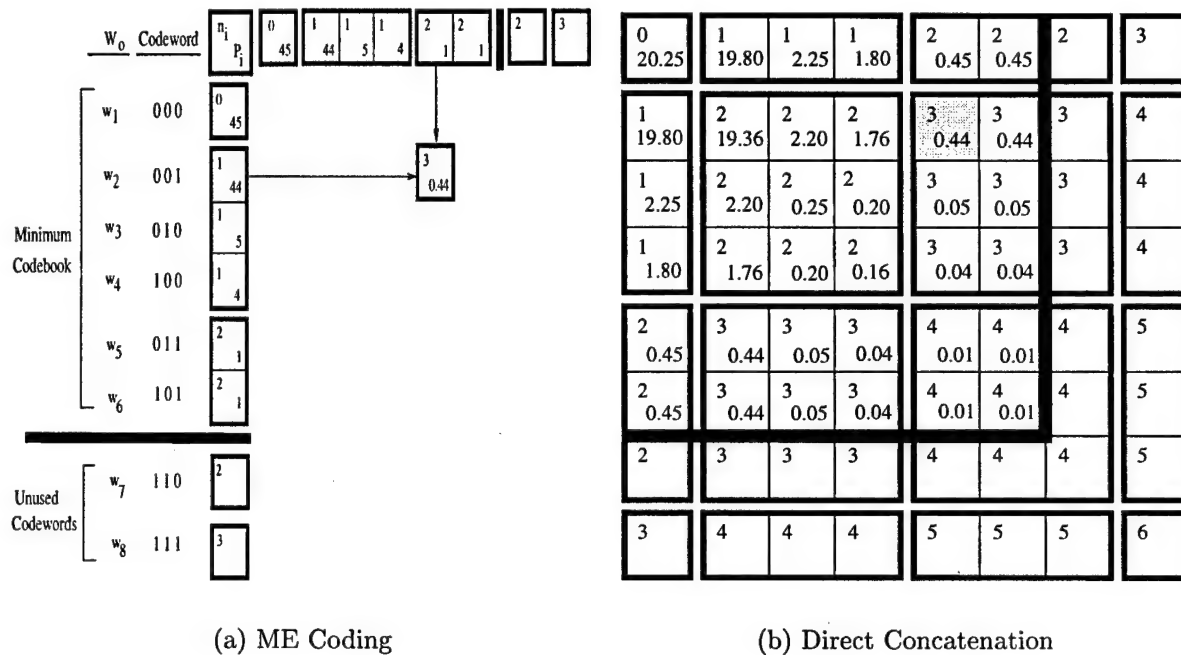


Figure 4: Generating Direct Concatenation (Probabilities in Percentages)

first column lists the entire usable codewords arranged in the ascending number of high bits. The first  $q = 6$  codewords form the minimum codebook, leaving two codewords  $w_7$  and  $w_8$  unused. The third column consisting of square blocks indicates the number of high bits  $n_i$  at the left top corner and the probability  $P_i$  in percentage at the bottom right corner. Note that the probabilities have been assigned in descending order from the top,  $w_1$ , to the bottom,  $w_6$ . Note also that the square blocks are grouped into rectangles in terms of the number of high bits, as shown by the thick lines in the figure.

The second order direct concatenation of this ME Code can be generated by arranging the same ME Code in a row and combining two codewords: one taken from the column and the other from the row, as shown in Figure 4-(a). For example, the shaded block in the figure is the concatenation of  $w_2$  from the column and  $w_5$  from the row having  $n_2 + n_5 = 1 + 2 = 3$  high bits and the probability of  $P_2 \times P_5 = 0.44 \times 0.01 = 0.0044$ . Repeating this process for the entire pairs of the column and row codewords yields the complete direct concatenation of the original ME Coding. As indicated by the thickest solid line in Figure 4-(b), 36 codewords

arranged in a 6-by-6 matrix are obtained. In the following two steps, we investigate the codebook and coding optimality of direct concatenation for this given example. Showing that direct concatenation does not necessarily result in an optimal codebook or coding, we re-optimize the codebook and coding, thereby demonstrating the performance improvement mechanism.

**Step 1: Codebook Optimization.** For a code  $C(W, S)$  to be optimal, the necessary condition is that the codebook  $W$  is a minimum codebook (Theorem 2, Section 3.1). Hence, we check if the direct concatenation codebook is a minimum codebook. Elimination of the probabilities from Figure 4-(b) results in Figure 5-(a), which illustrates the set of available codewords and the codebook for direct concatenation of fixed-length ME Coding. The

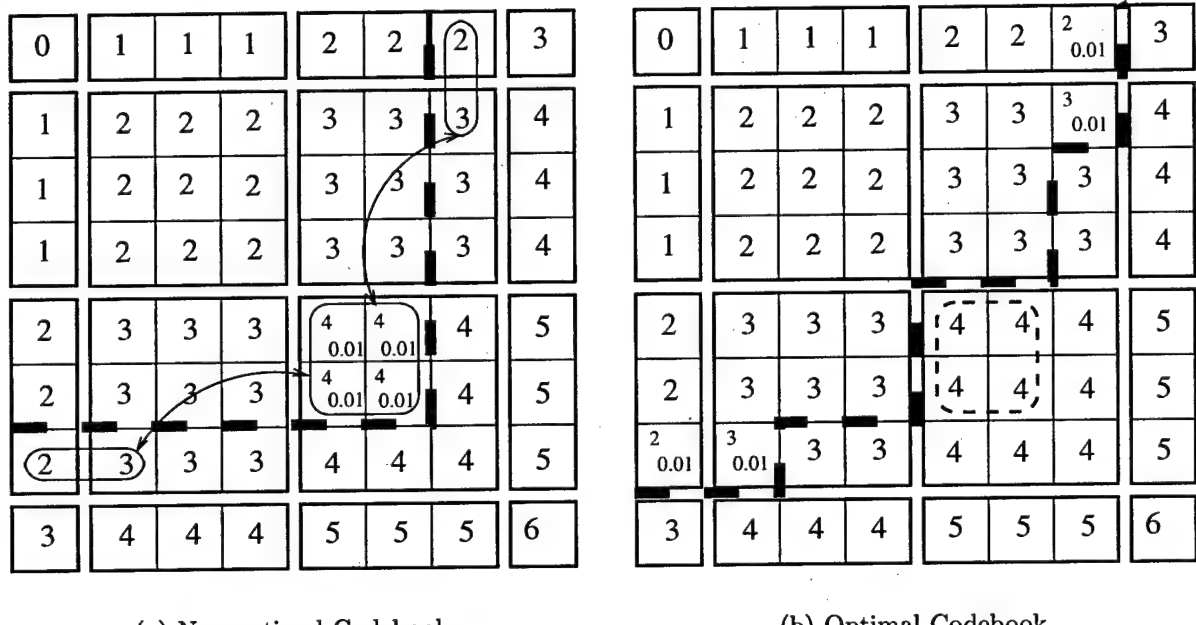


Figure 5: Codebook Optimization for Direct Concatenation (Probabilities in Percentages)

codebook for direct concatenation is represented by the 6-by-6 matrix enclosed by the thick dashed line. In this figure, it is seen that direct concatenation uses codewords having a maximum of 4 high bits marked by a round edged square, while the set of unused codewords contains codewords with  $\{2, 2, 3, 3\}$  high bits as marked by the two ellipses. Hence, the codebook is not optimal, since the total number of high bits in the codebook can be reduced. Thus, these unused codewords having less high bits should replace the ones with more high bits to reduce the average number of high bits per source symbol. This results in the minimum codebook shown in Figure 5-(b). As seen in this figure, symbols originally assigned to 4 high bit codewords (i.e.,  $P=0.01$ ) move to the newly available codewords

having  $\{2, 2, 3, 3\}$ . Note, however, that the global code optimality is not guaranteed until the symbol-to-codeword assignment is optimized.

**Step 2: Coding Optimization.** The optimal coding proven in Theorem 1 is now applied to the minimum codebook. A code is not optimal, if there exists two symbol-to-codeword assignments  $(P_i, n_i)$  and  $(P_j, n_j)$ , such that  $P_i > P_j$  and  $n_i > n_j$ . Hence, the mappings exhibiting the non-optimality condition (marked by ellipses in Figure 6-(a)) are swapped. For example, the symbol having a probability of 19.36% was originally assigned

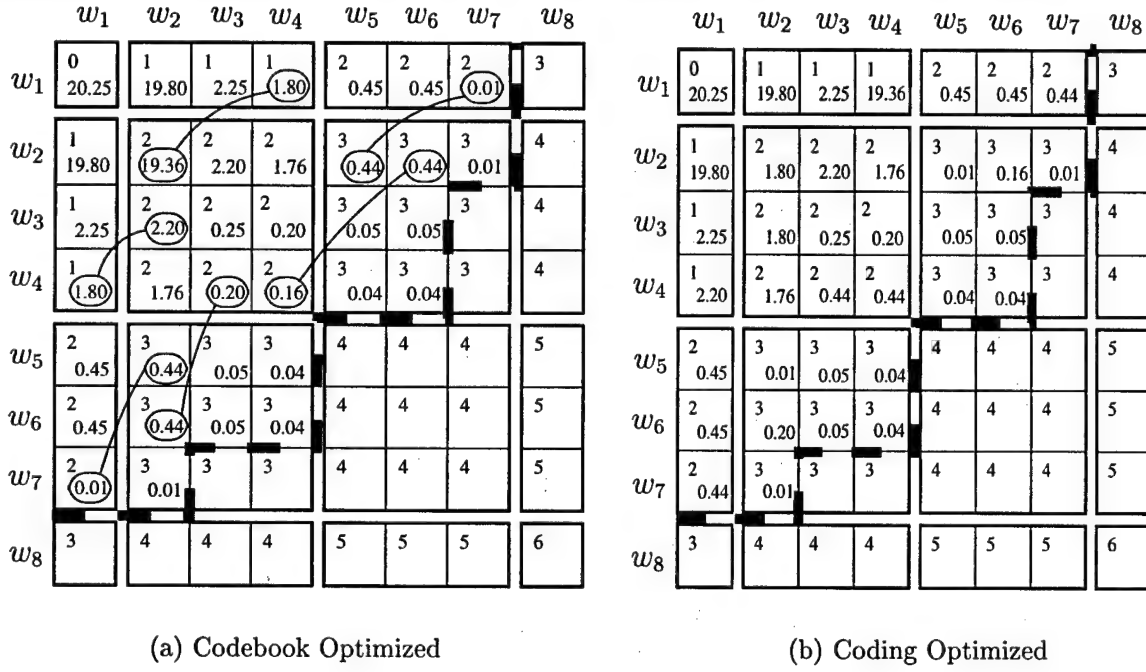


Figure 6: Coding Optimization for Direct Concatenation (Probabilities in Percentages)

to a 2 high bit codeword in the minimal codebook ( $w_2 - w_2$  codeword), while a symbol having a probability of 1.80% was assigned to a 1 high bit codeword ( $w_1 - w_4$  codeword). Thus, the two symbols are swapped in Figure 6-(b) to reduce the average number of high bits per source symbol. Swapping is continued until the non-optimality condition does not hold between any pairs of mappings. The resulting optimal code, i.e., ME Code, is shown in Figure 6-(b).

### 3.2.3 Concatenation Theory

In this section, we present some theoretical results concerning analysis of concatenation mechanism. We first prove that direct concatenation yields an energy performance that is identical to the Memoryless ME Coding performance. Then, we show that concatenation

always improves memoryless ME Coding performance, given some conditions on the codebook parameters. Next, using a counterexample, we show that this improvement is not a monotonically increasing function of concatenation order. Finally, we extend the ME Coding optimality bound to concatenations.

**Theorem 3: Direct Concatenation.** *Let  $S^1$  be a  $q$ -symbol source with statistically independent symbol probabilities  $P^1 = \{P_1, \dots, P_q\}$ ,  $W^1$  be a codebook having the set of number of high bits  $N^1 = \{n_1, \dots, n_q\}$ , and  $C^1(W^1, S^1)$  be a code representing the  $q$  symbols in  $S^1$  by the  $q$  individual codewords in  $W^1$ . Furthermore, let  $S^p$ ,  $W^p$ , and  $C^p(W^p, S^p)$  be the source, the codebook, and the code associated with the  $p$ -th extension of the original source and codebook. There exists at least one code, whose average number of high bits per symbol  $\bar{n}^p/p$  is equal to that of the fixed-length ME Coding of the original, non-extended case,  $\bar{n}_{ME}^1$ ,*

$$\forall p \geq 2, \exists C^p(W^p, S^p) \text{ such that } \frac{\bar{n}^p}{p} = \bar{n}_{ME}^1. \quad (10)$$

*Proof.* See Appendix.

**Theorem 4: Concatenation.** *Let  $S^1$  be a  $q$ -symbol source with statistically independent symbol probabilities  $P^1 = \{P_1, \dots, P_q\}$ ,  $W^1$  be a codebook having the set of number of high bits  $N^1 = \{n_1, \dots, n_q\}$ , and  $C^1(W^1, S^1)$  be a code representing the  $q$  symbols in  $S^1$  by the  $q$  individual codewords in  $W^1$ . Furthermore, let  $S^p$ ,  $W^p$ , and  $C^p(W^p, S^p)$  be the source, the codebook, and the code associated with the  $p$ -th extension of the original source and codebook. There exists at least one code, whose average number of high bits per symbol  $\bar{n}^p/p$  is less than that of the fixed-length ME Coding of the original, non-extended case,  $\bar{n}_{ME}^1$ ,*

$$\forall p \geq 2, \exists C^p(W^p, S^p) \text{ such that } \frac{\bar{n}^p}{p} < \bar{n}_{ME}^1 \quad (11)$$

*if there exists at least one unused codeword in the original fixed-length ME Codebook (i.e.,  $q < 2^L$ ) and the number of used codewords is not equal to 1 or  $L + 1$ .*

*Proof.* See Appendix.

The conditions on  $(q, L)$  for energy efficiency improvement are illustrated in Figure 7 for a codeword length of 3 bits. Next we will show that the improvement is not monotonic with concatenation order.

**Remark 1.** *Average number of high bits per symbol for concatenation,  $\bar{n}_{ME}^p/p$ , is not a monotonically decreasing function of the concatenation order  $p$ . The following is a counterexample. Let a source  $S^1$  having the probabilistic distribution  $P^1 = \{0.48, 0.4, 0.1, 0.02\}$  and originally coded with  $L = 2$  bit codewords, be extended and coded according to the ME Coding algorithm. The resultant average numbers of high bits per symbol for the ME Codes for  $p = 1, 2, 3$  and  $4$  are  $\bar{n}_{ME}^p/p = 0.5400, 0.4840, 0.45287$ , and  $0.45595$ , respectively. Note that the the average number of high bits per symbol increases as concatenation order*

$q=1$	
$q=L+1$	
$q=2^L$	

Figure 7: Concatenation Improvement Conditions on Codebook Parameters

increases from 3 to 4 (i.e.,  $0.45287 \rightarrow 0.45595$ ). Therefore, the average number of high bits of ME Codes is not a monotonically decreasing function of the concatenation order.

This behavior is similar to that of Huffman Coding, for which counterexamples have been found [10]. In ME Coding, Theorem 4 guarantees that, under the mild conditions, concatenation of an arbitrary order decreases  $\bar{n}_{\text{ME}}^p/p$  compared with the original ME Coding  $\bar{n}_{\text{ME}}^1$ , but it does not say that the average number of high bits per symbol always decreases from  $p$  to  $p+1$ . For the above counterexample, however, it can be shown by using Theorem 4 that  $\bar{n}_{\text{ME}}^2/2 > \bar{n}_{\text{ME}}^4/4$ . Treating the concatenation of order  $p_0 = 2$  as an original ME Code, we can guarantee that  $\bar{n}_{\text{ME}}^{p_0}/p_0$  is higher than that of concatenation for  $p = 2p_0, 3p_0, \dots$ . Figure 8 shows these relations among the first six concatenations. Each directed arc indicates that

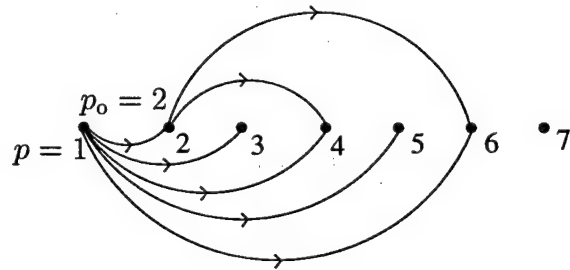


Figure 8: Relations among different concatenation orders:  $\bar{n}_{\text{ME}}^p/p$  decreases in the direction of arrows

$\bar{n}_{\text{ME}}^p/p$  decreases from the origin to the destination in concatenation order  $p$ . Note that there is no directed arc from  $p = 3$  to  $p = 4$ , which agrees with the above counterexample.

**Remark 2.** Optimality bound for fixed-length ME Coding can be extended to provide an optimality bound for concatenation. As a source and a codebook are extended according to concatenation, the following changes take place: (i)  $q \rightarrow q^p$ , (ii)  $L \rightarrow pL$ , and (iii)

$H(S) \rightarrow H(S^p) = pH(S)$ . Hence, making these substitutions into the original optimality bound (7) gives the following optimality bound for concatenation

$$\frac{k^{(H_k - \frac{\bar{n}^p}{p})}}{\sqrt[p]{\sum_{i=1}^{q^p} k^{-n_i}}} \leq 1. \quad (12)$$

## 4 Energy Efficient Error Correction

In the previous section, we discussed the question of how to most efficiently encode source information for transmission over a noiseless channel, where we did not need to be concerned with correcting errors. Now we are ready to consider the question of how to encode source information efficiently, and at the same time, minimize the probability of uncorrected errors when transmitting over a noisy channel.

### 4.1 Setting the Scene

Figure 9 shows the major blocks of a communication system. The definitions that follow

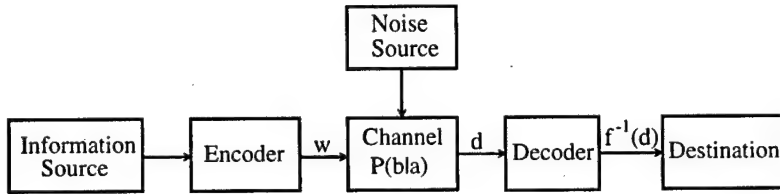


Figure 9: Block Diagram of a Communications System

will explain each block in this model of a communication system. In the previous section, we concentrated on the encoder block. However, we investigated this block only in terms of source coding, where we coded for noiseless channels. In this section, we will first introduce the noisy channel, and then we will consider the encoder and decoder blocks in terms of energy efficient error correction.

#### 4.1.1 The Channel

The communication channel is the medium through which the information bearing signal is transmitted. In this report, we will consider transmission over discrete memoryless channels, hence let us start by giving a formal definition of a discrete memoryless channel.

**Definition: Discrete Memoryless Channel.** A *discrete memoryless channel* consists of an input alphabet, an output alphabet, and a set of channel transition probabilities  $p(b_j|a_i)$  satisfying

$$\sum_{j=1}^t p(b_j|a_i) = 1$$

for all  $i$ . Intuitively, we think of  $p(b_j|a_i)$  as the probability that  $b_j$  is received given that  $a_i$  was sent through the channel. This is pictured in Figure 10.

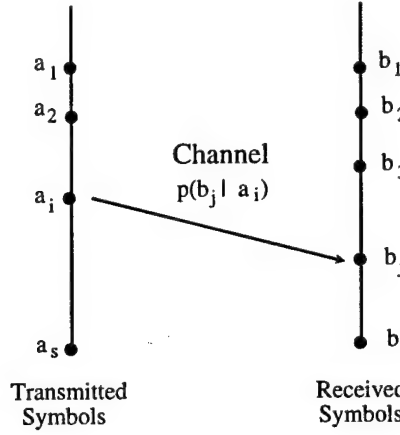


Figure 10: Discrete Memoryless Channel

Furthermore, if a sequence of source symbols  $a_1 a_2 \dots a_n$  represented as a codeword  $\mathbf{w} = w_1 w_2 \dots w_n$  is transmitted and a codeword  $\mathbf{d} = d_1 d_2 \dots d_n$  is received, the probability  $p(\mathbf{d}|\mathbf{w})$  is given by

$$p(\mathbf{d}|\mathbf{w}) = \prod_{i=1}^n p(d_i|w_i),$$

where  $a_i = w_i$  and  $b_i = d_i$ .

One of the most important discrete memoryless channels is the binary symmetric channel, which has input and output alphabets  $\{0, 1\}$  and channel probabilities

$$p(1|0) = p(0|1) = p \quad \text{and} \quad p(0|0) = P(1|1) = 1 - p.$$

These characteristics of the binary symmetric channel are summarized in the *channel transition matrix* given as

$$P(b|a) = \begin{bmatrix} p(0|0) & p(1|0) \\ p(0|1) & p(1|1) \end{bmatrix} = \begin{bmatrix} 1-p & p \\ p & 1-p \end{bmatrix}. \quad (13)$$

This channel is pictured in Figure 11. In this report, we focus on transmission over binary symmetric channels.

The binary symmetric channel is a noisy channel causing bit and thereby codeword errors in transmission if  $p \neq 0$ . Let us first explain what we mean by single *bit errors* or *codeword errors*. In the binary symmetric channel, a bit error occurs if a symbol 0 is sent and a 1 is received or a symbol 1 is sent and a 0 is received. Thus, the probability of a bit error, or the *crossover probability*, is  $p$ . This can be seen in Figure 11. When a codeword  $\mathbf{w}$  consisting of the string  $w_1 w_2 \dots w_n$  is sent through the channel and a codeword  $\mathbf{d}$  consisting of the string  $d_1 d_2 \dots d_n$  is received, we say that a codeword error has occurred if  $\mathbf{w} \neq \mathbf{d}$ , and the incorrect

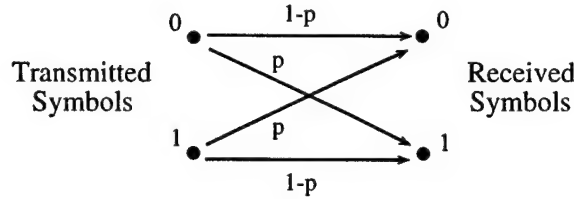


Figure 11: Binary Symmetric Channel

$\mathbf{d}$  is not corrected. Next, we discuss the types of errors that may occur when transmitting over a noisy channel.

Errors, in general, can be of four types: *(i)* isolated bit errors, *(ii)* burst errors, *(iii)* erasures, and *(iv)* insertions. Isolated bit errors, as the name implies, occur when the errors in transmission are independent. However, this can be unrealistic in certain situations, where there is a strong correlation among the bit errors. In this case, we speak of burst errors. For example, electrical interferences often last longer than the time it takes to transmit a single bit, defects on magnetic tape or disk are usually larger than the space required to store a single bit, and noise in wireless channels may corrupt multiple bits at the same time. The third type of errors, namely, erasures, are characterized by situations, where the decoder knows that a single bit is occurring at a point, but cannot determine its value. Finally, insertions occur when extra bits are inserted into the bit stream of transmitted data. Coding Theory aims to develop codes correcting certain types of errors. Much work has been put into developing structured codes correcting isolated bit errors. Hence, in this report we look into codes correcting isolated bit errors.

#### 4.1.2 The Decoder and Error Probability

**Definition: Decoder.** A decoder is a partial fraction  $f$  from the set of received words to the set of codewords. The word partial refers to the fact that  $f$  may not be defined for all received words. The intention is that if a received word  $\mathbf{d}$  is received, and if  $f(\mathbf{d})$  is defined, then the decoder decides that  $f(\mathbf{d})$  is the codeword that was sent. If  $f(\mathbf{d})$  is not the codeword that was sent, we say that a decoding error has been made. The decoder is shown in Figures 9 and 12.

By letting

$$B_i = f^{-1}(\mathbf{w}) = \{\mathbf{d} | f(\mathbf{d}) = \mathbf{w}\}$$

be the set of all outputs for which we decide that the correct input was  $\mathbf{w}$ , we can also think of a decoder as a collection  $\{B_{w_1}, \dots, B_{w_m}\}$  of disjoint subsets of the set of received words. This is illustrated in Figure 12. One important measure of decoder performance is the error

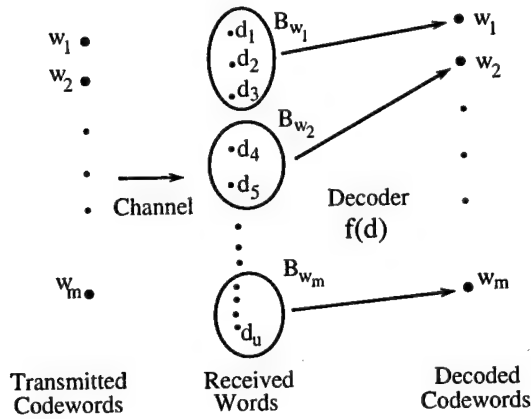


Figure 12: Decoder

probability, hence we now define error probability.

**Definition: Error Probability.** For any decoder, the error probability given that a codeword  $\mathbf{w}$  is transmitted is given by

$$P(\text{error}|\mathbf{w} \text{ sent}) = \sum_{\mathbf{d} \notin f^{-1}(\mathbf{w})} p(\mathbf{d}|\mathbf{w}).$$

Hence, the *error probability* for the whole code,  $p_e$ , is given by

$$p_e = \sum_{\mathbf{w}} P(\text{error}|\mathbf{w})p(\mathbf{w}) = \sum_{\mathbf{w}} \sum_{\mathbf{d} \notin f^{-1}(\mathbf{w})} p(\mathbf{d}|\mathbf{w})p(\mathbf{w})$$

A desirable decoder is one that offers a minimal error probability in the most computationally practical way. In order to see how we can design a decoder that minimizes the error probability, let us compute this probability by conditioning on the output, rather than the input. If the output of the channel is  $\mathbf{d}$ , then correct decoding will be made iff  $f(\mathbf{d})$  was the actual input. Hence,

$$P(\text{error}|\mathbf{d}) = 1 - p(f(\mathbf{d})|\mathbf{d})$$

Averaging over all possible outputs, we have

$$p_e = \sum_{\mathbf{d}} P(\text{error}|\mathbf{d})p(\mathbf{d}) = 1 - \sum_{\mathbf{d}} p(f(\mathbf{d})|\mathbf{d})p(\mathbf{d})$$

Now, this probability can be minimized by choosing a decision scheme that maximizes the sum on the far right. But since each term in the sum is nonnegative, and since the factors  $p(\mathbf{d})$  do not depend on the decoding algorithm, we can maximize the sum by choosing  $f(\mathbf{d})$  so that  $p(f(\mathbf{d})|\mathbf{d})$  is large as possible for all  $\mathbf{d}$ .

**Definition: Ideal Observer** For a given input distribution, any decoder  $f$  for which  $f(\mathbf{d})$  has the property that

$$p(f(\mathbf{d})|\mathbf{d}) = \max_{\mathbf{w}} p(\mathbf{w}|\mathbf{d})$$

for all received words  $\mathbf{d}$ , is called an *ideal observer*. In words, an ideal observer is one for which  $f(\mathbf{d})$  is a codeword most likely to have been sent, given that  $\mathbf{d}$  is received.

The ideal observer decoder has the advantage that it yields optimal probability of error; however, it uses backward channel probabilities, which depend on the input distribution. This suggests that the ideal observer will be computationally impractical. Thus, we seek ways to eliminate this dependency on the input distribution. We can eliminate this dependency by assuming a uniform input distribution. This results in the desirable feature that maximizing the backward channel probabilities become equivalent to maximizing forward channel probabilities. This is extremely practical, because it reduces the computation requirements. The undesirable feature is that the error probability performance is not as good as the ideal observer.

**Definition: Maximum Likelihood Decoder.** Any decoder  $f$  for which  $f(\mathbf{d})$  has the property that

$$p(\mathbf{d}|f(\mathbf{d})) = \max_{\mathbf{w}} p(\mathbf{d}|\mathbf{w})$$

for all received words  $\mathbf{d}$ , is called a *maximum likelihood decoder*. In words,  $f(\mathbf{d})$  is a transmitted codeword with the property that for no other codeword would it be more likely that the output  $\mathbf{d}$  was received.

Although the maximum likelihood decoding eliminates the dependence of decoder on the input distribution, it still exhibits a coupling between the decoder and the forward channel probabilities. Thus, we seek ways to eliminate this coupling. First, let us define the Hamming Distance.

**Definition: Hamming Distance.** Let  $\mathbf{x}$  and  $\mathbf{y}$  be codewords of the same length, over the same alphabet. The *Hamming Distance*  $d(\mathbf{x}, \mathbf{y})$  between  $\mathbf{x}$  and  $\mathbf{y}$  is the number of positions in which  $\mathbf{x}$  and  $\mathbf{y}$  differ. For instance, if  $\mathbf{x} = 10110$  and  $\mathbf{y} = 10101$ , then  $d(\mathbf{x}, \mathbf{y}) = 2$ , since the two codewords differ only in positions 4 and 5.

We will now state without proof, a fundamental result in Coding Theory and use this result in deriving energy optimal codes for wireless communications. The fundamental result is that the maximum likelihood decoder reduces to minimum distance decoding for binary symmetric channels with crossover probability  $p < 1/2$ . This result is also true for binary erasure channels and some other channels of interest. However, at this point we will only consider binary symmetric channels.

#### 4.1.3 The Main Energy Efficient Error Correction Problem

Before describing some coding schemes for energy efficient and reliable communication, we should describe the desirable characteristics of an *efficient* coding scheme and elucidate the main problem of energy efficient error correction. The characteristics of an efficient coding scheme can be summarized as

- minimizing the energy consumption in the RF transmitter,
- offering a desirable reliability performance in information transmission,
- requiring a computationally feasible decoding scheme,
- resulting in reasonable transmission rates.

In designing energy efficient codes for wireless communications, we will initially focus on the first three requirements and will not concern ourselves with the third requirement. Our objective will be to design energy optimal codes, offering a given error correction capability in a computationally feasible manner. Due to the computational feasibility requirement, we will consider linear block codes.

The problem of energy efficient error correction is in fact a codebook design problem upon which ME Coding is performed. This problem is illustrated in Figure 13. For a given

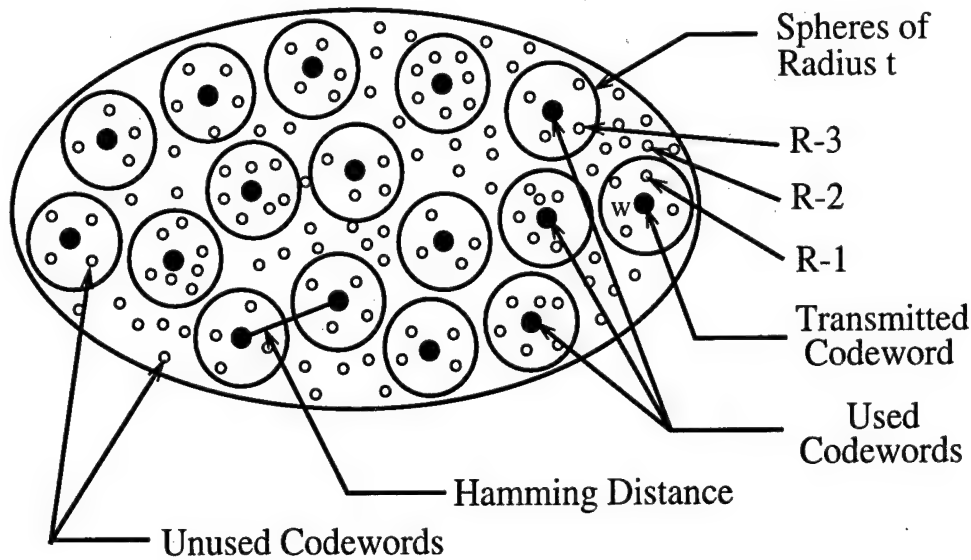


Figure 13: The Main Energy Efficient Error Correction Problem

codeword length the set of available codewords is shown by all the larger filled and the smaller unfilled circles in this figure. The larger filled spheres are the codewords used in the

codebook and the smaller unfilled spheres are unused codewords. The problem is *how to select the codewords such that all the codewords we have selected are (i) at least  $2t + 1$  units apart in terms of Hamming Distance, and (ii) constitute the elements of a minimum codebook*. Since we use linear block codes, the first requirement is automatically determined by the type of code we use. The second requirement is unfortunately not always satisfied by linear block codes. Satisfying the second requirement involves the use of nonlinear codes which are computationally impractical. This illustrates the tradeoff between energy efficiency and computational complexity. Since in our design computational feasibility is a hard constraint, we will ignore the second requirement for the time being. Going back to the first requirement, we see that this requirement is necessary for  $t$ -error correction. This  $t$ -error correction can be explained as follows.

Suppose a codeword  $\mathbf{w}$  is transmitted as indicated in Figure 13 and suppose that all the used codewords are at least  $2t + 1$  units apart, meaning that the spheres of radius  $t$  around any used codewords will be non-intersecting. Thus, during the transmission, if  $e$  errors occur in transmission,  $e \leq t$ , the received codeword (R-1) will still be in the sphere of the sent codeword and can be decoded correctly as that codeword. However, if the number of errors in transmission is  $e > t$ , then the received codeword (R-2 or R-3) will not be in the sphere of radius  $t$  and will most probably not be decoded correctly. Thus, any number of error less than or equal to  $t$  will be corrected with this code of minimum distance  $2t + 1$ . Once the codewords having a minimum distance of  $2t + 1$  are selected, energy efficiency in transmission will be optimized by performing ME Coding. That is the higher probability symbols will be mapped to codewords with less high bits. This way, we will achieve optimal energy efficient for a given reliability performance in a computationally feasible manner. Next, we introduce energy efficient linear codes for reliable communication.

## 4.2 Energy Efficient Linear Codes

Many practical error-correcting codes used today are linear. The reasons why linear codes are so popular can be summarized as follows.

- Evaluation of distance between codewords is much easier.
- Encoding is fast and requires little storage.
- Determination of which errors are correctable/detectable is much easier.
- Probability of correct decoding is much easier to calculate.
- Very cunning decoding techniques exist for linear codes.

Due to these advantages we will investigate the use of linear codes for energy efficient error recovery. In what follows, we will describe Hamming Codes, Golay Codes, and Reed-Muller Codes used for energy efficient and reliable information transmission.

### 4.2.1 Minimum Energy Hamming Codes

Hamming Codes are perfect linear block codes offering single error correction capability. Hamming Codes provide this single error correction capability due to their minimum distance of 3 bits. This is illustrated in Figure 14, where codewords 1 and 2 denote any two codewords in the Hamming codebook. Any single bit error in transmission of a codeword results in a

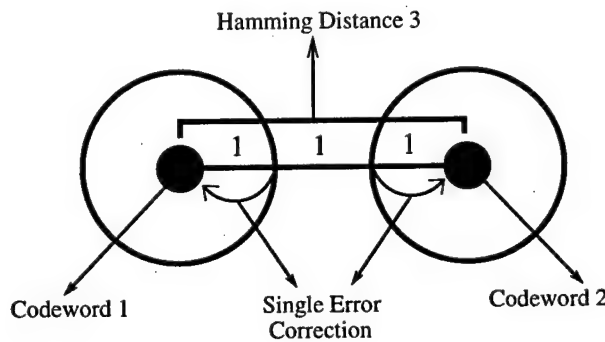


Figure 14: Single Error Correcting Hamming Codes

received codeword, which is on the circumference of the unit circles. Since this received codeword is still closest to the codeword that is originally transmitted, any single error can be corrected as it is seen in Figure 14.

*How do we combine ME Coding and Hamming Codes?* Hamming Codes are basically usable codewords sets,  $W_0$ s, for single error correction. Since Hamming Codes impose no

constraints on the mapping between the codeword set and the source symbols, we can combine ME Coding with Hamming Codes just by regarding the given Hamming Code as the usable codeword set  $W_o$  in Theorem 2 and performing ME Coding on this set. Rather than giving formal definitions and general descriptions of the coding and decoding algorithms of ME Hamming Codes, we will give an example that demonstrates these procedures. More detailed information on Hamming Codes and extended Hamming Codes can be found in [11,12]

**ME Hamming Code Example.** Let  $S$  be a  $q = 10$  symbol source with probabilities given in Table 2. In order to generate a ME Hamming Code for this source, we first construct

Table 2: ME Hamming Code

S	Prob.	MEH	S	Prob.	MEH
$s_1$	0.19	0000000	$s_9$	0.04	0001111
$s_2$	0.15	0010110	$s_{10}$	0.02	0110011
$s_3$	0.13	0011001			0111100
$s_4$	0.12	0100101			1010101
$s_5$	0.11	0101010			1011010
$s_6$	0.10	1000011			1100110
$s_7$	0.08	1001100			1101001
$s_8$	0.06	1110000			1111111

the set of usable codewords: the Hamming Code.

**Codebook Generation of ME Hamming Code.** We construct this set of codewords by choosing the longest Hamming Code (i.e., longest  $L$ ) that satisfies the transmission rate and error probability constraints and provides enough codewords to code all  $q$  symbols. We choose the longest code because this maximizes the number of codewords with less high bits, thereby optimizing the energy performance. Assuming that these constraints result in the Hamming (7, 4) Code being the only feasible code in this example, we generate the usable codeword set for this code and perform ME Coding. The usable codeword set is generated using the parity check equations

$$c H^T = 0, \quad (14)$$

where  $c$  is each codeword in the codeword set  $W_o$  and  $H^T$  is the transpose of the parity check matrix  $H$ . The parity check matrix for the Hamming (7, 4) Code is

$$H = \begin{bmatrix} 0 & 0 & 0 & 1 & 1 & 1 & 1 \\ 0 & 1 & 1 & 0 & 0 & 1 & 1 \\ 1 & 0 & 1 & 0 & 1 & 0 & 1 \end{bmatrix}. \quad (15)$$

The resulting set of usable codewords, ordered in ascending number of high bits, is given in the third and sixth columns in Table 2. From this Hamming Code, we choose the minimum

codebook consisting of the first 10 codewords, and assign codewords having less high bits to more probable symbols. The resulting code is the ME Hamming Code (see Table 2).

**Decoding of ME Hamming Codes.** The decoding of Hamming Codes is as follows. Assume that the codeword 0011101 containing a single bit error is received. This erroneous codeword is multiplied by the parity check matrix of the Hamming Code which results in the error vector  $\mathbf{e}$  given as

$$\mathbf{e} = \mathbf{H}\mathbf{w}^T = \begin{bmatrix} 0 & 0 & 0 & 1 & 1 & 1 & 1 \\ 0 & 1 & 1 & 0 & 0 & 1 & 1 \\ 1 & 0 & 1 & 0 & 1 & 0 & 1 \end{bmatrix} [0 \ 0 \ 1 \ 1 \ 1 \ 0 \ 1]^T = [1 \ 0 \ 1]^T.$$

This error vector represents the bit position of the error in binary coded decimal form. That is there is an error occurring in the fifth binary digit, and this bit can be complemented to correct this error: 0011101  $\rightarrow$  0011001.

**Extended Hamming Codes.** We should also note that Hamming Codes can be extended to provide double error detection by adding an overall parity check bit. This overall parity check bit merely increases the minimum distance of Hamming Codes to four bits, thereby enabling double error detection. Extended Hamming Codes are illustrated in Figure 15, where we see that by achieving a minimum distance of 4, extended Hamming Codes realize that a codeword containing double errors is not a legal codeword and that a double error has occurred. Once the decoder detects a double error, it can ask for a retransmission.

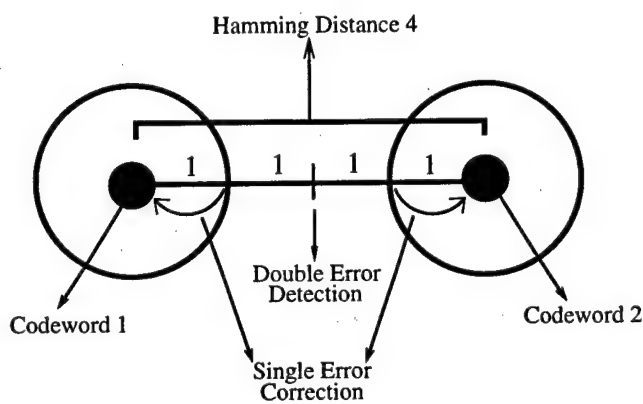


Figure 15: Single Error Correcting and Double Error Detecting Hamming Codes

While constructing the ME Hamming Code, we realize the trade-off among the three performance metrics: energy efficiency, reliability, and transmission rate. The ME Hamming Code in Table 2 is using codewords having zero, three, and four high bits. This code clearly provides a degraded energy performance compared to ME Codes in Section 3, which would use zero, one, and two high bit codewords only. Hence, this illustrates the trade-off

between energy efficiency and reliability. Furthermore, if the codeword length of the present ME Hamming Code is increased, more three high bit codewords would become available, thereby improving the energy efficiency of the current ME Hamming Code. However, this would degrade the transmission rate performance, re-introducing the trade-off between energy efficiency and transmission rate. Hence, energy efficient transmission is a trade-off among energy efficiency, reliability, and transmission rate.

#### 4.2.2 Minimum Energy Golay Codes

We start explaining Golay Codes with extended Golay Code. Extended Golay Code is used to correct three or fewer isolated bit errors. Extended Golay Code was in fact used in the Voyager spacecraft program in the early 1980's and brought us the close-up photographs of Jupiter and Saturn. Contrary to what we did in the previous section, in this and the next sections we will give formal definitions and generalized coding/decoding algorithms of ME Golay and Reed-Muller Codes.

**Definition: Extended Golay Codes.** Let  $B$  be the  $(12 \times 12)$  matrix

$$B = \begin{bmatrix} 0 & 1 & 1 & 1 & 1 & 1 & 1 & 1 & 1 & 1 & 1 & 1 \\ 1 & 1 & 1 & 0 & 1 & 1 & 1 & 0 & 0 & 0 & 1 & 0 \\ 1 & 1 & 0 & 1 & 1 & 1 & 0 & 0 & 0 & 1 & 0 & 1 \\ 1 & 0 & 1 & 1 & 1 & 0 & 0 & 0 & 1 & 0 & 1 & 1 \\ 1 & 1 & 1 & 1 & 0 & 0 & 0 & 1 & 0 & 1 & 1 & 0 \\ 1 & 1 & 1 & 0 & 0 & 0 & 1 & 0 & 1 & 1 & 0 & 1 \\ 1 & 1 & 0 & 0 & 0 & 1 & 0 & 1 & 1 & 0 & 1 & 1 \\ 1 & 0 & 0 & 0 & 1 & 0 & 1 & 1 & 0 & 1 & 1 & 1 \\ 1 & 0 & 0 & 1 & 0 & 1 & 1 & 0 & 1 & 1 & 1 & 0 \\ 1 & 0 & 1 & 0 & 1 & 1 & 0 & 1 & 1 & 1 & 0 & 0 \\ 1 & 1 & 0 & 1 & 1 & 0 & 1 & 1 & 1 & 0 & 0 & 0 \\ 1 & 0 & 1 & 1 & 0 & 1 & 1 & 1 & 0 & 0 & 0 & 1 \end{bmatrix}$$

Let  $G$  be the  $(12 \times 24)$  matrix  $G = [I, B]$ , where  $I$  is the  $(12 \times 12)$  identity matrix. The linear code  $C$  with generator matrix  $G$  is called the *extended Golay Code* and will be denoted by  $C_{24}$ . By inspection we see that  $B^T = B$ ; that is,  $B$  is a symmetric matrix.

**Characteristics of Extended Golay Codes and the Codebook Generation Algorithm.** Let us now summarize some important facts about the extended Golay Code  $C_{24}$  with the generator matrix  $G = [I, B]$ :

1.  $C_{24}$  has length  $L = 24$ , dimension  $k = 12$  and  $2^{12} = 4096$  codewords.
2. A parity check matrix for  $C_{24}$  is the  $(24 \times 12)$  matrix  $\begin{bmatrix} B \\ I \end{bmatrix}$ . Another parity check matrix for  $C_{24}$  is the  $(24 \times 12)$  matrix  $H = \begin{bmatrix} I \\ B \end{bmatrix}$ .

3. Another generator matrix for  $C_{24}$  is the  $(12 \times 24)$  matrix  $[B, I]$ .
4. The distance of  $C$  is 8.
5.  $C_{24}$  is a three-error-correcting code.

Thus spanning the generator matrix using all codewords of length 12 bits, we can obtain the  $(24, 12, 4)$  extended Golay Code. In other words, the Golay Code  $C_{24}$  can be obtained using the following matrix equation

$$C_{24} = uG$$

where  $u$  represents all binary strings of length 12 and  $G = [I, B]$  is the generator matrix with  $I$  being the identity matrix of size  $(12 \times 12)$ . Thus, a binary string  $u=001010000000$  would result in the codeword  $001010000000, 101101001100$  through simple matrix multiplication. Next, let us summarize the decoding algorithm for the extended Golay Code.

**Extended Golay Code Decoding Algorithm.** Let  $o_i$  be the word of length 12 with a 1 in the  $i$ -th position and 0s elsewhere,  $e$  be the error vector, and  $b_i$  be the  $i$ -th row of  $B$ . Then, the decoding algorithm of extended Golay Code comprises the following seven steps:

1. Compute the  $s = dH$ , where  $s$  is called the syndrome,  $d$  is the received codeword, and  $H$  is the parity check matrix given by  $H = \begin{bmatrix} I \\ B \end{bmatrix}$ .
2. If  $wt(s) \leq 3$ , then  $e = [s, 0]$ , where  $wt(s)$  is the weight of the syndrome which is equal to the number of 1s in the syndrome.
3. If  $wt(s + b_i) \leq 2$  for some row  $b_i$  of  $B$ , then  $e = [s + b_i, o_i]$ .
4. Compute the second syndrome  $sB$ .
5. If  $wt(sB) \leq 3$ , then  $e = [0, sB]$ .
6. If  $wt(sB + b_i) \leq 2$  for some row  $b_i$  of  $B$ , then  $e = [o_i, sB + b_i]$ .
7. If  $e$  is not yet determined, then request retransmission.

This algorithm requires at most 26 weight calculations in the decoding procedure. Of course, once  $e$  is determined, then no further steps in the algorithm need to be done. The transmitted codeword can simply found by  $w = e + d$ . Let us give some examples illustrating this decoding procedure.

Suppose a codeword  $d=10111110111, 010010010010$  is received. The syndrome is found to be

$$s = dH = 101111101111 + 001111101110 = 100000000001,$$

which has weight 2. Since  $wt(\mathbf{s}) \leq 3$ , we find that

$$\mathbf{e} = [\mathbf{s}, 0] = 10000000001, 000000000000$$

and conclude that the transmitted word is

$$\mathbf{w} = \mathbf{e} + \mathbf{d} = 001111101110, 010010010010.$$

As another example suppose a codeword  $\mathbf{d} = 001001001101, 101000101000$  is received. The syndrome for this word is

$$\mathbf{s} = \mathbf{d}H = 001001001101 + 111000000100 = 110001001001,$$

which has weight 5. Proceeding to step 3 of the decoding algorithm, we compute

$$\begin{aligned}\mathbf{s} + b_1 &= 000110001100 \\ \mathbf{s} + b_2 &= 011111000010 \\ \mathbf{s} + b_3 &= 101101011110 \\ \mathbf{s} + b_4 &= 001001100100 \\ \mathbf{s} + b_5 &= 000000010010.\end{aligned}$$

Since  $wt(\mathbf{s} + b_5) \leq 2$ , we find that

$$\mathbf{e} = [\mathbf{s} + b_5, o_5] = 000000010010, 000010000000$$

and conclude that

$$\mathbf{w} = \mathbf{e} + \mathbf{d} = 001001011111, 101010101000$$

was the transmitted codeword.

**ME Extended Golay Codes.** The extended Golay Code coding and decoding algorithms are used to derive a codebook enabling 3-error correction. The extended Golay Code enables us to transmit  $2^{12}$  different codeword, thereby enabling to code  $2^{12}$  symbols. The procedure for constructing the ME Extended Golay Code is described in the following three steps: (i) generate the Extended Golay Codebook, (ii) choose the minimum codebook, and (iii) map the source symbols to the minimum codebook according to the ME Coding algorithm. Hence, we can perform ME Coding for the available codewords in the extended Golay Code to achieve energy efficient transmission. Furthermore, if we have much less than  $2^{12}$  symbols, we can simply encode extensions of the source alphabet using the extended Golay Code, which might enable further energy savings.

**Golay Codes.** Another interesting 3-error correcting code can be obtained by puncturing  $C_{24}$ , that is removing a digit from every word in  $C_{24}$ . The same digit must be removed from each word. We shall remove the last digit.

**Decoding of Golay Codes.** Let  $\hat{B}$  be the  $(12 \times 11)$  matrix obtained from the matrix  $B$  by deleting the last column. Let  $G$  be the  $(12 \times 23)$  matrix  $G = [I_{12}, \hat{B}]$ . The linear code with generator matrix  $G$  is called the Golay Code and is denoted by  $C_{23}$ . The Golay Code has length  $n = 23$ , dimension  $k = 12$ , and contains  $2^{12} = 4096$  codewords. The Golay Code has minimum distance of 7 and will correct any 3 bit or less errors.

The decoding algorithm for the Golay Code is based on the decoding algorithm of the extended Golay Code. This algorithm can be summarized as follows

1. Form  $\mathbf{d}_0$  or  $\mathbf{d}_1$ , whichever has odd weight.
2. Decode  $\mathbf{d}_i$  ( $i$  is 0 or 1) using the extended Golay Code decoding algorithm to codeword  $\mathbf{w}$  in  $C_{24}$ .
3. Remove the last digit from  $\mathbf{w}$ .

**ME Golay Codes.** Golay Codes can be used for 3 or less error correction. These codes can be mapped to source symbols using the ME Coding algorithm to provide energy efficient reliable transmission. The procedure for constructing the ME Golay Code is the same as that of ME Hamming Codes and ME extended Golay Codes: (i) generate the Golay Codebook, (ii) choose the minimum codebook, and (iii) map the source symbols to the minimum codebook according to the ME Coding algorithm. In the following section, we will extend the Hamming and Golay Codes to  $t$ -error correcting Reed-Muller Codes, where  $t$  is any positive number.

#### 4.2.3 Minimum Energy Reed-Muller Codes

**Definition: Reed-Muller Codes.** The  $r$ -th order Reed-Muller Code of length  $2^m$  is  $RM(r, m)$ ,  $0 \leq r \leq m$ . A recursive definition of the Reed-Muller Code is such that

1.  $RM(0, m) = \{00\dots0, 11\dots1\}$ ,  $RM(m, m) = K^{2^m}$ ,
2.  $RM(r, m) = \{(x, x + y) | x \in RM(r, m - 1), y \in RM(r - 1, m - 1)\}$ ,  $0 < r < m$ .

**Codebook Generation of Reed-Muller Codes.** Rather than using this definition of the Reed-Muller Code, we will use a recursive construction of the generator matrix of  $RM(r, m)$ , which we will denote by  $G(r, m)$ . For  $0 < r < m$ , we define  $G(r, m)$  by

$$G(r, m) = \begin{bmatrix} G(r, m - 1) & G(r, m - 1) \\ 0 & G(r - 1, m - 1) \end{bmatrix}.$$

For  $r = 0$  we define

$$G(0, m) = [11\dots1]$$

and for  $r = m$ , we define

$$G(m, m) = \begin{bmatrix} G(m-1, m) \\ 0\dots01 \end{bmatrix}.$$

**Characteristics of Reed-Muller Codes** Let us summarize the properties of an  $r$ -th order Reed-Muller Code  $RM(r, m)$ .

- Length  $L = s^m$
- Distance  $d = 2^{m-r}$
- Dimension  $k = \sum_{i=0}^r \binom{m}{i}$
- $RM(r-1, m)$  is contained in  $RM(r, m)$ ,  $r > 0$
- Dual code  $RM(m-1-r, m)$ ,  $r < m$ .

By arbitrarily choosing the values for  $(r, m)$ , we can construct a Reed-Muller code that can correct up to  $(2^{m-r} - 1)/2$  errors.

Let us now give some examples demonstrating the recursive construction of the Reed-Muller Code. The generator matrices for  $RM(0, 1)$  and  $RM(1, 1)$  are

$$G(0, 1) = [11] \quad \text{and} \quad G(1, 1) = \begin{bmatrix} 11 \\ 01 \end{bmatrix}.$$

Let  $m = 2$ , then the length is  $n = 2^2 = 4$  and for  $r=1,2$  we have

$$G(1, 2) = \begin{bmatrix} G(1, 1) & G(1, 1) \\ 0 & G(0, 1) \end{bmatrix}, \quad G(2, 2) = \begin{bmatrix} G(1, 2) \\ 0001 \end{bmatrix}.$$

Substituting for  $G(0, 1)$  and  $G(1, 1)$ , we get

$$G(1, 2) = \begin{bmatrix} 1111 \\ 0101 \\ 0011 \end{bmatrix}, \quad \text{and} \quad G(2, 2) = \begin{bmatrix} 1111 \\ 0101 \\ 0011 \\ 0001 \end{bmatrix}.$$

For  $m = 3$ ,  $m = 2^3 = 8$ , we have

$$G(0, 3) = [11111111], \quad G(3, 3) = \begin{bmatrix} G(2, 3) \\ 00000001 \end{bmatrix}$$

$$G(1, 3) = \begin{bmatrix} G(1, 2) & G(1, 2) \\ 0 & G(0, 2) \end{bmatrix}, \quad G(2, 3) = \begin{bmatrix} G(2, 2) & G(2, 2) \\ 0 & G(1, 2) \end{bmatrix}.$$

Thus, substituting for  $G(0, 2)$ ,  $G(1, 2)$  and  $G(2, 2)$ , we get

$$G(1, 3) = \begin{bmatrix} 11111111 \\ 01010101 \\ 00110011 \\ 00001111 \end{bmatrix}.$$

Considering the first order Reed-Muller Code  $RM(1, m)$ , we realize that the code has a dimension  $2^m - m - 1$ , a distance of 4, and length  $2^m$ . Thus, the first order Reed-Muller Code is an extended Hamming Code.

The decoding of Reed-Muller Codes is a simple operation. However, explanation of the decoding operation requires some detailed background information. Hence, decoding of Reed-Muller Codes is not included here. A detailed treatment of the decoding operation in Reed-Muller Codes can be found in [12, 13]. The use of Reed-Muller Codes for energy efficient information transmission is similar to that of Hamming and Golay Codes. Basically, Reed-Muller Code is used to construct a codebook of codewords that are a given distance apart, and ME Coding is performed on this codebook to achieve energy efficient transmission. In conclusion, we can use ME Hamming, ME Golay, and ME Reed-Muller Codes for energy efficient and reliable information transmission.

## 5 Major Findings and Conclusions

In this report, we investigate the problem of energy efficient information transmission in wireless communications. The major findings and conclusions of this investigation are as follows.

### **The Main Energy Efficient Information Transmission Problem.**

- The major energy consuming component in most portable communication devices is the transmitter, hence optimization of the transmitter energy consumption would enable significant energy savings.
- Current approaches to the energy efficient transmission problem include on-time reduction, power level adaptation, and error control adaptation, which do not provide the overall optimal performance.
- Energy optimal information transmission can be accomplished by using codes that minimize the occurrence of high bits in representing the information.

### **Information Transmission over Noiseless Channels: Source Coding.**

- ME Coding is proposed as a novel memoryless coding algorithm that provides energy optimal codes for sources with known statistics.
- The conditions and parameters determining optimality are identified and an optimality bound is derived.
- Concatenation is introduced as a technique that improves the optimal memoryless performance via a simple memory mechanism.
- Energy efficiency improvement by concatenation is clearly explained and the conditions of improvement are determined.

### **Information Transmission over Noisy Channels: Error Control Coding.**

- The main problem of energy efficient and reliable information transmission over noisy channels is explained.
- Minimum Energy Hamming Codes, Minimum Energy Golay Codes, and Minimum Energy Reed-Muller Codes are proposed for energy efficient and reliable information transmission over noisy channels.

We conclude that energy efficient information transmission can be accomplished via proper source and channel coding algorithms that optimize the transmitter operation.

## References

- [1] T. S. Rappaport. *Wireless Communications: Principles and Practice*. Prentice Hall, 1996.
- [2] M. Zorzi and R. R. Rao. Energy-Constrained Error Control for Wireless Channels. *IEEE Personal Communications*, 4(6):27–33, Dec 1997.
- [3] N. Bambos. Toward Power-Sensitive Network Architectures in Wireless Communications: Concepts, Issues, and Design Aspects. *IEEE Personal Communications*, 5(3):50–59, June 1998.
- [4] E. Biglieri, G. Caire, and G. Taricco. Coding and Modulation under Power Constraints. *IEEE Personal Communications*, 5(3):32–39, Jun 1998.
- [5] E. Ayanoglu, S. Paul, T. F. LaPorta, K. K. Sabnani, and R. D. Gitlin. AIRMAIL: A Link-Layer Protocol for Wireless Networks. *Wireless Networks*, 1(1):47–60, 1995.
- [6] J. M. Rulnick and N. Bambos. Mobile Power Management For Wireless Communication Networks. *Wireless Networks*, 3(1):3–14, 1997.
- [7] P. Lettieri, C. Fragouli, and M. B. Srivastava. Low Power Error Control for Wireless Links. In *MobiCom 1997. Proceedings of the Third Annual ACM/IEEE International Conference on Mobile Computing and Networking*, pages 139–150, 1997.
- [8] P. Agrawal, B. Narendran, J. Sienicki, and S. Yajnik. An Adaptive Power Control and Coding Scheme For Mobile Radio Systems. In *Proceedings of the 1996 IEEE International Conference on Personal Wireless Communications*, pages 283–288. IEEE, Feb 19-21 1996.
- [9] J. R. Smith. *Modern Communication Circuits*. McGraw-Hill, 1998.
- [10] P. M. Fenwick. Huffman Code Efficiencies for Extensions of Sources. *IEEE Transactions on Communications*, 43(2-4):163–165, Feb-Apr 1995.
- [11] R. W. Hamming. *Coding and Information Theory*. Prentice-Hall, 1986.
- [12] J. Baylis. *Error-Correcting Codes: A Mathematical Introduction*. Chapman and Hall Mathematics, 1998.
- [13] S. G. Wilson. *Digital Modulation and Coding*. Prentice Hall, 1996.

## Appendix

### Proof of Theorem 1

Let  $i$  and  $j$  be arbitrary integers such that  $1 \leq i < j \leq q$ . From equations (4) and (5),

$$P_i \geq P_j \quad \text{and} \quad n_i \leq n_j. \quad (16)$$

Consider the two terms involved in  $\bar{n} = \sum_{i=1}^q P_i n_i$ ,

$$\text{Old : } P_i n_i + P_j n_j.$$

Interchanging the codewords for the  $i$ -th and  $j$ -th symbols yields

$$\text{New : } P_i n_j + P_j n_i.$$

Subtracting Old from New and using (16), the net change in the average number of high bits due to this re-assignment becomes

$$\text{New} - \text{Old} = (P_i - P_j)(n_j - n_i) \geq 0.$$

Therefore, the average number of high bits,  $\bar{n}$ , does not decrease for any interchange of codewords. Hence, this coding algorithm provides optimal codes for a given codebook with respect to energy consumption.  $\square$

### Proof of Theorem 2

Let  $n_1 \leq n_2 \leq \dots \leq n_i \leq \dots \leq n_q$  be the number of high bits in the codewords  $w_1$  through  $w_q$  involved in the minimum codebook  $W_{\min}$ . The proof is given by showing that replacing an arbitrary codeword  $w_i$  involved in  $W_{\min}$  with an arbitrary codeword  $w_j$  not involved in  $W_{\min}$  does not decrease the minimum average number of high bits  $\bar{n}$ . Since  $1 \leq i \leq q < j \leq q_0$  and  $n_i \leq n_{i+1} \leq \dots \leq n_q \leq n_j$ , the following inequalities hold

$$n_{i+1} - n_i \geq 0, \quad n_{i+2} - n_{i+1} \geq 0, \quad \dots, \quad n_q - n_{q-1} \geq 0, \quad n_j - n_q \geq 0. \quad (17)$$

Multiplying  $P_i, P_{i+1}, \dots, P_q$  by the above inequalities individually and summing them yield

$$P_i(n_{i+1} - n_i) + \dots + P_{q-1}(n_q - n_{q-1}) + P_q(n_j - n_q) \geq 0$$

or

$$P_i n_i + \dots + P_{q-1} n_{q-1} + P_q n_q \leq P_i n_{i+1} + \dots + P_{q-1} n_q + P_q n_j.$$

Adding  $P_1n_1 + \dots + P_{i-1}n_{i-1}$  to both sides,

$$\begin{aligned} P_1n_1 + \dots + P_{i-1}n_{i-1} + P_in_i + \dots + P_{q-1}n_{q-1} + P_qn_q &\leq \\ P_1n_1 + \dots + P_{i-1}n_{i-1} + P_in_{i+1} + \dots + P_{q-1}n_q + P_qn_j. \end{aligned} \quad (18)$$

The left hand side gives the minimum average number of high bits for the minimum codebook, while the right hand side provides  $\bar{n}$  for a non-minimum codebook where  $w_i$  is replaced by  $w_j$ . The former is always smaller than or equal to the latter. Therefore, the codebook must be a minimum codebook in order to minimize  $\bar{n}$  for available  $W_o$  and given  $P$ .  $\square$

## Derivation of ME Coding Optimality Bound

Consider the binomial bound given by

$$K = \frac{1}{\left(\frac{k+1}{k}\right)^L} \sum_{i=1}^q k^{-n_i} \leq 1. \quad (19)$$

Using this inequality, we define numbers  $Q_1$  through  $Q_q$ ,

$$Q_i = \frac{k^{-n_i}}{K\left(\frac{k+1}{k}\right)^L}, \quad (20)$$

which sum to 1,  $\sum_{i=1}^q Q_i = 1$ . These numbers may be regarded as a probability distribution, hence, the following Gibbs inequality applies:

$$\sum_{i=1}^q P_i \log_2 \left( \frac{Q_i}{P_i} \right) \leq 0. \quad (21)$$

Expanding the logarithmic term and dividing both sides by  $\log_2 k$  yields the entropy of the source symbols separated from the rest of the above inequality,

$$H_k = \sum_{i=1}^q P_i \log_k \left( \frac{1}{P_i} \right) \leq \sum_{i=1}^q P_i \log_k \left( \frac{1}{Q_i} \right). \quad (22)$$

Substituting (19) and (20) into (22) yields the lower bound to the average number of high bits,  $\bar{n} = \sum_{i=1}^q P_i n_i$ ,

$$\bar{n} \geq H_k - \log_k B_k \quad (23)$$

where  $B_k$  is a characteristic parameter of the codebook, referred to as *codebook capacity*, given by

$$B_k = \sum_{i=1}^q k^{-n_i} \quad (24)$$

Inequality (23) can also be expressed in an exponential form,

$$\frac{k^{(H_k - \bar{n})}}{B_k} \leq 1. \quad (25)$$

Hence, this completes the derivation.

### Proof of Theorem 3

The average number of high bits for the ME Code is given by  $\bar{n}_{ME}^1 = \sum_{i=1}^q P_i n_i$ . Let the  $p$ -th concatenation be performed via direct concatenation, where the number of high bits involved in each new codeword is given by  $n_{i_1} + n_{i_2} + \dots + n_{i_p}$ , and its probability by  $P_{i_1} P_{i_2} \dots P_{i_p}$ . Therefore, the average number of high bits for the  $p$ -th direct concatenation is given by

$$\bar{n}^p = \sum_{i_1=1}^q \dots \sum_{i_p=1}^q P_{i_1} P_{i_2} \dots P_{i_p} (n_{i_1} + n_{i_2} + \dots + n_{i_p}) \quad (26)$$

Separating the terms including  $n_{i_1}$  from others yields

$$\begin{aligned} \bar{n}^p &= \left( \sum_{i_1=1}^q P_{i_1} n_{i_1} \right) \left( \sum_{i_2=1}^q \dots \sum_{i_p=1}^q P_{i_2} \dots P_{i_p} \right) + \sum_{i_1=1}^q P_{i_1} \left( \sum_{i_2=1}^q \dots \sum_{i_p=1}^q P_{i_2} \dots P_{i_p} (n_{i_2} + \dots + n_{i_p}) \right) \\ &= \left( \sum_{i=1}^q P_i n_i \right) + \left( \sum_{i_2=1}^q \dots \sum_{i_p=1}^q P_{i_2} \dots P_{i_p} (n_{i_2} + \dots + n_{i_p}) \right). \end{aligned}$$

Repeating this process for  $i_2$  through  $i_p$  yields

$$\bar{n}^p = p \sum_{i=1}^q P_i n_i = p \bar{n}_{ME}^1 \quad (27)$$

This completes the proof. □

### Proof of Theorem 4

From Theorem 3 it follows that for any source  $S^1$  and any codeword length  $L$ , direct concatenation results in codes having  $\bar{n}^p/p = \bar{n}_{ME}$ . Let  $n_{max}$  be the maximum number of high bits in  $N^1$ ;  $n_{max} \geq n_i, 1 \leq i \leq q$ . Then, among all unused codewords, the unused codeword with the minimum number of high bits must have either  $n_{max}$  or  $(n_{max} + 1)$  high bits (This can be seen in Figure 4-(a)). When the  $p$ -th concatenation is generated according to direct concatenation, the resulting codebook includes a codeword with  $p \times n_{max}$  high bits, that is, the largest number of high bits. Since the minimum number of high bits in unused codewords,  $u_{min}$ , is either  $n_{max}$  or  $(n_{max} + 1)$ , this unused codeword has fewer high bits than that of the used codeword with  $p \times n_{max}$  high bits;  $u_{min} < p \times n_{max}$ . Note that, when  $q = L + 1$ ,

$n_{\max} = 1$  and  $u_{\min} = 2$ , hence this inequality does not hold for  $p = 2$ . Thus, for  $(q, L)$  pairs, where (i)  $q \neq 1$ , (ii)  $q \neq L + 1$ , and (iii)  $q < 2^L$ , the codebook for direct concatenation is not minimum in any concatenation order. Hence, the unused codewords having less high bits ( $n_{\max}$  or  $(n_{\max} + 1)$ ) can be incorporated into the codebook to reduce the total number of high bits

$$n_1 + \dots + n_{q^p-1} + (n_{\max} + 1) < n_1 + \dots + n_{q^p-1} + p x n_{\max} \quad (28)$$

Multiplying this equation through by the source symbol probabilities shows that concatenation always improves the energy efficiency of the original unconcatenated ME Code

$$\begin{aligned} \bar{n} &= P_1 n_1 + \dots + P_{q^p-1} n_{q^p-1} + P_{q^p} (n_{\max} + 1) \\ &< P_1 n_1 + \dots + P_{q^p-1} n_{q^p} + P_{q^p} (p x n_{\max}) = \bar{n}_{\text{direct}}^p = p \bar{n}_{\text{ME}} \end{aligned}$$

This is true for any  $p$ , such that  $p \geq 2$ . Hence, this proves the Theorem 4. □